Lecture Notes in Electrical Engineering 1497

Corrado Di Natale
Leandro Lorenzelli
Viviana Mulloni *Editors*

Sensors and Microsystems

Proceedings of AISEM 2025

Springer

Lecture Notes in Electrical Engineering 1497

Series Editors

The book series *Lecture Notes in Electrical Engineering* (LNEE) publishes the latest developments in Electrical Engineering—quickly, informally and in high quality. While original research reported in proceedings and monographs has traditionally formed the core of LNEE, we also encourage authors to submit books devoted to supporting student education and professional training in the various fields and applications areas of electrical engineering. The series cover classical and emerging topics concerning:

- Communication Engineering, Information Theory and Networks
- Electronics Engineering and Microelectronics
- Signal, Image and Speech Processing
- Wireless and Mobile Communication
- Circuits and Systems
- Energy Systems, Power Electronics and Electrical Machines
- Electro-optical Engineering
- Instrumentation Engineering
- Avionics Engineering
- Control Systems
- Internet-of-Things and Cybersecurity
- Biomedical Devices, MEMS and NEMS

For general information about this book series, comments or suggestions, please contact leontina.dicecco@springer.com.

To submit a proposal or request further information, please contact the Publishing Editor in your country:

China

Jasmine Dou, Editor (jasmine.dou@springer.com)

India, Japan, Rest of Asia

Swati Meherishi, Editorial Director (Swati.Meherishi@springer.com)

Southeast Asia, Australia, New Zealand

Ramesh Nath Premnath, Editor (ramesh.premnath@springernature.com)

USA, Canada

Michael Luby, Senior Editor (michael.luby@springer.com)

All other Countries

Leontina Di Cecco, Senior Editor (leontina.dicecco@springer.com)

**** This series is indexed by EI Compendex and Scopus databases. ****

Corrado Di Natale · Leandro Lorenzelli ·
Viviana Mulloni
Editors

Sensors and Microsystems

Proceedings of AISEM 2025

Springer

Editors
Corrado Di Natale
Department of Electronics Engineering
University of Rome Tor Vergata
Rome, Italy

Viviana Mulloni
Fondazione Bruno Kessler
Povo (TN), Italy

Leandro Lorenzelli
Fondazione Bruno Kessler
Povo (TN), Italy

ISSN 1876-1100 ISSN 1876-1119 (electronic)
Lecture Notes in Electrical Engineering
ISBN 978-3-032-08270-1 ISBN 978-3-032-08271-8 (eBook)
https://doi.org/10.1007/978-3-032-08271-8

This Springer imprint is published by the registered company Springer Nature Switzerland AG
The registered company address is: Gewerbestrasse 11, 6330 Cham, Switzerland

Preface

This book collects papers presented at the XXIII Italian Conference on Sensors and Microsystems (AISEM 2025) held at the Fondazione Bruno Kessler (Trento, February 11–14, 2025).

The conference has been organized by the "Associazione Italiana Sensori e Microsistemi" (AISEM) with the close collaboration and support of the Center for Sensors and Devices of the Fondazione Bruno Kessler (Trento, Italy).

Since 1996, the national conference on Sensors and Microsystems has been a consolidated event in the variegated community of researchers in the broad field of sensors. The main motivation of this conference series is still to promote and build a common ground for researchers of different scientific backgrounds.

The AISEM 2025 Conference is an interdisciplinary forum encompassing a wide range of topics in the research in physics, chemistry, biology, technology, engineering, and materials science with the aim of providing an ideal environment for researchers and innovators to discuss practical and theoretical research aspects.

Miniaturization-led advances in conventional micro/nanoelectronics over the last sixty years have revolutionized digital technologies that have served well the needs of almost every socio-economic sector. Yet, as revolutionary as these advances have been, the miniaturization route alone appears now to be insufficient, as several emerging applications demand new features like embedded intelligence and distributed computing. The concept of "extreme edge" in sensors is a glaring example where computing capabilities are needed, but conventional technology cannot be used alone. Examples of applications of extreme edge include the prediction of food freshness in smart packaging for logistics and monitoring of consumer goods, the evaluation of wound healing status, the classification of human malodour score in wearable and textiles, and prediction of plant growth in agriculture. For this reason, in this edition, we have also explored research sectors complementary to sensor ones, such as IoT, AI, and machine learning, of current interest and capable of unquestionably providing added value to microsystem and sensor technology.

In light of the above considerations, AISEM conferences have always been organized in multidisciplinary common sessions where researchers can listen and be inspired by talks on topics apparently distant from their immediate interests.

This methodological approach has contributed over the years to the education of dozens of researchers who are still active in the field.

Our thanks to the members of the AISEM steering committee for their commitment and to the conference's sponsors for providing excellent support to the event.

Leandro Lorenzelli
Viviana Mulloni
Fondazione Bruno Kessler
Corrado Di Natale
University of Rome Tor Vergata

Organization

Associazione Italiana Sensori e Microsistemi
www.aisem.eu

Steering Committee

Bruno Ando	University of Catania
Dario Compagnone	University of Teramo
Elisabetta Comini	University of Brescia
Sabrina Conoci	University of Messina
Francesco Baldini	CNR–Institute of Applied Physics, Firenze
Giovanni Betta	University of Cassino
Girolamo Di Francia	ENEA-Portici
Corrado Di Natale (chairperson)	University of Rome Tor Vergata
Vittorio Ferrari	University of Brescia
Leandro Lorenzelli	Foundation Bruno Kessler, Trento
Giovanna Marrazza	University of Firenze
Anna Grazia Mignani	CNR–Institute of Applied Physics, Firenze
Giovanni Neri	University of Messina
Pietro Siciliano	CNR–Institute of Microelectronics and Microsystems, Lecce
Sara Tombelli	CNR–Institute of Applied Physics, Firenze

Best Poster Award Winners

A. M. Carluccio, A. Manni, A. Caroppo, P. A. Siciliano, A. Leone.
Performances and Usability of Remote PPG Technology on Consumer Smartphones
A. Scroccarello, F. Della Pelle, P. Di Battista, D. El Fadil, D. Compagnone.
Laser-Induced Metal Nanoparticles Writing on Cellulosic Substrates for Colorimetric Paper based Analytical Kits Development
Licheri, B. Ercolani, C. D'Elia, A. Maffucci, S. Orlanducci, L. Micheli.
Advanced Electrochemical Sensors Integrated in Textiles for Real-Time Emotional State Assessment: Preliminary Results
F. Liu, R. Dahiya, L. Lorenzelli.
Contact Printed Nanowires for Next-Generation Electronic Skin

Conference's Sponsors

STMicroelectronics NV, Italy
Fondazione Bruno Kessler. Italy
FemtoRays Srl, Italy
Seensit Technologies, US
VSParticle B.V., NL
Nextron Corporation, Korea
NanoTech Analysis S.r.l. Italy
Trentingrana Consorzio dei Caseifici Sociali Trentini s.c.a. Italy

Contents

Chemical and Gas Sensors

Wearable and Flexible Sensors

Optical Sensors

Neural Networks and Machine Learning For Sensing

Chemical and Gas Sensors

Characterization of *Pseudomonas aeruginosa* Volatilome Using a QMB-Based Gas Sensor Array for the Diagnosis of Lung Infections in Cystic Fibrosis Patients

R. Capuano[1,2(✉)], S. Ammendola[3], F. Pacello[3], A. Battistoni[3], A. Catini[1,2], M. Stefanelli[2,4], R. Paolesse[2,4], and C. Di Natale[1,2]

[1] Department of Electronic Engineering, University of Rome Tor Vergata, Via del Politecnico 1, Rome, Italy
capuano@ing.uniroma2.it

[2] Interdepartmental Centre for Volatilomics "A. D'Amico", University of Rome Tor Vergata, Via del Politecnico 1, Rome, Italy

[3] Department of Biology, University of Rome Tor Vergata, Via Della Ricerca Scientifica, Rome, Italy

[4] Department of Chemical Science and Technologies, University of Rome Tor Vergata, Via della Ricerca Scientifica, Rome, Italy

Abstract. *Pseudomonas aeruginosa* (Pa) is a significant respiratory pathogen for patients with cystic fibrosis (CF), a leading cause of chronic lung infections, which are correlated with lung function decline. The actual detection methods, based on Pa microbiological identification, are time-consuming and are typically performed on expectorated sputum, that sometimes is challenging to obtain for CF treated and pediatric patients. Volatile organic compounds (VOCs) may be evaluated as indicators of Pa colonization. In this study, the aim was to characterize the VOC profile associated with Pa cultured *in vitro*, using a gas sensor array based on quartz crystal microbalance coated with porphyrinoids, and comparing it to that released by another common airway pathogen, such as *Staphylococcus aureus.* Sensor measurements were complemented by gas chromatography-ion mobility spectrometry evaluations. Results showed that both techniques are able to discriminate *Pseudomonas aeruginosa.*

Keywords: QMB-based gas sensor array · *Pseudomonas aeruginosa* · volatile organic compounds · GC-IMS

1 Introduction

1.1 A Subsection Sample

Airway inflammation represents a central feature in the pathogenesis of chronic pulmonary diseases, particularly in cystic fibrosis (CF), a genetic disorder characterized by impaired mucociliary clearance and recurrent respiratory infections. Among the

C. Di Natale et al. (Eds.): AISEM 2025, LNEE 1497, pp. 3–9, 2025.
https://doi.org/10.1007/978-3-032-08271-8_1

pathogens associated with CF lung disease, *Pseudomonas aeruginosa* (Pa) plays a predominant role. Once established in the lower airways, *P. aeruginosa* is remarkably difficult to eradicate and frequently transitions to a chronic infection state that can persist for years or even decades [1]. Chronic *P. aeruginosa* infections are strongly associated with accelerated pulmonary function decline, increased frequency of hospitalizations, and elevated mortality rates in CF patients [2].

Given the clinical impact of *P. aeruginosa*, timely and accurate diagnosis of initial infections is a key therapeutic goal, aimed at preventing chronic colonization and its associated complications [3]. Currently, standard diagnostic approaches rely primarily on culture-based identification from respiratory specimens, such as expectorated sputum. However, sputum collection is often unfeasible in certain patient populations, including pediatric patients and individuals undergoing highly effective CFTR modulator therapies, which tend to reduce sputum production. These limitations highlight a critical need for non-invasive, rapid diagnostic tools capable of detecting respiratory infections at the point of care.

In recent years, increasing attention has been directed toward the use of volatile organic compounds (VOCs) as potential biomarkers of microbial presence and activity. Gas sensor arrays have emerged as promising tools for detecting and discriminating VOC profiles associated with different pathogens [4]. The volatilome—the complex mixture of VOCs emitted by microorganisms—offers a potential avenue for real-time, non-invasive diagnosis, especially when integrated with advanced sensor technologies.

In this study, we investigate the *in vitro* VOC signature of *P. aeruginosa* using a gas sensor array composed of QMB sensors functionalized with porphyrinoid coatings. VOC patterns released by *P. aeruginosa* were compared to those of another common CF-associated pathogen, *Staphylococcus aureus*. Sensor measurements were further complemented with gas chromatography-ion mobility spectrometry (GC-IMS) analysis to enhance compound resolution and provide additional validation. The primary objective is to assess the potential of this combined approach in distinguishing *P. aeruginosa* from other respiratory pathogens, laying the groundwork for the development of a volatilome-based diagnostic tool for use in CF clinical practice.

2 Materials and Methods

2.1 Sample Preparation

P. aeruginosa PAO1 and *Staphylococcus aureus* (SH1000) were cultured in Artificial Sputum Medium (ASM) [5] at 37 °C for 18 h in 25 cm^2 vented flasks. A total of three independent samples were prepared for each bacterial species, and experiments were performed twice to test the reproducibility. Following incubation time, 3 ml of culture were transferred to 20 ml headspace glass vials for analysis. The headspace of bacteria samples was analyzed by a porphyrinoid QMB-based gas sensor array and gas chromatography coupled with an ion mobility spectrometer (GC-IMS). Not-inoculated ASM was analyzed as a reference sample.

2.2 GC-IMS Analysis

Bacteria samples were analysed by GC coupled to an ion mobility spectrometer (GC-IMS; FlavourSpec, GAS Dortmund, Germany), equipped with an automatic sampler (HT2000H, HTA, Italy). Samples were agitated and heated to 40 °C for fifteen minutes. 700 µl of bacteria headspace were automatically sampled by a 2.5 ml gas syringe and injected into the GC-IMS. Volatile organic compounds composing the bacteria headspace were first separated by GC, equipped with a MXT-5 column (Restek Corporation, Bellefonte, Pennsylvania) 30 m 0.53 mm I.D. 1 µm, having a phase equivalent to 5% methylolysiloxane. Carrier gas flow was initially constant at 5 ml/min for 5 min, then increased to 50 ml/min in 5 min and held for 5 min, resulting in a total analysis time of 15 min per sample. Once eluted from chromatographic column, compounds were ionized and separated into a 5.3 cm drift tube using a constant carrier gas flow rate of 150 ml/min at a stable voltage of 2.7 kV in positive ion mode. Analysis was performed keeping the GC and IMS temperature at 45 °C and inlet injector at 80 °C [6]. Nitrogen used as carrier and drift gas, was obtained by means of a nitrogen generator that guarantees a gas purity higher than 99.9995%. GC-IMS data were extracted using the VOCal software (GAS Dortmund, Germany), provided with the instrument.

2.3 Electronic Nose Measurements

The used electronic nose consists of an array of 12 quartz crystal microbalances (QMBs), functionalized by different metalloporphines or corrol metals and it is developed at University of Rome Tor Vergata [7].

The tool management software was developed in Matlab (Mathworks, USA). The device is also equipped with a microfluidic system that allows you to manage the flows inside the instrument. A calcium chloride trap has the function of filtering moisture from the ambient air, in order to obtain the reference gas for measurements. During measurements, sensors were exposed 40 s to sample headspace and 240 s to filtered air. The airflow is maintained at 100 SCCM during the measurements.

Samples were thermalized at 37 °C ± 2 °C in a water bath for 5 min before measurement and during analysis.

3 Results and Discussion

The data of GC-IMS and gas sensor array were analysed using Principal component Analysis (PCA) [8] in Matlab R2022b.

3.1 GC-IMS

GC-IMS measurements produced a two-dimensional spectrum with drift time on the x-axis and retention time on the y-axis. Figure 1 shows the comparison between spectra obtained by headspace analysis of ASM, *P. aeruginosa* and *S. aureus* culture samples. A total of 98 regions of interest (ROI) have been detected considering all measurements, using the VOCal Software platform (G.A.S. Dortmund, Germany). Each ROI corresponds to a compound.

For each selected region, the volume was extracted considering the signal intensity in the plane of drift time vs retention time, obtaining a vector with 98 volume values for each measure. A preliminary feature selection was carried out using the Kruskal-Wallis rank test, considering the binary comparison between *P. aeruginosa* samples and the others, where only features with a p-value < 0.05 were retained for further analysis (Fig. 2). This process reduced the dataset to 15 variables. Data were previously normalized at null media and unitary variance and analyzed with Principal Component Analysis. The obtained score plot is reported in Fig. 3. The obtained result demonstrated that this proposed approach allowed for full discrimination of *P. aeruginosa* samples with respect to those of *S. aureus* and ASM.

3.2 Gas Sensor Array

The analysis of sensor array data was performed using a similar method. The frequency shift registered between the baseline and the minimum value recorded during sample measurement was considered as feature for each sensor. Three consecutive measurements were taken for each sample, and the average value was considered for the analysis. Prior to Principal Component Analysis, the data were normalized to have a mean of zero and unit variance. The resulting score plot, related to 1st and 3rd principal components, is presented in Fig. 4. The obtained results showed the capability of the gas sensor array to discriminate the volatilome of *P. aeruginosa* samples with respect to *S. Aureus* and ASM.

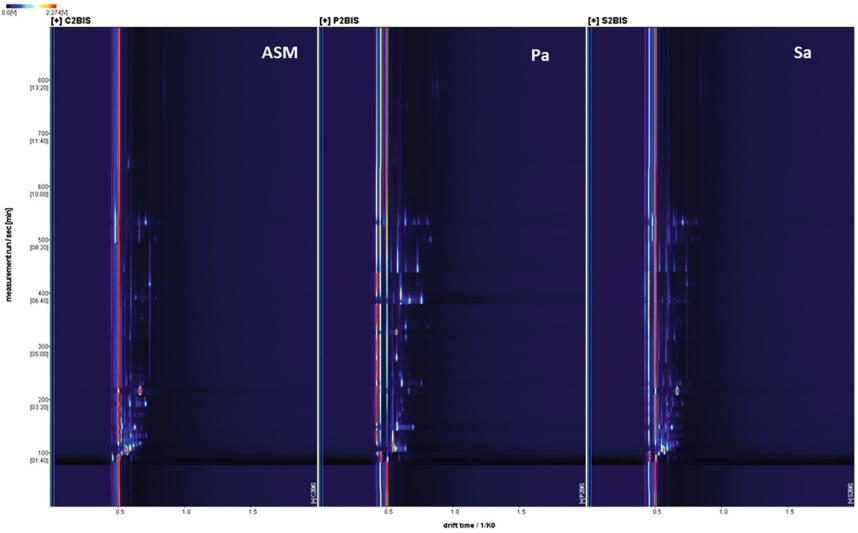

Fig. 1. Comparison between 2-D representation of a GC-IMS spectra obtained by headspace analysis of artificial sputum medium (ASM), *Pseudomonas aeruginosa* (Pa) and *Staphylococcus aureus* (Sa) cultures. X-axis reports the drift time, normalized respect that of the reactant ion peak (RIP); y-axis reports the retention time.

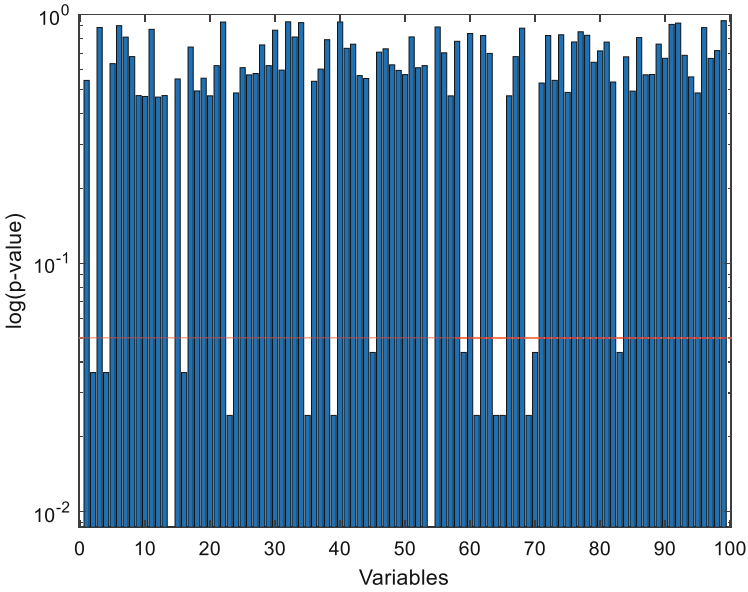

Fig. 2. Trend of p-values associated with 98 compounds present in the volatilome of artificial sputum medium (ASM), *Pseudomonas aeruginosa* (Pa) and *Staphylococcus aureus* (Sa) cultures

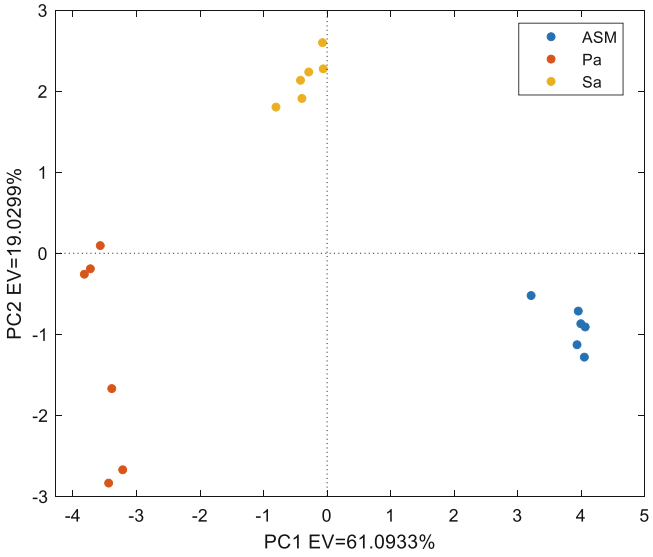

Fig. 3. Score plot obtained by Principal Component Analysis (PCA) of data obtained by GC-IMS measurement of artificial sputum medium (ASM), *Pseudomonas aeruginosa* (Pa) and *Staphylococcus aureus* (Sa) cultures headspace, performed considering the 15 selected variables.

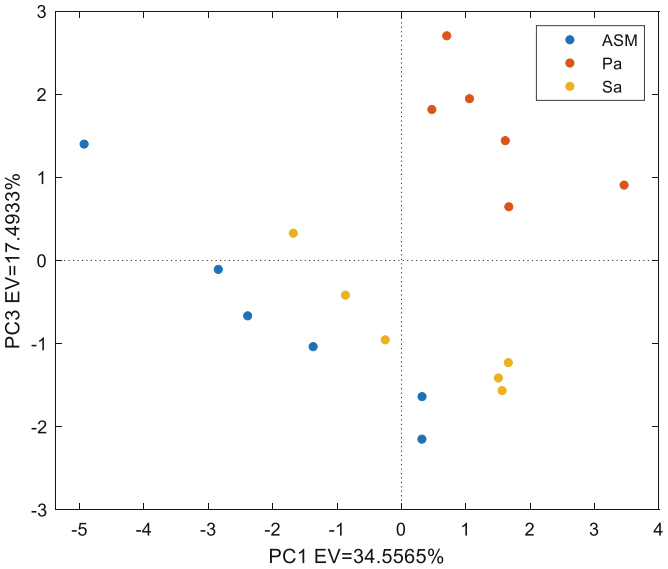

Fig. 4. Score plot obtained by Principal Component Analysis (PCA) performed considering the 12 sensor responses of electronic nose to volatilome analysis of artificial sputum medium (ASM), *Pseudomonas aeruginosa* (Pa) and *Staphylococcus aureus* (Sa) cultures

4 Conclusions

The aim of this study was the characterization of the *in vitro* volatilome of *P. aeruginosa* with respect to *S. aureus,* another common CF-associated pathogen, using a gas sensor array and GC-IMS. PCA performed on GC-IMS data revealed the capability of this technique to discriminate Pa with respect to other considered samples, considering a pattern of 15 VOCs.

Also, the gas sensor array has proven to be able to detect the volatilome differences of *P. aeruginosa* with respect to *Staphylococcus aureus* and the ASM.

The results obtained enabled the distinct characterization of the *P. aeruginosa* volatilome compared to other respiratory pathogens, providing a foundation for the development of a volatilome-based diagnostic tool applicable in CF clinical practice.

References

1. Gellatly SL, Hancock REW (2013). Pseudomonas Aeruginosa: New Insights Into Pathogenesis and Host Defenses. https://doi.org/10.1111/2049-632X.12033
2. Garcia-Clemente M et al (2020) Impact of pseudomonas aeruginosa infection on patients with chronic inflammatory airway diseases. J Clin Med 9:1–32. https://doi.org/10.3390/jcm9123800
3. Davidson AGF, Chilvers MA, Lillquist YP (2012) Effects of a Pseudomonas aeruginosa eradication policy in a cystic fibrosis clinic. Curr Opin Pulm Med 18:615–621. https://doi.org/10.1097/MCP.0b013e328358f5a2
4. Capuano R et al (2023) A pilot study for legionella pneumophila volatilome characterization using a gas sensor array and GC/MS techniques. Sensors 23:1–14. https://doi.org/10.3390/s23031401

5. Kirchner S et al (2012) Use of artificial sputum medium to test antibiotic efficacy against Pseudomonas aeruginosa in conditions more relevant to the cystic fibrosis lung. J Vis Exp 1–8. https://doi.org/10.3791/3857
6. Gasparri R et al (2022) Volatolomic urinary profile analysis for diagnosis of the early stage of lung cancer. J Breath Res 16. https://doi.org/10.1088/1752-7163/ac88ec
7. Paolesse R, Nardis S, Monti D, Stefanelli M, Di Natale C (2017) Porphyrinoids for chemical sensor applications. Chem Rev 117:2517–2583. https://doi.org/10.1021/acs.chemrev.6b00361
8. Jolliffe IT, Cadima J: Principal component analysis: a review and recent developments. https://doi.org/10.1098/rsta.2015.0202

Hydrogen Sensing with Graphene-Wo3Pt: AC/DC Measurements and Admittance Spectroscopy

T. Polichetti[1(✉)], B. Alfano[1], E. Massera[1], M. L. Miglietta[1], L. Di Benedetto[2], R. Liguori[2], N. Rinaldi[2], and A. Rubino[2]

[1] ENEA Research Center, Piazzale E. Fermi, 1, 80055 Portici (Naples), Italy
tiziana.polichetti@enea.it
[2] University of Salerno, Via Giovanni Paolo II, 132, 84084 Fisciano, SA, Italy

Abstract. This study investigates a hydrogen sensor based on platinum and graphene-enriched tungsten oxide, synthesized via impregnation and deposited as a chemoresistor. The sensor was evaluated using both DC and AC impedance spectroscopy at 200 °C.

DC measurements showed a linear, reversible response to hydrogen (2500–25000 ppm), demonstrating sensitivity. The combined DC and AC approach yields multiple parameters correlated with a specific analyte, suggesting a pathway for improved discrimination between different target gases.

Keywords: hydrogen sensor · chemoresistive sensor · Metal Oxide Semiconductor (MOX) · impedance spectroscopy · graphene-tungsten oxide composite · selectivity enhancement

1 Introduction

Chemoresistive gas sensors, particularly those employing noble metal-functionalized metal oxide semiconductors (MOXs) [1], exhibit high sensitivity. This sensitivity arises from conductivity changes upon gas exposure. However, the conventional direct current (DC) resistive transduction [2] presents selectivity challenges. To address these limitations, alternating current (AC) impedance spectroscopy has become a significant technique [3, 4]. In this study, a platinum and graphene-enriched tungsten oxide (G-WO_3-Pt) material was synthesized via impregnation and subsequently deposited as a chemoresistor on gold interdigitated electrodes supported by an alumina substrate. The G-WO_3-Pt chemoresistor was characterized using both DC and AC impedance spectroscopy. DC measurements at 200 °C demonstrated a proportional and reversible response to 2500–25000 ppm hydrogen concentrations, confirming sensitivity.

C. Di Natale et al. (Eds.): AISEM 2025, LNEE 1497, pp. 10–14, 2025.
https://doi.org/10.1007/978-3-032-08271-8_2

2 Experimental

The sensitive layer of tungsten trioxide (WO_3) nanopowder (Sigma Aldrich, Ø < 100nm) was functionalized via impregnation. WO_3 was dispersed in deionized water using sonication, followed by the addition of a colloidal platinum (Pt) solution (0.2 wt% relative to WO3, Metrohm DropSense). This mixture was stirred, resulting in Pt nanoparticle impregnation into the WO_3, forming WO_3-Pt. Liquid Phase Exfoliation (LPE) graphene was then mixed with WO_3-Pt to reduce resistance and improve electrical compatibility. The resulting dispersion was drop-cast onto an alumina substrate with gold interdigitated electrodes and subsequently dried and annealed to stabilize the G-WO_3-Pt composite and its adhesion.

Morphological and structural characterization was performed using FE-SEM/EDS (LEO 1530–2 microscope, acceleration voltage: 5 kV), AFM (Dimension 3100, Nanoscope IV in non-contact mode), and Raman spectroscopy (Renishaw InVia Reflex, excitation wavelength 514.5 nm in reflection mode). The hydrogen sensing properties were evaluated in a controlled atmosphere chamber using pre-mixed gases, with precise flow control and environmental monitoring. DC and AC impedance data were acquired using specialized instruments at a working temperature of 200 °C and 50% relative humidity.

3 Results and Discussion

The morphological characterization of the G-WO_3-Pt film, conducted via scanning electron microscopy (SEM), revealed a microstructure composed of 80–100 nm WO_3 microcrystal grains, with discernible graphene flakes dispersed throughout. However, platinum nanoparticles, due to their sub-5 nm size, remained undetectable through SEM. Energy-dispersive X-ray spectroscopy (EDX) confirmed the elemental composition, identifying tungsten, oxygen, carbon and platinum, along with silicon originating from the substrate (Fig. 1).

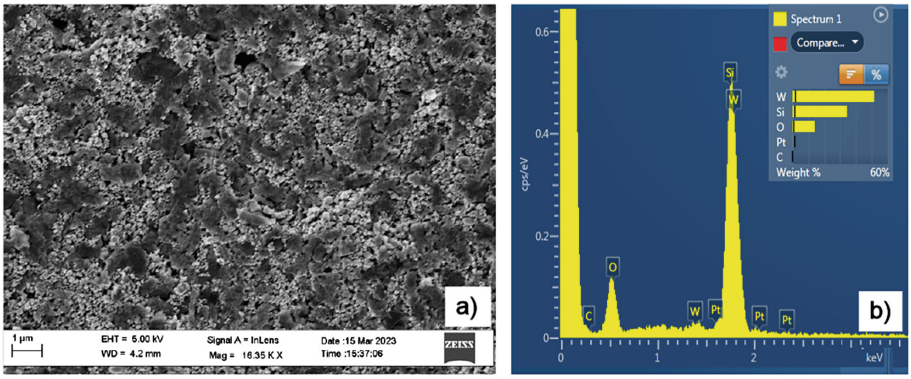

Fig. 1. A) SEM image and b) EDX spectrum of G-WO_3-Pt sample.

Raman spectroscopy identified the crystalline structure of the composite material as monoclinic WO_3, a phase known for its enhanced reactivity towards hydrogen (Fig. 2).

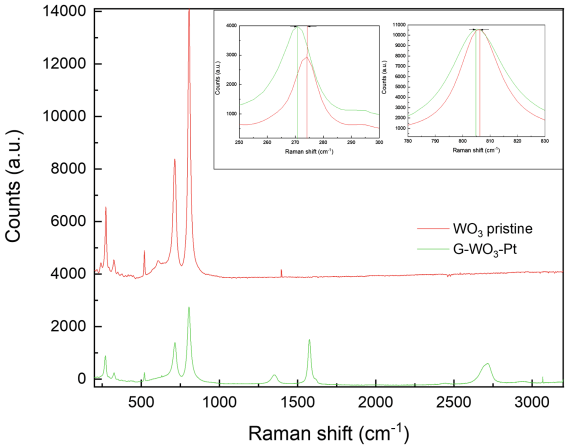

Fig. 2. Raman spectrum of monoclinic G-WO_3-Pt on a Si/SiO_2 substrate

Characteristic peaks at 270, 325, 710, and 805 cm⁻1 confirmed WO_3 presence. A slight redshift observed in the 270 and 805 cm⁻1 peaks indicated structural deformation, likely resulting from Pt functionalization. Peaks in the 1300–2700 cm⁻1 range confirmed graphene incorporation.

The WO_3-H_2 interaction is well-established [5], and the sensing mechanism is governed by surface oxygen species. Upon air exposure, oxygen anions form on the material's surface, creating a depletion layer by extracting electrons from the conduction band [6]. When exposed to a reducing gas like hydrogen (H_2), these anions react, releasing electrons back to the conduction band and shrinking the depletion layer, increasing conductivity for n-type semiconductors like WO_3. An optimal operating temperature maximizes surface oxygen species, thereby enhancing gas interaction. Typically, WO_3-based hydrogen sensors operate at high temperatures. The addition of Pt nanoparticles is expected to reduce the working temperature. Indeed, Pt nanoparticles dissociates H_2 into H^+ ions and electrons, H^+ ions spillover onto WO_3, reducing the potential barrier while electrons traverse the Pt-WO_3 junction, increasing conductivity [7].

Within the WO_3 bulk, H_2 forms WO_3-x•xH_2O, creating oxygen vacancies (1). This adsorption process is reversed during desorption (2), where oxygen spillover reduces electron density (Fig. 3).

$$WO_3 + xH_2 \rightarrow WO_3 - x \cdot xH_2O \tag{1}$$

$$WO_3 - x \cdot xH_2O + (x/2)O_2 \rightarrow WO_3 + xH_2O \tag{2}$$

The hydrogen sensing properties of the G-WO_3-Pt film were analyzed using both DC and AC measurements, over a concentration range of 2500 to 25000 ppm at 35% relative humidity. The DC characterization employed a three-phase gas exposure protocol,

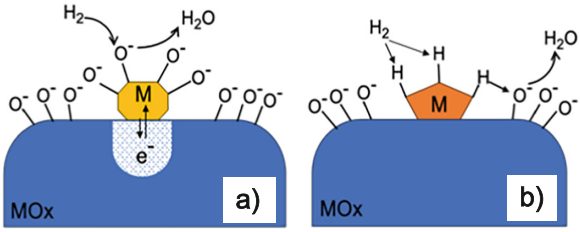

Fig. 3. Graphical representation of electrical and chemical sensitization followed by the spillover mechanism during a) adsorption and b) desorption phases.

encompassing stabilization, exposure to varying H_2 concentrations, and recovery, all performed under a constant 1V bias. Preliminary tests determined 200 °C as the optimal operating temperature for maximum sensitivity, testifying the beneficial effect of the Pt functionalization on the reduction of the working temperature. In AC measurements, under the same exposure protocol, the complex impedance $Z(f,t) = R(f,t) + jX(f,t)$ was recorded, using an LCR meter at fixed frequencies (245 Hz, 4175 Hz, and 71 kHz).

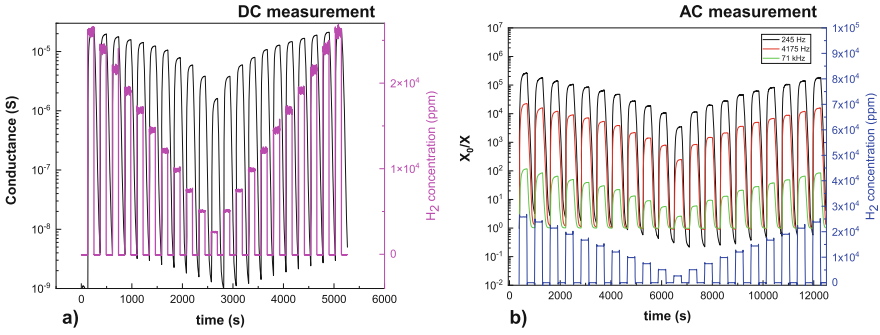

Fig. 4. a) DC dynamic response under multi-step H_2 concentration exposure cycle (2500–25000 ppm) at 35% RH. b) AC normalized response transients at a frequency of 245Hz, 4175Hz and 71kHz under different H_2 concentrations.

In DC regime (Fig. 4 a)), the sensor exhibited an increase in conductance proportional to the increasing H_2 concentration; however, this was accompanied by a pronounced baseline drift. Consistently with established literature, this baseline drift is attributed to the reduction of metal oxide materials under humid conditions, wherein water vapor inhibits reoxidation and decreases surface charge while operating in AC regime may mitigate this effect [4, 8]. Figure 4 b) illustrates the normalized time response of the imaginary component, $X(f *,t)/X_0$, where X_0 is the baseline value. Across all tested frequencies, the electrical signal showed a clear correlation with H_2 injection and concentration, demonstrating good repeatability. The effect of baseline drift reduction is clearly visible and becomes progressively more pronounced with increasing frequency.

Conversely, a gradual decrease in the response intensity is observed; therefore, it is necessary to adopt an appropriate trade-off in the selection of the operating frequency to optimize device performance.

4 Conclusions

The integration of platinum nanoparticles and graphene within the WO_3 matrix enabled the fabrication of a G-WO_3-Pt chemoresistive sensor exhibiting noticeable hydrogen detection capabilities. DC characterization confirmed a reversible and quasi-linear conductometric response in the 2500–25000 ppm range at 200 °C, validating the material's sensitivity and the effectiveness of Pt-induced catalytic activation. AC impedance spectroscopy, performed at multiple frequencies, provided complementary information, mitigating baseline drift. The observed trade-off between signal intensity and drift reduction highlights the relevance of frequency tuning in optimizing sensor performance. The combined DC/AC approach establishes a multidimensional sensing paradigm that enhances the robustness of MOX-based sensors, paving the way for advanced detection strategies in complex gaseous environments.

Acknowledgement. This work was supported by the European Union – NextGenerationEU – M2C2 Investment 3.5 through the "Hydrogen Research and Development" Operational Plan (POR H2).

References

1. Tereshkov M, Dontsova T, Saruhan B, Krüger S (2024) Metal oxide-based sensors for ecological monitoring: progress and perspectives. Chemosensors 12(3):42
2. Malik R, Tomer VK, Mishra YK, Lin L (2020) Functional gas sensing nanomaterials: a panoramic view. Appl Phys Rev 7(2):021301
3. Dutta K (2021) Potential of impedance spectroscopy towards quantified analysis of gas sensors: a tutorial. IEEE Sens J 21(20):22220–22231
4. Barsan N, Weimar U (2003) Understanding the fundamental principles of metal oxide based gas sensors; the example of CO sensing with SnO_2 sensors in the presence of humidity. J Phys: Condens Matter 15(20):R813
5. Mirzaei A, Kim J-H, Kim HW, Kim SS (2019) Gasochromic WO_3 nanostructures for the detection of hydrogen gas: an overview. Appl Sci 9(9):1775
6. Yamazoe N, Miura N (1992) Some basic aspects of semiconductor gas sensors. Chem. Sen. Technol. 4:19–42
7. Chang C-H, et al (2020) Study of a WO_3 thin film based hydrogen gas sensor decorated with platinum nanoparticles. Sensors and Actuators B: Chemical 317: 128145
8. Potyrailo RA et al (2020) Extraordinary performance of semiconducting metal oxide gas sensors using dielectric excitation. Nature Electronics 3(5):280–289

A Low-Cost Hydrogel-Based Pressure Sensor for the Glucose Monitoring System

Mohammedhusen Manekiya(✉), Irene Dal Chiele, and Massimo Donelli

Department of Civil, Environmental and Mechanical Engineering (DICAM), University of Trento, 38123 Trento, Italy
{m.manekiya,irene.dalchiele,massimo.donelli}@unitn.it

Abstract. The increasing prevalence of diabetes worldwide necessitates the advancement of blood glucose monitoring technologies. Traditional methods, which require frequent blood sampling, can be inconvenient and painful for patients. Consequently, there has been a significant shift towards continuous monitoring solutions. Recent advancements in glucose sensors, particularly non-invasive methods that assess blood glucose levels through tears, saliva, and sweat, show considerable promise in enhancing patient comfort and accuracy. Although implantable sensors may reduce the frequency of blood samples, their invasive nature and need for regular replacements pose challenges. This research focuses on hydrogel-based pressure sensors that effectively convert physical changes into electrical signals, thereby providing a wireless and efficient approach to glucose monitoring. These innovations enhance sensitivity and stability and facilitate real-time monitoring, paving the way for more sophisticated health systems integrated with the Internet of Things (IoT). Ultimately, this study aims to improve diabetes management and patient care through non-invasive solutions.

Keywords: Glucose monitoring · Non-invasive methods · Hydrogel sensors · Diabetes management

1 Introduction

The rise of diabetes worldwide demands improved blood glucose monitoring technologies, as traditional methods involving frequent blood samples can be inconvenient and painful. Recent advancements in glucose sensors enable continuous monitoring for diabetes patients. Blood glucose readings are vital health indicators, especially for diabetes mellitus. With many individuals affected by diabetes, various measurement methods have been tested for ongoing and accurate monitoring. An implantable glucose sensor could minimize blood sample needs; however, its invasiveness and the necessity for frequent replacements due to biofouling and limited lifespan present challenges. Researchers are thus pursuing non-invasive methods to measure blood glucose levels via tears, saliva, interstitial fluid, and sweat. The development of glucose sensors, including materials, device designs, manufacturing processes, and system engineering, has been discussed in [2]. This study examines both invasive and non-invasive techniques for blood glucose monitoring. Glucose sensors are classified into two types: in vitro devices that

C. Di Natale et al. (Eds.): AISEM 2025, LNEE 1497, pp. 15–20, 2025.
https://doi.org/10.1007/978-3-032-08271-8_3

measure glucose in blood samples and in vivo devices that continuously monitor glucose levels in the body. In vivo technologies include needle-type amperometric enzyme electrodes and microdialysis probes, typically implanted in subcutaneous tissue [3]. Smartwatch devices employing reverse iontophoresis are widely available for personal glucose level measurement; however, these methods are not as clinically accepted as invasive blood sampling techniques due to a prevalence of false positives. Hydrogels, which are materials capable of undergoing reversible volume changes in response to physical and chemical stimuli, are suitable for sensor applications. Hydrogel-based sensors offer distinct advantages over traditional electrochemical sensors by eliminating the need for counter and reference electrodes. Research has demonstrated that a hydrogel pressure sensor with a gradient hierarchical structure exhibits enhanced sensitivity, and a broader sensing range compared to conventional planar sensors [4–8]. This research proposes a wireless glucose sensor, focusing on hydrogel-based pressure sensors that efficiently convert physical changes into electrical signals, enabling remote detection of patients' vital signs and allowing for comparisons with therapeutic parameters to measure adherence levels [5–8]. This research introduces a wireless glucose sensor centred on hydrogel-based pressure sensors that effectively convert physical changes into electrical signals, offering substantial advantages over conventional electrochemical sensors. The proposed sensors demonstrate enhanced sensitivity, an expanded sensing range, and stability under high-pressure conditions, allowing for effectively monitoring various human movements. These innovations represent a significant advancement in diabetes management and patient care by providing non-invasive monitoring solutions, paving the way for smarter health monitoring systems integrated with the Internet of Things (IoT) [9, 10]. Ultimately, this research aims to improve measurement and facilitate remote detection of vital signs.

2 Sensor Measurements and Description

Galvanic skin resistance (GSR) can be measured using two electrodes on the hand with a weak electric current (a few microamperes) passing between them. GSR measurement can be performed with either direct (DC) or alternating (AC) current through a circuit that consists of a voltmeter, a battery, and a subject to detect variations in electrodermal activity (EDA). However, DC currents are more frequently used than AC currents for assessing blood glucose levels [6]. The configuration of the measurement system and the circuit model of the two electrodes are depicted in Fig. 1. The following equation represents the voltages recorded by the voltmeter, which allows for the estimation of the GSR and, consequently, the blood glucose level:

$$VGSR() = V_s \frac{R_M}{\frac{1}{R_{P1}+\frac{1}{j\omega C_{P1}}} + Rs(\alpha) + \frac{1}{R_{P2}+\frac{1}{j\omega C_{P2}}} + R_M} \tag{1}$$

where Vs denotes the voltage generator (3.3 V), α represents the glucose blood level, RP1, CP1, and RP2, CP2 are the resistance and capacitance at the electrode contact points, respectively. Rs signifies the measured skin resistance, and Rm = 470 KΩ. An analog-to-digital converter (ADC) is employed to measure the voltage amplitude across the resistance Rm.

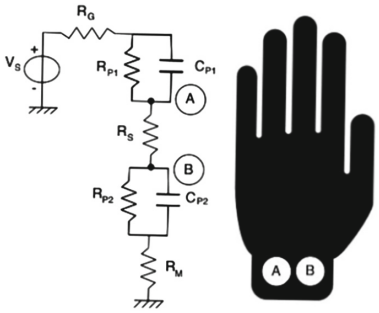

Fig. 1. Schema of the glucose sensor with Hydrogel and galvanic skin resistance measurement

Given that the measurement is conducted with DC current and the electrodes exhibit very low resistance, RP1, RP2, CP1, and CP2 can be approximated as zero, allowing for the easy estimation of the GSR using the following relation:

$$R_s(\alpha) = \frac{R_M\,(V_S - VGSR(\alpha))}{VGSR(\alpha)} \tag{2}$$

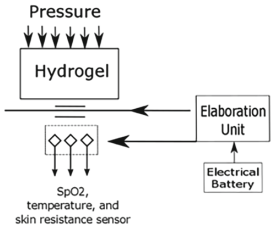

Fig. 2. Schematic general illustration of Hydrogel Pressure sensor attached with other sensors.

Stimuli-responsive volume changes are key to hydrogel sensors. Hydrogel pressure sensors mainly use capacitive or piezoresistive mechanisms. In capacitive sensing, the hydrogel serves as a dielectric between two electrodes, where pressure changes capacitance, as shown in Fig. 2. A notable example is a sensitive, transparent hydrogel pressure sensor created through soft lithography, featuring a pyramid structure that enhances sensitivity while balancing high sensitivity (48.7 kPa^{-1}) and durability through optimal cross-linker ratios [9]. The conductivity of the hydrogel, crucial for glucose sensor performance, is calculated using the following formula:

$$\sigma = \frac{L}{(R * S)} \tag{3}$$

In this equation, σ represents the conductivity, L is the length of the Hydrogel, R denotes its resistance, and S is the cross-sectional area. This calculation is pivotal as it reflects the Hydrogel's ability to conduct electric currents, which is critical for accurate

sensor readings. Furthermore, the total capacitance (C) of the Hydrogel is determined by the expression:

$$C = \frac{\varepsilon_0 \varepsilon_m \left(S_{A_{max}} + S_{B_{max}} + S_c\right)}{d} \tag{4}$$

where ε_m is material's dielectric constant, while $S_{A_{max}}$, $S_{B_{max}}$ and C represents the contact areas of the electrode pairs, and d indicates the thickness of the dielectric layer. Together, these calculations underscore the Hydrogel's role in enhancing the efficacy of the glucose sensor. The system uses an ESP32-beetle microcontroller ideal for wearables. It features WiFi, Bluetooth, and several ADC channels. A 3.3 V button battery powers it. The system is housed in 3D-printed plastic with antibacterial filament for safety, and its dimensions are similar to a wristwatch.

3 Experimental Assessment

This section presents an experimental evaluation of the proposed technique by analyzing the glycemic curve across various individuals. The glycemic response of 20 participants who volunteered was measured using a standard glucose meter (model INR Coaguchek InRange, Roche) from their blood samples. These measurements were compared to the readings obtained from the proposed GSR sensor. In healthy individuals, the body releases a specific quantity of insulin when glucose enters the bloodstream. Insulin is crucial in keeping blood glucose levels below the maximum tolerable limit, storing any surplus in the liver. Surpassing this limit indicates impaired glucose tolerance (IGT), suggesting a relative insulin deficiency that may lead to diabetes. The glycemic curve is a clinical assessment tool for examining carbohydrate metabolism and identifying abnormalities. Commonly known as the Oral Glucose Tolerance Test (OGTT), this curve evaluates blood sugar levels before and after consuming a glucose solution. This test is vital for determining normal blood glucose levels, thus acting as both a screening and diagnostic tool for diabetes and pre-diabetes, and monitoring individuals with hyperglycemia or hypoglycemia. Suppose the glucose curve reports values between 140 and 200 mg/dL after ingestion, alongside fasting levels between 110 and 126 mg/dL. In that case, the condition is classified as impaired glucose tolerance, which is significant due to its association with future diabetes mellitus. The oral glucose load test, whereby a predetermined amount of glucose is administered in a water solution followed by blood samples at defined intervals, is crucial for diagnosing diabetes when initial findings are ambiguous.

This test consists of administering 75 g of glucose dissolved in 250–300 mL of water within 30 s to 5 min. Blood samples are collected at hourly intervals, and if glycemia surpasses 200 mg/dL after 2 h, it confirms the existence of diabetes mellitus, even if fasting glycemia remains under 126 mg/dL. Figure 3 illustrates the glycemic curve measurements following glucose solution administration. The sampling frequency was set to assess GSR hourly for 8 h. After the measurement period, the data was transmitted via Bluetooth to a personal computer for further analysis or storage. Figure 3 shows glucose levels normalizing about one hour after ingestion, with the GSR curve mirroring this trend. Data from participants (one shown for brevity) indicate a correlation between

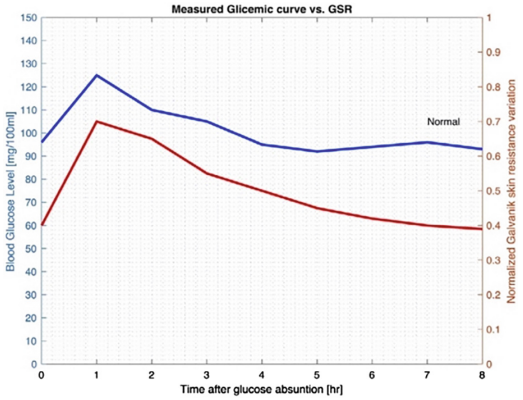

Fig. 3. Behaviour of blood glucose level and galvanic skin resistance versus time

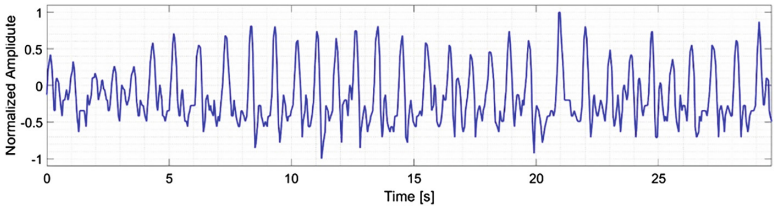

Fig. 4. Different pressure steps due to hand/wrist movement of the patient wearing the prototype, recoded with the Hydrogel.

GSR and glucose levels. Figure 4 depicts pressure variations from hand movements detected by the Hydrogel sensor, with the x-axis showing time in seconds and the y-axis displaying voltage. Sensor output reveals peaks correlating with increased hand pressure, returning to baseline when the hand is stable. This sensitivity is crucial for tracking real-time glucose changes. When analyzed with glycemic data from Fig. 3, these findings suggest potential for non-invasive monitoring. The relationship between GSR and blood glucose, along with the sensor's pressure detection capacity, emphasizes the system's promise for continuous physiological monitoring. Remote detection capabilities also offer reassurance to patients and healthcare providers.

4 Conclusion

This work proposed a non-invasive low-cost hydrogel-based Glucose measurement system for the measurement of galvanic skin resistance, and the system was experimentally assessed to measure glucose blood levels. The sensor has been integrated into a wearable bracelet equipped with a microcontroller to measure, store, and transmit real-time data through a wireless channel. Additionally, incorporating a hydrogel-based pressure sensor enhances the device's functionality, allowing for monitoring physiological changes related to pressure around the glucose sensor due to hand movement. The obtained results

are quite promising and demonstrate the potential of Hydrogel based pressure system as a device as an efficient tool for smart wearable system for the early diagnosis of level two diabetes and for monitoring glucose blood levels in patients with diabetes.

References

1. Pickup JC (2004) Glucose sensors: present and future. In: DeFronzo, Ferraninni, Keen, Zimmet (eds.) International Textbook of Diabetes Mellitus, 1st ed. Wiley
2. Lee H, Hong YJ, Baik S, Hyeon T, Kim D (2018) Enzyme-based glucose sensor: from invasive to wearable device. Adv Healthc Mat 7(8):1701150
3. McNichols RJ, Coté GL (2000) Optical glucose sensing in biological fluids: an overview. J Biomed Opt 5(1):5–16
4. Guo Z, Zhang H, Xie W, Liu W (2024) Structurally designed hydrogel-based pressure sensors for wearable sensing. IEEE Sensors J 24(13):20394–20401
5. Athauda T, Banerjee PC, Karmakar NC (2020) Microwave characterization of chitosan hydrogel and its use as a wireless pH sensor in smart packaging applications. IEEE Sensors J 20(16):8990–8996
6. Schulz V, Ebert H, Gerlach G (2013) A closed-loop hydrogel-based chemical sensor. IEEE Sensors J 13(3):994–1002
7. Bian C, Cheng Y, Zhu W, Tong R, Hu M, Gang T (2020) A novel optical fiber mach-zehnder interferometer based on the calcium alginate hydrogel film for humidity sensing. IEEE Sensors J 20(11):5759–5765
8. Herzog J, Sobczyk M, Schuster C, Härtling T, Wallmersperger T, Gerlach G (2024) Determination of specific volume fractions in multicomponent liquids using hydrogel-functionalized plasmonic sensors. IEEE Sensors J 24(9):13720–13729
9. Franke D, Binder S, Gerlach G (2017) Performance of fast-responsive, porous crosslinked poly(N-Isopropylacrylamide) in a piezoresistive microsensor. IEEE Sens Lett 1(6):1–4
10. Zikulnig J, Lengger S, Rauter L, Neumaier L, Carrara S, Kosel J (2022) Sustainable printed chitosan-based humidity sensor on flexible biocompatible polymer substrate. IEEE Sens. Lett. 6(12):1–4

Multiparametric Microwave Sensor for Environmental Measurements

V. Mulloni[1(✉)], G. Marchi[1], L. Lorenzelli[1], A. Gaiardo[1], M. Valt[1], M. Donelli[2], C. Duc[3], and S. Vassaux[3]

[1] Center for Sensors and Devices, Fondazione Bruno Kessler, 38123 Trento, Italy
mulloni@fbk.eu

[2] Department of Civil Environmental and Mechanical Engineering, University of Trento, Trento, Italy

[3] IMT Nord Europe, École Mines-Télecom, Univ. Lille, 59000 Lille, France

Abstract. In this paper, we propose the use of multiple passive microwave sensors to monitor several environmental parameters simultaneously. The system can be easily integrated into a chipless RFID system to obtain sensing and identification in a single, simple tag, which is also inexpensive, completely passive, suitable for harsh environments and easy to fabricate. We demonstrate the capability to detect humidity, NO_2, ozone and ammonia. The main challenges, related to the selection of suitable sensing materials and the detection system, are also discussed, together with possible directions for future work.

Keywords: Chipless RFID · microwave sensor · gas sensing · wireless detection

1 Introduction

Chipless Radio Frequency Identification (RFID) technology represents a significant evolution in wireless identification, offering a lower-cost alternative to traditional chip-based RFID systems. Conventional RFID tags rely on silicon chips to store and transmit data. Chipless RFIDs, in contrast, eliminate this need, encoding data through the physical design and properties of the tag itself, typically through printed structures that resonate at specific frequencies.

Microwave sensors can be easily embedded into chipless RFID solutions, adding the sensing function to the identification technology. This can be done seamlessly by merging specific sensing resonating structures with the ID geometries [1, 2]. The integrated systems, containing identification and sensing on a single tag, are intensively studied for their advantages related to the absence of electronics, making them very attractive due to their low price, mechanical stability, very low energy consumption and suitability for harsh environments.

In this work, we focus on the sensing function and the performance of the microwave sensors. The key to transforming a microwave resonator into a wireless sensor is the availability of a suitable sensing material that can modify its structure and dielectric properties when exposed to a specific chemical or physical parameter. Once this material

C. Di Natale et al. (Eds.): AISEM 2025, LNEE 1497, pp. 21–26, 2025.
https://doi.org/10.1007/978-3-032-08271-8_4

has been identified, a layer of convenient thickness can be added on top of the microwave resonator [3]. The variation of the dielectric properties of the layer changes the resonator Q-factor and frequency, thus enabling a quantitative determination that can be read wirelessly, together with the identification code.

These characteristics of microwave sensors allow the exploitation of gas-sensing materials already used in established wired sensing approaches, combining them with innovative wireless detection strategies [4].

In this work, we discuss the realization of a multiparameter wireless sensor for environmental monitoring based on a microwave multi-resonator platform. The final goal is to obtain a complete system for wireless detection of several environmental parameters with the same functionality as a classic array of MOS sensors, but with the important advantages of being wireless, completely passive, low-cost, working at room temperature and printable. Moreover, the targeted environmental parameters may be varied by changing the selected sensing materials, making the whole system very flexible and adaptable.

This ambitious goal encounters two crucial challenges. The first one is related to the sensitive materials. Suitable sensing materials must be adapted to the alternative transduction mechanism. This involves optimizing the sensitive layers' thickness, resistivity and dispersion/deposition techniques. The second and probably most difficult challenge is developing a suitable detection strategy that allows for the precise and simultaneous determination of all the resonators' peaks [7].

The first step towards this ambitious passive environmental platform is to design, fabricate, and test structures with only two resonators and select the target parameters using an appropriate choice of sensing materials. The structure of this paper is aligned with this preliminary aim.

2 Materials and Methods

2.1 The Resonating Structures: Design and Fabrication

The design of the two resonators is reported in Fig. 1. The geometry of the metallic structures was that of a square electric inductive-capacitive (ELC) resonator and were simulated to have the lowest resonant peak for the bare structures at around 1.7 and 2.2 GHz. The frequencies may vary slightly with the detection system but are a direct function of the geometrical dimensions.

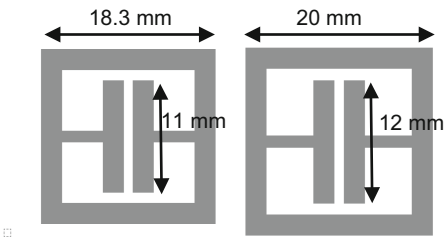

Fig. 1. The geometry of the chipless tag with two resonators.

The resonating structures were made of a metallic copper (17 μm-thick) on a 168 μm-thick Rogers 4350 substrate (Rogers Corp.) and were realized by microlithography and chemical etching. In order to sense two environmental parameters, different sensing materials were placed over the two resonators. The choice of the sensing materials is discussed in the following subsection.

2.2 The Selection of the Sensing Materials

The selected sensitive materials are: 1) Nafion NRE 212, which is commercially available, 2) reduced SnO_2, prepared as described in [4], and 3) acidic-doped polyaniline (PAni)/polyurethane (PU) [5]. Nafion is extremely sensitive to humidity and responds rapidly, while reduced SnO_2 can detect both NO_2 and ozone. Finally, PAni/PU is a suitable sensing material for NH_3[5] that can work at room temperature. Using these materials for microwave sensing requires some adaptation, especially for their conductivity. While highly conductive materials are ideal for chemoresistive sensors, high-resistivity layers are needed for microwave sensors to have a high quality-factor resonance. This was a problem with both Nafion and PAni/PU, (a solution of 20% was selected), because both are known to have good conductivity. In both cases, the thickness of the layers has been reduced to obtain a signal of sufficient intensity. In the case of PAni/PU, a thin layer of Kapton was also interposed between the metallic resonator and the layer [6]. Both these adjustments, however, reduce sensor sensitivity, so a trade-off had to be found. For reduced tin oxide, the main difficulty was related to the room-temperature recovery time [4], which was very long and, therefore, non-compatible with real-time operation. The solution found in this case is the use of a UV lamp during gas testing to accelerate the sensing process. Both reduced tin oxide and PAni/PU were deposited by drop casting from a convenient solution and then let dry overnight. Nafion NRE 212 is available as a 50 μm thick membrane and was directly applied on the resonator. Thicker Nafion membranes lead to higher sensitivity but do not provide a sufficient signal intensity [6].

2.3 Sensor Measurement

The sensor RF measurements were performed by using a dedicated apparatus with a custom-made gas-flow test chamber coupled with a two-ports Agilent E5061B ENA vector network analyzer (VNA) [6]. The RF reading apparatus was composed of two directional E-plane linearly polarized Vivaldi Horn antennas with gain $G = +11$ dBi, connected with low-loss RF cables to the VNA. The distance between the transmitting and receiving antenna was 30 cm, with the test chamber in between. Gas sensing measurements were conducted at room temperature (20 °C). Relative humidity (%RH) was detected by a digital humidity sensor at the chamber's exit and the %RH control was achieved by injecting a fixed fraction of the total dry air, namely 200 sccm (20% O_2 and 80% N_2), through mass flow controllers into a gas bubbler filled with deionized water to create the desired humidity conditions. Ozone, NO_2 and ammonia were fluxed and mixed with dry air through calibrated mass-flow controllers, achieving a constant total flow of 500 sccm. A detailed description of the measuring system is reported in refs. [4] (gas sensing equipment and setup) and [6] (antenna configuration).

3 Results and Discussion

The sensors examined in this work enable the determination of two independent sensor characteristics, the peak frequency and intensity. The resonating peak may change both its peak frequency and intensity upon exposure to the target environmental parameter, reflecting changes in the dielectric constant and the loss factor of the sensing material, respectively. For sensing purposes, this means that the sensor can be flexibly adapted to the application-specific needs, and the simultaneous determination of both features increases the reliability and accuracy of the determination [7]. In this work, we will concentrate only on the intensity variations because they are more precise and sensitive, and it is easier to explain the variation trends of a single feature when multiple target analytes are involved. First, we checked the correct functioning of the whole system, performing a baseline measurement with only the bare resonators. The result is reported in Fig. 2.

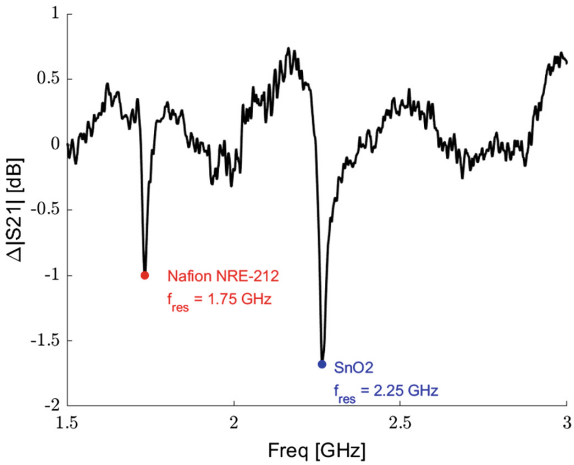

Fig. 2. Measurement of the bare resonators in the range 1.5–3 GHz.

The two distinct peaks are evident in the plot of Fig. 2, centered at 1.75 and 2.25 GHz, in accordance with the simulated values. After this preliminary check, we decided to evaluate the system Nafion/SnO_2, targeting the detection of NO_2, ozone and humidity. The system, with the two resonators covered with either Nafion 212 (1.75 GHz) or reduced SnO_2 (2.25 GHz), was initially tested for response to humidity and then to NO_2 and O_3. The results are reported in Figs. 3 and 4. As can be seen in Fig. 3, reduced SnO_2 is sensitive to all three environmental parameters, as expected. However, its response to O_3 is more pronounced than that to NO_2, and the response to humidity is in the opposite direction, which means that the peak becomes larger and less intense in humid environments. The recovery times were, however, quite long, and the illumination with a UV source was necessary [4].

The response of Nafion to the same environmental parameters is completely different. This material is very sensitive to humidity and does not react to NO_2 and O_3. Moreover,

the intensity variation in this case is more pronounced, probably because the thickness of the sensing layer is much higher. Even in this case, the response to humidity is in the opposite direction compared to the negligible response to NO_2 and O_3. The response and recovery in this case were very fast (a few seconds and 2–3 min, respectively, for full recovery).

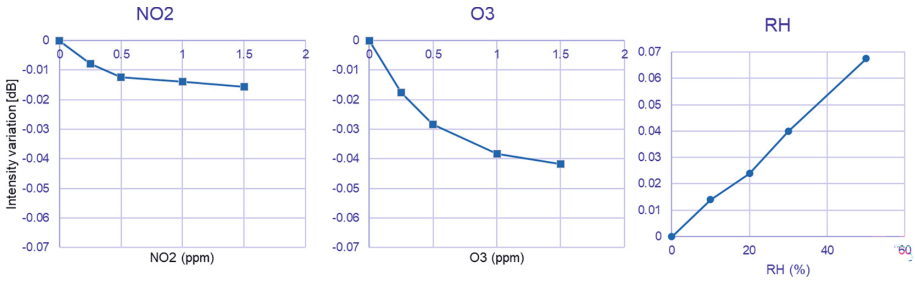

Fig. 3. Variation of intensity of the resonator covered with reduced Tin Oxide exposed to NO_2, O_3 and humidity.

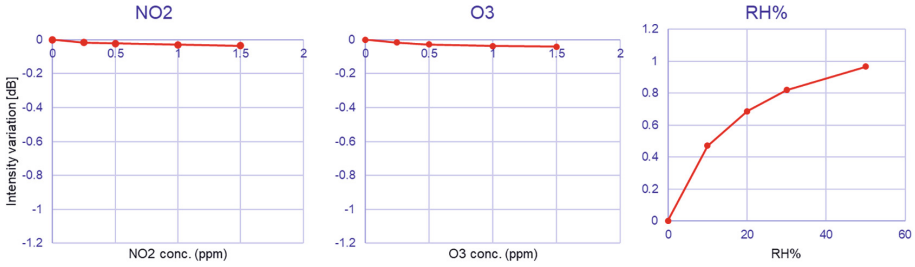

Fig. 4. Variation of intensity of the resonator covered with Nafion NRE 212 exposed to NO_2, O_3 and humidity.

PAni/PU was also tested because it is a known sensing material for ammonia. This material was tested separately because its conductivity is high compared to the other materials and is not expected to be sensitive to NO_2 and O_3. It reacts to humidity, but in this preliminary assessment, the focus was on the optimization of the material deposition parameters to have a sufficiently high-quality factor for the resonator, so we performed only measurements in dry air. For this purpose, we used the bare resonator centered at 1.7 GHz, and a thin layer of PAni/PU was drop-cast on it. The resonator peak was noisier and broader than hoped, and consequently, measurements had to be repeated to obtain a meaningful result. Further adjustments are needed to improve the data quality before we can test it for more parameters. The results, averaged over multiple measurements, are reported in Fig. 5. Both the response and the recovery times were around a few minutes. The most reasonable approach to signal improvement is to try to increase the

layer resistivity by increasing the content of polyurethane. This should increase the Q-factor of the resonator but could reduce the material sensitivity to ammonia. Tests are still in progress.

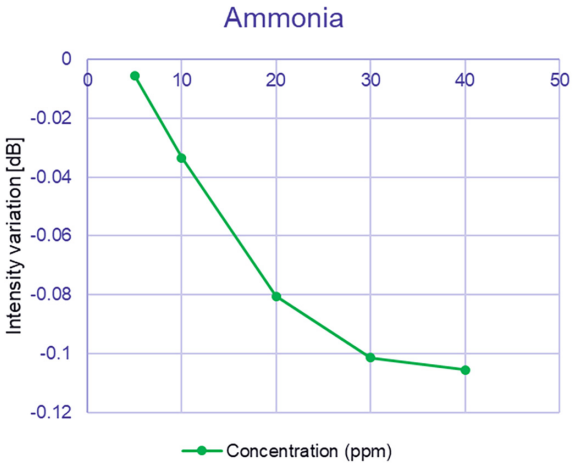

Fig. 5. Variation of intensity of the resonator covered with PAni/PU exposed to NH_3.

4 Conclusion

Microwave sensors can add the sensing function to the chipless RFID technology. The integrated systems, containing identification and sensing on a single tag, are very attractive due to their low price, very low energy consumption and suitability for harsh environments. In this paper, we have preliminarily shown that a multisensing platform for environmental monitoring based on passive microwave sensors is feasible, targeting humidity, NO_2, ozone and ammonia with the same measuring platform.

References

1. Dey S, Saha JK, Karmakar NC (2015) Smart sensing: chipless RFID solutions for the internet of everything. IEEE Microw Mag 16:26–39
2. Javed N, Azam MA, Qazi I, Amin Y (2020) Data-Dense Chipless RFID Multisensor for Aviculture Industry. IEEE Microw. Wirel. Compon. Lett. 30: 1193–1196
3. Amin EM, Karmakar NC, Jensen BW (2016) Fully Printable Chipless RFID Multi-Parameter Sensor. Sens Actuators A: Physical 248:223–232
4. Mulloni V et al (2023) Sub-Ppm NO_2 Detection through Chipless RFID Sensor Functionalized with Reduced SnO_2. Chemosensors 11:408
5. Da Silva EA, Samuel C, Furini LN, Constantino CL, Redon N, Duc C (2023) Poly(aniline)-based ammonia sensors: understanding the role of polyurethane on structural/morphological properties and sensing performances. Sens Actuators B: Chemical 397:134664
6. Marchi G, et al (2024) Chipless and batteryless microwave sensor cell for remote detection of humidity. 2024 IEEE International Symposium on AP-S/INC-USNC-URSI, pp. 2245–2246. IEEE, Firenze, Italy
7. Mulloni V, Marchi G, Gaiardo A, Valt M, Donelli M, Lorenzelli L (2024) Applications of chipless RFID humidity sensors to smart packaging solutions. Sensors 24:2879

Detection of 2-Furaldehyde in Transformer Oil in the Presence of Fatty Acids by SPR Sensor Modified with Molecularly Imprinted Polymer

S. Prosperi[1,2], L. De Maria[1(✉)], D. Merli[2], and G. Alberti[2]

[1] Technologies for Transmission and Distribution Department, RSE S.p.A., 20134 Milano, Italy
letizia.demaria@rse-web.it

[2] Department of Chemistry, University of Pavia, 27100 Pavia, Italy

Abstract. 2-Furaldehyde (2-FAL) is a furan compound that can be found in various environmental and food contexts, including food, wine, and milk. It is often analyzed as a quality marker, but its potential health risks make it a concern. In industrial liquids, like natural esters, which are used in oil-filled transformers, 2-FAL concentrations can be high due to insulating paper degradation, making it essential to monitor solid insulation. An SPR optical sensor has been previously reported for this aim. It is based on a plastic optical fiber and a sensing receptor for 2-FAL, specifically a Molecular Imprinted Polymer layer, which directly performs in the ester matrix. However, natural ester is also subjected to hydrolysis, releasing fatty acids. In this work, as a first step, the response of the SPR sensors to 2-FAL in standard solutions of virgin ester and in the presence of different stearic acid content has been investigated. It turns out that the response to 2-FAL only varies with high levels of fatty acid, which are typical for an oil that has lost its functionality.

Keywords: 2-Furaldehyde · SPR sensor · Natural ester · Insulating oil · Fatty acids · Aging detection

1 Introduction

The presence of acids in transformer oil is a critical issue for the longevity and reliability of the insulation system. The formation of organic acids within the insulating system results from the decomposition and oxidation of the oil itself. These organic acids increase the viscosity of the oil. An increase in acidity indicates the deterioration rate of the oil, with inevitable sludge production [1]. The acidity of the oil in a transformer should never exceed the threshold value of 0.25 mg of KOH/g of oil, namely, the amount of KOH (in mg) necessary to neutralize 1 g of oil. Oil deterioration rapidly increases once this level is exceeded [2].

Generally, antioxidants are used to slow down the oxidation process in transformer oils. These additives react with free radicals and other oxidation products, blocking the reaction and thus reducing the rate of oxidation [3].

C. Di Natale et al. (Eds.): AISEM 2025, LNEE 1497, pp. 27–32, 2025.
https://doi.org/10.1007/978-3-032-08271-8_5

In recent years, the use of alternative insulating liquids for transformers has become an important topic due to the high demand for environmental safety. Natural esters present numerous advantages in terms of sustainability since they originate from renewable natural sources, are biodegradable, and are less flammable than mineral oils. On the other hand, they are more susceptible to oxidation and show higher viscosity compared to mineral oils.

However, it has been shown that natural esters produce a higher number of acids compared to mineral oil and especially acids with high molecular weight due to their chemical structure. In fact, esters are formed from glycerol and fatty acids and are referred to as triglycerides. They can undergo oxidation processes, specifically free radical reactions that, in the final stage, lead to the formation of aldehydes, ketones, alcohols, and fatty acids [4].

It has been demonstrated that, while compromising the characteristics of the oil, the hydrolysis by-products are not harmful to the insulating paper. Indeed, it is hypothesized that fatty acids tend to stabilize the OH groups present on the cellulose surface; this process is called transesterification and protects the paper from further degradation [5].

One of the main byproducts of paper degradation in transformer is the 2-Furaldehyde (2-FAL); this compound, once released in oil, is relatively stable and, therefore, it is generally used as a chemical marker of accelerated paper aging. A way to detect 2-FAL amount directly in insulating oil samples is the use of an optical sensor which exploits the SPR phenomenon at the interface between a gold nanofilm and a synthetic receptor for 2-FAL, specifically a Molecular Imprinted Polymer (MIP) layer, which directly performs in oil matrix [6]. This optical sensor has been extensively tested on standards of virgin oil fortified with different 2-FAL amounts and various oil matrices (mineral oil, vegetable oil, natural ester).

With reference to the 2-FAL detection in insulating ester, one challenge is represented by the presence of fatty acids in the oil matrix, which could impair or alter the optical response to 2-FAL.

In this work, the influence of fatty acids concentration in oil on the optical response is investigated. As a model of fatty acid, a long-chain saturated stearic acid generally found in natural oils is considered.

2 Optical Sensor

The optical sensor was realized by removing the cladding and part of the core of a plastic optical fiber (POF) embedded in a resin block [7]. A D-shaped profile of the POF fibre is thus obtained by polishing the fibre along half the circumference. Then, a buffer layer of photoresist Microposit S1813, approximately 1.5 μm thick, is spun over the exposed core; finally, a gold nanofilm (60 nm) is sputtered over the photoresist. Successively, a layer of a MIP selective for 2-FAL ($MIP_{2\text{-}FAL}$) is deposited over the flat surface of the sensing fiber, approximately 10 mm long.

The prepolymeric mixture for the preparation of $MIP_{2\text{-}FAL}$ consists of a solution containing methacrylic acid (MAA) as the functional monomer, 2-Furaldehyde (2-FAL) as the template analyte, divinylbenzene (DVB) acting as the crosslinking agent and solvent, and azobisisobutyronitrile (AIBN) as the radical initiator of the polymerization

reaction. A few μL (40–50 μL) of this mixture are drop-coated on the surface of the SPR platform. The polymerization is carried out thermally in a laboratory oven at a temperature of 50–70 °C. After cooling the platform, the removal of the template and unreacted monomer is performed by washing with absolute ethanol.

The scheme of the optical sensor is shown in Fig. 1.

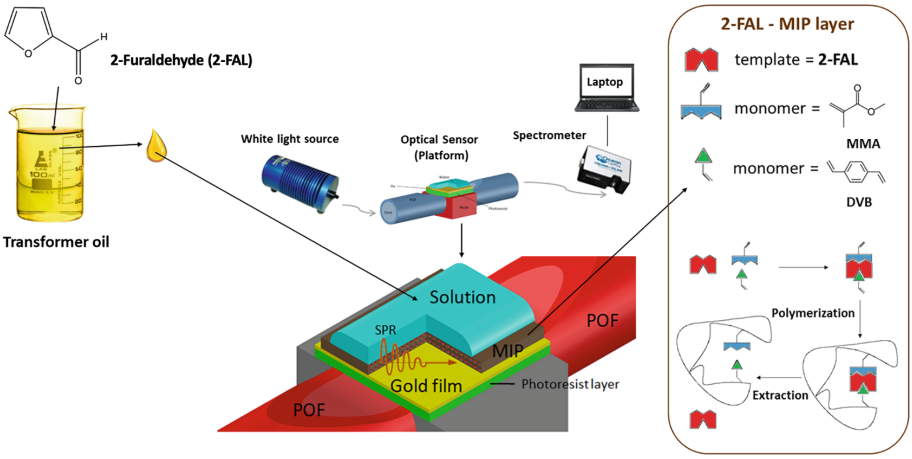

Fig. 1. Scheme of the SPR-POF-MIP$_{2\text{-FAL}}$ sensor and the apparatus used [6].

The experimental setup consists of a white light source and a spectrometer. A halogen lamp (model HL-2000-LL, manufactured by Ocean Optics, Dunedin, FL, USA) is generally used with spectral emission range from 360 nm to 1700 nm, while the spectrometer (Ocean Optics USB2000 + VIS-NIR-ES) has a detection range from about 330 nm to 1100. The SPR transmission spectra, normalized to the spectrum of the sensor before MIP deposition and with air as the surrounding medium, are displayed online on the computer screen [7].

3 Standard Preparation and Test Procedure

The standard solutions of 2-FAL have been prepared in ester oil (FR3) for subsequent dilutions starting from a stock solution with a concentration of 11358 mg/L. This solution was obtained by taking an appropriate amount of the standard (98%, d = 1.159 g/mL, Alfa Aesar Chemicals) and dissolving it in ethanol (absolute for analysis EMSURE®, Supelco).

The standard 2-FAL solutions containing stearic acid were prepared by adding appropriate volumes of the stock solutions of fatty acid (at a concentration of 50 mg/g), which were previously prepared in oil. The concentrations of fatty acid are expressed as a percentage in relation to the starting stock solution.

Table 1 shows the conversions from percentages of fatty acid to mg KOH/g oil, which is the unit of measurement generally used to report the total amount of acids in transformer oils [2].

Table 1. Conversion from % stearic acid to mg KOH/g of oil (amount of KOH needed to neutralize the acids contained in 1 g of oil).

% stearic acid	mg KOH/g oil
0.1	0.01
0.25	0.025
0.5	0.05
1	0.1
2	0.2

The SPR spectra were acquired by drop-coating the solution containing 2-FAL at different concentrations on the MIP platform. Each spectrum was normalized to the reference spectrum previously acquired in air. Between one measurement and the subsequent, conditioning with virgin oil was carried out. The same procedure was adopted for the experiments with solutions containing stearic acid. For each measurement set, the acid percentage varied while keeping the concentration of 2-FAL constant.

4 Results

SPR spectra obtained with the procedure described above for different concentrations of 2-FAL (from 0 mg/L to 1 mg/L) are shown in Fig. 2.

With the increasing concentration of the analyte, a red shift around 800 nm of the resonance wavelength minimum can be observed.

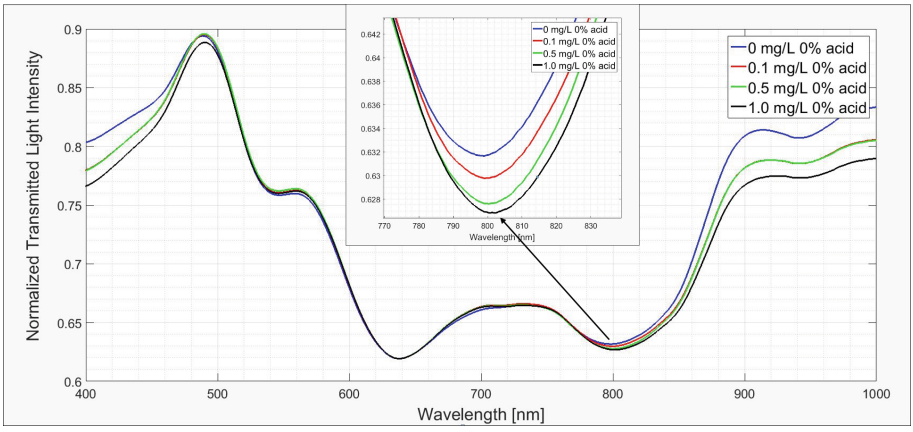

Fig. 2. Normalized SPR spectra at different concentrations of 2-FAL (in the absence of acid) and a zoom of the resonance wavelength minimum.

To evaluate the response of the SPR-MIP$_{2\text{-FAL}}$ sensor to the analyte in the presence of stearic acid, experiments were conducted at increasing concentrations of acid (from

0.1% = 0.01 mg KOH/g to 2% = 0.2 mg KOH/g) in ester oil in absence and presence of a fixed concentration of 2-FAL (0.1 mg/L). Experiments were replicated using three different platforms to assess the data's reliability and reproducibility.

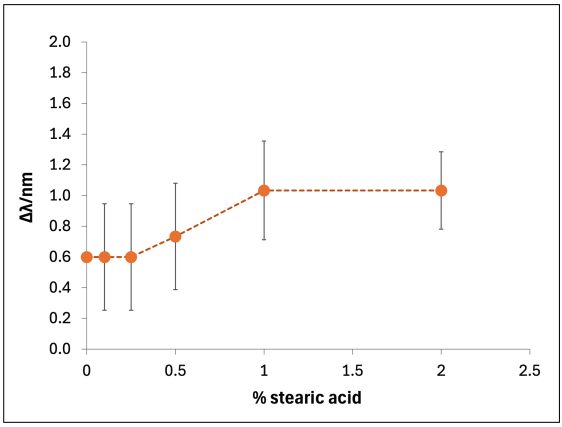

Fig. 3. Graph Δλ (nm) vs. % of stearic acid at a constant concentration of 2-FAL (0.1 mg/L) for three different SPR-MIP$_{2\text{-FAL}}$ sensors (the orange dots represent the average of the three sensors with their respective standard deviation).

From the graph of Fig. 3, it is evident that stearic acid percentages below 0.25% (corresponding to an acidity of 0.025 mg KOH/g of oil) do not affect the response of the sensor to 2-FAL. The Δλ value then linearly increases up to 1% of stearic acid (corresponding to an acidity of 0.1 mg KOH/g of oil) and reaches a plateau for higher acid percentages.

To try to understand and provide a justification for this experimental evidence, a test was conducted on a single platform measuring Δλ for samples containing only stearic acid ad different percentages in FR3 ester oil (Fig. 4).

It is immediately noticeable that, even in the absence of 2-FAL, there is a red shift in the wavelength of plasmonic resonance (around 770–800 nm) with a Δλ similar to that observed for samples containing 2-FAL. It seems that stearic acid somehow interacts with the recognition cavities of the MIP, and this interaction increases with the concentration of stearic acid. In the presence of 2-FAL and an acid concentration of 0.25%, the measurement of 2-FAL is not affected by the presence of the acid. Therefore, up to concentrations of stearic acid lower than 0.5%, there is no interference in the measurement. At higher concentrations of stearic acid, specifically above 0.5% and up to 1%, there is an increase in Δλ, which remains constant even when further increasing the amount of acid.

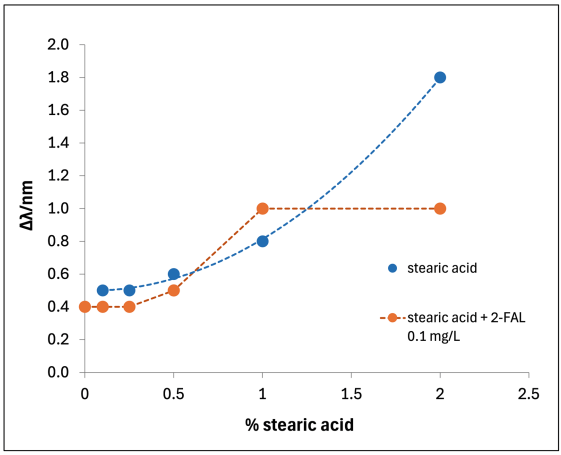

Fig. 4. Graphs of Δλ (nm) vs. % of stearic acid at a constant concentration of 2-FAL (0.1 mg/L, orange dots) and in the absence of 2-FAL (blue dots) for the same SPR-MIP$_{2\text{-FAL}}$ platform.

5 Conclusion

The results of the tests performed for the detection of 2-FAL in virgin natural ester at fixed concentration and increasing stearic acidity percentages confirm that the optical response varies only with high levels of fatty acid, which is typical of an ester that has lost its functionality. Further analyses will be necessary to consolidate the results obtained and extend the investigation to other decomposition compounds of a natural ester.

Acknowledgement. This work has been financed by the Research Fund for the Italian Electrical System under the Three-Year Research Plan 2025–2027 (MASE, Decree n.388 of November 6*th*, 2024), in compliance with the Decree of April 12*th*, 2024.

References

1. Kouassi KD, Fofana I, Cissé L, Hadjadj Y, Yapi KML, Diby KA (2018) Impact of low molecular weight acids on oil impregnated paper insulation degradation. Energies 11:1465
2. IEC 62975 (2021) Natural esters - Guidelines for maintenance and use in electrical equipment
3. Totzauer P, Trnka P (2019) Different ways to improve natural ester oils. Transport Res Procedia 40: 102–106. ISSN 2352-1465
4. Danikas MG, Sarathi R (2020) Alternative fluids – with a particular emphasis on vegetable oils – as replacements of transformer oil. Eng Technol Appl Sci Res 10(6):6570–6577
5. Azis N, Wang ZD (2011) Acid generation study of natural ester. XVII International Symposium on High Voltage Engineering. Hannover, Germany
6. Pesavento M, Cennamo N, Zeni L, De Maria L (2021) A molecularly imprinted polymer based SPR sensor for 2-furaldehyde determination in oil matrices. Appl Sci 11:10390
7. Cennamo N, De Maria L, D'Agostino G, Zeni L, Pesavento M (2015) Monitoring of low levels of furfural in power transformer oil with a sensor system based on a POF-MIP platform. Sensors 15:8499–8511

Qualitative Carbohydrates Analysis Using Yeast-Direct Catalytic Fuel Cell Bio-Device and Chemometrics

Mauro Tomassetti[1(✉)], Corrado Di Natale[2(✉)], Federico Marini[1], Mauro Castrucci[1], and Luigi Campanella[1]

[1] Department of Chemistry, University of Rome, "La Sapienza", P.le A. Moro 5, 00185 Rome, Italy
mauro.tomassetti@uniroma1.it
[2] Department of Electronic Engineering, University of Rome "Tor Vergata", Via del Politecnico 1, 00133 Rome, Italy
dinatale@uniroma2.it

Abstract. Fuel cells have been used in the past, by present authors, to quantify alcohol or glucose content in foods, or drinks, while in more recent papers authors investigated the analytical survey of the Direct Catalytic Fuel Cell (DCFC) for "qualitative" analysis too of aliphatic alcohols and so on, using suitable chemometric methods for DCFC data elaboration. In the present research authors tried to extend the same format, for qualitative determination to several carbohydrates (Glucose, Xylose, Fructose, Galactose, Sucrose), using the same simple experimental apparatus for batch analytical measurements, i.e., a Direct Catalytic Fuel Cell, obviously after incubation of carbohydrates by Yeast, to obtain corresponding alcohol from carbohydrates. Lastly obtained experimental data has been processed by different chemometric strategies. At first, the whole response curves' data have been subjected to Principal Component Analysis (PCA). Lastly, applying, to only initial response data of Fuel Cell, a multi-block exploratory approach, using the ComDim algorithm, so that best separation and recognitions were achieved.

Keywords: Direct Catalytic Fuel Cell (DCFC) · chemometrics multi-block exploratory approach (ComDim) · carbohydrates recognition · qualitative analysis

1 Introduction

In recent times we have demonstrated [1] that different substances possessing an alcohol group can be qualitatively identified, using a completely innovative method. It is sufficient, in this case, to only use appropriate chemometric methods to process the discharge curves of a DCFC (Direct Catalytic Fuel Cell) type, to obtain good separations in the scores of PCA representations, obtained from all the data of the Fuel Cell discharge curves, and therefore to be able to carry out valid qualitative recognitions of any unknown alcoholic substances under examination.

C. Di Natale et al. (Eds.): AISEM 2025, LNEE 1497, pp. 33–39, 2025.
https://doi.org/10.1007/978-3-032-08271-8_6

However, if the substances to be recognized are very similar from a chemical standpoint, such as monoalcohols differing only for the length of the linear aliphatic chains, the possibility of univocally identifying the analytes, even with the help of chemometric models [1], becomes more difficult, given the "chemical" similarity of the different alcoholic molecules and therefore the probable similarity of the subsequent oxidative processes (leading to the formation of H_2O and CO_2), which take place in the catalytic fuel cell, which uses, in the anodic section, classical catalysts, based on Platinum and Ruthenium [2]. However, we have recently tried to successfully overcome this difficulty [1], since we realized that if, in addition to recording and processing data of the discharge curves of the catalytic Fuel Cell, the fitting parameters of the initial, quasi-linear part of the curves themselves were also calculated, the possibility of exploiting data fusion strategies (in particular, by means of ComDim, a multi-block generalization of Principal Component Analysis) allowed to a good separation in the corresponding scores plot, even with alcohols of the same type [1]. In the present research we tried to extend the same format for qualitative determination to several carbohydrates (Glucose, Xylose, Fructose, Galactose, Sucrose); but in this case, obviously, carbohydrates had to be firstly converted into alcohol, using yeast in buffer-isotonic glycine solution.

2 Materials and Methods

Carbohydrates had to first be converted into alcohol using yeast solution [3]. For this purpose, 50 mL glass flask, properly closed and filled with 30 mL of yeast-glycine solution (0.03 mol L^{-1} in the tested carbohydrate), was kept at a constant temperature, for 12 h. At the end of the incubation time, 2 mL of solution was quickly extracted from the flask with a device made by graduated syringe, equipped with two small filters (see Fig. 1), and injected in the DCFC. The Fuel Cell was obtained from Fuel Cell Store (College Station, TX, USA). The end plate of the electrode of DCFC was made of a Pt-Ru black catalyst, assembled with a Nafion™ membrane. The Fuel Cell was used in potentiostatic mode, by measuring continuously the so-called supplied current until to steady state, using an EmStat potentiostat from PalmSens, connected to a PC. The fuel cell was connected to the EmStat, with PSTrace Software ver. 4.6 data interface, supplied on a Compaq Presario PC. In the Fuel Cell the anode acts as working electrode, while the cathode acts as reference and counter electrode. Before the current measurement, the EmStat automatically measured the Open Circuit Voltage (OCV) value, for a time of about 200 s, and then the anode potential was set to a value corresponding to the Optimized Applied Potential (OAP = OCV-100 mV) [4–6].

The collected data was then subjected to single- or multi-block exploratory chemometric techniques for the differentiation of the analytes, which constitutes the basis for their successive identification. Single-block data (i.e., individual data matrices) have been processed by Principal Components Analysis (PCA) [7, 8].

When more than a single block of data, i.e., more than a single matrix, was collected to describe the same set of samples, data analysis can profit from the integration of the information from the different data blocks through data fusion approaches; in the present study, the Common Dimensions (ComDim) [9, 10] algorithm was adopted.

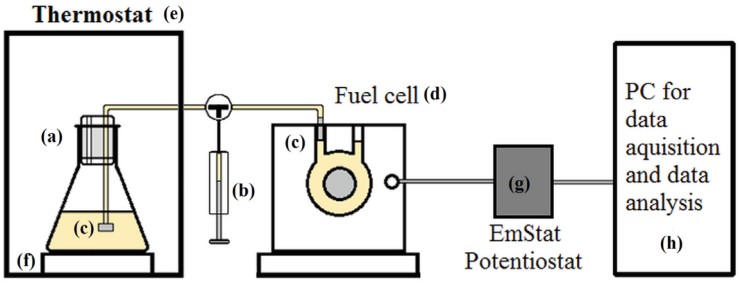

Fig. 1. Representation of incubation with yeast, Fuel Cell DCFC system and recording apparatus, by operating in batch mode; (a) glass vessel for yeast - glucose incubation, under stirring, (b) systems to transfer the obtained alcohol solution into the fuel cell (syringe), (c) suitable filter, (d) fuel cell, (e) thermostat, (f) magnetic stirrer, (g) potentiostat, (h) PC. All carbohydrates were analyzed at the same concentrations (0.03 mol L^{-1}). Incubation performed with 0.6 g of yeast, in glycine buffer, at 28.5 °C, for a period of 12 h, and each discharge curve was recorded for 4000 s, up to approximately steady state.

3 Results

Current response trends to five different investigated carbohydrate molecules have been recorded until about the steady state (Fig. 2).

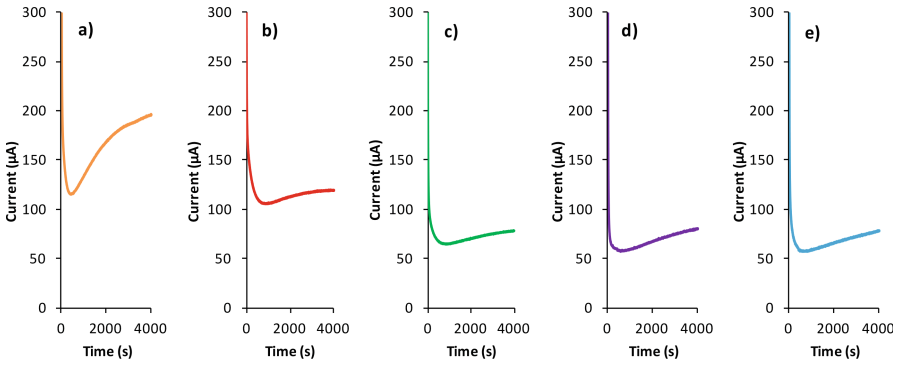

Fig. 2. Entire current response trend of each of the five investigated carbohydrate molecules: (a) sucrose, (b) fructose, (c) glucose, (d) galactose, (e) xylose. For each of the reported trends, at least three determinations were carried out, to check, in each case, their repeatability.

Principal component analysis (PCA) [7, 8] was then applied to the data set obtained by gathering all the data points of the response curves, after mean centering. The results of PCA are graphically displayed in Fig. 3, in terms of scores plot along the first two principal components, accounting for more than 99.9% of the total variance. The differences in the behavior among carbohydrates, can be appreciated by inspecting the scores plot reported in Fig. 3.

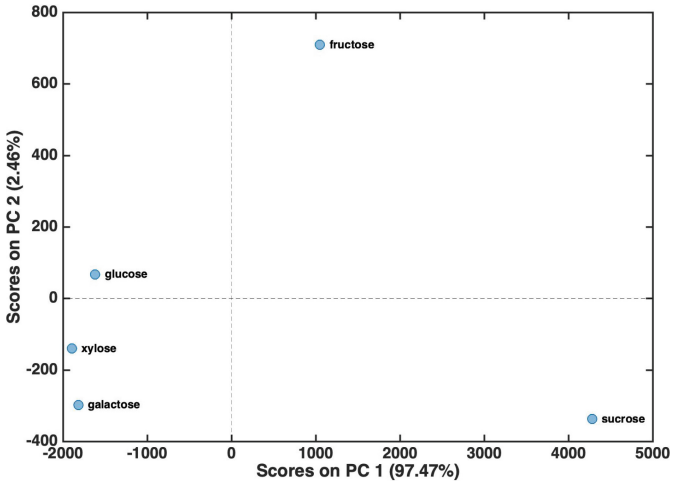

Fig. 3. PCA scores plot: results for the dataset comprising complete current response curves up to 4000 s. Projection of the five analyzed carbohydrates, onto the first first principal components, (explaining 99.9% of the total variance).

To try to shorten the time needed for recording the experimental data, a second strategy was then developed: to this end, a second model was built considering only the initial points (up to 120 s) of the recorded curves (see Fig. 4).

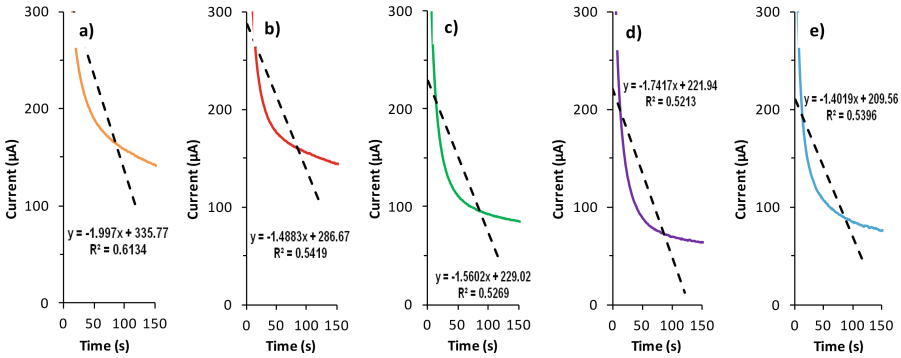

Fig. 4. Current response trend, only up to 150 s, of each of the five investigated carbohydrate molecules, a) sucrose, b) fructose, c) glucose, d) galactose, e) xylose, and results of linear fitting (dotted lines) of the data recorded on the five studied carbohydrates solutions, all at the same concentration (30 mmol L^{-1}) and after the same incubation time (12 h) at 28.5 °C, obtained using only the points of the curves up to 120 s. For each of the reported trends, at least three determinations were carried out, to check, in each case, their repeatability.

Together with the experimental data (up to 120 s only), the results of linear fitting (slope, intercept and their R^2) of the same data up to 120 s, reported in Fig. 4, were then jointly processed, through a multi-block exploratory approach using the ComDim

algorithm [9, 10]. The scores' representation, resulting from the fusion of the first part of the discharge curves and the parameters of the linear fitting of the same set of data points (reported in Fig. 4) shows excellent separation of five carbohydrates, as can be clearly seen in Fig. 5, thus providing a support for the possible good recognition of the carbohydrates themselves, but needing a much shorter time, to obtain the experimental data (only up to about 120 s).

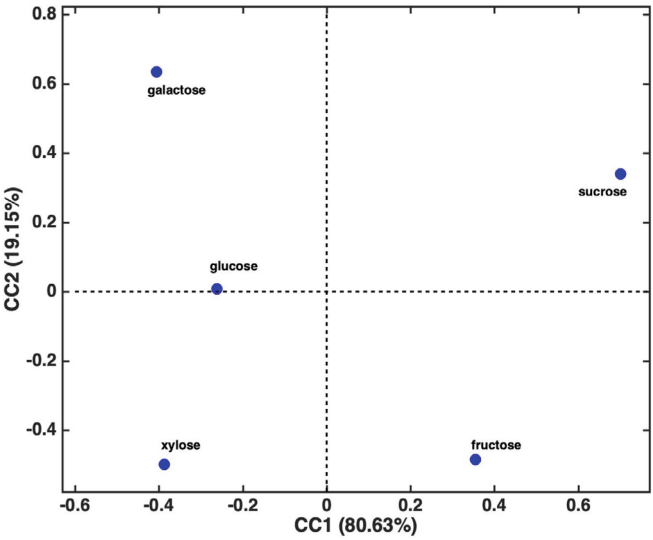

Fig. 5. Projection of the five analyzed carbohydrates, onto the first two common components, extracted by Data "Fusion", using the ComDim algorithm (explaining 99.8% of the total variance).

4 Discussion

Looking at carbohydrates discharge curves, reported in Fig. 2, it can be observed as the sucrose shows the higher current response at the steady state, in comparison with other carbohydrates. Obviously, it can be assumed that this is due to the fact that the sucrose is a disaccharide [11], and this seems to justify its higher steady-state current, if its response, with that of the other four monosaccharides, is compared.

This naturally leads to the admission that the enzymatic system, present in yeast metabolism, is also able to split the disaccharide into the two different monosaccharides, both able to produce alcohol. It is also interesting to observe as, of the four determined monosaccharides [11], two of them (glucose and galactose), are aldohexoses and show almost the same response (as μA); xylose, which is an aldopentose, has a similar, but slightly lower, response, while the fructose, that is a ketohexose, shows a significantly higher response, and this seems to be in accordance too with the very high response of sucrose, i.e., a disaccharide containing a fructose molecule, in addition to that of glucose. It could perhaps be hypothesized that, since fructose is a ketohexose, instead of an aldohexose, can be transformed in alcohol, by the yeast, more easily and quickly,

while xylose (aldopentose), less quickly, by the yeast cells, than the other two aldohexoses above mentioned. However, these statements have been studied and demonstrated, once it has been just verified that our system is also able to operate well with different carbohydrates too.

5 Conclusions

An important aspect of the present research was the fact that the proposed qualitative analytical method was found to work very well, not only in the case of direct analysis of different aliphatic alcohols [1], but also when it is necessary to first transform a different non-alcoholic fuel into alcohol, as, for example, in the case of carbohydrates, by means of a biological process, based on the action of yeasts [3]. In fact, it has been definitely established in this research that the discharge curves of the Fuel Cell, which are obtained, always depend on the diversity of the different original fuels used, even if not alcoholic [4], such as, for example, carbohydrates [3]. The discharge curves, i.e., the responses of the Fuel Cell, in fact retain information, which is always correlated to the original fuels (as different carbohydrates), and therefore allow qualitative analysis to be carried out, also for these original organic compounds, even if not alcoholic, despite the necessary preventive transformation, into alcohols, of the possible different organic compounds under investigation.

Another important aspect of this research it's the fact that we've been trying to reduce to the minimum the number of data points from the Fuel Cell response curves used for model building and, at the same time, to investigate what the best suited chemometric data processing approach could be. The result is that, to shorten the analysis times, it is sufficient to use only the initial part of the response curves obtained with the Fuel Cell, and at the same time apply to a multi-block exploratory approach, using the ComDim algorithm [9], which seems, up to now, to be the approach that provides the best results.

Lastly, despite several instrumental chemical methods for the qualitative identification of organic substances are well-known, such as chromatography, coupled, or not by (MS) [12, 13], or nuclear magnetic resonance (NMR) spectroscopy [14], however these methods are time expensive for application, or they have need of expensive equipment. In contrast, the method described in this study requires only inexpensive equipment, as modern Direct Catalytic Fuel Cells are available at low cost, and require relatively little experience to be used.

Acknowledgments. This work has been logistically supported by the University of Rome "La Sapienza" and University of Rome "Tor Vergata".

References

1. Tomassetti M, Marini F, Pezzilli R, Castrucci M, Di Natale C, Campanella L (2024) Improvement of qualitative analyses of aliphatic alcohols using direct catalytic fuel cell and chemometric analysis format. Sensors 24(10):3209–3220

2. Tomassetti M, Angeloni R, Merola G, Castrucci M, Campanella L (2016) Catalytic fuel Cell used as an analytical tool for methanol and ethanol determination. Application to ethanol determination in alcoholic beverages. Electrochim. Acta 191:1001–1009
3. Tomassetti M, Dell'Aglio E, Castrucci M, Sammartino MP, Campanella L, Di Natale C (2021) SimpleYeast-direct catalytic fuel cell bio-device: analytical results and energetic properties. Biosensors 11(2):45–54
4. Tomassetti M, Merola G, Angeloni R, Marchiandi S, Campanella L (2016) Further development on DMFC device used for analytical purpose: real applications in the pharmaceutical field and possible in biological fluids. Anal Bioanal Chem 408(26):7311–7731
5. Zhang J, Zhang H, Wu J, Zhang J (2013) Chapter 7 - fuel cell open circuit voltage. In: Pem Fuel Cell Testing and Diagnosis. Elsevier (Amsterdam, The Netherlands), pp. 187–200 (2013). ISBN 9780444536884
6. Sparks D et al (2005) Uncasville (Hartford). Connecticut, USA
7. Pearson K (1901) On lines and planes of closest fit to systems of points in space. Philos Mag 2:559–572
8. Jolliffe IT (2002) Principal Component Analysis, 2nd Ed. Springer Series in Statistics, New York, NY (2002)
9. Qannari EM, Wakeling I, Courcoux P, MacFie HJH (2000) Defining the underlying sensory dimensions. Food Qual Prefer 11:151–154
10. Jouan-Rimbaud Bouveresse D, Rutledge DN (2024) A synthetic review of some recent extensions of ComDim. J Chemom 38(5): e3454. https://doi.org/10.1002/cem.3454
11. Alén R (2018) Carbohydrate Chemistry: Fundamentals and Applications. World Scientific Publishing Company, p. 596 (2018). ISBN: 9813223642
12. Badawy MEI, El-Nouby MAM, Kimani PK, Lim LW, Rabea EI (2022) A review of the modern rinciples and applications of solid-phase extraction techniques in chromatographic analysis. Anal Sci 38:1457–1487
13. Ranjan Maji S, Roy C, Kumar Sinha S (2023) Gas chromatography–mass spectrometry (GC-MS): A comprehensive review of synergistic combinations and their applications in the past two decades. J Anal Sci Appl Biotechnol 5:72–85
14. Mitschke N, Vemulapalli SPB, Dittmar T (2023) NMR spectroscopy of dissolved organic matter: a review. Environ Chem Lett 21:689–723

Hybrid Nanozyme System: Gold-Decorated Nanodiamonds for Advanced Electrochemical Sensing

B. Ercolani[1(✉)], A. Licheri[1], V. Guglielmotti[1], S. Tosi[1], R. Matassa[2,3], R. Salvio[1], L. Sansone[4], L. Micheli[1], and S. Orlanducci[1]

[1] Department of Chemical Sciences and Technologies, University of Rome Tor Vergata, Via della Ricerca Scientifica 1, 00133 Rome, Italy
beatrice.ercolani@alumni.uniroma2.eu
[2] Physics Division, School of Science and Technology, University of Camerino, 62032 Camerino , MC, Italy
[3] Department of Anatomical, Histological, Forensic and Orthopedic Sciences, Section of Human Anatomy, Sapienza University of Rome, Via A. Borelli 50, 00161 Rome, Italy
[4] Institute for Polymers, Composites and Biomaterials, National Research Council of Italy, IPCB-CNR, 80055 Portici, Italy

Abstract. The text discusses the use of nanozymes, specifically gold nanoparticles (AuNPs), for electrochemical sensing owing to their benefits over natural enzymes in stability, reusability, and cost. Traditional synthesis methods for AuNPs can hinder efficiency, leading to the development of a new synthesis strategy utilizing nanodiamonds (NDs) as a support. NDs provide high surface area and chemical stability, resulting in ND-AuNPs hybrids exhibiting enhanced catalytic activity and stability. Additionally, a second hybrid using sp^2 nanocarbons derived from cellulose-based waste was created. When applied to screen-printed electrodes, both hybrid systems demonstrate improved electron transfer and heightened sensitivity, validating their potential integration into electrochemical sensors for detecting hydrogen peroxide. This study emphasizes the potential of using nanodiamonds and sustainable materials to advance nanozyme-based, enzyme-free electrochemical sensors for environmental and biomedical applications.

Keywords: Nanozymes · Biosensors · Nanodiamonds · Gold Nanoparticles

1 Introduction

Although natural enzymes are extensively utilized in biosensors for their specificity and efficiency, their high costs and lack of stability limit their long-term application. To overcome these issues, nanozymes have emerged as promising alternatives. The term *nanozyme* refers to nanomaterial-based artificial enzymes that not only replicate the catalytic functions of their biological counterparts but also offer superior properties [1]. They offer advantages such as improved stability under harsh conditions, lower production costs, ease of surface modification, and better recyclability.

C. Di Natale et al. (Eds.): AISEM 2025, LNEE 1497, pp. 40–46, 2025.
https://doi.org/10.1007/978-3-032-08271-8_7

Oxidoreductase-mimicking nanozymes are of interest for the development of biosensors due to their catalytic properties. Gold nanoparticles (AuNPs) have demonstrated exceptional peroxidase-like behavior, catalyzing the oxidation of substrates in the presence of hydrogen peroxide [2, 3]. However, the traditional synthesis of AuNPs involves reducing and stabilizing agents that can interfere with their catalytic performance [4]. Therefore, the development of innovative, cleaner, and more effective synthesis strategies remains a key focus to enhance sensor functionality.

This study explores a novel method of synthesizing AuNPs using nanodiamonds (NDs) and sp^2 carbon from pyrolyzed cigarette butts (CB) as support platforms [5]. These hybrids, ND-AuNP [6, 7] and CB-AuNP, show enhanced features and promising catalytic activity [8], demonstrated by evaluating the reaction between TMB (3,3′,5,5′-Tetramethylbenzidine) and H_2O_2. To assess the feasibility of integrating both systems into electrochemical platforms, the materials were deposited onto the graphite working electrodes of screen-printed electrodes (SPEs). In this preliminary study, the conductive properties of the materials were evaluated to assess their potential applicability in electrochemical systems and to facilitate the transfer of hydrogen peroxide sensing within an electrochemical framework.

2 Experimental

2.1 Materials Synthesis

The synthesis of ND-AuNPs was carried out as already reported in ref [9]. The concentration of the material dispersions was expressed in terms of carbon content to ensure comparable conditions between systems. Specifically, both detonation nanodiamonds (DND) and the carbonaceous material obtained from the pyrolysis of cigarette butts (CB) were used at a concentration of 0.1% (w:w) carbon and mixed with an aqueous solution of Au complex at 10^{-4} M. In the case of ND-AuNPs, DNDs purchased from the International Nanotechnology Center (ITC, USA) were first treated for 12 h with $NaBH_2$ to increase their reducing power and favor the formation of AuNPs. The DND dispersion and Au complex solution were mixed in equal volumes and sonicated for 30 min. After at least 48 h, the reaction was stopped by separating the supernatant from the powder products. The procedure was similar for synthesizing AuNPs using CB as the carbonaceous substrate. The CB dispersion and Au complex solution were mixed and left to react for seven days. Over time, the formation of nanometric gold was indicated by the disappearance of the yellow color of the gold complex in solution and the appearance of a red color due to the surface plasmon resonance (SPR) effect.

2.2 Raman Spectroscopy

The samples were analyzed on a silicon <100> substrate. The Raman analysis was conducted using the MicroRaman LabRAM Odyssey (Horiba) using laser source at 532 nm and 785 nm, employing a 600 gr/mm diffraction grating. Acquisition times were set to 2 s for the ND-AuNPs samples and 10 s for the CB-AuNPs samples.

2.3 UV-Vis Catalytic Activity Measurements

The optical measurements were conducted using a Shimadzu 1800 spectrophotometer (Mettler Toledo, Italy). The catalytic activity of the synthesized materials was evaluated by following the oxidation of 3,3′,5,5′-tetramethylbenzidine (TMB) into a product absorbing at 652 nm, as a marker of H_2O_2 reduction to H_2O. The reaction was carried out in a 10 mM acetate buffer solution pH 4, with 0.2 M H_2O_2, 0.5 mM TMB, and 0,05% (w:w) of the nanozyme material. The absorbance at 652 nm was measured over time up to 60 min.

2.4 Electrochemical Characterization

To evaluate the electroanalytical performance of the materials, they were drop-casted on the surface of the working electrode (WE) of screen-printed electrodes (SPEs). The SPEs have been printed at the University of Rome Tor Vergata on PET substrates with a graphite working and counter electrode (CE) and a silver reference electrode (RE) system. Preliminary measurements have been carried out and focused on evaluating the conductivity of the materials produced. Cyclic Voltametric (CV) measurements were performed using a 5 mM solution of potassium ferrocyanide ($K_4[Fe(CN)_6]$) and potassium ferricyanide ($K_3[Fe(CN)_6]$) prepared in KCl 0.1M, and conducted between -1 and 1 V at a scan rate of 0.05 V/s using a PalmSens4 potentiostat.

3 Results and Discussion

3.1 Morphological and Structural Characterization

The water dispersions of the ND-AuNPs and CB-AuNPs materials, synthesized as reported in Sect. 2.1, were analyzed by Raman spectroscopy. Raman maps of an area of about 100 to 200 μm^2 were recorded, and a false color map was superimposed on the optical image. The ND-AuNPs material (Fig. 1a-c) is composed of nanodiamond clusters with a spongy-like structure, which are decorated by quasi-spherical gold nanoparticles of different dimensions, visible in the picture as black dots. The map, see Fig. 1b, highlights regions of different optical responses. Green areas indicate zones with higher background signal intensity, possibly related to nanodiamond-associated fluorescence. Red regions correspond to stronger Surface Enhanced Raman Spectroscopy (SERS) signals from the gold nanoparticles. SERS enhances Raman scattering through localized surface plasmon resonance effects of metal nanoparticles such as gold [10]. Yellow zones represent areas where both contributions overlap. The spectra in Fig. 1c are representative of areas with the strongest SERS effect compared to those without it. Both spectra show the peak at ~1340 cm^{-1}, which is attributed to nanodiamonds [11]. However, only in the spectrum from the SERS-active zone multiple additional bands are visible, corresponding to functional groups typically present on the nanodiamond surface [12]. The CB-AuNPs material (Fig. 1d and f) is composed of different forms of sp^2 carbon. Like the nanodiamond-based sample, the reducing functional groups present on the carbon surface promote the formation of gold nanoparticles, which are clearly visible as yellow clusters, even if in smaller quantity and with larger size distribution, as depicted in

Fig. 1d. In the Raman map shown in Fig. 1e, the regions where the gold nanoparticles exhibit a SERS effect are highlighted in red. In the corresponding spectrum (Fig. 1f), the D and G bands typical of Csp^2 nanomaterials (~1350 and ~ 1580 cm^{-1}) show higher intensity compared to the spectrum acquired from areas lacking the SERS effect, mainly due to the absence of gold nanoparticles.

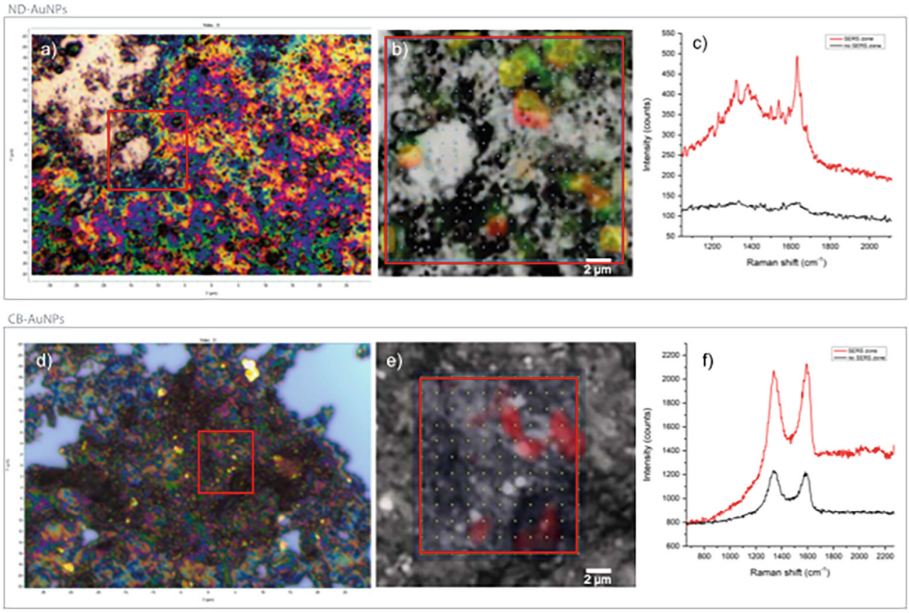

Fig. 1. Raman mapping and spectral analysis of ND-AuNPs and CB-AuNPs hybrid materials. (a-c) ND-AuNPs: (a) Optical image overlaid with false-color Raman map; (b) magnified view of the mapped area showing distinct optical features: green (fluorescent nanodiamond regions), red (SERS-active zones due to AuNPs), and yellow (overlap of both signals); (c) Raman spectra from a SERS-active area (red) and a non-SERS area (black). (d-f) CB-AuNPs: (d) Optical image with Raman mapping overlay; (e) magnified map showing SERS-active zones (red); (f) Raman spectra from a SERS-active area (red) and a non-active area (black).

3.2 Catalytic Activity Assessment

The peroxidase-like activity of the synthesized materials was assessed through the catalytic oxidation of TMB in the presence of H_2O_2, as illustrated in Fig. 2a. In this reaction, H_2O_2 is reduced to water, while TMB is oxidized, producing a blue-colored product with a characteristic absorption peak at 652 nm. The progression of the reaction was monitored by measuring the absorbance at 652 nm at different time intervals for the ND-AuNPs, CB-AuNPs, and DNDs (Fig. 2b-d). Among the tested materials, ND-AuNPs exhibited a significantly higher catalytic activity, as evidenced by the rapid increase in absorbance even at the earliest time point (Fig. 2b).

This enhanced performance can be attributed to both the higher density of gold nanoparticles on the nanodiamond surface, facilitated by the favorable surface chemistry

of DNDs, and the intrinsic catalytic properties of the nanodiamonds themselves. In comparison, the CB-AuNPs (Fig. 2c) showed lower activity, while bare DNDs (Fig. 2d) exhibited moderate catalytic behavior, surpassing that of CB-AuNPs, demonstrating that nanodiamonds contribute independently to the catalytic process.

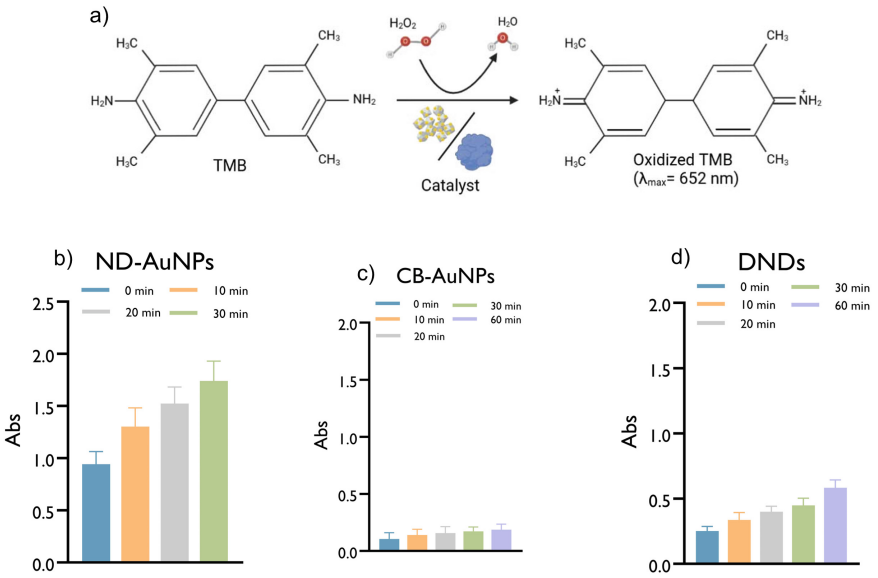

Fig. 2. (a) Schematic representation of the catalytic oxidation of TMB by H_2O_2 in the presence of a catalyst. (b-d) Time-dependent absorbance measurements at 652 nm for the reaction catalyzed by (b) ND-AuNPs, (c) CB-AuNPs, and (d) DNDs.

4 Preliminary Electrochemical Evaluation

After deposition on the working electrode (WE) of screen-printed electrodes (SPEs), the conductive performance of the materials was assessed. Table 1 shows the electrochemical parameters extracted from the cyclic voltammograms obtained using a redox probe. As expected, the CB-AuNPs material exhibited the highest current response due to the high conductivity of sp^2 carbon and the presence of gold nanoparticles. In contrast, the DNDs displayed a lower current than the bare electrode. Interestingly, the ND-AuNPs hybrid showed significantly higher current than the bare electrode, likely due to the conductive contribution of the gold nanoparticles.

Table 1. Electrochemical parameters extracted from CV curves of modified and unmodified SPEs: anodic (I_p^a) and cathodic (I_p^c) peak currents, their ratio (I_p^a/I_p^c), formal potential (E^0), and peak-to-peak separation (ΔE).

	i_p^a (μA)	i_p^c (μA)	i_p^a/i_p^c	E^0 (V)	ΔE(V)
Bare	81.78	-63.10	1.29	0.14	0.47
ND-AuNPs	120.04	-107.18	1.12	0.15	0.26
DNDs	56.94	-50.49	1.13	0.12	0.61
CB-AuNPs	156.01	-152.50	1.02	0.15	0.14

5 Conclusions

The study explores the use of nanodiamond-based and waste-derived carbon-based hybrid materials as nanozymes for electrochemical sensing. By using nanodiamonds (NDs) and carbon from pyrolyzed cigarette butts (CB) to synthesize gold nanoparticles (AuNPs), two materials, ND-AuNPs and CB-AuNPs, were developed, both demonstrating peroxidase-like activity. ND-AuNPs showed superior catalytic performance in the H_2O_2-TMB assay, attributed to higher AuNP density and intrinsic catalytic activity of the nanodiamonds. Electrochemical analysis confirmed the effectiveness of integrating these materials on screen-printed electrodes, with CB-AuNPs displaying the best conductivity. The study concludes that ND-AuNPs and CB-AuNPs are promising, sustainable nanozyme candidates for enzyme-free electrochemical sensors, with potential applications in biomedical and environmental fields.

Acknowledgments. The research leading to these results has received funding from the Project "SENS-AI, Environmental Sensing with Artificial Intelligence" CUP H53D23000520006 (Italian "Bando Prin 2022-D.D. 104 del 02-02-2022" by MUR (2023–2025), Project "Dress the future; novel combined wearable integrated system (Stargate)" CUP E53D22014620001 by MUR (2023–2025)(MUR-PRIN 2022 PNRR Decreto Direttoriale n. 1409 del 14-9-2022) and Grant MUR Dipartimento di Eccellenza 2023-27 X-CHEM project "eXpanding CHEMistry: implementing excellence in research and teaching".

References

1. Zandieh M, Liu J (2024) Nanozymes: definition, activity, and mechanisms. Adv Mater 36(10):2211–2241
2. Gerlache M, Senturk Z, Quarin G, Kauffmann JM (1997) Electrochemical behavior of H2O2 on gold. Electroanalysis 9(14):1088–1092
3. Huang S, Xiang H, Lv J, Guo Y, Xu L (2024) Propelling gold nanozymes: catalytic activity and biosensing applications. Anal Bioanal Chem 416(27):5915–5932
4. Wang S, Chen W, Liu AL, Hong L, Deng HH, Lin XH (2012) Comparison of the peroxidase-like activity of unmodified, amino-modified, and citrate-capped gold nanoparticles. ChemPhysChem 13(5):1199–1204

5. De Fenzo A, Giordano M, Sansone L (2020) A clean process for obtaining high-quality cellulose acetate from cigarette butts. Materials 13(21):4710
6. Reina G, Orlanducci S, Tamburri E, Matassa, R, Rossi M, Terranova ML (2016) Nanodiamonds and gold nanoparticles: a promising couple for CRM-free photonics. Phys Status Solidi (C) Curr Top Solid State Phys **13**(10–12):972–978
7. Orlanducci S (2018) Gold-Decorated nanodiamonds: powerful multifunctional materials for sensing, imaging, diagnostics, and therapy. Eur J Inorg Chem 48:5138–5145
8. Vezzoni CA, Casnati A, Orlanducci S, Sansone F, Salvio R (2024) Enzyme mimics based on guanidinocalix[4]arene/ nanodiamond hybrid systems with phosphodiesterase activity. ChemCatChem 16(6):e202301477
9. Orlanducci S et al (2024) Gold-diamond nanocomposites efficiently generate hydrated electrons upon absorption of visible light. ACS Appl Opt Mater 2(6):1180–1187
10. Le Ru EC, Etchegoin PG (2009) Principles of surface-enhanced Raman spectroscopy : and related plasmonic effects. Elsevier
11. Mermoux M, Chang S, Girard HA, Arnault JC (2018) Raman spectroscopy study of detonation nanodiamond. Diam Relat Mater 87:248–260

Detection of Mineral Oil Aging by Free Space Transmission Measurements with Microstrip Patch Antennas

E. Proietti[1(✉)], A. Capoccia[2], D. S. Joseph[1], M. Bernabei[3], and R. Marcelli[1]

[1] CNR-Institute for Microelectronics and Microsystems, Via del Fosso del Cavaliere, 100, 00133 Roma, Italy
emanuela.proietti@cnr.it

[2] Department of Civil Engineering and Computer Science Engineering, University of Rome Tor Vergata, Via del Politecnico, 100133 Roma, Italy

[3] University of Central Lancashire, Preston, UK

Abstract. In this paper, a non-invasive electromagnetic method using free-space transmission measurements with patch antennas is presented as a promising approach for real-time detection of dielectric property variations induced by oil aging. This measurement technique eliminates the need to extract oil samples and transport them to a laboratory for chemical analysis, allowing the oil condition to be assessed directly in situ. As such, it represents a significant advancement toward the development of smart, integrated oil condition monitoring systems for industrial and energy infrastructures.

Keywords: Free Space Measurements · Patch antennas · Mineral oil Aging · Dielectric Permittivity

1 Introduction

Lubricating oils are essential for maintaining the reliability and efficiency of mechanical systems and industrial equipment. Mineral oils, in particular, are extensively used in oil-immersed transformers, internal combustion engines, and various industrial applications to reduce friction, prevent wear and corrosion, dissipate heat, and remove contaminants from critical surfaces. However, during operation, lubricating oils undergo complex physical and chemical degradation processes that progressively impair their performance, potentially leading to costly maintenance interventions or equipment failure if not properly monitored [1–3].

The degradation of mineral oils primarily occurs through oxidation, thermal breakdown, and compressive heating. Among these, oxidation is the most significant, with its rate doubling for every 10 °C increase above 75 °C. Thermal breakdown, induced by elevated temperatures, results in discoloration and the formation of carbonaceous residues and oxides, while compressive heating under high pressures causes molecular structural changes. These degradation mechanisms adversely affect key oil parameters, such as

C. Di Natale et al. (Eds.): AISEM 2025, LNEE 1497, pp. 47–52, 2025.
https://doi.org/10.1007/978-3-032-08271-8_8

viscosity, acidity, and dielectric strength, ultimately compromising both insulating and lubricating functions [4, 5].

Conventional oil condition monitoring typically relies on off-line laboratory analyses, including viscosity measurements, acid number titrations, and spectroscopic techniques. While accurate, these methods are time-consuming, costly, and require specialised personnel. To overcome these limitations, recent research has explored the development of faster, low-cost, and automated diagnostic techniques, such as impedance and dielectric spectroscopy [6, 7]. Since the dielectric properties of lubricant oils are linked to their chemical composition and physical structure, they can be used to assess lubricant aging.

In this study, a novel approach based on patch antennas in a free-space measurement setup is proposed to evaluate the dielectric properties of oxidized lubricating oils. By analyzing the transmitted signal, the dielectric constant of the oil can be determined, enabling the assessment of its degradation state in a rapid and non-invasive manner.

2 Material and Methods

2.1 Oil Samples: Accelerated Aging Tests by Temperature Heating

A temperature heating approach is used to simulate the oil degradation causing a change in oil dielectric properties [8]. Three 120 ml samples of Mineral Oil Merck (CAS 8042–47-5, [9]), were heated on a hot plate (Fig. 1a) for 8 h, 16 h, and 24 h at 180 °C (Fig. 1b), producing different degradation states, as shown by the change of colours of the sample.

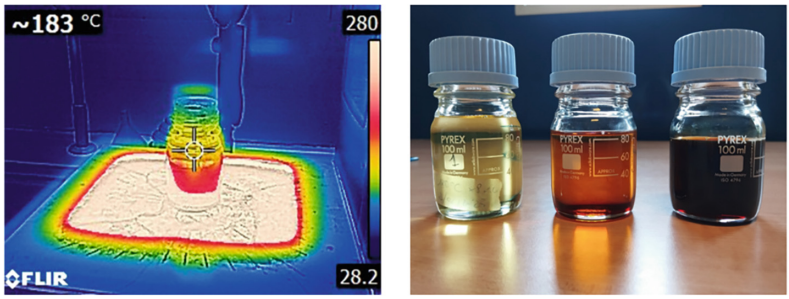

(a) (b)

Fig. 1. (a) FLIR (Forward-Looking Infra-Red) camera image of the hot plate heated sample, (b) 8 h, 16 h and 24 h heated samples.

2.2 Experimental Set up: Transmission Measurements

To detect changes in the dielectric properties of mineral oil as it undergoes thermal degradation, we implemented a measurement system based on two microstrip patch antennas operating at ~1.56 GHz.

The antennas are positioned 15 cm apart from each other to guarantee the plane wave incidence on the sample at 1.56 GHz with the sample oil placed in a custom-designed holder manufactured via 3D printing. As the oil ages, its chemical structure alters, and

these changes affect how the electromagnetic waves are transmitted by the sample, and the phase of the transmission signal S_{12} changes accordingly.

The set up was simulated using CST 2022 software. Figure 2 shows the simulation model of the measurement system (a) and the corresponding simulated transmission phase (S_{12}) over the frequency range of interest for sample materials with relative permittivity ranging from 1 to 4. The simulation results indicate that the phase of S_{12} decreases as the dielectric constant increases. As the permittivity of the lubricant oils increases with the oil aging, we expect a decrease in the S_{12} phase value with the increasing degradation levels.

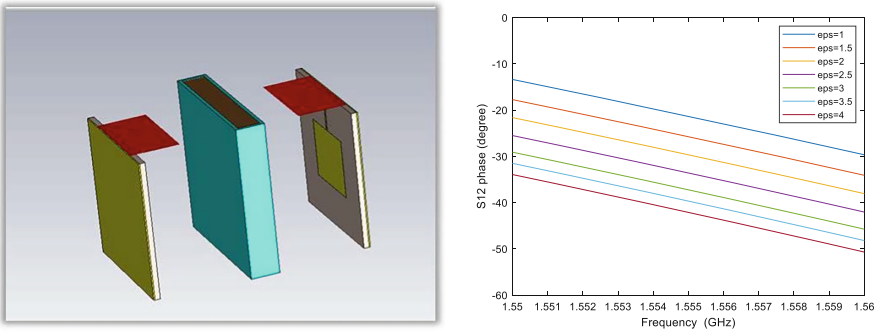

(a) (b)

Fig. 2. Parametric simulation of the transmission phase in our measurement system. (a) Simulation model of the two patch antennas positioned 15 cm apart from each other, with the oil holder filled with the sample material placed between the antennas. (b) Simulated transmission phase (S_{12}) in the frequency range 1.55 - 1.56 for sample materials with dielectric constants ranging from 1 (empty holder) to 4.

Figure 3a shows the real setup in our lab. It was used to measure the S_{12} transmission parameter of 4 sample oils: the fresh oil sample, and the 3 aged samples prepared as described above. Figure 3b and c show the module and phase of S_{12}, respectively.

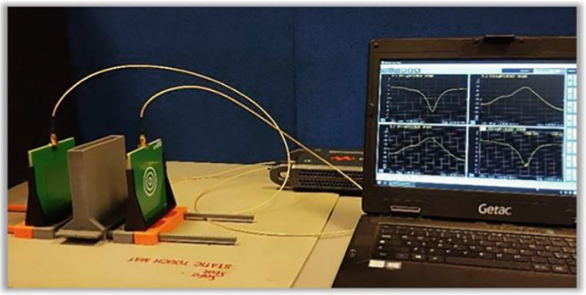

(a)

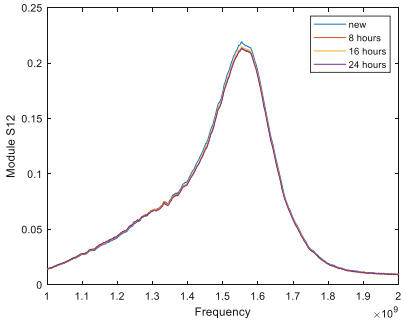

(b)

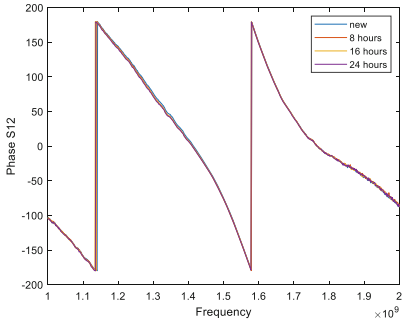

(c)

Fig. 3. (a)Transmission measurements set-up: the aged oil samples are placed in a 3D-printed holder in-between two patch antennas operating at 1.56 GHz. Transmission parameter is measured by a Keysight P9375A Vector Network Analyzer, (b) S_{12} module, (c) S_{12} phase.

The measurements show a S_{12} phase decreasing with the oil aging, confirming the simulated results.

3 Results and Discussion

The key idea to evaluate the mineral oil samples' permittivity is to observe how the aging of the oil affects the phase of the electromagnetic wave propagating through it, under the assumption of plane wave propagation. To do this, two measurements need to be taken: one with the oil sample inserted in a custom 3D-printed holder placed between the antennas and another with the holder empty (effectively measuring in air). The difference in the measured phase ($\Delta\Phi$) between these two configurations represents the additional phase delay introduced by the oil, due to its higher dielectric constant compared to air.

Since electromagnetic waves travel more slowly in a high dielectric medium than in the air, this delay is directly related to the relative permittivity (ε_r) of the oil. Assuming the wave propagates as a plane wave, the phase delay can be modeled by the expression:

$$|\Delta\phi| = |\phi_{oil} - \phi_{air}| = \left(\frac{2\pi}{\lambda_{oil}} - \frac{2\pi}{\lambda_{air}}\right) \cdot d = \left(\frac{2\pi}{\lambda_{air}} \cdot \sqrt{\varepsilon_r} - \frac{2\pi}{\lambda_{air}}\right) \cdot d = \\ = \frac{2\pi}{\lambda_{air}} \cdot \left(\sqrt{\varepsilon_r} - 1\right) \cdot d \tag{1}$$

where λ_{air} is the wavelength in air, and d is the thickness of the sample.

Choosing a thickness d < λ avoids phase ambiguity because it ensures the measured phase shift remains within the principal value range [0, 2π], preventing aliasing.

This allows a unique correspondence between the phase delay and the dielectric constant, avoiding multiple valid solutions due to phase wrapping.

From this equation, the dielectric constant ε_r can be extracted and calculated.

$$\varepsilon_r = \left(1 + \frac{|\Delta\phi| \cdot \lambda_{air}}{2\pi \cdot d}\right)^2 \tag{2}$$

Using Eq. (2), the dielectric constant of the samples under test was calculated as a function of frequency over a broadband range (1–2 GHz), showing an increasing trend as the oil degrades (Fig. 4a). To provide a more precise quantification, a narrowband calculation, around the antenna working frequency of ~1.56 GHz, was also performed, as illustrated in Fig. 4b, where the phase difference between the oil measurements and the free-space reference is shown for the fresh oil and the three degraded samples.

Figure 4c displays the corresponding dielectric constant values.

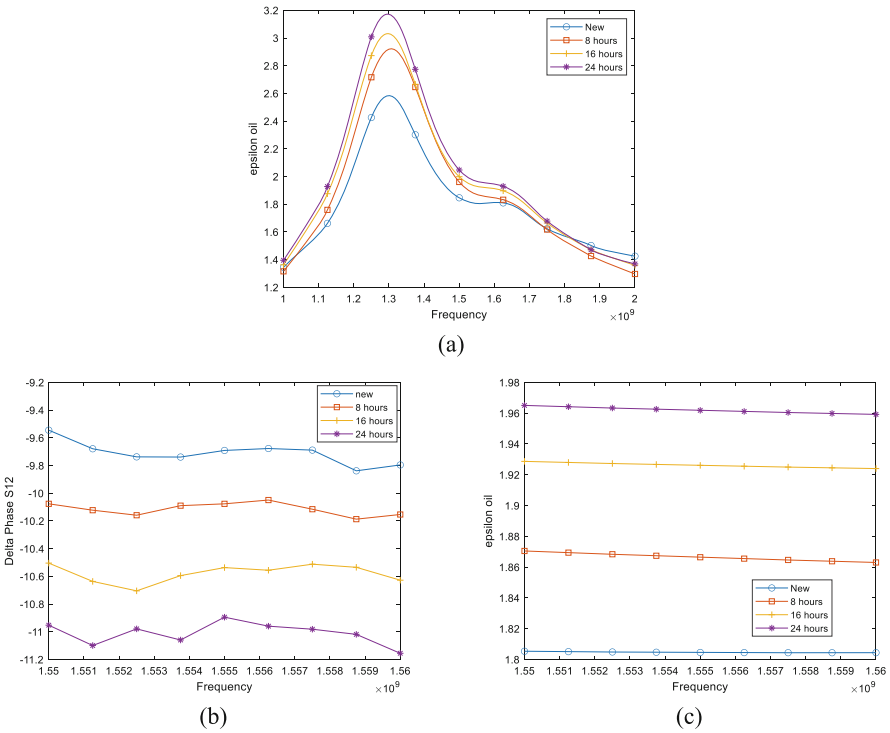

Fig. 4. (a) Dielectric constant of the samples under test calculated as a function of frequency over a broadband range (1–2 GHz), (b) phase difference (sample-freespace) ΔΦ of the transmission signal S_{12} of the fresh, 8 h, 16 h and 24 h degraded oil, (c) dielectric constant of the samples, retrieved using Eq. (2).

The results show an increasing trend of the permittivity constant as the oil degrades, aligning with existing literature. The observed increase in permittivity with aging can be attributed to the formation of oxidation by-products, such as acids, aldehydes and ketones, which introduce polar molecules into the oil,

4 Conclusion

In this paper, we studied mineral oil aging effects on the permittivity constant. Oil aging was emulated by heating fresh sample oils at 180 C for different times. The samples' transmission parameter was measured by free-space microwave transmission measurements, and the samples' permittivity was calculated using the measured S_{12} paramters. The results confirm that aging affects the dielectric properties of mineral oil and this is reflected in changes of the permittivity constant of the oil. The findings support the feasibility of free-space microwave transmission measurements as a non-invasive diagnostic tool for assessing the health of lubricating oils. The set up developed allows simple in-situ analysis that does not requires specialized personnel to be run.

References

1. Abner YEJr (1983) Lubricant degradation in service. In: Booser, E.R. (ed.) CRC Handbook of Lubrication: Theory and Practice of Tribology, vol I, pp 517–530. CRC Press
2. https://www.machinerylubrication.com/Read/475/oil-breakdown
3. Pérez AT, Hadfield M (2011) Low-cost oil quality sensor based on changes in complex permittivity. Sensors 11:10675–10690. https://doi.org/10.3390/s111110675
4. Loiselle L, Rao UM, Fofana I (2020) Influence of aging on oil degradation and gassing tendency for mineral oil and synthetic ester under low energy discharge electrical faults. Energies 13:595. https://doi.org/10.3390/en13030595
5. Zhu J, He D, Bechhoefer E (2013) Survey of lubrication oil condition monitoring, diagnostics, and prognostics techniques and systems. J. Chem. Sci. Technol. 2(3):100–115
6. Guan L et al (2011) Application of dielectric spectroscopy for engine lubricating oil degradation monitoring. Sens Actuators A Phys 168:22–29. https://doi.org/10.1016/j.sna.2011.03.033
7. European Patent EP 3417273 B1. (2023) Method and system for in-situ identification of working fluids. European Patent Office
8. Aljohani OM, Abu-Siada A (2015) Impact of power transformer insulating mineral oil degradation on FRA polar plot. In: Proc IEEE Int Symp Industrial Electronics (ISIE), pp [insert page numbers if available]
9. Sigma-Aldrich: Oil data sheet. https://www.sigmaaldrich.com/IT/it/sds/sigma/m5904

A Wireless, RFID-Based Solution for Hydrogen Sensing

T. Polichetti[1(✉)], E. Massera[1], B. Alfano[1], M. L. Miglietta[1], R. Parente[2], F. P. Monaco[2], M. Consales[2], A. M. Cusano[2], A. Micco[2], G. Quero[2], and A. Cusano[2]

[1] ENEA Research Center, Piazzale E. Fermi, 1, 80055 Portici, Naples, Italy
tiziana.polichetti@enea.it

[2] Centro Regionale Information Communication Technology (CeRICT Scrl), Via Traiano, Benevento, Italy

Abstract. Hydrogen is a versatile energy carrier which has gained significant attention in different fields. Because of its flammable nature, it necessitates robust safety measures, including reliable hydrogen sensors. These devices play a crucial role in monitoring hydrogen concentration, preventing accidents, and ensuring operational efficiency. The application scenario described in the following study involves a network for transporting and distributing methane/hydrogen mixtures. The project aims to equip this network with a series of completely passive sensors that are distributed extensively. This setup is intended to enable rigorous monitoring during storage, transportation, and distribution of hydrogen, particularly in natural gas networks where hydrogen is utilized as a transition gas or additive.

Keywords: Hydrogen Sensing · RFID-based sensor · Graphene-platinum chemo-resistor · Wireless gas monitoring · Passive sensor platform · UHF RFID technology

1 Introduction

Accurate and safe hydrogen monitoring is critical in various sectors (industrial, energy, chemical, electronic) due to its flammable nature [1]. Recent advancements have significantly improved sensor sensitivity, response times, and selectivity [2]. Concurrently, RFID (Radio-Frequency Identification) technology has emerged for automatic identification and tracking. Traditionally used in logistics and access control, RFID is evolving to integrate sensing functionalities, meeting the demand for wireless, low-cost, and often battery-less solutions [3]. This work presents a novel hydrogen sensing platform Ultra High Frequency (UHF) RFID combined with a chemo-resistive sensing element based on graphene flakes decorated with platinum nanoparticles (Gr-Pt). The sensor is integrated directly into the analog interface of the RFID chip, enabling direct hydrogen concentration measurement via DC resistance. This direct and practical approach is ideal for environmental and safety monitoring, being easily interrogated by standard RFID readers.

C. Di Natale et al. (Eds.): AISEM 2025, LNEE 1497, pp. 53–57, 2025.
https://doi.org/10.1007/978-3-032-08271-8_9

2 Experimental

The sensing element comprises graphene flakes decorated with platinum nanoparticles (Gr-Pt). The Gr-Pt material was synthesized by first preparing graphene flakes dispersion via graphite exfoliation in an eco-friendly water/isopropanol solvent [4]. A composite dispersion was prepared by mixing 0.02 g of $PtCl_2$ with 10 mL of a graphene suspension and 4 ml of aqueous solution of sodium dodecyl sulfate (SDS, at 1 mg/ml). The mixture was treated in ultrasonic bath at 60 °C for 2 h. The solid residue was then collected by centrifugation and washed three times with MilliQ water. Morphological characterization was carried out using field-emission scanning electron microscopy (FE-SEM) coupled with energy-dispersive X-ray spectroscopy (EDX) (LEO 1530–2, operated at an acceleration voltage of 5 kV).

Chemoresistive device was realized by drop-casting Gr-Pt dispersion onto alumina substrate where five pairs of gold interdigitated electrodes (fingers 350 μm wide, 4650 μm long and 350 μm spaced) are printed.

The sensing element was interfaced with the Asygn AS3212 RFID chip, which enabled passive, wireless data acquisition via the EPC Gen2 protocol. Gain control on the chip (G = 2–20) allowed for the optimization of the sensor's dynamic range and readout sensitivity.

Hydrogen sensing performance was investigated in a custom-built controlled atmosphere chamber, employing pre-mixed hydrogen containing gas blends. Measurements were conducted under precisely regulated flow rates and environmental parameters to ensure repeatability and accuracy.

3 Results

Scanning electron microscopy analysis of the Gr-Pt film revealed a microstructure consisting of graphene flakes with lateral dimensions ranging from 200 to 400 nm, decorated with platinum nanoparticles (<10 nm) and sparse aggregates (Fig. 1 on the left). Energy-dispersive X-ray spectroscopy confirmed the elemental composition, detecting the presence of carbon and platinum, as well as silicon attributed to the underlying substrate (Fig. 1 on the right).

The hydrogen sensing performance of the Gr-Pt film was primarily evaluated by exposing the chemoresistive device to 25000 ppm of H_2 at 50% relative humidity and at room temperature, under a constant applied bias of 1 V.

The chemoresistive sensor exhibited a baseline resistance of approximately 22 kΩ, increasing to ~30 kΩ upon exposure to 25000 ppm of H_2, followed by a near-complete baseline recovery within the time window of the measurement protocol (see Fig. 2).

Prior to interfacing the sensing device with the Asygn AS3212 RFID chip [5], reported in Fig. 3 on the right, functional simulations of the platform were conducted using reference resistors to emulate the two limiting resistance states of the sensor, namely, the baseline value R_0 and the maximum resistance R_{sense} observed upon hydrogen exposure. The resistive network connected to the chip pins is in a half-bridge configuration, with a 24 kΩ reference resistor and a commercial resistance to be measured. 22 kΩ (simulating hydrogen absence) and 33 kΩ (simulating hydrogen saturation) resistors were used (Fig. 3 on the left).

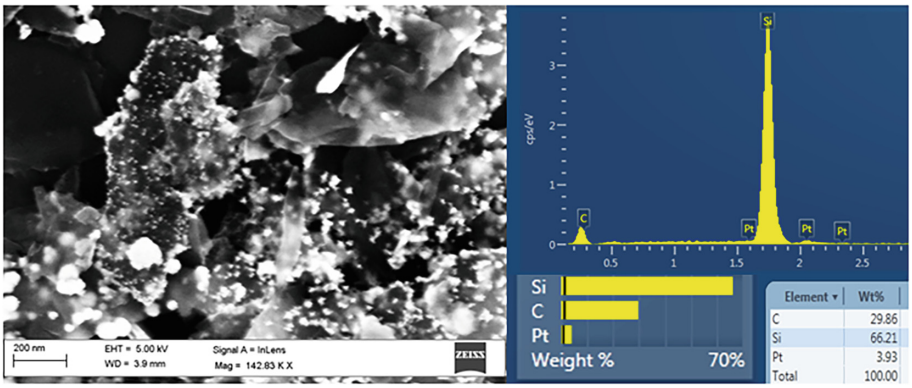

Fig. 1. SEM image of graphene flakes coated with Pt NPs on the left (confirmed via EDX analysis on the right).

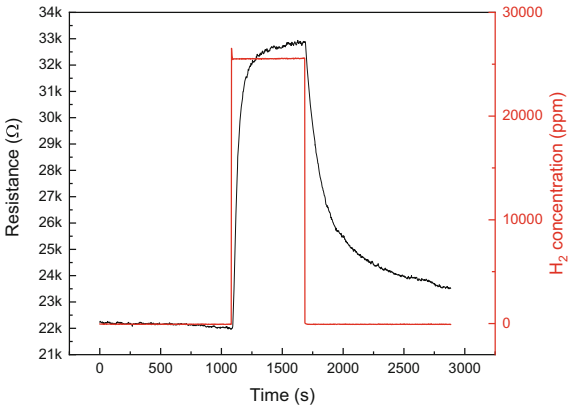

Fig. 2. Dynamic response of the Gr-Pt based chemoresistor.

Fig. 3. On the left, half bridge employed to simulate the sensor behavior ($R_0 = 27$ kΩ $R_{sense} =$ 22 kΩ, 33 kΩ); on the right, the Asygn AS3212 RFID chip.

The ADC's dynamic response of the RFID chip was optimized by adjusting the gain parameter (G = 1–20) to match the resistance range of the sensing element. External sensor acquisition was enabled, and measurements were performed at discrete gain values (G = 1, 2, 10, and 20). At G = 1, the output signal exhibited minimal variation (~50 units). Increasing the gain to G = 2 expanded the output range to 450–580, while

G = 10 further extended the dynamic range to approximately 600 units (200–800). At G = 20, the full output scale of the RFID chip (0–1023) was utilized, confirming that gain tuning enables complete exploitation of the sensor's dynamic range (Fig. 4).

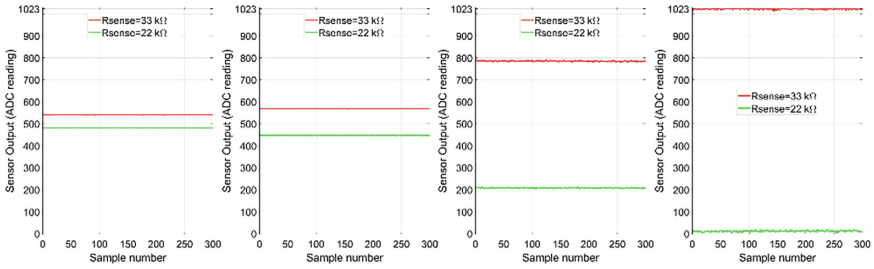

Fig. 4. Emulation of the chip output signal through commercial resistors: the 4 tests were carried out by varying the gain G of the tag chip from 1 to 20.

Following parameter optimization, the Gr-Pt-based chemoresistor was integrated into the wireless platform, and the complete device was subjected to the same testing protocol previously applied to the standalone chemoresistor. As shown in Fig. 5b), the signal transmitted by the wireless system (red curve) closely tracks the hydrogen concentration profile within the test chamber (black curve), demonstrating reliable signal correspondence.

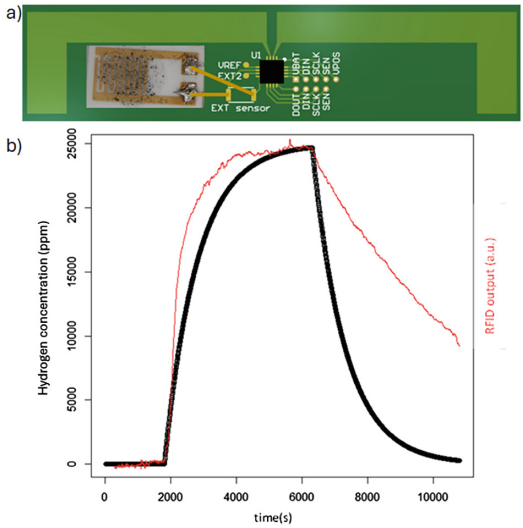

Fig. 5. a) Designed UHF GEN2 RFID tag, with pads for chemo-resistor connection; b) Kinetics of test chamber filling during H_2 injection (black curve) and corresponding sensor dynamic response (red curve).

Signal acquisition through the RFID interface demonstrated stable, linear behavior with increasing hydrogen concentration. Gain optimization enabled full exploitation of the chemoresistor's dynamic range, achieving a resolution of approximately 29.3 ppm per sensor output level at $G = 20$. Experimental validation using discrete resistors confirmed accurate emulation of both hydrogen-present and hydrogen-free environments.

4 Conclusions

A passive, wireless hydrogen sensor was developed by integrating a graphene–platinum (Gr-Pt) chemo-resistor with an RFID platform based on the Asygn AS3212 chip. The sensing material, deposited via drop-casting onto an alumina substrate, showed a reversible resistance response to hydrogen exposure. Direct integration with the RFID chip enabled battery-free detection and wireless readout via standard EPC Gen2 readers.

System performance was validated through simulations and experimental tests, confirming reliable operation and effective signal resolution. Gain tuning allowed full exploitation of the chip's dynamic range, with a sensitivity of ~29.3 ppm per ADC level at maximum gain. The device demonstrated stable and responsive behavior in controlled hydrogen environments, supporting its suitability for scalable, low-power gas monitoring applications.

Acknowledgement. This work was supported by the European Union–NextGenerationEU–M2C2 Investment 3.5 through the "Hydrogen Research and Development" Operational Plan (POR H2).

References

1. Calabrese M et al (2024) Hydrogen safety challenges: a comprehensive review on production, storage, transport, utilization, and CFD-based consequence and risk assessment. Energies 17(6):1350
2. Wang L, Song J (2024) Review—Recent progress in the design of chemical hydrogen sensors. J Electrochem Soc 171(1):017510
3. Costa F, Genovesi S, Borgese M, Michel A, Dicandia FA, Manara G et al (2021) A review of RFID sensors, the new frontier of internet of things. Sensors 21(9):3138
4. Fedi F et al (2015) A study on the physicochemical properties of hydroalcoholic solutions to improve the direct exfoliation of natural graphite down to few-layers graphene. Mater Res Express 2(3):035601
5. Asygn: https://asygn.com/as3212-external-resistive/. Last accessed 26 May 2025

Reusable *Lavandula multifida*-Based Fluorescent Platform for Ultra-Trace Mercury Detection in Seawater

Meryam Chelly[1,2(✉)], Sabrine Chelly[1,2], Angelo Ferlazzo[1,3], Hanen Bouaziz-Ketata[2], and Giovanni Neri[1]

[1] Department of Engineering, University of Messina, C.da Di Dio, 98166 Messina, Italy
chelly.meryam@gmail.com
[2] Laboratory of Toxicology-Microbiology Environmental and Health, LR17ES0, Faculty of Sciences, University of Sfax, Sfax, Tunisia
[3] Department of Chemical Sciences, University of Catania, Viale A. Doria 6, 95125 Catania, Italy

Abstract. *Lavandula multifida* (Lm), a Mediterranean aromatic plant, was investigated as a natural fluorescent sensor for mercury ion (Hg^{2+}) detection. The plant powder was characterized using Fourier Transform Infrared Spectroscopy (FTIR), confirming the presence of bioactive molecules like polyphenols, flavonoids, and terpenes. Aqueous extracts of Lm exhibited strong intrinsic fluorescence, which was efficiently quenched upon the addition of Hg^{2+} ions in seawater, demonstrating high sensitivity with a limit of detection (LOD) of 2.7 nM. A solid-state sensor was further developed by incorporating Lm extract into a Nafion/PET platform, retaining fluorescence properties and allowing visual detection of mercury via color change. These results highlight Lavandula multifida as a promising eco-friendly material for sensitive, selective, and real-time detection of mercury in environmental samples.

Keywords: *Lavandula multifida* · Fluorescent sensor · Mercury detection · Seawater analysis

1 Introduction

Mercury contamination poses significant risks to human health and marine ecosystems due to its toxicity, persistence, and bioaccumulation [1]. Detecting Hg^{2+} in complex environmental matrices like seawater is challenging, requiring methods that are both sensitive and selective. Traditional detection techniques—such as atomic absorption —often involve costly instrumentation and time-consuming procedures [2]. In this context, optical biosensors can offer a simple and low-cost alternative. In the last years, the use of natural dyes coming from plants has been proposed to make greener and more sustainable the production processes of optical sensors [3]. *Lavandula multifida* (Lm), a Mediterranean plant known for its rich content of bioactive compounds, is gaining attention in green chemistry and sustainable sensing. Recent studies have highlighted the

C. Di Natale et al. (Eds.): AISEM 2025, LNEE 1497, pp. 58–63, 2025.
https://doi.org/10.1007/978-3-032-08271-8_10

strong photoluminescent behavior of plant-derived materials, attributed to their natural fluorophores [4]. This work explores, for the first time, the use of Lavandula multifida as a dual-mode liquid and solid-state fluorescent sensor for mercury detection in seawater.

2 Materials and Methods

2.1 Plant Extraction and Characterization

Dried *Lavandula multifida* powder was infused in hot distilled water, filtered, and stored for fluorescence analysis [4]. Functional groups in the Lm powder were identified using FTIR spectroscopy [4].

2.2 Fluorescence Testing

The aqueous extract was tested under varying excitation wavelengths. Mercury sensing was performed by adding Hg^{2+} (0–10 nM) to seawater samples, followed by fluorescence quenching analysis. A solid-state sensor was developed by immobilizing the Lm extract onto a PET substrate using Nafion, enabling portable detection [4].

3 Results and Discussion

3.1 Characterization of *Lavandula Multifida*

3.1.1 FTIR Analysis

FTIR analysis of *Lavandula multifida* (Lm) powder (Table 1) revealed key functional groups, including O–H (3306 cm^{-1}), C–H (2932 cm^{-1}), CO_2 (2317 cm^{-1}), isothiocyanates (2083 cm^{-1}), C = C (1622 cm^{-1}), and C–O (1245, 1024 cm^{-1}), with a weak C–I band at 533 cm^{-1}. These indicate the presence of polyphenols, flavonoids, and terpenes—bioactive compounds with antioxidant and fluorescent properties. No toxic groups were detected, confirming Lm as a safe, green material for sustainable use [5, 6].

Table 1. FTIR assignments of *Lavandula multifida.*

Wavenumber (cm^{-1})	Functional group
533	C-I stretching (halo compound)
1024	C-O stretching
1245	C-O stretching (aromatic ester)
1395	O-H bending (carboxylic acid)
1622	C = C stretching (conjugated alkene)
2083	N = C = S stretching (isothiocyanate)
2317	O = C = O stretching (carbon dioxide)
2932	C-H stretching (alkane)
3306	O-H stretching (phenol)

3.2 Photoluminescence of *Lavandula Multifida* Aqueous Extract

The aqueous extract of Lm displayed characteristic fluorescence under various excitation wavelengths (Fig. 1). A redshift in the emission peak with increasing excitation wavelength suggests the presence of multiple fluorophores, each contributing differently to the emission profile. The dominant blue fluorescence (BF), with a maximum emission at 450 nm upon 390 nm excitation, was accompanied by a shoulder at ~530 nm corresponding to green fluorescence (GF). This spectral pattern is consistent with natural plant fluorophores, typically comprising polyphenolic compounds and other secondary metabolites [7, 8].

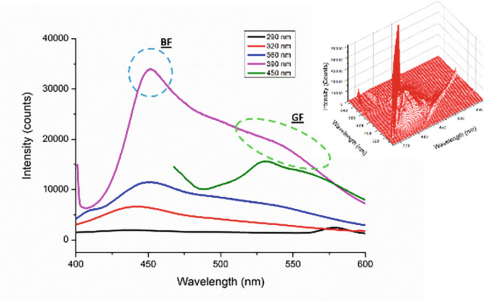

Fig. 1. Photoluminescence spectra of *Lavandula multifida* aqueous extract at various excitation wavelengths.

3.3 Mercury Detection in Seawater

Mercury detection in environmental samples is critical due to its toxicity and associated health risks. Various strategies have been developed for sensitive and selective mercury detection in complex matrices like seawater [9]. To assess the applicability of our liquid fluorescent sensor, we tested it on seawater samples. As shown in Fig. 2, Lm retained strong fluorescence in seawater (1V/1V), confirming its potential as a liquid-state sensor. To evaluate sensitivity, $Hg2^{+}$ ions were added at 1, 5, and 10 nM (Fig. 2a), resulting in progressive fluorescence quenching (Fig. 2b). A linear response was observed over 0–10 nM with a regression of $y = 279.41 + 500.71x$ (R2 = 0.97823) and a detection limit (LOD) of 2.7 nM. This LOD outperforms other reported liquid-state fluorescent sensors, such as those by Tümay Had et al. [10] (LOD = 3.65 nM), Karuk Elmas et al. [11] (8.12 nM), and Jia et al. [12] (53 nM). The enhanced sensitivity may be due to the high content of natural fluorescent polyphenols in *Lavandula* extracts [7, 8]. Additionally, our sensor achieved a recovery rate of 116.6% and a relative standard deviation (RSD) of 1.861% in mercury analysis.

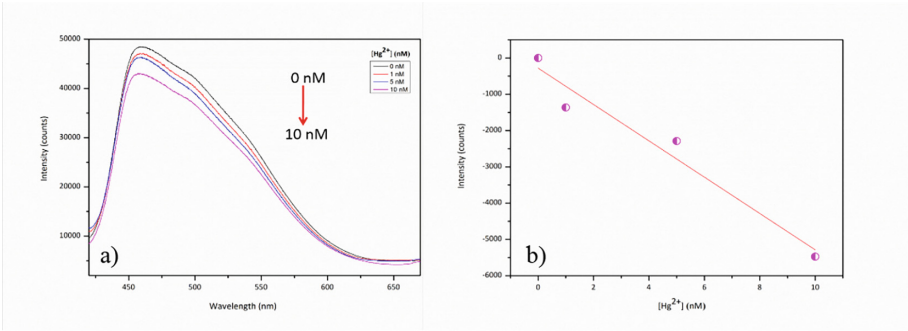

Fig. 2. (a) Fluorescence quenching of *Lavandula multifida* extract with increasing concentrations of $Hg2^{+}$ (0–10 nM) in seawater. (b) Linear relationship between fluorescence intensity and $Hg2^{+}$ concentration.

3.4 Solid-State Fluorescent Sensor

To facilitate the practical use, a solid-state sensor was fabricated by immobilizing Lm extract in a Nafion matrix on a PET substrate. Nafion's sulfonate groups promote strong interactions with polar components in the extract, while its transparency allows optimal fluorescence transmission. Under visible light, the sensor appeared yellow, while under UV (365 nm) it emitted strong blue fluorescence (Fig. 3), indicating successful retention of the photoluminescent properties of Lm in the solid state.

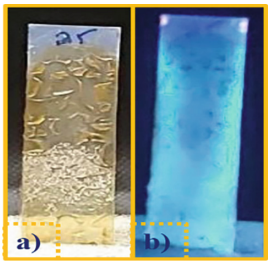

Fig. 3. *Lavandula multifida* sensor under visible and UV (365 nm) lights

The fluorescent mechanism in the present of mercury ions is shown in Fig. 4. Lm solid film was also tested for regenerating *Lavandula multifidia* sensor's sensitivity to mercury. After washing with water, Hg^{2+} was slightly stripped, and the surface of sensing film gets free of mercury (Fig. 4). The mercury has a particular binding to H_2O because of its coordination site (hydroxyl group). Therefore, the fluorescence intensity of Lm sensor is recovered and switched to the "on" state after adding water. These results demonstrate that the sensing film could be reused for more than one time.

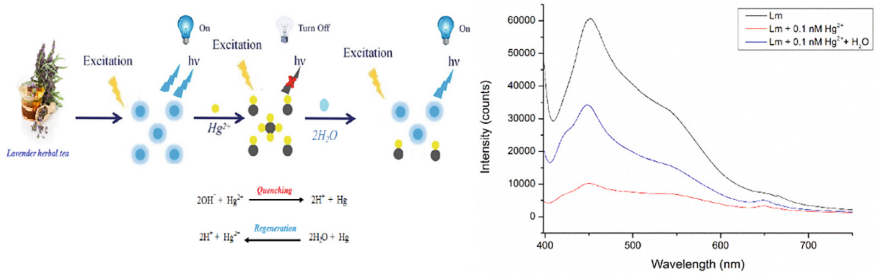

Fig. 4. *Lavandula multifidia* sensor mechanism and sensor regeneration.

4 Conclusion

This study demonstrates the potential of *Lavandula multifida* as a natural, eco-friendly fluorescent sensor for the ultra-trace detection of mercury ions in seawater. The aqueous extract exhibited strong intrinsic fluorescence, which was highly sensitive to Hg^{2+} quenching, achieving a low detection limit of 2.7 nM. Incorporation into a solid-state Nafion/PET platform enabled portable and visual mercury detection while retaining photoluminescent properties. Notably, the sensor showed regeneration after water treatment, suggesting its potential for a reuse. These findings highlight *Lavandula multifida* as a promising candidate for sustainable, low-cost, and regenerative optical sensing of mercury in environmental monitoring applications.

Acknowledgements. This work was partially supported by the European Union (NextGeneration EU), project SAMOTHRACE (ECS00000022).

References

1. Morgado F et al (2021) Chronological trends and mercury bioaccumulation in an aquatic semiarid ecosystem under a global climate change scenario in the northeastern coast of Brazil. Animals 11(8):2402
2. Cinnirella S et al (2019) Mercury concentrations in biota in the Mediterranean Sea, a compilation of 40 years of surveys. Sci. Data 6(1):205
3. Chelly M et al: (2024) Fluorescent properties and detection of heavy metals of hydrochar samples obtained by hydrothermal carbonization of *Lavandula multifida* plant: a preliminary study. In: AISEM Annual Conference on Sensors and Microsystems, pp 132–139. Springer, Cham
4. Chelly M, Chelly S, Ferlazzo A, Neri G, Bouaziz-Ketata H (2024) *Lavandula multifida* as a novel eco-friendly fluorescent-blue material for mercury ions sensing in seawater at femto-molar concentration. Chemosphere 352:141409
5. Dhivya SM, Kalaichelvi K (2017) UV-Vis spectroscopic and FTIR analysis of Sarcostemma brevistigma, wight and Arn. Int. J. Herb. Med. 9(3):46–49
6. Dobros N, Zawada K, Paradowska K (2022) Phytochemical profile and antioxidant activity of *Lavandula angustifolia* and Lavandula x intermedia cultivars extracted with different methods. Antioxidants 11(4):711

7. Lopes CL et al: Phenolic composition and bioactivity of *Lavandula pedunculata* (Mill.) Cav. samples from different geographical origin. Molecules **23**(5):1037 (2018)
8. Kageyama A, Ueno T, Oshio M, Masuda H, Horiuchi H, Yokogoshi H (2012) Antidepressant-like effects of an aqueous extract of lavender (*Lavandula angustifolia Mill.*) in rats. Food Sci Technol Res **18**(3):473–479
9. Liu X, Wu Z, Zhang Q, Zhao W, Zong C, Gai H (2016) Single gold nanoparticle-based colorimetric detection of picomolar mercury ion with dark-field microscopy. Anal Chem 88(4):2119–2124
10. Tümay SO, Şanko V, Şenocak A, Demirbas E (2021) A hybrid nanosensor based on novel fluorescent iron oxide nanoparticles for highly selective determination of Hg^{2+} ions in environmental samples. New J Chem 45(32):14495–14507
11. Elmas SNK et al: (2020) A novel fluorescent probe based on isocoumarin for Hg^{2+} and Fe^{3+} ions and its application in live-cell imaging. Spectrochim Acta Part A Mol Biomol Spectrosc 224:117402
12. Jia P, Yang K, Hou J, Cao Y, Wang X, Wang L (2021) Ingenious dual-emitting Ru@UiO-66-NH_2 composite as ratiometric fluorescence sensor for detection of mercury in aqueous. J Hazard Mater 408:124469

Spirulina as a Natural Dye for Dual Colorimetric and Fluorescent Detection of Biomolecules

Sabrine Chelly[1,2(✉)], Meryam Chelly[1,2], Alberto Giacobbe[1], Fakher Frikha[3], Hanen Bouaziz-Ketata[2], and Giovanni Neri[1]

[1] Department of Engineering, University of Messina, C.da Di Dio, 98166 Messina, Italy
Sabrine.chelly@yahoo.com
[2] Laboratory of Toxicology-Microbiology Environmental and Health, LR17ES0, Faculty of Sciences, University of Sfax, Sfax, Tunisia
[3] Laboratory of Molecular and Cellular Screening Processes, Centre of Biotechnology of Sfax, University of Sfax, Sidi Mansour Road, P. Box 1177, 3018 Sfax, Tunisia

Abstract. Spirulina *platensis*, a microalga known for its bioactive pigments, presents an eco-friendly source of dyes with remarkable optical and fluorescent properties. This study investigates the dual-functionality of Spirulina-derived chlorophyll and phycocyanin as natural dyes for the selective and sensitive detection of biomolecules. The pigments were extracted and analyzed using UV-Vis, FTIR, and photoluminescence spectroscopy, which highlighted their strong interactions with riboflavin (vitamin B2). Both the intrinsic fluorescence and colorimetric responses of the dyes enabled dual-mode detection, with results confirmed using a portable platform. The findings emphasize the significant role of Spirulina-derived compounds in biosensing applications, demonstrating that these natural dyes offer an affordable, sustainable, and effective alternative to synthetic dyes. The dyes' sensitivity to riboflavin and their ability to function in both fluorescence and colorimetric modes make them promising candidates for various applications, including diagnostics and environmental monitoring. Spirulina-based dyes provide an innovative solution in green sensing technology, prioritizing sustainability without compromising performance. This work contributes to the growing trend of utilizing natural, renewable materials in the development of sustainable sensing platforms, offering a path toward more environmentally friendly biosensing and diagnostic solutions.

Keywords: Spirulina platensis · phycocyanin · chlorophyll · natural dyes · fluorescence sensing · riboflavin

1 Introduction

Spirulina platensis, a blue-green microalga, has garnered increasing attention due to its unique bioactive compounds, notably phycocyanin and chlorophyll, which possess strong colorimetric and fluorescent properties [1]. These natural pigments offer a sustainable, biocompatible, and efficient alternative to synthetic dyes in sensing applications. Their optical characteristics i.e. intense absorption in the visible range and distinct fluorescence, make them excellent candidates for biosensing platforms [2].

C. Di Natale et al. (Eds.): AISEM 2025, LNEE 1497, pp. 64–68, 2025.
https://doi.org/10.1007/978-3-032-08271-8_11

In this study, we introduce a novel, eco-friendly approach to biomolecule detection using a dual-mode (colorimetric and fluorescent) sensing system that exploits the photophysical behavior of Spirulina-derived dyes. Unlike traditional detection methods requiring complex instrumentation, our approach emphasizes natural materials as functional elements, with the sensing readout conveniently visualized via a smartphone interface. We demonstrate this strategy through the sensitive detection of riboflavin (RF), an essential biomolecule, by leveraging the optical response of Spirulina pigments.

2 Materials and Methods

2.1 Chemicals and Materials

Spirulina platensis was sourced from the Pasteur Institute, France. Riboflavin and all other reagents were of analytical grade and used as received. Distilled water was obtained from a Millipore purification system.

2.2 Cultivation and Processing of Spirulina

Cultivation of Spirulina was conducted at AlGreen Tunisia Farm under optimized conditions. After harvesting, the biomass was processed into flakes or powder for characterization and dye extraction.

2.3 Characterization of Spirulina-Derived Pigments

The extracted Spirulina biomass was characterized using UV-Vis spectroscopy, Fourier transform infrared (FTIR) spectroscopy, and photoluminescence spectroscopy [3].

3 Results and Discussion

3.1 Structural and Chemical Characterization

FTIR analysis highlighted the presence of characteristic bonds such as O–H, C–H, C = C, and C–O, which support the strong optical behavior of the extracted dyes. These functional groups play a crucial role in the photoluminescent efficiency of Spirulina (Fig. 1) [3].

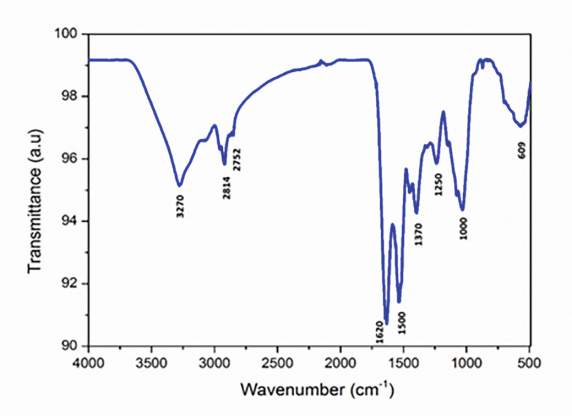

Fig. 1. ATR-FT-IR pattern of *Spirulina platensis.*

3.2 Optical Response of Spirulina to Riboflavin

UV-Vis spectra of Spirulina extracts displayed peaks associated with aromatic systems and phycocyanin at ~600 nm, confirming the presence of active chromophores (Fig. 2).

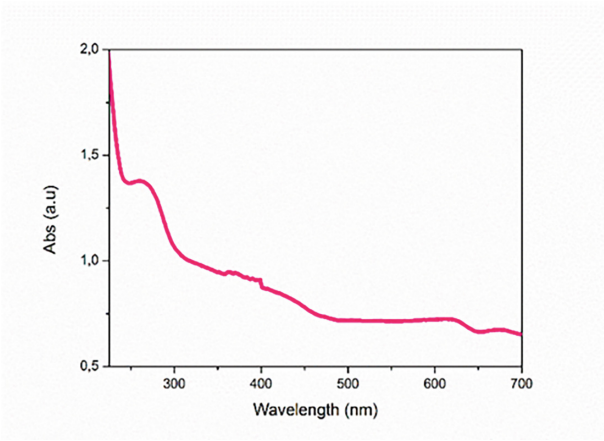

Fig. 2. UV–Vis absorption of *Spirulina platensis.*

Upon addition of riboflavin, a visible color shift and enhanced fluorescence were observed, with no significant response from other biomolecules or metal ions, indicating high selectivity. Spirulina exhibited a distinct fluorescent response under UV excitation at 365 nm. Fluorescence measurements showed that riboflavin uniquely intensified the emission spectrum, underscoring its potential as a specific probe in biosensing applications (Fig. 3).

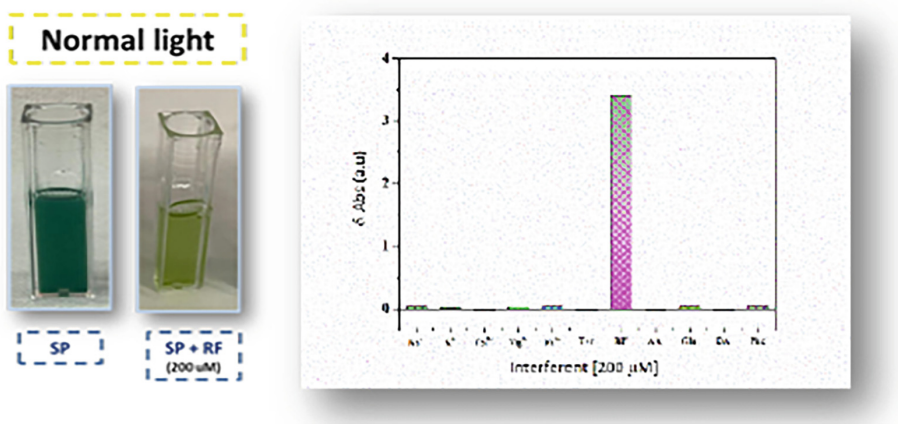

Fig. 3. Colorimetric tests under visible light of *Spirulina platensis* in absence and in the presence of RF and other metal ions and biomolecules.

3.3 Smartphone-Enabled Optical Sensing: Demonstrating Spirulina's Sensing Capabilities

To validate the practical application of Spirulina-derived pigments, we integrated them into a simple smartphone-assisted optical sensing setup. The portable device comprised basic light sources (white and UV LEDs) and an RGB color sensor interfaced with a microcontroller [4, 5]. The smartphone served only as a visualization and data interface, while the dyes from Spirulina provided the functional detection capability (Fig. 4).

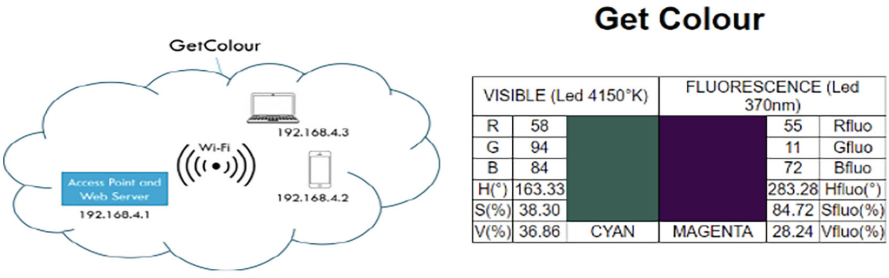

Fig. 4. Architecture of the detection system with the associated "GetColour" Wi-Fi network, for in field and real time tests.

Calibration curves generated for riboflavin showed distinct linear responses in both the RGB colorimetric parameters and fluorescence intensity. The detection relied solely on the interaction between riboflavin and the Spirulina dyes, confirming that Spirulina pigments can serve as powerful and selective natural probes in bioanalytical platforms (Fig. 5).

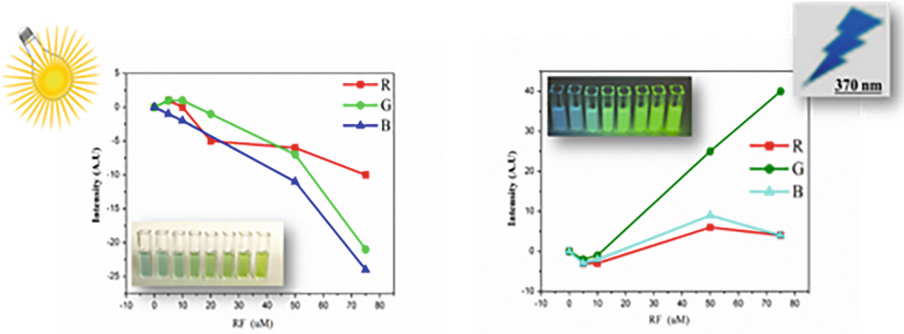

Fig. 5. Colorimetric and fluorescent calibration curves for RF, by reporting the values of the R, G, and B parameters acquired by the developed optical platform.

4 Conclusion

This work highlights the central role of Spirulina-derived pigments as effective and sustainable optical probes for the detection of biomolecules such as riboflavin. Their strong and selective optical responses, combined with easy integration into simple optical systems, offer a compelling alternative to synthetic sensing elements. The success of this Spirulina-based strategy in a smartphone-compatible platform underscores its potential for portable, eco-friendly, and cost-effective biosensing applications.

Acknowledgements. This work was partially supported by the European Union (NextGeneration EU), project SAMOTHRACE (ECS00000022).

References

1. Prasanna R, Sood A, Suresh A, Nayak S, Kaushik B (2007) Potentials and applications of algal pigments in biology and industry. Acta Bot Hung 49(1–2):131–156
2. Allouzi MMA et al (2022) Current advances and future trend of nanotechnology as microalgae-based biosensor. Biochem Eng J 187:108653
3. Chelly M, Chelly S, Ferlazzo A, Neri G, Bouaziz-Ketata H (2024) *Lavandula multifida* as a novel eco-friendly fluorescent-blue material for mercury ions sensing in seawater at femto-molar concentration. Chemosphere 352:141409
4. Chandra Kishore S et al (2022) Smartphone-operated wireless chemical sensors: a review. Chemosensors 10:55
5. Lu W et al (2023) Smartphone-assisted colorimetric sensing platform based on molybdenum-doped carbon dots nanozyme for visual monitoring of ampicillin. Chem Eng J 468:143615

Biosensors and Medical Devices

Point-of-Care Sensor for the Electrochemical Detection of miRNA Biomarker of Alzheimer's Disease

G. Bella[1(✉)], E. L. Sciuto[1], N. Yadav[2], P. Calorenni[1], A. Giacobbe[1], L. M. De Plano[1], S. Oddo[1], C. Potrich[2], L. Lorenzelli[2], A. A. Messina[3], M. Chelly[4], G. Neri[4], and S. Conoci[1,5]

[1] Department of Chemical, Biological, Pharmaceutical and Environmental Sciences, University of Messina, V.le Ferdinando Stagno d'Alcontres, 31, Messina, Italy
gbella@unime.it
[2] Center for Sensors & Devices (SD), FBK—Foundation Bruno Kessler, Via Sommarive 18, 38123 Trento, Italy
[3] STMicroelectronics, Stradale Primosole 50, Catania, Italy
[4] Department of Engineering, University of Messina, C. da Di Dio, 98166 Messina, Italy
[5] Department of Chemistry "Giacomo Ciamician", University of Bologna, Via Selmi 2, 40126 Bologna, Italy

Abstract. The analysis of microRNA (miRNA or miR-) expression profile is very appealing in the biomedical field since it allows to explore at a molecular level the onset and progression of different human diseases. Numerous miRNAs in literature have been identified as important biomarkers of a series of neurological disorders mostly concerning Alzheimer's disease (AD), the most diffused neurodegenerative disorder having a tremendous impact on our society. So far, there is no evidence of accurate, sensitive, and non-invasive diagnostic solutions able to provide precise diagnosis and adequate therapies. The study of miRNA profiles, however, opens towards a new frontier of diagnostics by which it would be possible to screen and predict AD at an early stage, making therapies more effective against the pathological onset. Moreover, the importance of using miRNAs as biomarkers is exploited by the fact that many of them are free to circulate in the bloodstream, thus, simplifying the genetic material extraction and facilitating the sensing technology integration into PoC devices and opening to the possibility of decentralizing AD screening. In this work, we present the development and characterization of a portable electrochemical sensor for the accurate and sensitive detection of a microRNA associated with the human AD, in a Point-of-Care (PoC) format.

Keywords: microRNA · thiolate probes · electrochemical impedance spectroscopy · Alzheimer's disease · PCR-free detection · PoC applications

C. Di Natale et al. (Eds.): AISEM 2025, LNEE 1497, pp. 71–75, 2025.
https://doi.org/10.1007/978-3-032-08271-8_12

1 Introduction

MicroRNAs (miRNAs) are small non-coding RNAs, of 18 to 24 nucleotides, that play a crucial role in regulating mRNA translation [1]. They are essential in various biological processes such as apoptosis, proliferation, and differentiation [2]. In the nervous system miRNAs influence neuronal patterning, synaptogenesis, neuronal plasticity, and the progression of neurodegeneration [3, 4], as in the case of Alzheimer's disease (AD). This is a widely diffuse complex age-related condition that causes a progressive neurodegeneration, (especially dementia cases) representing a significant contributor to mortality and disability among older populations [5]. The current methods for AD screening are precarious, costly and limited to the advanced stage of the disorder making curative or preventive treatments ineffective and highlighting the crucial need for the development of low-cost, non-invasive biomarkers [6]. In this perspective, given their key function in modulating gene expression, miRNAs have emerged as potential biomarkers for AD, especially those that circulate in various bodily fluids such as plasma, serum, and cerebrospinal fluid [7]. These characteristics simplify miRNAs extraction and detection, making them suitable candidates for non-invasive and early diagnosis of AD. Additionally, miRNAs are stable and resistant to RNase degradation, maintaining their integrity even after prolonged storage, exposure to high temperatures, extreme pH levels, or undergoing multiple freeze-thaw cycles [1]. With these premises, we developed an electrochemical sensor for AD-associated miRNAs detection. As a use-case target, we selected miR-146a, whose dysregulation can affect neuronal apoptosis, inflammation and Aβ metabolism in AD [8, 9]. The sensing system hinges on an electrochemical chip integrating three micro-fabricated electrodes of which the working one (WE) has been functionalized with oligonucleotide probes selective for miR-146a. The chip combines the electrochemical impedance spectroscopy (EIS)-based detection with a PCR-free approach for the fast and accurate detection of miRNA target without its long and expensive amplification [10, 11], making the AD screening more accessible and suitable for PoC diagnostic applications.

2 Results and Discussion

The fabricated sensor chip consisted of 3 micro-electrodes arranged in a concentric circle geometry with a platinum working electrode (WE) placed in the center and a gold reference (RE) and counter (CE) electrodes placed around it. The WE was used as the sensing surface, schemed in Fig. 1a. The WE surface was functionalized as schemed in Fig. 1b, c and d.

More precisely, an array of thiol-modified oligonucleotide probes, selective for the miR-146a target, was anchored onto of the platinum surface of the WE and used to capture the miRNA target via direct on-chip DNA-RNA hybridization, without the need for any pre-amplification of the miRNA, as is required by commercial RT-PCR-based diagnostic kits. This PCR-free approach simplifies the time and costs of analysis, promoting the sensor's suitability for PoC applications and enabling the decentralization of AD screening.

The WE surface functionalization for miR-146a sensing has been validated via contact angle and surface free energy (SFE) analysis, which reported an increase in surface

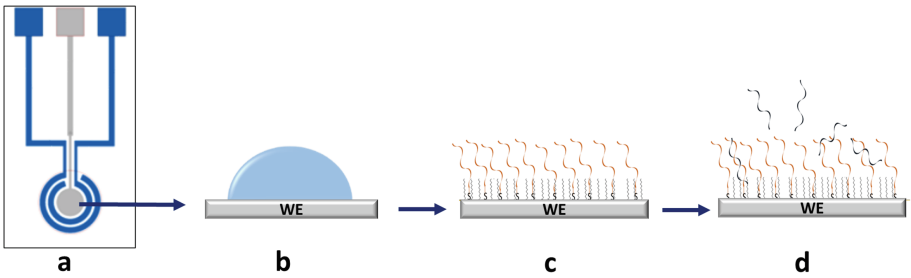

Fig.1. (a) Electrochemical chip. Chemical functionalization of WE surface for miRNA detection: (b) surface cleaning; (c) probes anchoring; (d) miRNA hybridization.

wettability and polarity, consistent with the anchoring of probes and miRNA. The sensing tests, instead, were performed by detecting the hybridized miRNA via Electrochemical Impedance Spectroscopy (EIS) and cyclic voltammetry (CV). These were done by spotting a few drops of an electro-active analyte on top of the functionalized WE of the chip into a properly assembled analytical system.

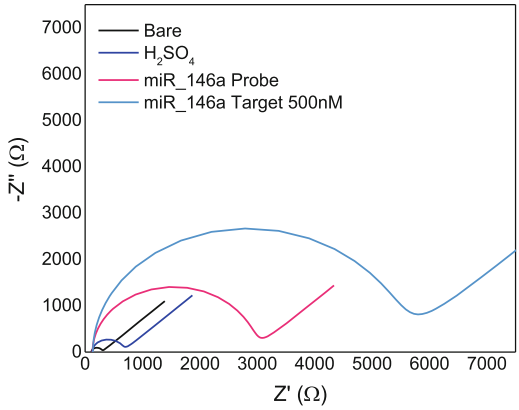

Fig. 2. EIS qualitative analysis of miRNA: comparison of resistances measured on bare (black line), cleaned (blue line), probe grafted (magenta line) and the miRNA hybridized (light blue line) chip.

Results, summarized in the Nyquist plot of Fig. 2, reported a very high level of sensitivity for miR-146a with a progressive increment of the measured impedance after the duplex formation (light blue line), which allowed qualitative and accurate discrimination of the target's presence without PCR amplification.

3 Conclusions

A PoC sensor for the electrochemical PCR-free detection of miRNA146a as a biomarker for AD screening has been presented. The results spotlighted the effective functionalization of probes on the sensor surface and the capture and recognition of the miRNA

targets without any time-/cost- consuming amplification by RT-PCR. Moreover, the miniaturized dimensions of the sensor support its suitability for decentralized diagnostic applications.

4 Methods

4.1 WE Functionalization

The chip WE functionalization was performed (exploiting the chemical reactivity of sulfur pendants toward platinum [12, 13]) in drop-casting mode, after a cleaning step with H_2SO_4. Subsequently, thiol-modified probes and a passivating thiolate molecule were grafted on the top of the WE surface to form a self-assembled monolayer for hybridization with the miRNA target. Lastly, functionalized WE was exposed to 40 μL of synthetic miR-146a for the perfect match hybridization. The PCR-free detection of miRNA target was carried out by using an electro-active analyte $[Fe(CN)_6]^{3-}$ that triggered a current signal, detected by EIS analysis.

4.2 EIS Measurements

For the EIS measurements, the electrochemical chip was spotted with a solution of 5 mM of $[Fe(CN)_6]^{-3/-4}$ in PB, used as redox mediator. Measurements have been done at 100 kHz to 0.1 Hz frequency range and 1mA current.

Fundings. This work has been funded by the European Union (NextGeneration EU) through the MUR-PNRR project SAMOTHRACE (ECS00000022).

References

1. Zhao Y, Zhang Y, Zhang L, Dong Y, Ji H, Shen L (2019) The potential markers of circulating microRNAs and long non-coding RNAs in Alzheimer's disease. Aging Dis 10(6):1293–1301
2. Congur G, Erdem A (2019) PAMAM dendrimer modified screen printed electrodes for impedimetric detection of miRNA-34a. Microchem J 148:748–758
3. Nunomura A, Perry, G, Izadpanah E (2020) RNA and oxidative stress in Alzheimer's disease: focus on microRNAs, Oxid Med Cell Longev pp 1–16
4. Wu Y, Li Q, Zhang R, Dai X, Chen W, Xing D (2021) Circulating microRNAs: biomarkers of disease. Clin Chim Acta 516:46–54
5. Wong W (2020) Economic burden of Alzheimer disease and managed care considerations. Am J Manag Care 26:177–183
6. Song Z et al (2021) Microarray microRNA profiling of urinary exosomes in a 5XFAD mouse model of Alzheimer's disease. Anim Models Exp Med 4(3):233–242
7. Galimberti D et al (2014) Circulating miRNAs as potential biomarkers in Alzheimer's disease. J. Alzheimers Dis. JAD 42(4):1261–1267
8. Li Y, Fu Q, Guo M, Du Y, Chen Y, Cheng Y (2024) MicroRNAs: pioneering regulators in Alzheimer's disease pathogenesis, diagnosis, and therapy. Transl Psychiatry 14:367
9. Kou X, Chen D, Chen N (2020) The regulation of microRNAs in Alzheimer's disease. Front Neurol 11:288

10. Calorenni P et al (2023) PCR-Free innovative strategies for SARS-CoV-2 detection. Adv Healthc Mater 12:2300512
11. Nikolaou P, et al.: (2022) Ultrasensitive PCR-Free detection of whole virus genome by electrochemiluminescence. Biosens. Bioelectron. **209**
12. Giannetto A, Nastasi F, Puntoriero F, Bella G, Campagna S, Lanza S (2021) Fast transport of HCl across a hydrophobic layer over macroscopic distances by using a Pt(II) compound as the transporter: micro- and nanometric aggregates as effective transporters. Dalton Trans 50:1422–1433
13. Bella G, Milone M, Bruno G, Santoro A (2022) Which DFT factors influence the accuracy of 1H, 13C and 195Pt NMR chemical shift predictions in organopolymetallic square-planar complexes? New scaling parameters for homo- and hetero-multimetallic compounds and their direct applications. Phys Chem Chem Phys 24:26642–26658

Emerging Biosensors for Detecting Marine Biotoxins in Mussels

M. Carbone[1], A. Szymczyk[1,2], G. Selvolini[1], and G. Marrazza[1(✉)]

[1] University of Florence, Via Della Lastruccia 3-13, 50019 Sesto Fiorentino, Italy
giovanna.marrazza@unifi.it
[2] Chair of Medical Biotechnology, Faculty of Chemistry, Warsaw University of Technology, Noakowskiego 3, 00-664 Warsaw, Poland

Abstract. Microalgae are one of the main problems in the management of marine resources around the world. Harmful algal blooms (HABs) have significantly impacted on marine ecosystems worldwide, affecting open ocean, deep sea, and coastal ecosystems. Phycotoxins are toxic compounds produced in large quantities during HABs, particularly accumulating in shellfish, and thus capable of entering the food chain. Consuming a sufficient amount of contaminated seafood may therefore lead to intoxication in humans. Biosensors play a crucial role as efficient and reliable analytical tools for the screening of these toxic compounds. This mini-review aims to summarize the latest advancements in biosensors for detecting marine biotoxins in mussels.

Keywords: Biotoxin · biosensor · phycotoxin · mussels

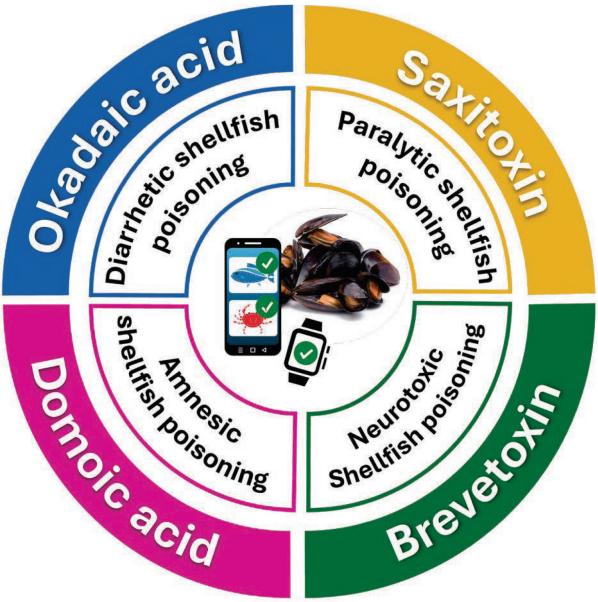

C. Di Natale et al. (Eds.): AISEM 2025, LNEE 1497, pp. 76–81, 2025.
https://doi.org/10.1007/978-3-032-08271-8_13

1 Introduction

Biotoxins are natural chemical compounds produced by certain organisms as a defense mechanism. Marine environments are often impacted by biotoxin contamination from specific types of algae such as phycotoxins, including *Karenia*, *Pseudo-nitzschia*, *Alexandrium*, *Dinophysis*, and *Gymnodinium spp.* [1].

During harmful algal blooms (HABs), high concentrations of phycotoxins in seawater can harm nearby organisms and the environment. These toxins accumulate in the tissues of marine animals, like bivalve mollusks and fish, posing a threat to human health [2]. Algal biotoxins are estimated to cause between 50,000 and 500,000 cases of foodborne illness worldwide each year, with a mortality rate of around 1.5% [3, 4].

Due to the common occurrence of mussel contamination and their widespread consumption, there is a growing need for rapid, cost-effective, and accessible contamination testing. Recently, biosensors have emerged as a valuable alternative to chromatographic methods and ELISA tests, which are commonly used for detecting marine biotoxins. The main benefits of biosensors include cost-effectiveness, time efficiency, and the capability to conduct on-site analyses while maintaining high accuracy. In this review, we examine the most recent advancements in biosensors for detecting four of the most frequently recurring phycotoxins in mussels.

1.1 Biosensors for Marine Biotoxins

Shellfish toxins are basically divided into five types according to their poisoning symptoms and mechanism of action, as listed below:

- paralytic shellfish poisoning (PSP) toxins, such as saxitoxin (STX) and gonyautoxin (GTX);
- diarrheic shellfish poisoning (DSP) toxins, such as okadaic acid (OA) and dinophysistoxin (DTX);
- neurotoxin shellfish poisoning (NSP) toxins, such as brevetoxins (BTX);
- amnesic shellfish poisoning (ASP) toxins, such as domoic acid (DA);
- azaspiracid shellfish poisoning (AZP) toxins, such as azaspiracids (AZAs).

In 2004, the joint Food and Agriculture Organization of the United Nations, World Health Organization and Intergovernmental Oceanographic Commission of UNESCO (FAO/IOC/WHO) expert meeting classified the shellfish toxins into eight groups based on their chemical structure, *i.e.*, saxitoxin (STX), brevetoxin (BTX), okadaic acid (OA), domoic acid (DA), azaspiracid (AZA), cyclic imines, pectenotoxin (PTX), and yessotoxin (YTX). In the following sections, we discuss the biosensors realized to detect phycotoxins classified as just explained.

1.1.1 Saxitoxins

Saxitoxin (STX) is a light carbamate alkaloid with a tetrahydropurine core. In marine environments, STX is produced by some species of dinoflagellates, such as *Protogonyaulax sp.* And *Coolia sp.,* and generally accumulates in the viscera and/or digestive glands of lobsters, carnivorous snails, crabs, and especially bivalve mollusks, which are

potent vectors to humans s [1, 3]. Currently, over 50 STX derivatives have been discovered. This group of molecules is well recognized for its neurotoxicity and its role in inducing PSP in humans, whose symptoms vary and can include nausea, vomiting, abdominal pain, among others. Additionally, individuals may experience neurological symptoms such as weakness, dizziness, dysarthria, paresthesia, double vision, and loss of coordination. In the most severe cases, symptoms progress rapidly to severe respiratory problems, which can ultimately lead to the patient's death [2, 5].

A bioassay for STX detection was developed by Wu L. et al. [6]. The assay was based on molecularly imprinted polymer (MIP), realized on Au-Pt nanoparticles-modified Fe_3O_4 magnetic nanozymes (MS@Au-Pt NZs). The MS@Au-Pt NZs catalyzed the oxidation of 3,3′,5,5′-tetramethylbenzidine (TMB). The cavities blocked by the STX analyte were unable to oxidize the TMB substrate. The oxidized TMB was measured using both a colorimetric assay and Raman spectroscopy. The results showed that linear ranges from 0.01 μM to 100 μM and 0.1 nM to 100 nM were retrieved for the two detection techniques, respectively, with limits of detection of 3.1 nM and 0.03 nM. The recoveries were between 78.0% and 92.6% and 86.0% and 96.2%.

Liu et al. [7] used a different method to develop an electrochemical sensor based on peptides. Glassy carbon electrodes (GCEs) were treated with reduced graphene oxide (rGO) and gold nanoparticles (AuNPs) in order to encapsulate a specific peptide (peptides/rGO-AuNPs/GCE). Differential pulse voltammetry (DPV), which was performed following an incubation with sample solutions, showed a decrease in the current signal when STX was present in the sample. The measured STX concentrations varied in the range 10–1000 ng/L, with a limit of detection (LOD) of 6.9×10^{-4} μg/L and a recovery rate of 87.3%–116.2%.

1.1.2 Brevetoxins

Brevetoxins (BTXs) are a class of chemicals that are primarily generated by the dinoflagellate *Karenia Brevis* and are distinguished by their lipophilic cyclic polyether structure. Because BTXs may be lethal to fish, aquatic mammals, and many other aquatic invertebrates, it is uncommon to find reports of BTXs buildup in fish and shellfish in the literature [1, 5]. The majority of recorded BTXs intoxications in humans were caused by the inhalation of aerosolized BTXs, instances of BTXs poisoning from eating tainted mussels, clams, and oysters have also been documented [8]. Human NSP, which is characterized by a collection of neurological and gastrointestinal symptoms such as nausea, vomiting, diarrhea, paresthesia, paralysis, seizures, coma, and, in severe instances, death, is caused by consuming a high enough concentration of BTXs [9].

A biosensor using biolayer interferometry (BLI) and a specific aptamer for BTX-1 as a recognition element was developed [10]. The biotinylated aptamer was immobilized onto the surface of streptavidin-coated sensor chips. When the toxin binds to the aptamer, it alters the thickness of the sensing layer, leading to a wavelength shift in the interferometry spectrum that correlates directly with the toxin concentration in solution. The aptasensor showed a linear response in the range from 100 nM to 2000 nM of BTX-1, with a limit of detection (LOD) of 4.5 nM. Furthermore, it did not recognize BTX-2 or other cyclic polyether marine toxins, demonstrating high specificity for BTX-1. Finally,

the recovery rates ranged from 104% to 108% in shellfish extracts, suggesting minimal interference from the shellfish matrix on the aptasensor response.

1.1.3 Okadaic Acid

Okadaic acid (OA) is a lipophilic molecule, member of a group of molecules called polyketides, characterized by a complex structure that includes multiple spiroketals along with fused ether rings. Mainly produced by dinoflagellates species belonging to the genus *Dinophysis*, *Prorocentrum*, and *Phalacroma*, OA enters the food chain by accumulating in the fatty tissues of fish and shellfish. Among the shellfish, mussels, clams, scallops, and oysters are the most common vectors [11, 12]. OA is the main toxin causing DSP in humans, with symptoms such as diarrhea, nausea, vomiting, and abdominal cramps, which typically appear from 30 min to a few hours after eating contaminated shellfish [8]. Although these symptoms are typically self-limiting and last for few days, there is a chance of more severe medical complications over time based on preliminary data [2].

An organic light-emitting diode (OLED)-based biosensor was developed, utilizing monoclonal antibodies as the recognition element [13]. The immunosensor was realized using a disposable plastic cartridge with a transparent polyethylene (PE) bottom part, to which the conjugate of OA and keyhole limpet hemocyanin (OA-mcKLH), a large, multisubunit, oxygen-carrying, metalloprotein, was attached: the antibody reaction was carried out using a sample mix of the mussel methanolic extract and the anti-okadaic acid monoclonal antibody (mAb-OA). When OA is present in the sample solution, it binds to mAb-OA, thereby preventing its binding to the OA-mcKLH immobilized on the bottom of the cartridge. Then, a second polyclonal antibody, specific for mAb-OA, attached with the fluorophore ATTO-430LS (PAb-430LS), an anionic dye, is fixed, and finally, fluorescence is detected. To analyze the results, the images were processed by setting a threshold to automatically find and measure the round glowing areas. The fluorescence intensity was determined by averaging the pixel values in the bright spots of the image. The biosensor showed its capability of detecting amounts as low as 60 μg/kg of toxin and up to 350 μg/kg.

Another approach for OA detection was adopted with an electrochemiluminescence (ECL)-based biosensor [14]. In this scenario, a microfluidic sensing chip based on aggregation-induced electrochemiluminescence (AIECL) was created, utilizing a hafnium-based metal-organic framework (Hf-MOF) derived from 4′,4″,4‴,4⁗-(ethene-1,1,2,2-tetrayl) tetrabiphenyl-4-carboxylic acid (TPE) as the emitter. Aptamers, linked to carboxylated magnetic beads (MB), are used as bioreceptors, and the specific recognition of OA leads to the beginning of catalytic hairpin assembly (CHA), activating clustered regularly interspaced short palindromic repetitions (CRISPR)-associated (Cas) systems. The activated CRISPR systems cleave the catalytic hairpin immobilized on the Hf-MOF, resulting in a "signal-on" state. This enables the establishment of a quantitative relationship between the concentration of OA and the difference in electrochemiluminescence (ECL) luminescence. The aptasensor showed a LOD of 1.61 ng/mL, a good response in the range of 5.0–1.5 $\times$ 10^4 ng/mL and a recovery rate in the range 96–101%.

1.1.4 Domoic Acid

Domoic acid (DA) is a water-soluble kainic acid-type neurotoxin, characterized by a cyclic tricarboxylic amino acid structure [1]. DA is primarily produced by the marine diatoms of the genus *Pseudo-nitzschia.* And has been detected in numerous bivalves and some other species, such as crabs, octopuses and fish [3]. Since DA mostly accumulates in the digestive tract of these species, hardly any or no toxin is usually found in tissues suitable for human consumption. Razor clams and scallops are significant vectors as they can retain the toxin for up to one year in the natural environment and even several years after processing, canning, or freezing [15]. DA poisoning is responsible for ASP, whose symptoms can range from gastrointestinal effects to neurological disorder signs and include nausea, vomiting, confusion, lethargy, disorientation, paresthesia, short-term memory loss, brain damage, leading to, in extreme cases, coma or death [3, 15].

A BLI-based aptasensor was developed for the detection of DA [16], utilizing streptavidin-coated sensors. The specific biotin-modified aptamers, selected through Capture-SELEX in vitro, were immobilized on the sensor surface, and, through the real-time monitoring of the optical interference signals, the response of the sensor to different DA concentrations was recorded. The BLI-based aptasensor had a process of detection that could be completed in 7 min, and displayed a linear range from 0.625 μM to 10 μM, with a LOD of 13.7 nM, demonstrating also high specificity and exhibiting good precision and repeatability. The aptasensor showed high recovery rates for real samples, ranging from 95% to 110%.

A different approach for DA detection was adopted with an electrochemical MIP sensor based on polydopamine-reduced graphene oxide/polyacrylamide composite (PDA-rGO/PAM), constructed on screen-printed electrode (SPE) [17]. Electrochemical impedance spectroscopy (EIS) and DPV techniques were applied to monitor the response towards domoic acid at SPE-MIP sensors under the optimal conditions. The sensor displayed a satisfactory response both in DPV and EIS results, with a linear range from 1 nM to 600 nM and a LOD of 0.31 nM, while recoveries rates ranges were 90–98% for DPV and 90–94% for EIS.

2 Conclusions

This mini-review presents the most important strategies applied for the detection of algal biotoxins in mussels developed in the last years. The mentioned biosensors were applied for the detection of STX, BTXs, OA and DA; all showing good analytical performances, with sensitivity, reproducibility and selectivity suited for accurate on-field analysis.

Acknowledgments. This project has received funding from the European Union's Horizon Europe program under grant agreement no. 101060712.

References

1. Dutta T, Mandal SK, Biswas JK (2025) Biosensors for the Detection of Biotoxins in Finfish and Shellfish. Biotoxins 27–53

2. Grattan LM, Holobaugh S, Morris JG Jr (2016) Harmful algal blooms and public health. Harmful Algae 57:2–8
3. Pinto A, Botelho MJ, Churro C, Asselman J, Pereira P, Pereira JL (2023) A review on aquatic toxins-do we really know it all regarding the environmental risk posed by phytoplankton neurotoxins? J. Environ. Manag. 345
4. Wang DZ (2008) Neurotoxins from marine dinoflagellates: a brief review. Mar Drugs 6(2):349–371
5. Nicolas J et al (2017) Marine biotoxins and associated outbreaks following seafood consumption: prevention and surveillance in the 21st century. Glob Food Sec 15:11–21
6. Wu L et al (2024) A dual-mode optical sensor for sensitive detection of Saxitoxin in shellfish based on three-in-one functional Nanozymes, J Food Compos Anal 130
7. Liu B, Chen L, Zhu Y, Zhao X, Wang H, Wang S (2024) A novel screening on the specific peptides by molecular simulation and development of the highly-sensitive electrochemical sensor for saxitoxin, Microchem J 200
8. Visciano P, Schirone M, Berti M, Milandri A, Tofalo R, Suzzi G (2016) Marine biotoxins: occurrence, toxicity, regulatory limits and reference methods. Front Microbiol 7
9. Watkins SM, Reich A, Fleming LE, Hammond R (2008) Neurotoxic shellfish poisoning. Mar Drugs 6:431–455
10. Hu B et al (2024) Brevetoxin aptamer selection and biolayer interferometry biosensor application. Toxins 16:411
11. Corriere M, Soliño L, Costa PR (2021) Effects of the marine biotoxins okadaic acid and dinophysistoxins on fish. J Mar Sci Eng 9
12. James KJ, Carey B, O'halloran J, Škrabáková Z (2010) Shellfish toxicity: human health implications of marine algal toxins. Epidemiol Infect 138, 927–940
13. Daniso E, Melpignano P, Cocchi M, Susmel S, Tulli F (2025) Development of a point of care (POC) test as an immunobiosensor for okadaic acid detection in mussels. Appl. Food Res. 5
14. Jia Y et al (2024) Analysis of okadaic acid using electrochemiluminescence imaging on microfluidic biosensing chip. Biosens Bioelectron 264
15. Farabegoli F, Blanco L, Rodríguez LP, Vieites JM, Cabado AG (2018) Phycotoxins in marine shellfish: origin, occurrence and effects on humans. Mar Drugs 16:188
16. Zhao L et al (2022) A rapid and sensitive aptamer-based biosensor for amnesic shellfish toxin domoic acid. Bioengineering 9:684
17. Jiang M et al (2022) Rapid electrochemical detection of domoic acid based on polydopamine/reduced graphene oxide coupled with in-situ imprinted polyacrylamide. Talanta 236

Innovative, Bio-Based Probes for the Detection of Protozoan Parasites

M. S. Nicolò[1(✉)], G. Bella[1], E. L. Sciuto[1,2,3,4], S. Morselli[2], T. Gritti[2], M. Ortalli[2], S. Varani[2], S. P. P. Guglielmino[1], and S. Conoci[1,3,4]

[1] Department of Chemical, Biological, Pharmaceutical and Environmental Sciences, University of Messina, Viale F. Stagno d'Alcontres 31, 98166 Messina, Italy
mnicolo@unime.it

[2] Department of Medical and Surgical Sciences, University of Bologna, Via Massarenti 9, 40138 Bologna, Italy

[3] Department of Chemistry "Giacomo Ciamician", University of Bologna, Via Selmi 2, 40126 Bologna, Italy

[4] URT Lab Sens DSFTM-CNR, Viale F. Stagno D'Alcontres 37, 98166 Messina, Italy

Abstract. Innovative biosensors for the detection of microbial pathogens require selective and robust probes for target recognition. Filamentous bacteriophages, or phages, are viruses that multiply in bacterial cells. They are composed of a proteic shell, called capsid, which contains the single stranded DNA codifying for all the phage proteins and are very robust structures. A phage library is a population of genetically-modified phages, each displaying a random peptide on the capsid surface. Phages displaying target-specific peptides can be selected from the library and used as probes for biosensors. In this study, we selected phages able to recognize the protozoan parasite *Leishmania infantum*, which can cause a range of clinical manifestations, including visceral leishmaniasis (VL), a disease that can be fatal if untreated. Phages were evaluated in the ability to recognize and bind *L. infantum*-infected macrophages, with or without cell lysis. The specific interaction of the phages with whole or lysed infected macrophages was analysed by using an enzyme-linked immunosorbent assay (ELISA).

Keywords: Biosensors · Probes · Phage Display · Pathogen Detection · Leishmania

1 Introduction

Innovative biosensors for the detection of microbial pathogens require selective and robust probes for target recognition. The efficiency of traditional probes, *e.g.* antibodies or synthetic peptides, depends on factors, such as pH and temperature, which can hinder the conformation of the target-recognizing domain [1].

Filamentous bacteriophages, or phages, are viruses that infect and multiply in bacterial cells. A proteic shell, called capsid, contains the DNA, which encodes all the proteins required for infection and replication.

C. Di Natale et al. (Eds.): AISEM 2025, LNEE 1497, pp. 82–86, 2025.
https://doi.org/10.1007/978-3-032-08271-8_14

Phage display technology is based on phage libraries, which are populations of genetically-modified phages, each bearing a random exogenous peptide, displayed on the capsid surface [2]. Up to 10^{10}–10^{12} different peptides can be expressed. Phage display can be used to select probes specific and selective against a target. By a procedure called biopanning, the phage library is incubated with a desired target, allowing phages displaying target-specific peptides to bind. Unbound phages are washed away and bound phages are recovered and allowed to replicate in bacteria (Fig. 1).

In this study, we identified and selected phages capable of targeting the protozoan parasite *Leishmania infantum*, which causes a range of clinical manifestations, including visceral leishmaniasis (VL). VL represents the most severe form of *Leishmania* infection and is invariably fatal if left untreated. The diagnosis of VL remains a significant challenge due to the limited sensitivity of microscopy, the suboptimal performance of serological assays in immunocompromised patients, and the lack of standardization of molecular tests [3]. Consequently, the development of novel, more sensitive, and reliable diagnostic tools is needed.

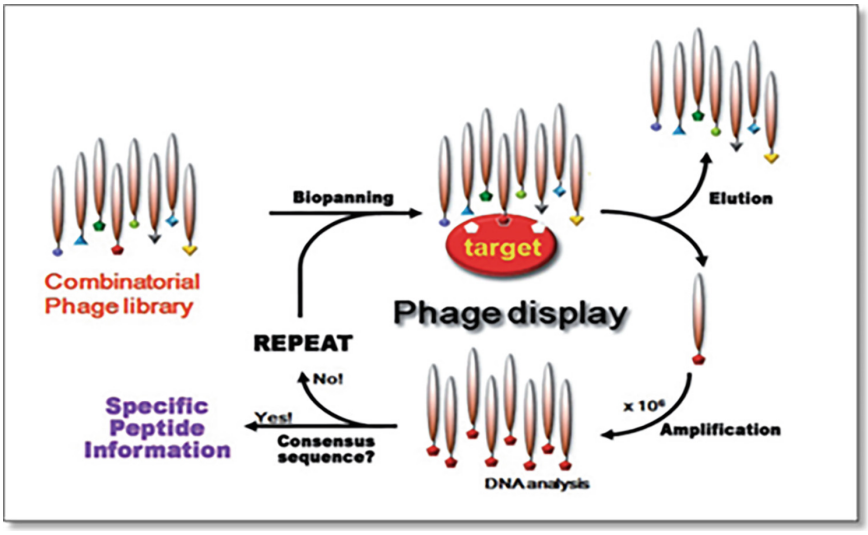

Fig. 1. Biopanning scheme. After the 1st round of selection, bound phages are recovered and multiplied by an amplification procedure, then undergo a new round of selection. Finally, the aminoacidic sequence of the specific peptide is determined.

2 Methods

Phages were isolated from a pVIII M13 9-mer phage library incubated with L. infantum soluble antigens immobilized on the bottom of a 96-wells microplate and al-lowed to replicate in Escherichia coli TG1 cells. After two rounds of biopanning, the phages ability to recognize whole or lysed *L. infantum*-infected macrophages was evaluated, and mock-infected (healthy) macrophages were used as control. Macrophages were fixed by paraformaldehyde (PFA) or methanol to the bottom of a polystyrene 96-wells

microplate. The specific interaction of the phages with the samples was analysed by an enzyme-linked im-munosorbent assay (ELISA). Phages were incubated with the samples, then a HRP-labeled antibody antiphage was used. After the enzimatic reaction with the chromo-genic substrate (TMB), absorbance was measured at 450 nm.

Each experiment was performed in triplicate.

3 Results and Discussion

Three of the selected phages, namely LEI6, LEI7 and LEI8, were tested on PFA- or methanol-fixed samples by ELISA.

Results are presented in Figs. 2 and 3.

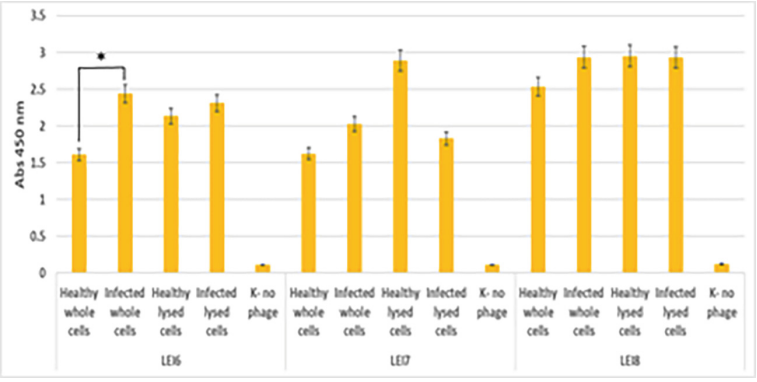

Fig. 2. ELISA performed on PFA-fixed whole or lysed, mock-infected (healthy) and *L. infantum*-infected macrophages.

In PFA-fixed samples (Fig. 2), LEI6 was able to significantly (*) discriminate between intact mock-infected and *L. infantum*-infected cells, whereas LEI7 and LEI8 were not.

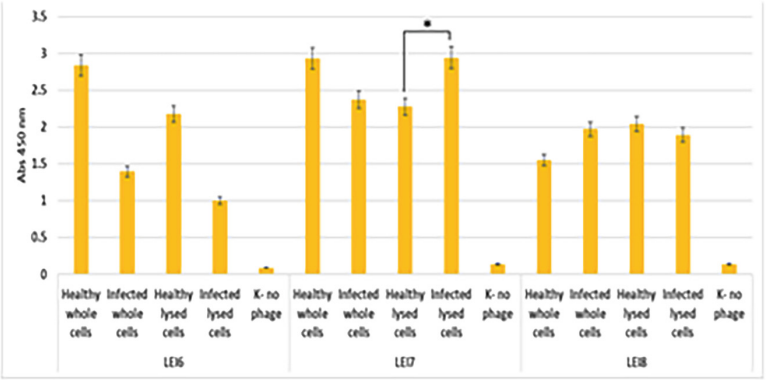

Fig. 3. ELISA performed on methanol-fixed whole or lysed, mock-infected (healthy) and *L. infantum*-infected macrophages.

In methanol-fixed samples (Fig. 3), LEI7 was able to significantly (*) discriminate between lysed mock-infected (healthy) and *L. infantum*-infected cells, whereas LEI6 and LEI8 were not.

Data indicates that the LEI6 clone effectively differentiated PFA-fixed intact mock-infected from *L. infantum* infected macrophages, whereas the LEI7 clone could significantly distinguish methanol-fixed lysed mock-infected from *L. infantum* infected macrophages.

It is well known that antigen preservation may be altered by chemicals fixating agents as they might affect antigen conformation [4]. With this premise, the two fixating procedures are likely to preserve different antigens, which have been recognized by the two phage clones investigated in this study. As consequence, the two phage clones ensure the detection of *Leishmania* antigens independently on the fixation procedure used.

4 Conclusions

Biosensors for detection of microbial pathogens very often suffer of the lack of reliable probes, as the efficiency of traditional ones (antibodies or synthetic peptides) is susceptible to several physico-chemical parameters.

For such reason, engineered bacteriophages, expressing a foreign peptide on their surface, can be used as innovative probes.

In this study, two phage clones, namely LEI6 and LEI7, have been selected and tested against intact or lysed, mock-infected (healthy) and *L. infantum*-infected macrophages.

The two clones are likely to recognize diverse antigens, as consequence of the different fixating procedures adopted, then they could be used as a mixture for a more efficient detection of *Leishmania* antigens.

References

1. Wang J, Song Q, Yang T et al (2024) The challenges and breakthroughs in the development of diagnostic monoclonal antibodies. VIEW 5(4):20240017

2. Felici F, Castagnoli L, Musacchio A, Jappelli R, Cesareni G (1991) Selection of antibody ligands from a large library of oligopeptides expressed on a multivalent exposition vector. J Mol Biol 222:301–310
3. Dondi A et al (2023) A 10-year retrospective study on pediatric visceral Leishmaniasis in a European endemic area: diagnostic and short-course therapeutic strategies. Healthcare (Basel) 12(1):23
4. Beckstead JH (1994) A simple technique for preservation of fixation-sensitive antigens in paraffin-embedded tissues. J Histochem Cytochem 42(8):1127–1134. https://doi.org/10.1177/42.8.8027531

Insights into Microbial Fuel Cell: Recovering Energy from Microbial Electrolysis Cells for Low Power Applications

A. Pietrelli[1(✉)], N. Lovecchio[1], S. Khorvash[2], M. Zeppilli[3], A. Marchetti[3], G. Gagliardi[2], V. Ferrara[1], B. Allard[4], F. Mieyeville[4], and D. Borello[2]

[1] Department of Information Engineering Electronics and Telecommunications, Sapienza University of Rome, Rome, Italy
andrea.pietrelli@uniroma1.it
[2] Department of Mechanical and Aerospace Engineering, Sapienza University of Rome, Rome, Italy
[3] Department of Chemistry, Sapienza University of Rome, Rome, Italy
[4] Université de Lyon, INSA Lyon, UCBL 1, Ecole Centrale de Lyon, CNRS, Ampère, UMR5005, 69621 Villeurbanne, France

Abstract. This paper examines the fundamentals, operational parameters, and applications of MFCs, in particular wastewater MFCs (WWMFCs), The WWMFCs were fed with the output effluent from a MEC (microbial electrolysis cell), coupling the system with a MEC (microbial electrolysis cell) which produces hydrogen and the MFCs which recover energy. Experimental data show a maximum power output of 600 μW from a single WWMFC at the maximum power point (MPP), highlighting their potential for powering low-energy devices while addressing environmental challenges.

Keywords: Microbial fuel cell · Microbial electrolysis cell · bioelectrochemistry · low power electronics · Wireless sensor networks

1 Introduction

Microbial fuel cells (MFCs) are a promising technology to supply low power devices of a node of a wireless sensor net-works (WSN) for environmental monitoring [1, 2] as well as for application like environmental bioremediation [3]. Moreover, MFCs can be a useful power source for applications as robotics [4], smartphone recharge [5] and lighting [6]. Furthermore, MFCs can be used itself for biosensing purpose [7]. It exists different reactor typologies of MFCs as Terrestrial microbial fuel cells (TMFCs) [8, 9], Benthic microbial fuel cells (BMFCs) [10, 11], Plant microbial fuel cells (PMFCs) [12] or Waste-water microbial fuel cells (WWMFCs) [13] (which also include urine as fuel [14]), they have different designs characteristics and specific electrical performances.

A large bibliography exists for each MFCs typologies concerning the improvement of power density and the influence on electrical performance from key parameter as

C. Di Natale et al. (Eds.): AISEM 2025, LNEE 1497, pp. 87–93, 2025.
https://doi.org/10.1007/978-3-032-08271-8_15

pH [15], temperature [16], water content [17] and the substrate used [18]. TMFCs are influenced by soil pH and water content as well as substrate used, instead in WWMFCs temperature is a key factor which influence electrical performance.

MFCs offer a sustainable and innovative approach to waste reduction, wastewater treatment, and bioelectricity generation. By leveraging the metabolic activities of microorganisms, MFCs convert chemical energy from organic compounds into electrical energy.

This paper examines the fundamentals, operational parameters, and applications of MFCs, with a focus on wastewater MFCs (WWMFCs) and coupling the system with a MEC (microbial electrolysis cell) which produces hydrogen. Experimental data show a maximum power output of 600 μW from a single WWMFC at the maximum power point (MPP) after 3 s of discharge, highlighting their potential for powering low-energy devices while addressing environmental challenges.

2 Microbial Fuel Cell

Microbial Fuel Cells are bioelectrochemical systems that exploit the electrocatalytic properties of microorganisms to generate electricity. Wastewater MFCs are of particular interest as they combine the dual functions of energy production and bioremediation. These systems operate by oxidizing organic matter in an anaerobic anodic chamber, generating electrons and protons. Electrons travel through an external circuit to the cathode, while protons pass through a proton exchange membrane (PEM), completing the circuit and producing water.

In addition to power generation, MFCs serve as biosensors for parameters such as pH and biological oxygen demand (BOD), enhancing their applicability in environmental monitoring. The presented results underscore the feasibility of wastewater MFCs as scalable energy solutions, particularly for small-scale applications.

Machine learning techniques and artificial intelligence can be a valuable solution to address the challenge predict the status and the health of the cells [19]. In 2021, neural networks was used to improve soft robots independence using microbial fuel cell as power source, namely a nonlinear autoregressive network with exogenous inputs was employed to predict the electrical output of MFCs, given its previous outputs and feeding volumes. Thus, predicting MFC outputs as a time series, enables accurate determination of feeding intervals and quantities required for sustenance that can be incorporated in the behavioural repertoire of a soft robot [20].

MFCs are versatile energy harvesting technique which offer remarkable advantages, such as electricity generation from renewable resources and applications in wastewater treatment as well as biosensing.

The integration of microbial fuel cells with advanced energy harvesting systems such as the EH4295 micropower Step-Up low voltage booster module from Linear and the AEM30300 from e-peas represents a significant advancement in sustainable energy technologies. The EH4295, with its self-starting oscillator and ability to operate at ultra-low input power levels (60 uW), is ideal for harnessing the energy output from a single MFC. Its compatibility with low-voltage, low-energy sources ensures efficient energy transfer and power management for various applications as: empowering remote sensors

nodes in wireless sensor networks (WSNs), enabling environmental monitoring, wastewater treatment supervision, and agricultural applications. Moreover, other applications are suitable as energy storage and backup, standalone energy solutions for maintenance-free systems in off-grid locations, and Hybrid power systems like solar or thermoelectric generators to enhance reliability and extend operating cycles.

The synergy between MFCs and cutting-edge booster technologies and energy harvesting technologies underscores the potential of bioelectrochemical systems in revolutionizing energy harvesting and environmental sustainability. By addressing both energy and environmental challenges, this integrated approach aligns with the growing demand for eco-friendly and reliable power solutions.

3 Material and Methods

3.1 MFCs Prototypes

The experimental activities on this work was set up using a single-chamber air cathode lab-scale Wastewater MFC. The WWMFCs prototypes of cylindrical shape are made of PVC draining tube of 0.7 L using a stainless-steel mesh anode with a projected area of 100 cm^2.

The distance between the electrodes is about 4 cm with an anode made with carbon fiber brush. An air cathode of 120 cm^2 of carbon cloth ((30% Teflon treated, Fuel Cell Earth LLC, USA) was manually made, using a paintbrush with 1.56 mg of black carbon and 0.5 mg of platinum for every cm^2 of the cathode surface area (Fig. 1).

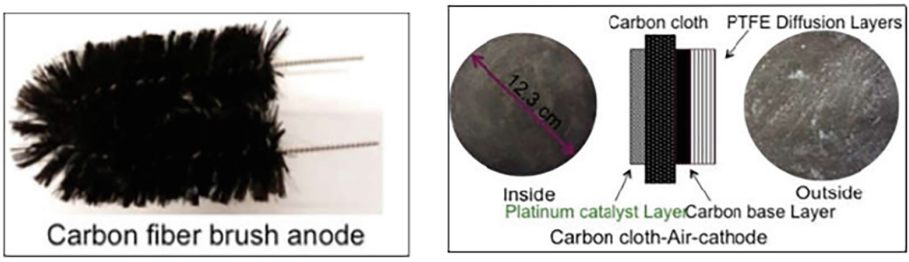

Fig. 1. Left: Carbon fiber brush anode. Right: Carbon cloth Air-cathode

3.2 MEC System

The WWMFCs reactors, with a capacity of 0.7 L, were fed with synthetic wastewater, which was the output of a MEC system designed for hydrogen production. Microbial electrolysis cell (MEC) is a technology which can help to produce cleaner hydrogen gas. MEC generally uses carbon-rich compounds like sewage water, organic compounds, and waste from treatment facilities to produce high-quality hydrogen. In MEC, bacteria in the anode chamber extract the electrons from the organic compound and break it into simpler forms, simultaneously creating electrons, protons, and carbon dioxide [21]. External power is provided to the reactor for biohydrogen production (>0.2 V vs. SHE). The

MEC was continuously fed with a synthetic mixture of organic substrates simulating the composition of municipal wastewater. The MEC's anodic chamber was operated under continuous flow with an organic loading rate (OLR) of 4 g COD/L·d and a hydraulic retention time (HRT) of 0.3 days. The influent solution composition was: sodium acetate (0.088 g/L), glucose (0.34 g/L), yeast extract (0.075 g/L), peptone (0.088 g/L), COD (255 mg/L), and pH (5.95). The MEC achieved a hydrogen productivity of 0.88 L/Ld, with a Coulombic efficiency of 103% and energy efficiency of 109%. During the steady state operation, feeding solution concentration was on average 584 ± 5 mg COD/L while the effluent showed an average value of 342 ± 4 mg COD/L resulting in a COD abatement standing at around 59%. The MEC was operated under a three electrode configuration using a reference AgAgCl electrode (E = +0.199 V vs SHE) controlling the anodic potential at +0.3 V vs SHE. This coniditions promoted the establishment of an average current of 99 ± 2 mA and a cell voltage of −1.35 ± 0.02 V. The WWMFCs was fed with the MEC's fresh effluent directly without any modifications, only the acetate concentration was brought to the level of 1 g/l.

3.3 Measurement System

The measurements was performed with a custom measurement board specific developed for MFC electrical characterization (Fig. 2). The system is low cost and it was developed for the characterization of Microbial fuel cell with high precision. A large set of option and feature are available which allow long term measurement and large flexibility to set up measurement and timing of experiments [22].

Indeed, the system can perform multi-step discharge protocols to accurately measure the power output of MFCs, and has been calibrated to ensure high precision and low noise measurements. One of the key features of the proposed measuring system is its ability to conduct long-term measurements with variable time steps.

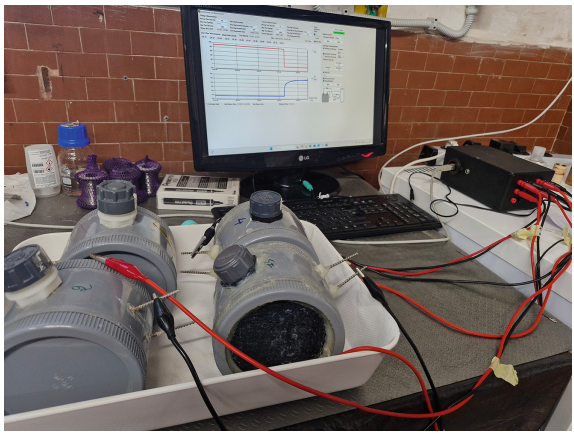

Fig. 2. MFCs system with Measurement Unit

4 Results

The experimental setup yielded a maximum power output of **600 µW** for a single WWMFC at a load of 224 Ω for a sample time of 3 s. This value reflects significant advancements in optimizing materials, fuel and operational conditions. Indeed, the power obtained shows improved results from past experimentation on the same reactor [3]. The results was the best among a set of four reactor in the same condition tested for two months continuously. The open circuit voltage was found around 600 mV. A model of the reactor was developed on PSpice to simulate reactor performance. The system actually use as input fuel, the output of the MEC system, coupling hydrogen generation and electrical energy recovery.

A full electrical characterization was performed using the measurement system, evaluating power output and internal resistance across a load range of 100–1000 Ω with a measurement interval of 3 s as in Fig. 3. The internal resistance, a key factor influencing performance, was found approximately as 225 Ω.

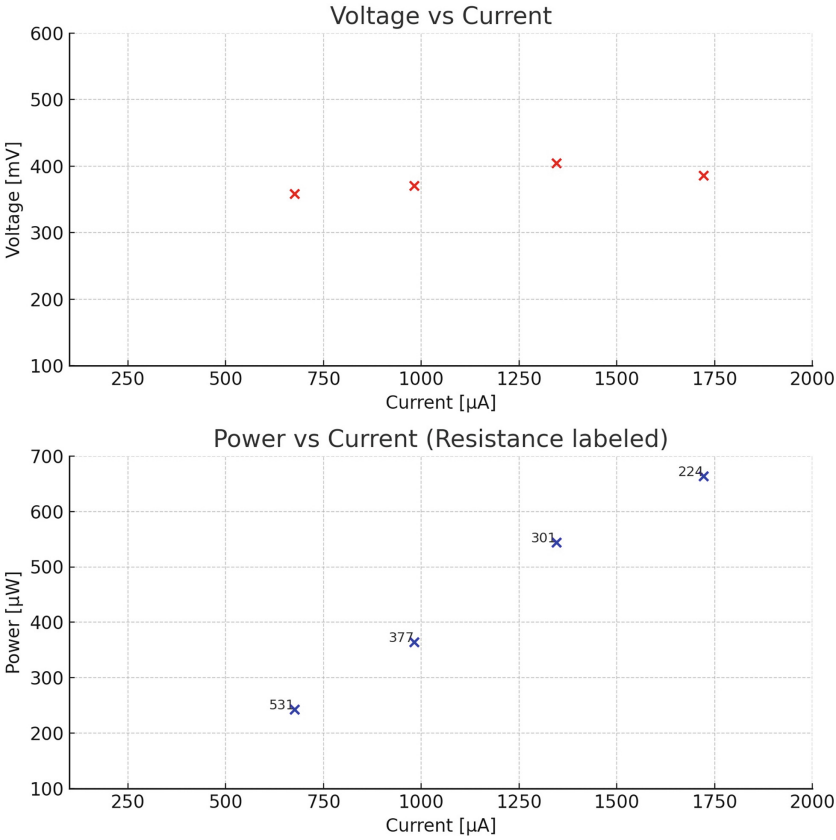

Fig. 3. Power chart results with labelled corresponding resistance, showing the MPP at 224 Ω

5 Discussions and Future Development

MFCs are versatile, offering applications in decentralized power generation, wastewater treatment, and biosensing. Future research should focus on reducing internal resistance, enhancing electrode durability, and integrating renewable energy systems for improved efficiency. Expanding the database of MFC performance under varied conditions will be instrumental in refining their design and application.

Moreover, leveraging natural wastewater as a source of microorganisms and nutrients offers a cost-effective path toward commercialization. Coupling MFCs and MECs system bring the technologies into a sustainable circle were biohydrogen is produced using bioenergy. Future research activities will focus on the hydraulic and electrical interconnection of the systems and on the prototypes improvements. In order to enhance the electrical performances, it will be tested different effluent composition in different operating condition, using distinct prototypes of the cells.

Further development of MFC systems paired with boosting modules as EH4295 should focus on optimizing the energy conversion efficiency and scalability with cluster configurations of MFC, constructive and electrodes material advancements, system Integration and adaptive control systems.

References

1. Cooke, K.G., Gay, M.O., Radachowsky, S.E., Guzman, J.J., Chiu, M.A.: BackyardNet: distributed sensor network powered by terrestrial microbial fuel cell technology. In: Unattended ground, sea, and air sensor technologies and applications XII, vol 7693. SPIE, pp 223–233 (2010)
2. Pietrelli A et al (2014) Wireless sensor network powered by a terrestrial microbial fuel cell as a sustainable land monitoring energy system. Sustainability 6(10):7263–7275
3. Ancona V, Caracciolo AB, Borello D, Ferrara V, Grenni P, Pietrelli A (2020) Microbial fuel cell: an energy harvesting technique for environmental remediation. Int J Environ Impacts 3(2):168–179
4. Ieropoulos IA, Greenman J, Melhuish C, Horsfield I (2012) Microbial fuel cells for robotics: energy autonomy through artificial symbiosis. Chemsuschem 5(6):1020–1026
5. Walter XA, Stinchcombe A, Greenman J, Ieropoulos I (2017) Urine transduction to usable energy: a modular MFC approach for smartphone and remote system charging. Appl Energy 192:575–581
6. Walter XA, Merino-Jiménez I, Greenman J, Ieropoulos I (2018) PEE POWER® urinal II–Urinal scale-up with microbial fuel cell scale-down for improved lighting. J Power Sources 392:150–158
7. Logroño W et al (2016) A terrestrial single chamber microbial fuel cell-based biosensor for biochemical oxygen demand of synthetic rice washed wastewater. Sensors 16(1):101
8. Zhang D, Ge Y, Wang W (2013) Study of a terrestrial microbial fuel cell and the effects of its power generation performance by environmental factors. In: Proceedings of the 2013 international conference on advanced mechatronic systems, pp 445–448. IEEE
9. Zhang D, Zhu Y, Pedrycz W, Guo Y (2016) A terrestrial microbial fuel cell for powering a single-hop wireless sensor network. Int J Mol Sci 17(5):762
10. Tavakolian M, Taleghani HG, Khorshidian M (2020) New design of benthic microbial fuel cell for bioelectricity generation: comparative study. Int J Hydrogen Energy 45(43):23533–23542

11. Guzman JJ et al (2010) Benthic microbial fuel cells: Long-term power sources for wireless marine sensor networks. In: Sensors, and Command, Control, Communications, and Intelligence (C3I) Technologies for Homeland Security and Homeland Defense IX, vol 7666, pp 586–596. SPIE
12. Osorio-de-la-Rosa E et al (2020) Arrays of plant microbial fuel cells for implementing self-sustainable wireless sensor networks. IEEE Sens J 21(2):1965–1974
13. Zhuang L, Zheng Y, Zhou S, Yuan Y, Yuan H, Chen Y (2012) Scalable microbial fuel cell (MFC) stack for continuous real wastewater treatment. Biores Technol 106:82–88
14. Chouler J et al (2016) Towards effective small-scale microbial fuel cells for energy generation from urine. Electrochim Acta 192:89–98
15. Puig S, Serra M, Coma M, Cabré M, Balaguer MD, Colprim J (2010) Effect of pH on nutrient dynamics and electricity production using microbial fuel cells. Biores Technol 101(24):9594–9599
16. Barbato RA, Foley KL, Toro-Zapata JA, Jones RM, Reynolds CM (2017) The power of soil microbes: Sustained power production in terrestrial microbial fuel cells under various temperature regimes. Appl Soil Ecol 109:14–22
17. Casula E et al (2021) Modelling the influence of soil properties on performance and bioremediation ability of a pile of soil microbial fuel cells. Electrochim Acta 368:137568
18. Chae KJ, Choi MJ, Lee JW, Kim KY, Kim IS (2009) Effect of different substrates on the performance, bacterial diversity, and bacterial viability in microbial fuel cells. Biores Technol 100(14):3518–3525
19. Gyaneshwar A et al (2022) A survey of applications of MFC and recent progress of artificial intelligence and machine learning techniques and applications, with competing fuel cells. Eng Res Express 4(2):022001
20. Tsompanas, M.A., You, J., Philamore, H., Rossiter, J., Ieropoulos, I.: Neural networks predicting microbial fuel cells output for soft robotics applications. Front. Robot. AI, 8, Front. Robot. AI **8** (2021). https://doi.org/10.3389/frobt.2021.633414
21. Kadier A, Simayi Y, Kalil MS, Abdeshahian P, Hamid AA (2014) A review of the substrates used in microbial electrolysis cells (MECs) for producing sustainable and clean hydrogen gas. Renew Energy 71:466–472
22. Lovecchio N, Di Meo V, Pietrelli A (2023) Customized multichannel measurement system for microbial fuel cell characterization. Bioengineering 10(5):624. https://doi.org/10.3390/bioengineering10050624

Materials for Biosensor Designation of DNA Comet Assay for Radiotherapy Patients' Exposure Monitoring

Cem Gök[1,2], Arzum Işıtan[3,4(✉)], Massimo Bersani[4], and Ahmet Koluman[5]

[1] Department of Biomedical Engineering, Izmir Bakırçay University, Izmir, Turkey
[2] Biomedical Technologies Design Application and Research Center, Izmir Bakırçay University, Izmir, Türkiye
[3] Department of Mechanical Engineering, Pamukkale University, Denizli, Turkey
aisitan@pau.edu.tr
[4] Center for Sensors and Devices, Fondazione Bruno Kessler, Trento, Italy
[5] Department of Biomedical Engineering, Pamukkale University, Denizli, Turkey

Abstract. The accurate monitoring of DNA damage in radiotherapy patients is essential for evaluating the effects of radiation exposure and the effectiveness of treatment. The comet assay, a widely used technique to detect DNA strand breaks at the single-cell level, is recognized for its sensitivity and adaptability in radiation biodosimetry. However, enhancing the throughput, sensitivity, and automation of the assay is vital for clinical applications. The innovations presented in material selection, sensor design, and automation mark a significant step forward in the use of the comet assay for radiation exposure monitoring, paving the way for personalized medicine approaches in radiotherapy and beyond. This study aims to discuss material recommendations for biosensors using advanced materials to improve the functionality of the DNA comet assay for radiation exposure monitoring.

Keywords: DNA Comet Assay · Biosensor · DNA Damage · Carbon Nanotubes · Radiation Damage

1 Introduction

Radiotherapy remains one of the most effective treatment modalities for cancer, utilizing ionizing radiation to destroy tumor cells while preserving surrounding healthy tissues. However, despite technological advances in precision targeting, inadvertent damage to normal tissues remains a significant clinical challenge. Ionizing radiation induces various forms of DNA damage, including base modifications, single-strand breaks (SSBs), and double-strand breaks (DSBs), with DSBs being the most critical and cytotoxic lesions [1–3].

Traditional dosimetry techniques, such as thermoluminescent dosimeters and ionization chambers, accurately measure the physical dose delivered to a patient. However, these approaches fail to capture biological variability among individuals, such as differences in DNA repair capacity, age-related radiosensitivity, and genetic predispositions

C. Di Natale et al. (Eds.): AISEM 2025, LNEE 1497, pp. 94–99, 2025.
https://doi.org/10.1007/978-3-032-08271-8_16

[2, 3]. Consequently, there is an increasing need for biological dosimetry techniques that can assess the actual biological impact of radiation exposure rather than merely the physical dose administered.

Among various biodosimetry methods, the DNA comet assay, also known as single-cell gel electrophoresis (SCGE), has emerged as a powerful and sensitive tool for quantifying DNA damage at the individual cell level [4]. The assay involves embedding cells in agarose gel, lysing the cells to release DNA, and subjecting the DNA to electrophoresis under specific conditions. Fragmented DNA migrates more readily than intact DNA, forming a "comet tail" whose extent correlates with the amount of damage. Variants of the assay—alkaline, neutral, or modified versions—allow for the detection of different types of DNA lesions, including single- and double-strand breaks.

The comet assay provides several advantages: minimal cell numbers required, high sensitivity to low levels of DNA damage, relatively low cost, and adaptability for automation and high-throughput screening. This makes it an ideal platform for integrating into biosensor systems designed for real-time radiation exposure monitoring during radiotherapy.

This study focuses on developing a material-based biosensor system to enhance the functionality of the DNA comet assay for clinical applications. By improving the assay's throughput, sensitivity, and reproducibility through advanced materials and sensor technologies, we aim to support the evolution of radiotherapy into a more personalized, biologically guided practice.

2 DNA Comet Assay and Its Clinical Significance

The DNA comet assay has become an essential technique for detecting DNA strand breaks and alkali-labile sites at the level of individual eukaryotic cells [1, 4]. Its sensitivity to low levels of damage makes it a valuable tool in radiation biology, genetic toxicology, and clinical diagnostics. Compared to traditional methods like chromosome aberration assays or micronucleus tests, the comet assay offers a faster, more cost-effective, and less labor-intensive alternative for evaluating genotoxicity.

Clinically, the assay's application in radiotherapy offers several advantages. By assessing DNA damage immediately following radiation exposure, it allows clinicians to monitor how patients' cells respond in real time, offering a dynamic biomarker for radiosensitivity [2, 5]. This is crucial, as individual variability in DNA repair kinetics can significantly affect treatment outcomes and the risk of radiation-induced late effects, such as fibrosis, cardiovascular disease, or secondary malignancies.

Furthermore, the assay can be adapted to different experimental conditions to detect specific types of damage. The alkaline version, using high pH electrophoresis, reveals single-strand breaks and alkali-labile sites, while the neutral version focuses on double-strand breaks—both of which are critical in evaluating radiation damage severity [4].

Recent efforts to automate and miniaturize the comet assay have increased its clinical potential. Platforms combining automated electrophoresis, standardized staining, and image analysis have reduced user-dependent variability, making results more reproducible and suitable for large-scale clinical studies [5].

Given its capacity to offer personalized biological dosimetry, the comet assay holds great promise for tailoring radiotherapy regimens to individual patients, optimizing therapeutic efficacy while minimizing adverse effects. In the context of emerging biosensor technologies, integrating the comet assay into sensor platforms could transform radiation exposure monitoring into a rapid, real-time clinical practice.

3 Materials for Biosensor Development

The selection of materials for biosensor construction is critical to achieving high sensitivity, stability, and biocompatibility, all of which are essential for clinical applications such as radiation exposure monitoring through the DNA comet assay. Recent advances in nanotechnology have enabled the use of carbon-based and metallic nanomaterials, along with biopolymer matrices, to enhance biosensor performance.

Graphene, a two-dimensional sheet of carbon atoms arranged in a hexagonal lattice, offers exceptional properties, including high electrical conductivity, mechanical strength, and biocompatibility [6]. Its high surface area promotes efficient electron transfer, facilitating rapid and sensitive detection of DNA damage. However, complex synthesis routes and handling issues remain technical challenges.

Carbon nanotubes (CNTs), particularly single-walled and multi-walled variants, are widely used for their excellent conductivity and mechanical resilience [7]. Their unique tubular structure allows for enhanced charge mobility and improved signal amplification in biosensors. Despite their promising properties, concerns regarding cytotoxicity and high production costs have limited their broader clinical adoption.

Gold nanoparticles (AuNPs) are valued for their large surface area, biocompatibility, and ability to facilitate electron transfer between biological elements and electrode surfaces [8]. AuNPs enhance signal stability and sensitivity in biosensor platforms but may suffer from aggregation issues and high production expenses.

Chitosan, a natural polysaccharide derived from chitin, provides a biodegradable and biocompatible matrix ideal for DNA immobilization [9]. Its film-forming properties help maintain the structural integrity of biological samples during electrophoresis. However, due to its inherently low conductivity, chitosan often needs to be combined with conductive materials like CNTs or graphene for improved performance.

Agarose gel, commonly used in electrophoresis, offers a stable and supportive medium for embedding cells and DNA. While agarose ensures sample integrity during the electrophoretic process, its poor electrical conductivity necessitates the addition of conductive elements to optimize sensor efficiency [10].

The synergistic integration of these materials—combining the conductivity of graphene and CNTs with the biocompatibility of chitosan and agarose, and the signal-enhancing properties of AuNPs—creates a composite biosensor system capable of detecting low levels of DNA damage with high sensitivity and reliability. Such material combinations are pivotal for automating the comet assay, improving throughput, and enabling real-time, point-of-care applications in clinical radiation monitoring. The proposed biosensor leverages carbon-based materials, including graphene and carbon nanotubes, for their excellent electrical conductivity and high surface area, which enhance electron transfer efficiency [6–10] (Table 1).

Table 1. Comparison of material variations for the biosensor.

Material	Advantages	Disadvantages
Graphene	High surface area, excellent conductivity, biocompatibility	Complex synthesis and handling
Carbon Nanotubes	High conductivity, mechanical strength, enhances sensitivity	Potential cytotoxicity, expensive
Gold Nanoparticles	Large surface area, biocompatibility, efficient electron transfer	High cost, aggregation issues
Chitosan	Biodegradable, good film-forming properties for DNA immobilization	Limited conductivity may require composites for better performance
Agarose Gel	Provides a stable matrix for DNA during electrophoresis	Poor conductivity requires additional conductive elements

4 Sensor Automation and Clinical Impact

The automation of DNA comet assay biosensors represents a significant advancement in clinical radiation monitoring. Traditional comet assays, while sensitive, are labor-intensive, require meticulous manual handling, and are subject to operator variability. Automation addresses these limitations by standardizing sample processing, electrophoresis conditions, staining procedures, and data analysis, thereby enhancing reproducibility and throughput [5].

Integrating biosensors into automated platforms allows for real-time, point-of-care analysis of radiation-induced DNA damage. Rapid feedback can be crucial for clinical decision-making during radiotherapy sessions, enabling dose adjustments based on a patient's individual radiosensitivity profile. Such personalization has the potential to reduce side effects, improve tumor control rates, and optimize therapeutic outcomes [3, 4].

Automation also facilitates large-scale population screenings in radiation emergency scenarios. In the event of accidental exposures, automated comet assay-based biosensors could rapidly assess biological doses in affected individuals, helping prioritize medical interventions. Furthermore, sensor miniaturization and integration with wireless technologies, such as Internet of Medical Things (IoMT) frameworks, may allow continuous or remote monitoring of radiation exposure in vulnerable populations, such as healthcare workers or astronauts [11].

Clinical trials have already demonstrated the feasibility of using semi-automated comet assay platforms in assessing DNA damage among cancer patients undergoing radiotherapy [1–3, 5, 12]. Combining these systems with advanced materials—such as cellulose-based composites, graphene, and gold nanoparticles—further enhances sensitivity, stability, and biocompatibility, paving the way for fully automated, patient-centered monitoring tools.

Ultimately, the development of robust, user-friendly biosensors capable of quantifying DNA damage in real time holds transformative potential for radiotherapy, personalized medicine, and public health surveillance.

5 Conclusion

The integration of advanced materials into DNA comet assay biosensors offers a promising approach for real-time radiation exposure monitoring during radiotherapy. By combining highly conductive nanomaterials such as graphene and carbon nanotubes with biocompatible matrices like chitosan and agarose, sensor platforms achieve enhanced sensitivity, reproducibility, and clinical applicability. Automation further transforms the traditionally manual comet assay into a standardized, high-throughput method capable of supporting personalized treatment planning and rapid emergency response.

Cellulose-based composites, gold nanoparticles, and other innovative materials provide additional avenues for improving biosensor performance while aligning with the growing need for sustainable healthcare technologies. Future developments focusing on miniaturization, wireless integration, and AI-assisted data interpretation will further cement the role of biosensor-based comet assays in personalized medicine and radiation safety.

By bridging material science, biotechnology, and clinical practice, these advances pave the way for patient-centric, efficient, and environmentally responsible healthcare solutions.

References

1. Azqueta A, Collins AR (2013) The essential comet assay: a comprehensive guide to measuring DNA damage and repair. Arch. Toxicol. 87:949–968. https://doi.org/10.1007/s00204-013-1070-0
2. Azqueta, A., et al.: Application of the comet assay in human biomonitoring: an hCOMET perspective. Mutation Res./Rev. Mutation Res. **783**, 108288 (2020). https://doi.org/10.1016/J.MRREV.2019.108288
3. Collins AR (2004) The comet assay for DNA damage and repair: Principles, applications, and limitations. Appl. Biochem. Biotechnol. – Part B Molecular Biotechnol. 26:249–261. https://doi.org/10.1385/MB:26:3:249
4. Bushmanov A, Vorobyeva N, Molodtsova D, Osipov AN (2022) Utilization of DNA double-strand breaks for biodosimetry of ionizing radiation exposure. Environ. Adv. 8:100207. https://doi.org/10.1016/J.ENVADV.2022.100207
5. Vidya, G., Gladwin, V., Chand, P.: A comprehensive review on clinical applications of comet assay. J. Clin. Diagn. Res. **9**, GE01 (2015). https://doi.org/10.7860/JCDR/2015/12062.5622
6. Novoselov, K.S., Fal'Ko, V.I., Colombo, L., Gellert, P.R., Schwab, M.G., Kim, K.: A roadmap for graphene. Nature. **490**, 192–200 (2012). https://doi.org/10.1038/nature11458
7. De Volder MFL, Tawfick SH, Baughman RH, Hart AJ (2013) Carbon nanotubes: present and future commercial applications. Science 1979(339):535–539. https://doi.org/10.1126/science.1222453
8. Dykman L, Khlebtsov N (2012) Gold nanoparticles in biomedical applications: recent advances and perspectives. Chem. Soc. Rev. 41:2256–2282. https://doi.org/10.1039/C1CS15166E

9. Rinaudo M (2006) Chitin and chitosan: properties and applications. Prog. Polym. Sci. 31:603–632. https://doi.org/10.1016/J.PROGPOLYMSCI.2006.06.001
10. Jiang F et al (2023) Extraction, modification and biomedical application of agarose hydrogels: a review. Mar Drugs 21:299. https://doi.org/10.3390/MD21050299
11. Joyia, G.J., Liaqat, R.M., Farooq, A., Rehman, S.: Internet of medical things (IOMT): applications, benefits and future challenges in healthcare domain. J. Commun.. **12**, 240–247 (2017). https://doi.org/10.12720/jcm.12.4.240-247
12. Olive PL, Banáth JP (2006) The comet assay: a method to measure DNA damage in individual cells. Nat. Protocols 1:23–29. https://doi.org/10.1038/nprot.2006.5

PCR-Free Strategies for Pathogens Molecular Detection in Biosensing Applications

E. L. Sciuto[1(✉)], G. Bella[1], P. Calorenni[1], M. S. Nicolò[1], K. Buonasera[2], A. A. Messina[3], T. Gritti[4], S. Varani[4], M. V. Balli[5], G. Valenti[5], L. Prodi[5], and S. Conoci[1,5]

[1] Department of Chemical, Biological, Pharmaceutical and Environmental Sciences, University of Messina, V.le Ferdinando Stagno d'Alcontres, 31, Messina, Italy
emanueleluigi.sciuto@unime.it

[2] Consiglio Nazionale delle Ricerche (CNR), Institute for Microelectronics and Microsystems (IMM), V.le F. Stagno d'Alcontres 31, Messina, Italy

[3] STMicroelectronics, Stradale Primosole 50, Catania, Italy

[4] Department of Medical and Surgical Sciences, University of Bologna, Via Massarenti 9, Bologna, Italy

[5] Department of Chemistry "Giacomo Ciamician", University of Bologna, Via Selmi 2, Bologna, Italy

Abstract. The diagnosis of infectious diseases mostly relies on PCR-based analytical methods that, although consolidated and accurate, are strictly constrained to specialized personnel and dedicated laboratories, due to the complex procedures and the system architectures required. This limits the urgent expansion of the diagnostics towards massive and decentralized applications in countries lacking appropriate lab and health assistance. The PCR-free biosensing represents the most appealing solution since it provides the detection of an infectious pathogen without its genetic material amplification by PCR, thus, overcoming the technological limitations of the conventional diagnostics. In this contribution we present three electrochemical PCR-free biosensing strategies for the selective detection of pathogens, including severe acute respiratory syndrome coronavirus (SARS-CoV)-2, *Pseudomonas aeruginosa* and *Leishmania infantum*. The detection is based on the capacitive quantification, through electrochemical impedance spectroscopy (EIS), of the three pathogens' nucleic acids (NAs) interacting via cooperative hybridization with complementary oligonucleotide probes anchored on top of commercial gold electrodes. The strategies allowed to directly reveal and quantify the target genomes without amplification and with a high level of selectivity.

Keywords: PCR-free biosensing · electrochemical impedance spectroscopy · pathogens detection · infectious disease · cooperative hybridization

C. Di Natale et al. (Eds.): AISEM 2025, LNEE 1497, pp. 100–105, 2025.
https://doi.org/10.1007/978-3-032-08271-8_17

1 Introduction

The field of infectious diseases has predominantly attracted biomedical research efforts, as it represents a crucial global public health challenge especially in low-resource countries where undernutrition, poor hygiene conditions and resource-limited healthcare settings limit the access to proper diagnostics and therapies. The COVID-19 pandemic caused by severe acute respiratory syndrome coronavirus (SARS-CoV)-2 virus further highlighted the global need for valid diagnostic tools capable of delivering fast, cheap and reliable molecular detection of infections to improve disease monitoring and management. Nevertheless, conventional molecular and immunological diagnostic methods for COVID-19 faced significant limitations, including the high time and cost demands, the requirement for a well-equipped laboratory to perform PCR-based analysis and the low sensitivity and accuracy of antigen/antibody-based assays. These challenges led to an urgent need for new solutions to address these limitations, allowing reliable and large-scale molecular screening while being adaptable to Point-of-Care (PoC) biosensing applications [1]. In this scenario, PCR-free biosensing represents the most appealing approach, as it can provide the molecular detection of pathogens without their genetic material amplification by PCR, thus simplifying the long and expensive experimental procedures and complex system architectures of PCR-based methods, all by keeping high sensitivity and selectivity levels [2–4].

The PCR-free approach can be also implemented by the combination with the electrochemical transduction that, compared to other detection strategies affected by dyes stability, complexity of measurement equipment and sensitivity to environmental noise [5–9], offers a high level of accuracy together with the possibility of integration into portable and miniaturized biosensing systems.

In this study, we developed effective electrochemical impedance spectroscopy (EIS)-based strategies for the high throughput PCR-free biosensing of the virus SARS-CoV-2 (SC), the bacterium *Pseudomonas aeruginosa* (PA) and the protozoan parasite *Leishmania infantum* (LI), which are representative of pathogens causing severe human diseases. These targets were detected through the direct recognition of their nucleic acids (NAs), including 1. The 29 Kb ssRNA genome of SC; 2. The 6.2 Mbp dsDNA genome of PA, a ubiquitous and opportunistic Gram-negative bacterium responsible for severe respiratory tract and bloodstream infections; 3. The 0.8 Kbp circular double-stranded kinetoplast (k)DNA of LI, an hemoflagellate protozoan parasite causing visceral leishmaniasis. The EIS measurements for PCR-free detection and quantification of pathogens' NAs were performed on commercial gold working electrodes (WE) functionalized by anchoring thiol-modified oligonucleotide capture probes properly designed for the NA cooperative hybridization. In parallel, the WE surface functionalization was validated by contact angle (CA) analysis.

2 Materials and Methods

2.1 Chemicals

Phosphate buffered saline (PBS) 0.01 M solution, phosphate buffer (PB) 0.2 M at pH 6.01, acetic acid/acetate buffers 0.2 M at pH 5.05, 4.01 and 3.7, hydrochloric acid at 0.01 M at pH 2, sulfuric acid (H_2SO_4) 0.5 M, potassium hexacyanoferrate

$[Fe(CN)_6]^{3-/4-}$ (ratio 1:1) 5×10^{-3} M, 6-mercapto-1-hexanol ($C_6H_{14}OS$) and ethanol (C_2H_6O) 100%, ammonium hydroxide solution (NH_4OH), NH_3 basis, and hydrogen peroxide (H_2O_2) 30% (w/w) solution were from Merck. All chemicals were used without further purification.

2.2 Oligonucleotides Probes and Pathogens' NAs

The oligonucleotide probes were purchased from Ella Biotech. For the cooperative hybridization, probes sequences were designed as complementary to two (PA and LI) and three (SC) regions of a conserved gene inside each specific target NA, so that probes could simultaneously hybridize the same target increasing both yield and stability of the NA capture. Moreover, probes were customized at their 5' end with a chain of 6 carbon atoms, working as spacer for the right orientation during the anchoring, and a thiol group used to covalently bind the gold surface in a self-assembled monolayer configuration.

Target NAs were extracted and purified via spin-column kit (Qiagen). Then, dsDNA genome of PA and kDNA of LI were diluted in PBS 0.01 M to the final concentration of 10^4–10^2-10–1 copies/μL, while ssRNA of SC was diluted to 10^2–10-1–10^{-1} copies/μL. A 10^4 copies/μL dsDNA of Hepatitis-B Virus was also extracted and used as unspecific (US) target for the cross-reactivity test.

2.3 Gold Electrode Surface Functionalization

CH101 gold electrodes (from CH Instruments) were functionalized with probes and targets as schemed in Fig. 1. They were first modified by a cleaning step, performed with alumina slurry and CV cycles with H_2SO_4. Then, the thiolate capture probes have been anchored at 25 °C for 4 h on top of the WE surfaces that, subsequently, have been passivated with 6-mercapto-1-hexanol at 25 °C overnight. For the CA validation and the EIS analysis, the biosensing surfaces have been dipped into NAs working solutions (see Sect. 2.2) and incubated at 50 °C for 3h30 to let the cooperative hybridization occurring.

2.4 Contact Angle Analysis

The CA analysis of functionalized electrodes surfaces have been performed by spotting 1 μL drop of ultrapure water on top and acquiring after 10 s. The CA was compared between a clean WE, used as reference, and surfaces after cleaning step, probes anchoring and probes–NAs target cooperative hybridization. All CA values have been collected in four replicas ($n = 4$).

2.5 EIS Measurements

For the EIS measurements the functionalized gold electrodes were included as WE into an electrochemical cell that has been properly assembled with a Pt wire as counter electrode (CE) and an Ag/AgCl reference electrode (RE). Then, the cell has been filled with a solution of 5 mM of $[Fe(CN)_6]^{-3/-4}$ in PB that was used as redox mediator. Measurements have been done at 100 kHz to 0.1 Hz frequency range, 1mA current and 0.234 V potential.

3 Results and Discussion

Commercial gold electrodes were functionalized for PCR-free NAs biosensing as reported in Fig. 1a. The effectiveness of electrodes modification has been first validated by CA analysis investigating the surface wettability after each step of treatment, as shown in Fig. 1b. By comparing a reference electrode (dashed bar) with electrodes after SC (green bar), PA (orange bar) and LI (purple bar) functionalization, the analysis revealed a marked increase of wettability after the Au cleaning step, with a decrease of ~30 °CA, possibly due to the hydroxyl layer formation on surface. After the probes anchoring and NAs target hybridization the wettability continues to increase and the average CA value fell to ~20° of CA, due to the additional charges of lateral groups of the attached oligo probes and NAs.

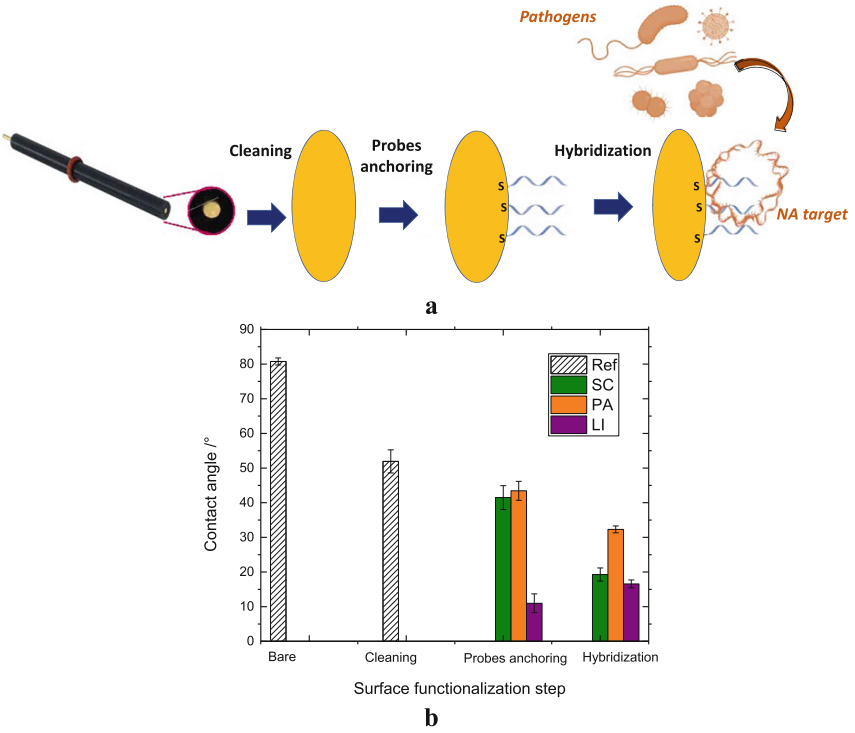

Fig. 1. (a) Gold electrodes surface functionalization for pathogens' NAs PCR-free biosensing. (b) CA analysis of electrodes surface wettability during functionalization.

Once validated their surface modification, functionalized electrodes were tested in their PCR-free biosensing ability by EIS. Nyquists plots, in Fig. 2, showed the trend of resistance values measured after probes-NA hybridization, normalized with respect to the values measured with only probes, which decreased consistently with the NA concentrations for SC(a), PA(b) and LI(c) pathogens, proving the effectiveness of the

biosensing strategy for pathogen NA detection and quantification. In addition, the strategy avoided the cross-reactivity, as confirmed by the low resistances measured with the unspecific (US) NA target at 10^4 copies/μL for all type of probes arrays.

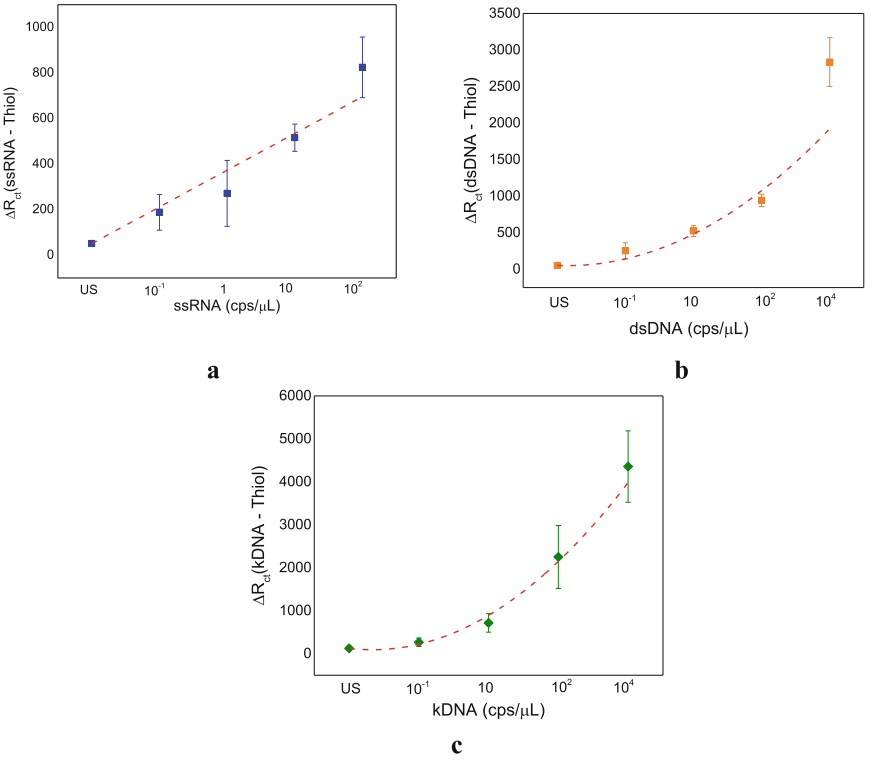

Fig. 2. Nyquists plots of EIS resistance values measured on functionalized gold electrodes after hybridization with different concentrations of SC(a), PA(b) and LI(c) NAs targets.

4 Conclusions

Three biosensing strategies based on EIS for the PCR-free detection and quantification of viral, bacterial and parasitic NAs were presented. The biosensing surfaces were prepared by the functionalization of commercial gold electrodes with oligonucleotide probes that can selectively and cooperatively hybridize with the genetic targets.

The CA analysis of electrodes after functionalization showed a gradual increase of the surface wettability as a function of the probes-NAs duplex formation and the relative charges addition, validating the electrodes modification.

The EIS measurements proved that the three strategies were able to detect and quantify the genetic targets, as shown by the marked increase of resistances measured after the NA hybridization, without their amplification by PCR and with a good level of sensitivity and selectivity, as confirmed by the low resistance measured after electrodes exposure to the US target.

5 Fundings

The research was supported by the European Union's Horizon Europe EIC Pathfinder Open programme "ECLIPSE project" (Grant Agreement Nr. 101046787).

References

1. Sciuto EL et al (2021) Nucleic acids analytical methods for viral infection diagnosis: state-of-the-art and future perspectives. Biomolecules 11:1585. https://doi.org/10.3390/biom11111585
2. Calorenni P et al (2023) PCR-free innovative strategies for SARS-CoV-2 detection. Adv. Healthc. Mater. 12:2300512. https://doi.org/10.1002/adhm.202300512
3. Petralia S, Sciuto EL, Pietro MLD, Zimbone M, Grimaldi MG, Conoci S (2017) An innovative chemical strategy for PCR-free genetic detection of pathogens by an integrated electrochemical biosensor. Analyst 142:2090–2093. https://doi.org/10.1039/C7AN00202E
4. Nikolaou P et al (2022) Ultrasensitive PCR-Free detection of whole virus genome by electrochemiluminescence. Biosens Bioelectron. https://doi.org/10.1016/j.bios.2022.114165
5. Cho I-H, Kim DH, Park S (2020) Electrochemical biosensors: perspective on functional nanomaterials for on-site analysis. Biomater. Res. 24:6. https://doi.org/10.1186/s40824-019-0181-y
6. Sciuto EL et al (2019) Biosensors in monitoring water quality and safety: An example of a miniaturizable whole-cell based sensor for Hg2+ optical detection in water. Water (Switzerland). https://doi.org/10.3390/w11101986
7. Sciuto EL et al (2015) Photo-physical characterization of fluorophore Ru(bpy)32+ for optical biosensing applications. Sens. Bio-Sens. Res. 6:67–71. https://doi.org/10.1016/j.sbsr.2015.09.003
8. Santangelo, M.F., et al.: Silicon photomultipliers applications to biosensors. Presented at the Proceedings of SPIE – The International Society for Optical Engineering (2014). https://doi.org/10.1117/12.2037765
9. Favetta M et al (2015) Development of Si-based electrical biosensors: simulations and first experimental results. Sens. Bio-Sens. Res. 6:72–78. https://doi.org/10.1016/j.sbsr.2015.11.012

Performance and Usability of Remote PPG Technology on Consumer Smartphones

Anna Maria Carluccio(✉), Andrea Manni, Andrea Caroppo, Pietro Aleardo Siciliano, and Alessandro Leone

Institute for Microelectronics and Microsystems, National Research Council of Italy, 73100 Lecce, Italy
annamariacarluccio@cnr.it

Abstract. Remote photoplethysmography has emerged as a promising technology for non-invasive and continuous estimation of vital signs, such as heart rate, breath rate and blood oxygen saturation. This study evaluated the performance and perceived usability of a remote photoplethysmography-based computational pipeline implemented on four consumer smartphones. The devices tested, Samsung Galaxy A35, Samsung Galaxy S23 +, HUAWEI Mate 50 Pro and Google Pixel 7, were evaluated under controlled conditions to assess their accuracy in vital signs estimation. Performance metrics were used to compare the results of the remote photoplethysmography estimations with reference measurements from medical-grade devices. The Samsung Galaxy A35 demonstrated the best performance among the smartphones assessed. Additionally, usability was evaluated using the System Usability Scale and the short version of the User Experience Questionnaire, yielding high scores indicative of a positive user experience. These findings suggest that remote photoplethysmography technology can be effectively deployed on consumer smartphones, offering a cost-effective and accessible solution for remote health monitoring. This study underscores the importance of camera sensor specifications in achieving accurate vital signs estimation and highlights the potential of smartphone-based remote photoplethysmography systems for widespread telemedicine applications.

Keywords: Remote photoplethysmography · rPPG · Smartphones · Vital Signs estimation · Usability · User Experience

1 Introduction

In the field of vital signs monitoring and estimation, remote photoplethysmography (rPPG) has gained significant attention for its potential in continuous, non-invasive monitoring. This technique allows the estimation of Heart Rate (HR), Breath Rate (BR) and blood oxygen saturation (SpO2) by capturing subtle variations in skin color associated with fluctuations in blood volume [1]. rPPG analyzes video recordings of the skin, typically from the face, to detect periodic changes in light absorption caused by blood flow [2]. This technique eliminates the need for wearable sensors and enables real-time monitoring by using affordable consumer-grade digital cameras.

C. Di Natale et al. (Eds.): AISEM 2025, LNEE 1497, pp. 106–113, 2025.
https://doi.org/10.1007/978-3-032-08271-8_18

The implementation of this solution on mobile devices, such as smartphones equipped with sensing, processing and gateway capabilities, allows the system to be utilized anywhere and at any time without the need for complicated configurations or the presence of dedicated specialists [3]. Several studies have investigated the potential applications of rPPG technology. It has been recognized in clinical settings for remote patient monitoring, fitness applications for heart rate tracking, and in mental health research for stress detection. Furthermore, its integration into consumer devices has made it an appealing option for telehealth and personalized healthcare solutions [4]. Despite these advantages, rPPG has certain limitations. Motion artifacts and variations in the skin tone can introduce noise into the signal, resulting in less reliable measurements. In addition, ambient lighting conditions and camera specifications significantly influence the quality of the extracted signal. While wearable devices ensure direct skin contact for more stable readings, smartphone-based rPPG offers the benefits of accessibility and ease of use without the need for additional hardware [5].

The present work represents the evolution of [6], in which an rPPG-based system capable of estimating vital signs, specifically HR, BR and SpO2, was tested exclusively on a smartphone. The accuracy in the vital signs estimation of the proposed pipeline was initially evaluated using four commercial smartphones equipped with different optical sensors. Subsequently, the usability of this solution was assessed on the smartphone with the best performance, ensuring that technological capabilities were aligned with user needs and expectations. To demonstrate that the use of expensive devices is unnecessary, the four devices selected for comparison were chosen for their wide availability, affordability and versatility in various applications, despite their medium-to-low quality. Our approach seeks to assess the feasibility of using smartphone-based rPPG for precise vital signs estimation under realistic conditions. This paper is organized as follows. Section 2 shows the description of the rPPG system for remote vital signs estimation, the description of the four selected smartphones and the perceived usability assessment methods. The obtained results are reported in Sect. 3. Finally, Sect. 4 shows our conclusions and some ideas for future work.

2 Materials and Methods

This section begins with an overview of the rPPG system used in this study. Subsequently, a summary of the camera capabilities of the four smartphones utilized for contactless vital signs estimation is provided. In conclusion, a summary of the tools employed to evaluate usability is given.

2.1 RPPG System Overview

In this research, the smartphone acts as a vision sensor to capture a video of the user's face (using the front camera) and functions as the processing unit where the vital sign estimation pipeline is executed. The pipeline for vital sign estimation operates directly on a smartphone, enabling real-time on-device processing. The complete pipeline for vital signs estimation was developed in our previous study [7]. This pipeline consists of two algorithmic steps: the preprocessing step and the feature extraction and vital

signs estimation step. For clarity, a flow diagram of the algorithmic pipeline is presented in Fig. 1a. In addition, a mobile application incorporating a graphical user interface (GUI) was implemented to enhance user interaction and data visualization. The GUI is illustrated in Fig. 1b. The acquisition lasted for 30s, after which the estimated vital signs were displayed to the user.

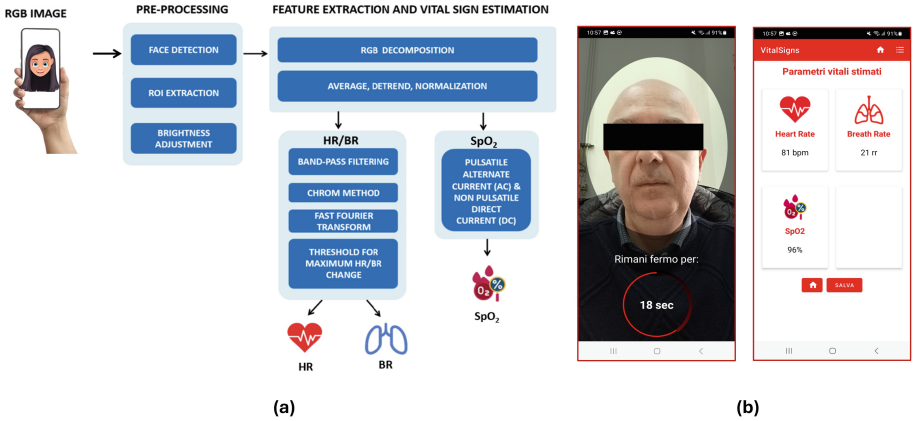

Fig. 1. Overview of the pipeline for vital signs estimation (a) and (b) GUI of the implemented app.

2.2 Smartphones Features

The study involved four different smartphones: the Samsung Galaxy A35, Samsung Galaxy S23 +, HUAWEI Mate 50 Pro and Google Pixel 7. These devices were selected for their affordability and varied optical sensor specifications. The characteristics of their camera sensors are summarized below, while Fig. 2 reports the four smartphones with details of the frontal camera used for face capture.

The android smartphone Samsung Galaxy A35 5G is equipped with a low-power octa-core processor (4x 2.4 GHz Cortex-A78 + 4x 2.0 GHz Cortex-A55), SAMSUNG Exynos 1380 as chipset, a dedicated graphic processor (Mali-G57 MC3), 4 GB of RAM and 128 GB of storage memory. The lens of the camera has the following features: a CCD/CMOS sensor model Sony IMX682, a focal length of 16 mm with an aperture (expressed in terms as the f-number) equal to 2.2, a physical sensor size equal to 3.20 mm $\times$ 2.40 mm (1/4″) and a pixel size of 1.12 μm.

Moreover, Samsung Galaxy S23+ has also an octa-core processor (1x 3.2 GHz Cortex-X3 + 2x 2.8 GHz Cortex-A715 + 2x 2.8 GHz Cortex-A710 + 3x 2.0 GHz Cortex-A510), Snapdragon 8 Gen 2 Qualcomm SM8550-AB as chipset, an Adreno 740 as GPU, 8 GB of RAM and 256 GB of storage memory. The lens of the camera has the following features: a CCD/CMOS sensor model Sony IMX564, a focal length of 25 mm with an aperture equal to 2.2, a physical sensor size equal to 5.75mm x 4.32mm (1/2.55”) and a pixel size of 1.4 μm.

HUAWEI Mate 50 Pro is equipped with the following processor: 1x 3.19 GHz Cortex-X2 + 3x 2.75 GHz Cortex-A710 + 4x 2.0 GHz Cortex-A510; it also integrates

the Snapdragon 8 Plus Gen 1 4G Qualcomm SM8475 as chipset and Adreno 730 as GPU. The device has 8GB of RAM and 256 GB of available physical space. The lens of the camera has the following features: a CCD/CMOS sensor model OmniVision OV64B, a focal length of 18 mm with an aperture equal to 2.4, a physical sensor size equal to 6.40mm x 4.80mm (1/2") and a pixel size of 0.7 μm.

Finally, Google Pixel 7 is equipped with 2x 2.85 GHz Cortex-X1 + 2x 2.35 GHz Cortex-A78 + 4x 1.80 GHz Cortex-A55 as processor, Google Tensor G2 as chipset, Mali-G710 MP07 as GPU, 8 GB of RAM and 256 GB of storage memory. The lens of the camera has the following features: a CCD/CMOS sensor model Samsung ISOCELL GN1, a focal length of 16 mm with an aperture equal to 2.2, a physical sensor size equal to 4.96mm x 3.72mm (1/2.9") and a pixel size of 1.25 μm.

Fig. 2. Image of the four smartphones used in the study with their frontal camera: a) Samsung Galaxy A35 5G, b) Samsung Galaxy S23 +, c) HUAWEI Mate 50 Pro, d) Google Pixel 7 Pro.

2.3 Usability Assessment

The perceived usability of the rPPG system was assessed using two standardized questionnaires: the System Usability Scale (SUS) [8] and the User Experience Questionnaire-Short version (UEQ-S) [9]. The SUS is a ten-item questionnaire in which participants rate each item on a 5-point Likert scale, ranging from "Strongly Disagree" to "Strongly Agree". The SUS produces a single score ranging from 0 to 100, with higher scores indicating better usability. According to the literature, a score higher than 68 indicates good usability. The UEQ-S is a short version of the User Experience Questionnaire designed to evaluate user experience with minimal respondent burden. It comprises eight items that assess two dimensions: Pragmatic Quality (efficiency and usability) and Hedonic Quality (stimulation and novelty). Participants rated each item on a 7-point semantic differential scale ranging from "−3" to "+3", with higher scores indicating a more positive user experience.

3 Results and Discussions

The experiment included 20 participants (9 males and 11 females) aged between 26 and 41 years (mean age = 34.8), all Caucasian ethnicity, with foreheads and cheeks free of beards and hair. Each participant was equipped with a commercial OXI-200 pulse oximeter manufactured by GIMA [10] to simultaneously collect baseline HR and SpO2 measurements. Additionally, participants wore a commercial smart device, Zephir Bio-Harness 3.0 [11], which is equipped with piezoresistive sensors capable of providing ground truth data for BR. These physiological signals served as reference values for validating the rPPG-based estimations. All experimental procedures were performed in a controlled indoor environment. Ambient illumination was maintained within a standardized range of 51–100 lx, and a fixed distance of 30cm was maintained between the participant's face and the camera to ensure consistency across the recordings. The performance of the rPPG estimation algorithms was evaluated using two widely adopted error metrics: Mean Absolute Error (MAE) and Root Mean Square Error (RMSE). These metrics were used to quantify the accuracy of the rPPG-derived values in comparison with those obtained from reference medical-grade instruments. Table 1 presents the MAE and RMSE values for HR, BR and SpO_2 estimated by the four smartphone models used during the trials.

Table 1. MAE and RMSE in the estimation of vital signs of the four smartphones.

		Samsung Galaxy A35	Samsung Galaxy S23 +	HUAWEI Mate 50 Pro	Google Pixel 7
HR	MAE	**4.47**	5.38	7.21	6.78
	RMSE	**7.83**	8.38	10.23	9.42
BR	MAE	**2.4**	3.18	3.56	3.29
	RMSE	**4.11**	4.76	5.04	4.85
SpO_2	MAE	**0.57**	0.82	0.68	0.63
	RMSE	**0.95**	1.36	1.21	1.18

Among the four smartphones evaluated, the Samsung Galaxy A35 demonstrated superior performance, exhibiting the lowest error rates across all measured physiological parameters (HR, BR and SpO_2). Under controlled experimental conditions, these performance differences are likely attributable to variations in camera sensor specifications and image processing capabilities. The better performance of the Galaxy A35 can be attributed to a combination of hardware and software advantages, including a larger sensor size, higher pixel density, improved light sensitivity and more effective noise reduction algorithms. Additionally, the device's image signal processor (ISP) may enhance frame stability and color fidelity, both of which are critical for accurate rPPG signal extraction. In contrast, the HUAWEI Mate 50 Pro and Google Pixel 7 exhibited higher estimation errors. These discrepancies may stem from smaller effective pixel areas or less optimized image enhancement pipelines, which can affect signal quality in low-light or motion-sensitive conditions. The Samsung Galaxy S23+ still reported

marginally higher error metrics, potentially due to differences in focal length or sensor architecture that impact facial region resolution and consistency of illumination. These findings underscore the influence of camera hardware characteristics and image processing strategies on the performance of smartphone-based rPPG systems and highlight the importance of sensor selection in the design of non-contact health monitoring solutions.

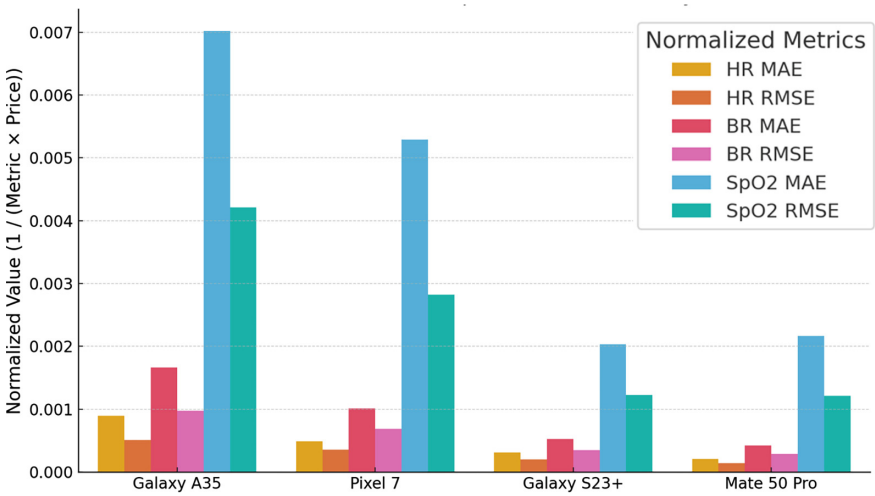

Fig. 3. Smartphones Cost-Performance Comparison.

To compare cost-performance across smartphones, MAE and RMSE values were normalized for each estimated vital sign. This process produced two unitless ratios—normalized MAE and RMSE—representing the performance error per euro spent. A higher value indicates a more advantageous cost-performance ratio. In Fig. 3 a graphical representation of the cost-performance comparison is reported. Devices are organized from left to right in ascending order of price, allowing for a direct comparison of both performance and cost-efficiency across the various models. The Samsung Galaxy A35 exhibits the most favorable cost-performance ratio among all devices tested, despite being the most affordable option at approximately €250. This indicates that it provides the most accurate vital sign estimations for each euro spent. Although the absolute differences in MAE and RMSE may not appear significant on a linear scale, normalization highlights relative inefficiencies in more expensive models.

The usability and acceptability of the rPPG system were evaluated in two elderly care facilities with 27 participants, including 20 older adults (mean age 74.5) and 7 staff members. Training was provided to ensure proper device usage, and tests were conducted in a controlled setting. Both groups completed SUS and UEQ-S questionnaires to assess perceived usability. Staff scored the system very highly on usability (SUS: 97.5), while elderly users gave a lower, but still positive, score (SUS: 80), indicating minor challenges linked to accessibility and technological familiarity. UEQ-S results showed elderly users rated the system higher in hedonic quality, likely due to its engaging design, while staff emphasized functionality. Overall quality scores were 2.625 for users and 2.125 for staff.

These findings highlight the system's strong usability but also suggest that improving accessibility, through interface adjustments such as larger fonts or guided interactions, could further enhance the experience for elderly users. The study also notes the need for broader evaluations across diverse populations and during extended use.

4 Conclusion

This study demonstrates the feasibility, accuracy and usability of an rPPG system implemented on consumer-grade smartphones for non-contact vital signs monitoring. By leveraging the built-in front-facing cameras and on-device processing capabilities of four different smartphones, we successfully estimated HR, BR and SpO_2 without the need for wearable sensors or specialized equipment. Among the tested devices, the Samsung Galaxy A35 5G stood out for its superior performance across all physiological parameters, achieving the lowest MAE and RMSE. Notably, despite its lower cost compared to flagship models, it provided the best cost-performance ratio, highlighting the potential for affordable yet accurate mobile health solutions. These results underline the critical role of camera sensor characteristics in determining rPPG accuracy. Usability assessments conducted with both healthcare staff and elderly users further confirmed the system's practical applicability. While staff members rated the system extremely high on usability, older adults also reported a generally positive experience, especially appreciating the engaging and user-friendly interface. Minor usability barriers for elderly suggest future design refinements—such as larger text, clearer guidance, and simplified navigation—could further enhance accessibility.

Overall, the findings support the adoption of smartphone-based rPPG systems for telehealth and continuous health monitoring. Further research should explore long-term usage in diverse populations and real-world environments to validate and expand the system's applicability.

Acknowledgment. This research was developed within the project funded by Next Generation EU – "Age-It – Ageing well in an ageing society" project (PE0000015), National Recovery and Resilience Plan (NRRP) – PE8 – Mission 4, C2, Intervention 1.3". The views and opinions expressed are only those of the authors and do not necessarily reflect those of the European Union or the European Commission. Neither the European Union nor the European Commission can be held responsible for them.

References

1. Rouast PV, Adam MTP, Chiong R et al (2018) Remote heart rate measurement using low-cost RGB face video: a technical literature review. Front Comput Sci 12:858–872
2. Wang W, Den Brinker AC, Stuijk S, De Haan G (2016) Algorithmic principles of remote photoplethysmography. IEEE Trans Biomed Eng 64(7):1479–1491
3. Qiao D, Amtul AH, Zulkernine F, Jaffar N, Masroor R (2022) ReViSe: Remote vital signs measurement using smartphone camera. IEEE Access
4. Yu Z, Li X, Zhao G (2021) Facial-video-based physiological signal measurement: recent advances and affective applications. IEEE Signal Process Mag 38(6):50–58

5. Pirzada P, Wilde A, Doherty GH, Harris-Birtill D (2023) Remote photoplethysmography: A state-of-the-art review. medRxiv
6. Carluccio AM, Manni A, Caroppo A, Siciliano PA, Leone A (2025) Cost-effective camera-based mobile architecture for contactless vital signs monitoring. In: Conoci S, Di Natale C, Prodi L, Valenti G (eds) Sensors and Microsystems. AISEM 2024. Lecture Notes in Electrical Engineering, vol 1334. Springer, Cham, pp 176–184
7. Caroppo, A., Manni, A., Rescio, G., Siciliano, P.A., Leone, A.: Vital signs estimation in elderly using camera-based photoplethysmography. Multimed Tools Appl (2024)
8. Brooke J (1996) SUS: A "quick and dirty" usability scale. In: Jordan PW, Thomas B, Weerdmeester BA, McClelland IL (eds) Usability evaluation in industry. Taylor & Francis, London, pp 189–194
9. Schrepp M, Hinderks A, Thomaschewski J (2017) Design and evaluation of a short version of the User Experience Questionnaire (UEQ-S). Int J Interact Multimed Artific Intell 4:103–108
10. GIMA, OXI-200. https://www.gimaitaly.com/prodotti.asp?sku=35213&dept_selected=622&dept_id=6220. Accessed May 2025
11. Zephyr, BioHarness 3.0. https://www.zephyranywhere.com/system/overview. Accessed May 2025

Point-of-Care Tests for Ultra-Low Detection of Pathogens Exploiting SPR-POF Sensors

Chiara Marzano, Rosalba Pitruzzella, Francesco Arcadio, Laura Pasquardini, Luigi Zeni, and Nunzio Cennamo(✉)

Department of Engineering, University of Campania Luigi Vanvitelli, Via Roma 29, Aversa, Italy

nunzio.cennamo@unicampania.it

Abstract. Following the pandemic due to SARS-CoV-2, the need for rapid, sensitive, and accessible methods to detect viral and bacterial pathogens in different biological matrices has become evident. In this context, a point-of-care test (POCT) device has gained significant attention for its potential to provide rapid diagnosis outside traditional laboratory environments. An ideal POCT system should be compact, low-cost, highly selective and sensitive, operable by unskilled personnel, and capable of real-time data transmission through integration with the Internet of Things (IoT) paradigm. This overview presents a POCT, based on plastic optical fibers (POFs), for the pathogen detection exploiting surface plasmon resonance (SPR) phenomena. The plasmonic-sensitive gold surface can be combined with selective receptor layers for membrane protein detection of specific pathogens. To this purpose, biological receptors, such as antibodies and aptamers, and synthetic receptors, such as molecularly imprinted polymers (MIPs), can be employed to tailor the sensor for different targets of interest. The reported POCT is designed to support IoT integration, enabling real-time data transmission, cloud processing, and remote monitoring. The SPR-POF platform functionalized with different types of receptors shows strong potential for decentralized diagnostics, offering rapid analysis (about ten minutes), no sample pretreatment, and high scalability.

Keywords: Point-of-care Test (POCT) · Surface plasmonic resonance (SPR) · Plastic optical fibers (POFs) · Bio/chemical Optical sensors · viruses · bacteria

1 Introduction

Rapid and accurate detection of viruses and bacteria is a key priority for public health and clinical diagnostics. The COVID-19 pandemic has highlighted the urgent need for affordable diagnostic tools for virus detection, while bacterial pathogens continue to be a menace due to their high infectivity and persistence [1]. Early diagnosis is essential for effective patient management and outbreak control. Point-of-care test (POCT) devices offer a promising solution, enabling rapid and decentralized diagnosis without the need for specialized personnel or complex sample preparation [2]. Their integration with

C. Marzano and R. Pitruzzella—These authors contributed equally to this work.

C. Di Natale et al. (Eds.): AISEM 2025, LNEE 1497, pp. 114–121, 2025.
https://doi.org/10.1007/978-3-032-08271-8_19

Internet of Things (IoT) technologies [3] enables real-time data transmission, remote monitoring, and improved epidemiological tracking. In contrast, gold standard methods such as reverse transcription polymerase chain reaction (RT-PCR), while ensuring sensitivity and reliability, are limited by high costs, long processing times, and dependence on laboratory infrastructure [4].

A significant challenge for POCT development consists of ensuring sensitivity and selectivity, enabling detection in highly diluted biological matrices, and minimizing matrix effects [5]. Among emerging POCT technologies, those based on surface plasmon resonance (SPR) and plastic optical fibers (POFs) are well known for their label-free operation, high sensitivity, and miniaturization potential [6]. The SPR-POF platforms can be functionalized with specific receptor layers for selective detection of analytes such as proteins, small molecules, and viruses and bacteria via membrane proteins. These receptors can be biological (e.g., antibodies, aptamers) or synthetic (e.g., molecularly imprinted polymers, MIPs), offering versatility and robustness in real samples [7].

This overview presents SPR-POF sensor chips employed in a reader device for pathogen detection via POCT, focusing on different recognition strategies (i.e., antibodies, aptamers, and MIPs) for targeting membrane proteins. The sensitivity and selectivity of each functionalized probe are evaluated and are recalled here, demonstrating the strong potential of this approach for rapid and on-site diagnostics of pathogens.

2 Point-of-Care Test (POCT)

2.1 Experimental Setup

Figure 1a shows the first prototype of a POCT based on SPR-POF chips [8, 9]. This setup exploits the SPR phenomenon and is based on a spectral configuration scheme. Therefore, the POCT comprises a white light source (model HL-2000-LL, manufactured by Ocean Insight, Orlando, FL, USA), a 3D-printed holder, a plasmonic POF chip, and a spectrometer (FLAME-S-VIS-NIR-ES, Ocean Insight). The disposable chip is an SPR-POF probe combined with receptor layers to obtain a selective detection of the substances of interest. The data are acquired using proprietary software (SpectraSuite 6.2, Ocean Optics) and then processed by MATLAB R2024a software. Figure 1b shows an even more compact version of this POCT prototype, developed together with Moresense srl (Spectra 340, Moresense srl, Milan, Italy) [10], as a further advancement in technological readiness level (TRL). In [10], a white LED is used instead of a halogen lamp.

In the [10] version, a software tool developed together with Moresense srl is used to acquire and process the experimental data of the POCT (Moresense Capture Spectrum Data ver. 2.3). This tool offers the possibility of connecting the POCT to the Internet. In particular, the IoT approach was used to process, visualize, and share the acquired data and produce statistical analyses [10].

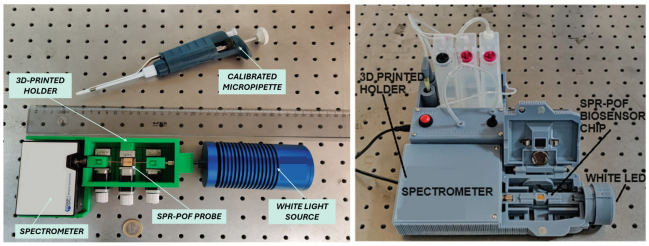

Fig. 1. Two POCT prototypes based on SPR-POF chips: (a) first experimental setup version; (b) more compact version with a higher TRL.

2.2 SPR-POF Probe Combined with Different Receptors

The SPR-POF platform is based on a well-established protocol [11]. Briefly, a 1 mm POF (having a 980 μm thick PMMA core and a 20 μm thick fluorinated polymer cladding) is fixed in the trench (1 mm wide, 1 mm deep, and 10 mm long) of a resin cube to facilitate the following manufacturing step involving polishing. In fact, through a lapping step with two different types of abrasive paper (5 and 1 μm grain), the cladding and part of the core are removed, obtaining the D-shaped POF. Subsequently, a Microposit S1813 photoresist layer (1.5 μm thick) was spin-coated onto the exposed core, as it has a higher refractive index than the core to enhance the SPR phenomenon [11]. Finally, a nanometric gold film (60 nm thick) was sputtered onto it using a sputter coater machine (Safematic CCU-010, Zizers, Switzerland) [11].

The SPR-POF sensor described above was functionalized with different kinds of receptors. In the case of *Brucella* detection, an antibody was used as the receptor [12]. Gold functionalization was optimized and extensively characterized by physicochemical techniques, as reported in [13]. The antibody immobilization protocol and optimal conditions (antibody layer oriented at the appropriate density) were selected [13] and then used for functionalization and testing of SPR-POF probes.

In the case of SARS-CoV-2 detection, a specific aptamer for the recognition of the SARS-CoV-2 spike glycoprotein was chosen as the receptor. The formation of the self-assembled monolayer (SAM) was achieved as described in detail in [8].

Finally, a specific synthetic receptor was used for the detection of SARS-CoV-2 through its membrane protein [9]. This MIP was synthesized using functional monomers able to interact with the functional groups of the S1 subunit of the SARS-CoV-2 spike protein.

Figure 2 shows outlines of the same SPR-POF platform functionalized for the detection of Brucella with an antibody (Fig. 2a) and SARS-CoV-2 with an aptamer (Fig. 2b), and an MIP (Fig. 2c), respectively.

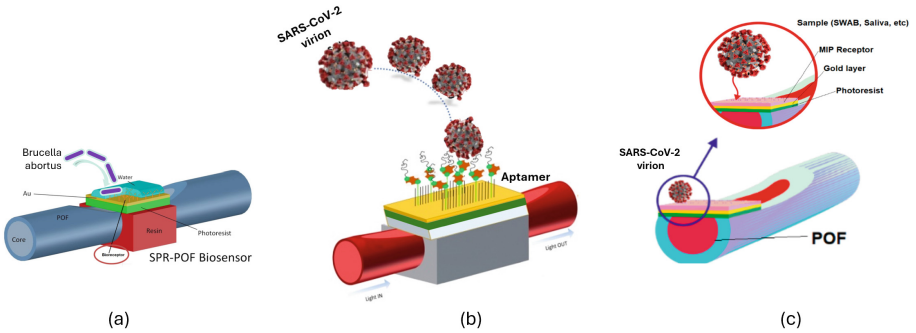

Fig. 2. Outline of SPR-POF platform functionalized with different kinds of receptor layers relative to a) *Brucella abortus* bacterium detection via antibody. SARS-CoV-2 detection via aptamers b) and MIP c).

3 Capabilities of the POCT Based on SPR-POF Chips for Pathogen Detection in Aqueous Solutions

3.1 *Brucella* Detection by SPR-POF Biosensors Based on an Antibody

The SPR-POF biosensor was evaluated for its ability to detect *Brucella abortus* over a wide concentration range, from 1 to 10^6 bacteria/mL [12]. In this overview, the key experimental results are recalled. After a short 5-min incubation and buffer wash steps, the sensor showed clear shifts in the resonance wavelength as the bacterial concentration varied. As shown in Fig. 3a, when the bacterial concentration under test increased, the resonance wavelength shifted toward lower values (blue-shift), demonstrating its efficacy in detecting the target pathogen even at low concentrations. When the binding/detection occurs, the refractive index of the receptor layer decreases. The resulting dose-response curve, shown in Fig. 3b, was fitted using the Langmuir equation. Based on the calibration data, the limit of detection (LoD) was estimated to be 2.8 bacteria/mL, confirming the high sensitivity of the POCT [12]. The selectivity of the sensor was validated by testing the proposed biosensor against *Salmonella*, where no significant signal was observed at low concentrations and only minimal nonspecific binding occurred at higher levels, likely due to physical deposition rather than specific interactions [12].

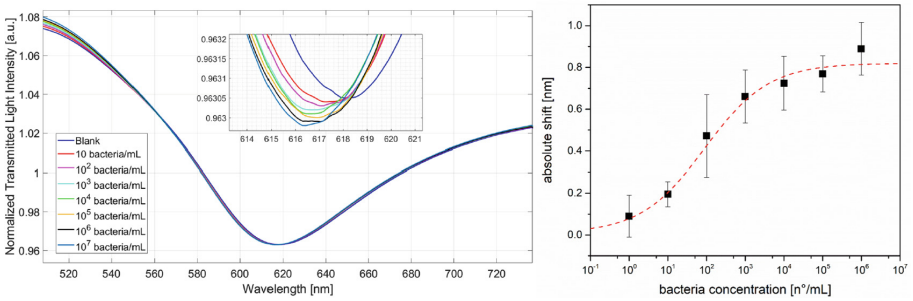

Fig. 3. (a) SPR spectra obtained by testing the SPR-POF biosensor with *Brucella* solutions at different dilutions in buffer solution [12]; (b) Dose-response curve obtained by fitting the experimental values with the Langmuir model: absolute value of the shift in resonance wavelength (calculated with respect to the blank) versus the bacterial concentration [12].

3.2 SARS-CoV-2 Detection via SPR-POF Sensors Based on an Aptamer

The SPR-POF aptasensor was initially evaluated by testing its response to different concentrations of the SARS-CoV-2 spike protein in buffer solution. The experimental data obtained and here recalled were successfully fitted using the Langmuir adsorption model to obtain the dose-response curve, as shown in Fig. 4a. From the fitting parameters, an affinity constant between the aptamer and the spike protein equal to 0.015 $(\text{nM})^{-1}$ and a LoD of about 10 nM were estimated [8]. To evaluate its performance in real biological matrices, the aptasensor was further tested with negative and positive nasopharyngeal (NP) swab samples. First, the SPR-POF aptasensor was tested with a negative swab in universal transport medium (UTM), which did not show a response in terms of resonance wavelength shift, and then with a positive swab in UTM (confirmed by RT-PCR), both diluted 1:2 with physiological solution (0.9% NaCl). The positive swab was collected from a COVID-19 positive patient, confirmed by RT-PCR (27th cycle of RT-PCR) [14]. The samples were incubated on the sensor surface for 10 min. As illustrated in Fig. 4b, SARS-CoV-2 virions induced a resonance wavelength shift (red-shift) of approximately 1.8 nm, clearly indicating the sensor's ability to detect the virus in complex matrices directly.

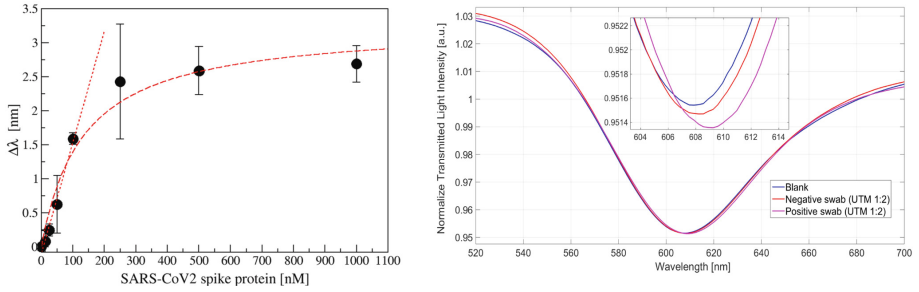

(a) (b)

Fig. 4. (a) Dose-response curve of the SPR-POF aptasensor: resonance shift with respect to blank ($\Delta\lambda$) versus the SARS-CoV-2 spike protein concentration [8]. (b) Comparison of the response obtained by the SPR-POF aptasensor with a negative and a positive SARS-CoV-2 swab in UTM (confirmed by RT-PCR), both diluted 1:2 in physiological solution.

3.3 SARS-CoV-2 Detection via SPR-POF Sensors Based on MIPs

The SARS-CoV-2 detection via SPR-POF platforms can be carried out exploiting MIPs instead of bio-receptors. To validate the synthesis of the MIP specifically designed for the S1 subunit spike protein of SARS-CoV-2, the SPR-POF-MIP sensor was tested with a commercial standard of the target protein at increasing concentrations [9]. The experimental data obtained by evaluating the shift of the resonance wavelength (red-shift) with increasing analyte concentration versus SARS-CoV-2 Spike protein concentration were fitted using the Langmuir model to obtain the dose-response curve, from which a LoD of 58 nM was estimated [9]. To evaluate the selectivity of the MIP-based sensor, specificity tests were performed comparing its response to solutions of SARS-CoV-2 and MERS-CoV spike proteins in buffer solution. The sensor demonstrated a strong selectivity for the SARS-CoV-2 spike protein, confirming its selective binding capacity [9]. Next, the sensor was tested for its ability to detect SARS-CoV-2 virions in clinical samples. NP swab samples collected from COVID-19 positive patients were diluted in physiological solution (0.9% NaCl) and analyzed for sensitivity in real matrices. Figure 5a presents the sensor responses at different dilutions of the positive swab. The sensor detected positive samples diluted up to 1:500, with each test taking approximately 10 min, demonstrating the ability to identify even minimal viral loads. In contrast, RT-PCR confirmed positivity only in the 1:2 dilution of the same samples. Finally, positive and negative NP swab samples, in physiological solution and UTM, were tested and cross-validated with RT-PCR results [9]. In particular, Fig. 5b reports the results obtained by testing the SPR-POF-MIP sensor with negative and positive swabs in physiological medium, confirming its potential for reliable and rapid detection of SARS-CoV-2 in real biological matrices.

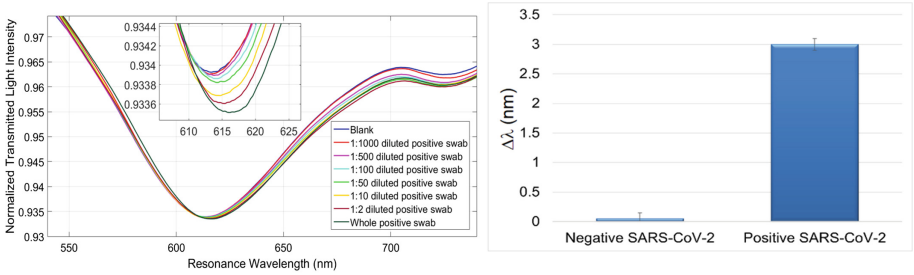

Fig. 5. (a) SPR response spectra of a positive swab for SARS-CoV-2 (36th cycle of RT-PCR) in physiological medium, at different dilutions with physiological solution, tested with the SPR-POF-MIP sensor [9]. (b) Comparison of the response obtained by the SPR-POF-MIP sensor with a negative and a positive SARS-CoV-2 swab (physiological medium) [9].

4 Conclusion

The sensing strategy presented in this overview, through three different examples of pathogen detection using the same SPR-POF platform combined with different receptor layers, demonstrates the versatility and effectiveness of these sensors for the detection of a wide range of viruses and bacteria via their membrane protein, simply by modifying the selective receptor layer. This adaptable approach, combined with the small-sized and low-cost setup, enables the development of POCT with detection limits several orders of magnitude lower than those obtained with conventional RT-PCR methods. Furthermore, the measurement time is significantly reduced, from several hours to a few minutes. In addition, sample pretreatment and highly trained personnel are not required. All this offers a powerful tool for on-site rapid, selective, and sensitive diagnoses.

References

1. Guo Y-R et al (2020) The Origin, Transmission and Clinical Therapies on Coronavirus Disease 2019 (COVID-19) Outbreak – an Update on the Status. Military Med Res, 7
2. Wangping D, Lihua W, Shipping S, Xiaolei Z (2016) Biosensors in POCT Application. Prog. Cherm. 28:1341–1350
3. Singh P (2018) Internet of things based health monitoring system: opportunities and challenges. ijarcs 9: 224–228
4. Shen M, et al (2020) Recent Advances and Perspectives of Nucleic Acid Detection for Coronavirus. J Pharmaceut Analy 10: 97–101
5. Kumar S, Seo S (2023) Plasmonic sensors: a new frontier in nanotechnology. Biosensors 13:385
6. Caucheteur C, Guo T, Albert J (2015) Review of plasmonic fiber optic biochemical sensors: improving the limit of detection. Anal Bioanal Chem 407:3883–3897
7. Cennamo N, Pesavento M, Arcadio F, Marzano C, Zeni L (2024) Advances in plastic optical fiber bio/chemical sensors to realize point-of-care-tests. TrAC Trends Anal Chem 177:117797
8. Cennamo N et al (2021) SARS-CoV-2 spike protein detection through a plasmonic D-shaped plastic optical fiber aptasensor. Talanta 233:122532

9. Cennamo N et al (2021) Proof of concept for a quick and highly sensitive on-site detection of SARS-CoV-2 by plasmonic optical fibers and molecularly imprinted polymers. Sensors 21:1681
10. Capasso F, et al (2024) The BETTER project: development of a tool for the measurement of SARS-CoV-2 via internet of medical things POCT. 2024 IEEE Sensors Applications Symposium (SAS), pp. 1–5
11. Cennamo N, Massarotti D, Conte L, Zeni L (2011) Low cost sensors based on SPR in a plastic optical fiber for biosensor implementation. Sensors 11:11752–11760
12. Pasquardini L, et al (2023) Immuno-SPR Biosensor for the Detection of Brucella Abortus. Sci Rep 13
13. Pasquardini L, et al (2023) Optimization of the immunorecognition layer towards brucella Sp. on Gold Surface for SPR Platform. Colloids and Surfaces B: Biointerfaces 231: 113577
14. Cennamo N et al (2021) (INVITED) quantitative detection of SARS-CoV-2 virions in aqueous mediums by IoT optical fiber sensors. Results in Optics 5:100177

Design of a Voltage-Conveyor Based Read-Out Circuit for ECG Monitoring

R. Olivieri[1](✉), G. Barile[1], V. Stornelli[1], A. Zompanti[2], and G. Ferri[1]

[1] Department of Industrial and Information Engineering and Economics, University of L'Aquila, L'Aquila, Italy
riccardo.olivieri1@graduate.univaq.it

[2] Unit of Electronics for Sensor Systems, Department of Engineering, University Campus Bio-Medico di Roma, Rome, Italy

Abstract. This paper presents the design of a VCII-based read-out circuit for ECG monitoring employing second generation voltage conveyors (VCIIs) as active blocks. Starting from a quick overview of VCII, the paper describes the whole interface, composed by three active blocks and one passive filter, and its basic operation. The proposed circuit was simulated by LT-SPICE firstly designing the internal blocks at transistor level, in 0.18 µm standard CMOS technology, and then using the commercially available device AD844 to demonstrate the validity of the designed circuit also with experimental measurements. The voltage gain is tunable by changing some resistance values in the different stages of the amplifier. In the proposed solution, the differential voltage gain has been set to more than 60 dB, while the common mode gain is about −25 dB. The aim of this research is to test the performance of biological signal amplifiers using the current-mode approach (in particular, VCII) which is still underutilized in this context.

Keywords: ECG · VCII · Current-mode · analog front-end · biomedical electronics

1 Introduction

In sensor interface applied to biomedical engineering, precision and accuracy of the read-out electronic circuit holds a significant importance, particularly in vital monitoring systems like ElectroCardioGraphy (ECG). ECG analog interface circuits serve as the foundation for acquiring, processing, and interpreting physiological signals, directly impacting diagnosis and patient care. By applying electrodes to the body surface, the ECG records the changes in electrical potential generated by cardiac cells during the cardiac cycle as graphical traces. These traces commonly consist of P waves, QRS complex, and T waves, and reflect the temporal sequence of electrical events in the heart during contraction and relaxation. Recent advancements in the design of sensor interfaces also in biomedical applications have opened new possibilities in the design of amplifier blocks to increase the readability of the measurand variation [1, 2].

One of these breakthroughs lies in the utilization of the second-generation voltage conveyor (VCII) as active block [3–6], heralding a paradigm shift in circuit design

C. Di Natale et al. (Eds.): AISEM 2025, LNEE 1497, pp. 122–127, 2025.
https://doi.org/10.1007/978-3-032-08271-8_20

methodologies. By exploiting the enhanced capabilities of these voltage conveyors, analog designers can overcome complexities inherent to ECG monitoring with improved features [7–9]. This article explores the new opportunities given by the employment of VCIIs in ECG monitoring systems, by examining underlying principles, design considerations, and practical implications of integrating them in the amplification of ECG signal. In Section II we give an overview of the active block as well as the proposed VCII-based interface for ECG signal, also described at transistor level. In Section III, simulation and measurement results are given. Finally, conclusions and future steps will be drawn.

2 VCII and VCII-Based Interface

In this section, the main current-mode active block employed for this analog front-end is presented: the second-generation Voltage Conveyor (VCII), a current-mode block that plays a key role in the design of modern analog circuit, in particular analog interfaces, due to its peculiar characteristics and improved performance over traditional operational amplifiers.

Figure 1 shows the symbol (a) and the equivalent internal structure (b) of a VCII. This block is the dual configuration of the second-generation current conveyor (CCII). It consists of a current buffer between the Y and X terminals and a voltage buffer between the X and Z terminals. Unlike the CCII, the Y terminal of the VCII is a low impedance current input port with an ideal value of zero, X is a high impedance current output port with an ideal value of infinite, and Z is a low impedance voltage output port with an ideal value of zero. The relations between terminals voltage and currents of VCII are represented as:

$$i_x = \pm\beta i_y;\ V_z = \alpha V_x;\ V_y = 0 \tag{1}$$

where β and α (ideally close to unity) are current gain between Y and X terminals and voltage gain between X and Z terminals, respectively. The − β relates to a VCII − while + β to a VCII + [3]. In Fig. 2, a possible schematic, at transistor level, of the VCII is shown.

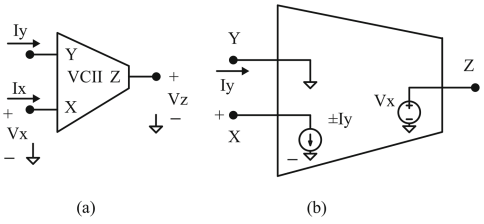

Fig. 1. Second generation voltage conveyor (VCII): (a) Symbol; (b) Internal structure.

Fig. 2.CMOS implementation of a VCII.

The proposed electronic system (shown, at block level, in Fig. 3) uses two main electrodes and a driven right leg (DRL) electrode, a low-noise amplification (LNA)

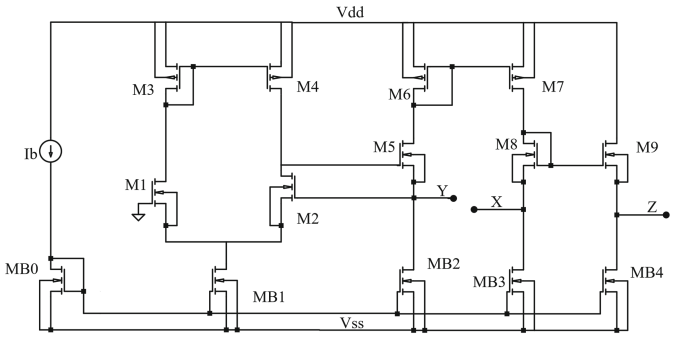

Fig. 2. CMOS implementation of a VCII.

stage, a filtering stage, which comprises a NOTCH filter designed to eliminate the 50 Hz power line frequency and a first order active low-pass (LP) filter with a cutoff frequency of 200 Hz, and a final single ended conversion stage (AMP). In all the active blocks, VCII is the employed active block.

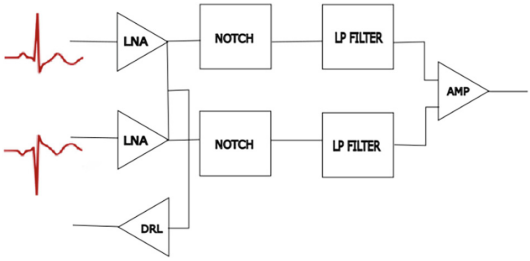

Fig. 3. ECG Proposed Block Diagram.

Cardiac signals were acquired with dry electrodes. In our design, cardiac signals have been generated as piecewise linear functions (PWL) and introduced with an amplitude of approximately 2 mV. The initial signal is differential, so a differential input configuration for the amplifier is needed. For this aim, we employed amplifiers designed with VCIIs. The input stage consists of two VCII voltage amplifiers. The input voltage is converted to current via a resistor and fed into the low impedance Y terminal of the VCII. The two VCII devices have their X terminals connected through resistors. The outputs of this input stage are taken as voltage signals at the low impedance Z terminal. The gain of these amplifiers is adjustable by varying the ratio between the output and the input resistances. This feature enables fine-tuning of amplification parameters for varying input signal amplitudes and optimizes signal-to-noise performance. In addition to signal amplification, the initial stage of the proposed ECG circuit incorporates a third electrode that serves as DRL, ensuring common-mode rejection as well as safety, by stabilizing the baseline voltage and reducing interference, thereby minimizing the risk of electrical shocks or discomfort during ECG acquisition [10].

Following signal amplification, the proposed interface has a filtering stage, significant for removing unwanted noise and artifacts while preserving the integrity of the cardiac signal. This stage comprises two key components: a classic passive notch filter to eliminate the 50 Hz frequency interference and an active first-order low-pass filter employing a VCII. Notably, the gain of this filter is adjustable via the input resistance [11]. This input resistance sets the current value at the Y terminal, which is then converted into a voltage at the X terminal and then copied to Z.

The output stage of proposed ECG read-out circuit is a VCII-based differential voltage amplifier. This stage is used to convert the differential-ended signal to single-ended one. The design of this stage incorporates five VCIIs, strategically arranged to amplify and process the incoming signal.

The differential amplifier has a voltage buffer for each of the two inputs, whose voltage output is converted to current using a resistor. The input current at the Y terminal in the second pair of VCIIs is the same as that at the X terminal due to the characteristic properties of the VCII. The voltage difference occurs in the final VCII, where the conversion from differential to single-ended also takes place. The gain of this amplifier is adjustable, primarily being determined by the ratio between the output and the input resistances.

3 Simulations and Measurements

The interface has been simulated firstly designing the VCII at transistor level, then using the commercial device named AD844 as VCII.

LT-Spice software was used for the simulations. Input signal amplitude was set at 2 mV in both the simulations, so emulating typical cardiac signal levels encountered in clinical scenarios. Non-idealities were added to the input signals for the simulation. Specifically, a 50 Hz sinusoidal waveform was injected to simulate power-line interference, mimicking real-world environmental conditions. Furthermore, to assess the circuit ability to mitigate noise and artifacts, a high-frequency noise source was incorporated into the simulation setup. This enabled the observation of the circuit total filtering performance, highlighting its efficacy in removing extraneous noise while preserving the essential features of the cardiac signal.

Figure 4 shows the cardiac signal with superimposition of a 50 Hz sinusoidal noise wave before notch filter stage and after the whole interface circuit. Table 1 summarizes the gain comparison made between the discrete version with AD844 and the simulated version with VCII designed with standard 0.18 μ CMOS technology. In Fig. 5 experimental input and output voltages are reported, showing a gain higher than 60 dB and the noise removal.

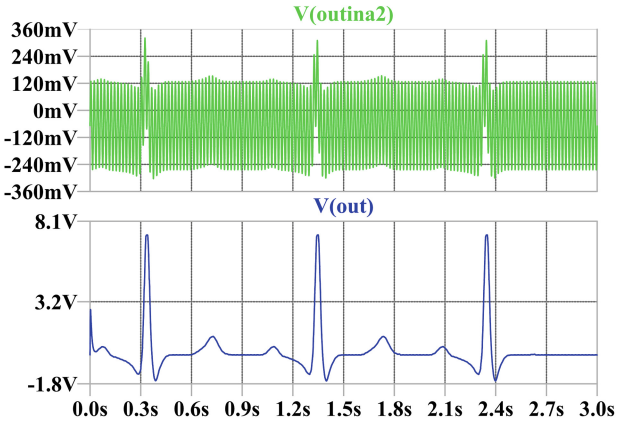

Fig. 4. Voltages at first amplification stage output (upper) and after the final output (lower).

Table 1. Gain comparison between simulated CMOS 0.18 µm version and fabricated AD844-based version.

Stage	Voltage Gain (dB) - AD844 version	Voltage Gain (dB) - CMOS 0.18 µm
First Amplification Stage	49.1 dB	41.5 dB
Notch Filter	−14 dB	−12 dB
Low-Pass Filter	15 dB	10.7 dB
Final Amplification Stage	23 dB	20.3 dB
Output Voltage	73 dB	60.5 dB

Fig. 5. Experimental output voltage (lower), input voltage (upper).

References

1. Scarsella M, Barile G, Stornelli V, Safari L, Ferri G (2023) A survey on current-mode interfaces for bio signals and sensors. Sensors 23(6):3194
2. Ferri G, Stornelli V, Fragnoli M (2006) An integrated improved CCII topology for resistive sensor application. Analog Integr Circ Sig Process 48:247–250
3. Safari L, Barile G, Stornelli V, Ferri G (2019) An Overview on the second generation voltage conveyor: features, design and applications. IEEE Trans Circuits Syst II Express Briefs 66(4):547–551
4. Olivieri R, Colaiuda D, Barile G, Stornelli V, Ferri G (2025) A novel low-power differential input current summing second-generation voltage conveyor. J Low Power Electron Appl 15(1):7
5. Barile G, Safari L, Stornelli V, Ferri G, Colaiuda D (2023) CMOS Adaptive Biased Second Generation Voltage Conveyor. 2023 IEEE International Workshop on Biomedical Applications, Technologies and Sensors (BATS), 62–67
6. Yuce E, Safari L, Minaei S, Ferri G, Barile G, Stornelli V (2021) A new simulated inductor with reduced series resistor using a single VCII. Electronics 10(14):1693
7. Ferri G, Stornelli V, Di Simone A (2011) A CCII-based high impedance input stage for biomedical applications. J Circ Sys Comp 20(8):1441–1447
8. Zompanti A et al (2021) Development and test of a portable ECG device with dry capacitive electrodes and driven right leg circuit. Sensors 21(8):2777
9. Thakor NV, Webster JG (1980) Ground-Free ECG recording with two electrodes. IEEE Trans Biomed Eng 27(12):699–704
10. Winter BB, Webster JG (1983) Driven-right-leg circuit design. IEEE Transact Biomed Eng BME 30(1): 62–66
11. Safari L, Barile G, Ferri G, Stornelli V (2018) High performance voltage output filter realizations using second generation voltage conveyor. Int J RF Microw Comp Aided Eng 28(9):e21534

Mems and Physical Sensors

A New Lead-Free Piezo-Composite MEMS Acoustic Transducer

A. Esposito(✉), P. S. Barbato, C. Verrengia Caporossi, V. Casuscelli, and R. Scaldaferri

Analog, Power and Discrete, MEMS and Sensors Group (APMS), STMicroelectronics, Via Remo de Feo 1, Arzano, Italy
Annachiara.esposito@st.com

Abstract. A microphone is a sensor that converts sound waves into an electrical signal, typically using a diaphragm and a transducer. Traditional microphones are often capacitive, but the new generation is moving towards piezoMEMS technology due to its advantages, such as insensitivity to particles, waterproofness, and improved wake-up modes. However, commercially available piezoelectric microphones often use PZT, which contains toxic PbO.

This article presents a prototype of a composite, non-toxic, and lead-free piezoelectric microphone capable of operating in harsh environments. The fabricated prototype consists of a 2 μm thin film spun over a platinum-coated silicon wafer, with a top electrode sputtered through a mask. The device was cut to form a cantilever, simulating a transducer in receiver mode.

The prototypes were characterized ferroelectrically and vibrometrically, allowing us to extract the piezoelectric parameters and compare them with well-known lead-containing piezoelectric materials (PZT) and green materials (AlN). Vibromechanical characterization revealed a resonance frequency of approximately 4 kHz, within the audible range.

The acoustic response was validated by comparing the device's response to a sound wave with that of a commercial microphone. The sensitivity of our device was measured at -55 dBV, which, while lower than the typical range, might be adequate considering the fabrication limitations.

Keywords: MEMS technology · Lead-free materials · Piezoelectric microphone · Composite material

1 Introduction

In the world of MEMS, microphones can be divided into two main categories: capacitive and piezoelectric. Capacitive microphones consist of two parallel plates: a fixed backplate and a movable diaphragm. The backplate contains multiple holes to equalize pressure and reduce elastic return, Fig. 1a. Piezoelectric microphones, on the other hand, consist of two flexible plates with piezoelectric material in the center, typically configured as opposing cantilevers. The diaphragm in piezoelectric microphones is designed to have greater rigidity, reducing the need for holes to equalize pressure, Fig. 1b. When

C. Di Natale et al. (Eds.): AISEM 2025, LNEE 1497, pp. 131–137, 2025.
https://doi.org/10.1007/978-3-032-08271-8_21

sound pressure waves reach the diaphragm, it vibrates or deforming the piezoelectric material, changing it capacitance or generating an electric charge, thereby producing an electrical signal.

Fig. 1. Schematic MEMS Microphone: a) Capacitive and b) Piezoelectric

Capacitive microphones have high sensitivity and low noise floor. However, they require a battery for power and can suffer from the pull-in effect. Piezoelectric microphones are robust, low power consumption, do not require an external battery, and are water-resistant. However, they have slightly lower sensitivity and can be affected by background noise [1]. Focusing on piezoelectric microphones, the most used material is PZT, which contains highly toxic lead oxide. Therefore, more environmentally friendly alternatives are being considered. Aluminum Nitride (AlN) is a promising material due to its high piezoelectric performance, thermal and chemical stability, and lead-free composition. However, its fabrication process is complex and expensive. An alternative is polyvinylidene fluoride (PVDF), a semicrystalline polymer that exhibits good piezoelectric, pyroelectric, and ferroelectric properties in its β phase.

2 Materials and Methods

2.1 Production of the Composite Thin Film

The 2 μm thick composite thin films were produced by spin coating a suspension containing PVDF and the lead-free piezo nanocrystals (LFPNC) made of Nb-doped BZT-BCT [2], over a commercial platinum coated silicon wafer (700 μm thick). After, 120 nm Pt electrodes were sputtered through a shadow mask and the via to the Pt bottom electrode was obtained by manually etching the composite to obtain the structure reported in Fig. 2.

Fig. 2. a) Transducer prototype and b) Stack schematic

2.2 Characterizations

The prototype was characterized in various aspects to evaluate its ferroelectric, vibromechanical and acoustic properties.

Ferroelectric characterization was performed to determine the electrical properties of the devices by measuring their polarization cycle. For this purpose, an Aixaact Thin Film Analyzer 2000E was used to obtain a dielectric hysteresis measurement (DHM), which provides information on the switching of ferroelectric domains under the influence of an electric field. This electric field was generated by sending a triangular wave at a known frequency and voltage. The measurement was performed on both the pure PVDF sample and the PVDF_LFPNC sample under examination, both fabricated in our laboratories.

Vibromechanical characterization was performed to evaluate the dynamic behavior of the developed material, obtaining the resonance frequency and its maximum displacement at that frequency. To achieve this, the device under test (DUT) was stimulated with a Laser Doppler Vibrometer (Polytec MSA 500). Two different measurement modes were performed: the FFT (Fast Fourier Transform) mode allows obtaining the entire vibration spectrum of the device. While the Time Mode enables measuring the maximum displacement of the device at the resonance frequency found in the previous mode. To perform the measurement, the device was placed on a metal plate under the laser interferometer. A custom adapter was used to fix the device to the base, ensuring accurate measurements and minimizing noise sources while keeping the cantilever free to move.

Acoustic characterization was performed to evaluate the device's response to an external mechanical stimulus, comparing it with that of a commercial microphone. The measurement was carried out by observing the response of our device to an external acoustic wave emitted by a speaker and comparing it with the response of the same wave recorded by a commercial microphone. The setup required for this measurement includes an external waveform generator (Waveform Generator – Keysight), an emitting speaker, a commercial microphone with its amplifier (Brüel & Kjær), a current amplifier (Stanford – Low-Noise Current Preamplifier) to amplify the signal received from our device, and an oscilloscope (Teledyne Lecroy Oscilloscope) to visualize the waveforms, one input and two outputs. The device was positioned on the Polytec anti-vibration plate, which also allows easy contact with the device, Fig. 3.

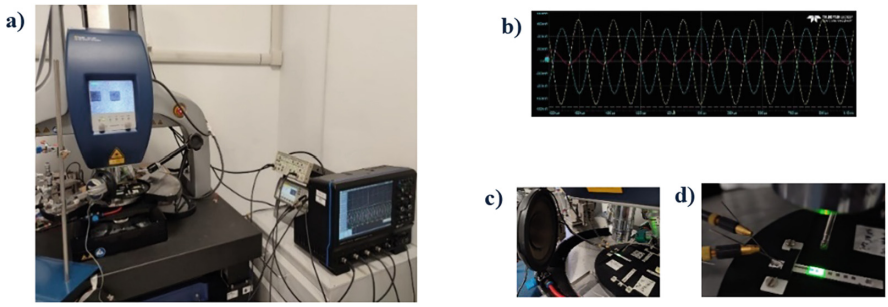

Fig. 3. a) Complete Acoustic Characterization Setup; b) Waveform input and output signal; c) Speaker, DUT, microphone; d) DUT and Microphone

The speaker was positioned at a 45-degree angle in front of the DUT and powered by external function generator, varying the frequency within the audible range. The

sound pressure generated by the speaker was directed towards the device and the commercial microphone. The device's response was measured using a current amplifier and visualized on an oscilloscope, comparing it with that of a commercial microphone.

3 Results

3.1 Ferroelectric and Vibromechanical Characterizations

The ferroelectric characterization results were analyzed to understand the behavior of the developed material compared to pure PVDF. To obtain the hysteresis cycle, samples were subjected to an electric field by sending a triangular wave at a frequency of 5 kHz with a peak-to-peak voltage of 30 V.

The hysteresis curve of PVDF (in blue) shows a wide polarization cycle, indicative of high dielectric losses. This behavior is attributed to the presence of conductive paths in the PVDF matrix, which may emerge due to impurities or inhomogeneities in the material. The hysteresis curve of the PVDF_LFPNC composite material shows a narrower hysteresis, suggesting a significant reduction in dielectric losses and a more defined and stable ferroelectric behavior, Fig. 4. The comparison between the two curves highlights the improvements brought by the developed composite material compared to pure PVDF, making it more suitable for applications requiring a stable and reliable ferroelectric response.

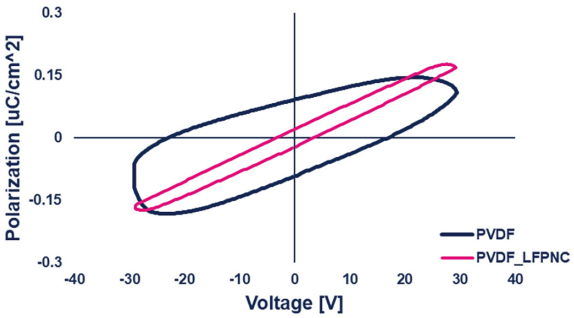

Fig. 4. Hysteresis Curves of PVDF and PVDF_LPNC

The vibromechanical characterization results were analyzed to understand the dynamic behavior of the device. From the FFT mode measurement, we obtained the frequency spectrum of the device stimulated with a chirp signal within a fixed frequency range. The response in the graph, Fig. 5a, shows a prominent peak at 4 kHz, corresponding to the first vibration mode of the device.

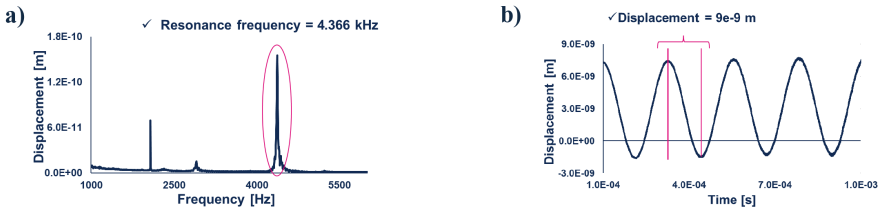

Fig. 5. a) Displacement spectrum; b) Displacement time response.

Once the resonance frequency was identified, the device was stimulated with a sinusoidal signal at that frequency with a fixed amplitude of 3 V, allowing the cantilever to reach its maximum extension. As shown in the graph, Fig. 5b, the maximum displacement was found to be 9 nm.

This characterization allowed us to calculate the piezoelectric coefficients of our device, specifically the $e_{31,f}$ coefficient, Eq. (1), representing the transverse piezoelectric response of the material [3].

$$e_{31,f} = \frac{1}{3V} \frac{Y(t_{Si})^2}{(1 - v)c_f} \frac{w(x_2)}{[2x_2 - x_1]x_1} \tag{1}$$

Comparing the measured piezoelectric coefficient with well-known piezoelectric materials, such as PZT, we observe that the coefficient of the composite material is distinct from those of PZT but slightly higher than that of other green films. The following values were extrapolated in our laboratories, Table 1.

Table 1. Comparison of piezoelectric coefficients $e_{31,f}$ on different materials

Piezoelectric coefficient $e_{31,f}$ $[C/m^2]$				
PVDF_LFPNC	PVDF	AlN	PNZT	PNZT PVD
~ 4	~ 2	~ 1	~ 16	~ 14

3.2 Acoustic Characterization

The results of the acoustic characterization were analyzed to understand the device's behavior in response to an external acoustic stimulus. The measurements were performed by measuring the device's response to varying frequencies sent to the speaker. The frequency range spanned from 0.5 to 20 kHz, noting that the audible range is from 20 Hz to 20 kHz. The measurements showed that the device responds to sound pressure similarly to a commercial microphone. Both responses tend to rise until reaching a peak value and then stabilize. The response of our device was compared with that of a commercial microphone, showing good correspondence in the waveforms, Fig. 6. The

device exhibits linearity in response up to 6.5 kHz, like the commercial microphone, with a response difference of a factor of 10.

$$S_{DUT} = \frac{mV_{rms}}{Pa} \sim 3.5\frac{mV}{Pa}; S_{Ref} = 1000\,mV/Pa \tag{2}$$

$$S_{dBV} = 20\log_{10}\frac{S_{DUT}}{S_{Ref}} \sim -55\,dBV \tag{3}$$

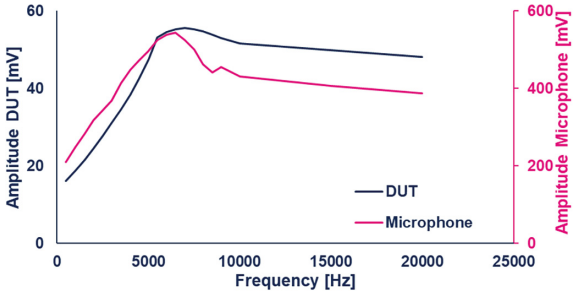

Fig. 6. Comparison of acoustic response of our DUT with commercial microphone

One of the fundamental parameters used to describe a microphone is sensitivity, representing the ability of a device to convert sound pressure into electrical voltage, expressed in dBV. The sensitivity measured for our device is −55 dBV, Eq. (2) and (3), which is lower than the typical range of commercial microphones (−28 dBV to −42 dBV). However, this sensitivity is considered a good response, considering that it is a prototype not yet optimized.

4 Conclusions

In this study, a new lead-free piezoMEMS microphone composite prototype was developed and characterized. The composite material exhibits reduced dielectric losses, and a more stable ferroelectric behavior compared to pure PVDF. Additionally, the vibromechanical characterization revealed a resonance peak around 4 kHz, within the audible range, with a maximum displacement of 9 nm. The acoustic characterization confirmed that the prototype responds to sound pressure similarly to a commercial microphone. Although the sensitivity of −55 dBV is lower than typical commercial standards, it represents a promising result for a non-optimized (not released) prototype. Overall, the developed microphone demonstrates the feasibility of using lead-free materials for piezoelectric applications. Future work will focus on optimizing the fabrication process to improve sensitivity and exploring potential applications in various fields, such as consumer electronics and medical devices.

References

1. Tseng, S.-H., et al.: Implementation of Piezoelectric MEMS Microphone for Sensitivity and Sensing Range Enhancement. In: 2020 IEEE 33rd International Conference on Micro Electro Mechanical Systems (MEMS), pp. 845–848. IEEE, Vancouver (2020). https://doi.org/10.1109/MEMS46641.2020.9056150.Author, F.: Article title. Journal 2(5), 99–110 (2016)
2. Barretta L, Barbato PS, Scaldaferri R, Casuscelli V, Esposito A (2025) Dielectric, Ferroelectric, and Piezoelectric Performances of Poled Nb-Doped BZT-BCT Prototypes. IEEE Sens J 25(5):7792–7797. https://doi.org/10.1109/JSEN.2024.3378530
3. Mazzalai, A., Balma, D., Chidambaram, N., Jin, L., Muralt, P.: Simultaneous piezoelectric and ferroelectric characterization of thin films for MEMS actuators. In: 2013 Joint IEEE International Symposium on Applications of Ferroelectric and Workshop on Piezoresponse Force Microscopy (ISAF/PFM), pp. 363–366. IEEE, Prague (2013). https://doi.org/10.1109/ISAF.2013.6748724

Analysis of the Effect of Interdigital Transducer Electrode Number in Lamb Wave Piezoelectric MEMS

Stefano Bertelli(✉), Alessandro Nastro, Marco Baù, Marco Ferrari, and Vittorio Ferrari

Department of Information Engineering, University of Brescia, 25123 Brescia, Italy
stefano.bertelli@unibs.it

Abstract. This work investigates the influence of the number *N* of electrode pairs of the interdigital transducers (IDTs) over the frequency response of a flexural plate wave (FPW) piezoelectric MEMS transducer. The number of electrode pairs *N* located over the diaphragm of a FPW MEMS directly affects the bandwidth and the frequency response of the transducer. Specifically, this paper addresses the case of a one-port piezoelectric MEMS transducer having the IDT positioned near the diaphragm edge. The electrical conductance *G(f)* of the IDT is analysed using FEM and LTspice simulations. The developed analysis was experimentally validated on a fabricated AlN-based piezoelectric MEMS transducer. The number of multiple waves was correctly detected within the expected bandwidth, in good agreement with theoretical predictions.

Keywords: flexural plate waves · Lamb waves · MEMS · piezoelectric · FEM · COMSOL Multiphysics · LTspice

1 Introduction

Lamb wave piezoelectric MEMS transducers have been employed in several fields such as industrial, consumer, and biomedical [1, 2]. They usually embed a micromachined piezoelectric diaphragm in which Lamb waves are generated by electrically actuating metal interdigital transducers placed on the piezoelectric layer. The IDT typically consists of two interleaved comb-shaped metal arrays each comprised with equally spaced electrodes, with a pitch *p* much larger than the diaphragm thickness. By applying a sinusoidal voltage across the IDT electrodes, a perturbation of the diaphragm thickness is induced which produces mechanical vibrations in the diaphragm in the form of Lamb waves. Therefore, the design of the IDTs must be carefully analyzed and tuned according to the target application. One of the key parameters is the number *N* of electrode pairs as it directly affects the bandwidth and the transducer frequency response [3]. In this context, this paper examines the influence of *N* on the IDT conductance in one-port MEMS piezoelectric transducers with the IDT located close to the edge of the diaphragm. Specifically, the first antisymmetric vibration mode (A_0) and the corresponding generated standing flexural plate waves (FPWs) were considered. The IDT

C. Di Natale et al. (Eds.): AISEM 2025, LNEE 1497, pp. 138–143, 2025.
https://doi.org/10.1007/978-3-032-08271-8_22

electrical conductance *G(f)* was analyzed by means of finite element method (FEM) and LTspice simulations.

2 Working Principle of the Lamb Wave MEMS Transducer

Figure 1a schematically represents the top view of the considered MEMS device. The structure consists of a squared diaphragm featuring an IDT positioned close to the edge of the diaphragm. The IDT comprises two interleaved comb-shaped metal arrays, each consisting of a series of N equally spaced electrodes with pitch p deposited on a piezoelectric layer. When a sinusoidal voltage is applied across the IDT electrodes, it induces a thickness perturbation in the piezoelectric layer, and consequently in the diaphragm, as illustrated in the cross-section view A–A' in Fig. 1b. At specific frequencies, the applied excitation generates mechanical vibrations in the diaphragm in the form of Lamb waves [4]. The IDT electrical conductance *G(f)* was analyzed for different values of N by means of FEM and LTspice simulations using the electrical configuration shown in Fig. 2. One metal array was grounded and the other was driven by a sinusoidal excitation voltage V_{AC}. The geometrical and material properties used in the simulations were those of the fabricated FPW MEMS transducer presented in [5]. A 2D FEM model was derived in COMSOL Multiphysics by considering a composite diaphragm with a $t_{Si} = 10$ µm thick silicon (Si) layer and a $t_{AlN} = 0.5$ µm thick aluminum nitride (AlN) layer. The diaphragm length was set to $L = 6$ mm, and the IDT pitch was defined as $p = 112$ µm.

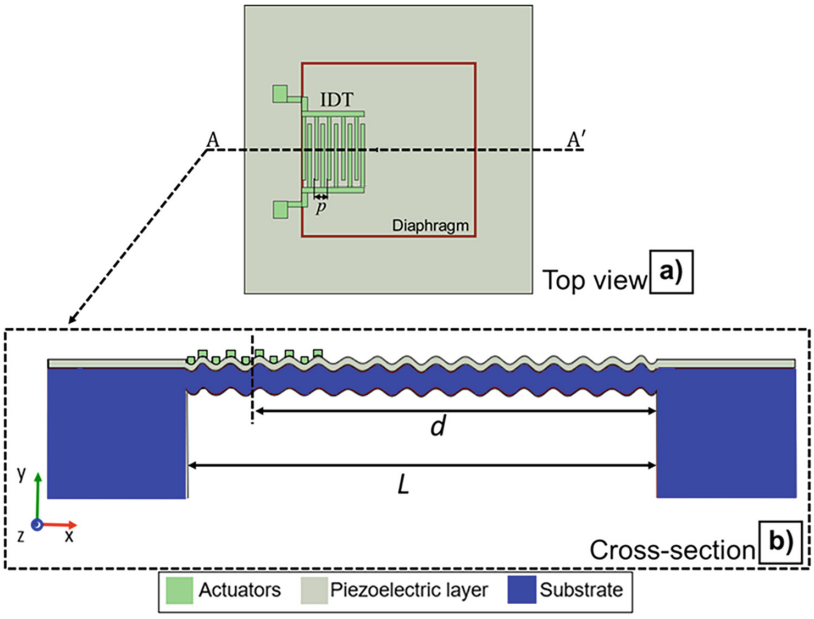

Fig. 1. Top a) and cross-section b) schematic views of the proposed piezoelectric MEMS transducer.

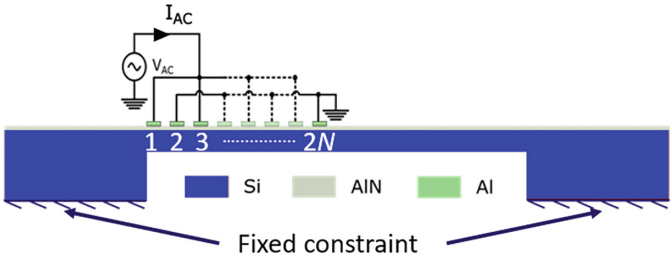

Fig. 2. Cross-section schematic view of the MEMS transducer and electrical configuration employed for the conductance analysis at different number of electrode pairs *N*.

A Mason equivalent circuit in cross-field configuration [6] was derived and simulated in LTspice. A representation of the implemented circuit is shown in Fig. 3. Figure 3a represents the cross-section schematic view of the MEMS transducer. To model the mechanical condition of fixed constraint at the diaphragm edges, i.e., total wave reflection, the beginning of the IDT and the end of the transmission line are set to open circuits, as shown in Fig. 3b. Each electrode pair of the IDT, shown in Fig. 3a, can be represented by an equivalent circuit composed of impedances forming two T-shaped networks connected to transformers [6, 7], as shown in Fig. 3c. The transformers represent the piezoelectric coupling between the electrical and mechanical/acoustic domains. The portion of the diaphragm between the end of the IDT and the edge can be approximated by a transmission line represented by impedances forming a T-shaped network, as shown in Fig. 3d. All the impedances were implemented by adopting voltage-driven current generators with gain expressed in the Laplace domain [8].

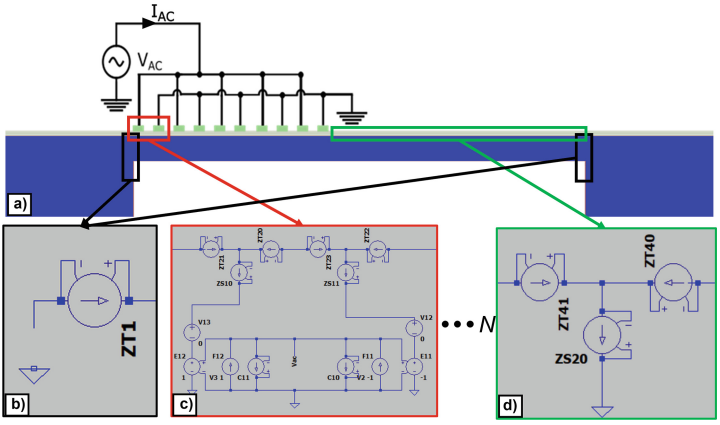

Fig. 3. Cross-section schematic view of the MEMS transducer a). Mason Equivalent circuit representation in LTSpice for the fixed constraint b), for a pair of electrodes c), and for the diaphragm d).

3 Simulation and Experimental Results

The normalized conductances *G(f)* simulated via both FEM and LTspice at different *N* as a function of the excitation frequency are shown in Fig. 4a and Fig. 4b, respectively. The obtained conductance patterns show multiple peaks within the considered bandwidth *B* that are function of *N*. The frequencies corresponding to the peaks of *G(f)* indicate the presence of standing FPWs. The number of conductance peaks N_p can be theoretically predicted as $N_p = (2d/\lambda_L) - (2d/\lambda_H)$, where λ_H and λ_L are the wavelengths of the upper f_H and lower f_L frequency boundaries of *B* [9] where $d = L - [(2N - 1/2)(p/4)]$ is the distance between the center of the IDT and the far diaphragm edge as shown in Fig. 1. Figure 5 compares the FEM simulation and measurement results of *G(f)* of a single IDT for the MEMS shown in the inset with $N = 10$. The conductance *G(f)* of the single IDT was measured by means of an HP4194A impedance analyzer over the 10–15 MHz frequency range, with the remaining IDTs left floating i.e., electrically unconnected. Figure 6 shows a comparison of the theoretically expected N_p as a function of N with the N_p values obtained through FEM, LTspice, and measurements. The results successfully confirm the theoretical predictions and simulations.

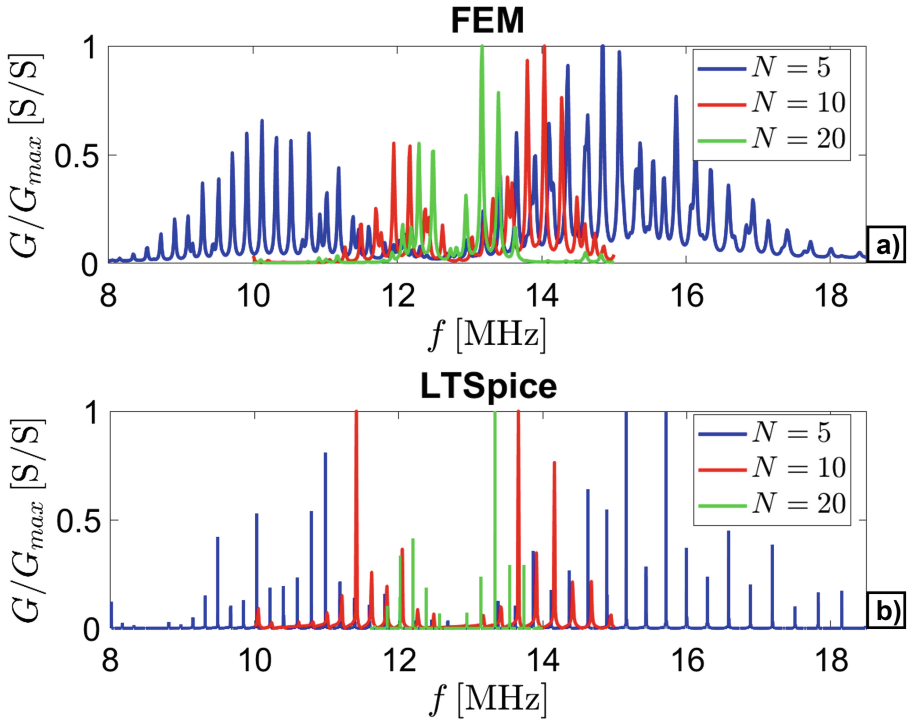

Fig. 4. FEM a) and LTSpice b) simulation results of the normalized conductance G/G_{max} as a function of the excitation frequency f for $N = 5$ (blue), 10 (red), and 20 (green).

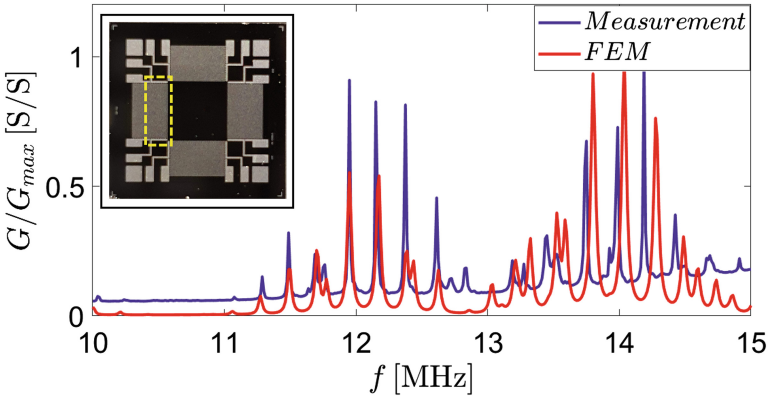

Fig. 5. Comparison between FEM (red), and measured (violet) normalized conductances of the single IDT (yellow dotted square) with $N = 10$ electrode pairs as a function of f. The top view of the manufactured MEMS is shown in the inset.

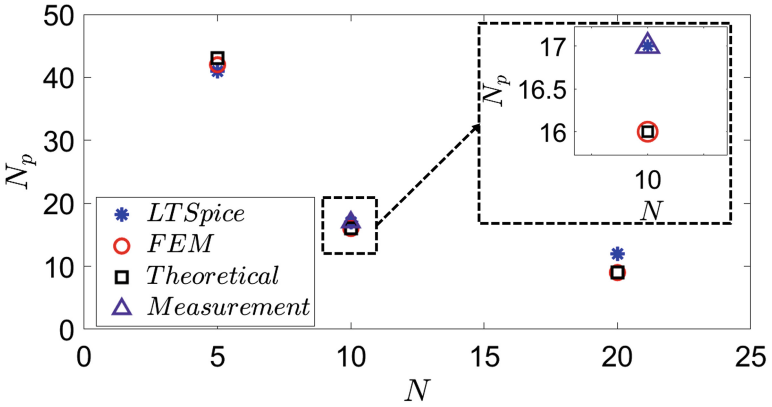

Fig. 6. Comparison of the number of conductance peaks (N_p) as a function of the number of electrode pairs N, obtained from LTSpice (blue asterisks), FEM (red circles), theoretical predictions (black squares) and measurement (violet triangle).

4 Conclusions

A comprehensive investigation combining theoretical modelling, 2D finite element simulations using COMSOL Multiphysics®, and LTspice analysis based on a Mason equivalent circuit in cross-field configuration was conducted to analyze a FPW MEMS transducer operating as a one-port device. The theoretical analysis enabled the estimation of the number of electrical conductance peaks N_p as a function of the number of electrode pairs N in the IDT structure. Both FEM and LTspice simulations successfully confirmed the predictions. Measurements of the electrical conductance *G(f)* on a fabricated device with $N = 10$ electrode pairs validated the theoretical and simulation results. The developed FEM and LTspice models provided accurate predictions of the conductance

pattern, as confirmed by measurements. The analysis proposed in this work allows to further enhance the insight in the design process of FPW MEMS transducers.

Acknowledgments. SB acknowledges funding under the European Union NextGenerationEU initiative.

References

1. Yu Z et al (2024) Physical sensors based on Lamb wave resonators. Micromachines 15:1243. https://doi.org/10.3390/mi15101243
2. Bryzek J et al (2006) Marvelous MEMs: Advanced IC sensors and microstructures for high volume applications. IEEE Circuits Devices Mag 22:8–28. https://doi.org/10.1109/MCD.2006.1615241
3. Mansoorzare H, Abdolvand R (2022). Micromachined heterostructured Lamb mode waveguides for acoustoelectric signal processing. In: IEEE Transactions on Microwave Theory and Techniques, vol. 70, no. 11, pp. 5195–5204. https://doi.org/10.1109/TMTT.2022.3194723
4. Nastro A, et al (2023) Cell alignment in aqueous solution employing a flexural plate wave piezoelectric MEMS transducer. In: IEEE Access, vol. 11, pp. 130755–130762. https://doi.org/10.1109/ACCESS.2023.3333694
5. Nastro A, Rufer L, Ferrari M, Basrour S, Ferrari V (2019) Piezoelectric micromachined acoustic transducer with electrically-tunable resonant frequency. In: 2019 20th International Conference on Solid-State Sensors, Actuators and Microsystems & Eurosensors XXXIII (TRANSDUCERS & EUROSENSORS XXXIII), IEEE, pp. 1905–1908. https://doi.org/10.1109/TRANSDUCERS.2019.8808488
6. Rasolomboahanginjatovo AH, Domingue F, Dahmane AO (2013) A New SAW Device Simulator Based on Mason's Equivalent Circuit Model. SENSORDEVICES 2013: The Fourth International Conference on Sensor Technologies and Applications, IARIA. ISBN: 978-1-61208-297-4
7. Mishra D, Singh A, Akbar Hussain DM, Dabas S, Dhankar M (2016) Inter digital transducer modelling through Mason equivalent circuit model: Design and simulation. 2016 3rd International Conference on Computing for Sustainable Global Development (INDIACom), pp. 1941–1946. New Delhi, India. ISBN: 978-9-3805-4421-2
8. Reskal H, Bybi A, Maimouni LE, Boujenoui A, Lakbib A (2023) Modeling of a high frequency ultrasonic transducer using Mason's equivalent circuit implemented in LTspice. Lecture Notes in Networks and Systems, vol 668. Springer, Cham. https://doi.org/10.1007/978-3-031-29857-8_58
9. Bertelli S, Nastro A, Ferrari M, Baù M, Ferrari V (2024) Simulation and experimental validation of a flexural plate wave piezoelectric MEMS transducer. IEEE Sensors Applications Symposium (SAS), pp. 1–6. Naples, Italy. https://doi.org/10.1109/SAS60918.2024.10636618

Electric Characterization of Thin Silicon Sensors for Beam Monitoring in Advanced Radiotherapy Techniques

D. M. Montalvan Olivares[1,2(✉)], A. Ferro[1,2], M. Centis Vignali[3], R. Cirio[1,2], E. Data[1,2], S. De Astis[1,2], U. Deut[1,2], M. D. Fernandez Moreira[2], M. Ferrero[2], S. Giordanengo[2], F. Mas Milian[2,4], E. Medina[1,2], F. Mostardi[1,2], G. Paternoster[3], V. Sola[1,2], R. Sacchi[1,2], and A. Vignati[1,2]

[1] Department of Physics, University of Turin, Via P. Giuria 1, Turin, Italy
diangomanuel.montalvanolivares@unito.it
[2] National Institute of Nuclear Physics (INFN)- Turin Division, Via P. Giuria 1, Turin, Italy
[3] Fondazione Bruno Kessler (FBK), Via Santa Croce 77, 38122 Trento, Italy
[4] Department of Exact and Technological Sciences, University of Santa Cruz, Ilhéus, Brazil

Abstract. The INFN projects FRIDA and MIRO aim to optimize and test segmented thin silicon sensors for real-time monitoring of clinical beams, particularly under the conditions required by emerging radiotherapy techniques such as Ultra-High Dose Rate and Spatially Fractionated Radiotherapy. This study presents the electric characterization of thin PIN silicon sensors, segmented into pads, with active thicknesses ranging from 15 μm to 45 μm. Current-voltage (I-V) and capacitance-voltage (C-V) measurements were conducted at room temperature, revealing breakdown and full depletion voltages, as well as variations in doping concentration and active thickness. The results showed that the sensors demonstrate consistent behavior across a broad voltage range. The C-V measurements indicated a correlation between variations in full depletion voltage and bulk doping concentration. Doping profile analysis revealed discrepancies of up to 12% between nominal and actual active thicknesses. These findings underscore the importance of static characterization in ensuring sensor accuracy and operational reliability.

Keywords: Segmented silicon sensor · I-V & C-V curves · Doping profile analysis · Nominal values deviations

1 Introduction

Thin planar silicon sensors with segmented electrodes offer reduced sensitive volumes, enabling excellent timing performance (<1 *ns*) and high spatial resolution (~ 10 μm) [1]. These characteristics make them suitable for monitoring clinical beams delivered at Ultra-High Dose Rates (UHDR, > 40 *Gy/s*) and/or as narrow beamlets (*e.g.*, minibeams), which are conditions required by emerging radiotherapy modalities such as UHDR and Spatially Fractionated Radiotherapy (SFRT) [1, 2].

C. Di Natale et al. (Eds.): AISEM 2025, LNEE 1497, pp. 144–150, 2025.
https://doi.org/10.1007/978-3-032-08271-8_23

The INFN projects FRIDA and MIRO aim to optimize segmented thin silicon sensors specifically designed for real-time beam monitoring in these advanced radiotherapy modalities. This work presents the laboratory-based electric characterization of thin multipad silicon sensors, an essential step in verifying their performance and functionality prior to testing in clinical particle beam environments.

2 Materials and Methods

2.1 Sensor Description

The devices under test (DUTs) are thin, planar, no-gain silicon detectors fabricated by Fondazione Bruno Kessler (FBK, Trento, Italy) as part of the ExFLU project [3], using a thin epitaxial layer (Epi) grown on low-resistivity silicon substrates. The sensor architecture is based on a standard PIN diode configuration, consisting of an n^{++} layer on a high-resistivity p^{-} substrate, with a p^{++} layer serving as the anode. Electrical isolation between electrodes is achieved through the implementation of p-doped regions (p-stops) surrounding each contact.

Each sensor has a total area of 4.5 × 4.5 $mm^2$and is segmented into a variety of geometries, including single-pad, multi-pad, and strip structures. The active areas of these segments range from 0.03 mm^2 to 2.33 mm^2 (see Fig. 1). The detectors feature active thicknesses between 15 μm and 45 μm, with total device thicknesses of less than 655 μm.

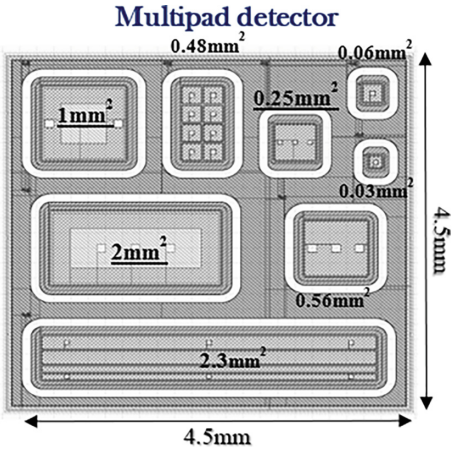

Fig. 1. Schematic diagram (not to scale) illustrating the detector geometry. The pads selected for testing are indicated with underlines

2.2 Static Characterization

Laboratory characterization of the sensors was conducted at the Department of Physics, University of Turin and INFN, using a dedicated probe station. Current–voltage (I-V) and capacitance–voltage (C-V) measurements were performed to identify any anomalous

behavior across the entire device and on three selected pads with active areas of 0.25 mm^2, 1 mm^2, and 2 mm^2.

The sensors were mounted on a support (chuck) connected to a High Voltage Source Monitor Unit (HV-SMU, model *B1513C*) to supply the bias voltage. Electrical contact with the sensor pads was established using tungsten–rhenium (W–Re) probe needles, positioned with micrometric manipulators. The needle contacting the pad was connected to a Medium Power Source Monitor Unit (MP-SMU), selected for its high current resolution (*10–100 fA*) [4]. A second needle, contacting the guard ring, was grounded (0 V) via the HV-SMU. For C-V measurements, the setup was complemented with a Multi-Frequency Capacitance Measurement Unit (MF-CMU, model *B1520A*), capable of generating signals with tunable amplitudes and frequencies from 1 kHz to 5 MHz.

During both I-V and C-V measurements, a negative bias voltage was applied to the chuck, with a compliance current of 20 μA to prevent damage from excess leakage current. This configuration enabled the measurement of total leakage current, individual pad leakage current, and their capacitance as functions of the applied reverse bias voltage, incremented in 2 V steps. All test were performed at room temperature.

From the I-V and C-V curves, the breakdown voltage (V_{BD}) and full depletion voltage (V_{FD}) were extracted. Furthermore, the bulk doping concentration (N_A) as a function of depth (d) was calculated using the measured capacitance (C), active area of the sensor (A), silicon dielectric constant (ε_{si}), and elementary charge (q), following the relations [4]:

$$N_A = \frac{2}{\varepsilon_{Si} q A^2 \frac{\partial 1/C^2}{\partial V}} \tag{1}$$

$$d = \frac{\varepsilon_{\mathrm{Si}} A}{C} \tag{2}$$

3 Results

Figure 2 presents representative I-V curves from the measured devices. The leakage current remains approximately constant (~ 10^{-11}-10^{-10} A) until the onset of breakdown, where it increases sharply and exponentially. For a given sensor thickness, this behavior is consistent across pads of different areas (Fig. 2a). In contrast, when comparing pads of identical area but differing thicknesses (Fig. 2b), a clear trend is observed: thinner sensors exhibit lower breakdown voltages (V_{BD}). This is attributed to the higher electric field intensity generated within the depleted region of the thinner sensors.

Since the sensor can be modeled as an RC network with low-pass filter characteristics, a 1 kHz-1 MHz capacitance–frequency (C-f) scan was performed prior to the C-V tests to determine the optimal measurement frequency. The C-f results showed frequency-independent capacitance, consistent with expected behavior of PIN sensors [4]; therefore, a frequency of 1 kHz was selected for subsequent measurements.

Figure 3a shows the C-V curves for 2 mm^2 pads on sensors of varying thickness. For thicker sensors (30 μm and 45 μm), the capacitance stabilizes at approximately 8 V. In contrast, the 15 μm and 20 μm sensors display a more gradual decrease, reaching a

constant capacitance value above 20 V. These voltages correspond to the full depletion voltage (V_{FD}) of the devices. Table 1 reports the measured capacitance values for the three pads on each sensor, which scale proportionally with the active pad area, as illustrated in Fig. 3b.

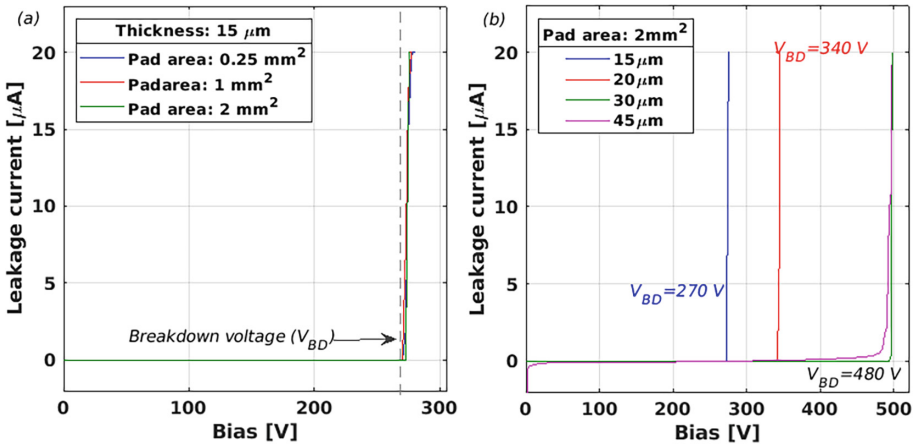

Fig. 2. Current-voltage characteristic curves of: (a) Pads with different areas for a 15 μm-thick sensor. (b) The 2 mm^2 pad for sensors with varying active thicknesses.

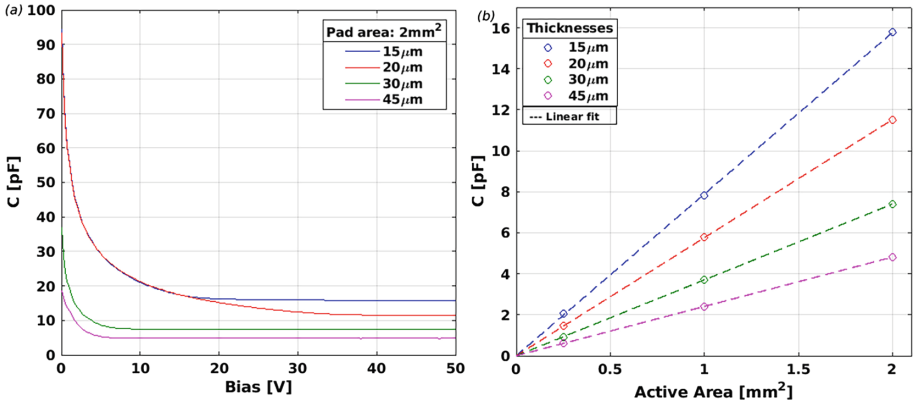

Fig. 3. (a) Capacitance-voltage characteristics of the 2 mm^2 pad for sensors with varying active thicknesses. (b) Measured capacitance values as a function of pad area for each sensor, fitted with a linear function ($r^2 > 0.9999$) to illustrate proportionality.

Table 1. Measured capacitance values for the three pad sizes tested on each sensor.

Pad Area (mm^2)	*15 µm*	*20 µm*	*30 µm*	*45 µm*
0.25	1.9	1.4	0.92	0.25
1.00	7.8	5.8	3.7	2.4
2.00	15.7	11.5	7.4	4.8

The doping concentration as a function of depth (d) can be calculated from the C-V characteristics using Eqs. (1) and (2). Within the bulk region, the doping profile remains relatively uniform, exhibiting a sharp increase near the end of the active volume due to the presence of the p^{++} electrode. As illustrated in Fig. 4, thinner sensors exhibit doping concentrations on the order of 1.5×10^{14} m^{-3}, whereas thicker sensors display concentrations one to two orders of magnitude lower. This variation in doping concentration accounts for the higher V_{FD} observed in the thinner devices.

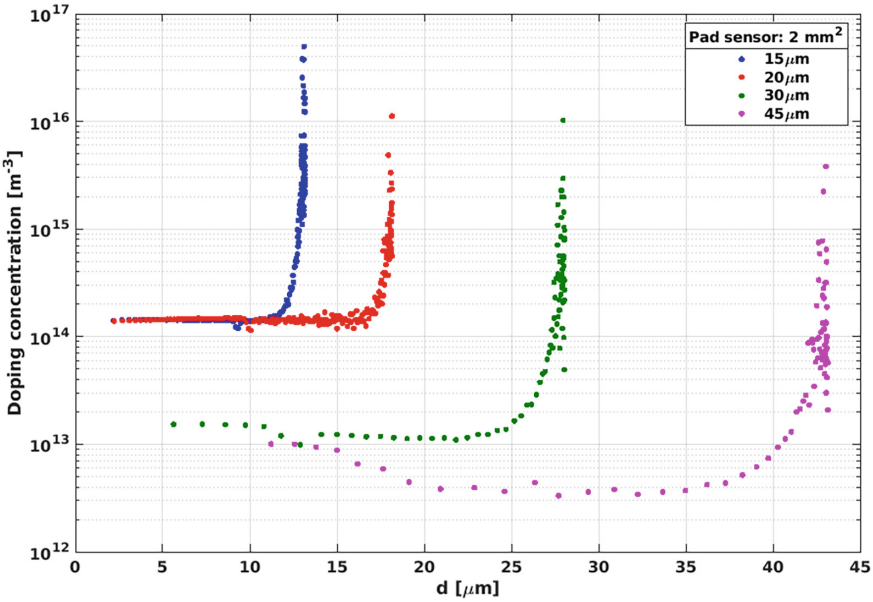

Fig. 4. Doping concentration profiles as a function of depth (d), shown on a semi-logarithmic scale, for the 2 mm^2 pad across sensors with varying active thicknesses.

It is important to note that the depth at which the doping concentration sharply increases defines the effective active thickness of the sensor. As shown in the previous figure, the actual active thicknesses are: 13.2 µm, 18.1 µm, 28.0 µm, and 43.1 µm. These values deviate from the nominal specifications by at least 2 µm, corresponding to discrepancies of up to 12% in the case of the thinnest sensor. The reduction in active

thickness, typically between 7% and 9%, is primarily attributed to the thermal bonding process of the p-type Float-Zone wafer to the thicker silicon support substrate [5].

Figure 5 presents the capacitance ratios of the 2 mm^2 pad for sensors with varying active thicknesses. The analysis focuses on the voltage region above 40 V, where the C-V curves stabilize for all four sensors. As illustrated, the measured capacitance ratios deviate from the nominal thickness ratios (dotted lines) but closely match those based on the extracted active thicknesses (solid lines). This consistency underscores the importance of experimentally verifying actual sensor parameters, as reliance on nominal specifications alone may lead to inaccurate interpretations of device behavior.

4 Conclusions

The static electrical characterization confirmed the proper operation of these sensors. The I-V curves exhibited behavior consistent with PIN structures, ensuring reliable performance across a broad bias range. The C-V measurements revealed that variations in the full depletion voltage correlated with differences in bulk doping concentration. Moreover, doping profile analysis identified deviations of up to 12% between actual and nominal active thicknesses.

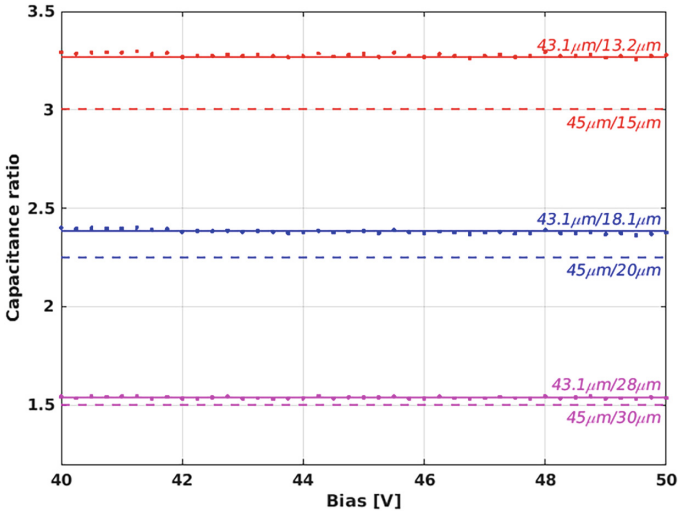

Fig. 5. Comparison of measured capacitance ratios for the 2 mm^2 pad with nominal (dotted lines) and extracted actual (solid lines) active thickness ratios.

These findings underscore the importance of electric characterization in accurately determining the effective active dimensions of silicon sensors and verifying their operational integrity, which is essential for the reliable interpretation of charge collection measurements.

Acknowledgements. The authors kindly acknowledge INFN CSN5 "ExFLU" project. The research was supported by the INFN CSN5 projects "FRIDA" and "MIRO".

References

1. Medina E et al (2024) First experimental validation of silicon-based sensors for monitoring ultra-high dose rate electron beams. Front Phys 12:1258832
2. Medina E et al (2024) Monitoring electron and proton beam profiles with segmented silicon sensors. Nucl Instrum Methods A 1069:169897
3. White RS et al (2024) Characterization of the FBK EXFLU1 thin sensors with gain in a high fluence environment. Nucl Instrum Methods A 1068:169798
4. Ferrero M et al (2021) An Introduction to Ultra-Fast Silicon Detectors. CRC Press, Florida
5. Sola V et al (2019) First FBK production of 50 μm ultra-fast silicon detectors. Nucl Instrum Methods A 924:360–368

Lead-Free Composite Bimorph Actuator for Energy Harvesting and Active Sensing

Paola Sabrina Barbato(✉), Christian Verrengia Caporossi, Valeria Casuscelli, Annachiara Esposito, and Rossana Scaldaferri

Analog, Power and Discrete, MEMS and Sensors Group (APMS) STMicroelectronics, Via Remo de Feo 1, Arzano, Italy
paolasabrina.barbato@st.com

Abstract. This study presents a self-standing bimorph actuator made from a lead-free piezoelectric composite material. The composite consists of nanocrystalline lead-free piezoelectric fillers dispersed in a piezo polymeric matrix. Electric field-induced polarization measurements showed significant polarization enhancement in the flexible bimorph structure compared to unimorph actuators. Piezoelectric measurements indicated higher displacement and lower resonance frequency for the flexible substrate compared to the rigid one. The bimorph actuator exhibited more than double the displacement of the flexible unimorph and demonstrated excellent fatigue resistance over 10^11 cycles without signs of aging.

Keywords: PiezoMEMS · Composite · Bimorph · lead-free

1 Introduction

Many applications, such as personal devices that provide real-time health monitoring and facilitate seamless communication with healthcare providers, and intelligent industrial machinery that autonomously plans maintenance and improves performance, rely on a network of sensors to collect data which is processed in the Cloud, and actuators to execute actions in the physical domain. Therefore, it is crucial to develop both highly efficient sensors and effective actuators.

Regarding the last topic, piezoelectric bimorph structures, consisting of two distinct layers of piezoelectric materials, represent a fascinating class of engineering devices that exploit piezoelectric properties to generate electrically controlled movements. These devices are fundamental in a range of applications, from robotics to the aerospace industry and many other industrial applications such as textile machines, fluid control devices and beam steering [1].

Bimorph piezoceramic actuators are also promising for energy harvesting due to their large motions and low power consumption [2]. However, they suffer from brittleness and toxicity issues, primarily due to the Si substrate [3] and PZT ceramic [4] materials used. Moreover, usually the two piezoelectric ceramic plates are stuck together using an adhesive whose spontaneous degradation also enhances the proneness of this kind of piezoceramic actuator. Polymeric or composite materials, with their low density, low

C. Di Natale et al. (Eds.): AISEM 2025, LNEE 1497, pp. 151–157, 2025.
https://doi.org/10.1007/978-3-032-08271-8_24

stiffness, and high fatigue resistance, offer a viable alternative to increase the fatigue resistance [5].

In the present work, a bimorph actuator based on a lead-free piezoelectric composite material and on a flexible conductive substrate is presented. The proposed composite material exhibits good piezoelectric properties and high fatigue resistance. The composite layers were grown directly on the metallic substrate avoiding the use of an organic adhesive whose ageing is often the cause of the actuator degradation [1].

2 Materials and Methods

2.1 Device Fabrication

The composite thin films were produced starting with a suspension containing PVDF and the lead-free piezo nanocrystals (LFPNC). These piezo ceramic nanocrystals are made of barium zirconate titanate-barium calcium titanate (BZT-BCT) doped with 2%Nb. The filler nanocrystals were obtained from a precursor solution containing all the metals in stochiometric amounts according to the formula: $0.5Ba(Zr_{(0,19)}Ti_{(0,79)})Nb_{0.02}O_3 - 0.5Ba_{0,7}Ca_{0,3}(Ti_{0.98}Nb_{0,02})O_3$. The preparation details of the precursor solution are reported elsewhere [6]. To obtain the powders, the precursor solution was dried at 150 °C and the obtained powders were first subjected to dry milling, then calcined at 1400 °C for 12h to obtain the crystalline phase. Finally, the calcined powders were wet milled in ethanol to decrease their size down to few hundred nanometers. On one hand, PVDF pellets were dissolved in two solvents, namely dimethyl sulfoxide (DMSO) and acetone, to realize a 15% wt/wt concentration of polymer. The previously prepared nanocrystals were added to the PVDF solution, thus obtaining a suspension with a filler loading equal to 20% wt/wt. To create the bimorph structure, the precursor suspension was applied to both sides of a flexible copper foil that had been previously coated with (3-Aminopropyl)triethoxysilane. This was followed by a drying step at 70 °C and a curing step at 90 °C, each conducted on separate hot plates. After the fabrication of the first film, the sample was flipped to allow deposition on the other side. In addition, to prevent contamination of the film from the contact with the wafer chuck, a clean silicon wafer was used to protect the first film from contaminations and overheating. Each deposited film was approximately 2 μm thick. After, 120 nm Pt electrodes were sputtered on the top surface of the composite in one case through a shadow mask to obtain the structure reported in Fig. 1.

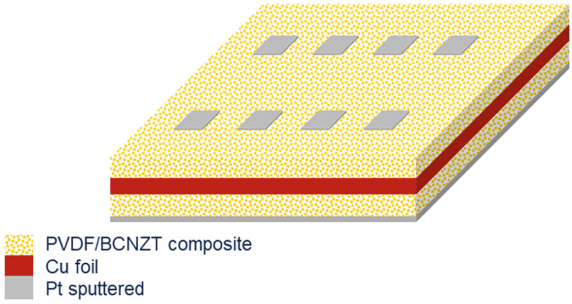

Fig. 1. Schematic of the bimorph stack

2.2 Electrical Characterizations

The electrical properties of the bimorph were analyzed by measuring their polarization cycles (PE loops) using an Aixacct Thin Film Analyzer 2000E. This implied applying a triangular wave at a known frequency and voltage to obtain dielectric hysteresis measurements (DHM), which provide insights into the switching behavior of ferroelectric domains under an external electric field. The PE loops of the bimorph actuator were obtained in series mode [7] by contacting the top electrode capacitor of $1mm^2$ area and the bottom Pt (see Fig. 2 a).

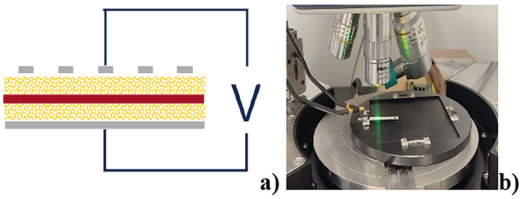

Fig. 2. **a)** Series operation mode **b)** custom adapter.

The Aixacct Thin Film Analyzer 2000E was also used for Fatigue Measurement (FM). After an initial measurement, a treatment signal sequence was applied to the sample, with regular interruptions for single measurements, thus obtaining the remanent polarization of recorded hysteresis loops against the logarithm of the total number of applied cycles. These measurements are equally spaced in a logarithmic plot.

The dynamic behavior of the bimorph structure in series operation mode was studied through vibromechanical characterization, determining the fundamental frequency and its maximum displacement at that frequency. The device under test (DUT) was stimulated using a Laser Doppler Vibrometer (Polytec MSA 500). For the measurement, the device was placed on a metal plate beneath the laser interferometer. A custom adapter (Fig. 2b) secured the device to the base, ensuring accurate measurements and minimizing noise while allowing the cantilever to move freely. The bimorph operated in series mode (Fig. 2a) by connecting the platinum bottom and top electrodes of the actuators.

Two measurement modes were performed sequentially:

FFT (Fast Fourier Transform) Mode: This mode captures the entire vibration spectrum of the device.

Time Mode: This mode measures the maximum displacement of the device over time by sending a sinusoidal signal at the resonance frequency identified in the FFT mode.

3 Results

Figure 4 presents the polarization versus voltage curves obtained at a fixed frequency of 5 kHz and 30 V for the bimorph actuator. These curves are compared to those of a unimorph actuator, using both rigid (Pt-coated silicon wafer) and flexible substrates. As expected, no improvement in ferroelectricity was observed when switching from a rigid to a flexible substrate, based on the unimorph actuator results. Ferroelectric characterizations highlight the effect of the flexible bimorph structure as also reported in the Table 1 in which the main parameters of the ferroelectric properties of the films are summarized (Fig. 3).

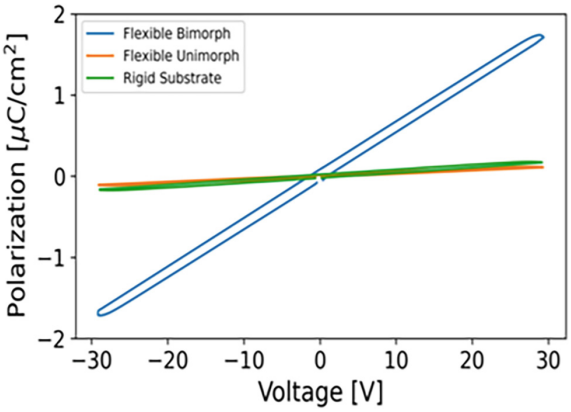

Fig. 3. Hysteresis Curves of the bimorph actuator (blue line) compared to the unimorph flexible substrate (orange line) and rigid one (green line).

Figure 4 presents displacement spectrum and time response of the bimorph flexible substrates. The displacement data for the unimorph rigid substrate are reported elsewhere [8].

Table 1. Ferroelectric and vibromechanical results

Samples	ΔPr, μC/cm^2	ΔEc, kV/cm	Displacement, nm	Res. Frequency, Hz
unimorph rigid substrate	0.04	4.7	9	4366

(*continued*)

Table 1. (*continued*)

Samples	ΔPr, μC/cm^2	ΔEc, kV/cm	Displacement, nm	Res. Frequency, Hz
unimorph flexible substrate	0.03	19.99	171	391
Bimorph flexible substrate	0.15	6.5	850	325

As shown in Table 1, Piezoelectric characterizations highlighted the benefits of the flexible bimorph structure, which resulted in an amplified polarization effect and higher displacement compared to the rigid substrate. The resonance frequency decreased significantly with the flexible substrate due to its lower stiffness. Bimorph actuation produced more than twice the displacement of the flexible unimorph.

Finally, Fig. 5 presents the results of fatigue testing over 10^11 cycles, showing no signs of aging. This demonstrates that using a flexible substrate and a polymer composite material reduces the occurrence of cracking and breaking under vibrational motion, thereby ensuring long-term operation.

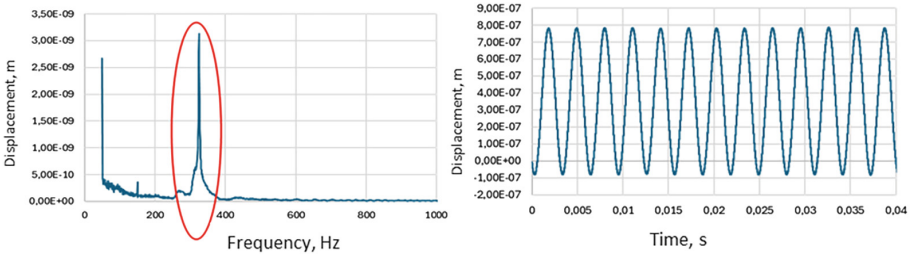

Fig. 4. Displacement spectrum (left) and time response (right) of the bimorph flexible substrate

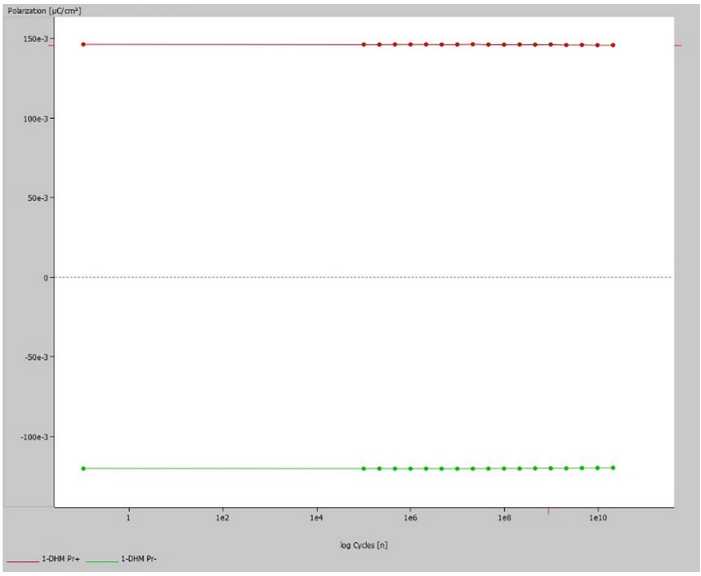

Fig. 5. Fatigue testing of the bimorph flexible substrate

4 Conclusions

In conclusion, this work demonstrated a simple, industrially compatible method to fabricate a lead-free bimorph composite actuator with notable advantages: non-toxicity, high performance, and high stability. The self-standing bimorph actuator was made from a new lead-free piezoelectric composite material, consisting of nanocrystalline Nb-doped barium zirconate titanate-barium calcium titanate lead-free piezoelectric fillers dispersed in a piezo polyvinylidene polymeric matrix. Electric field-induced polarization measurements showed significant polarization enhancement in the flexible bimorph structure compared to unimorph actuators. Piezoelectric measurements indicated higher displacement and lower resonance frequency for the flexible substrate compared to the rigid one. The bimorph actuator exhibited more than double the displacement of the flexible unimorph and demonstrated excellent fatigue resistance over 10^{11} cycles without signs of aging.

References

1. Rios SA, Fleming AJ (2015) A new electrical configuration for improving the range of piezoelectric bimorph benders. Sens Actuators, A 224:106–110. https://doi.org/10.1016/j.sna.2015.01.031
2. Chilibon C, Dias P, Inacio P (2007) PZT and PVDF bimorph actuators. J Optoelectron Adv Mater 9(6):1939–1943
3. Kanno I (2018) Piezoelectric MEMS: Ferroelectric thin films for MEMS applications. Jpn J Appl Phys 57:040101
4. Wang L et al (2023) Fabrication of a pressure sensor using 3D printed light-cured piezoelectric composites. Sens Actuators, A 362:114586. https://doi.org/10.1016/j.sna.2023.114586

5. Zuo P, Srinivasan DV, Vassilopoulos AP (2021) Review of hybrid composites fatigue. Compos Struct 274:114358. https://doi.org/10.1016/j.compstruct.2021.114358
6. Barbato PS, et al (2023) Green Synthesis of Piezoelectric Thin Films based on Niobium Doped Barium Zirconate Titanate - Barium Calcium Titanate (Nb-BZT-BCT). Chemical Engineering Transactions
7. Chattaraj N, Ganguli R (2015) Electromechanical Analysis of Piezoelectric Bimorph Actuator in Static State Considering the Nonlinearity at High Electric Field. Mechanics of Advanced Materials and Structures
8. Esposito A, et al. A new lead-free piezo-composite MEMS acoustic transducer. Lecture Notes in Electrical Engineering. Submitted

Light Stability of Amorphous Silicon Photosensors for Biomolecular Recognition

Giulia Petrucci[1,2(✉)], Fabio Cappelli[1], Martina Baldini[1], Augusto Nascetti[2], Francesca Costantini[3], Giampiero de Cesare[1], Nicola Lovecchio[1], and Domenico Caputo[1]

[1] Department of Information Engineering, Electronics and Telecommunications, Sapienza University of Rome, Via Eudossiana 18, Rome, Italy
g.petrucci@uniroma1.it

[2] School of Aerospace Engineering, Sapienza University of Rome, Via Salaria 851/881, Rome, Italy

[3] Research Center for Plant Protection and Certification, CREA-DC, Via G. Betero, 23, 00179 Rome, Italy

Abstract. Hydrogenated amorphous silicon (a-Si:H) is widely adopted in thin-film electronics due to its compatibility with large-area deposition, low fabrication temperatures, and cost-effectiveness. In recent years, a-Si:H photodiodes have gained interest for integration into Lab-on-Chip (LoC) systems, where they are used to detect light signals generated during biomolecular recognition events. However, a key concern in such applications is light-induced degradation (LID), which can affect the reproducibility and stability of the photodiode's response during continuous operation. This study investigates the light stability of a-Si:H photodiodes with varying intrinsic layer thicknesses (0.4 µm, 1.25 µm and 2.5 µm), exposed to monochromatic light at 450 nm, 550 nm, and 620 nm—wavelengths relevant to fluorescence and chemiluminescence detection. Devices were fabricated using conventional thin-film microfabrication techniques and a comprehensive characterization was conducted, including quantum efficiency (QE) measurements and photocurrent monitoring under continuous illumination for one hour. Despite the relatively high illumination intensities used (up to 2.3 µW), no appreciable degradation in photocurrent or QE was observed for any of the devices or wavelengths tested. These results indicate a high level of photoresponse stability across a range of device thicknesses and operational wavelengths. The findings confirm the suitability of a-Si:H photosensors for long-term use in LoC systems and support their application in sensitive and repeatable optical biosensing platforms.

Keywords: Hydrogenated amorphous silicon · Light-induced degradation · Photosensors · Photoresponse stability · Lab-on-Chip · Biomolecular recognition

1 Introduction

Hydrogenated amorphous silicon (a-Si:H) devices are widely used in electronic applications, such as switching elements in active-matrix displays, photosensors and photovoltaics [1–4].

C. Di Natale et al. (Eds.): AISEM 2025, LNEE 1497, pp. 158–163, 2025.
https://doi.org/10.1007/978-3-032-08271-8_25

A well-known issue affecting this semiconductor is light-induced degradation (LID), which causes performance loss over time. Specifically, in photovoltaics it reduces the power conversion efficiency, consequently extensive research has addressed this problem [5]. To mitigate it, thin intrinsic layer thicknesses (below 0.5 μm) in homojunction solar cells or tandem/triple junctions have been introduced [6–8].

One emerging application field for a-Si:H photosensors is in the development of Lab-on-Chip (LoC) systems [9–13], which can perform among the others biomolecular recognition [14–16]. This process relies on the detection of monochromatic radiation, generated by the recognition event that occurs within a microfluidic network optically coupled to the photosensors [17–19]. In this case, LID can influence the sensors response, as prolonged exposure to light could affect photocurrent stability.

The aim of this work was to investigate the stability of a-Si:H photodiodes under long-term operation in LoC systems by analysing their photoresponse to different radiation wavelengths. The selected wavelengths—450 nm, 550 nm and 620 nm—were specifically chosen as they are commonly used in LoC applications. Indeed, these wavelengths correspond to the radiation typically emitted during chemiluminescence or fluorescence processes occurring within the microfluidic network.

2 Device Structure

Figure 1a shows the schematic cross-section of the photosensor, highlighting its optical coupling with the microfluidic network, where luminescence is generated during the biomolecular recognition process.

The devices were fabricated on 5 × 5 cm^2 glass substrates using standard thin-film microfabrication techniques, including Physical Vapour Deposition (PVD) and Chemical Vapour Deposition (CVD) techniques, optical lithography for patterning and both wet and dry etching for selective material removal.

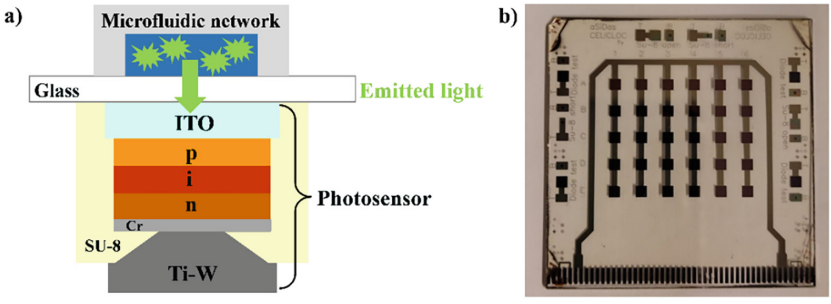

Fig. 1. a) Cross-section of a photosensor coupled with the microfluidic network. The green arrow represents the monochromatic radiation emitted during the recognition event; b) Fabricated photosensor array. The photosensors are the small squares, while the top contact is the U-shaped form (color figure online).

As shown in Fig. 1b, the device comprises an array of 30 photodiodes, each with an active area of 2×2 mm^2, including an individual bottom electrode and a shared top contact.

The photodiode features a bottom electrode made of indium tin oxide (ITO), a transparent conductive oxide deposited via magnetron sputtering. Subsequently, an a-Si:H p-type/intrinsic/n-type junction was realized by Plasma Enhanced Chemical Vapor Deposition (PECVD). To protect the junction and ensure good ohmic contact at the top interface, the a-Si:H stack was coated with a thin chromium layer using thermal evaporation. This step was followed by the application of a negative photoresist (SU-8) layer, patterned to define via holes for inter-layer electrical connection. Finally, a titanium–tungsten (Ti-W) alloy was deposited via sputtering to form the U-shaped shared top electrode.

3 Device Characterization

The evaluation of the photosensor's light stability was conducted through a series of electrical and optical measurements. This study examined three sensors with identical design, but differing intrinsic layer thicknesses: 0.4 µm, 1.25 µm and 2.5 µm.

For each photodiode, we performed an initial quantum efficiency (QE) measurement, a monitoring of the photocurrent under monochromatic illumination over one hour and a subsequent QE measurement. The last two steps were repeated for each wavelength, with all measurements conducted at 0 V bias.

QE measurements were carried out using a double-arm setup (Fig. 2a and b), which includes a reference crystalline silicon (c-Si) photodiode to monitor light intensity. In this configuration, a lamp's light is passed through a monochromator, and a beam splitter directs part of the radiation to the device under test and part to the c-Si sensor. The photocurrent monitoring was conducted through a Source Measure Unit (Keithley 236).

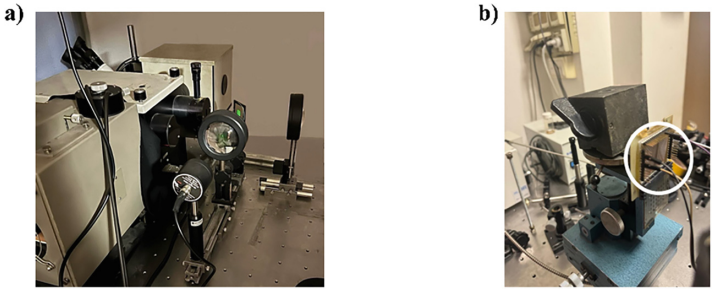

Fig. 2. a) Double-arm setup used for quantum efficiency measurements; b) Close up of the device under test in the white circle.

4 Results and Conclusions

The photocurrents of the three investigated photosensors generated under monochromatic radiation at the selected wavelengths are visible in Fig. 3.

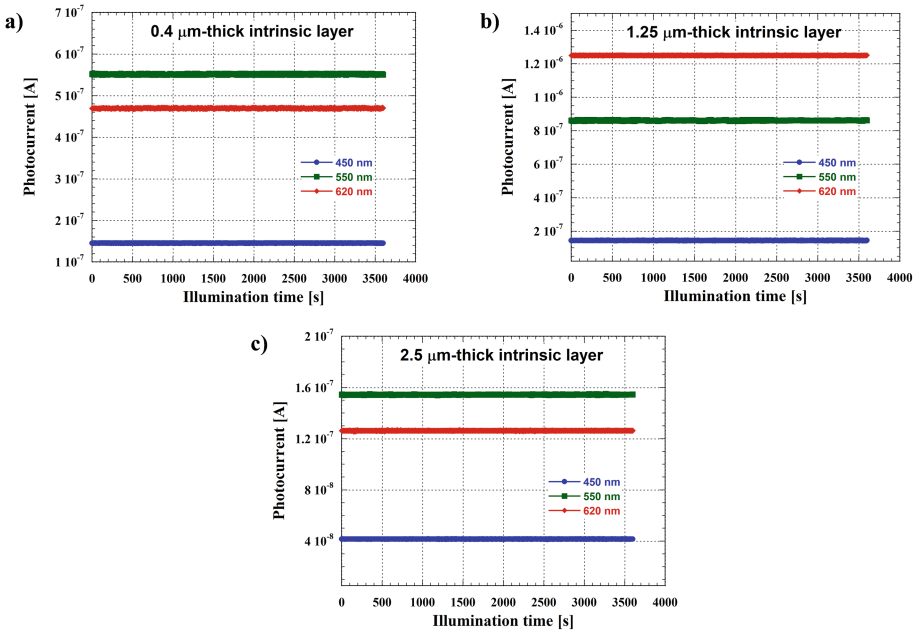

Fig. 3. Photocurrents generated at the selected wavelengths by the sensors with different intrinsic thicknesses: a) 0.4 μm; b) 1.25 μm; c) 2.5 μm.

As evident, for all the investigated wavelengths, the registered photocurrents did not exhibit any significant degradation throughout the testing period.

Similarly, the measured QEs revealed no substantial variation before and after illumination; in Fig. 4 QEs for the three photosensors before and after illumination at 620 nm are reported. Very similar curves have been achieved for the other two wavelengths.

Therefore, both the registered photocurrents and QEs highlighted the absence of response degradation.

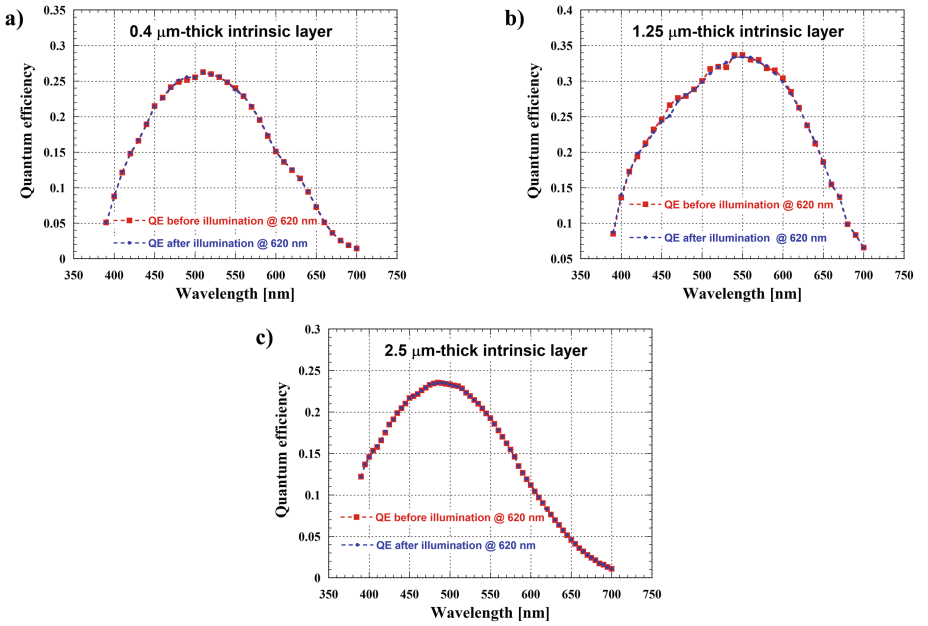

Fig. 4. Quantum efficiency measurements before (in red) and after (in blue) illumination at 620 nm of the sensors with different intrinsic thicknesses: a) 0.4 μm; b) 1.25 μm; c) 2.5 μm (color figure online).

Finally, the reference c-Si photodiode allowed us to calculate the power intensities of the monochromatic radiation (Table 1). These values exceed those typically encountered in biomolecular recognition processes.

Table 1. Monochromatic light power intensities used for photosensor illumination.

Wavelength [nm]	Monochromatic radiation power intensity [μW]
420	**1.9**
550	**2**
620	**2.3**

The absence of photocurrent degradation and the negligible variation in quantum efficiency across all tested wavelengths and device structure confirm both the stability and the robustness of the a-Si:H photosensor response in LoCs.

These results demonstrate that the devices can maintain consistent performance even under conditions that are more severe than those expected in practical applications.

In conclusion, these findings support the integration of these devices into Lab-on-Chip platforms for reliable, long-term optical biosensing, even in scenarios involving repeated or prolonged exposure to excitation light.

References

1. Flewitt AJ (2016) Hydrogenated Amorphous Silicon Thin-Film Transistors (a-Si: H TFTs). In: Chen J, Cranton W, Fihn M (eds) Handbook of Visual Display Technology. Springer, Berlin, Heidelberg, pp 627–646
2. Chen C-W et al (2005) High-performance hydrogenated amorphous-Si TFT for AMLCD and AMOLED applications. IEEE Electron Device Lett 26(10):731–733
3. Stiebig H et al (2007) Photodetectors based on amorphous and microcrystalline silicon. Thin Solid Films 515(19):7522–7525
4. Kang H (2021) Crystalline Silicon vs. Amorphous Silicon: the Significance of Structural Differences in Photovoltaic Applications. In: 2nd International Conference on Resources and Environmental Research, IOP Conf Ser Earth Environ Sci 726: 012001
5. Piliougine et al (2022) Analysis of the degradation of amorphous silicon-based modules after 11 years of exposure by means of IEC60891. Progress Photovoltaics Res Appl 30(10): 1176–1187
6. Matsui T, et al (2012) Amorphous-silicon-based thin-film solar cells exhibiting low light-induced degradation. Jpn J Appl Phys 51(10S): 10NB04
7. Veldhuizen LW et al (2016) Very thin and stable thin-film silicon alloy triple junction solar cells by hot wire chemical vapor deposition. J Appl Phys 120(9):095301
8. Stuckelberger M et al (2014) Comparison of amorphous silicon absorber materials: Kinetics of light-induced degradation. J Appl Phys 116(15):154509
9. Zhu H et al (2020) Recent advances in lab-on-a-chip technologies for viral diagnosis. Biosens Bioelectron 153:112041
10. Karthik V et al (2022) Development of lab-on-chip biosensor for the detection of toxic heavy metals: A review. Chemosphere 299:134427
11. Alexandrou G et al (2021) Detection of multiple breast cancer esr1 mutations on an isfet based lab-on-chip platform. IEEE Trans Biomed Circuits Syst 15(3):380–389
12. Silva IE et al (2024) A versatile platform for point-of-care detection of molecular biomarkers. IEEE Sens J 24(16):26388–26396
13. Staicu CE et al (2022) Glass lab-on-a-chip platform fabricated by picosecond laser for testing tumor cells exposed to X-ray radiation. Appl Phys A 128(9):770
14. Yang L et al (2021) Application of lab-on-chip for detection of microbial nucleic acid in food and environment. Front Microbiol 12:765375
15. Lovecchio N et al (2022) Thin-film-based multifunctional system for optical detection and thermal treatment of biological samples. Biosensors 12(11):969
16. Rosa C et al (2021) Label-free biosensing using thin-film amorphous silicon photodiodes integrated with microfluidics. IEEE Sens J 21(14):15999–16005
17. Costantini F et al (2018) Integrated sensor system for DNA amplification and separation based on thin film technology. IEEE Trans Compon Packag Manuf Technol 8(7):1141–1148
18. Mirasoli M et al (2018) On-chip LAMP-BART reaction for viral DNA real-time bioluminescence detection. Sens Actuators B Chem 262:1024–1033
19. Lovecchio N et al (2018) Integrated optoelectronic device for detection of fluorescent molecules. IEEE Trans Biomed Circuits Syst 12(6):1337–1344

MEMS Variable Reluctance Sensor Based on a Micromachined Coil

D. Nasr[1,2,3(✉)], Marco Baù[1], A. Nastro[1], S. Bertelli[1], M. Ferrari[1], M. H. Said[3], D. Flandre[4], M. Mansour[2], F. Tounsi[4], and V. Ferrari[1]

[1] Department of Information Engineering, University of Brescia, Brescia, Italy
{dorra.nasr,marco.bau}@unibs.it
[2] Laboratory of Microelectronics and Instrumentation, Faculté des Sciences de Monastir, Université de Monastir, Monastir, Tunisia
[3] Center for Research in Microelectronics and Nanotechnology (CRMN), Sousse, Tunisia
[4] SMALL Group, UCLouvain, ICTEAM Institute, Louvain-la-Neuve, Belgium

Abstract. This work explores the potential of using a MEMS micromachined coil combined with an external magnet and front-end electronics as a variable-reluctance (VR) microsensor. The development of VR microsensors using MEMS technology represents a significant advance, as it could enable high spatial resolution for focused detection of small metallic/ferromagnetic target components and parts. To validate the principle, a squared micromachined coil with a side length of 2180 μm was adopted to detect the rotation of a ferromagnetic drill bit within the magnetic field generated by a neodymium magnet. The temporal variation of the associated flux due to the reluctance change induces a voltage in the micromachined coil that can be correlated with the target rotation speed. The VR microsensor signal was compared with a reference signal from an optical sensor used to monitor the drill bit rotation. Rotation speeds of up to 1551 and 1393 rpm were detected for drill bits with diameters of 5 and 8 mm, respectively, at a stand-off distance from the micromachined coil of approximately 2 mm, validating the proposed approach.

Keywords: Variable reluctance sensor · micro coil · ferromagnetic target · MEMS technology

1 Introduction

Variable reluctance (VR) sensors are adopted in several harsh applications, such as in automotive and industrial systems, to detect the rotational speed [1, 2] or angular position [3, 4] of metallic/ferromagnetic targets without physical contact. These sensors essentially consist of a magnet and one or more coils, where the presence of a ferrous object can change the magnetic reluctance across the coil(s) [5]. Industrial development and emerging technologies require more compact and energy-efficient sensors [6]. In response to this need, the development of VR microsensors in Micro-Electro-Mechanical Systems (MEMS) technology represents a significant advance, as they may enable high spatial resolution for focused detection of small target components and parts [7, 8], such as details of machining tools.

C. Di Natale et al. (Eds.): AISEM 2025, LNEE 1497, pp. 164–169, 2025.
https://doi.org/10.1007/978-3-032-08271-8_26

This work explores the possibility of using a MEMS planar coil, combined with an external magnet and appropriate front-end electronics, as a complete VR microsensor. The paper is structured as follows: Sect. 2 deals with the design and operating principle of the sensor, Sect. 3 examines the adopted setup and test results, and Sect. 4 is devoted to conclusions.

2 Sensor Design and Operating Principle

A variable reluctance sensor typically comprises a magnetic circuit consisting of a coil placed in a static magnetic field and a moving ferromagnetic target. The moving target changes the reluctance of the magnetic circuit, inducing a voltage across the coil, or equivalently, a change in its inductance/impedance. Figure 1a illustrates the scenario considered in this work, where a rotating ferromagnetic drill bit is placed within the magnetic field generated by a permanent magnet, causing a time-variant flux Φ_B linked to a planar coil across which an induced voltage can be sensed. A simplified model of the working principle can be formulated by denoting the equivalent magnetomotive force of the magnet as $\mathcal{F}_m$, and the reluctances of the magnet, the magnetic path in the air, and the drill bit as $\mathcal{R}_m$, $\mathcal{R}_{air}$, $\mathcal{R}_{bit}$, respectively. Since most of the magnetic path is in air and magnet, it can be assumed that $\mathcal{R}_{air} + \mathcal{R}_m >> \mathcal{R}_{bit}$. The linked flux Φ_B through the planar coil can be obtained by Hopkinson's law [9] applied to the magnetic circuit of the magnet, air and, bit as:

$$\Phi_B = \frac{N\mathcal{F}_m}{\mathcal{R}_m + \mathcal{R}_{air} + \mathcal{R}_{bit}} \approx \frac{N\mathcal{F}_m}{\mathcal{R}_m + \mathcal{R}_{air}}\left(1 - \frac{\mathcal{R}_{bit}}{\mathcal{R}_m + \mathcal{R}_{air}}\right) \tag{1}$$

where N is the number of turns of the coil, the flux is assumed to be the same for all the coil turns, and the flux was expanded in a Taylor's series stopping at the first order.

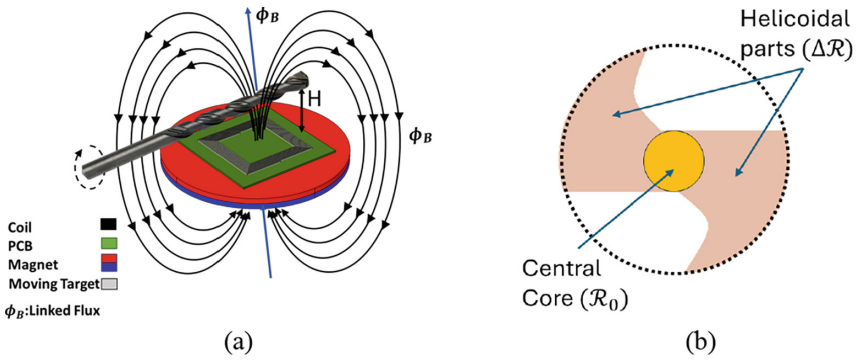

Fig. 1. Working principle of a variable reluctance sensor (a). Cross-section of the drill bit (i.e., $\mathcal{R}_0$ represents the reluctance of the central core of the drill bit, while $\Delta\mathcal{R}$ is the reluctance of the helicoidal part) (b).

If the drill bit is rotating around its longitudinal axis with an angular velocity ω, then when observing the cross-section of the bit in Fig. 1b, it can be assumed that the associated reluctance $\mathcal{R}_{\text{bit}}$ changes with time t as:

$$\mathcal{R}_{\text{bit}} = \mathcal{R}_0 + \Delta\mathcal{R}\sin(2\omega t) \tag{2}$$

where $\mathcal{R}_0$ is the reluctance of the central core of the drill bit, while $\Delta\mathcal{R}$ is the reluctance of the helicoidal part. From Eqs. (1) and (2), the induced open-circuit voltage V_S across the coil is then given by Faraday's law as:

$$V_S = -\frac{d\Phi_B}{dt} = \frac{N\mathcal{F}_{\text{m}}}{(\mathcal{R}_{\text{m}} + \mathcal{R}_{\text{air}})^2}\frac{d\mathcal{R}_{\text{bit}}}{dt} = \frac{2\omega N\mathcal{F}_m\Delta\mathcal{R}}{(\mathcal{R}_{\text{m}} + \mathcal{R}_{\text{air}})^2}\cos(2\omega t) \tag{3}$$

From Eq. (3), the output signal is expected to have an angular frequency twice the bit rotation frequency. Also, the amplitude of V_S is directly proportional to 2ω and the coil turn number N.

Figure 2a illustrates the layout of the square spiral micromachined coil. The coil features a number of turns $N = 11$, an outer side $D = 2180\,\mu$m, an inner side $d = 1470\,\mu$m, a trace width $W = 25\,\mu$m, and a turn spacing $s = 10\,\mu$m. The micromachined Al-based coil was fabricated on a 500 μm-thick high-resistivity silicon substrate combined with a trap-rich (TR) polysilicon layer using a MEMS microfabrication process involving four photolithography steps [10]. Figure 2b shows the layer stack adopted in the fabrication process of the micromachined coil featuring the thicknesses of the different layers.

3 Experimental Setup and Results

Figure 3 illustrates the experimental setup employed to test the micromachined coil as a VR microsensor with relevant dimensions. The micromachined coil was wire-bonded to a customized printed circuit board (PCB) with a thickness of $t_{\text{pcb}} = 1.6$ mm. The PCB was placed on top of a circular neodymium magnet with a diameter of $D_{\text{m}} = 20$ mm and a thickness of $t_{\text{m}} = 10$ mm, which generated the magnetic field.

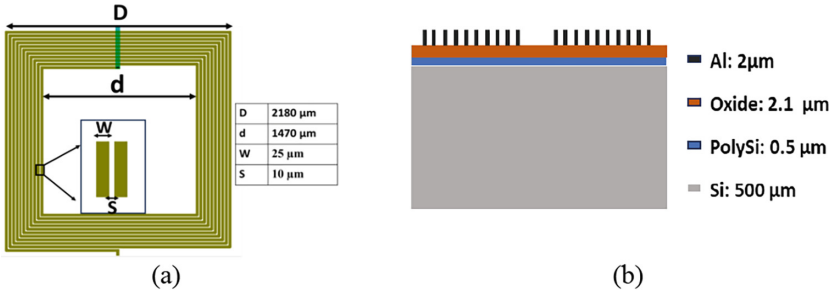

Fig. 2. Layout of the micromachined coil with relevant dimensions (a). Layer stack of the adopted fabrication process (b).

The magnet is of grade N42, with a typical residual magnetic induction of $B_r \approx 1.32$ T. A drill was used to rotate a drill bit kept at a fixed distance of $H \approx 2$ mm from the micromachined coil. An OPB8329 optical sensor was placed near the drill spindle to measure the rotation speed. More specifically, a highly reflective target was glued to the spindle so that the optical sensor generated a voltage spike for each revolution of the spindle. The adopted micromachined coil has low impedance at low frequencies, and given the expected low amplitude of the induced voltage, it is essential to amplify the readout signal and keep electronic noise and picked-up interference to a minimum. Figure 4 shows the block diagram of the electronic front-end of the VR microsensor. The micromachined coil is modeled by its equivalent parameters: the series inductance $L_s = 82$ nH and resistance $R_s = 69\ \Omega$ measured at 100 kHz. The time derivative $-d\Phi_B/dt$ of the flux linked to the micromachined coil, as expressed in Eq. 3, is modeled by the generator V_S. The signal V_S is amplified with a multistage amplifier with an overall voltage gain $G = G_1G_2G_3 \approx 10000$, which consists of two low-pass filters and one high-pass filter to enhance the signal-to-noise ratio.

The signals detected by the VR microsensor, V_{OUT}, and by the optical sensor, V_{OPB}, for two drill bits with diameters of 5 and 8 mm are illustrated in Fig. 5a and Fig. 5b, respectively. The downward peaks of V_{OPB} represent spindle revolutions from which the rotation speed can be determined. The V_{OUT} signal is directly correlated with the speed and proximity of the rotating target. Indeed, both figures show that for each spindle revolution, V_{OUT} has two peaks and two dips, consistently with the cross-sectional geometry of the drill bits shown in the insets and with what is predicted by Eq. (3). The results obtained indicate that both the rotational speed and the geometric shape of the bit can be detected and monitored.

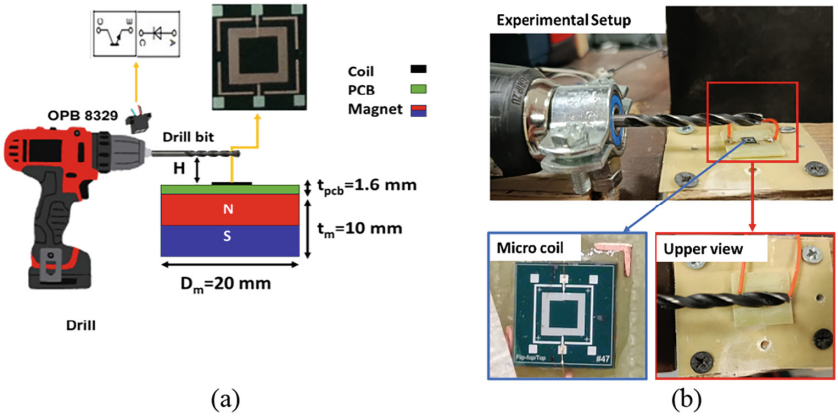

Fig. 3. Experimental setup for the validation of the micromachined coil as a VR microsensor (a). Enlarged views of the experimental setup (b)

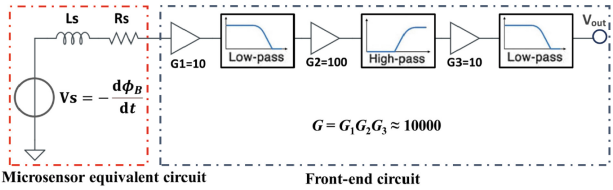

Fig. 4. Block diagram of the microsensor equivalent circuit (V_S, L_S, and R_S) and the multistage amplifier.

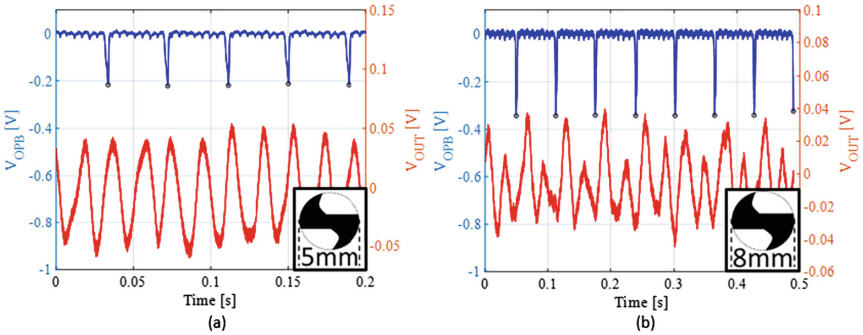

Fig. 5. Measured OPB (blue) and VR microsensor (red) signals for a 5 mm drill bit at a rotation speed of 1551 rpm (a) and for an 8 mm drill bit at a rotation speed of 1393 rpm (b) (color figure online).

4 Conclusions

This study presents the development of a variable reluctance microsensor. The sensor comprises a micromachined coil and an external permanent magnet and is used to sense the rotation of a ferromagnetic drill bit used as the tested target. An optical sensor is used to determine the reference value of the rotation speed. A dedicated front-end electronic circuit was developed to amplify the readout signal ensuring an appropriate signal-to-noise ratio. Experimental results demonstrate that the proposed microsensor successfully detects both the rotation speed and the geometric properties of the target. Future work will focus on detailed finite element simulations and further development in the electronic circuitry.

Acknowledgment. DN and this work were supported by the Italian Ministry of Foreign Affairs and International Cooperation (MAECI) within the framework of the scientific and technological collaboration between Tunisia and Italy.

References

1. Ge X, Zhu ZQ, Ren R, Chen JT (2016) A novel variable reluctance resolver for HEV/EV applications. In: IEEE Transactions on Industry Applications, vol. 52, no. 4, pp. 2872–2880. https://doi.org/10.1109/TIA.2016.2533600

2. Addabbo T, et al (2019) Instantaneous rotation speed measurement system based on variable reluctance sensors for torsional vibration monitoring. In: IEEE Transactions on Instrumentation and Measurement, vol. 68, no. 7, pp. 2363–2373. https://doi.org/10.1109/TIM.201
3. Kumar SA, George B, Mukhopadhyay SC (2023) Design and development of a variable reluctance-based thin planar angle sensor. IEEE Trans Industr Electron 70(9):9653–9662. https://doi.org/10.1109/TIE.2022.3210585
4. Pattanayak S, Dash SK, Sivakumar S, Shanmugam G (2021) Variable reluctance type speed sensor for acidic and radiation environment. In: Proc IEEE 5th Int Conf Condition Assessment Techn Elect Syst, pp. 011–016. https://doi.org/10.1109/CATCON52335.2021.9670477
5. Lemarquand G (1989) A variable reluctance sensor. IEEE Trans Magn 25(5):3827–3829. https://doi.org/10.1109/20.42446
6. Bahari M, Davoodi A, Saneie H, Tootoonchian F, Nasiri-Gheidari Z (2020) A new variable reluctance PM-resolver. In: IEEE Sensors Journal, vol. 20, no. 1, pp. 135–142. https://doi.org/10.1109/JSEN.2019.2941554
7. Tavakkoli H, Cabot J, Chen W, Lee Y-K (2024) Design, fabrication, and characterization of micro variable reluctance sensors. In: IEEE Sensors Letters, vol. 8, no. 3, pp. 1–4, Art no. 2500604. https://doi.org/10.1109/LSENS.2024.3368077
8. Nastro A, et al (2024) Inductive sensor based on micromachined coil for conductive target detection. In: IEEE Sensors Letters, vol. 8, no. 8, pp. 1–4, Art no. 2502604. https://doi.org/10.1109/LSENS.2024.3426102
9. Furlani EP (2001) Chapter 4 - permanent magnet applications. In: Furlani EP (ed.) In Electromagnetism, Permanent Magnet and Electromechanical Devices, pp. 207–333. Academic Press. ISBN 9780122699511. https://doi.org/10.1016/B978-012269951-1/50005-X
10. Zeidi N et al (2023) Symposium on design, test, integration & packaging of MEMS/MOEMS (DTIP). Valetta, Malta 2023:1–4. https://doi.org/10.1109/DTIP58682.2023.10267935

Monolithically Integrated RF-MEMS for Beamforming Applications: A Multi-functional Module with Both Amplitude and Phase Control

G. Tagliapietra(✉), J. Iannacci, and L. Lorenzelli

Center for Sensors and Devices, Fondazione Bruno Kessler (FBK), Via Sommarive 18, 38123 Trento, Italy
gtagliapietra@fbk.eu

Abstract. The significant data rates associated with current and forthcoming telecommunication standards depend on access points functioning within the millimeter-wave (mmWave) frequency bands, which are distinguished by their antenna array configurations. The anticipated increase in Small Cells (SC) deployment raises concerns about the power consumption of these numerous nodes, thereby rekindling interest in passive electronic solutions for the development of hardware beamforming (BF) architectures. In this regard, the low power requirements, combined with the exceptional and broadband electrical characteristics of Radio Frequency Micro Electro-Mechanical Systems (RF-MEMS), present a viable option for the creation of future reconfigurable BF architectures. This paper illustrates this potential through a monolithic general-purpose module that includes a 3-bit attenuator, three phase-shifting cells, and a switch, all within a compact footprint of 3.36×9.51 mm^2. The low driving voltage for this network is achieved through the use of movable membranes with meandered beams, which require an actuation voltage of 7 V. Preliminary simulations indicate wideband isolation performance ranging from -25 dB up to -27.22 GHz, alongside amplitude control from -5.39 to -13.51 dB and phase control from 14.03° to 158.46° at the center frequency of 25.87 GHz within the examined spectrum.

Keywords: RF-MEMS · MIMO · Beamforming · Switch · Phase Shifter · Attenuator

1 Introduction

The 5G and forthcoming communication standards are designed to accommodate an increasing user base and a diverse array of services, resulting in substantial data transmission. Meeting these demands necessitates a fundamental shift in the system-level approach compared to earlier standards. At the physical layer, advancements such as the utilization of high-frequency bands, a greater concentration of access points, and improved spectral efficiency facilitate the implementation of these sophisticated applications.

C. Di Natale et al. (Eds.): AISEM 2025, LNEE 1497, pp. 170–177, 2025.
https://doi.org/10.1007/978-3-032-08271-8_27

The utilization of microwave bands (3–30 GHz) and millimeter-wave bands (30–300 GHz) introduces challenges related to atmospheric absorption, to mitigate which, 5G and future networks employ various types of access points, including macrocells and microcells for outdoor coverage, as well as the so-called SC (picocells and femtocells) for indoor and localized deployments. Femtocells, in particular, are experiencing significant interest in both research and market sectors [1] due to their ease of installation and substantial market potential [2].

Beside the access point densification, a fundamental aspect of 5G technology is the incorporation of Multiple-Input-Multiple-Output (MIMO) antenna systems alongside beamforming (BF) techniques. MIMO technology enhances spectral efficiency by facilitating multiple simultaneous data streams between the base station and users, thereby augmenting channel capacity and throughput [3].

The incorporation of MIMO techniques with Small Cell Base Stations (SCBS) is anticipated to increase as 5G networks develop into more intricate infrastructures [4]. This growing interest is attributed to the capacity of SCBS to improve coverage, alleviate congestion, and provide advantages such as cost-effectiveness, compact size, and energy efficiency [5]. Moreover, a widespread adoption of SCs in dense heterogeneous networks determines a significantly improved energy efficiency as compared to networks relying only on few high-power nodes (macro or micro BS) [6].

The anticipated growth of Small Cells (SC) within future telecommunication networks raises significant concerns about the total power consumption associated with such small cell base stations (SCBS) [7].

The demand for miniaturized and low-power passive components with broadband electrical characteristics can be effectively met through RF-MEMS technology. In relation to BF architectures, numerous instances of MEMS-based applications can be found in the scientific literature, showcasing RF-MEMS phase shifters that are integrated with radiating elements in either a heterogeneous manner [8] or a monolithic approach [9], facilitating the development of antenna-in-package or subarray modules. Nevertheless, while monolithic integration and the utilization of electrostatic actuation for the movable membrane result in reduced losses and minimal power consumption, the current implementations are subject to two primary limitations. The first consists in the fact that only phase shifters are utilized, precluding the implementation of tapering schemes that could reduce the Side Lobe Level (SLL) of the radiation pattern through amplitude control of the feeding signal. Secondly, the electrostatic actuation mechanism typically requires high driving voltages (e.g. 200 in [9]), significantly exceeding the voltages used in corresponding commercial modules that rely on active electronics (such as 3.3 V in [10]), thereby complicating the integration of these RF-MEMS modules with the broader beamforming circuitry.

This paper introduces a low-voltage RF-MEMS module operating at 25.87 GHz, that incorporates both amplitude and phase control. The module consists of a 3-bit attenuator, three phase-shifting cells, and a Single-Pole-Double-Throw (SPDT) switch, all monolithically integrated into a single layout.

The paper is organized as follows: after the brief explanation of Sect. 2, concerning the single components of the module and their electrical features, the layout of the complete module is outlined in Sect. 3, showing its most significant configurations.

Finally, considerations on the future developments and final remarks are given in the conclusive Sect. 4.

2 The Single RF-MEMS Components

The reconfigurable module that incorporates passive RF-MEMS components features a 3-bit attenuator, three phase shifting cells, and a SPDT switch for integration with a typical RF front-end. Each of the three components was designed and optimized individually, focusing on the addressed frequency range (24.25–27.5 GHz, the N258 band for 5G communications in Europe), and they were subsequently combined in a final layout that has been optimized.

The majority of the signal line in the 3-bit attenuator illustrated in Fig. 1a is constructed from a buried multi-metal layer, depicted in blue. The two series resistors and the shunt resistor (in red) may load the line when their membranes are elevated and actuated, respectively. The approach of incorporating cascaded attenuation cells with either series or shunt resistors facilitates this compact multi-bit design measuring 1.50 $\times$ 1.52 mm^2, allowing for optimizations of the resistivity, width, and length of the buried poly-crystalline silicon resistors to achieve different attenuation levels.

The normalized voltage amplitudes of 1, 0.9, 0.72, 0.51, and 0.4, resulting from the tapering scheme applied to the antenna array of [11], correspond to power attenuations of 0, −0.91, −2.85, −5.84, and −7.95 dB and they have been chosen as target values. The targeted attenuations are closely aligned with the S-Parameters presented in Table 1 and illustrated in Fig. 1b, which are the results of optimization and simulations.

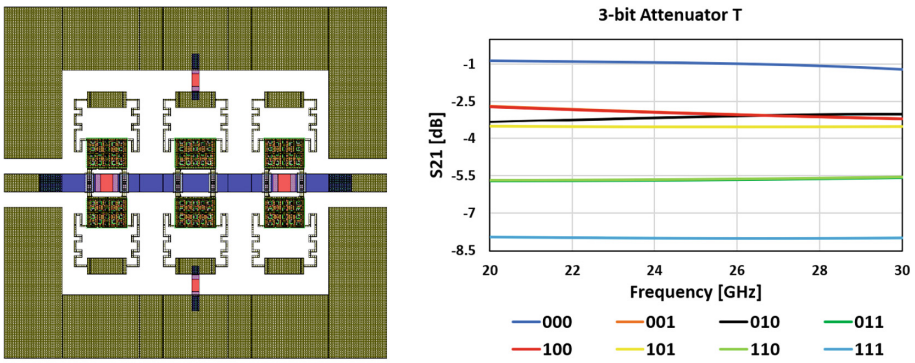

a b

Fig. 1. The 3-bit attenuator in its (a) complete layout and (b) insertion loss (attenuation levels) curves.

Evaporated gold layer is the material composing the RF signal line (depicted in light green) of the SPDT switch illustrated in Fig. 2a. The membranes consist of a first layer of electroplated gold, while the second layer (in dark green) functions as a supportive framework and it covers also the ground planes of the coplanar waveguide. The low

Table 1. S-Parameters of the optimized 3-bit attenuator of Fig. 1 at the center frequency.

Series Left Shunt Series Right	S21 at 25.87 GHz [dB]	S11 at 25.87 GHz [dB]
0 0 0	−0.99	−23.77
0 0 1	−3.01	−9.91
0 1 0	−3.08	−12.68
0 1 1	−5.67	−19.83
1 0 0	−3.02	−8.68
1 0 1	−3.55	−12.60
1 1 0	−5.64	−8.32
1 1 1	−8.01	−10.43

operational voltage of the displayed membranes (7 V) is also the actuation voltage of the membranes of the 3-bit attenuator (and of the following phase shifting cells). The T-junction within this SPDT configuration has been optimized to minimize insertion loss across the entire frequency range of interest, revealing a commendable return loss (<−10.8 dB), alongside minimal insertion loss (>−1.14 dB) and isolation (<−25.1 dB) up to 27.5 GHz, as visible in Fig. 2b.

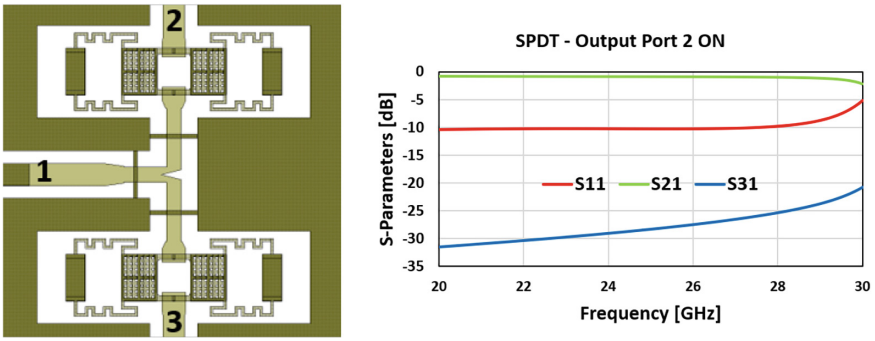

a b

Fig. 2. The SPDT switch in its (a) simplified layout and (b) S-Parameters.

In relation to phase control, three phase-shifting cells have been developed utilizing the switched-line topology illustrated in Fig. 3a, based on the previous SPDT design. In this configuration, the corresponding membrane pair is capable of selecting either the longer shifting signal path or the reference path. The three versions of the cells are designed to achieve phase shifts of 22.5°, 45°, and 90° in relation to the reference path. The optimized cells ensure minimal insertion losses and they demonstrate a phase error of less than 1° at the center frequency compared to the target values, with the reference branch reaching 38.96°, and the 22.5°, 45° and 90° shifting paths realizing

60.63°, 83.79° and 129.44°, respectively, in Fig. 3b. Due to their extended shifting paths, all cells maintain a moderate footprint width of 2.904 mm, with lengths of 2.887 mm, 3.052 mm, and 3.359 mm for the 22.5°, 45°, and 90° configurations, respectively.

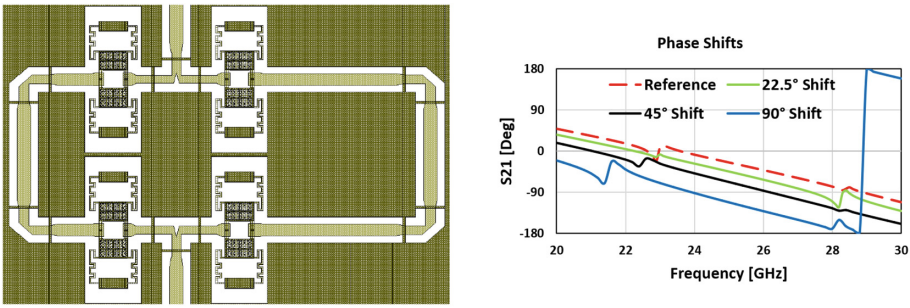

a b

Fig. 3. The optimized phase-shifting cells, in their (a) simplified layout and (b) the introduced phase shifts as compared to the reference path (dashed red).

3 The Complete Reconfigurable Module

The phase-shifting cells were integrated by means of segments of CPW transmission line, characterized by variable-length, to create a unified configuration including also the attenuator and the SPDT switch. The optimization of the spacing between the individual components led to the final design depicted in Fig. 4a, featuring a total footprint of 3.36×9.51 mm^2. To evaluate the layout's capability for amplitude control, various attenuation levels imposed by the attenuator are initially considered when output Port 2 is activated and the phase-shifting cells do not induce any phase shift. In this scenario, a maximum attenuation level of -12.64 dB can be achieved at 25.87 GHz, starting from a baseline insertion loss of -5.39 dB (reported in Fig. 4b). The optimized layout also maintains return loss curves below -10 dB across the frequency range of 25.2–26.3 GHz (illustrated in Fig. 4c).

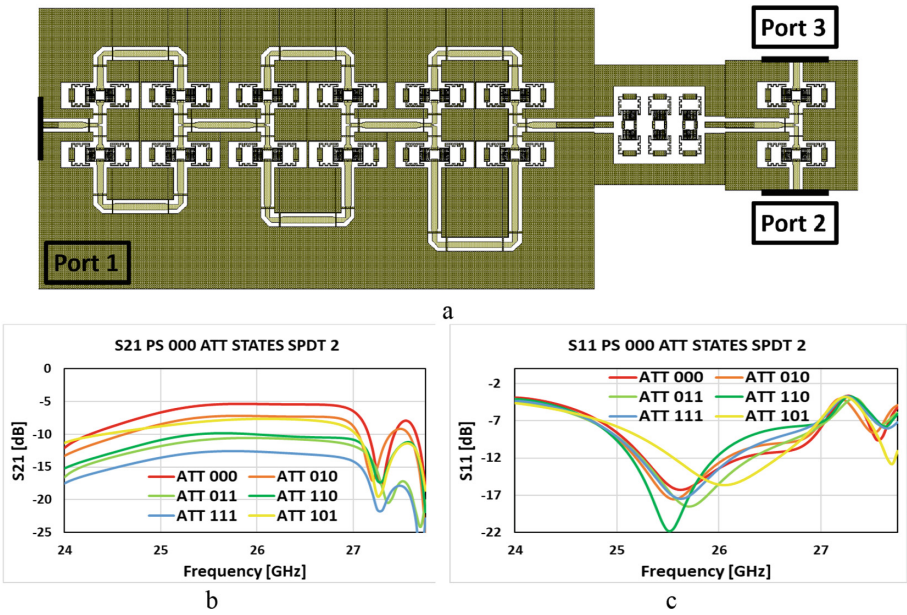

Fig. 4. The optimized final module in its (a) simplified layout reporting the port numbering. S-Parameters of the optimized module in case of no enforced phase shift and the sole variation of the attenuation states, in its (b) introduced amplitude variations and (c) return loss curves.

To ensure overall brevity, few selected phase shifts in the attenuation conditions ATT000 and ATT111 will be displayed. In this context, the code PS110 ATT010 refers to the state where attenuation is produced by the single central shunt resistor, and the induced phase shift results from the leftmost (90°) and central (45°) cells, as depicted in the arrangement of Fig. 4a. Concerning the achievable phase shifts, Fig. 5 demonstrates the linearity of the different phase rotations attained across the various attenuation states, while Table 2 offers a comprehensive breakdown. In this table, it is evident that the discrepancies (in comparison to the desired values) of the phase shifts in the ATT000 condition are more significant than those in the other attenuation state (ATT111), which align more closely with expectations.

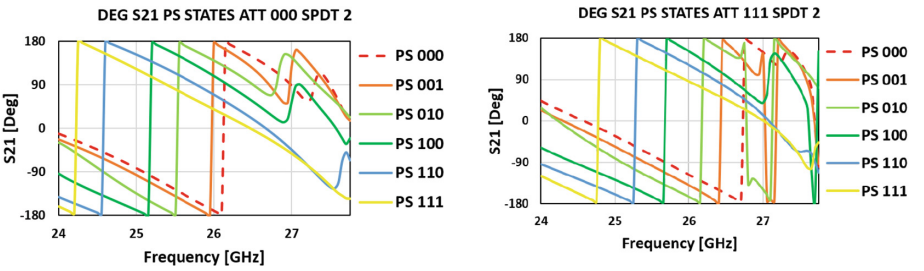

Fig. 5. Phase shifts caused by the activation of different combinations of phase-shifting cells, in case of the attenuation states (a) ATT000 and (b) ATT111, with the dashed line representing the case of no enforced shift.

Table 2. The different phase shifts introduced by the states reported in Fig. 5.

State	Target	Simulated	State	Target	Simulated
ATT000 PS001	22.5°	14.03°	ATT111 PS001	22.5°	22.61°
ATT000 PS010	45°	50.33°	ATT111 PS010	45°	48.12°
ATT000 PS100	90°	80.76°	ATT111 PS100	90°	90.63°
ATT000 PS110	135°	120.66°	ATT111 PS110	135°	122.68°
ATT000 PS111	157.5°	152.01°	ATT111 PS111	157.5°	158.46°

4 Conclusions

The proposed module design utilizes single low-voltage RF-MEMS components optimized for an operating frequency of 25.87 GHz, starting from a range of attenuation levels defined by a real case scenario. The simulated monolithic integration of these components resulted in operational states that exhibit S-Parameters with broadband characteristics for such a reconfigurable module characterized by noteworthy reconfigurability. Specifically, the module has a footprint of 3.36×9.51 mm^2 and demonstrates low driving voltage and negligible power consumption, due to the electrostatic actuation mechanism. It also allows for amplitude control ranging from -5.39 to -12.64 dB and phase control spanning from 14.03° to 158.46° over the routed signal. The proposed module illustrates the potential of RF-MEMS passives in developing low-power, low-voltage, and reconfigurable networks for beamforming applications within the context of future MIMO SC access points.

References

1. Fortune Business Insights. Small cell 5g market size. https://www.fortunebusinessinsights.com/industry-reports/5g-small-cell-market-101600. Last accessed 18 September 2024

2. Kaur S, Kuttan DB, Sharma T (2021) A survey of diverse antennas in an emerging 5G small cellular base stations. In: 2021 2nd International Conference on Smart Electronics and Communication (ICOSEC), pp. 317–322. IEEE, New Jersey, USA
3. Ghanbarisabagh M, Vetharatnam G, Giacoumidis E, Malayer SM (2019) Capacity improvement in 5G networks using femtocell. Wireless Pers Commun 105:1027–1038
4. Alvarez JAM, Paz F, Zurbriggen IG, Ordonez M (2020) Optimization-based design of power architecture for 5G small cell base stations. In: Proceedings of the 2020 IEEE Energy Conversion Congress and Exposition (ECCE), pp. 3092–3097
5. Shen Y, Chen Y, Kang H, Sun X, Chen Q (2024) Energy-efficient indoor hybrid deployment strategy for 5G mobile small-cell base stations using JAFR algorithm. Pervasive Mob Comput 100:101918. https://doi.org/10.1016/j.pmcj.2024.101918
6. Ahmed AH, Thair Al-Heety A, Al-Khateeb B, Mohammed AH (2020) Energy efficiency in 5G massive MIMO for mobile wireless network. In: 2022 3rd International Conference on Intelligent Engineering and Management (ICIEM), pp. 1–6. IEEE, New Jersey, USA
7. Leyva-Mayorga I, Mahmood NH, Lauridsen M, Rodriguez I (2017) Performance evaluation of 5G millimeter-wave cellular access networks using a capacity-based network deployment tool. In: Proceedings of the 2017 IEEE 86th Vehicular Technology Conference (VTC-Fall), pp. 1–5. IEEE, New Jersey, USA
8. Raeesi A, et al (203) A low-profile 2D passive phased-array antenna-in-package for emerging millimeter-wave applications. IEEE Trans Antennas and Propagation 71(1): 1093–1098
9. Sundaram A, Maddela M, Ramadoss R, Feldner LM (2008) Mems-based electronically steerable antenna array fabricated using pcb technology. J Microelectromech Syst 17(2):356–362
10. Renesas Electronics Corporation. F5288, 28ghz 8-channel, half-duplex transceiver ic. https://www.renesas.com/us/en/document/sds/f5288-short-form-datasheet?r=1050916. Last accessed 18 September 2024
11. Xu T, Yao M, Zhang F, Wang X (2020) Design of low sidelobe series microstrip array antenna with non-uniform spacing and excitation amplitude. Electron Lett 56(21):1099–1101

Structural Health Monitoring Based on Multimodal Sensors to Detect Barely Visible Impact Damage

A. De Luca, A. Polverino, A. Aversano, F. Caputo, D. Perfetto, E. Catalano, A. Coscetta, R. Vallifuoco, L. Zeni, and A. Minardo(✉)

Department of Engineering, University of Campania Luigi Vanvitelli, Via Roma 29, 81031 Aversa, Italy
aldo.minardo@unicampania.it

Abstract. In this study, we explore the application of multimodal sensors for structural health monitoring (SHM) in carbon fiber reinforced polymers (CFRP) composite panels. The effects of Barley Visible Impact Damages (BVIDs) resulting from Low Velocity Impact (LVI) events were analyzed using three different technologies: distributed optical fiber sensors, piezoelectric transducers, and ultrasonic C-scan. Our preliminary results show that the multimodal sensor approach is beneficial in determining the evolution of BVIDs under compressive fatigue loads, potentially helping in estimating the remaining fatigue life of the monitored structure.

Keywords: Structural health monitoring · barely visible impact damage · distributed optical fiber sensors · piezoelectric transducers

1 Introduction

Carbon fiber reinforced polymer (CFRP) composites exhibit excellent mechanical properties such as high specific stiffness, high strength, and fatigue/corrosion resistance. This has led to their widespread use in many fields, such as aerospace, automative and civil engineering [1]. However, composite structures are deteriorated by barely visible impact damage (BVID) resulting from Low Velocity Impact (LVI) events, such as bird or lightning strike, runway debris, or tool drop during maintenance procedures. Under structural loads, these BVIDs can grow and even compromise the load-bearing functionality of the structure. Therefore, it is essential to detect these BVIDs at an early stage [2].

Monitoring the structures without recurring inspections is highly desirable, as this reduces the downtime and inspection costs. Optical fiber sensors represent excellent candidates for in-situ, permanent monitoring of composite structures, owing to their advantages of low size, light weight, immunity to electromagnetic interference, possibility of embedding within the composite material, and distributed sensing capabilities [3]. Distributed optical fiber sensors measure the local strain conditions with a given spatial resolution and are especially valuable when regions with anomalous strain are

C. Di Natale et al. (Eds.): AISEM 2025, LNEE 1497, pp. 178–183, 2025.
https://doi.org/10.1007/978-3-032-08271-8_28

not known in advance [4]. In fact, BVIDs may be missed by point sensors if they are not positioned in the vicinity of the defect [5].

Another valuable technology is constituted by piezoelectric transducers, which can be employed as either sensors or actuators to realize a variety of methods, including electromechanical impedance, ultrasonic propagation monitoring, acoustic emission, and stress monitoring [6]. Furthermore, piezoelectric transducers can be interrogated to actuate and record ultrasonic guided waves (UGW) [7], which are particularly sensitive to material local changes induced by damage. Combining multiple information from various sensor types may increase the reliability of the sensory system [8, 9].

The present study explores the application of multimodal sensor technologies to detect the evolution of a BVID in a CFRP panel subjected to compressive fatigue loads. The data provided by a high spatial resolution distributed optical fiber sensor and piezoelectric transducers are correlated with the presence of a BVID and the number of fatigue cycles. Ultrasonic C-scans are also performed to follow the evolution of the BVID.

2 Experimental Setup

Our experimental campaign was carried out on a composite panel of size 100 mm × 150 mm × 2.7 mm, manufactured in accordance with the ASTM D7136 Standard. Optical fiber measurements were provided by a custom Brillouin Optical Frequency-Domain Analysis (BOFDA) sensor operating at a spatial resolution of 8 mm [10]. The BOFDA sensor was applied to measure the strain distribution along a 145-μm polyimide-coated optical fiber glued on top of the panel, following the path indicated in Fig. 1(a).

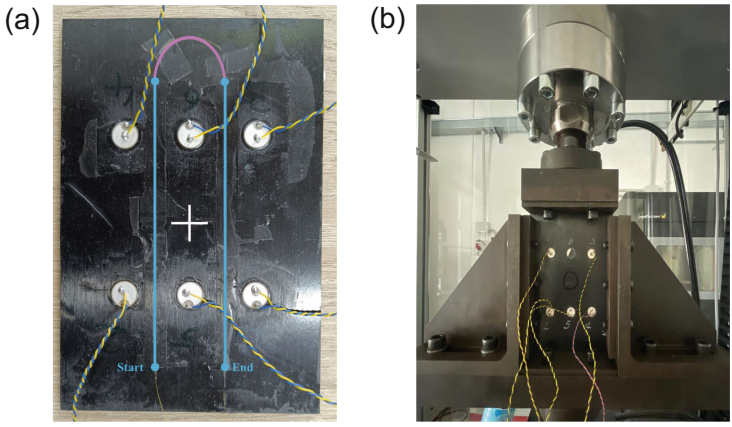

Fig. 1. (a) CFRP panel with optical fiber and piezoelectric transducers. The blue line indicates the active path of the optical fiber glued on the panel surface, while the " +" symbol marks the impact location; (b) Composite panel under the load test machine.

For strain measurements, the load test machine shown in Fig. 1(b) was employed to apply a compressive load. Six lead zirconate titanate (PZT) transducers were glued on the same surface to excite and detect the UWGs. A network of six transducers was

arranged in a 2 × 3 matrix configuration on the panel surface, as shown in Fig. 1a. The sensors were aligned in two horizontal rows of three elements each, with 25 mm spacing between adjacent sensors along the horizontal direction. The two rows were vertically spaced by 60 mm. This sensor network, centered on the panel, allowed wave propagation analysis along horizontal, vertical and diagonal directions.

The instrumentation adopted for the measurements consists of an Handyscope oscilloscope HS5 (TiePie Engineering) with a built-in arbitrary waveform generator and an Handyscope oscilloscope HS6 (TiePie Engineering) connected in parallel. The excitation signal used is a 5-cycle tone burst modulated in amplitude with a Hanning window characterized by a peak-to-peak amplitude of 12 V (The highest value allowed by the instrumentation employed) and a central frequency equal to 200 kHz. This process is repeated 64 times to ensure an adequate number of averages, effectively reducing environmental noise. Subsequently, a low-pass Butterworth filter (order 4) with a cut-off frequency of 0.01 Hz is applied to clean the signal without compromising the damage-related information. This parameter has been chosen by an iterative procedure. Due to the small planar dimensions of the inspected panel, the acquired time window is 80 μs. The strain distribution and UWGs responses (for all actuator-receiver combinations) were acquired with the panel in pristine configuration, and then after the formation of a BDIV upon a calibrated impact with an energy of 15 J. The panel response was then acquired in subsequent compression-after-impact (CAI) fatigue tests, in accordance with ASTM D7137. Fatigue tests were interrupted at multiple stages (with a periodicity of 250×10^3 cycles), to monitor the damage evolution using optical fiber and piezoelectric sensors. For each stage, the panel under test was also inspected by ultrasonic C-scan using an OmniScan SX system equipped with an Olympus 5L32-A31 phased array transducer and an SA31-OL-IHC wedge. The scan was performed with a step-motor controlled scanning stage. The encoder resolution was set to 10 step/mm in both directions, enabling a detailed assessment of delamination growth on the impacted area throughout fatigue life.

3 Experimental Results

We report in Fig. 2(a) the strain profiles provided by the BOFDA sensor with the panel subjected to a compressive load L = 5 kN. In detail, the figure reports the strain distribution acquired before (blue line) and after (red line) the calibrated impact, as well as after each stage of fatigue cycles. Each profile was calculated adopting, as a reference, the strain measured immediately the application of the compressive load. We see that the number of fatigue cycles N has a profound impact on the measured strain profiles, with the compressive strain on the initial and final portions of the glued fiber gradually reducing and even becoming a tensile strain after a certain number of cycles. Such behavior is attributed to the progressive growth of the delamination created by the impact. Note that the fatigue tests were interrupted after $1{,}01 \times 10^6$ cycles, due to panel failure. It is interesting to analyze the strain evolution at a selected position, as a function of the number of fatigue cycles. The results related to the position z = 0.112 m are shown in Fig. 2(b), for three different loads (L = 5 kN, L = 10 kN, L = 15 kN). Note that the strain values for N = 0 refer to the measurement taken after the impact, while the measurement at N

$= 1.01 \times 10^6$ cycles was possible only for L = 5 kN due to subsequent panel failure. The figure highlights the consistency of the measured strain profiles under different loads: in each case, we observe a progressive reduction of the load-induced compressive strain at increasing fatigue cycles. For completeness, we also report in the same figure the strain measured with the unloaded panel (L = 0 kN), taking as a reference the strain measured before the impact. In such a case, the fatigue cycles induce a compression of the fiber at growing delamination size, consistently with previous observations [4].

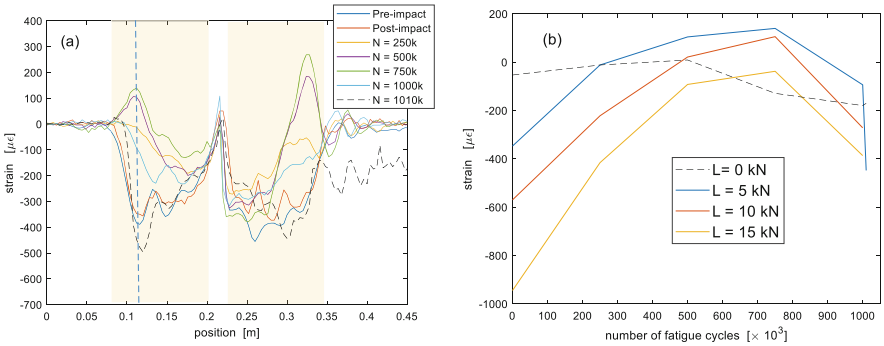

Fig. 2. (a) Strain measurements for L = 5 kN. The shaded areas represent the portions of the fiber disposed vertically along the panel; (b) Strain measured at z = 0.112 m (indicated with a dashed line in Fig. 2(a)), as a function of fatigue cycles.

Figure 3 shows the signal envelopes acquired along a selected actuator–receiver path for the pre-impact, post-impact and the five fatigue stages. As the number of cycles increases, a progressive attenuation and distortion of the first wave packet of the received signal is observed, with its peak occurring around 25 μs, indicating the accumulation of damage. The envelope representation allows a clearer comparison of signal amplitude variations across the fatigue evolution. In parallel, ultrasonic C-scan inspections were carried out after each fatigue stage. Figure 4 reports the corresponding C-scan acquisitions, which reveal a gradual enlargement of the delaminated area. Starting from an initially localized defect, the damaged region evolves with the number of cycles, confirming the progressive nature of the internal failure mechanism. The C-scan maps provide spatial context to the changes observed in UGW signals.

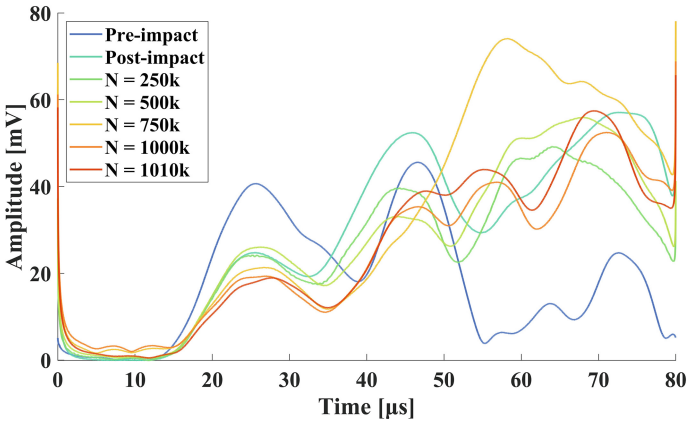

Fig. 3. Evolution of UGW signal envelope for different fatigue stages.

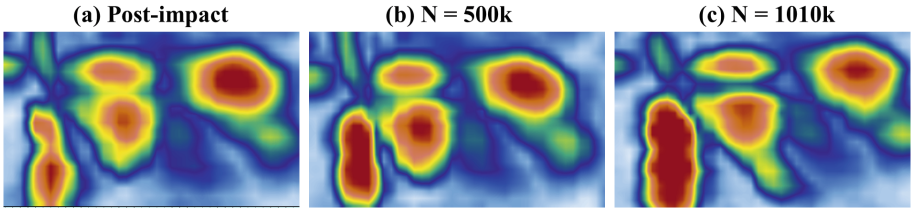

Fig. 4. C-scan images showing damage evolution (a) after LVI; (b) at N = 500 k cycle; (c) at N = 1010 k cycle.

4 Conclusions

In this study, we demonstrated the effectiveness of a multimodal sensor approach for SHM of CFRP composite panels subjected to compressive fatigue loading after a low-velocity impact. By combining distributed optical fiber sensors and piezoelectric transducers, it was possible to monitor the evolution of BVID over time with high spatial resolution and sensitivity. The distributed strain measurements provided by the BOFDA system revealed progressive strain variations associated with delamination growth, while piezoelectric transducers confirmed the presence and evolution of damage through ultrasonic guided waves. Ultrasonic C-scans supported these findings by offering visual confirmation of the delamination progression. These results highlight the complementary strengths of each sensing modality and confirm that their integration enhances reliability and diagnostic accuracy in SHM applications. Furthermore, the correlation between sensor outputs and the number of fatigue cycles suggests that this approach could be instrumental in estimating the remaining fatigue life of critical structures. Future developments may include real-time monitoring strategies and advanced damage localization algorithms to further support the use of these technologies in industrial and aerospace applications.

References

1. Gay D, Hoa SV, Tsai SW (2002) Composite materials: Design and applications, 1st edn. CRC Press
2. Goossens S, Muñoz K, Jiménez M, Mendíaz MM, Berghmans F (2024) Barely visible impact damage detection and location on a real scale curved CFRP fuselage panel with optical fibre Bragg grating sensors. Procedia Struct Integ 52:647–654
3. Lopez-Higuera JM, Rodriguez Cobo L, Quintela IA, Cobo A (2011) Fiber optic sensors in structural health monitoring. J Light Technol 29(4):587–608
4. Goossens S et al (2021) Practicalities of BVID detection on aerospace-grade CFRP materials with optical fibre sensors. Compos Struct 259:113243
5. Kim SW (2017) Effect of sensing distance of aluminum-coated FBG sensors installed on a composite plate under a low-velocity impact. Compos Struct 160:248–256
6. Ju M et al (2023) Piezoelectric materials and sensors for structural health monitoring: fundamental aspects, current status, and future perspectives. Sensors 23:543
7. De Luca A, Perfetto D, Polverino A, Minardo A, Caputo F (2023) Development and validation of a probabilistic multistage algorithm for damage localization in piezo-monitored structures. Smart Mater Struct 32(8):085015
8. Zahoor R et al (2022) Lamb Wave Detection for Structural Health Monitoring Using a ϕ-OTDR System. Sensors 22:5962
9. Zahoor R, Catalano E, Vallifuoco R, Zeni L, Minardo A (2023) Automated Damage Detection Using Lamb Wave-Based Phase-Sensitive OTDR and Support Vector Machines. Sensors 23:1099
10. Bernini R, Minardo A, Zeni L (2012) Distributed sensing at centimeter-scale spatial resolution by BOFDA: measurements and signal processing. IEEE Photon J 4(1):48–56

Study of Amorphous Silicon Temperature Sensors in Saline Solution for Microwave Thermal Ablation

F. Cappelli[1(✉)], M. Baldini[1], G. Petrucci[1,2], A. Nascetti[2], G. de Cesare[1], N. Lovecchio[1], M. Cavagnaro[1], and D. Caputo[1]

[1] Department of Information, Electronic and Telecommunications Engineering, University of Rome La Sapienza, Via Eudossiana 18, Rome, Italy
cappelli.1840513@studenti.uniroma1.it

[2] School of Aerospace Engineering, Sapienza University of Rome, Via Salaria 851/881, Rome, Italy

Abstract. This work explores the use of amorphous silicon temperature sensors for temperature monitoring in Microwave Thermal Ablation (MTA). MTA is a minimally invasive technique that uses the heat generated by microwave electromagnetic fields (EMF) to destroy pathological tissues. MTA is performed by inserting an antenna in the target tissue; then, the antenna is allowed to radiate an EMF which is absorbed by the tissue, thus raising the tissues' temperature.

To optimize MTA and to avoid damage to the surrounding healthy tissues, it is fundamental to monitor the temperature during the treatment.

Here we investigate a solution based on hydrogenated amorphous silicon (a-Si:H) temperature sensors, that, thanks to their small dimensions and low deposition temperature, are suitable to be integrated directly on the MTA antennas.

This work is focused on a study of the sensors' stability in a dissipative environment similar to human tissues; the scope is to analyze the feasibility of temperature monitoring in MTA through a-SI:H diodes.

Keywords: Amorphous Silicon · Microwave Thermal Ablation · Temperature Sensors · Stability Study · Dissipative Environment

1 Introduction

MTA is a minimally invasive technique that uses the heat generated by microwave electromagnetic fields (EMF) to destroy pathological tissues. MTA's procedure involves inserting an antenna into the target tissue and allowing it to emit a high power EMF. This EMF is then absorbed by the tissue, thus leading to a rise in tissue's temperature [1].

To optimize MTA and to avoid damage to the surrounding healthy tissues, it is fundamental to monitor the temperature during the treatment. Nowadays, temperature monitoring is performed mainly using ultrasounds probes (US), but the sensor becomes blind during the procedure because of the water vapour created by the raising temperature. Other techniques such as thermistors, optical fibers and thermocouples increase

C. Di Natale et al. (Eds.): AISEM 2025, LNEE 1497, pp. 184–190, 2025.
https://doi.org/10.1007/978-3-032-08271-8_29

the invasiveness of the treatment and provide only local information [2]. Computed tomography (CT) uses ionizing radiation [3]. Finally, magnetic resonance (MRI) has both compatibility issues and high costs [4].

Here we investigate a solution based on hydrogenated amorphous silicon (a-Si:H) temperature sensors [5–7], that, thanks to their small dimensions and low deposition temperature, are suitable to be integrated directly on the MTA antennas (Fig. 1).

As it is well known, diodes can be used as temperature sensors by measuring the voltage drop across them when biased at a constant direct current [5]. A previous study showed that a-Si:H sensors can be used in dissipative environments (as biological tissues). The same study showed that they couple with the EMF; however, the coupling is systematic so that the possibility to remove it was demonstrated [8].

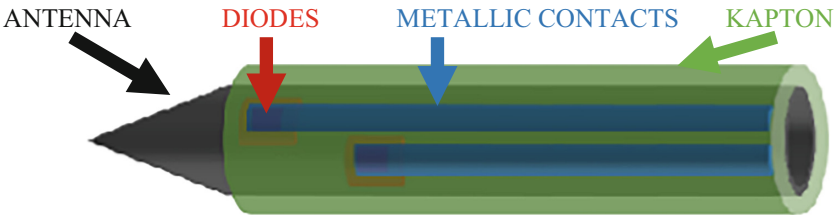

Fig. 1. Example of sensors' integration on the MTA antenna

This work reports the study about the stability of a-Si:H sensors performances in a dissipative environment as well as the study of different geometries and dimensions, to look for structures that could be integrable directly on the shaft of the antenna whose diameter is around 2.5 mm.

2 Device's Structure

The realized devices are p-i-n junctions with a metal/a-Si:H p-type/a-Si:H intrinsic/a-Si:H n-type/metal stacked structures fabricated on glass substrate as shown in Fig. 2. They are fabricated using standard microelectronic techniques.

To deposit the layers, the following processes were used:

a. thermal evaporation for the bottom metal layer;
b. sputtering for the top metal layer;
c. Plasma Enhanced Chemical Vapor Deposition (PECVD) for the hydrogenated amorphous silicon films.

Each deposition step was followed by photolithography and etching:

a. wet etching for the metal layers;
b. Reactive Ion Etching (RIE) for the hydrogenated amorphous silicon films.

The sensors are also insulated and passivated with layers of SU8. Two different geometries were studied: smaller and larger diodes with area equal to 0.25×0.25 mm^2 and 0.5×0.5 mm^2, respectively.

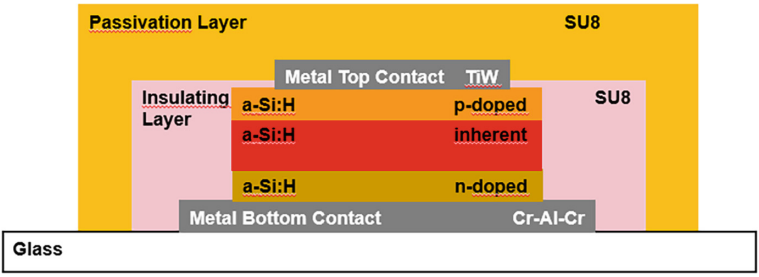

Fig. 2. Diodes structure

3 Experimental Setup and Measurements

Experiments were carried out to investigate the sensor stability in a dissipative environment. Voltage-temperature (V-T) curves were measured as well as the voltage across the diode when biased at constant forward current (B-O) in a saline solution. In particular, the following sequential steps were performed:

a. I-V characteristics to determine the more suitable working current.
b. V-T characteristics to check the initial sensitivity at the working current determined in a.
c. B-O measurement for 2 h to investigate the long-term stability as temperature sensor at the working direct current as determined in a.
d. V-T characteristics to check if the sensor maintains the same characteristics as in point b.

Figure 3 shows the experimental setup which includes:

o a beaker with 900 ml of saline solution, with NaCl concentration of 4.79 g/l,
o the a-Si:H sensors inserted in the solution,
o a 20-pad 100 mils-pitch Edge Card Connector which enables the electrical connection of the sensors to the Source Measure Unit (Keithley K236).

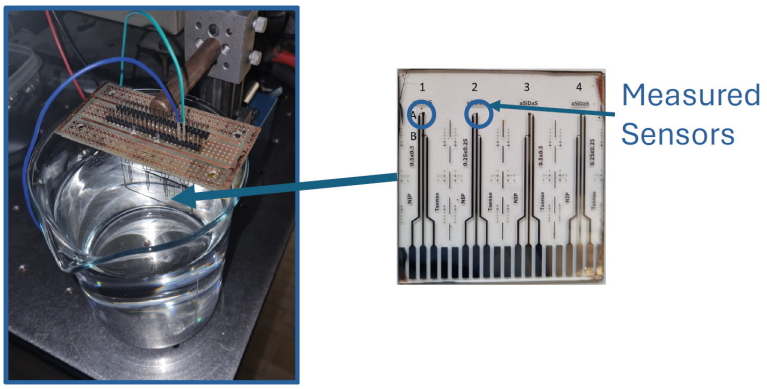

Fig. 3. (left) Experimental setup. (right) the 5 × 5 cm^2 glass hosting four 0.5 × 0.5 mm^2 and four 0.25 × 0.25 mm^2 sensors

4 Results and Discussion

From the initial I-V curves (not shown here), we found that a forward current of 10 nA biases both diodes in the exponential region of both diodes ensuring a correct behavior of the devices as temperature sensors. This current has been therefore chosen as the current working condition in the stability study. Figure 4 shows the voltage across the diodes during the B-O procedure. Upper and lower panels report the results for the smaller and larger diodes, respectively. It can be noted that the voltage drop across the devices has a drift of 2.92 mV for the 0.25 × 0.25 mm^2 area sensor and 2.85 mV for the one with sensor area 0.5 × 0.5 mm^2.

Figures 5 and 6 report the voltage vs temperature behavior before and after the B-O procedure, respectively. From the figures it can be noted that the V-T curves don't present significant differences which corroborates the stability of the sensor's sensitivity. Additionally, they allow deriving a sensitivity of the sensors of about 3.4 ÷ 3.5 mV/°C. Therefore, the expected temperature variation during the B-O procedure can be estimated to be around 0.85 °C. These values are widely acceptable for the proposed use. Indeed, the accuracy needed in MTA is about 1 °C. Furthermore, the typical MTA procedure times are about 15 min, so the observed temperature drift would be not significant for the proposed use.

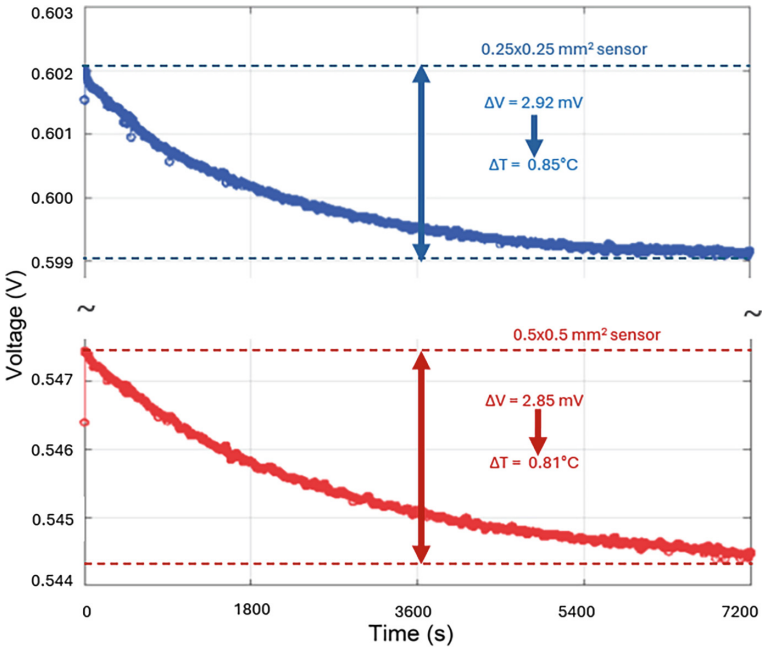

Fig. 4. Stability study at 10 nA forward current for 0.5×0.5 mm^2 (bottom) and 0.25×0.25 mm^2 (top) sensors

As a final comment, results in Figs. 5 and 6 indicate that the sensors do not degrade their performances in a saline environment under working conditions and suggests that these devices are suitable for the proposed MTA application.

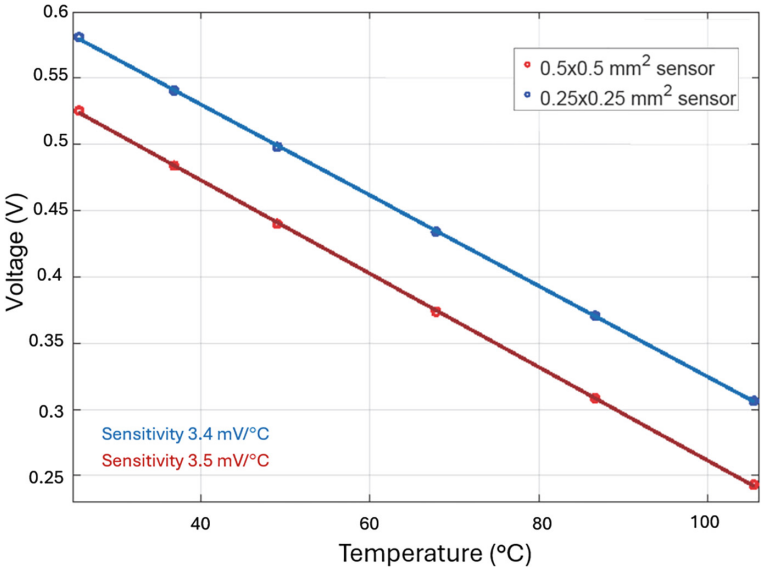

Fig. 5. Voltage vs Temperature before stability study

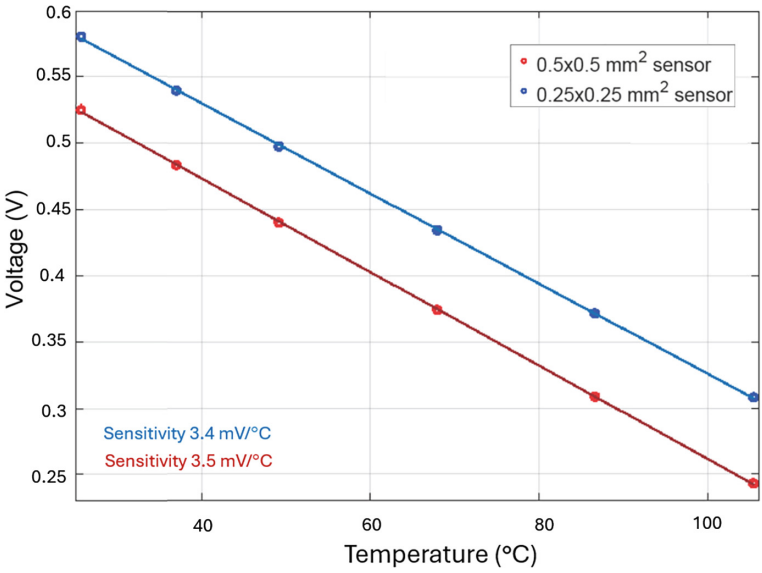

Fig. 6. Voltage vs Temperature after stability study

5 Conclusions

This study shows the stability and the absence of degradation of a-Si:H temperature sensors in a dissipative environment with electrical properties close to those of human tissues. The reported results demonstrate the feasibility of the use of a-Si:H temperature

sensors during a MTA procedure. Given that the antenna's interference is systematic and so removable, and that MTA procedure's duration is shorter than 15 min, this type of device would allow a real-time measurement throughout the MTA procedure while maintaining minimal invasiveness.

References

1. Goldberg SN et al (2003) Image-guided tumor ablation: proposal for standardization of terms and reporting criteria. Radiology 228(2):335–345
2. Nahirnyak VM, Moros EG, Novàk P, Klimberg VS, Shafirstein G (2010) Doppler signals observed during high temperature thermal ablation are the result of boiling. Int J Hyperth 26(6):586–593
3. Shiand L, Tashiro S (2018) Estimation of the effects of medical diagnostic radiation exposure based on DNA damage. J Radiat Res 59(Suppl. S2): ii121–ii129
4. Lopresto V, Pinto R, Farina L, Cavagnaro M (2017) Treatment planning in microwave thermal ablation: clinical gaps and recent research advances. Int J Hyperthermia 33(1):83–100
5. Lovecchio N, Caputo D, Costantini F, Di Meo V, Nascetti A, de Cesare G (2020) On the stability of amorphous silicon temperature sensors. IEEE Trans Electron Devices 67(8):3348–3354
6. Rojwal V, Singha MK, Mondal TK (2020) Amorphous silicon and carbon nanotubes layered thin-film based device for temperature sensing application. IEEE Sens J 21(3):2627–2633
7. Rao S, Pangallo G, Della Corte FG (2016) Integrated amorphous silicon pin temperature sensor for CMOS photonics. Sensors 16(1): 67
8. Caputo D, Lovecchio N, De Cesare G, Cavagnaro M (2024) Amorphous silicon diodes as temperature sensors in microwave thermal ablation applications: an initial assessment. IEEE Sens J 24(17):27198–27204

Energy Harvesting and Sensor Interfaces for Maritime Applications

R. Olivieri[1(✉)], L. Nazzicone[1,2], L. Pantoli[1], V. Stornelli[1], A. Zompanti[3], and G. Ferri[1,4]

[1] Department of Industrial and Information Engineering and Economics, University of L'Aquila, L'Aquila, Italy
riccardo.olivieri1@graduate.univaq.it
[2] Department of Industrial and Information Engineering, University of Pavia, Pavia, Italy
[3] Unit of Electronics for Sensor Systems, Department of Engineering, University Campus Bio-Medico di Roma, Rome, Italy
[4] Department of Electrical and Information (DEI), Polytechnic of Bari, Bari, Italy

Abstract. This work presents the basic concepts of energy harvesting (EH) techniques and circuits, with reference to maritime applications. The main EH sources are recalled as well as boost DC-DC conversion circuits. Multi-input energy sources, in particular piezoelectric and thermoelectric (TEG), have been considered. Two Matlab-Simulink models for TEG are finally described.

Keywords: Boost converter · energy harvesting · sensors · continuous/discontinuous conduction mode · power scavenging · TEG · piezo · synchronous DC-DC converter

1 Introduction

Harvesting is commonly defined the technique for energy recovery from environmental power sources. It is an innovative and appealing way to capture and store energy. By means of energy harvesting (EH) systems, the environmental available and not exploited energy can be converted into other useful forms, mainly electrical [1, 2]. Off-shore EH is also gaining popularity, since many sources (ocean waves, sun, wind, heat, etc.) could be directly used to convert original form of energy into electric to gather electrical power.

EH technique is employed into small, wireless autonomous devices, like those used in wearable electronics and wireless sensor network systems. For this transduction, EH systems need of suitable sensors and interfaces to optimize system performances. The kind of available sources depends on the site where energy must be recovered. The main considered energy sources for EH are the following: radiofrequency (RF), thermal, solar (light), vibrational and motion.

In this paper, where we consider, as an applicative example, maritime sites, also off-shore (platforms), many different energy sources that are abundant, natural and clean, like wind, wave, tidal/current, heat, and solar, can be considered. Their exploitation in the maritime area (e.g., Mediterranean Sea) needs of important research efforts due to

C. Di Natale et al. (Eds.): AISEM 2025, LNEE 1497, pp. 191–196, 2025.
https://doi.org/10.1007/978-3-032-08271-8_30

the characteristics of the area and boundary conditions. Natural resources offer also other forms of renewable energy that can be harvested for innovative applications, as, for example, geothermal energy which offers further possibilities for energy conversion and storage. From the point of view of general interest, this specific activity in maritime sites is very widespread. It can consider, among many, floating wind turbines, electric machines, geophysical resources as well as different kinds of converters for the recovery of waste or environmental energy (magnetocaloric, magneto-elastic, water pressure recovery systems, etc.).

In this sense, research must consider also the development of new devices, which must be designed and fabricated, but also modeled and characterized. Not only, a fundamental aspect is related to the technologies, as magneto-caloric, magneto-elastic, piezo- and thermostat-electric, spintronic, nanomaterials and nanofabrication for sensing, environmental monitoring and telecommunications. Multifunctional materials could represent the paradigm for stand-alone low power environmental sensors with the EH facility in the same device, then it must have multiple input structure that can optimize multiple energy harvesting sources [3–5]. Another important aspect is related to energy storage, through the design and realization of battery management systems featuring innovative management and estimation algorithms to determine the inner state (charge, health, power, etc.), as well as the modeling of physical-chemical phenomena in batteries.

An important topic is related to the DC-DC conversion. As an example, a preliminary design of a dual-input hybrid energy conversion topology to get a constant output voltage is reported. The two considered inputs come from a piezoelectric source and a thermoelectric generator (TEG), respectively, but could be different. Matlab-Simulink models are also described.

2 DC-DC Conversion

2.1 Boost Converter

EH sources gives either AC or DC voltage levels. In the first case, a suitable AC-DC conversion is employed. In the second case, a DC-DC converter can help to increase the DC output level [6–9]. Here we consider, two DC sources (of piezoelectric and TEG kind), so only the DC-DC conversion will be described. Capacitors can be used as a load since the ripple of the voltage across the capacitor can be neglected when compared with its DC value. Its gain is typically related to the duty cycle (D) value of the switch gate voltage. Considering V_i the input voltage, T the period, L the inductance and I_0 the output current, the traditional boost converter has the following gain:

$$CCM\ Voltage\ gain = \frac{1}{1-D} \tag{1}$$

$$DCM\ Voltage\ gain = 1 + \frac{V_i D^2 T}{2LI_0} \tag{2}$$

CCM operation occurs when inductance conducts current continuously in the switching period, whereas DCM happens when it carries current for only part of the switching period, with the current dropping to zero before the end of the period.

2.2 Dual Input Boost Converter

The proposed basic idea of dual input converter employs two switches, S1 and S2, in counter-phase (Fig. 1). When S1 is ON and S2 is OFF, C1 is charged, while when switch S1 is OFF and S2 is ON, C1 is discharged. Gain for the proposed converter is twice the gain of one-input converter. For the start-up phase of the proposed converter, a transformer-based oscillator circuit (TBO) with high turns ratio was used. In addition to its simple design, the TBO has a very low voltage start-up capability. The start-up circuit allows the control signal of the S1 transistor to be generated directly from the piezoelectric sensor, making it necessary to have only one control signal for the S2 transistor, as in a single-input boost.

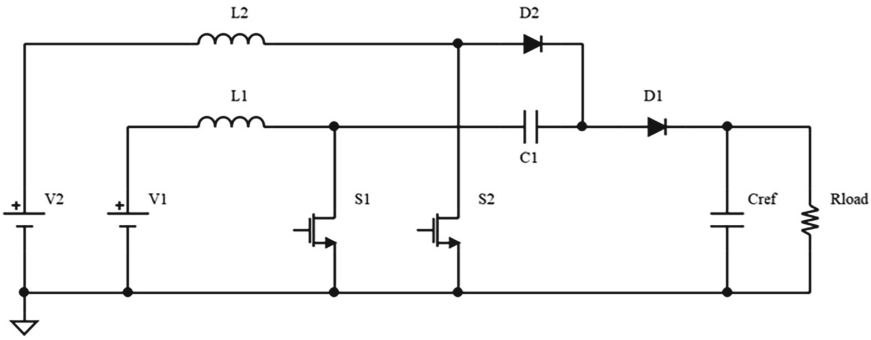

Fig. 1. Two-input DC-DC boost converter with start-up circuit.

3 TEG Modeling and Simulation

Thermoelectric generators (TEGs) convert waste heat into electrical energy via the Seebeck effect, offering a promising solution for energy harvesting. However, most accessible heat sources provide only small temperature gradients (ΔT), resulting in low output voltages—typically in the millivolt range. To maximize power under these conditions, TEGs must exhibit low internal resistance (on the order of ohms or less). While the generated power may suffice, the low voltage often necessitates a DC-DC boost converter. For optimal power transfer, the input resistance of the converter should closely match the TEG internal resistance (RTEG).

A TEG can be modeled as a DC voltage source in series with RTEG. The open-circuit voltage is given by $V_{TEG} = n \cdot S \cdot \Delta T$, where n is the number of thermocouples and S is the Seebeck coefficient. Miniaturized TEGs with small n and low ΔT produce very low voltages; however, thermally series and electrically parallel configurations can maintain ΔT while reducing overall resistance. Despite relatively low efficiency (5–10%), TEGs offer solid-state durability and are well suited for powering IoT nodes. In this project, TEC1-12706 modules were used. Since RTEG can vary, a variable resistor is included in simulations to model this behavior.

Fig. 2 shows the electrical model of a DC-DC boost converter created in Matlab Simulink. The model is composed by: input voltage (1), the inductor with parasitic

resistance (2), the MOSFET transistor (3), used as a switch controlled by the PWM signal (4), the diode (5), the smoothing capacitor (6) and the output resistance (7).

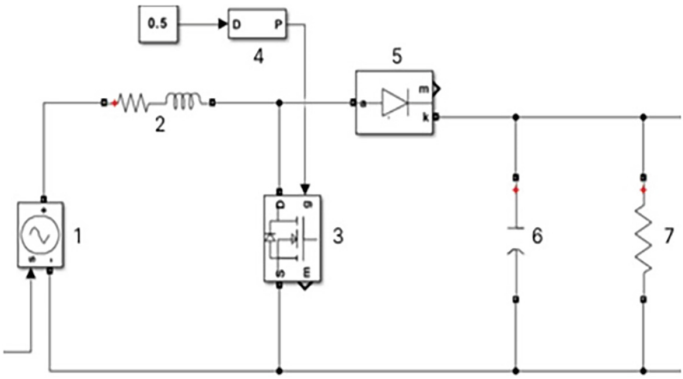

Fig. 2. DC-DC Booster electrical Simulink model.

In the following a solution that uses only one DC-DC booster is presented. The main part of the task is to find a solution for managing the energy inputs to the DC-DC Booster. The issue is that the voltage obtained from energy harvesting is low, and since using an external voltage source is not recommended due to system efficiency, we cannot use a summing amplifier. Two solutions are proposed for passive management of energy inputs: in the first solution the system operates by selecting the source that provides a higher voltage level while disconnecting the other one. This solution is suitable for different types of sensors. The circuit shown in Fig. 3 is based on the use of diodes. Standard diodes are not suitable for this purpose due to their forward voltage drop of about 0.7 V. In this circuit, Schottky diodes are used, as they have a forward voltage drop of about 0.3 V.

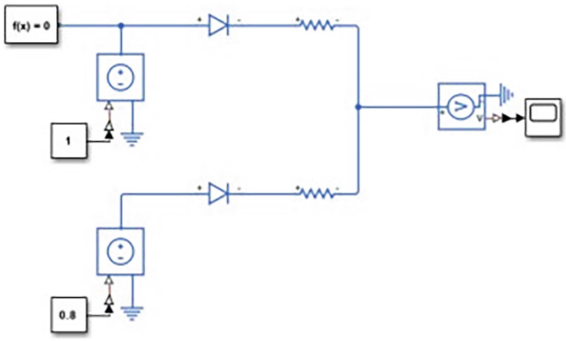

Fig. 3. First DC-DC boost solution.

Fig. 4 shows another solution (in Simulink) for managing the input signal in a DC-DC booster. MOSFET switches and capacitors are key components in this circuit. In the first half- cycle, switch S1 is *on* while switch S4 is *off* (the same applies to switches S2 and S3, but in the opposite phase). In the second half cycle, the situation is reversed. This approach slices the two input signals into fragments and combines them. At the output, we get two signals with opposite phases, oscillating from the voltage level of the first input to the voltage level of the second input. After passing through a capacitor, which smooths these oscillating signals, the signals (now at equal voltage levels) are combined at a single point, thereby summing the energy of the input signals.

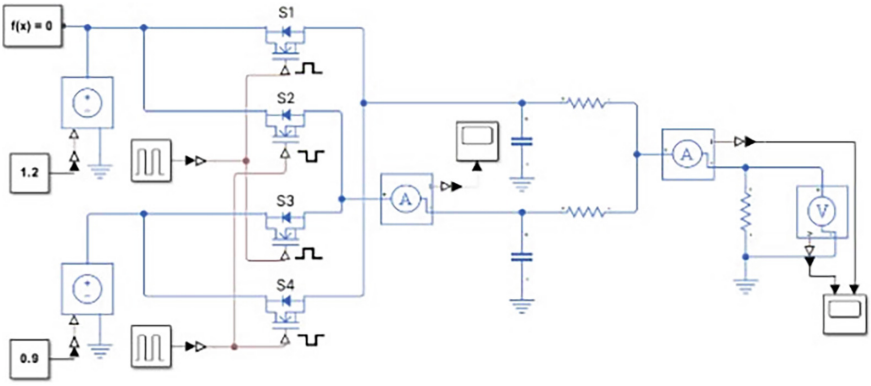

Fig. 4. Second DC-DC boost solution.

Acknowledgement. This Project has been funded under the National Recovery and Resilience Plan (NRRP), Mission 4 Component 2 Investment 1.3 - Call for tender No. 1561 of 11.10.2022 of Ministero dell'Università e della Ricerca; funded by the European Union – NextGenerationEU. Award Number: Project code PE0000021, Concession Decree No. 1561 of 11.10.2022 adopted by Ministero dell'Università e della Ricerca (MUR), CUP - to be indicated by each Beneficiary, according to attachment of Decree No. 1561/2022, Project title "Network 4 Energy Sustainable Transition –NEST".

References

1. Nguyen-Vinh K, Nguyen-Quang N, Dewasurendra H (2015) A review of Low-Power energy harvesting technologies in Industry 4.0. 2023 5th International Conference on Electrical, Control and Instrumentation Engineering (ICECIE), 41: 521–539
2. Fan PM-Y, et al (2015) Energy harvesting techniques: energy sources, power management and conversion. 2015 ECCTD Conference. Trondheim
3. Lavanya A, Navamani JD, Vijayakumar K, Rakesh R (2016) Multi-input DC-DC converter topologies—a review. 2016 International Conference on Electrical, Electronics, and Optimization Techniques (ICEEOT), pp. 2230–2233. Chennai, India
4. Lavanya A, Navamani JD, Kumar KV, Suman PD, Mishra S (2021) Selection of renewable energy materials for dual input DC–DC converter-based hybrid energy system. Materials Today: Proceedings 34(2):379–385

5. Carli D, Brunelli D, Benini L, Ruggeri M (2011) An effective multi-source energy harvester for low power applications. 2011 Design, Automation & Test in Europe (DATE), pp. 1–6. Grenoble, France
6. Rehman Z, Al-Bahadly I, Mukhopadhyay S (2015) Multi-input DC–DC converters in renewable energy applications – an overview. Renew Sustain Energy Rev 41:521–539
7. Soldado-Guamán J, Herrera-Perez V, Pacheco-Cunduri M, Paredes-Camacho A, Delgado-Prieto M, Hernandez-Ambato J (2023) Multiple input-single output DC-DC converters assessment for low power renewable sources integration. Energies 16:1652
8. Lavanya A, Jayaseelan N, Navamani JD, Kumar KV (2017) Dual input DC-DC converter for renewable energy systems. 2017 International Conference on Inventive Systems and Control (ICISC), pp. 1–5. Coimbatore, India
9. Ahrabi RR, Ardi H, Elmi M, Ajami A (2017) A novel step-up multi-input DC–DC converter for hybrid electric vehicles application. IEEE Trans Power Electron 32(5):3549–3561

Optimization of Thin Film Heaters for Spatial Polymerase Chain Reaction

Martina Baldini[1,3(✉)], Giulia Petrucci[1,3], Fabio Cappelli[1,3], Augusto Nascetti[1,3], Francesca Costantini[2,3], Giampiero de Cesare[1,3], Domenico Caputo[1,3], and Nicola Lovecchio[1,3]

[1] Department of Information Engineering, Electronics and Telecommunications, Sapienza University of Rome, Via Eudossiana 18, Rome, Italy
baldini.1637322@studenti.uniroma1.it

[2] School of Aerospace Engineering, Sapienza University of Rome, Via Salaria 851/881, Rome, Italy

[3] Research Center for Plant Protection and Certification, CREA-DC, Via G. Betero, 23, 00179 Rome, Italy

Abstract. Lab-on-Chip (LoC) technology has emerged as a powerful tool for biomedical diagnostics, chemical analysis, and environmental monitoring, offering compact and portable solutions. One key application is DNA amplification via Polymerase Chain Reaction (PCR), which replicates specific DNA sequences through thermal cycling. A challenge in conventional PCR is the time required for heating and cooling cycles. Spatial PCR addresses this limitation by allowing the sample to flow through a microfluidic network, where dedicated heaters maintain optimal thermal conditions across different regions of the chip. However, real-time detection of amplified products remains a challenge. Integrating photosensors in the annealing zone enables real-time monitoring of DNA amplification. This study focuses on the design, fabrication, and testing of thin-film heaters for spatial PCR. Using COMSOL Multiphysics, we simulated coupled thermal and electrical phenomena to optimize heater performance. The heaters, fabricated as a Cr/Al/Cr stack on a 5 × 5 cm^2 glass substrate, were designed to ensure uniform temperature distribution while minimizing thermal crosstalk. The configuration included a central heater for the denaturation phase (95 °C) and two lateral heaters for the annealing phase (62 °C). Thermal imaging confirmed uniform heating, assessing the integration of spatial PCR into LoC systems for efficient, real-time DNA amplification.

Keywords: Lab-on-Chip (LoC) · Polymerase Chain Reaction (PCR) · Spatial PCR · Thin-Film Heaters · Microfluidics · Real-Time Detection

1 Introduction

In recent years, Lab-on-Chip (LoC) technology has emerged as an innovative tool for performing analyses in a compact and portable format, with applications in biomedical diagnostics, chemical analysis, and environmental monitoring [1–7].

C. Di Natale et al. (Eds.): AISEM 2025, LNEE 1497, pp. 197–202, 2025.
https://doi.org/10.1007/978-3-032-08271-8_31

One important application of LoC devices is the DNA amplification via Polymerase Chain Reaction (PCR) [8–10]. This technique enables the replication of specific DNA sequences by subjecting the sample to repeated thermal cycles between three temperatures: 95 °C for denaturation to separate the DNA strands, 55 °C for primer binding to the target sequence (annealing) and 72 °C for elongation [11–13]. A common variant of PCR involves two-step per cycle: denaturation, and annealing (~60 °C), during which primers bind, allowing DNA polymerase to initiate synthesis [14–16].

One drawback of this technique is the time required for the thermal cycling process, which is influenced by the heating and cooling rates. A potential solution to this limitation is spatial or continuous-flow PCR. In this approach, the sample moves through a microfluidic network and undergoes thermal cycles within different regions of the chip, where dedicated heaters integrated onto the device are strategically positioned to maintain the required thermal conditions.

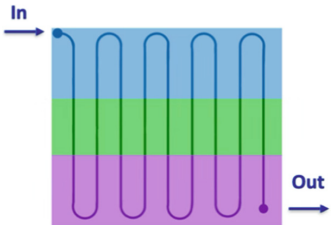

Fig. 1. Colors represent three temperature zones: denaturation (blue), annealing (green), and elongation (purple).

Figure 1 illustrates an example of Continuous-flow PCR, where the continuous meander represents the microfluidic channel. Starting from the inlet, the fluid goes through the regions at different temperatures, enabling the DNA amplification. As for the standard PCR, the DNA amplification is mainly monitored by fluorescence.

However, conventional implementations of this method typically lack real-time detection of the amplified products [12]. Indeed, while the flow of samples and reagents goes through temperature-specific zones, the amplified products are collected and analyzed at a last stage rather than in real time. To address this issue and implement a real-time PCR in a compact device, it is necessary to design the heaters and the microfluidic network to easily include the photosensors for monitoring the DNA amplification in each PCR cycle.

Within this framework, the focus of this research was the development of thin-film heaters capable of reaching the target temperatures, associated with the required thermal zones, that can be easily integrated with a custom-designed microfluidic layout and with photosensors enabling real-time monitoring of the amplification process.

2 Structure of the LoC

The scheme of the proposed LoC, which implements a spatial two-step PCR is depicted in Fig. 2. The dark-grey line represents the central heater, while the light-grey lines represent two lateral heaters. The blue rectangle encircles the denaturation zone; the

red rectangles designate the annealing/elongation zones. Within each region, there are two temperature sensors (blue squares). Additionally, the light blue shapes represent six independent microfluidic channels, each containing a dedicated photosensor (orange rectangles) for real-time monitoring.

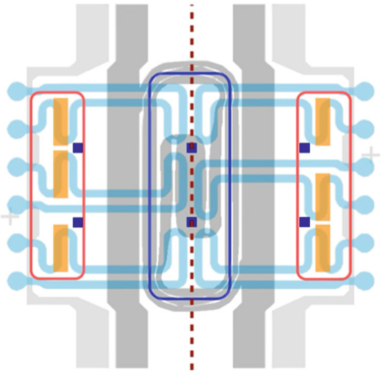

Fig. 2. Proposed LoC device: Temperature sensors (dark blue), photo-sensors (orange), and three heaters—one central (dark grey) and two laterals (light grey) are deposited on the bottom glass substrate. The microfluidic channels (light blue) are patterned on a top glass layer, aligned with the underlying glass. The dashed brown line highlights the structural symmetry designed for simultaneous amplification.

In this scheme the fluid flow through the microfluidic network can be precisely controlled using electronic micro-pumps, ensuring accurate and reliable movement between the different thermal zones required for the two-step PCR protocol.

3 Thin-Film Heaters

The research presented in this work is focused on the design, fabrication and testing of thin-film heaters.

3.1 Design Optimization

Design optimization was performed using coupled thermal and electrical simulations in COMSOL Multiphysics to evaluate whether the heaters could reach the target temperatures and to assess heat distribution across the chip. The heaters were modeled as a Cr/Al/Cr stack deposited on a 3D 5×5 cm^2 glass substrate. Their geometry was specifically designed to ensure uniform heating of the target zones and minimize thermal interference between adjacent regions. The electrical resistance of each heater—determined by material composition, thickness, and length—plays a critical role, as higher resistance results in greater heat generation at a given current. The layout features a central heater ($R = 10.9\ \Omega$) for the denaturation phase and two lateral heaters ($R = 2.8\ \Omega$) for the annealing phase. This symmetric configuration enables simultaneous amplification across six independent microfluidic sites. To improve thermal efficiency and

uniformity, the conductive film was patterned into serpentine or grid-like structures. Figure 3 presents the simulation results, showing the central heater reaching 95 °C and the lateral heaters maintaining 62 °C.

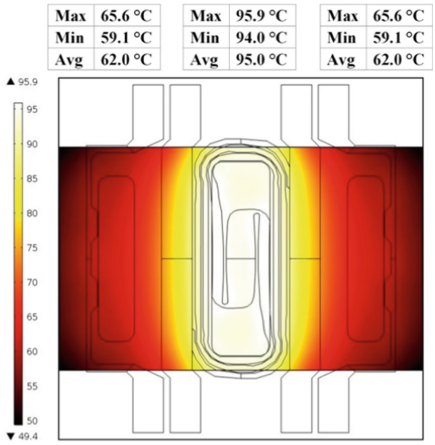

Fig. 3. COMSOL simulation results.

3.2 Fabrication

The microelectronic device is fabricated using a layer-by-layer approach, which enables the construction of complex and precise structures through the controlled deposition of thin films. Following the deposition of each layer, photolithography and etching are employed to define the desired patterns by selectively removing unwanted material. This sequence—deposition, photolithography, and etching—is repeated for each subsequent layer until the entire device is completed. A photograph of the heaters fabricated on a 5 $\times$ 5 cm^2 Borofloat glass substrate is shown in Fig. 4.

Fig. 4. Picture of the fabricated device.

3.3 Measurement Setup

Once the heaters were fabricated, an experimental setup was assembled to perform thermal measurements using a FLIR 320A thermal camera. These measurements were used to validate the simulation results. The heat generated by each heater was controlled by adjusting the applied voltage or current, in accordance with the Joule effect.

Each of the three heaters was powered independently using separate power supplies, allowing precise control of the thermal conditions in each zone.

4 Results

To reproduce the experimental setup during DNA amplification. The microfluidics, a 3×5 cm^2 glass slide was placed on top of the LoC device to mimic the microfluidic layer.

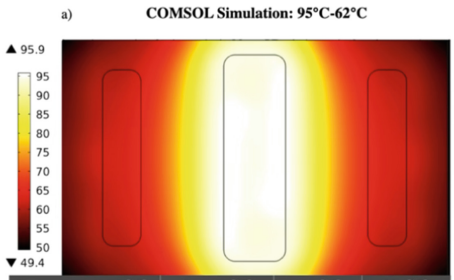

Areas temperature [°C]	Average [°C]	Max[°C]	Min[°C]
Central	95.00	95.92	94.00
Lateral	62.00	65.90	59.10

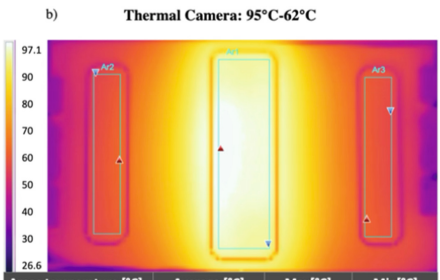

Areas temperature [°C]	Average [°C]	Max[°C]	Min[°C]
Central Ar1	95.00	97.2	92.00
Lateral Ar2	62.00	65.00	59.10
Lateral Ar3	62.00	64.10	59.90

Fig. 5. a) COMSOL simulation data. b) Thermal Camera data.

The images reported in Fig. 5a and b show the temperature distributions achieved with simulation and measurement, respectively. Both the simulation and experimental results demonstrated good temperature uniformity, with a maximum deviation of ± 2 °C observed in the corner regions. Thermal camera measurements (Fig. 5b) revealed a difference between the maximum and minimum temperatures of the lateral heaters. This variation is attributed to inhomogeneities in the thin films of the two smaller resistors, which affected their thermal performance.

5 Conclusions

In this work, we designed, fabricated and tested this film heaters for implementing a two-temperature-step spatial PCR. Experimental results confirmed that the optimized heater geometries provide the required temperature distribution with minimal thermal crosstalk between zones. These findings assess the feasibility of integrating this type of spatial PCR into LoC systems.

References

1. Zhu H et al (2020) Recent advances in lab-on-a-chip technologies for viral diagnosis. Biosens Bioelectron 153:112041
2. Karthik V, Karuna B, Kumar PS, Saravanan A, Hemavathy RV (2022) Development of lab-on-chip biosensor for the detection of toxic heavy metals: a review. Chemosphere 299:134427
3. Lovecchio N et al (2022) Thin-film-based multifunctional system for optical detection and thermal treatment of biological samples. Biosensors 12(11):969
4. Staicu CE et al (2022) Glass lab-on-a-chip platform fabricated by picosecond laser for testing tumor cells exposed to X-ray radiation. Appl Phys A 128(9):770
5. Rahad R et al (2024) A polarization independent highly sensitive metasurface-based biosensor for lab-on-chip applications. Measurement 231:114652
6. Lovecchio N, et al (2021) Transparent oxide/metal/oxide thin film heater with integrated resistive temperature sensors. IEEE Sensors Journal 21(17): 18847–18854
7. Krakos A (2024) Lab-on-chip technologies for space research—current trends and prospects. Microchim Acta 191(1):31
8. Baltrušis P, Johan H (2023) Digital PCR: modern solution to parasite diagnostics and population trait genetics. Parasit Vectors 16(1):143
9. Mirasoli M et al (2018) On-chip LAMP-BART reaction for viral DNA real-time bioluminescence detection. Sens Actuators, B Chem 262:1024–1033
10. Maren NA, et al (2023) Stepwise optimization of real-time RT-PCR analysis. Plant Genome Engineering: Methods and Protocols, pp. 317–332. Springer US, New York, NY
11. Costantini F et al (2018) Integrated sensor system for DNA amplification and separation based on thin film technology. IEEE Trans Compone Packag Manufact Technol 8(7):1141–1148
12. Ahrberg CD, Manz A, Chung BG (2016) Polymerase chain reaction in microfluidic devices. Lab Chip 16(20):3866–3884
13. İnce GT, et al (2023) Micro-polymerase chain reaction for point-of-care detection and beyond: a review microfluidics and nanofluidics. Microfluidics and Nanofluidics 27(10): 68.A
14. Huang S, et al (2023) Ultra-fast, sensitive and low-cost real-time PCR system for nucleic acid detection. Lab on a Chip 23(11): 2611–2622
15. Mackay IM et al (2002) Real-time PCR in virology. Nucleic Acids Res 30(6):1292–1305
16. Zhou R et al (2022) Spatial continuous-flow polymerase chain reaction structure controlled by single-temperature driver. Advanced Science 9(6):2203174
17. Li, Z, et al (2023) Lower fluidic resistance of double-layer droplet continuous flow PCR microfluidic chip for rapid detection of bacteria. Analytica Chimica Acta 1251: 340995
18. Hsieh, H-Y, et al (2022) Continuous polymerase chain reaction microfluidics integrated with a gold-capped nanoslit sensing chip for Epstein-Barr virus detection. Biosensors and Bioelectronics 195: 113672
19. Han W, Chen X (2021) A review on microdroplet generation in microfluidics. J Braz Soc Mech Sci Eng 43(5):247

The Design of Piezoelectric Cantilever for Blood Sensor Device

Mohammed Mahdi[1](✉), Rania Boudissa[3], Iman Laribi[3], Bouasla Chafia[1,2], and Belhani Imadeddine[4]

[1] Centre de Développement des Technologies Avancées CDTA, MEMS & Sensor Team, Algires, Algeria
mmahdi.usto@gmail.com
[2] Platform MEMS, Center for Development of Advanced Technologies CDTA, Algires, Algeria
[3] Electric Engineering Department, University of Science and Technology Houari Boumediene USTHB, Agiers, Algeria
[4] Laboratory of Theoretical Physics and Material Physics (LPTPM), Faculty of Technology, Hassiba Benbouali University of Chlef, B.O. Box 151, Hay Salem, 02000 Chlef, Algeria

Abstract. This work aims to design a biocompatible microsystem device using piezoelectric materials. The device is 1000 μm in length, and 100 μm wide, and the thickness is 10 μm for the Silicon plus 2 μm for the piezo-material (ZnO, PZT, BNN, and AlN). The COMSOL analysis shows that the ZnO (which is a biocompatible material) has 6.4 μV/Pa of sensitivity and the output voltage is from 0.7 to 1 mV under normal blood pressure (80 to 120 mmHg) the maximum cantilever displacement is 79.9 μm. The second piezo material is the AlN. This material is biocompatible, and CMOS compatible, which makes it an excellent candidate for mass production. Its sensitivity is 4.4 μV/Pa and the output voltage is 0.2 to 0.4 mV under normal blood pressure with low deformation under the pressure at 120 mmHg the total displacement is 57.8 μm.

Keywords: Cardio-MEMS · blood pressure · piezoelectric materials · health care · telemedicine

1 Introduction

Today, real-time health assessment has become a significant public health concern. There is a growing need for smart wearable devices to monitor health parameters such as arterial pressure or glycemic levels. This is important for preventing complications related to heart failure and diabetes, ensuring overall quality of life, and reducing the risk of serious health issues. Microelectromechanical systems (MEMS) offer great solutions for telemedicine and related applications. Advanced research and development are underway to invent new solutions with high accuracy, cost-effectiveness, and to streamline the fabrication process for mass production.

Currently, pressure measurement is mainly conducted using capacitive MEMS or piezoresistive MEMS. However, for blood pressure measurement, the device should be

C. Di Natale et al. (Eds.): AISEM 2025, LNEE 1497, pp. 203–208, 2025.
https://doi.org/10.1007/978-3-032-08271-8_32

biocompatible and the output signal easy to handle. For instance, Rao, K.S et al. [1] show in their work on capacitive MEMS for blood sensors. They indicate a sensitivity in femtofarad range (7.979 Ff/bar), which is challenging to manage, requiring heavy electronics to handle the device. On the other hand, Jakati et al. [2] present a comparative study of different pressure sensor types and conclude that the capacitive pressure sensor gives a nonlinear response, while the piezoresistive pressure sensor achieves high linearity. They suggest that the piezoelectric sensor has the highest sensitivity in dynamic pressure conditions. Lahreche et al. [3] propose a new C-Shaped Slot Design for a capacitive blood pressure sensor, achieving high sensitivity of 1.49 fF/mmHg, compared to the previous study. On the invasive MEMS device, Beyaz [4] presents finite element simulation on laminar flow and solid mechanics domains to evaluate the sensor effect on blood pressure. Their results show an improvement of 95% to 98% for the pressure and 66% to 88% for the flow compared with previous works. Vasudeva et al. [5] analyze the coagulation effect in veins by piezoelectric MEMS flow to design a stethoscope and wristband to measure heart health parameters through blood pressure. Finally, Dalin et al. [6] designed a square membrane with AlN piezoelectric material on the top, creating a blood pressure device with nano-generation sensitivity of 0.13V/kP.

In this study, we designed a cantilever device incorporating different piezoelectric materials (PZT, ALN, ZnO, and Barium Sodium Niobate BNN) on top of a silicon support. We conducted analysis under different blood pressures ranging from 80 mmHg (10665.8 Pa) to 120 mmHg (15998.7 Pa) and measured the corresponding output voltages for each piezoelectric material. The main aim of this work is to design high output voltage for biocompatible piezoelectric material for wearable technology solution.

2 Modeling on COMSOL

COMSOL is a multiphysics tool that allows us to analyze coupling physics phenomena. In the present work, we applied to the geometry: Solid Mechanics module: in which we define the piezoelectric material, and The Electrostatics (es) module: in which we define the floating voltage, meaning the electrical boundary conditions are not grounded or fixed at a particular potential but instead respond to the mechanical stress applied to the piezoelectric material. Finally, in the definition module, we applied the domain point probe at the top of the free edge of the beam cantilever to have the output voltage as a response to the applied stress. Then, the coupling physics, in our case the piezoelectric Effect couple the solid mechanics and electrostatics modules using the piezoelectric effect. This coupling allows the mechanical stress in the material to generate an electric potential (voltage) as a response, and vice versa, based on the piezoelectric properties of the material see Fig. 1.

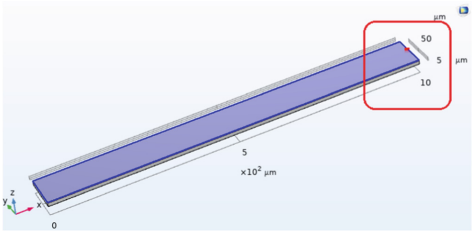

Fig. 1. 3D geometry of the cantilever on COMSOL

3 Results and Discussion

3.1 Geometry Definition

Our cantilever has 2 μm thickness of each pizo-materials listed in the Table 2 deposited on silicon beam (E = 190 GPa) of 10 μm thick and 10 μm width, the length is varied from 350 to 1000 μm see table 1. Therefore, the resulting stress under 80 and 120 mmHg pressure is calculated using equation

$$\sigma = (F\,L)/\left(6b\,t^2\right) \tag{1}$$

Table 1. The geometric parameters of the cantilever.

Shape parameters	Symbols	Value
Beam length	L	350–1000 μm
Beam width	b	100 μm
Piezo-material thickness	t_p	2 μm
Silicon beam thickness	t_s	10 μm

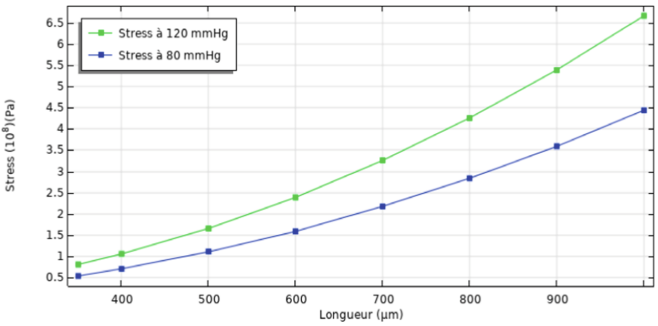

Fig. 2. Stress as function of the beam length under 80 mmHg and 120 mmHg pressure the highest stress is 6.66 10^8 Pa for 1000 μm beam length.

The overall stress as function of the beam cantilever length under 80 mmHg and 120 mmHg pressure is shown on the Fig. 2, we used Eq. (1) to calculate the stress with the thickness $t = t_p + t_s$.

The cantilever has two material the silicon with (E = 190 GPa) and the piezoelectric material with different young module see table 2. The equivalent elastic module for the beam cantilever is then calculated using the following equation.

$$E_{eq} = E_{piezo}(V_{piezo}/V_{total}) + E_{si}(V_{si}/V_{total}) \quad (2)$$

The deformation is calculated using the Eq. (3)

$$E = (\text{stress } (\sigma))/(\text{strain (s)}) \quad (3)$$

At the maximum stress of 6.66 10^8 Pa the strain is 4.1 10^{-3} therefore the deformation on the cantilever length would be ΔL is 4.1 μm (L = 10^3 μm).

Table 2. Module elastic for the piezoelectric material and the relative cantilever

materials	PZT-5H	Barium Sodium Niobate BNN	AlN	ZnO
E (GPa)	23.47	75.75	15.5	44.25
E_{eq} (GPa)	162.2	171	160.9	165.7

The total displacement for each cantilever under the blood pressure is shown in Table 3, and Fig. 3.

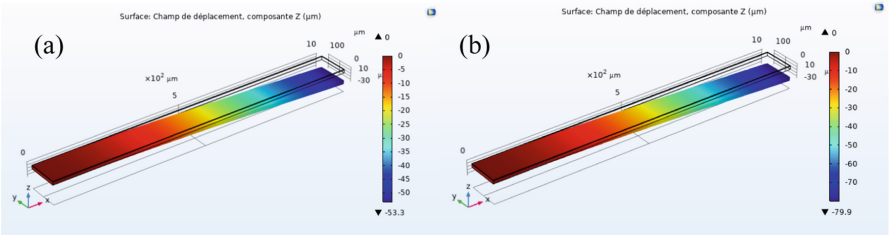

Fig. 3. The cantilevers displacement under the blood pressure for ZnO, a) and b) under 80 and 120 mmHg respectively.

Table 3. The cantilever displacement under the blood pressure

Pressure mmHg	Displacement (μm) PZT-5H	Displacement (μm) ZnO	Displacement (μm) BNN	Displacement (μm) AlN
80	69.7	53.3	57.4	38.5
90	78.5	59.9	64.5	43.4
100	87.2	66.6	71.7	48.2
110	95.9	73.2	78.9	53
120	105	79.7	86	57.8

3.2 Output Voltage for Each Geometry

The COMSOL analysis of the output voltage as function of the applied pressure for each piezo-material are traced on the Fig. 4. We have good linearity and the ZnO gives higher output voltage between 0.7 to 1 mV in normal blood pressure comparing to the other piezo-material see Table 4.

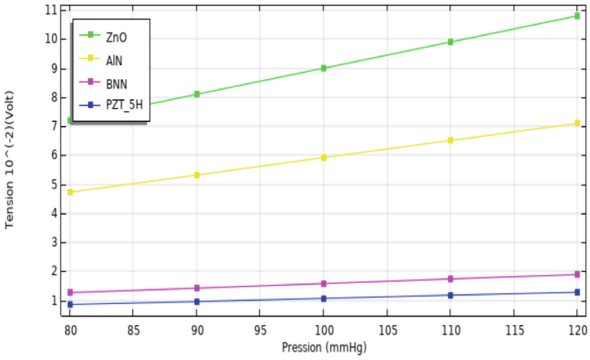

Fig. 4. The output voltage as function of the applied voltage for ZnO, AlN, BNN and PZT 5H materials using the classical geometry.

Table 4. The output voltage data for the normal blood pressure using different piezo-materials.

Pressure mmHg	PZT 5H	ZnO	BNN	AlN
80	$0.86\ 10^{-2}$	$7.2\ 10^{-2}$	$1.27\ 10^{-2}$	$4.73\ 10^{-2}$
90	$0.96\ 10^{-2}$	$8.1\ 10^{-2}$	$1.42\ 10^{-2}$	$5.32\ 10^{-2}$
100	$1.07\ 10^{-2}$	$9\ 10^{-2}$	$1.58\ 10^{-2}$	$5.92\ 10^{-2}$
110	$1.18\ 10^{-2}$	$9.9\ 10^{-2}$	$1.74\ 10^{-2}$	$6.51\ 10^{-2}$
120	$1.28\ 10^{-2}$	$10.8\ 10^{-2}$	$1.89\ 10^{-2}$	$7.10\ 10^{-2}$

Table 5. The dielectric properties of the piezo-materials used in this work.

Paramètres physique	PZT-5H	BNN	ZnO	AlN
d_{31} (pC/N)	−274	42	−5.43	−2,78
ε_r	3400	60000	12.64	10,26
g (Vm/N)	$-9.1\ 10^{-3}$	$0{,}079\ 10^{-3}$	$-48.52\ 10^{-3}$	$-30{,}6\ 10^{-3}$

Despite that, PZT has a large piezoelectric coefficient (d_{31}) see Table 5. The overall value of the piezoelectric voltage constant ($g = d\ /\ (\varepsilon_0\ \varepsilon_r)$) becomes less compared to the ZnO and AlN due to its large relative permittivity. This is exactly what COMSOL analysis shows us in those results [7, 8].

4 Conclusion

This study explores biocompatible ZnO for enhanced piezoelectric output, achieving 6.7 μV/Pa sensitivity, outperforming AlN (4.4 μV/Pa), BNN (1.1 μV/Pa), and PZT (0.1 μV/Pa). Compared to prior PZT studies (0.251×10^{-2} V [9]), our PZT analysis yielded 0.98×10^{-2} V at 1×10^{4} Pa. ZnO/AlN's higher piezoelectric coefficient (g) improves voltage, aligning with [6]'s AlN square membrane (0.13 mV/Pa). Structural optimization (e.g., square membranes) and materials like PVDF (110–180 mV/pulse [10]) suggest promising avenues for biomedical applications [11].

References

1. Rao KS, Samyuktha W, Vardhan DV et al (2020) Design and sensitivity analysis of capacitive MEMS pressure sensor for blood pressure measurement. Microsyst Technol 26:2371–2379. https://doi.org/10.1007/s00542-020-04777-x
2. Jakati RS, Balavalad KB, Sheeparamatti BG (2016) Comparative analysis of different micro-pressure sensors using comsol multiphysics. 2016 International Conference on Electrical, Electronics, Communication, Computer and Optimization Techniques (ICEECCOT), Mysuru, India, pp 355–360 https://doi.org/10.1109/ICEECCOT.2016.7955245
3. Lahreche T, Kandouci M (2024) Enhancing blood pressure sensitivity: innovative C-Shaped slot design in microsensor systems. https://doi.org/10.2478/sbeef-2024-0012
4. Beyaz Mİ (2022) An implantable sensor for arterial pressure monitoring with minimal loading: design and finite element validation. 2022 IEEE Sensors, Dallas, TX, USA, pp 01–04 https://doi.org/10.1109/SENSORS52175.2022.9967260
5. Reddy TV, Anirudh Reddy R, Reddy, PK, Reddy A (2022) Analysis of coagulation effect in veins using MEMS laminar flow for early heart stroke detection. 2022 International Conference on Automation, Computing and Renewable Systems (ICACRS), Pudukkottai, India, pp 39–44 https://doi.org/10.1109/ICACRS55517.2022.10029270
6. Dalin EM, Hasan SMR (2022) Modeling of a novel AlN nanogenerator-based self-powered MEMS arterial-pulse sensor. IEEE Sens J 22(9):8574–8582. https://doi.org/10.1109/JSEN.2022.3161026
7. Uchino K (2017) The development of piezoelectric materials and the new perspective. Adv Piezoelectr Mater https://doi.org/10.1016/B978-0-08-102135-4.00001-1
8. Stephen A. Campbell, The Senience and Engineering of Microelectronic Fabrication, second Edition
9. Mahdi M, Kadri M (2021) Effect of KrF laser irradiation on the morphology and microstructure of amorphous PZT thin films grown by RF magnetron sputtering. J Elec Mater 50:4450–4455. https://doi.org/10.1007/s11664-021-08980-y
10. Nath SS, Lingaraja D, Aravind P, Thangavel P, Arun Kumar P, Ram, GD (2023) Comparison of different shapes MEMS based Piezo electric pressure sensor for smart devices. 2023 5th International Conference on Smart Systems and Inventive Technology (ICSSIT), Tirunelveli, India, pp 1–5 https://doi.org/10.1109/ICSSIT55814.2023.10061138
11. Tan JY, Islam S, Li Y, Kim A, Kim J (2023) An optimization of perforation design on a piezoelectric-based smart stent for blood pressure monitoring and low-frequency vibrational energy harvesting. IEEE 36th International Conference on Micro Electro Mechanical Systems (MEMS), Munich, Germany, pp 396–399, https://doi.org/10.1109/MEMS49605.2023.10052623

Development of a Passive Skin for Glass Building Surfaces in a Smart Electromagnetic Environment

G. Marchi(✉), A. Bagolini, V. Mulloni, J. Iannacci, and L. Lorenzelli

Center for Sensors and Devices (SD), Fondazione Bruno Kessler, 38123 Trento, Italy
gmarchi@fbk.eu

Abstract. Electromagnetic metasurfaces (MTS), also referred to as Reconfigurable Intelligent Surfaces (RIS) in their dynamic form, have the potential to actively shape the wireless communication environment, particularly in 5G and 6G systems. They help overcome significant path loss issues, especially at millimeter-wave (mmWave) frequencies within the FR2 band. Our study focuses on MTS from a fabrication standpoint, highlighting the microfabrication methods employed to create a static and passive MTS prototype on a 6″-optically transparent wafer substrate. This MTS design is intended for integration onto large glass surfaces commonly found in urban settings.

Keywords: Electromagnetic Metasurfaces · Reconfigurable Intelligent Surfaces (RIS) · Wireless Communications · 5G-6G Communications · Optically-Transparent

1 Introduction

The emerging communication paradigms of 5G, Beyond-5G (B5G), and 6G are opening exceptional possibilities while also presenting significant technical and technological challenges. The complex propagation environments and the attenuation of millimeter waves (mmWaves) in these settings demand affordable communication infrastructure, which must also take into account the constraints on data rates per user, latency and reliability required in the transition from 5G to 6G. From the perspective of enhancing 5G/B5G communication infrastructure in a more environmentally friendly manner (e.g., without increasing the density of base stations), buildings in the environment can be transformed into a naturally enhanced communication infrastructure, referred to as a Smart ElectroMagnetic Environment (SEME). Rather than being seen as obstacles to electromagnetic (EM) radiation, buildings can be utilized to support non-line-of-sight communications by introducing passive skins or EM metasurfaces (MTS). In their static and passive version, these EM skins are identified in [1] as the Metasurface 2.0 typology. They are designed to redirect the signal in anomalous angular directions with respect to those identified by the standard Snell's laws, thus being defined as MTS for anomalous reflection (Rx) or transmission (Tx).

C. Di Natale et al. (Eds.): AISEM 2025, LNEE 1497, pp. 209–214, 2025.
https://doi.org/10.1007/978-3-032-08271-8_33

A challenge within this paradigm is identifying which parts of buildings can be covered with a MTS. In most studies [2, 3], solid sections of facades, such as concrete walls, are identified as suitable for MTS coverage, with panels incorporating this EM functionality typically added on top. In contrast, windows and doors are generally regarded as restricted areas.

In this work we want to focus on this aspect and to develop a prototype of EM smart skin for glass portions of buildings, microfabricating it and assessing its fabrication and electrical properties. Indeed, there is growing evidence in recent literature highlighting this as a recognized gap, where further research and technological advancements are needed to enhance the transparency of MTS [4–9]. For the purpose, we develop a transparent MTS by selecting the design proposed by the authors in [10], where the metasurface is designed for the specific functionality of anomalous reflection.

2 Microfabrication of the MTS

The MTS as in [10] is characterized by a periodic pattern of conductive cells or meta-atoms as the one proposed in Fig. 1(a), which is of Phoenix type. Eight cells with a gradient-based trend in the dimensions are repeated periodically throughout the MTS. When the EM metasurface is used as reflective mirror, it typically features a compact radio frequency (RF) groundplane that blocks the view and allows for the reflection of the signal, while the MTS for anomalous transmission is usually characterized by different layers of patterned surfaces (see both in Fig. 1(b)). The design in [10] is studied to operate at 28.25 GHz, and when an incident electromagnetic excitation impinges the metasurface at an angle $\theta_i = -30°$ the MTS reflects it into a new location at $\theta_r = +54°$. The layout in [10] was developed to be implemented on a standard FR4 substrate, which is not optically transparent. Instead, we have selected a transparent high-purity fused silica (HPFS) substrate in a 6″-wafer format, with dielectric properties $\varepsilon_r = 3.8$ and $\tan \delta = 0.0001$, which cover a similar range to those of FR4. This choice is strategic, as it moves us toward the development of smart EM skin for glass surfaces on buildings. Aluminum (Al) is chosen as the conductive material for fabrication, characterized by a nominal conductivity of $\sigma = 3.77 \times 10\text{^}7$ S/m and a thickness of $t = 3$ μm. The fabrication process is carried out within the FBK cleanroom classified ISO 4–5. The Al film is deposited on both the back and front sides of the wafer using a standard microelectronic-grade magnetron sputter physical vapor deposition (PVD) tool. A photoresist film is spin-coated onto the front side of the wafer, and the Phoenix meta-atoms are created using photolithography. The wafers are then etched in chlorine-based plasma to remove the Al from unprotected areas. Some details of the optical inspection are shown in Fig. 1(a).

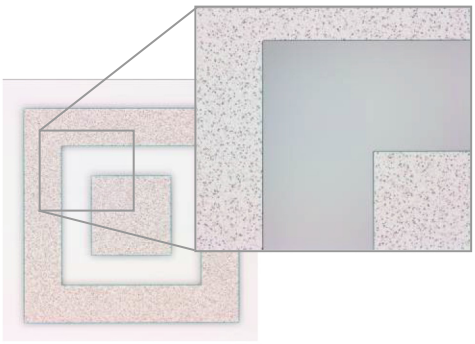

(*a*)

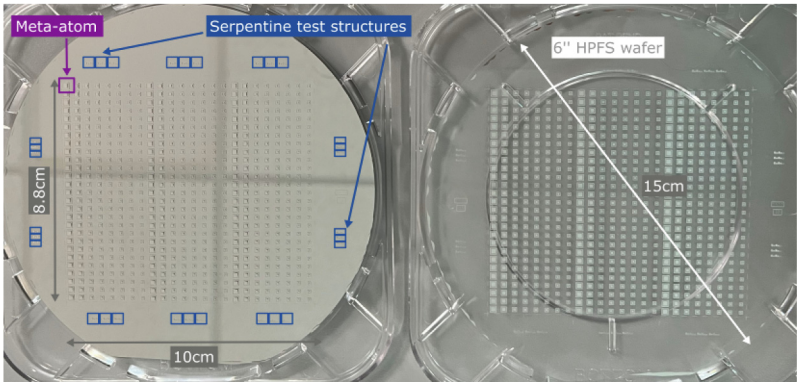

(*b*)

Fig. 1. In (*a*) MTS unit cell geometry with focus on the fabrication resolution, while in (*b*) the final MTS prototype on HPFS 6′′- wafers for anomalous reflection (first wafer) and transmission (second wafer).

3 Electrical and Morphological Characterization

As a further design feature, four serpentine-shaped electrical test structures are placed at the wafer's edges and replicated at regular intervals as indicated in Fig. 1(b). A set of structures *R1, R2, R3, R4* acquired at the Microscope Leica INM100 (1.25x) is proposed in Fig. 2. They allow us for the evaluation of the fabrication process accuracy, including the resolution and thickness of the strips and the electrical properties of the conductive layers, such as the deviation of conductivity from its nominal value. Indeed, they differ in both length and width parameters and contribute to a more insightful and meaningful evaluation. The thinnest line width is $w_{BASE} = 10$ µm, while the thickest is $w_{GROWN} = 15$ µm. The shortest serpentine lengths are $l_{R1} = l_{R3} = 11.58$ mm, and the longest are $l_{R2} = l_{R4} = 23.16$ mm.

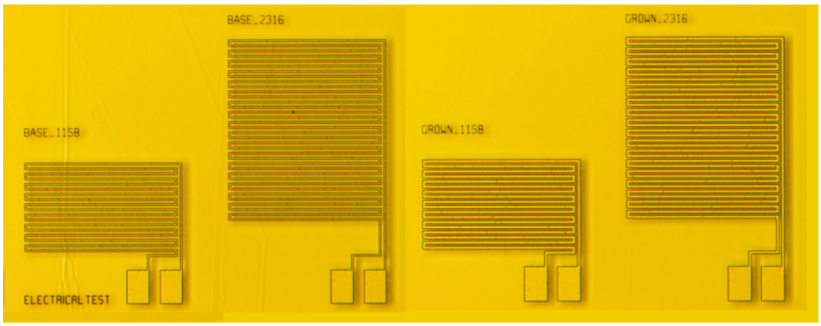

Fig. 2. Microscope Leica INM100 (1.25x) inspection after aluminum dry etching. In (*a*)-(*b*) the serpentine-shaped electrical test structures with line width w_{BASE}, and different serpentine lengths l_{R1} and l_{R2}, in (*c*)-(*d*) the serpentine-shaped electrical test structures with line width w_{GROWN}, and different serpentine lengths l_{R3} and l_{R4}.

The KLA Tencor P15 mechanical profilometer was used to quantitatively analyze the width and thickness of the serpentine-shaped electrical test structures. Figure 3 shows, in orange, the deviation of the serpentine width from its initial design value, highlighting a slight oversize due to the pattern transfer process. In contrast, the thickness values, shown in blue, closely match the expected design values.

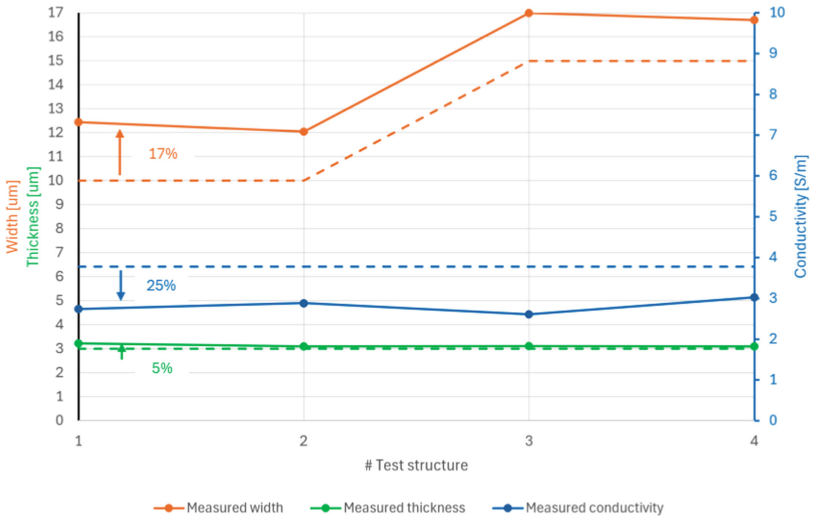

Fig. 3. Evaluation of the fabrication process accuracy. Nominal (dotted line) and measured (continuous line) trends result from tests on the four electrical test structures. We report the resolution and thickness of the strips, and Al material conductivity × 10^7 S/m calculated measuring the resistance of the different structures.

The patterns fabricated are also electrically characterized through two-point resistivity measurements. This evaluation aims to determine any deviations in the resistivity (and thus the conductivity) of the Al patterns with respect to the nominal values defined in Sect. 2. Figure 4 illustrates this measurement process using a manual electrical probing system, showing a magnified view captured through an optical microscope. The aluminum pattern, contacted by two fine probes placed on the dedicated pads, is clearly visible.

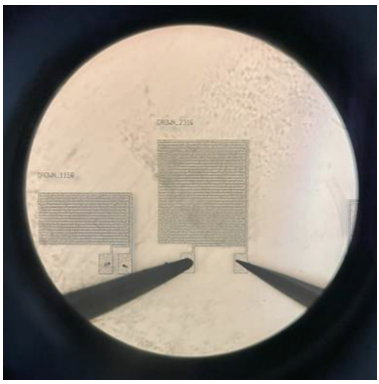

Fig. 4. Photo taken during two-point resistivity measurements to acquire the sheet resistance value of the R4 test structure.

By performing these measurements on test structures located in opposite regions of the wafer and using the average line thickness obtained from mechanical profilometry, it is possible to compute the resistivity ρ and derive the resulting average electrical conductivity σ of the Al layer. The aluminum conductivity in Fig. 4 is regarded as very close to the nominal value, since the overall order of magnitude is maintained (the 25% variation shown in the plot is based only on the leading digits).

Finally, the experimental EM evaluation of the MTS is currently underway, utilizing horn antennas and a vector network analyzer operating within the relevant frequency band.

4 Conclusions

This type of optically transparent MTS is particularly advantageous when the goal is to manipulate the wavefront to enhance transmission (Tx) in outdoor-to-indoor (O2I) 5G-6G communication links. Unlike traditional reflective MTS designs-such as the one described in [10] and here reproposed-it does not require a continuous metallic RF groundplane layer to optimize reflection. Although the prototype presented here functions as a "reflective screen," the focus on optical transparency remains highly relevant, as it supports the development of MTS solutions suitable for integration onto glass surfaces in modern buildings. The microfabrication process for our MTS module is here described in detail, and the resulting prototype underwent morphological and electrical characterization to evaluate the fabrication quality and performance.

Acknowledgement. This work has been supported by the Project "Smart ElectroMagnetic Environment in TrentiNo-SEME@TN" funded by the Autonomous Province of Trento (CUP: C63C22000720003).

References

1. Maci S (2024) Electromagnetic metamaterials and metasurfaces: a historical journey. IEEE Antennas Propag. Mag.
2. Da R'u P, Anselmi N, Rocca P, Massa A (2022) Passive and modular surface design for tailoring EM propagation in urban scenarios. In: 2022 16th European Conference on Antennas and Propagation (EuCAP), pp 1–4
3. Rocca P et al (2022) On the design of modular reflecting EM skins for enhanced urban wireless coverage. IEEE Trans Antennas Propag 70(10):8771–8784
4. Kitayama D, Hama Y, Goto K, Miyachi K, Motegi T, Kagaya O (2021) Transparent dynamic metasurface for a visually unaffected reconfigurable intelligent surface: controlling transmission/reflection and making a window into an RF lens. Opt Express 29:29292–29307. https://doi.org/10.1364/OE.435648
5. Choi H, et al (2024) Evaluation of glass metasurface using commercialized 5G mmWave small cell and phone. 2024 International Symposium on Antennas and Propagation (ISAP), Incheon, Korea, Republic of, 2024, pp 1-2 https://doi.org/10.1109/ISAP62502.2024.10846078
6. Suzuki M, Nakano K, Mori T, Takahashi H, Irie M (2024) Development of high optically transparent reconfigurable intelligent surface for 5G. 2024 IEEE International Symposium on Antennas and Propagation and INC/USNC-URSI Radio Science Meeting (AP-S/INC-USNC-URSI), Firenze, Italy, pp 1365–1366 https://doi.org/10.1109/AP-S/INC-USNCURSI52054.2024.10685859
7. Marasco I, Cantore C, Bianco GV, Bruno G, D'Orazio A, Magno G (2025) Transparent graphene-based RIS for 6G communications in the THz spectrum. IEEE Open J. Antennas Propagat 6(1):193–200. https://doi.org/10.1109/OJAP.2024.3487793
8. Suche M, Topsakal E (2025) A reconfigurable intelligent surface using transparent conductive oxide. 2025 United States National Committee of URSI National Radio Science Meeting (USNC-URSI NRSM), Boulder, CO, USA, p 295 https://doi.org/10.23919/USNCURSINRSM66067.2025.10906836
9. Liu B, Wang Q, Pollin S (2024) TAIS: transparent amplifying intelligent surface for indoor-to-outdoor mmWave communications. IEEE Trans Commun 72(2):1223–1238. https://doi.org/10.1109/TCOMM.2023.3328259
10. Hongnara T, et al: (2021) Dual-polarized broadbeam reflective metasurface based on multi-sheet configuration for local 5G application at 28.25 GHz. In: 2021 15th European Conference on Antennas and Propagation (EuCAP), pp 1–4

Lead-Free AlN pMUT Array: Acoustic Characterization in the Near Field

L. Barretta[1(✉)], D. Giusti[2], R. Scaldaferri[1], and A. Esposito[1]

[1] Analog, Power and Discrete, MEMS and Sensors Group (APMS), STMicroelectronics, Via Remo de Feo 1, 80022 Arzano, NA, Italy
luigi.Barretta@St.Com

[2] Analog, Power and Discrete, MEMS and Sensors Group (APMS), STMicroelectronics, Via Tolomeo 1, 20100 Cornaredo, Italy

Abstract. Piezoelectric Micromachined Ultrasonic Transducers (pMUTs) are increasingly utilized in industrial and biomedical applications due to their high sensitivity, miniaturized size, and ability to operate at high frequencies. However, traditional pMUTs often contain lead, posing significant environmental and health risks. This study focuses on the acoustic characterization of a lead-free Aluminum Nitride (AlN) pMUT array, highlighting its potential to provide high-performance sensing while eliminating the hazards associated with lead-based materials. The measurement setup includes a function generator to stimulate the lead-free AlN pMUT array and a Xarion ETA 450 Ultra laser microphone to capture the acoustic signals. The microphone, characterized by high sensitivity and a broad frequency range, enables precise acoustic measurements. A mechanical arm adjusts the distance between the microphone and the pMUT array, allowing measurements at distances ranging from 1 to 4 cm. Results show a clear attenuation of the acoustic signal with increasing distance, with peak-to-peak voltage decreasing from 16.81 V at 1 cm to 4.50 V at 4 cm. In conclusion, the lead-free AlN pMUT array demonstrates effective near-field acoustic performance, validating its potential for precise industrial and biomedical applications.

1 Introduction

Piezoelectric Micromachined Ultrasonic Transducers (pMUTs) are at the forefront of modern sensor technology, offering unique advantages due to their micromachined structure. These devices are renowned for their high sensitivity, compact size, and ability to operate at high frequencies, making them indispensable in a variety of industrial and biomedical applications [1, 2]. In the medical field, pMUTs are primarily used for diagnostic imaging, such as ultrasound, where they provide high-resolution images that are crucial for precise diagnostics. The miniaturization of pMUTs allows for the development of smaller, less invasive probes, enhancing patient comfort and image quality. Additionally, pMUTs are employed in distance measurement and motion detection, which are critical in wearable devices and advanced driver-assistance systems.

C. Di Natale et al. (Eds.): AISEM 2025, LNEE 1497, pp. 215–220, 2025.
https://doi.org/10.1007/978-3-032-08271-8_34

In the industrial sector, pMUTs play a vital role in non-destructive testing, a technique essential for inspecting materials and structures without causing damage. These sensors are instrumental in detecting defects or discontinuities in materials, ensuring the safety and reliability of infrastructures. Furthermore, pMUTs are used in automation systems for object detection and distance measurement, contributing to increased efficiency in manufacturing processes. Despite these advantages, traditional pMUTs often contain lead, an element that poses significant environmental and health risks. Lead is toxic, and its presence in electronic devices can lead to contamination during production, use, and disposal. As environmental regulations become increasingly stringent, the industry is compelled to seek lead-free alternatives to reduce environmental impact and enhance device safety.In response to these concerns, lead-free piezoelectric materials[3] such as aluminum nitride (AlN) and certain bismuth and sodium-based compounds have been developed. AlN is particularly promising due to its excellent piezoelectric properties, chemical stability, and compatibility with large-scale manufacturing processes. AlN-based transducers offer performance comparable to traditional lead-based ones, without the associated risks. Another emerging material is potassium sodium niobate (KNN), which has demonstrated good piezoelectric properties and can be integrated into pMUT devices. These alternative materials not only eliminate the risks associated with lead but also provide new opportunities to enhance sensor performance in terms of sensitivity and accuracy.

2 Material and Method

This study focuses on the development and characterization of a lead-free Aluminum Nitride (AlN) Piezoelectric Micromachined Ultrasonic Transducer (pMUT) array. The array consists of 25 individual membranes, each meticulously engineered to optimize acoustic performance. These membranes are constructed with a 4 μm thick PolySilicon base, layered with Molybdenum (Mo) and Aluminum Nitride (AlN) to form the active piezoelectric element. The choice of AlN as the piezoelectric material is pivotal, as it eliminates the environmental and health risks associated with traditional lead-based materials. This choice aligns with global efforts to comply with stringent environmental regulations and promote sustainable practices in electronic device manufacturing.

AlN is particularly advantageous due to its excellent piezoelectric properties, chemical stability, and compatibility with existing semiconductor fabrication processes. These properties make AlN a suitable candidate for high-frequency applications, as it supports the generation and detection of ultrasonic waves with high precision and sensitivity. The use of Mo/AlN/Mo layers enhances the mechanical robustness and piezoelectric efficiency of the membranes.

The measurement setup (see Fig. 1) was designed with precision to accurately characterize the acoustic performance of the lead-free AlN pMUT array. The setup includes several key components that work in tandem to facilitate comprehensive acoustic analysis:

- **Function Generator**: A function generator was employed to stimulate the lead-free AlN pMUT array. This device is crucial for providing a controlled and consistent signal to the array. By generating specific waveforms at desired frequencies, the function

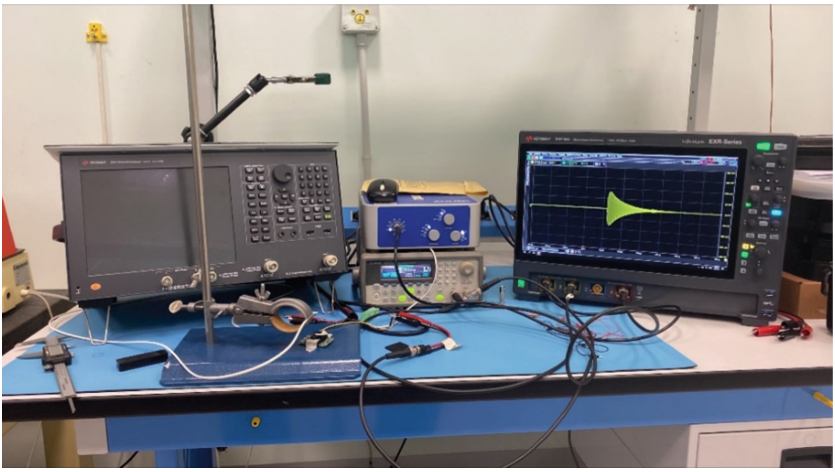

Fig. 1. Photo of the measurement setup, including the function generator, laser microphone (Xarion ETA 450 Ultra), pMUT array, and oscilloscope, during the acoustic characterization process.

generator ensures that the acoustic response of the pMUT array can be accurately captured and analyzed. The generator's ability to produce stable and repeatable signals is essential for the reliability of the measurements.

- **Xarion ETA 450 Ultra Laser Microphone**: This high-sensitivity laser microphone was used to capture the acoustic signals generated by the pMUT array. The Xarion ETA 450 Ultra is renowned for its broad frequency range, extending up to 2 MHz, and its non-contact measurement capability. These features make it ideal for precise acoustic measurements, as they allow for the detection of subtle changes in the acoustic signal without interfering with the pMUT array's operation. The laser microphone's high sensitivity ensures that even low-intensity signals are accurately recorded, providing detailed insights into the array's performance.
- **Oscilloscope**: An oscilloscope was utilized to collect and visualize the signals received by the laser microphone. This instrument plays a critical role in the measurement setup by allowing real-time monitoring and analysis of the acoustic signals. The oscilloscope's high-resolution display and advanced signal processing capabilities enable researchers to observe the waveform characteristics, such as amplitude and frequency, with great precision. This facilitates a detailed understanding of the pMUT array's performance and helps identify any anomalies or variations in the acoustic response.
- **Mechanical Arm**: A mechanical arm was incorporated to adjust the distance between the laser microphone and the pMUT array. This feature enabled measurements at various distances, specifically 1 cm, 2 cm, 3 cm, and 4 cm, allowing for a comprehensive analysis of the acoustic response at close proximity. The mechanical arm's precise positioning capabilities ensure that the distance adjustments are accurate and repeatable, which is essential for assessing how the acoustic response varies with distance.

This aspect of the setup is crucial for understanding the attenuation characteristics of the pMUT array and its potential applications in different sensing environments.

The experimental procedure was meticulously designed to evaluate the acoustic characteristics of the lead-free AlN pMUT array. The process involved several key steps to ensure comprehensive data collection and analysis.

3 Results

The acoustic characterization of the lead-free Aluminum Nitride (AlN) Piezoelectric Micromachined Ultrasonic Transducer (pMUT) array was conducted with meticulous attention to detail, aiming to evaluate its performance across varying distances in the near field. The results of this study provide significant insights into the acoustic capabilities of the AlN pMUT array, emphasizing its potential for various industrial and biomedical applications. The acoustic response of the lead-free AlN pMUT array was measured at distances ranging from 1 cm to 4 cm. Figure 2 graphically represents the peak-to-peak voltage recorded by the laser microphone at these distances, showcasing a clear trend of signal attenuation as the distance increases. This attenuation is a critical aspect of acoustic characterization, as it reflects the array's sensitivity and its ability to maintain signal integrity over varying proximities. At 1 cm, the peak-to-peak voltage was recorded at 16.81 V, corresponding to a pressure of 164.8 Pa. This measurement indicates a strong acoustic signal, demonstrating the array's high sensitivity and effective performance in the near field. As the distance increased to 2 cm, the peak-to-peak voltage decreased to 8.81 V, with a corresponding pressure of 86.37 Pa. This reduction in voltage and pressure is consistent with the expected attenuation of acoustic signals over distance, highlighting the predictable nature of the array's performance.

Further measurements at 3 cm and 4 cm showed peak-to-peak voltages of 6.22 V and 4.50 V, respectively, with pressures of 60.98 Pa and 44.12 Pa. These results, summarized in Table 1, confirm the trend of decreasing sensitivity with increasing distance. The data illustrates a linear attenuation pattern, which is crucial for understanding the operational limits and optimization potential of the pMUT array in real-world applications.

The consistent decrease in peak-to-peak voltage and pressure as the distance increases underscores the reliability and accuracy of the lead-free AlN pMUT array. This predictable attenuation allows for precise calibration and adjustment in various sensing environments, making the array a viable candidate for applications requiring high sensitivity and accuracy. The ability to maintain a strong signal at close distances is particularly beneficial for medical imaging and industrial non-destructive testing, where detailed and accurate measurements are essential. The results also highlight the effectiveness of the AlN material in providing high-performance sensing capabilities while eliminating the hazards associated with lead-based materials.

The use of AlN not only aligns with environmental regulations but also enhances the array's durability and performance, making it suitable for long-term application in demanding environments. The findings from this study validate the potential of the lead-free AlN pMUT array for a wide range of applications. In the biomedical field, the array's ability to provide accurate measurements at close distances can be leveraged for advanced imaging techniques, offering improved resolution and patient comfort.

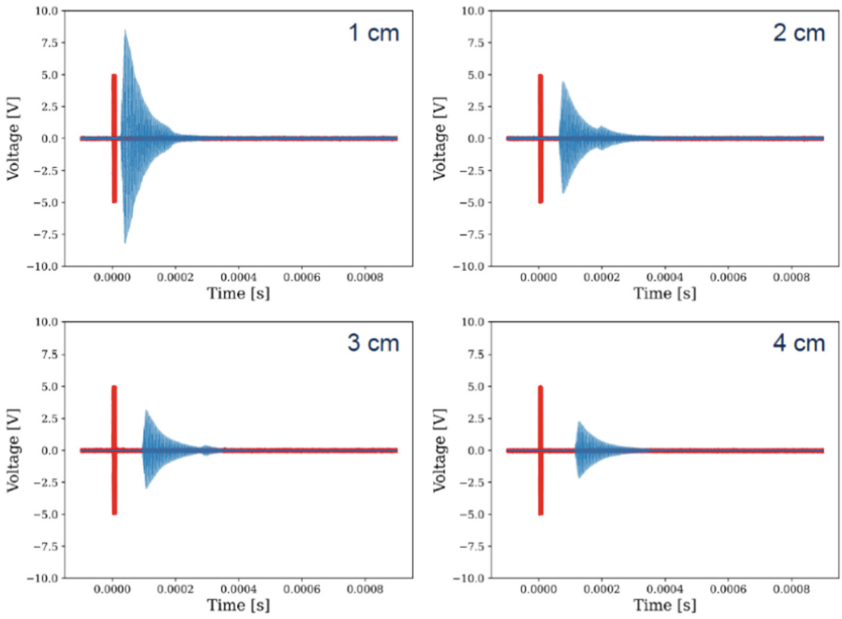

Fig. 2. Acoustic response graphs of the lead-free AlN pMUT array at various distances (1 cm, 2 cm, 3 cm, and 4 cm), showing the peak-to-peak voltage recorded by the laser microphone.

Similarly, in industrial settings, the array's predictable attenuation characteristics can be utilized for precise distance sensing and material inspection, contributing to enhanced safety and efficiency.

Moreover, the study opens avenues for further optimization of the pMUT array design.

Table 1. Table captions should be placed above the tables.

Distance (cm)	Vmax (V)	Vmin (V)	Peak-to-Peak Voltage (V)	Offset (V)	Peak-to-Peak Pressure (Pa)
1	8.56	−8.25	16.81	0.31	164.80
2	4.49	−4.32	8.81	0.17	86.37
3	3.18	−3.04	6.22	0.14	60.98
4	2.29	−2.21	4.50	0.08	44.12

By understanding the attenuation patterns and sensitivity limits, researchers can explore modifications to the membrane structure or material composition to enhance performance across broader distance ranges. This could lead to the development of pMUT arrays with tailored characteristics for specific applications, expanding their utility and impact in various sectors.

4 Conclusion

The study successfully demonstrates the acoustic characterization of a lead-free Aluminum Nitride (AlN) Piezoelectric Micromachined Ultrasonic Transducer (pMUT) array, highlighting its effective near-field performance. The results indicate a predictable attenuation of acoustic signals with increasing distance, validating the array's high sensitivity and reliability for precise sensing applications. The use of AlN as a piezoelectric material not only addresses environmental and health concerns associated with lead-based materials but also enhances the array's durability and performance. This positions the AlN pMUT array as a promising candidate for both industrial and biomedical applications, where accurate and reliable measurements are crucial.

The study provides a foundation for future research and development, suggesting avenues for optimization of the array design to extend its operational range and improve sensitivity. By leveraging the predictable attenuation characteristics, the array can be tailored for specific applications, enhancing its utility across diverse sectors. Overall, the lead-free AlN pMUT array offers a sustainable and high-performance solution, aligning with global efforts to promote environmentally friendly technologies while meeting the demanding requirements of modern sensing applications.

Acnowledgment. Research reported in this publication was supported by the PROUD project that received funding from the Italian Ministry of Enterprises and Made in Italy (MIMIT): Prog. n.: F/310211/01-05/X56 (Decree n. 4187, 19-12-2023).

References

1. He Y, Wan H, Jiang X, Peng C (2022) Piezoelectric micromachined ultrasound transducer technology:recent advances and applications. Biosensors 13(1):55
2. Atheeth S, Krishnan K, Arora M (2023) Review of pMUTs for medical imaging: towards high frequency arrays. Biomed Phys Eng Express 9(2):022001
3. Zhang S, Malič B, Li JF, Rödel J (2021) Lead-free ferroelectric materials: prospective applications. J Mater Res 36(5):985–995

Advanced Electrochemical Sensors Integrated in Textiles for Real-Time Emotional State Assessment: Preliminary Results

A. Licheri[1(✉)], B. Ercolani[1], C. D'Elia[2], A. Maffucci[2], S. Orlanducci[1], and L. Micheli[1]

[1] Department of Chemical Sciences and Technologies, University of Rome Tor Vergata, Via della Ricerca Scientifica 1, 00133 Rome, Italy
Antonio.licheri@students.uniroma2.eu

[2] Department of Electrical and Information Engineering, University of Cassino and Southern Lazio, 03043 Cassino, Italy

Abstract. Nowadays, predicting emotional arousal is becoming increasingly relevant in sensor research, due to its implications in fields ranging from healthcare to performance optimization. This study presents preliminary results from the Italian project *"Dress the Future: Novel Combined Wearable Integrated Systems (Stargate)"* (MUR, PRIN-PNRR - P2022CZA3P), which aims to develop a wearable, AI-integrated, multi-analyte sensor embedded in textiles for continuous monitoring of emotional and physiological states. Initially, we focus on the detection of one key marker, cortisol levels in sweat, through an electrochemical sensing platform. The results represent an early step toward a fully integrated, non-invasive monitoring system.

Keywords: Emotion · Wearable · Label-free · AI integrated sensor · Cortisol · Immunosensor · Screen Printed Electrode

1 Introduction

Over the last decade, increasing attention has been given to the strong link between a person's physical state and their emotional or physiological condition [1, 2]. An expanding body of research focuses on monitoring parameters such as heart rate (HR) [3], electrodermal activity (EDA) [3], skin temperature, pH, and biomarkers like cortisol to assess emotional states. While these studies demonstrate promising correlations, many of the proposed sensors lack applicability in real-life, everyday contexts. Key limitations include the disregard for inter-individual variability, the need for expert personnel for data acquisition and interpretation, and the discomfort of some body-worn devices that are not suitable for prolonged or daily use.

This study is part of the broader Italian project *"Dress the Future: Novel Combined Wearable Integrated Systems (Stargate)"* (PRIN-PNRR - P2022CZA3P), which aims to develop a game-changing wearable sensor. By integrating artificial intelligence (AI) and

C. Di Natale et al. (Eds.): AISEM 2025, LNEE 1497, pp. 221–225, 2025.
https://doi.org/10.1007/978-3-032-08271-8_35

machine learning (ML), the system is designed to adapt measurements to the individual user, avoiding rigid classification models and enabling personalized interpretation. The AI will also help verify signal quality, identifying and discarding unreliable data caused by sensor malfunction.

User-friendliness is a central goal: the project includes the development of intuitive, user-facing software and a comfortable wearable design to enhance both usability and patient well-being.

This work presents the preliminary results of the project, focusing on the detection of cortisol levels, using an electrochemical platform. Emotions such as fear, excitement, or panic trigger physiological responses mediated by the autonomic nervous system (ANS) [4, 5] and the hypothalamic-pituitary-adrenal (HPA) axis [6], which alter the composition of biological fluids [7] like sweat and saliva, ideal for non-invasive analysis. Cortisol, a hormone closely associated with stress, is detected via a label-free immunosensor that leverages sustainable carbon nanomaterials, which both enhance electrochemical performance and provide a covalent immobilization platform for antibodies.

2 Materials

All chemicals from commercial sources were of analytical grade. Sodium chloride (NaCl), potassium chloride (KCl) sodium dihydrogen phosphate (NaH_2PO_4), disodium hydrogen phosphate (Na_2HPO_4), ethanolamine, potassium ferricyanide, potassium ferrocyanide, 2-(N-morpholino)ethanesulfonic acid (MES, 99%), N-hydroxysuccinimide (NHS, 98%), 1-ethyl-3-(3-dimethylaminopropyl) carbodiimide (EDC, 97%), Polivinil-alcohol were purchased from Sigma-Aldrich (Darmstadt, DE). Anti-mouse IgG purchased by ThermoFisher Italy, Anti-cortisol and cortisol from Sigma Aldrich.

3 Methods

3.1 Protocol for Cortisol Immunosensor

The immunosensor was developed using screen-printed electrode (SPE) platform fabricated at the University of Rome Tor Vergata with a DEK 245 screen-printing machine (Weymouth, UK). The electrodes featured a working electrode (WE), and counter electrode (CE) printed with graphite ink, and a reference electrode (RE) made of silver/silver chloride ink. A dielectric layer defined the active area of the WE, limiting it to 0.07 cm^2.

The working electrode (WE) was modified with biochar, used to enhance electrochemical performances and enable antibody covalent immobilization. A biochar dispersion (1 mg/mL) was prepared in a water: ethanol (3:1 v/v) mixture and sonicated using a probe sonicator at 70% amplitude for 30 min. The resulting suspension was drop-cast onto the WE.

After deposition, the carboxylic groups on the biochar surface were activated using a mixture of 5 mM NHS and 4 mM EDC in MES buffer (pH = 6.0). Afterward, the electrode was rinsed three times with 50 μL of PBS buffer (pH = 7.4).

Next, anti-mouse IgG secondary antibodies were covalently immobilized on the activated surface.

To reduce non-specific interactions and passivate any remaining activated groups, a blocking step was performed using 2% (w/v) ethanolamine (ETA) prepared in PBS. The solution (10 μL) was drop-cast on the working electrode and left to react for 1 h at room temperature.

Subsequently, the cortisol-specific primary antibody (Ab1) (antibody solution in PBS pH = 7.4) was deposited on the electrode by drop-casting and incubating for 1 h at RT. After incubation, the standard washing protocol was applied.

Finally, 10 μL of cortisol solution, also prepared in PBS, was applied to the surface and incubated for 1 h to allow the formation of the Ab1–cortisol complex.

After the final wash, 80 μL of 10 mM $[Fe(CN)_6]^{3-/4-}$ in PBS was used as a redox probe. The electrochemical response was measured using square wave voltammetry (SWV).

4 Results and Discussion

4.1 Cortisol Immunosensor

All preparation steps of immunosensor are studied and optimized in order to improve the electrochemical performance and sensitivity of the proposed tool.

Antibody Concentration Optimization. To improve analytical performance within a clinically relevant window, four Ab1/Ab2 concentrations pairs were evaluated with cortisol at 100 and 300 ng/mL:

- Ab2 = 5 μg/mL, Ab1 = 2.5 μg/mL
- Ab2 = 5 μg/mL, Ab1 = 10 μg/mL
- Ab2 = 20 μg/mL, Ab1 = 2.5 μg/mL
- Ab2 = 20 μg/mL, Ab1 = 10 μg/mL

Each condition was run in triplicate. The largest signal difference between 100 and 300 ng/mL, and the smallest variability, was achieved with Ab2 = 5 μg/mL and Ab1 = 2.5 μg/mL. In contrast, the highest antibody load (20–10) produced opposite behavior and larger error, consistent with a hook effect due to antibody excess.

The optimized antibody concentrations (Ab2 = 5 μg/mL, Ab1 = 2.5 μg/mL) are used to obtain a calibration curve for eight cortisol levels (0-10-25–50-100-300-600-1200 ng/ml) in PBS (pH 7.4). Five replicates per point yielded a dose–response curve, fitted to the four-parameter logistic model (Eq. 1):

$$Y = bottom - \left[(top - bottom)/1 + (x/IC50)slope\right] \quad (1)$$

From this fit, the limit of detection (LOD) was calculated as 22 ng/mL and the limit of quantification (LOQ) as 60 ng/mL (Fig. 1). These figures demonstrate that the label-free immunosensor can reliably detect cortisol at physiologically relevant concentrations with good precision.

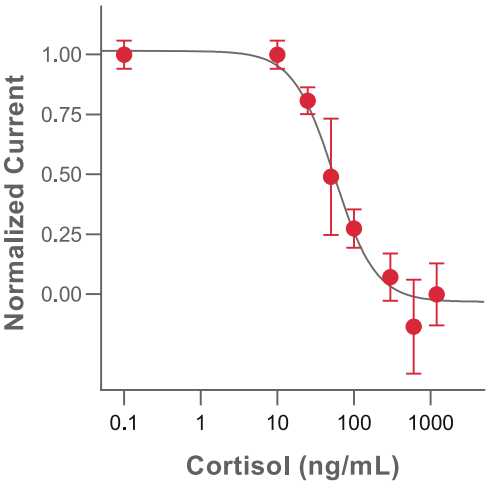

Fig. 1. Calibration curve of cortisol in PBS pH = 7.4.

5 Conclusion and Future Outlook

This work reports preliminary steps toward a textile-integrated, wearable platform for real-time emotional state assessment, based on cortisol sensing. The label-free immunosensor on screen-printed electrodes yielded encouraging repeatability and sensitivity in the lab. These early results validate the overall concept but also underscore the need to translate from bench-top SPEs into a truly wearable format.

Moving forward, the priority is to embed the sensor into a flexible, skin-contact patch, paired with a compact, low-power potentiostat. In parallel, a custom software suite, already capable of interpreting chronoamperometric data, flagging outliers, and identifying faulty measurements, will be extended with machine-learning algorithms. This AI layer will adapt calibration curves to individual users, recognize signal drift, and provide real-time feedback without requiring expert oversight.

Then, for cortisol immunosensor, the next phase will replace square-wave voltammetry with chronoamperometry, using the AI-enabled software to automate data processing and error rejection. Testing in real sweat samples and across a diverse volunteer cohort will determine robustness under physiological conditions. Ultimately, integrating both sensing modalities and their AI/ML backend into a single textile patch promises a significant leap toward unobtrusive, personalized monitoring potentially revolutionizing how emotional and physiological states are tracked in everyday life.

Acknowledgments. The research leading to these results has received funding from the Project "SENS-AI, Environmental Sensing with Artificial Intelligence" CUP H53D23000520006 (Italian "Bando Prin 2022 - D.D. 104 del 02–02-2022" by MUR (2023–2025), Project ""Dress the future; novel combined wearable integrated system (Stargate)" CUP E53D22014620001 by MUR (2023–2025) (MUR-PRIN 2022 PNRR Decreto Direttoriale n. 1409 del 14-9-2022) and Grant MUR Dipartimento di Eccellenza 2023–27 X-CHEM project "eXpanding CHEMistry: implementing excellence in research and teaching".

References

1. Can YS, Arnrich B, Ersoy C (2019) Stress detection in daily life scenarios using smart phones and wearable sensors: a survey. J Biomed Inform 92:103139
2. Picard RW (2016) Automating the recognition of stress and emotion: from lab to real-world impact. IEEE Multimedia 23:3–7
3. Yannakakis GN, Martínez HP, Jhala A (2010) Towards affective camera control in games. User Model User-Adap Inter 20:313–340
4. Liu G et al (2016) A wearable conductivity sensor for wireless real-time sweat monitoring. Sens Actuators B Chem 227:35–42
5. Ortega L, Llorella A, Esquivel JP, Sabaté N (2019) Self-powered smart patch for sweat conductivity monitoring. Microsyst Nanoeng 5:3
6. Zea M et al (2020) Electrochemical sensors for cortisol detections: almost there. TrAC Trends Anal Chem 132:116058
7. Marieke Van Dooren JJG, (Gert-Jan) De V, Joris H (2012) Janssen. Emotional sweating across the body: comparing 16 different skin conductance measurement locations. Physiol Behav **106**:298–304

QCM4PM – A Quartz Crystal Microbalance-Based Approach for Real-Time Particulate Matter Monitoring

E. Massera, B. Alfano, T. Polichetti, A. De Girolamo Del Mauro, and M. L. Miglietta(✉)

ENEA Research Center, Piazzale E. Fermi, 1, 80055 Portici, Naples, Italy
marialucia.miglietta@enea.it

Abstract. 1. The growing awareness of the health impacts of airborne particulate matter (PM) and the limitations of regulatory monitoring networks have catalyzed interest in low-cost particulate matter sensors (LCPMS). While optical sensors dominate the market, their accuracy is limited by factors such as particle shape, density, and surface contamination. This work presents the QCM4PM, a novel QCM-D (Quartz Crystal Microbalance with Dissipation) based device, as a compelling alternative. Capable of measuring both mass and viscoelastic properties of particles, it represents a promising approach for real-time, filter-free PM monitoring. Preliminary results show that QCM4PM provides stable and sensitive detection of PM2.5, potentially enhancing IoT-enabled air quality networks.

Keywords: Airborne particulate matter · QCM-D · low-cost sensors · real-time monitoring · IoT sensors · piezoelectric resonators · PM2.5

1 Introduction

Particulate matter (PM) represents one of the most pressing environmental and public health issues of our time, particularly due to the increasing evidence linking airborne particles to respiratory and cardiovascular diseases [1]. In response to this concern, European regulations, including Directive (EU) 2024/2881, have established stricter thresholds for PM10 and PM2.5 concentrations. However, traditional gravimetric monitoring systems used to ensure regulatory compliance are often large, expensive, and energy-consuming, making them unsuitable for widespread or mobile deployment [2, 3]. This has driven significant interest in developing low-cost particulate matter sensors (LCPMS) that are compact, energy-efficient, and suitable for integration into distributed air quality monitoring networks [4].

In recent years, efforts have focused primarily on optical sensing technologies due to their ability to provide real-time measurements in a relatively compact form factor. Nevertheless, limitations related to their sensitivity, accuracy, and long-term stability, particularly under conditions of variable humidity and particle composition, continue to hinder their broader adoption in critical applications [5]. This work briefly reviews the

C. Di Natale et al. (Eds.): AISEM 2025, LNEE 1497, pp. 226–231, 2025.
https://doi.org/10.1007/978-3-032-08271-8_36

main sensing technologies available per particle detection and addresses their shortcomings. Finally, an alternative sensing platform based on Quartz Crystal Microbalance with Dissipation monitoring (QCM-D), named QCM4PM is presented. This study explores the feasibility of employing the QCM4PM sensing elements in a highly simplified configuration, without the need for additional components such as airflow systems, particle sorters, or dryers - commonly required in LCPMS setups - thereby significantly reducing complexity and overall cost.

1.1 State of the Art in Low-Cost Particulate Matter Sensing

Optical sensors currently dominate the LCPMS market. These instruments rely on light scattering techniques, using either laser or LED sources to detect and quantify airborne particles [6]. By measuring the intensity and angular distribution of scattered light, these devices infer particle size and concentration. Although widely used due to their compactness and commercial availability, optical sensors exhibit notable drawbacks. Their performance often depends on assumptions about particle shape, density, and refractive index. Furthermore, long-term use can lead to contamination and degradation of optical components, thereby reducing measurement accuracy and necessitating frequent maintenance or recalibration. The use of proprietary algorithms to interpret the optical signal further complicates direct comparison across different devices and limits transparency for end-users.

Alternative approaches such as capacitive and image-based sensors have been explored. Capacitive sensors detect changes in permittivity when particles pass between electrodes [7, 8]. They are compatible with CMOS technology and offer scalability but are primarily sensitive to larger particles and require complex electronics for reliable detection of finer fractions (Fig. 1) [9]. Image-based sensors, on the other hand, use visual data captured by cameras to estimate particle load [10]. While innovative and inexpensive, these solutions typically suffer from limited sensitivity and slow response times, making them unsuitable for real-time monitoring in dynamic environments.

Resonant mass sensors, and in particular quartz crystal microbalances, have emerged as promising alternatives [11]. QCMs rely on a gravimetric method, in fact they operate by measuring shifts in the resonance frequency of a piezoelectric crystal due to particle deposition. The magnitude of the shift, described by the Sauerbrey equation, directly correlates with the added mass.

$$\Delta m = -\Delta fn/n\,C \tag{1}$$

where Δf_n is the measured shift of the resonance frequency at n^{th} overtone and C is the mass sensitivity constant of the QCM (typically, for a 5 MHz AT-cut quartz crystal, C is equal to 17.7 ng cm^{-2} Hz^{-1}) [12].

In Fig. 1 a summary of the existing technologies for PM detection compares the application size ranges and the ability to detect single particles or a set of particles.

An interesting feature that can be observed with QCMs is the oscillation decay time, which is due to dissipative energy losses induced by the deposited masses (*i.e.*, the so-called dissipation factor, D) and depends on their viscoelastic properties. The dissipation

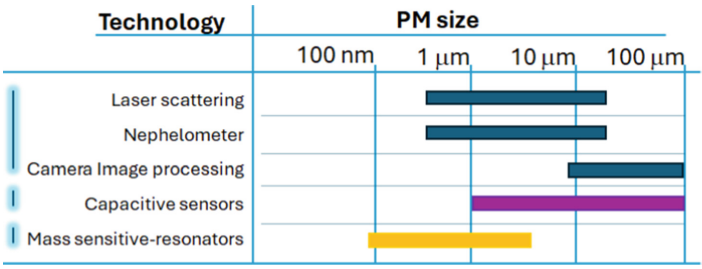

Fig. 1. A comparative chart amongst the existing technologies for particle detection [9].

factor can be derived from the width of the oscillation peak (*i.e.*, half-bandwidth at half-maximum, Γ) according to the Eq. (2):

$$2\Gamma = Dfn \tag{2}$$

where f_n is the quartz crystal resonance frequency at the nth overtone [13]. For a rigid and homogeneous layer of deposited particles the dissipative energy losses are small ($\Delta D_n/(\Delta f_n/n) < 10^{-7}$ Hz^{-1}), the adsorbed mass Δm is thus linearly proportional to the induced frequency shift according to the Sauerbrey relation (1). However, when the deposited masses establish an insufficient mass coupling to the QCM surface, then dissipative energy losses become significant, whereupon the Sauerbrey relation underestimates the adsorbed mass. To overcome this issue, it is possible to recall the work by Tellechea et al. [14], who showed that plotting the normalized dissipation (*ΔDn/Δfn* or *ΔΓn/Δfn*) versus normalized frequency shift (*Δfn/n*) yields a linear trend, where the intercept at *Δfn/n* corresponds to 100% surface coverage. As dissipation approaches zero at this point, Sauerbrey's relation becomes valid.

Therefore, the integration of dissipation monitoring in QCM-D systems enables the simultaneous evaluation of both mass and viscoelastic properties of the deposited particles such as particle stiffness or adhesion, providing more comprehensive information about airborne PM.

2 Experimental Methods and Sensor Preparation

To ensure the optimal functionality of the QCM membranes, a meticulous multistep procedure was adopted. Initial calibration was performed to verify sensor baseline behaviour, followed by a cleaning protocol based on ultraviolet/ozone treatment and chemical immersion in a heated solution of ammonia and hydrogen peroxide [15]. This process effectively removed contaminants while preserving the integrity of the piezoelectric surfaces. A second calibration confirmed that sensor performance remained stable after cleaning.

Subsequent functionalization involved the spin-coating of silicone oil dissolved in toluene, at 6000 rpm for 30 s. The film was then thermally cured to enhance adhesion and stabilize the coating. The sensors were exposed to a controlled aerosol of Arizona Test Dust generated with a commercial dust dispenser [16]. Simultaneous reference measurements were conducted using a DustTrak 8533 monitor, enabling direct comparison of QCM4PM readings with a certified optical instrument.

3 Results and Analysis

The experimental data confirmed the efficacy of QCM4PM in detecting particulate matter, particularly in the PM2.5 range. Frequency shifts recorded during exposure to the test aerosol showed consistent trends corresponding to particle deposition (Fig. 2).

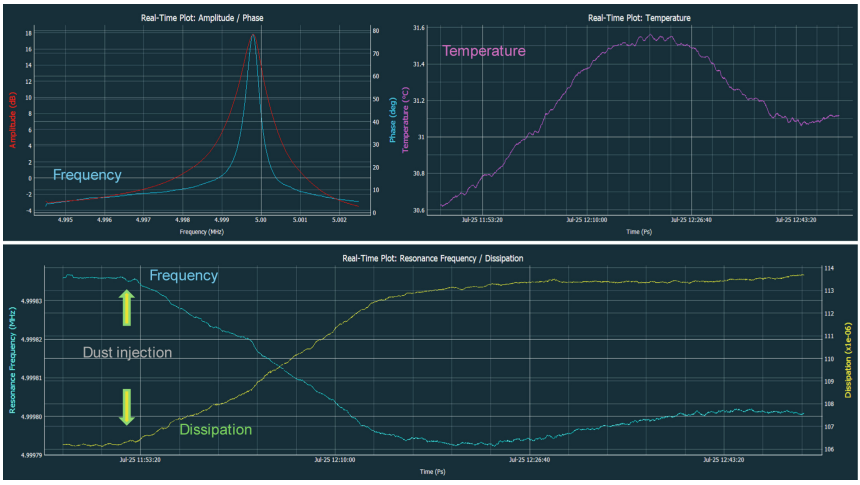

Fig. 2. Dynamic behaviour of silicon oil coated QCM under standard Arizona dust injection. The upper panel on the left shows the resonant frequency under dust exposure (red line) with respect to the calibration (blue line). On the right panel the temperature variation. The bottom panel shows the resonant frequency shift and dissipation factor.

The particle retention of the membranes coated with silicon oil was significantly higher than the one of bare QCMs [16]. These findings, along with the reduced signal drift, highlight the importance of surface engineering in sensor optimization. By considering ΔD and Δf along with the wave amplitude at t = 0 (just before dust injection) A_0 and the time evolution of the wave amplitude $A(t)$ and plotting them versus the total amount of PM injected ($\int_0^t PMdt$) it can be observed the linear correlation of the selected features with the PM exposure. The results are summarized in Table 1 while Fig. 3 shows the correlation of PM exposure with the dissipation factor.

Table 1. Sensitivity of silicon oil coated QCM and linear regression coefficients

	ΔD	Δf	$A(t)$	A_0
S (%/μg/m^3)	20	2x10^{-3}	17	22
$\mathbf{R^2}$	0,996	0,896	0,999	0,985

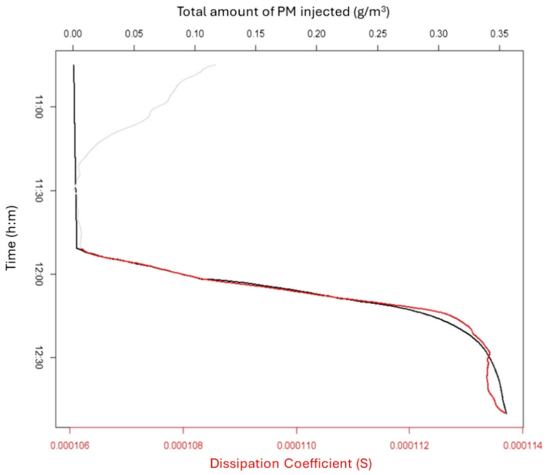

Fig. 3. Dissipation coefficient evolution plotted versus the total amount of PM injected.

These results suggest that appropriate surface treatments can significantly enhance both sensitivity and reliability, making QCM4PM a viable candidate for air quality monitoring applications.

4 Conclusions and Future Perspectives

This study demonstrates the potential of quartz crystal microbalance technology, particularly in its dissipation-enabled configuration, as a robust and sensitive platform for low-cost particulate matter monitoring. Preliminary results suggest a good correlation between QCM measurements and reference data, although further work is needed to establish calibration curves and validate performance in real-world conditions.

References

1. Kim K-H, Kabir E, Kabir S (2015) A review on the human health impact of airborne particulate matter. Environ Int 74:136–143
2. EEA. Air Quality in Europe - 2020 Report. https://www.eea.europa.eu/en/analysis/publications/air-quality-in-europe-2020-report. Last accessed 06 Feb 2025
3. Xie X et al (2017) Philips,W: a review of urban air pollution monitoring and exposure assessment methods. ISPRS Int J Geo Inf 6:389
4. Kumar P et al (2015) The rise of low-cost sensing for managing air pollution in cities. Environ Int 75:199–205
5. Alfano B et al (2020) A review of low-cost particulate matter sensors from the developers' perspectives. Sensors 20(23):6819
6. Sorensen CM, Gebhart J, O'Hern TJ, Rader DJ (2011) Optical measurement techniques: fundamentals and applications. John Wiley & Sons, Ltd, pp 269–312
7. Carminati M, et al (2014) Capacitive detection of micrometric airborne particulate matter for solid-state personal air quality monitors. Sens Actuators A Phys **219:**80–87

8. Ferlito U, Grasso AD, Vaiana M, Bruno G (2021) A time-based electronic front-end for a capacitive particle matter detector. Sensors 21(5):1840
9. Carminati M, Ferrari G, Sampietro M (2017) Emerging miniaturized technologies for airborne particulate matter pervasive monitoring. Measurement 101:250–256
10. Budde M, Leiner S, Köpke M, Riesterer J, Riedel T, Beigl M (2019) FeinPhone: low-cost smartphone camera-based 2D particulate matter sensor. Sensors 19:749
11. Johannsmann D (2015) The quartz crystal microbalance in soft matter research. Soft Biol Matter 1:143–168
12. Olsson AL, Quevedo IR, He D, Basnet M, Tufenkji N (2013) Using the quartz crystal microbalance with dissipation monitoring to evaluate the size of nanoparticles deposited on surfaces. ACS Nano 7(9):7833–7843
13. Reviakine I, Johannsmann D, Richter RP (2011) Hearing what you cannot see and visualizing what you hear: interpreting quartz crystal microbalance data from solvated interfaces. ACS Publications
14. Tellechea E, Johannsmann D, Steinmetz NF, Richter RP, Reviakine I (2009) Model-independent analysis of QCM data on colloidal particle adsorption. Langmuir 25(9):5177–5184
15. Kern W (1970) Cleaning solution based on hydrogen peroxide for use in silicon semiconductor technology. RCA Rev 31(2):187–206
16. Massera E, Barretta L, Miglietta ML, Alfano B, Polichetti T (2023) Quartz crystal microbalance study in controlled environment for particulate matter sensing. In: Sensors and Microsystems, Proceedings of the AISEM 2022, Rome, Italy, Springer Nature: Cham, Switzerland, pp 129–134

Wearable and Flexible Sensors

Comparison of Haptic Feedback in Upper-Limb Prostheses for Hand-Wrist Amputee Patients

Giuseppe Coviello[1], Giuseppe Brunetti[1], Marianna Pia Coccia[1], Damiano Cosma Potenza[2], and Caterina Ciminelli[1(✉)]

[1] Optoelectronics Laboratory, Department of Electrical and Information Engineering, Polytechnic University of Bari, Via E. Orabona 4, Bari, Italy
Caterina.ciminelli@poliba.it

[2] Department of Mechanics, Mathematics and Management, Polytechnic University of Bari, Via E. Orabona 4, Bari, Italy

Abstract. This study investigates two different actuator technologies, namely piezoelectric and linear resonant actuators (LRA), for delivering haptic feedback in upper-limb prosthetic devices. A dual-phase experimental protocol was conducted: the first phase aimed to identify optimal actuator placement on the user's body and within a prosthetic socket, while the second phase examined human sensitivity to more complex haptic patterns. The experiments involve both direct skin contact and integration into a rigid prosthetic structure, exemplified by the Adam's Hand developed by BionIT Labs. Results indicate that LRAs provide better spatial resolution and vibration propagation, particularly when placed near typical electrode sites. In contrast, piezoelectric actuators, while more energy-efficient and precise, produce weaker sensations, limiting user perception. Furthermore, the study indicates that humans struggle to distinguish intricate vibration patterns, highlighting the need for simple, intuitive feedback strategies to avoid excessive cognitive load. These findings inform the design of more effective and user-friendly haptic systems for prosthetic applications.

Keywords: Haptic feedback · Prosthetic hand · Piezoelectric actuator · Linear resonant actuator · Vibration perception · Sensory feedback

1 Introduction

The human hand plays a fundamental role in performing a vast array of complex activities essential to daily life, including grasping, object manipulation, and sensory exploration of the environment [1]. It functions not only as an instrument of interaction with the external world but also as a highly refined sensory organ, enabling intricate motor coordination and nuanced tactile perception. Despite notable advancements in prosthetic technology, particularly in the areas of materials science, actuation systems, and control algorithms, a considerable functional disparity persists between prosthetic hands and their biological counterparts. This gap is especially evident in the limited capacity of current devices to provide users with naturalistic sensory experiences. The integration

C. Di Natale et al. (Eds.): AISEM 2025, LNEE 1497, pp. 235–240, 2025.
https://doi.org/10.1007/978-3-032-08271-8_37

of graded, multimodal sensory feedback—encompassing tactile cues and proprioceptive information related to joint position and movement—represents a crucial step toward enhancing both user embodiment and task performance [2]. Moreover, the development of more intuitive control strategies, based on physiological or neurophysiological signals, may substantially reduce the cognitive load required to operate prosthetic limbs. Although contemporary electromyographic systems demonstrate significant capabilities in detecting muscle activity and generating control commands, they remain insufficient in conveying the internal state of the prosthesis to the user in the absence of visual monitoring. This limitation continues to represent a major obstacle to the widespread functional adoption of prosthetic hands in unstructured, real-world environments [3].

In most current prosthetic systems, sensory feedback is typically delivered through non-invasive techniques such as vibrotactile, electrotactile, or mechanotactile stimulation applied to the residual limb. These approaches aim to convey information regarding grip force, contact events, or joint positions by stimulating the skin in a manner that partially replicates natural sensations. However, such feedback remains limited in resolution and often lacks the temporal and spatial accuracy necessary for precise motor control and object discrimination.

This paper focuses on haptic feedback, employing tactile vibrations to transmit information about the physical environment or the operational status of the prosthesis. The objective is to enhance user perception and foster more intuitive interaction with the prosthetic device. Two different vibrotactile technologies are comparatively evaluated: piezoelectric actuators, known for their high-frequency response and compact form factor, and eccentric rotating mass (ERM) motors, commonly used for their simplicity and ease of integration. The comparative analysis aims to assess their effectiveness in delivering meaningful and perceivable tactile cues under conditions representative of everyday prosthesis use.

2 System Description

The haptic feedback system developed in this study is based on a central control unit built around an STM32 microcontroller, which simultaneously drives two different types of actuators. This configuration allows for a direct and synchronized comparison of their performance under identical operating conditions, thereby ensuring consistency in the experimental protocol. An overview of the experimental setup is provided in Fig. 1.

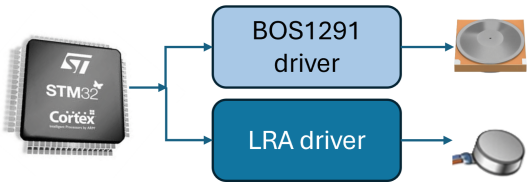

Fig. 1. Experimental setup illustrates the STM32-based central control unit connected to both piezoelectric and LRA actuators for comparative analysis.

The first actuator evaluated is a piezoelectric device from the PowerHap 1313 series manufactured by TDK. This actuator is designed to deliver high-speed, high-precision haptic feedback and operates with an input voltage ranging from 0 to 120 V, achieving a maximum displacement of 65 μm [4]. To meet the high-voltage driving requirements of the piezo element, the system incorporates the Boreas BOS1921 driver, a high-performance piezoelectric driver capable of converting a 3.3 V supply into output voltages reaching up to 190 V peak-to-peak (Vpp) [5].

The driver enables fine-grained control over several critical stimulation parameters, including vibration amplitude, which governs the perceived intensity, actuation frequency, duty cycle, and the shape of the waveform, particularly during the ramp-up and ramp-down transitions. This level of control is essential for tailoring tactile experience to mimic natural haptic sensations.

In contrast, the second actuator is based on a linear resonant actuator (LRA) architecture, driven by a Precision Microdrives LRA module. This actuator operates at a nominal voltage of 5 V and is controlled through a Pulse-Width Modulation (PWM) signal generated by the STM32 microcontroller. A dedicated MOSFET is employed as a load switch to modulate power delivery. The amplitude and temporal characteristics of the vibration are adjusted by varying the PWM frequency and duty cycle, which directly influence the intensity and duration of the feedback pulses. Although LRAs are less precise and offer limited flexibility in waveform shaping compared to piezoelectric actuators, they are widely used due to their low cost, mechanical simplicity, and ease of integration.

From a technical standpoint, piezoelectric actuators provide superior responsiveness, lower power consumption, and enhanced resolution in both temporal and spatial domains, making them well-suited for applications requiring fine-tuned haptic feedback. On the other hand, LRAs offer practical advantages in terms of affordability and system integration, albeit at the expense of higher energy requirements and reduced controllability.

3 Experimental Results

The primary objective of this study is to evaluate the comparative suitability of two actuation technologies (e.g. piezoelectric and LRA) for haptic feedback in upper-limb prosthetic devices. To this end, a two-part experimental protocol was implemented. The first part investigates the optimal positioning of the actuators on the user's body, both in direct contact with the skin and integrated into the prosthetic socket structure, to maximize perceptibility and comfort. The second part focuses on the sensory sensitivity of the human user to more complex vibrational patterns, assessing the ability to discern varied waveform parameters and their effects on the clarity of feedback. Four volunteers (one male and three females) with an average age of 43.5 years participated in both experimental phases, under approved ethical protocols. After completing the tasks, participants provided feedback through a structured questionnaire to capture quantitative assessments (e.g., position recognition rates) as well as qualitative impressions (e.g., clarity, comfort, and subjective ease of identifying different patterns).

3.1 Optimal Positioning of Actuators: Skin Contact vs Prosthetic Socket Integration

In the first experimental phase, actuators were positioned in direct contact with the skin on the volar region of the forearm to identify the most sensitive areas for effective feedback as shown in Fig. 2. This setup was chosen for its controlled conditions, allowing precise mapping of the skin's sensitivity to vibrational stimuli, and its relevance to real-world prosthetic applications where actuators might be integrated directly with the user's residual limb. Various waveform parameters, including frequency, amplitude, and the on/off cycle duration, were systematically varied to understand how these factors influenced the perception of intensity, clarity, and feedback's spatial resolution.

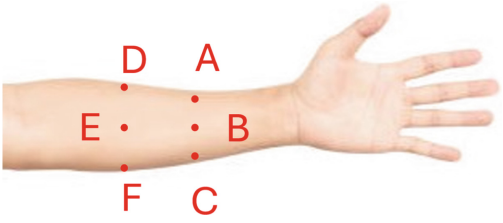

Fig. 2. Actuators positioning on the forearm.

The results of the first experiment demonstrated that the LRA actuator enables a satisfactory level of spatial discrimination accuracy. An optimal vibration duration of 100 ms or 150 ms allowed participants to correctly identify all six stimulation positions, as illustrated in Fig. 3a. In contrast, the piezoelectric actuator allowed for the identification of several sensitive positions by tuning the stimulation to an optimal frequency of 150 Hz. However, this configuration did not result in the correct recognition of all positions, indicating limited spatial resolution, as shown in Fig. 3b.

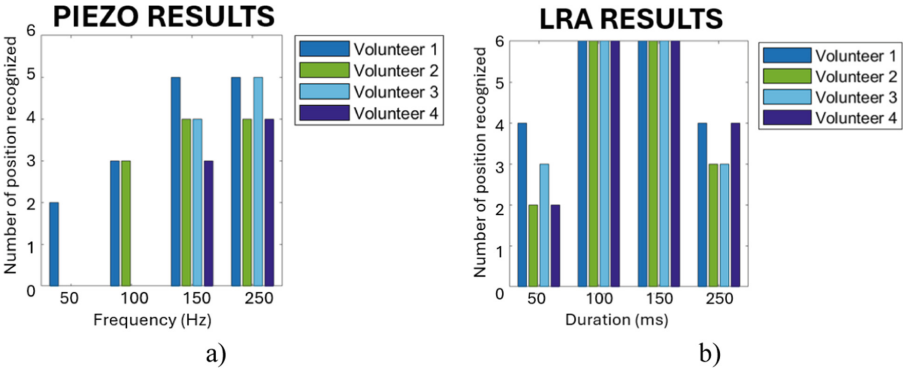

Fig. 3. Experimental results: a) positions recognized with piezo and b) positions recognized with LRA.

Fig. 4. Actuator placement on the prosthetic socket: Y indicates typical electrode locations; X denotes the area housing the residual limb.

Additionally, actuators were also integrated into the rigid structure of a prosthetic socket, as developed by BionIT Labs and illustrated in Fig. 4 [6], to simulate the conditions of indirect coupling where the actuator does not make direct contact with the skin. Y corresponds to the typical location of the electrodes, while X refers to the area where the residual limb is usually housed. It was found that the LRA, when placed near the electrode sites (e.g. Y position), tended to propagate vibrations more effectively throughout the device, while still maintaining a satisfactory level of user comfort. In contrast, the piezoelectric actuator produced vibrations that were slightly more comfortable but also weaker and more attenuated, thereby reducing tactile perceptibility and increasing the cognitive effort required to interpret the feedback. This aspect of the experiment aimed to assess the feasibility and effectiveness of delivering perceptible feedback through the material layers of the prosthetic for an easier integration in the prosthetic socket.

3.2 Sensory Sensitivity to Complex Feedback Patterns

The second experimental phase was designed to assess human sensitivity to complex vibrational patterns, including variations in waveform characteristics such as amplitude, frequency, shape, and activation duration. The goal was to determine the most effective and perceivable feedback characteristics, with a particular focus on how participants discriminated between different vibration patterns.

In this phase, participants were exposed to more complex feedback sequences, involving rapid modulations in frequency or amplitude and varying on/off cycle patterns. The actuator was positioned in the optimal location identified in the previous experiment to ensure consistent and maximized perceptual conditions. The duration and shape of the waveform were systematically adjusted to investigate their effect on the participants' ability to accurately recognize and differentiate the stimuli.

Analysis of the questionnaire responses revealed that more elaborate waveform patterns were generally not perceived with sufficient clarity. Participants reported difficulty in distinguishing between complex modulations, indicating that human tactile perception may have limited sensitivity to rapid and intricate variations in haptic feedback. This suggests that overly complex feedback strategies may compromise the intuitiveness and naturalness of interaction with the prosthesis, as they require increased cognitive attention and may not yield a proportionate benefit in user experience.

4 Conclusions

In this work, two technologies for haptic feedback in upper-limb prosthetics were compared: one using LRAs and the other using piezoelectric actuators. The LRAs provide a simpler, more cost-effective control system, while the piezoelectric actuators allow for more complex waveform generation but require a more expensive and intricate control mechanism.

Two types of experiments were conducted: the first focused on actuator placement and perceptual sensitivity, while the second aimed to assess the ability to discern complex feedback patterns. The results showed that the linear resonant actuators offered stronger and more noticeable feedback, while the piezoelectric actuators, despite offering more precision, produced less distinguishable sensations. Moreover, the second experiment revealed that users were not able to effectively distinguish between complex feedback patterns unless they paid close attention, which reduced the intuitive use of the prosthetic device.

In conclusion, the LRA system is favored for its simplicity, cost-effectiveness, and more intuitive user experience, making it a more practical choice for prosthetic applications.

References

1. Jones LA, Lederman SJ (2006) Human Hand Function. Springer
2. Antfolk C, D'Alonzo M, Rosén B, Lundborg G, Sebelius F, Cipriani C (2013) Sensory feedback in upper limb prosthetics. Expert Rev Med Devices 10(1):45–54
3. Farina D et al (2014) The extraction of neural information from the surface electromyogram for the control of upper-limb prostheses: emerging avenues and challenges. IEEE Trans Neural Syst Rehabil Eng 22(4):797–809
4. TDK Corporation (2022) PowerHap 1313H018V060 – Piezo actuator with haptic feedback. Datasheet [Online]
5. Boreas Technologies (2023) BOS1921 – Ultra-low power piezo haptic driver. Datasheet. [Online]
6. BionIT Labs (2023) Adam's Hand – World's first fully-adaptive bionic hand. https://bionitlabs.com/en/adams-hand/. Accessed 12 May 2025

Edge Shape Detection Based on Soft Piezoelectric Tactile Sensing System and Machine Learning

Razan Khalifeh(✉), Yahya Abbass, and Maurizio Valle

Department of Naval, Electrical, Electronics, and Telecommunications Engineering, University of Genoa, Genoa, Italy
Razan.Khalifeh@edu.unige.it

Abstract. This paper presents a tactile-sensing fingertip based on piezoelectric materials for edge shape detection. Two statistical features were extracted from the collected tactile signals and evaluated through ML algorithms such as the Support Vector Machine (SVM) and One-Dimensional Convolutional Neural Network (1D-CNN). The system was tested with two 3D-printed cubes featuring Bar and Roof edges, which were rotated in the hand to assess the tactile sensing system capability in edge detection. Results showed that the SVM algorithm attained an accuracy of 90.21%, with 87.93% for CNN and 87% for human perception. The proposed system demonstrated its effectiveness in discriminating between object edges, highlighting its potential for applications in robotics and prosthetics.

Keywords: Piezoelectric sensor · edge detection · machine learning · robotic hand · prosthetics

1 Introduction

Among several human senses, touch plays a crucial role in perceiving information about the surrounding environment. It allows humans to recognize objects by identifying the characteristics of their shape, material, and temperature [1]. Recently, researchers focused on improving tactile sensor technologies [2] due to their capability to mimic, to some extent, the human touch perception, with a particular focus on identifying the physical properties of the objects. Several artificial touch sensors made from various materials, including piezoresistive, capacitive, and piezoelectric [3], have been used to extract tactile information (e.g., force, slippage, edge, texture, etc.).

Across various tactile information, edge detection plays a crucial role in object exploration, thus affecting the grasp stability. For instance, a 2×2 tactile sensor to track and identify the edges of a 2D shape object has been presented in [4]. In [5], an object recognition method has been proposed for edge detection using 3D object images. Three images with varying edge complexities were used, captured from a camera setup used in augmented reality applications. Moreover, authors in [6] proposed a method for edge detection of concrete cracks from real 2D images of concrete surfaces containing noisy and accidental objects.

C. Di Natale et al. (Eds.): AISEM 2025, LNEE 1497, pp. 241–246, 2025.
https://doi.org/10.1007/978-3-032-08271-8_38

To improve the control of the robotic hand, edge detection algorithms have been discussed in [7]. Edge recognition is achieved through the implementation of artificial vision techniques, where the algorithms process images captured by a camera (webcam) to identify significant changes in pixel intensity that correspond to edges.

Although these methods effectively capture object edges, they tend to be bulky and are constrained by their reliance on visual data (images), limiting their versatility in dynamic environments and presenting challenges for real-time processing. To overcome these limitations, this paper presents a soft tactile sensing system for object edge detection based on flexible piezoelectric materials (PVDF). Time-series signals were acquired and processed through machine learning (ML) algorithms, including Support Vector Machine (SVM) and One Dimensional Convolutional Neural Network (1D-CNN), enabling the identification of two 3D-printed cubes with Bar and Roof edges.

2 Materials and Methods

2.1 Tactile Sensing System

The piezoelectric sensing array is composed of 8 P(VDF-TrFE) sensors screen-printed on a flexible substrate. In particular, the manufacturing process involves screen-printing repeated units of P(VDF-TrFE) poly (vinylidene fluoride trifluor-oethylene). Figure 1 shows the structure of a single sensing array. The single sensor is composed of a bottom electrode, a ferroelectric polymer P(VDF-TrFE) layer (5.1 μm thick), and a top electrode (PEDOT: PSS). To acquire the sensor's response, we developed compact embedded electronics (Fig. 1 (right)). It is composed of a low-power BL600 module (Laird Connectivity, US) microcontroller based on an ARM Cortex M0, a DDC232 (Texas Instrument, US) current-input analog-to-digital converter, and a USB data transfer interface (i.e., FTDI232). The electronics can collect and process tactile signals from 32 sensors at 2K samples/s.

The 2 kHz sampling rate is used to capture the full bandwidth of the sensor. The structure of the e-skin, the intrinsic flexibility of the sensing system, and its wide frequency bandwidth (0.5 Hz–1 kHz) make it a good candidate as a functional constituent of a flexible electronic skin measuring dynamic contacts.

2.2 Experimental Setup

To assess the sensing system's capability in detecting shape edges, two cubes characterized by two different edges were 3D printed. In particular, two edge types are selected, including" Roof edges" and" Bar edges," as shown in Fig. 1. Two experiments are planned to assess the capability of the sensing system to detect the different edges, as will be discussed in the next sections.

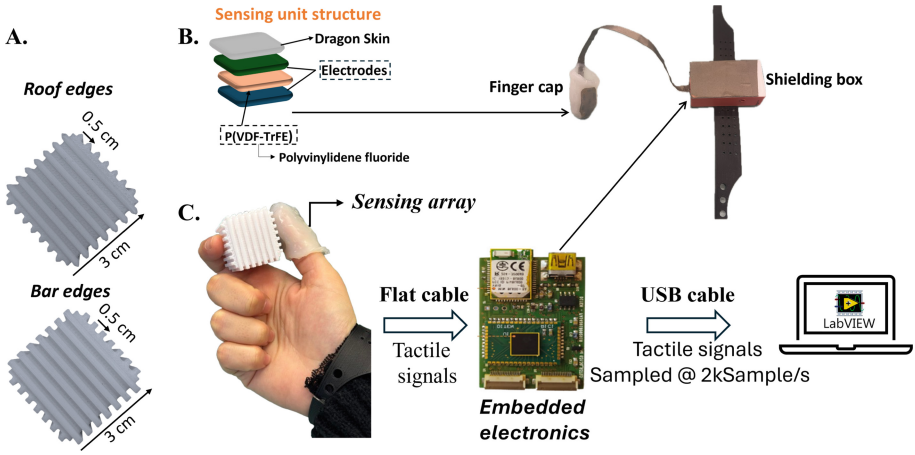

Fig. 1. Overview of the proposed sensory system. A. Two-dimensional cubes with two distinct edge types. B. Sensing unit structure and geometry: a fingercap equipped with eight PVDF sensors. C. A fingercap mounted on the subject's finger, with embedded electronics to acquire and process tactile signals at 2Ksample/s, and a PC running LabView software for signal collection.

2.3 Data Acquisition by the Sensing System

In the first experiment, three healthy subjects (two females and one male aged 26 ± 3 years) were asked to wear the sensing system (see Fig. 1) and try to explore the objects involving the sensorized finger (the thumb finger) for ≈ 3 s.

During the experiment, the response of the sensors is captured and saved by a Graphical User Interface developed on LabVIEW software. This procedure is repeated 30 times for each object from each subject, resulting in a dataset of 180 trials consisting of 30 trials × 2 cubes × 3 subjects. The resulting dataset can be formulated as: $D = \{(Xi, yi) \mid Xi \in R^{Nc \times Ns}, yi \in \{roof, bar\}, i = 1,\ldots, 180\}$, where $Nc = 8$ is the number of sensors and $Ns = 6000$ is the number of samples (2K samples/s × 3 s).

2.4 Edge Perception (Human Perception)

This experiment is conducted on the same healthy subjects, and they are asked to explore the edge cubes again. However, in this experiment, subjects were asked to guess the edge cube using their sensory perception. During this, the experimenter blindfolded and guided the subjects to grasp the cubes and rotate them in different directions with their hands. The cubes are shuffled and randomly presented.

The experiment is composed of two phases, including learning and reinforced learning. In the learning phase, the subjects are informed beforehand which cube will be presented. However, during the reinforced learning, the cubes are randomly presented, and the subjects are asked to guess the cube type within 3 s, and the correct answer is recorded by the experimenter. Each of the subjects performed 30 actions on each cube during each phase.

2.5 Data Pre-processing

Inspired by work done in [8], two features were extracted from the collected tactile signals, including Standard Deviation (SD) and mean. As a result, each Xi ∈ D is transformed to ˜Xi ∈ ˜D where ˜D = {(˜Xi, *y*i); ˜Xi ∈ $R^{2\times8}$; *y*i ∈ {roof, bar}}. These features were normalized using a standard scaler technique [9]. Moreover, a t-Distributed Stochastic Neighbor Embedding is used to visualize data by giving each datapoint a two-dimensional map was applied as illustrated in Fig. 2.

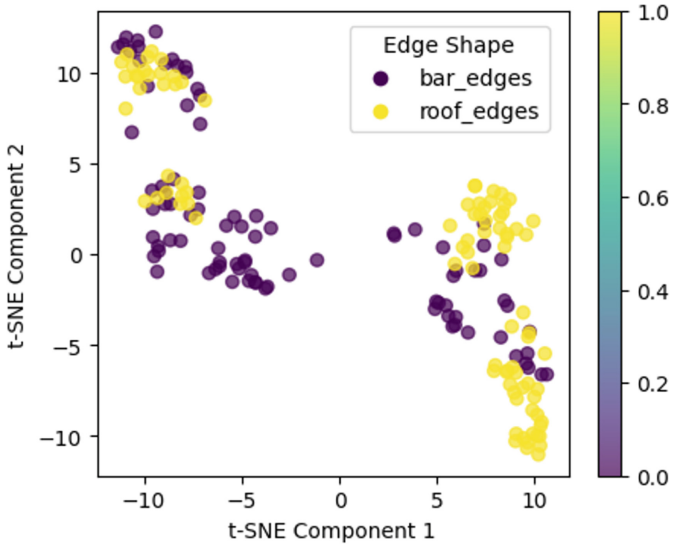

Fig. 2. Two-dimensional reduction results of the data.

The visualization results show that the two edge shapes exhibit a certain degree of clustering with some overlap, indicating that the t-SNE algorithm can extract meaningful features and identify key characteristics of tactile signals associated with different object edge shapes.

2.6 Implemented Algorithms

To detect the edge shape of cubes, the response of the eight sensors represented by D is processed and analyzed using a One-Dimensional Convolutional Neural Network (1D-CNN) algorithm [10], and the extracted features represented by the dataset ˜D are trained by a Support Vector Machine (SVM) algorithm [11].

The implemented SVM algorithm works by computing the hyperplane that maximizes the margin to the nearest samples of the two classes. In this study, the Radial Basis Function (RBF) was used.

The input raw data for the CNN algorithm is a two-dimensional tensor X × Y, where X represents the time features and Y is the number of channels (sensors). The model architecture consists of a 1D convolutional layer with a ReLU activation function,

utilizing various filters and kernel sizes. It includes batch normalization, max-pooling, global average pooling, and a SoftMax output layer with 2 neurons corresponding to the classified objects.

These models are trained and tested on fivefold using a stratified cross-validation technique. The dataset is split into training 80%, validation 10%, and testing 10%.

3 Results and Discussion

Table 1 shows the identification accuracy of human perception and the proposed models. The results demonstrated that the accuracy achieved by the SVM algorithm was 90.21% ±0.0024, highlighting the importance of the extracted features. Furthermore, while the CNN model exhibited a performance comparable to that of SVM, a slight drop in accuracy was observed, reaching 87.93%. In comparison, the subjects' accuracy in discriminating between the shape of the two edges was 87%.

This indicates that the finger cap, combined with the ML algorithms, proved its efficacy in differentiating between the edges.

Table 1. Identification accuracy of the proposed models and human perception.

Models	Accuracy
SVM	90.21%
1D-CNN	87.93%
Human perception	87%

4 Conclusion

To conclude, this paper presents a tactile sensing system based on PVDF combined with machine learning models for edge detection. The proposed system demonstrated its efficacy in accurately determining object edges. Future work could focus on expanding the range of shape sizes, evaluating the system on real-world objects, and exploring applications of the proposed algorithm in prosthetic and robotic hands.

References

1. Wang L, Qi X, Li C, Wang Y (2024) Multifunctional Tactile Sensors for Object Recognition. Advanced Functional Materials, 2409358
2. Yogeswaran N et al (2015) New materials and advances in making electronic skin for interactive robots. Adv Robot 29(21):1359–1373
3. Dahiya RS, Metta G, Valle M, Sandini G (2009) Tactile sensing—from humans to humanoids. IEEE Trans Rob 26(1):1–20
4. Phung TC, Ihn YS, Koo JC, Choi HR (2010) An enhanced edge tracking method using a low-resolution tactile sensor. Int J Control Autom Syst 8:462–467

5. Gao T, Yang Z (2020) 3D object recognition method based on improved canny edge detection algorithm in augmented reality. In: 2020 IEEE 5th International Conference on Image, Vision and Computing (ICIVC), pp. 19–23. IEEE
6. Nguyen HN, Kam TY, Cheng PY (2014) An automatic approach for accurate edge detection of concrete crack utilizing 2D geometric features of crack. J Sign Process Syst 77: 221–240
7. Arias Velásquez RM (2023) Edge detection algorithms to improve the control of robotic hands. In: Silhavy R, Silhavy P (eds.) Artificial Intelligence Application in Networks and Systems. CSOC 2023. Lecture Notes in Networks and Systems, vol 724. Springer, Cham
8. Abbass Y, Gianoglio C, Ali HA, Saleh M, Valle M (2024) Texture perception using tactile sensing glove based on PVDF sensors and machine learning. IEEE Sensors Letters
9. Huang L, Qin J, Zhou Y, Zhu F, Liu L, Shao L (2023) Normalization techniques in training dnns: Methodology, analysis and application. IEEE Trans Pattern Anal Mach Intell 45(8):10173–10196
10. Kiranyaz S, Avci O, Abdeljaber O, Ince T, Gabbouj M, Inman DJ (2021) 1D convolutional neural networks and applications: a survey. Mech Syst Signal Process 1(151):107398
11. Abdullah DM, Abdulazeez AM (2021) Machine learning applications based on SVM classification a review. Qubahan Acad J 1(2):81–90

Innovative Wearable Stress Monitoring System for Astronauts Using EEG and PPG

Giuseppe Coviello, Giuseppe Brunetti, Andrea Ignazio Larossa, Giuseppe Conti, and Caterina Ciminelli(✉)

Optoelectronics Laboratory, Department of Electrical and Information Engineering, Polytechnic University of Bari, Via E. Orabona 4, Bari, Italy
Caterina.ciminelli@poliba.it

Abstract. This paper presents a novel wearable system for real-time stress monitoring in space-like conditions, combining EEG and PPG signals acquired through a commercially available headband. The system integrates edge-based processing on a low-power microcontroller, enabling real-time classification and feedback without reliance on external computation. A key innovation is including physiological artifacts, such as eye closure and teeth grinding, as features for stress detection rather than noise to be discarded. Experimental results demonstrate high accuracy in multimodal stress identification, highlighting the system's potential for enhancing astronaut well-being and cognitive performance during long-duration space missions.

Keywords: PPG · EEG · Cognitive load · Data fusion · Wearable system

1 Introduction

Spaceflight exposes astronauts to various challenging physical and psychological conditions, including microgravity, radiation, disrupted sleep-wake cycles, social isolation, and confinement. These stressors often combine to create a state of ongoing psychological strain. As space agencies like NASA plan longer missions, such as those of the Artemis program to the Moon and, eventually, Mars, these stress factors are expected to intensify [1]. In such missions, preserving astronauts' mental health and cognitive performance becomes essential, not just for their well-being, but for the success of the mission itself.

Traditionally, stress and emotional well-being during spaceflight have been assessed using subjective tools such as interviews and self-report questionnaires. Instruments like the Profile of Mood States (POMS), State-Trait Anxiety Inventory (STAI), and NASA Task Load Index (NASA-TLX) are widely used to evaluate mood, anxiety, and cognitive workload [2, 3]. However, these tools depend on participants' willingness to report symptoms and are prone to bias. This has led to increasing interest in objective, real-time monitoring of stress using physiological signals [4].

Among the most promising techniques are electroencephalography (EEG) and photoplethysmography (PPG). EEG offers direct insights into brain activity and can detect

C. Di Natale et al. (Eds.): AISEM 2025, LNEE 1497, pp. 247–252, 2025.
https://doi.org/10.1007/978-3-032-08271-8_39

stress-related changes, such as increased beta activity and reduced alpha power [5]. It also reveals patterns like frontal alpha asymmetry, which are linked to emotional regulation and cognitive control [6, 7]. PPG, a simple and non-invasive optical method, measures blood volume changes and is commonly used to calculate heart rate variability (HRV), an established marker of stress and autonomic nervous system activity. Lower HRV typically indicates increased sympathetic activity and greater stress [8].

Combining EEG and PPG through multimodal data fusion can provide a more complete and reliable evaluation of stress level. Each signal contributes unique information: together, they capture both neurocognitive and physiological responses. Machine learning models using features such as power spectral density from EEG and time-domain HRV indices from PPG have shown high accuracy in classifying stress states [9]. Despite this progress, creating a wearable, non-intrusive, and low-power system suitable for space remains a complex challenge. Space hardware must be compact, efficient, and unobtrusive, able to function reliably without interfering with mission tasks.

In this paper, we propose a new data analysis approach that extracts more information than traditional methods by integrating the same EEG and PPG signals. Through data fusion, it is possible to obtain a more accurate and reliable assessment compared to traditional approaches.

2 System Description

This section presents the design and implementation of the wearable system that leverages multimodal signal fusion, combining EEG and PPG to achieve continuous, real-time stress monitoring in space-like conditions. At this stage, the system is engineered to be unobtrusive and computationally efficient, relying solely on commercially available hardware and custom-developed algorithms. A key innovation of the system is the inclusion and enhancement of signal features commonly dismissed as artifacts. When analyzing EEG signals, various artifacts caused by normal physiological activities, such as eye blinking, eye movements, or swallowing, can interfere with the brain signals. Therefore, in our approach, these artifacts are first isolated, amplified, and analyzed, as they may contain relevant physiological or emotional information. Only after this dedicated analysis are they filtered out to allow for a clearer interpretation of the underlying EEG activity.

Figure 1 illustrates the experimental setup employed in this study. The system utilizes the Muse 2 headband [10], a lightweight, commercially available wearable device equipped with dry EEG electrodes and an integrated PPG sensor. The device is wireless and provides sufficient spatial resolution for the extraction of frontal-lobe brain activity. The reference electrodes are FPz, FP1, and FP2, while the active electrodes AF7 and AF8 are positioned over the left and right frontal lobes, respectively. This configuration is well-suited for measuring hemispheric symmetry and detecting eye-related activity. The Muse 2 also includes a built-in PPG sensor positioned on the forehead, which captures volumetric changes in blood flow.

Muse 2 transmits data wirelessly via Bluetooth to a host computer, which subsequently forwards the signals through a serial interface to an STM32F401RE microcontroller evaluation board. This microcontroller performs real-time signal processing,

Fig. 1. Experimental setup.

including feature extraction and stress classification. The processed results are then transmitted back to the computer for visualization.

To facilitate a more comprehensive offline analysis, raw data were also processed using MATLAB, enabling detailed graphical representation and further validation of the signal processing pipeline.

A test was carried out on a sample of 10 volunteers, and all data was collected anonymously under ethical guidelines.

3 Experimental Results

3.1 EEG Processing and Feature Extraction

EEG data is first preprocessed using a bandpass filter (0.5–40 Hz) to eliminate both low-frequency drift and high-frequency noise. The resulting signal is analyzed using power spectral density (PSD) to isolate the alpha band (8–13 Hz), which is known to be sensitive to stress-related neural activity. The hemispheric symmetry index is computed as:

$$\text{Symmetry Index} = \frac{\text{PSD}_{\text{AF7}} - \text{PSD}_{\text{AF8}}}{\text{PSD}_{\text{AF7}} + \text{PSD}_{\text{AF8}}} \tag{1}$$

This metric captures lateralization patterns, with greater asymmetry often indicating increased cognitive load or emotional imbalance.

Figure 2 shows an example of typical values of symmetry's index associated with a calm and a stressed subject.

As stated, eye closure is not discarded as an artifact but is instead classified into different categories based on the amplitude and duration of EEG components in the delta band (1–4 Hz). A decision tree algorithm processes these features to distinguish between regular closures, forced closures, and the absence of closing. Figure 3a shows the filtered EEG signal, while Fig. 3b illustrates the isolated and enhanced eye closure pattern. The interpretation of these patterns provides a direct and immediate assessment of the subject's stress state, as they are compared to a baseline calibration performed

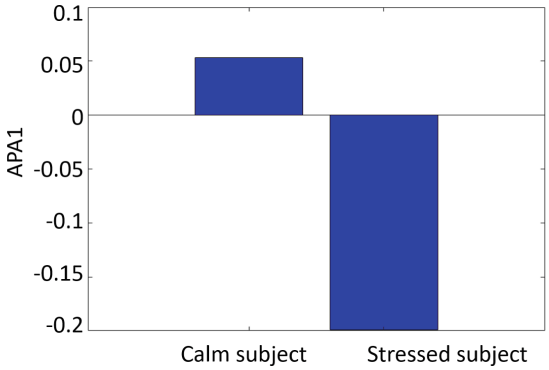

Fig. 2. Representative data for calm and stressed conditions.

on Earth, enabling more accurate and context-specific stress monitoring during space missions.

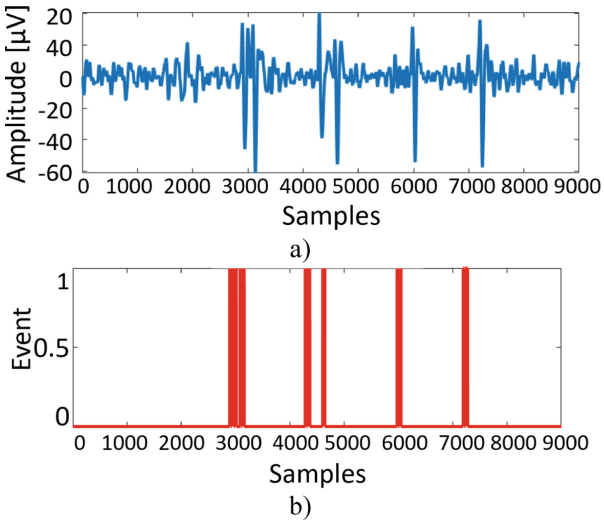

Fig. 3. a) Filtered EEG signal. b) Isolated and enhanced eye closure pattern.

3.2 PPG Processing and HRV Analysis

The raw PPG signal is bandpass filtered (0.5–4 Hz) to isolate the heart rate waveform.

HRV is calculated from the inter-beat intervals (IBIs) derived using peak detection algorithms The signal is then decomposed into frequency components using a fast Fourier transform (FFT). The power spectrum is computed and partitioned into low-frequency (LF: 0.04–0.15 Hz) and high-frequency (HF: 0.15–0.4 Hz) bands. The stress index is calculated as:

$$\text{Stress Index} = \frac{\text{PSD}_{\text{LF}}}{\text{PSD}_{\text{HF}}} \tag{2}$$

This index reflects autonomic nervous system activity: elevated values suggest increased sympathetic activation, a known marker of stress. Figure 4a shows the power spectrum for a low-stress state, while Fig. 4b corresponds to a high-stress state. Figure 4c shows typical values of the stress index associated with calm and stressed subjects, including the threshold.

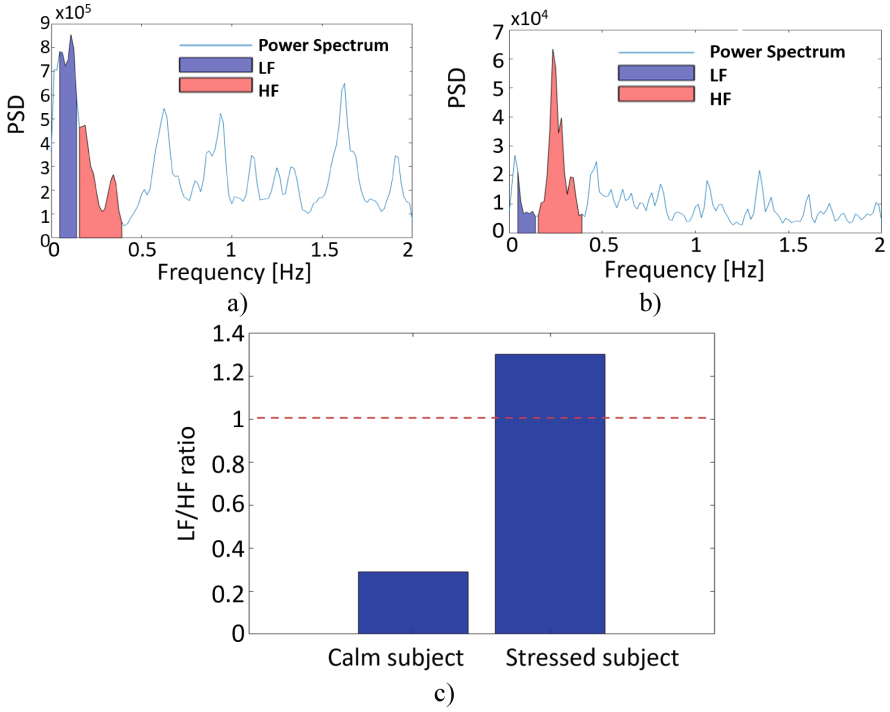

Fig. 4. a) Power spectrum during a low-stress state. b) Power spectrum during a high-stress state. c) Typical values for calm and stressed subjects, with indicated threshold for the stress index.

3.3 Data Fusion

The fusion of the three methods significantly improves accuracy, as it allows the system to rely on multiple inputs. This enables the implementation of weighted fusion algorithms as well as machine learning approaches. The fusion is performed in real time on the microcontroller. Initial tests conducted on a group of 10 volunteers confirmed that each method, when used independently, can detect stress-related features with good reliability. The current challenge lies in determining the most effective way to merge these signals and assign appropriate weights to each, a process that is the focus of our ongoing work.

4 Conclusions

In this paper we introduced a lightweight, wearable system for real-time stress monitoring based on EEG and PPG fusion, with a novel approach to leveraging physiological artifacts as stress indicators. The system demonstrated high identification, accuracy and low

latency, supporting its use in resource-constrained environments such as space missions. Future work will focus on refining the data fusion algorithm by identifying and assigning appropriate weights to each signal output, to enhance the reliability and interpretability of the combined stress assessment.

References

1. Al-Shargie F, et al (2023) Detection of Astronaut's Stress Levels During 240-Day Confinement using EEG Signals and Machine Learning. 45th Annual International Conference of the IEEE Engineering in Medicine & Biology Society (EMBC), pp. 1–6
2. McNair DM, Lorr M, Droppleman LF (1971) Manual for the Profile of Mood States. Educational and Industrial Testing Service, San Diego
3. Spielberger CD, Gorsuch RL, Lushene R (1983) STAI Manual for the State-Trait Anxiety Inventory. Consulting Psychologists Press, Palo Alto
4. Taskasaplidis G, Fotiadis DA, Bamidis PD (2024) Review of stress detection methods using wearable sensors. IEEE Access, 38219–38246
5. Becker L, Nilson T, Cowley A (2022) Electroencephalography (EEG), electromyography (EMG) and eye-tracking for astronaut training and space exploration. 73rd International Astronautical Congress (IAC), pp. 1–15
6. Murata A (2005) Evaluation of mental workload using the modified alpha attenuation coefficient. Int J Ind Ergon 35(8):761–770
7. Coan JA, Allen JJB (2004) Frontal EEG asymmetry as a moderator and mediator of emotion. Biol Psychol 67(1–2):7–49
8. Kim H-G, Cheon E-J, Bai D-S, Lee YH, Koo B-H (2018) Stress and heart rate variability: a meta-analysis and review of the literature. Psychiatry Investig 15(3):235–245
9. Konar D, De S, Mukherjee P, Roy AH (2023) A novel human stress level detection technique using EEG. International Conference on Network, Multimedia and Information Technology (NMITCON)
10. InteraXon (2020) Muse 2: The brain sensing headband. https://www.choosemuse.com/muse-2/

The Integration of Cellulose-Based Materials in Orthotic Devices as Flexible and Biodegradable Sensors

Ahmet Koluman[1], Arzum Işıtan[2,3(✉)], Cem Gök[4,5], Massimo Bersani[3], and Laura Pasquardini[6]

[1] Department of Biomedical Engineering, Pamukkale University, Denizli, Turkey
[2] Department of Mechanical Engineering, Pamukkale University, Denizli, Turkey
aisitan@pau.edu.tr
[3] Center for Sensors and Devices, Fondazione Bruno Kessler, Trento, Italy
[4] Department of Biomedical Engineering, Izmir Bakırçay University, Izmir, Turkey
[5] Biomedical Technologies Design Application and Research Center, Izmir Bakırçay University, Izmir, Turkey
[6] Indivenire Srl, Trento, Italy

Abstract. Cellulose (CE), a biodegradable and biocompatible biopolymer, can be used as a functional element in systems such as orthotics, where both high strength and flexibility are required. They can also be rapidly produced as embedded flexible sensors that can monitor pressure, strain, humidity and temperature in real time in orthoses produced using patient-specific anatomical data and additive manufacturing. These 'smart' orthotic devices not only improve user comfort and treatment outcomes but also align with the growing demand for environmentally friendly healthcare solutions.

In this study, the applications of CE as both the main structure and sensor material in reverse engineering and 3D printing applications in medical devices, especially in the design and manufacturing of personalized orthotics are discussed. The promising performance of cellulose-based sensors in experimental settings suggests a bright future for their clinical applications, particularly in rehabilitation, sports medicine, and long-term care.

Keywords: Flexible Sensors · Cellulose · Orthotic Devices · Reverse Engineering · 3D Printing

1 Introduction

Orthotic devices are auxiliary medical devices used to correct, support, immobilize or gain function in cases where there is no limb loss in the body but there is a disorder in the anatomical, physiological and mechanical structure of the limb [1, 2]. Traditionally, orthoses were fabricated through manual techniques such as plaster casting, molding, and trial-and-error adjustments—methods that are often time-consuming, labor-intensive,

C. Di Natale et al. (Eds.): AISEM 2025, LNEE 1497, pp. 253–258, 2025.
https://doi.org/10.1007/978-3-032-08271-8_40

and limited in personalization. Since the 1990s, reverse engineering (RE) and rapid prototyping (RP) have been widely applied in the design and manufacture of personalized medical devices, including implants, orthoses, prostheses, and surgical tools. Advancements in 3D printing (3DP) have significantly reduced production time and enabled complex geometries previously unachievable by traditional methods [3, 4]. RE allows for precise anatomical data capture through advanced imaging, supporting the creation of tailored orthotic devices [5]. The integration of RE and additive manufacturing (AM) has particularly transformed orthotic design. Figure 1 illustrates examples of foot, ankle, and leg modeling using RE and 3DP.

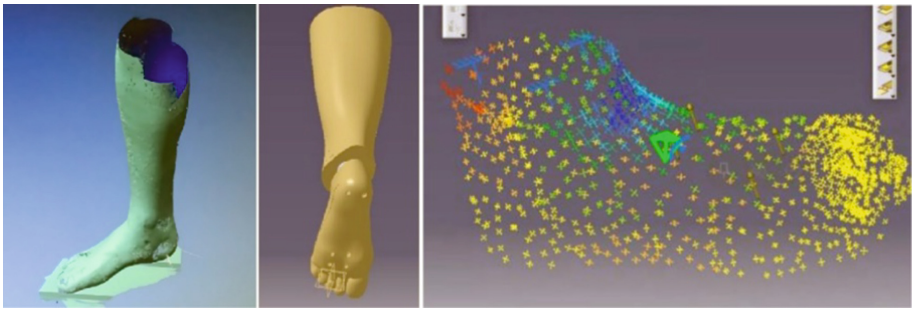

Fig. 1. Examples of foot, ankle, and leg numerical modelling with RE approach and 3DP.

Polymer matrix composites offer flexibility and adaptability, making 3DP ideal for patient-specific production [3, 4, 6]. However, petroleum-based plastics pose sustainability and waste management challenges [7, 8]. Cellulose (CE) emerges as a biodegradable, sustainable alternative with unique advantages. Its integration into orthotic sensors offers flexibility, biocompatibility, and environmental benefits. Progress in material synthesis, structure design, and fabrication has enhanced the mechanical, electrical, and chemical performance of CE-based sensors. Their high mechanical strength and surface area provide notable sensitivity for real-time monitoring of biomechanical forces and environmental factors [9–14]. One of the key applications of CE in orthotics is its use in pressure and strain sensors which can monitor mechanical forces exerted on the body through the orthotic device. These sensors detect and record pressure distribution and strain during movement, helping to optimize the fit and performance of orthotic devices. Studies show that CE nanocomposites exhibit remarkable sensitivity in strain sensing, owing to their high mechanical strength and surface area [9–14].

This work aims to explore the synergistic application of RE, 3DP and CE-based materials in the design and fabrication of personalized orthotic devices. By leveraging the precision of RE, the versatility of AM and the sustainability of CE-based sensors, a new approach is required to develop orthoses that are not only tailored to individual anatomical structures but also capable of real-time biomechanical monitoring. Such integration has the potential to increase patient comfort, improve therapeutic outcomes and contribute to environmentally sustainable healthcare solutions.

2 Integration of Cellulose in Reverse Engineering and 3DP

RE and 3DP have become indispensable tools in the development of personalized orthotic devices. The process begins with anatomical data acquisition via high-resolution imaging (MRI, CT, or 3D scanning), followed by CAD-based modeling to produce patient-specific 3D designs [3, 4]. This approach allows for the design of orthotic structures that precisely conform to a patient's morphology and functional needs (Fig. 1). A summarized scheme of the steps can be seen in Fig. 2.

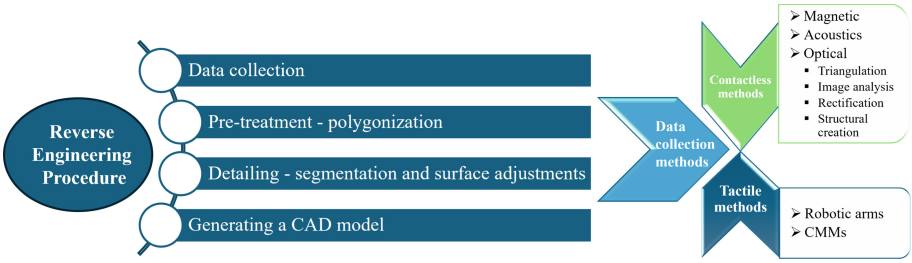

Fig. 2. RE process steps summary (left) and data collection methods (right).

Once the digital model is generated, AM technologies such as fused deposition modeling (FDM), stereolithography (SLA), or digital light processing (DLP) are employed to fabricate the physical orthosis (Fig. 3). Unlike traditional polymers, CE offers greater skin compatibility for prolonged use. Its hydrophilicity also supports humidity sensing in orthotic environments [14]. When functionalized with nanomaterials like graphene or CNTs, CE enables smart orthotics with flexible biosensors for real-time feedback [13, 15]. These sensors can provide feedback on the performance of the orthotic device, allowing for adaptive adjustments based on real-time data. As a biodegradable material, CE reduces the environmental impact of disposable medical devices, aligning with the growing trend toward eco-friendly healthcare solutions. The production of CE-based sensors is also energy-efficient, making them an attractive alternative to traditional materials used in similar applications [12, 13].

Nano-crystalline, fibril, or bacterial forms can be used in composites with PLA, TPU, or PCL, enhancing strength, elasticity, and printability [16–18]. The production process includes anatomical data collection, CAD modeling, CE-based filament preparation, printing via AM techniques, and post-processing for sensor integration [5, 6, 13, 16, 17].

2.1 Functional Properties of Cellulose-Based Sensors in Orthotics

CE-based materials combine high mechanical strength, surface tunability, biocompatibility, and environmental responsiveness. In orthotic applications, they are engineered to detect mechanical, thermal, and biochemical signals. Key functions include pressure and strain sensing via nanocomposites, moisture and temperature detection through

Fig. 3. Examples of foot and foot ankle orthosis

hydrophilicity, and biosensing of electromyographic (EMG) or electrodermal activity (EDA) signals when functionalized with conductive nanomaterials. These features enable real-time feedback for orthotic adjustment, enhancing comfort and therapeutic outcomes [13, 16, 17, 19, 20]. Compared to conventional materials, CE offers distinct technical and environmental advantages (Table 1), making it a promising material for sustainable healthcare innovations.

Table 1. Comparison of orthotic sensor materials.

Property	Cellulose-Based Materials	Traditional Polymers
Biodegradability and Biocompatibility	High / Excellent	Low / Variable
Environmental Impact	Sustainable	Polluting
Functionalization	High	Medium

2.2 Environmental and Clinical Relevance

CE, unlike traditional polymers, degrades under ambient conditions, offering technological and ecological benefits in orthotic devices [7, 21]. Its soft, flexible nature enhances patient comfort, especially during prolonged use for scoliosis, foot drop, or knee instability. Integration into wearable systems supports healthcare's shift toward sustainable materials, particularly for long-term or disposable applications. CE composites emit fewer greenhouse gases and use non-toxic processes [19, 20]. Clinically, CE sensors offer excellent biocompatibility, minimizing irritation risks during direct skin contact. Their flexibility further enhances comfort during extended wear. Functionalization with antimicrobial agents provides added infection protection. Pre-clinical and clinical studies show CE-based sensors effectively track physiological signals while maintaining comfort and safety [13, 15–20]. Studies confirm that CE sensors degrade within weeks to months, supporting their safe application in direct-contact medical devices [13, 20].

3 Conclusion and Future Directions

The combination of RE, 3DP, and CE-based sensors in orthotics offers a new generation of smart, sustainable healthcare devices. These systems provide real-time monitoring of biomechanical parameters while remaining biocompatible and environmentally friendly. CE-based sensors in orthotic devices hold great potential for advancing personalized healthcare. By offering flexibility and sensitivity, these materials enable the development of orthotics that are not only comfortable and efficient but also sustainable. The integration of advanced sensor technologies into orthotic devices marks a significant step toward smarter, more responsive medical devices that cater to individual patient needs. The promising performance of CE-based sensors in experimental settings suggests a bright future for their clinical applications, particularly in rehabilitation, sports medicine, and long-term care.

References

1. Kobak C, Abdulkadir YA, Işıtan A (2019) Türkiye'de Ortez Protez, Kullanımı ve Üretim Aşamaları. SETSCI Conference Proceedings 4:411–415
2. Alsancak S (2000) Ortez ve Protez Tarihçesi. Ankara Sağlık Hizmetleri Dergisi 1:27–33. https://doi.org/10.1501/ASHD_0000000003
3. Hieu LC, et al (2010) Medical reverse engineering applications and methods. In: Proceedings of International Conference on Innovations, Recent Trends and Challenges In Mechatronics, Mechanical Engineering And New High-Tech Products Development – MECAHITECH'10
4. Işıtan A, Uluşal T (2020) Tersine Mühendislik Yaklaşımıyla Protez Tasarımı. In: Uğur Çavdar, Çiğdem Gündoğan Türker, Pınar Sarı Çavdar, Feyza Gürbüz, Canan Başlak (eds.) Geleceğin Dünyasında Bilimsel Ve Mesleki Çalışmalar 2020 Mühendislik Bilimleri / I, pp. 190–204. Ekin Basım Yayın Dağıtım
5. Rengier F et al (2010) 3D printing based on imaging data: Review of medical applications. Int J Comput Assist Radiol Surg 5:335–341. https://doi.org/10.1007/S11548-010-0476-X
6. Yeleswarapu S, Vijayasankar KN, Chameettachal S, Pati F (2023) Recent trends in polymeric composites and blends for three-dimensional printing and bioprinting. Adv Biomed Poly Compos Mat Appl 131–157. https://doi.org/10.1016/B978-0-323-88524-9.00004-8
7. Işıtan A, et al (2025) Sustainable production of microcrystalline and nanocrystalline cellulose from textile waste using HCl and NaOH/Urea treatment. Polymers (Basel) 17. https://doi.org/10.3390/polym17010048
8. Işıtan A, et al (2022) Bioplastics/Biopolymers: How Aware Are We? European J Sci Technol 37: 36–41. https://doi.org/10.31590/EJOSAT.1129490
9. Ummartyotin S, Manuspiya H (2015) A critical review on cellulose: From fundamental to an approach on sensor technology. Renew Sustain Energy Rev 41:402–412. https://doi.org/10.1016/J.RSER.2014.08.050
10. Kamel S, Khattab TA (2020) Recent Advances in Cellulose-Based Biosensors for Medical Diagnosis. Biosensors (Basel) 10: 67. https://doi.org/10.3390/BIOS10060067
11. Langari MM, Nikzad M, Labidi J (2023) Nanocellulose-based sensors in medical/clinical applications: the state-of-the-art review. Carbohydr Polym 304:120509. https://doi.org/10.1016/J.CARBPOL.2022.120509
12. Liu Y et al (2024) Nanocellulose-based functional materials for physical, chemical, and biological sensing: A review of materials, properties, and perspectives. Ind Crops Prod 212:118326. https://doi.org/10.1016/J.INDCROP.2024.118326

13. Chen W, Ma J, Yu D, Li N, Ji X (2024) Transparent, super stretchable, freezing-tolerant, self-healing ionic conductive cellulose based eutectogel for multi-functional sensors. Int J Biol Macromol 266(Pt 2):131129. https://doi.org/10.1016/J.IJBIOMAC.2024.131129
14. An N, et al (2022) Recent progress in cellulose-based flexible sensors. J Renew Mater 10. https://doi.org/10.32604/jrm.2022.021030
15. Li K et al (2024) Nano-carbon/PIL modified cellulose wearable sensors by computer aided patterning. Mater Today Nano 26:100482. https://doi.org/10.1016/J.MTNANO.2024.100482
16. Fu Q, Cui C, Meng L, Hao S, Dai R, Yang J (2021) Emerging cellulose-derived materials: a promising platform for the design of flexible wearable sensors toward health and environment monitoring. Mater Chem Front. 5:2051–2091. https://doi.org/10.1039/D0QM00748J
17. Dandegaonkar G, Ahmed A, Sun L, Adak B, Mukhopadhyay S (2022) Cellulose based flexible and wearable sensors for health monitoring. Mater Adv. 3:3766–3783. https://doi.org/10.1039/D1MA01210J
18. Huang L, Hu Q, Gao S, Liu W, Wei X (2023) Recent progress and applications of cellulose and its derivatives-based humidity sensors: a review. Carbohydr Polym 318:121139. https://doi.org/10.1016/J.CARBPOL.2023.121139
19. Basarir F, Kaschuk JJ, Vapaavuori J (2022) Perspective about cellulose-based pressure and strain sensors for human motion detection. Biosensors 12: 187. https://doi.org/10.3390/BIOS12040187
20. Li A et al (2025) High-performance, breathable, and degradable fully cellulose-based sensor for multifunctional human activity monitoring. Chem Eng J 505:159564. https://doi.org/10.1016/J.CEJ.2025.159564
21. Zeidler H, et al (2018) 3D printing of biodegradable parts using renewable biobased materials. In: Procedia Manufacturing, pp. 117–124. Elsevier B.V. https://doi.org/10.1016/j.promfg.2018.02.101

Microwave Sensing of Humidity with a Transparent and Flexible Electromagnetic Metasurface

G. Marchi[1(✉)], L. Graziani[3], V. Mulloni[1], A. Gaiardo[1], M. Valt[1], T. Facchinelli[1], E. Negri[4], M. Donelli[2], A. Galli[3], and L. Lorenzelli[1]

[1] Center for Sensors and Devices (SD), Fondazione Bruno Kessler, 38123 Trento, Italy
gmarchi@fbk.eu
[2] Department of Civil Environmental and Mechanical Engineering (DICAM), University of Trento, 38123 Trento, Italy
[3] Department of Information Engineering, Electronics and Telecommunications (DIET), Sapienza University of Rome, 00184 Rome, Italy
[4] Institute for Microelectronics and Microsystems (IMM), National Research Council (CNR), 00133 Rome, Italy

Abstract. A planar, low-cost, and flexible microwave sensor is introduced, utilizing an electromagnetic metasurface of frequency-selective surface (FSS) type. This sensor concept relies on altering the inter-plate capacitance of the electric inductive-capacitive (ELC) resonators forming the FSS periodic array grid. When a material with varying electrical characteristics is placed between the plates, changes in capacitance and inductance lead to a shift and attenuation of the resonant frequency that are exploited as encoding mechanism for the sensing functionality. The metasurface approach offers the advantage of enhancing the sensor's radar cross section (RCS), which in turn improves either the reading distance or the strength of the sensor response.

Keywords: Frequency Selective Surface (FSS) · Electric-Inductive-Capacitive Resonator (ELC) · Sensing · Humidity · Nafion 117

1 Introduction

Frequency selective surfaces (FSS) have been widely studied and exploited for different applications, such as spatial filters where they act as band pass or band stop filters, integration with antennas to improve gain and directivity features, electromagnetic shielding [1]. Among all these practical scenarios, FSS have been recently proposed for sensing applications as well. In particular, microwave sensors based on electromagnetic metasurfaces of FSS type have lately gained significant attention due to their simplicity, non-contact wireless reading, and low cost. A microwave sensor based on FSS is proposed in [2], where a gammadion-shaped unit cell FSS is used to develop a corrosion sensor. In this case, the increase in corrosion thickness leads to a rise in surface impedance, causing a shift in resonances to lower frequencies. Similarly, a resonant cavity fabricated on

C. Di Natale et al. (Eds.): AISEM 2025, LNEE 1497, pp. 259–264, 2025.
https://doi.org/10.1007/978-3-032-08271-8_41

a coated metasurface is employed in [3] to create a glucose sensor using complementary rectangular cells. A structural health monitoring (SHM) FSS is presented in [4], where a cross-type metasurface element is fabricated on a flexible membrane. Structural damage is detected by monitoring changes in the resonance frequency. Lastly, wearable sensors are demonstrated in [5], where a dipole-based FSS is used for body temperature monitoring.

In this work, an original, planar, and cost-effective FSS metasurface has been proposed for humidity sensing at microwave frequency. The working principle of the device is based on a modification of the inter-plate capacitance of the unit cell because of the progressive incorporation of wet air. Specifically, by placing a material with electrical characteristics that are strongly sensible to the humidity level, the shift and attenuation of the resonant frequency due to the variation of the capacitance and inductance in the system are exploited for humidity detection. The design and experimental validation of the proposed device are presented in Sects. 2 and 3, respectively. Conclusions are finally drawn in Sect. 4.

2 Design and Simulation

Our FSS structure consists of an array of identical meta-atoms, as are commonly known the elements of a metasurface, of electric inductive-capacitive (ELC) type. The individual ELC cell is designed to resonate at 2.4 GHz in the absence of any sensing material incorporated into the sensor. This structure has been simulated with the Ansys HFSS electromagnetic simulation tool and the final layout is presented in Fig. 1.

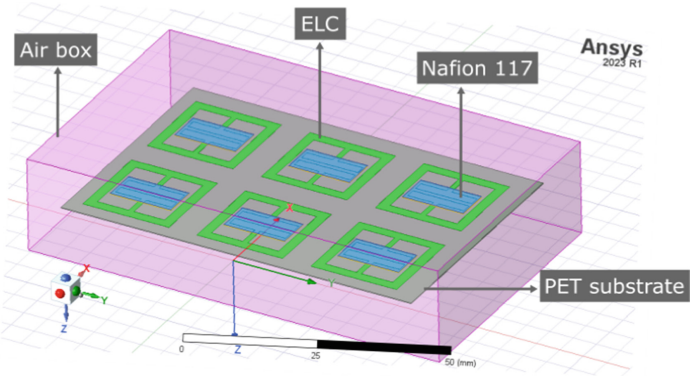

Fig. 1. Simulation layout in Ansys HFSS of the metasurface-based humidity sensor with ELC resonators and the Nafion 117 sensitive material.

The meta-atom has an area of 18 × 18 mm^2, and the periodicity of the array is carefully designed to minimize coupling effects between adjacent cells. This optimization aims to enhance the amplitude peak by maximizing each meta-atom's individual contribution. In previous studies [6, 7], the single ELC resonator was employed in chipless Radio-Frequency Identification (RFID) sensors. However, due to its passive nature,

its performance was limited to relatively weak scattering capabilities given the low radar cross section (RCS) σ of the tag. In contrast, the metasurface approach proposed here is expected to significantly enhance the sensor's response and scattering efficiency given its intrinsically higher RCS. This performance gain is accompanied by a moderate increase in footprint, which is a valuable trade-off considering the substantial functional improvement.

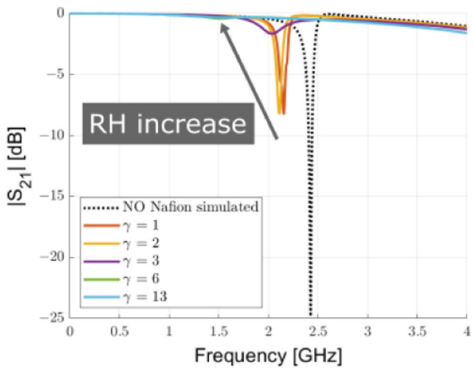

(*a*)

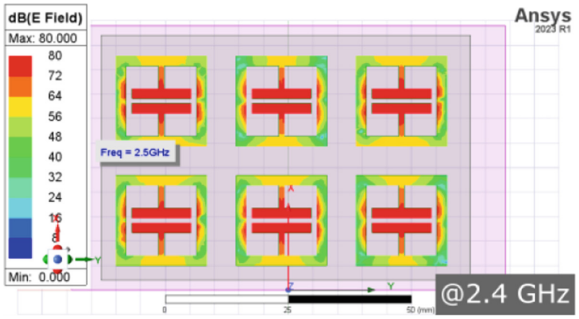

(*b*)

Fig. 2. In (*a*) the frequency shift and peak attenuation of the FSS sensor resonance peak as RH increases. In (*b*) the magnitude of the electric field at the resonance frequency, i.e., 2.4 GHz, without Nafion 117.

The frequency response and magnitude of the electric field at the resonance are proposed in Fig. 2. The tag is placed inside a rectangular air box where perfect electric and magnetic (PEC and PMC) boundary conditions are applied to confine the electromagnetic radiation. The excitation is provided through the mode of the waveguide ports placed parallel to the substrate with a plane wave impinging the sensor in the $+\hat{z}$ direction. Specifically, the simulation setup has been accurately studied to induce an electric field (E-field) between the capacitive plates, being the main mechanism to realize the

resonance, as shown in Fig. 2(b). The response of the tag is analyzed via the S_{21} scattering parameter, and particularly its negative peak in the magnitude. The FSS is indeed expected to allow signal transmission at all frequencies, except for the resonant one.

The metasurface sensor is designed on a transparent polyethylene terephthalate (PET) substrate of height $h_{\text{sub}} = 0.168$ mm, while the conductive material used for the ELC resonators is silver (Ag). The system operates at 2.4 GHz when no material is present (see black dotted line in Fig. 2(a)). Inserting the polymer between the plates causes the resonance frequency shift in relation to the material's complex dielectric constant variation. Specifically, the ELC internal plates are filled with Nafion 117, a polymer material recognized for its strong interaction with water, commonly used in fuel cells and explored in our previous studies [8, 9]. In simulation, the increasing γ states of Nafion 117 correspond to increasing relative-humidity (RH) states that are modeled through different complex permittivity values as in [8]. Simulations show the expected reduction of the peak and the shift of its resonant frequency as the γ value increases (see Fig. 2(a)).

3 Fabrication and Preliminary Experimental Validation

The metasurface humidity sensor has been fabricated with the Voltera NOVA microdispenser, that is suitable for the fabrication of flexible and printed electronics. The meta-atoms feature an Ag layer with a thickness $T_{\text{ELC}} = 30$ μm. The final prototype, reported in Fig. 3(a), is presented with dimensions of 50 × 80 mm, resembling a badge. A preliminary experimental validation of the device has been carried out utilizing double-ridge Horn antennas for wireless reading connected to an Agilent ENA Series Vector Network Analyzer (VNA) up to 3 GHz. The measurement setup is proposed in Fig. 3(b). The antennas are characterized by antenna gains $G = G_{Tx} = G_{Rx} = +11$ dBi and are positioned 60 cm apart, with the climatic chamber containing the FSS sensor placed centrally between them. The centers of the antennas are aligned with the center of the tag with the final aim to maximize the sensor response. The antennas generate a plane wave with its electric field oriented along the tag's x-axis, i.e. parallel to the field lines established between the capacitive plates.

In general, the magnitude of the insertion loss $|S_{21}|$ is calculated as the ratio between the transmitted power (P_{Tx}) and the received power (P_{Rx}). For a bistatic configuration, this is expressed according to the approach presented in [10] as follows:

$$|S_{21}| = \sqrt{\frac{P_{Rx}}{P_{Tx}}} = \sqrt{\sigma}\frac{G\lambda}{\left(2\sqrt{\pi}\right)^3 R^2},$$

where R is the reading distance and λ is the wavelength at the working frequency.

The formula indicates that the sensor response parameter, observed through $|S_{21}|$, can be enhanced by increasing the sensor's radar cross section σ, as achieved with the metasurface-based approach. Alternatively, for a fixed $|S_{21}|$ level, an increase in RCS enables a longer reading distance R, allowing the sensor to be monitored from greater distances.

The sensor response signal has been initially evaluated by placing the designed FSS metasurface between the transmitting (Tx) and the receiving (Rx) antennas obtaining

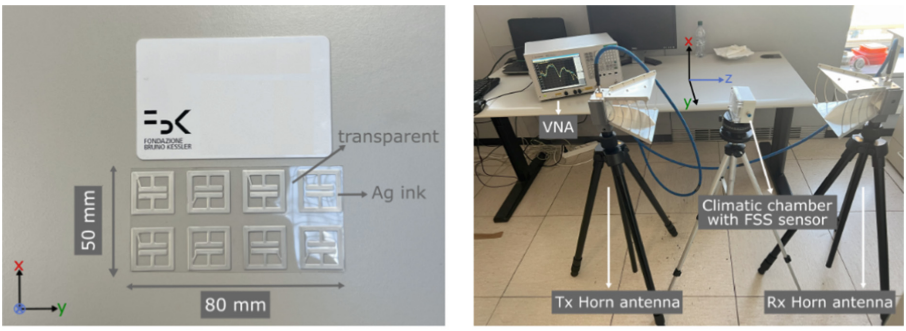

(*a*) (*b*)

Fig. 3. In (*a*) picture of the metasurface-based humidity sensor fabricated on the transparent and flexible PET substrate using a silver micro-dispensed solution. A badge is placed near the device for dimensional comparison. In (*b*) a picture of the measurement setup is shown with the FSS sensor placed in a climatic chamber between two commercial wideband double-ridge Horn antennas connected to a VNA for |S21| signal acquisition in dB.

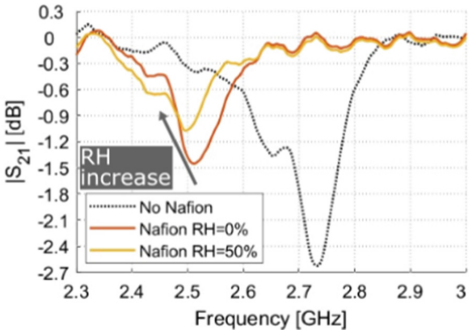

Fig. 4. Experimental results demonstrate the resonant behavior of the stand-alone metasurface-based sensor (black dotted line) and the expected frequency shift and attenuation of the resonance peak when Nafion 117 sensitive material is present on top of the ELC resonators and RH increases.

a resonant behavior of the tag shifted of about 0.4 GHz with respect to simulations (black dotted line in Fig. 4). The $|S_{21}|$ parameter has been, thus, measured in presence of the Nafion 117 material with two different levels of relative humidity: RH = 0% and RH = 50%. As expected, the negative peak of the transmitted signal decreases and shifts as the humidity level increases, corroborating the sensing behavior of the designed metasurface. Further experimental investigations are currently underway to assess the sensor's response and recovery times, sensitivity, and repeatability.

4 Conclusions

The proposed sensor is easy to produce and can be scaled to work across different frequency bands based on the microwave sensing application requirement. Its transparency and flexibility make it easy to seamlessly integrate it as a tag or label into any product.

We seek to merge in this study the passive nature of chipless RFIDs with the enhanced characteristics enabled by metasurfaces.

Acknowledgement. This work has been supported by the Project "Smart ElectroMagnetic Environment in TrentiNo-SEME@TN" funded by the Autonomous Province of Trento (CUP: C63C22000720003).

References

1. Katoch K, Jaglan N, Gupta SD (2019) A review on frequency selective surfaces and its applications. 2019 International Conference on Signal Processing and Communication (ICSC), NOIDA, India, pp 75–81
2. Jaya Marindra AM, Tian GY (2020) Chipless RFID sensor for corrosion characterization based on frequency selective surface and feature fusion. Smart Mater Struct 29(12):125010
3. Kandwal A, Dutt S, Liu LWY et al (2024) Frequency selective metasurface-based radio frequency glucose sensor with a periodic array of meta cells. Sci Rep 14:25716
4. Shishir IR, Mun MD, Kim H-C, Kim JW, Kim J (2017) Frequency-selective surface-based chipless passive RFID sensor for detecting damage location. Struct Control Health Monit 24:e2028
5. Lorenzo J, Guillén A, Villarino R, Girbau D (2016) Modulated frequency selective surfaces for wearable RFID and sensor applications. IEEE Trans Antennas Propag 64:4447–4456
6. Mulloni V et al (2023) Sub-ppm NO2 detection through chipless RFID sensor functionalized with reduced SnO2. Chemosensors 11:408. https://doi.org/10.3390/chemosensors11070408
7. Mulloni V, Marchi G, Gaiardo A, Valt M, Donelli M, Lorenzelli L (2024) Applications of chipless RFID humidity sensors to smart packaging solutions. Sensors 24:2879. https://doi.org/10.3390/s24092879
8. Marchi G, Mulloni V, Manekiya M, Donelli M, Lorenzelli L A (2020) Preliminary microwave frequency characterization of a nafion-based chipless sensor for humidity monitoring. 2020 IEEE SENSORS, Rotterdam, Netherlands, pp 1–4
9. Marchi G et al (2024) Chipless and batteryless microwave sensor cell for remote detection of humidity. 2024 IEEE International Symposium on Antennas and Propagation and INC/USNC-URSI Radio Science Meeting (AP-S/INC-USNC-URSI), Firenze, Italy, pp 2245–2246
10. Rance O, Perret E, Siragusa R, Lemaitre-Auger P (2017) RCS Synthesis for Chipless RFID, Theory and Design. Elsevier Science

Optical Sensors

Advancing Label-Free Biosensing Technologies Using Integrated Optical Circuits

R. Favaretto[1,2,3(✉)], N. Ardoino[2], G. Pucker[3], M. Bernard[3], N. Bellotto[2], N. Srocka[2], and C. Guardiani[2]

[1] Department of Physics, University of Trento, Via Sommarive 14, 38123 Trento, Italy
rachele.favaretto@unitn.it
[2] FTH s.r.l., Via Sommarive 18, 38123 Trento, Italy
[3] Fondazione Bruno Kessler, Via Sommarive 18, 38123 Trento, Italy

Abstract. Biosensors are powerful tools for detecting specific molecules by leveraging biological interactions to generate measurable signals. This research focuses on the development of advanced label-free biosensors using Silicon Nitride integrated optical circuits, employing Mach-Zehnder Interferometer (MZI) structures as the sensing elements. MZIs, which combine waveguiding and interferometry, offer high sensitivity by detecting phase shifts induced by analyte binding in real time. The development process encompasses component simulation, chip design, chip fabrication, packaging, optical and electrical characterization and biological testing. Although the Silicon Nitride sensor is still under development, preliminary results from silicon waveguide-based MZI devices have demonstrated their ability to accurately monitor binding kinetics. A key advantage of Silicon Nitride is its compatibility with visible wavelengths, where optical losses are lower when using aqueous cladding, as is common in biological testing. This research holds significant potential for advancing label-free optical biosensing technologies, with applications spanning healthcare, environmental monitoring, and beyond.

Keywords: Biosensor · Mach-Zehnder Interferometer · Photonic Integrated Circuit · Silicon Nitride · Label-free Detection · Point of Care

Biosensors are innovative tools that leverage the specificity of biological interactions to detect molecules of interest, such as proteins, viruses or bacteria. The analyte binds to a bio-recognition element (like an antibody or aptamer), triggering a reaction that is converted into a measurable signal by a transducer. The sensitivity of the sensor is defined as the output response per unit change of the total quantity of the target analyte molecules bound to the surface of the waveguide.

Waveguide-based optical biosensors are particularly interesting because they can be used as label-free sensors directly binding the biorecognition elements on their surface and because they can be integrated into miniaturized lab-on-chip technologies.

The light is directed in the waveguide, a transparent material with a refractive index higher than its surrounding environment, the silicon oxide substrate and the biofluid. What is important for sensing is the fact that the electric field is not strictly confined in the waveguide but has exponentially decaying tails in the surrounding materials as

C. Di Natale et al. (Eds.): AISEM 2025, LNEE 1497, pp. 267–273, 2025.
https://doi.org/10.1007/978-3-032-08271-8_42

shown in Fig. 1. Any refractive index changes near to the waveguide surface, like the one caused by the specific binding of an analyte to an antibody, yields to a detectable change of the effective refractive index of the mode.

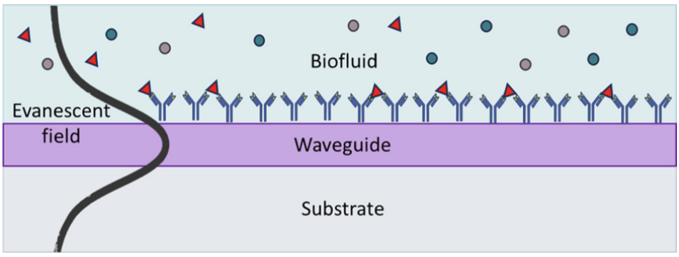

Fig. 1. Schematic of a biofunctionalized slab waveguide**.**

Among the various types of waveguide-based optical biosensors, microring resonators and integrated asymmetric Mach–Zehnder interferometers (MZIs) are among the most extensively studied. In particular, waveguide interferometers hold significant importance due to their ability to combine two highly sensitive techniques—optical waveguiding and interferometry—resulting in biosensors with enhanced sensitivity, well-suited for point-of-care applications [1]. The sensing mechanism [2] can be schematically described as follows. The input light beam is directed to the sensor's input and then equally split into two arms. One arm, the sensing arm, is biofunctionalized with biorecognition elements on the surface for detection, while the other, the reference arm, includes a phase shifter. The light is then recombined using a 2×2 coupler. The output optical power is converted by a photodiode into two complementary current signals having the shape of squared sine and cosine waves modulated by the phase difference between the two arms. When a binding event occurs, the refractive index of the medium around the sensing arm changes, introducing a phase shift. This phase shift can be counterbalanced by the phase shifter in the control arm.

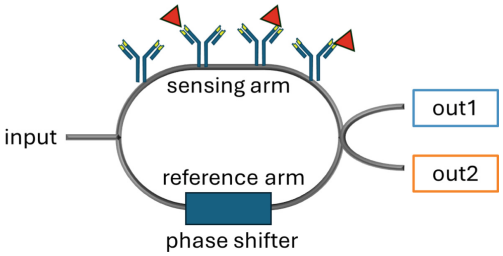

Fig. 2. Schematic of a Mach-Zehnder Interferometer bio sensor**.**

The power used to maintain the MZI in phase is proportional to the amount of analyte bound in the sensing arm, providing a quantitative measurement of the analyte concentration in the biofluid. A sketch of a MZI biosensor is shown Fig. 2.

The workflow to develop a biosensor based on Mach-Zehnder interferometers includes several key steps. In the first step, the key optical components are thoroughly simulated; then the integrated optical circuit is designed; the third step entails fabricating the circuit; and finally, the resulting physical structure is fully characterized by means of optical and biological tests.

1 Wavelength selection

The design of an optoelectronic biosensor chip begins with the selection of an appropriate operating wavelength. Photonic biosensors typically operate within the visible spectrum, as water, the primary constituent of most biofluids, exhibits minimum optical absorption in this range. Nonetheless, in a previous project, we employed the 1550 nm telecom wavelength using a silicon waveguide platform. Despite the relatively high absorption losses in water (~10 dB/cm), this wavelength offers practical advantages: it is supported by multiple foundries and chip fabrication at this wavelength is both mature and cost-effective, yielding reproducible results. In the present work, we investigated both the telecom-band (1550 nm) and near-visible band (780 nm), to evaluate their respective advantages in terms of technical performance and industrial scalability.

2 Waveguide Geometry

Following the selection of the operating wavelengths, the next step involved the simulations of key photonic chip components. A fundamental design decision at this stage was the determination of the optimal waveguide geometry, as this constitutes the fundamental building block of all optical components on the chip.

Simulations were conducted for waveguides with heights of 150 nm and 350 nm and widths ranging from 500 nm—the lithographic current resolution limit achievable at FBK cleanroom—to 2500 nm. A schematic of the simulated cross-section is shown in Fig. 3a while Fig. 3b illustrates a representative example of the resulting electric field. The simulations were performed using *modesolverpy* Python library. The structure consists of a silicon substrate with a 5 μm bottom oxide layer, overlaid by a silicon nitride waveguide with parameterized height and width. Finally, the cladding was evaluated in two configurations: water and oxide.

The simulation allowed us to calculate both the real and imaginary parts of the effective refractive index of the guided mode(s) as well as the spatial distribution of the electric field at each point within the simulation window. Key parameters that could be extracted from the simulation included the effective refractive index of guided modes, mode confinement within the waveguide core, mode fraction, absorption losses and bulk sensitivity—a metric that quantifies the sensitivity of the effective refractive index to variations in the cladding refractive index.

Only parameter combinations with water cladding that supported single-mode waveguides (TE00) and acceptable optical losses— defined as absorption below -15 dB/cm—were considered for further analysis. The 780 nm wavelength with a waveguide height of 350 nm was excluded, as it did not support single mode within the tested width range. Configurations wl780 nm-h150 nm and wl1550 nm-h350 nm exhibited

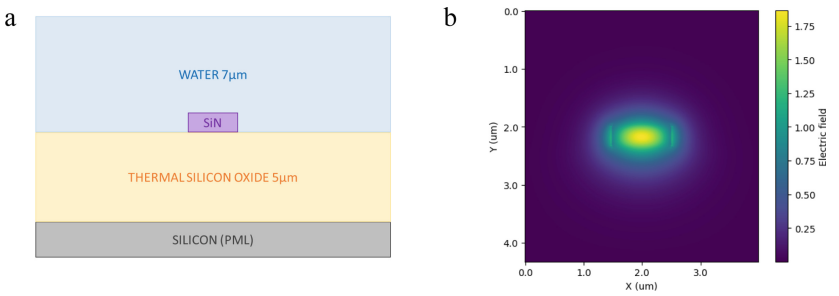

Fig. 3. **a** Cross-sectional design of the simulation window, from bottom to top: Silicon substrate, bottom oxide layer, Silicon nitride waveguide, water cladding. **b.** Example of the simulated electric field in the waveguide. The boundary conditions for the simulation are PML**.**

slightly higher effective indices than wl1550 nm-h150 nm, resulting in less confined optical modes. All configurations demonstrated a high TE mode fraction. As expected, wl1550 nm designs showed increased absorption losses in water but offered somewhat better sensitivity. The results for refractive index, optical absorption losses, and bulk sensitivity are reported in Fig. 4.

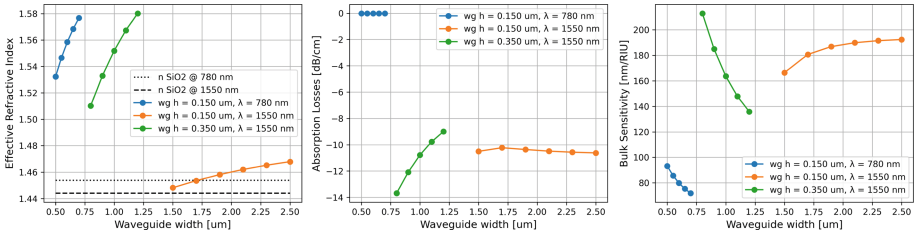

Fig. 4. Results of the simulations (water cladding) for the effective refractive index, absorption losses and bulk sensitivity of the 3 configurations wl780 nm-h150 nm, wl1550 nm-h150 nm and wl1550 nm-h350 nm in the widths range allowing single-mode TE00 propagation**.**

Among the valid configurations, a trade-off analysis considering loss, sensitivity, and the lithographic constraints of FBK fabrication process led to the selection of wl780 nm-h150 nm-w600 nm, wl1550 nm-h150 nm-w2100 nm and wl1550 nm-h350 nm-w1000 nm.

2.1 Bending Radius

Following the selection of the waveguide cross-sections, additional simulations were conducted to determine their minimum bending radii required to maintain low optical losses due to curvature. This was assessed by comparing the effective indices of bent vs. straight waveguides, within a <0.003% tolerance for the difference. The results indicated that the wl1550 nm-h150 nm-w2100 nm waveguide required a minimum bending radius of approximately 600 µm— due to weak mode confinement—which was unsuitable for

compact chip layouts. In contrast, the 780 nm and 1550 nm configurations exhibited significantly smaller bending radii (~80 μm and ~150 μm respectively) and were thus retained for further development.

3 Simulation of the Directional Couplers

Following definition of the two operating wavelengths and of their respective minimum bending radii, the next design step was to simulate the couplers required for the MZI configuration. One common method for implementing waveguide couplers is by using straight parallel sections where the evanescent field of one overlap with that of the adjacent guide, forming a directional coupler. This configuration allows optical power to transfer gradually from one waveguide to the other. By carefully optimizing the gap between the guides and the length of the coupling region, the coupling ratio can be precisely controlled. For our case the target splitting ratio was 50:50.

The first step to calculate the optimal coupling length L is to determine the refractive indices of the two modes propagating in the coupled waveguide system. The difference between these indices, Δn, is calculated. Assuming that initially all the input power is in waveguide 1 the coupling length to achieve a desired power transfer to waveguide 2, can be determined by solving Eq. (1):

$$L = [\lambda/(\pi \cdot \Delta n)] \cdot sin^{-1}\left[(P_2/P_1)^{1/2}\right] \quad (1)$$

The following table provides a summary of the resulting values that were found in this case (Table 1).

Table 1. Table captions should be placed above the tables.

Wavelength	Height	Width	Coupler gap	Coupler width
780 nm	150 nm	600 nm	600 nm	103.5 um
1550 nm	350 nm	1000 nm	835 nm	50 um

4 Chip Design

The sensor integrates all components onto a single photonic chip, including the optical input/output interfaces, waveguides, MZIs arms exposed to analyte-containing fluids, and metal structures for phase shifting.

As illustrated in Fig. 5 the chip layout is organized as follows: the left side hosts one optical input and 16 optical outputs. The middle section accommodates the phase shifters while all the MZI sensor are placed on the right side of the chip. This floorplan has been chosen to allow for a sharp separation between optical and electro-optical components – namely the phase shifters.

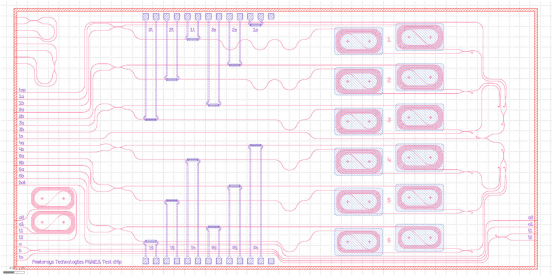

Fig. 5. Layout of the chip for telecom wavelength.

A well is etched above each MZI to allow biofluids to interact with the sensing region. This is accomplished by selectively removing the oxide dielectric above the interferometer arms through a combination of dry and wet etching processes. The exposed length of each MZI arm is varied across different instances in order to study the impact of interaction length on the sensor's sensitivity. In addition to MZI arm length, a second key parameter that is varied is the optical path difference (ΔL) between the two arms. This variation is intended to evaluate the optimal tradeoff between free spectral range (FSR) and sensitivity.

5 Chip Fabrication and Packaging

The design is realized through precise photolithographic processes, using multiple masks to pattern waveguides, metal structures, pad opening, sensor window areas and finally deep trenches and facets. Previous fabrication experience [3] has informed the current chip designs to ensure robustness and manufacturability. The next steps are packaging via wire bonding to a custom-designed PCB and encapsulation with the microfluidic chamber. The chip will then be used with the Diamir2 diagnostic read-out machine, owned by FTH S.r.l.

6 Biological Testing

After fabrication, the biosensor's functionality is validated using biological tests. Although the Silicon Nitride MZI-based sensor is still under fabrication, preliminary results from Silicon MZI sensors provide a basis for characterizing analyte-antibodies interactions, monitoring binding kinetics.

The Fig. 6 below shows an example of an outcome of a biological test on a Silicon MZI sensor, using a sandwich strategy to enhance the signal output. MZIs 2 and 6 were functionalized with a-CRP antibodies, MZIs 4 and 5 with a-PCT antibodies, and MZI 3 served as a reference. The sensors are primed with a buffer solution, then the bio-fluid with 0.1 nM CRP and 1 nM PCT protein is flowed on top of the sensors to bind the analytes. Finally, a step with two detection antibodies is applied after a short buffer cleaning step to complete the test sequence. The binding behavior matches theoretical models [3] and is consistent with previous experimental results in the literature, such

as [4], which employs a similar integrated MZI setup, though without a phase shifter, thus confirming the feasibility of MZI-based optical sensors for real-time quantitative analysis.

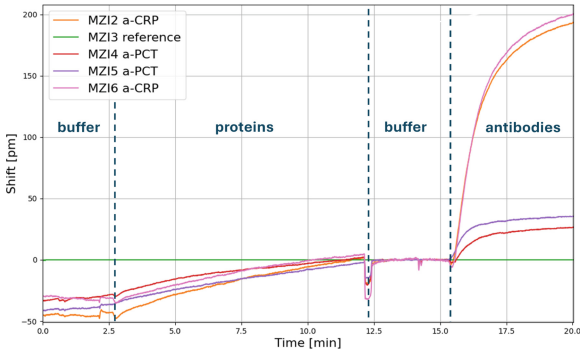

Fig. 6. Example of biological test.

While the fabrication of Silicon Nitride MZI-based biosensors is ongoing, this research holds significant promise for advancing label-free optical biosensing technologies. Key goals include achieving enhanced sensitivity, reducing optical losses and signal-to-noise ratios, and integrating alternative phase-shifting mechanisms to improve sensor performance.

Acknowledgments. This research was supported in part by the Autonomous Province of Trento, L.P. 6 luglio 2023, n. 6 e ss.mm.ii., project FANES Cup: C69J24000350001.

References

1. Armani A, Chalyan, T, Sampson D (eds.). (2024) Biophotonics and biosensing: from fundamental research to clinical trials through advances of signal and image processing. 1st Edition, pp 15–41. Elsevier
2. Patent (2019) Dispositivo opto-elettronico per la rilevazione di una sostanza dispersa in un fluido. Filed 23-01-2017 N. 102017000006640 Issued: 27 Sep 2019
3. Favaretto R, et al (2025) A ring resonators optical sensor for multiple biomarkers detection. Talanta
4. Besselink G et al (2022) Asymmetric mach-zehnder interferometric biosensing for quantitative and sensitive multiplex detection of Anti-SARS-CoV-2 antibodies in human plasma. Biosensors 12:553

Object Recognition with IMUs and Convolutional Neural Networks for Wearable Systems

Daniella Shebly[1,2(✉)], Christian Gianoglio[1], Hussein Chibli[2], and Maurizio Valle[1]

[1] DITEN, University of Genoa, Genoa, Italy
daniella.shebly@edu.unige.it
[2] MECRL Laboratory, Lebanese University, Beirut, Lebanon

Abstract. This study presents a lightweight 1D-Convolutional Neural Network (1D-CNN) for object recognition on edge devices utilizing Inertial Measurement Unit (IMU) sensors positioned on the thumb and index finger to capture motion data. The proposed system achieves a classification accuracy of 91%, underscoring its effectiveness in distinguishing four object shapes. Optimized for embedded applications, the model provides an inference time of 110.1 ms and energy consumption of 2.27 mJ per inference, highlighting its efficiency and suitability for real-time deployment. These results demonstrate the potential of the developed solution for enabling intelligent and energy-efficient wearable systems.

Keywords: 1D-Convolutional Neural Network · embedded system · wearable sensors

1 Introduction

The increase in technology allowing us to build wearable devices to improve the interaction of bodies and their surroundings has significantly advanced with integrating Inertial Measurement Units (IMUs) into wearable systems [1, 2]. IMUs—comprising accelerometers and gyroscopes—offer a non-visual approach to recognizing objects by capturing detailed motion dynamics during user interaction. Wearable systems can infer object properties by analyzing motion patterns during object manipulation, enhancing human-computer interaction (HCI), assistive technologies, and robotics applications.

Recent advances have expanded the applicability of IMU-based object recognition beyond simple classification tasks. For example, multi-IMU fusion techniques have been explored to improve recognition accuracy by integrating motion data from multiple body parts, such as wrists, fingers, and arms [3]. Moreover, sensor fusion with additional modalities, such as electromyography (EMG) and force sensors, has been investigated to improve the robustness of object recognition in complex manipulation tasks [2, 4]. These multimodal approaches improve classification performance and provide deeper insights into user intent and interaction patterns.

C. Di Natale et al. (Eds.): AISEM 2025, LNEE 1497, pp. 274–279, 2025.
https://doi.org/10.1007/978-3-032-08271-8_43

Several studies have demonstrated the potential of IMU-based object recognition. For example, Liang et al. [5] introduced dual-ring IMU systems, which excel at capturing fine motor tasks for detailed motion analysis. Similarly, Hazman et al. [6] leveraged IMU-based solutions for rehabilitation applications, tracking hand-object interactions to assess motor function. Other works, such as Connolly et al. and Lin et al. [7, 8], have validated the use of IMUs for real-time gesture recognition, paving the way for their application in identifying the shapes and sizes of objects. Additionally, Jaramillo et al. [9] discuss a system for real-time recognition of human activity using IMU and encoder sensors in a wearable exoskeleton robot, leveraging deep learning networks for enhanced performance. Despite these advancements, several challenges remain in adapting IMUs to precise and reliable object recognition, including power efficiency, real-time processing constraints, and variability in motion precision between different users. The application of deep learning methods, such as 1D-convolutional neural networks (1D-CNN), has demonstrated notable improvements in classification performance [10, 11], but achieving a balance between computational complexity and real-time execution remains an active area of research [12].

A low-power embedded system for object detection based on inertial data gathered from wearable IMUs is proposed in this paper. Using a lightweight 1D-Convolutional Neural Network (1D-CNN) designed for edge deployment, the system can classify four distinct 3D object shapes in real time. When manipulating objects, two 6-axis IMU sensors on the thumb and index finger record fine-grained motion patterns. The results underscore the feasibility and efficiency of IMU-based object recognition, highlighting its potential for integration into wearable devices and applications in robotics [12], human-computer interaction [6, 13, 14], and rehabilitation technologies. Future research should explore the integration of IMU-based recognition, enabling more intuitive and immersive human-computer interactions [15].

The key contributions of this work include:

- A 1D-Convolutional Neural Network (1D-CNN) model for IMU-based object recognition, achieving **91%** classification accuracy across four 3D geometric shapes.
- A lightweight and energy-efficient design, enabling real-time operation with an inference time of **110.1 ms** and energy consumption of **2.27 mJ** per classification task, making it suitable for edge devices.
- Deployment on an embedded **STM32** microcontroller, demonstrating the feasibility of real-time IMU-based classification in wearable applications.

The remainder of this paper is structured as follows: Sect. 2 details the methodology, including data collection, processing, and the CNN architecture. Section 3 presents the experimental results and performance evaluation. Finally, Sect. 4 concludes the paper and outlines future research directions.

2 Methodology

The proposed IMU-based object recognition framework is illustrated through the communication flow of the hardware in Figure 1. The experimental setup and the system architecture used for collecting and processing motion data are detailed in Figure 2. The

setup utilized two 6-axis Inertial Measurement Units (IMUs), each capable of capturing accelerometer and gyroscope data. These IMUs were strategically mounted on the top of the thumb and index finger to accurately measure fine-grained motion patterns associated with object manipulation. The motion data was sampled at a frequency of 200 Hz. The IMUs were connected to an STM32F401RE Nucleo-64 development board for data acquisition and pre- processing. The experimental protocol involved four subjects, each performing a series of object manipulation trials. The participants were instructed to handle four distinct geometric shapes: (1) a large cylinder with a radius of 2.5 cm and a height of 7 cm, (2) a small cylinder with a radius of 2 cm and a height of 4 cm, (3) a circle with a radius of 2 cm, and (4) a cube with a volume of (4 cm^3). Each subject performed 30 trials for each shape, each trial involving 3 seconds of continuous manipulation. This experimental design resulted in a total of 480 trials, providing a robust dataset for training and evaluating the proposed recognition system. The dataset can be represented as:

$$\mathrm{D} = (\mathrm{X}_i, y_i);\ \mathrm{X}_i \in R^{600\times 12},\ y_i \in \{\text{cube, sphere, smallcylinder, largecylinder}\};\quad (1)$$

$$i = 1, ..., 480\}$$

Fig. 1. Block diagram of the proposed system

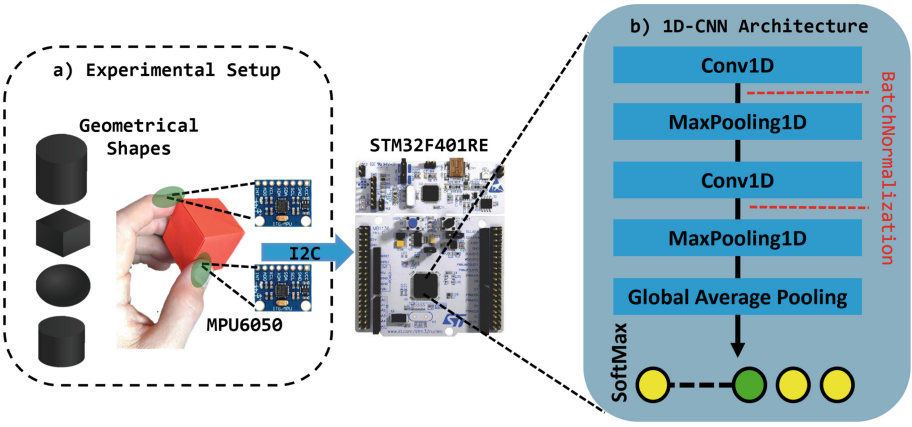

Fig. 2. a) Experimental Setup; b) 1-D CNN architecture.

The dataset was initially divided into training (70%), validation (15%), and testing (15%) subsets using stratified sampling to preserve class distribution. The IMU data, represented as a 600 × 12 tensor (600 samples, 12 channels, 6 axes from 2 IMUs), were processed. A grid search approach was used for model selection, evaluating multiple 1D-CNN architectures and hyperparameters. Early stopping was applied during training to prevent overfitting, with the final model selected based on validation performance. A 1D convolutional neural network (CNN) was designed using TensorFlow to process sequential IMU data and classify object manipulation patterns. This architecture was chosen because of its effectiveness in capturing spatial and temporal dependencies within time-series sensor data. The network consists of multiple Conv1D layers that apply learnable filters across the temporal dimension, enabling the extraction of local motion features from the IMU signals. Each convolutional layer is followed by batch normalization, which standardizes activations to improve stability and accelerate training convergence. To further refine feature selection and prevent overfitting, Max- Pooling1D layers are incorporated, reducing the dimensionality of the feature maps while preserving essential motion characteristics. After the convolutional and pooling layers, a global average pooling layer is applied to condense the extracted features into a compact representation. This approach significantly reduces the number of trainable parameters compared to fully connected layers, minimizing computational complexity while maintaining key information. The final classification layer is a softmax activation function, which outputs probabilities corresponding to one of four predefined object classes. Once trained, the model was converted to TensorFlow Lite to enable efficient deployment on edge devices with limited computational resources. The optimized model was then deployed on an STM32F401RE Nucleo-64 development board, allowing real-time inference of object manipulation patterns directly on embedded hardware. This deployment enables low-latency classification, making the system suitable for applications such as wearable devices, robotics, and human-computer interaction.

3 Results

The performance of the proposed 1D-CNN framework for real-time object classification is summarized in Table 1. The model achieved a classification accuracy of 91%, demonstrating its robustness and reliability in distinguishing between the four object classes based on IMU data. The framework's efficiency is evident in its inference time of 110.1 milliseconds, which ensures low-latency operation suitable for real-time applications such as wearable systems and embedded devices. Furthermore, the model exhibited an energy consumption of only 2.27 millijoules per inference.

Table 1. Experimental Results

Model	Accuracy (%)	Inference (ms)	Energy (mJ)
1-D CNN	91	110.1	2.27

4 Conclusion

In this study, we successfully developed and demonstrated a lightweight and efficient 1D-Convolutional Neural Network (1D-CNN) model optimized for real-time object recognition using IMU sensors in wearable systems. By positioning two strategically placed 6-axis IMUs on the thumb and index finger, we effectively captured detailed motion patterns associated with object manipulation, achieving a classification accuracy of 91% across distinct object types. The optimized 1D-CNN model not only proved highly accurate but also exhibited impressive performance on edge devices, with an inference time of 110.1 ms and low energy consumption of just 2.27 mJ per inference. These performance metrics under- score the suitability of the model for deployment in embedded systems where computational resources and power efficiency are critical.

Our results highlight the practical potential of IMU-based object recognition for integration into various wearable applications, including robotics, assistive technologies, rehabilitation devices, and advanced human-computer interaction systems. Moving forward, expanding the system to include additional IMU sensors and multi-finger wearable configurations could further enhance accuracy and enable the recognition of more complex manipulation patterns. This work lays a robust foundation for future advancements in intelligent wearable technologies.

References

1. Fei F et al (2021) Development of a wearable glove system with multiple sensors for hand kinematics assessment. Micromachines 12(4):362
2. Zhang X et al (2019) Cooperative sensing and wearable computing for sequential hand gesture recognition. IEEE Sens J 19(14):5775–5783
3. Noronha B et al (2021) Exoskeletal devices for hand assistance and rehabilitation: a comprehensive analysis of state-of-the-art technologies. IEEE Trans Med Robot Bionics 3(2):525–538
4. Li W et al (2021) Gesture recognition using surface electromyography and deep learning for prostheses hand: state-of-the-art, challenges, and future. Front Neuro Sci 15:621885
5. Liang C et al (2021) Dualring: Enabling subtle and expressive hand interaction with dual imu rings. Proc ACM Interact Mobile Wearable Ubiquit Technol 5(3):1–27
6. Hazman MAW et al (2020) Imu sensor-based data glove for finger joint measurement. Indonesian J Electr Eng Comput Sci 20(1):82–88
7. Connolly J et al (2017) Imu sensor-based electronic goniometric glove for clinical finger movement analysis. IEEE Sens J 18(3):1273–1281
8. Lin B-S et al (2017) Data glove system embedded with inertial measurement units for hand function evaluation in stroke patients. IEEE Trans Neural Syst Rehabil Eng 25(11):2204–2213
9. Jaramillo IE et al (2022) Real-time human activity recognition with imu and encoder sensors in wearable exoskeleton robot via deep learning networks. Sensors 22(24):9690
10. Gianoglio C et al: (2021) 1-d convolutional neural networks for touch modalities classification. In: 2021 28th IEEE international conference on electronics, circuits, and systems (ICECS). IEEE, pp 1–6
11. Kiranyaz S et al (2021) 1d convolutional neural networks and applications: a survey. Mech Syst Signal Process 151:107398

12. Yin C et al: (2021) Quantitative evaluation of hand functions using a wearable glove with multiple sensors:. In: 2021 IEEE International Conference on Real-time Computing and Robotics (RCAR). IEEE, pp 1093–1098
13. Wang D, et al: (2024) Wearable electronic glove and multi-layer para-lstm-cnn based method for sign language recognition. IEEE Internet Things J.
14. Knorr B, et al: (2005) Quantitative measures of functional upper limb movement in persons after stroke. In: Conference Proceedings. 2nd International IEEE EMBS Conference on Neural Engineering, 2005. IEEE, pp 252–255
15. Huang X, et al: (2023) Imu-based interaction in augmented reality. J Augmented Virtual Reality **7**(2):89–102. https://doi.org/10.1007/s41095-023-0256-7

A System for the Identification of Olive Oil Adulterations Based on Optical Sensors and Fuzzy Logic

I. Dal Chiele(✉), M. Manekiya, and M. Donelli

Department of Civil, Environmental and Mechanical Engineering, University of Trento, Via Mesiano 77, 38100 Trento, Italy
{irene.dalchiele,m.manekiya,massimo.donelli}@unitn.it

Abstract. Edible olive oil is a fundamental component of the Mediterranean diet, valued for its health benefits and economic importance. However, fraudulent practices involving the adulteration of virgin olive oil with lower-quality oils have become widespread, posing risks to both market integrity and consumer health. While conventional detection methods exist, they often require costly equipment or specialized operators. This study presents a novel, cost-effective, and compact optical sensor system designed to identify olive oil adulterations efficiently. The proposed device integrates three optical sensors and light sources operating in the Ultraviolet, Visible, and Infrared frequency bands. It functions in both reflection and transmission modes, providing a spectrogram analysis interpreted through a fuzzy logic system to detect oil adulterations based on reference samples. The system is equipped with wireless connectivity, enabling seamless data transmission to smartphones or computers. The analysis requires only a minimal oil sample and is completed within seconds. Experimental results demonstrate the device's ability to distinguish adulterated oil samples, highlighting its potential as a practical and accessible solution for ensuring olive oil authenticity.

Keywords: Olive oil adulteration · Optical sensor · Food fraud detection · Spectroscopy · Fuzzy logic analysis · Portable detection system

1 Introduction

Edible olive oil is the cornerstone of the Mediterranean diet, and due to its health benefits - as suggested by nutritionists - it should be the primary source of fat in the diet. Virgin olive oil not only contributes significantly to nutritional well-being but also holds high economic value, maintaining strong demand in global markets [1]. Its premium quality and widespread consumer preference have made it a valuable commodity, contributing substantially to international trade. However, the lucrative nature of the olive oil market has also given rise to fraudulent practices, most notably the mixing of lower-quality oils with genuine virgin olive oil. Such adulteration compromises the nutritional integrity of the product, erodes consumer trust, and introduces harmful chemical substances that can pose serious health risks.

C. Di Natale et al. (Eds.): AISEM 2025, LNEE 1497, pp. 280–290, 2025.
https://doi.org/10.1007/978-3-032-08271-8_44

The economy is greatly impacted and a diverse range of stakeholders are affected by the practice of diluting or contaminating genuine olive oil. Reputable producers and traders are financially burdened and the integrity of established brands are jeopardized by fraudulent practices that undermine the value of the product. Furthermore, these actions weaken consumer trust, complicate regulatory oversight, and impede international trade. The use of questionable additives can cause major health risks, making it crucial to have reliable and accessible methods to identify adulterated products.

To get a handle on this persistent issue, scientists created a variety of analytical tools to ferret out olive oil fraud. Older, more established techniques–well-documented in sources like [2] and [3]–typically involve chromatographic, spectroscopic, and even some good, old-fashioned chemical analyses to examine the oil's fundamental properties. Newer, more advanced methods, such as Nuclear Magnetic Resonance (NMR) spectroscopy [4] and Raman spectroscopy [5], provide a much more detailed picture of the oil's molecular structure, offering a more solid basis for confirming its authenticity. Even microwave sensor technology has demonstrated some potential for spotting adulteration in liquid foods, as outlined in [6, 7]. However, while these approaches generally offer high accuracy, they often require quite expensive equipment, fairly complex procedures, and specially trained personnel, which can make them less practical for routine use in smaller-scale settings.

Our approach combines artificial intelligence with fuzzy logic [8] to analyze spectrogram data from both reflection and transmission. By matching these optical "fingerprints" against a library of reference standards, our algorithm can detect when olive oil has been adulterated. Recognizing that many current methods are too expensive or require specialized skills, we've developed a compact, cost-effective, and user-friendly system based on an optical sensor [9, 10]. This method leverages how olive oil uniquely interacts with light, along with advanced data processing, to provide a reliable tool for protecting both economic interests and public health.

This work is structured as follows: Sect. 2 introduces the mathematical formulation related to the presented system, Sect. 3 describes the design of the system, Sect. 4 is devoted to the experimental assessment, Sect. 5 is focused on the results and Sect. 6 provides concluding remarks.

2 Mathematical Formulation

2.1 Spectroscopy Analysis

The system operates in both reflection and transmission modes, measuring spectral data in the range of 410 nm to 940 nm with an accuracy of 28.6 nW/cm^3 across eighteen channels. Mathematically, the intensity of the transmitted light I_t and reflected light I_r can be described using the Beer-Lambert law and Fresnel equations [11–13]:

1. **Transmission Mode**: The transmitted intensity is given by:

$$I_t = I_0 e^{-\alpha d} \tag{1}$$

where I_0 is the incident light intensity, α is the absorption coefficient of the sample, and d is the path length of light through the sample.

2. **Reflection Mode**: The reflected intensity at a given wavelength λ is governed by the Fresnel equations:

$$R = \left| \frac{n_1 - n_2}{n_1 + n_2} \right|^2 \tag{2}$$

where R is the reflectance, n_1 and n_2 are the refractive indices of the two media.

By analyzing the spectral data in both modes, the system provides a comprehensive assessment of the sample's optical properties, aiding in the detection of oil adulteration.

2.2 Fuzzy Logic

Fuzzy logic is a mathematical framework designed to handle imprecision and uncertainty, extending classical set theory by allowing elements to possess degrees of membership within a set rather than adhering to binary classification.

This study applies artificial intelligence techniques, specifically fuzzy logic, to assess oil adulteration. The fuzzy logic algorithm employed is based on the Mamdani inference method, originally introduced in [8].

The fuzzy inference system (FIS) comprises the following stages:

3. Fuzzification: Quantitative spectral data (ultraviolet, visible, and infrared frequencies) are mapped onto fuzzy sets using membership functions (Fig. 1).
4. Rule Base: A set of IF-THEN linguistic rules defines the correlation between spectral characteristics and the risk of adulteration.
5. Inference Engine: The Mamdani inference mechanism processes fuzzy inputs to derive a risk assessment (Fig. 1).
6. Defuzzification: The fuzzy output is converted into a crisp numerical value to quantify the level of adulteration risk (Fig. 3).

Mathematically, a fuzzy set A is defined by its membership function $\mu_A(x)$:

$$\mu_A(x) : X \rightarrow [0, 1] \tag{3}$$

where X represents the universe of discourse, and $\mu_A(x)$quantifies the degree to which x belongs to A. In this study, the risk factors associated with ultraviolet, visible, and infrared spectral data are modeled using membership functions $\mu_{UV}(x)$, $\mu_{VIS}(x)$, and $\mu_{IR}(x)$. These are represented using trapezoidal functions, which are defined as:

$$\mu_A(x) = \begin{cases} 0 & x \langle aorx \rangle d \\ \frac{x-a}{b-a} & a \leq x < b \\ 1 & b \leq x \leq c \\ \frac{d-x}{d-c} & c < x \leq d \end{cases} \tag{4}$$

where a, b, c, d define the trapezoidal shape, with b and c representing the core where membership is maximal.

The inference process follows the Mamdani approach, wherein fuzzy rules take the form:

$$IF\ x_1\ is\ A_1\ AND\ x_2\ is\ A_2\ THEN\ y\ is\ B \tag{5}$$

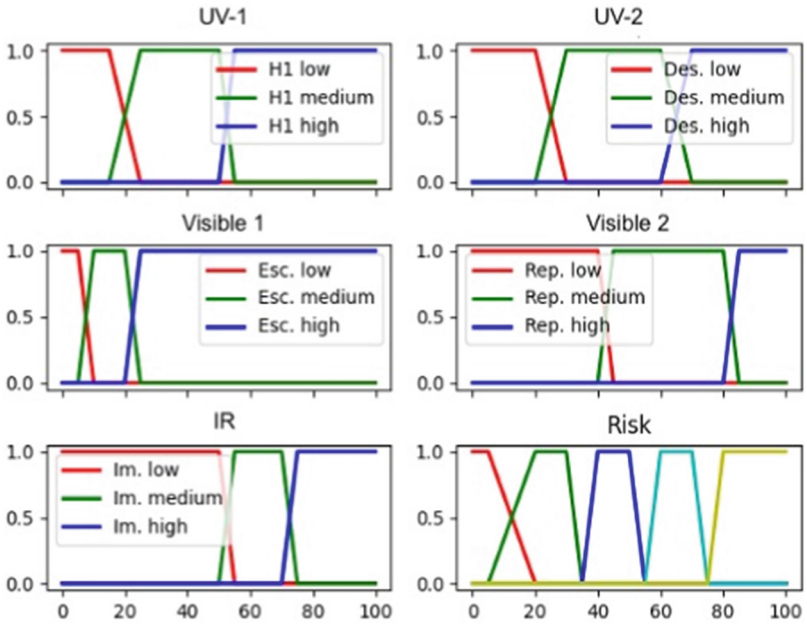

Fig. 1. Inference and risk fuzzy functions.

where A_1, A_2 are fuzzy sets representing spectral risk factors, and corresponds to the level of adulteration. Finally, defuzzification is executed using the centroid method: to derive a precise risk assessment value. This fuzzy logic-based approach offers a systematic and interpretable means of evaluating oil adulteration from spectral data.

$$y^* = \frac{\sum \mu_B(y) y}{\sum \mu_B(y)} \tag{6}$$

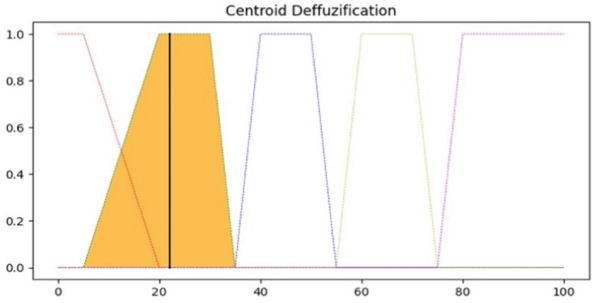

Fig. 2. Mapping of the risk factor using the risk functions.

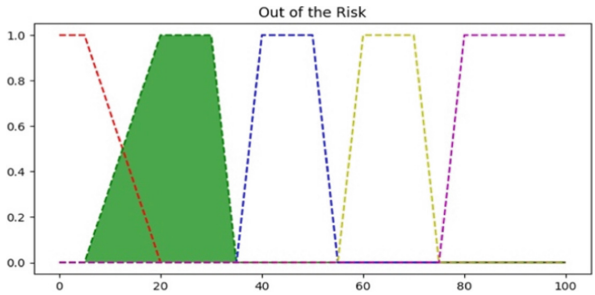

Fig. 3. Defuzzification of the membership functions and the corresponding identification of the risk percentage.

3 System Design

This work proposes a compact, low-cost, and simple system based on an optical sensor to identify olive oil adulteration and is shown in Fig. 4.

To detect signs of olive oil adulteration, the system relies on an AI-based fuzzy logic algorithm. The algorithm uses the Mamdani technique to assess risk factors that occur in all ultraviolet (UV), visible (VIS) and infrared (IR) spectral ranges. Figure 2 shows how these functions help to classify a sample of extra virgin olive oil as low risk, meaning that the likelihood of adulteration is low. In the final phase (defuzzification), shown in Fig. 3, all the collected data is summarized into a single probability value that is easy to understand and indicates the possibility of adulteration.

Fig. 4. Photo of the analysis system with all accessories.

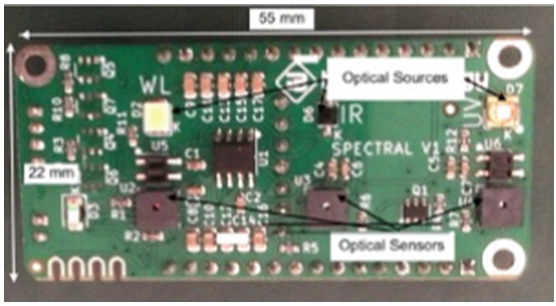

Fig. 5. Photo of the optical sensor prototype.

The system functions in both reflection and transmission modes, capturing spectrogram data across a range from 410 nm to 940 nm, with a stated accuracy of 28.6 nW/cm^3 across eighteen distinct channels. This data is then channeled into the fuzzy logic framework, which is designed to highlight any subtle indicators of adulteration. Figure 1 gives a simplified overview of the fuzzy rules, the mechanics of the inference process, and the risk assessment function–all based on reference samples of both authentic and adulterated oils.

The system's core is the ESP32 microcontroller that handles both optical sensors and electromagnetic sources. A lightweight and space-efficient design is achieved with the assembly of compact semiconductor sensors and LED-based reference light sources with surface-mount components. The ESP32 is responsible for collecting data, processing sensor readings, and transmitting this information to a computer via USB. For real-time data analysis, smartphones or laptops can be connected seamlessly through its built-in Bluetooth and Wi-Fi.

Before any actual analysis begins, the device first confirms that the temperature and reference voltage are within acceptable ranges. Once these conditions are met, electromagnetic pulses are emitted across various frequency bands, synchronized with the relevant sensors collecting data. The complete analysis–in both direct and reflected modes–takes around 10 s and needs only a small 5 ml sample of oil.

Figure 5 shows a photo of the optical sensor prototype. The device is compact, measuring 55 $\times$ 22 mm^2. Spectral sensors are combined with visible, UV, and IR LEDs to illuminate and test different surfaces for light spectroscopy, enabling the detection of potential adulteration in olive oil.

4 Experimental Assessment

Analysis was conducted on several cuvettes that contained samples of both pure and adulterated extra virgin olive oil during the experiments. To ensure accurate assessment of both purity and impurity levels, trustworthy reference models were created using careful adaptation of the fuzzy logic algorithm.

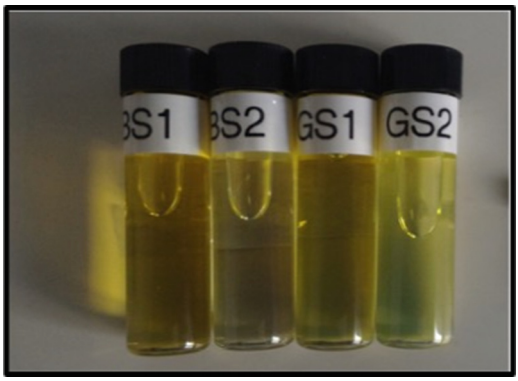

Fig. 6. Samples of adulterated extra virgin olive oil placed in borosilicate cuvettes.

Once the analysis procedure is initiated, electromagnetic pulses are generated across different spectral bands and synchronized with various acquisition sensors. A full analysis in both direct and reflective modes is completed in under 10 s.

In the experiments, different cuvettes were tested, containing samples of both pure and adulterated extra virgin olive oil (Fig. 6). To ensure accurate evaluation of purity and contamination levels, the fuzzy logic algorithm was rigorously refined to develop reliable reference models.

The sample is introduced via a 5 ml borosilicate glass cuvette into a designated compartment. To operate the spectrometer, the acquisition unit is connected to the processing system via a USB cable. Once the control software is activated, the user can select either direct or reflective analysis mode and obtain a graphical representation of the spectral data.

5 Results

The performance of the proposed system was evaluated using a total of 100 samples of extra virgin olive oil. Specifically, 80% of the samples were pure extra virgin olive oil, sourced from various farms, while the remaining 20% consisted of contaminated samples. The samples presented in Figs. 8 and 9 are representative of the entire dataset.

Figure 7 illustrates typical spectrograms obtained with the compact spectrometer: panel (a) shows a spectrogram of a pure extra virgin olive oil sample, while panel (b) depicts a contaminated sample. The spectral data span a range from 410 nm to 940 nm, with an accuracy of 28.6 nW/cm^3 across eighteen channels covering the UV, visible, and IR regions.

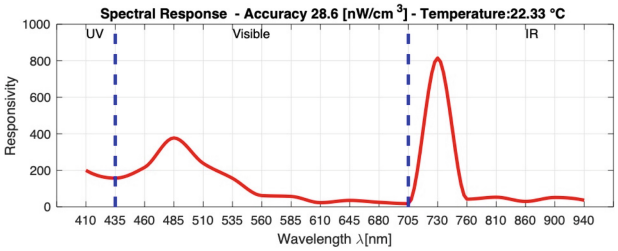

(a)

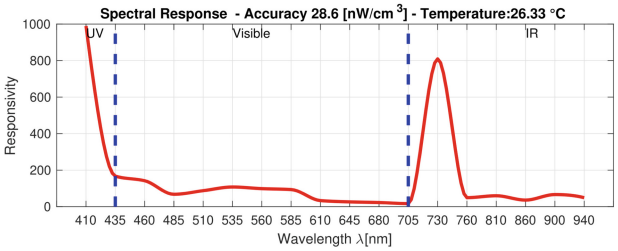

(b)

Fig. 7. Example sample spectrograms obtained with the compact spectrometer: (a) a pure sample and (b) a contaminated sample.

This section presents a selected set of significant results, specifically showcasing contaminated oil samples in Fig. 8 and pure, uncontaminated oil samples in Fig. 9. Figure 8 presents spectrograms of contaminated samples, including both adulterated extra virgin olive oil and non-edible oils, among them, three were adulterated extra virgin olive oil and two were non-edible oils (namely, construction lubricating oil and anti-corrosion oil).

In contrast, Fig. 9 displays spectrograms from five pure extra virgin olive oil samples of high quality.

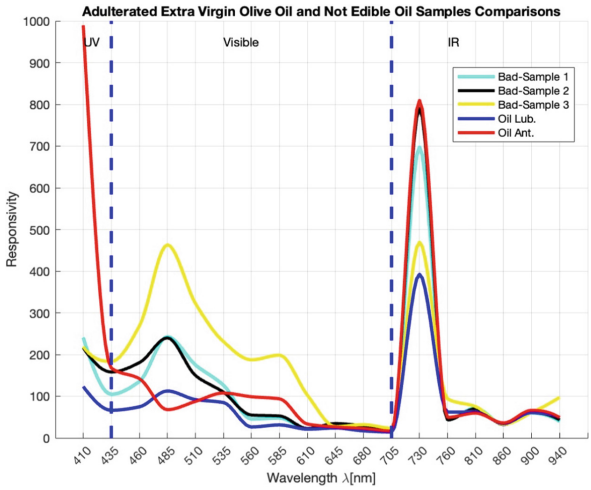

Fig. 8. Spectrograms of contaminated samples, including adulterated extra virgin olive oil and non-edible oils, obtained with the proposed system.

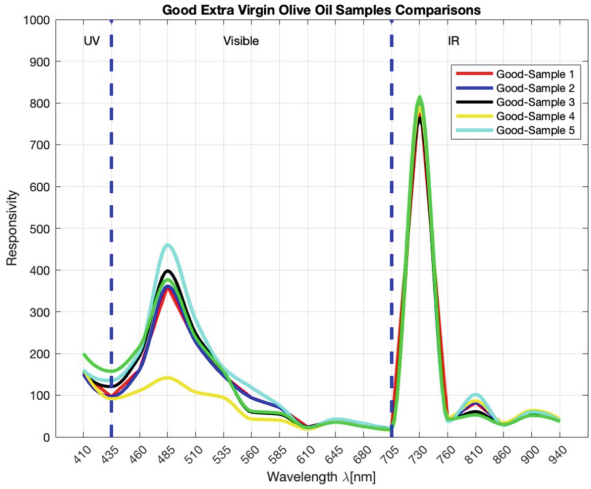

Fig. 9. Spectrograms of pure extra virgin olive oil samples obtained with the proposed system.

The fuzzy logic-based decision-making process is one of the key strengths of the system. A well-trained fuzzy logic algorithm can reliably distinguish pure and adulterated olive oil, even if visual inspection of spectrograms fails to clearly show their differences. The system is highly reliable and offers a quick, non-invasive, and user-friendly way to detect olive oil adulteration with a 95% classification accuracy.

6 Conclusions

To summarize, this study presents a system that utilizes fuzzy logic to detect adulteration in extra virgin olive oil through spectroscopic analysis. The method uses artificial intelligence and optical spectroscopy to assess oil quality quickly and without any damage. The early results indicate the system ability to distinguish between authentic and adulterated samples, and its ability to analyze UV, VIS, and IR wavelengths assures a comprehensive evaluation.

The system has been made to be fast, user-friendly, and economical, completing a full spectrum analysis in less than 10 s, making it appropriate for situations that require quick on-the-spot assessments. Additionally, since the method is non-destructive, the same oil can be kept for further testing, if necessary. The food industry can benefit from this promising advancement in quality assurance by using this approach, which offers a reliable, accessible, and cost-effective solution to oppose olive oil adulteration.

References

1. Trendeconomy. Olive Oil, Imports and Exports, Trend Economy 2023 (2022)
2. Hashempour-baltork F, et al: (2024) Recent methods in detection of olive oil adulteration: state-of-the-art. J Agric Food Res 16:101123 ISSN 2666-1543 https://doi.org/10.1016/j.jafr.2024.101123
3. Meenu M, Cai Q, Xu B (2019) A critical review on analytical techniques to detect adulteration of extra virgin olive oil. Trends Food Sci Technol 91:391–408
4. Maestrello V, Solovyev P, Bontempo L, Mannina L, Camin F (2022) Nuclear magnetic resonance spectroscopy in extra virgin olive oil authentication. Compr Rev Food Sci Food Saf 21(5):4056–4075
5. Li Y, Fang T, Zhu S, Huang F, Chen Z, Wang Y (2018) Detection of olive oil adulteration with waste cooking oil via Raman spectroscopy combined with iPLS and SiPLS, Spectrochim. Acta Mol. Biomol Spectrosc 189:37–43
6. Menon SA, Donelli SKMLM (2021) Development of a microwave sensor for solid and liquid substances based on closed loop resonator. Sensors 21:8506. https://doi.org/10.3390/s21248506
7. Aiswarya S, Meenu L, Unnikrishna Menon KA, Donelli M, Menon SK: A novel microstrip sensor based on closed loop antenna for adulteration detection of liquid samples. IEEE Sens J https://doi.org/10.1109/JSEN.2023.3332101
8. Mamdani EH, Assilian e S: (1975) An experiment in linguistic synthesis with a fuzzy logic controller. Int J Man-Mach Stud **7**(fasc. 1):1–13. https://doi.org/10.1016/S0020-7373(75)80002-2
9. Daurai B, Shrimanta SR, e Manashjit G: (2023) Comparison of Sparkfun TRIAD AS7265x spectroscopy sensor device with a Spectrophotometer for qualitative and quantitative analysis. In: 2023 4th International Conference on Computing and Communication Systems (I3CS), pp 1–3. https://doi.org/10.1109/I3CS58314.2023.10127282
10. Pérez-Ávila, AJ, Mesa-Simón MA, Martínez-Olmos, A, Palma, AJ, López-Ruiz e N: (2024) Assessment of the performance of a commercial spectral sensor for portable and cost-effective multispectral applications. In: 2024 27th Euromicro Conference on Digital System Design (DSD), pp 457–63 https://doi.org/10.1109/DSD64264.2024.00067
11. Stratton, JA: (2007) Electromagnetic Theory. John Wiley & Sons

12. Born, M, Wolf e E: (1999) Principles of optics: electromagnetic theory of propagation, interference and diffraction of light. 6. (corr.) ed. Repr. Cambridge, Cambridge University Press
13. Balanis CA: Advanced engineering electromagnetics. 2nd ed. Hoboken, NJ, Wiley, s.d

Achieving Photon Number Resolution with Linearly Multiplexed Single-Photon Detectors

Leonardo Limongi[1,2(✉)], Martino Bernard[2,3], Mirko Lobino[1,3], Alessandro Gaggero[4], Francesco Martini[4], Francesco Mattioli[4], and Andrea Salamon[5]

[1] Department of Industrial Engineering, University of Trento, Trento, Italy
leonardo.limongi@unitn.it, llimongi@fbk.eu
[2] Center for Sensors and Devices, Bruno Kessler Foundation, Trento, Italy
[3] INFN – TIFPA, Trento, Italy
[4] IFN – CNR, Roma, Italy
[5] INFN – Sezione di Roma 2, Roma, Italy

Abstract. This work studies a photon-number resolving detector (PNRD) made by a linearly multiplexed single-photon niobium nitride detector (SPD) array integrated on a silicon nitride strip-loaded waveguide platform, fabricated on a lithium niobate on insulator (LNOI) substrate. Linearity allows the device to maintain the mathematical model for the fidelity of already existing spatially multiplexed SPDs, while significantly changing the detector's geometry. Integrating such a device on a LNOI platform allows to exploit the unique properties of lithium niobate, such as the high electro-optic effect. Additionally, niobium nitride SPDs are one of the best superconductor devices available nowadays, allowing for tunable, and overall high, detection efficiency and low dark counts rate, making them one of the best candidates for our platform.

Keywords: Integrated Photonics · Superconducting Nanowire Single Photon Detector · Photon-number Resolving Detector · Lithium Niobate on Insulator

1 Introduction

Photon-number-resolving detectors (PNRDs) are becoming pivotal for many integrated and quantum optics applications, such as photon-number measurements, quantum key distribution, LIDAR, and single-photon source calibration.

Nowadays, most PNRDs implementations rely on spatially multiplexed single-photon detectors [1] (SPDs): the incoming waveguide ends in a binary-tree structure which splits the input among 2^k branches and terminates in an array of high-efficiency SPDs.

Superconducting nanowire single-photon detectors (SNSPDs) are versatile devices able to combine the possibility of tuning the nanowire interaction with the waveguide while keeping a low level of dark counts [2]. Such technology is widely employed in

C. Di Natale et al. (Eds.): AISEM 2025, LNEE 1497, pp. 291–294, 2025.
https://doi.org/10.1007/978-3-032-08271-8_45

commercially-available spatially multiplexing PNRDs, but few works have been done to integrate PNRDs made of linearly multiplexed SNSPDs.

In this work [3], we propose a new linearly multiplexed PNRD architecture, replacing conventional binary-tree with a straight single waveguide. On top of the straight waveguide, an array of N niobium-nitride (NbN) SNSPDs is evanescently coupled. We derived the optimal length of each SPD, which is tuned to tailor the coupling strength to the desired value. This geometry preserves the analytic fidelity of spatial multiplexing devices while greatly simplifying the circuit layout and footprint. Such PNRD sits directly atop a silicon nitride (Si_3N_4 or SIN) strip-loaded waveguide on thin-film lithium niobate ($LiNbO_3$ or LN)-on-insulator (LNOI) substrate. This material stack let us exploit SIN's low propagation losses and well-established CMOS fabrication technology together with LN's electro-optic properties.

We also analyze different shapes of SNSPDs, impacting significantly both performance and fabrication feasibility. While, performance wise, the best nanowire shape would be the *wavy-wall* type, the choice changes once the fabrication constrains are considered. In this work we will analyze a process featuring the well-established meander structure.

2 Fidelity Scaling

In the binary-tree multiplexing, each SPD has an equal probability of collecting a single-photon due to the tree structure. To optimize the fidelity F of this system, that is the probability of correctly measuring the number of photons, each SPD must have $\eta = 100\%$ detection efficiency, which is the probability of coupling, absorbing and detecting a single-photon.

In the linear multiplexing, instead, to maintain for each SPD an equal probability to measure a single-photon it is necessary to modify the detection efficiency, by means of the coupling coefficient, of every SPD in the array. By performing combinatorial calculations, we obtained that, indexing the SPDs in the array with i ranging from N to 1, each detector's efficiency must satisfy $\eta_i = 1/i$.

Evaluating the fidelity of measuring m photons with N SPDS leads to the formula in Eq. (1),

$$F(m, N) = \Pr\big[\text{detected} = m | \text{incoming} = m\big] = m! \binom{N}{m} \frac{1}{N^m} \tag{1}$$

which is valid for the ideal case (waveguide is lossless, detector has unitary internal quantum efficiency and no dark counts), and it essentially represents the probability of distributing m photons in N SPDs with at most one photon per SPD.

Realistic propagation loss ($\alpha_w < 0.3$ dB/cm) and nanowire absorption ($\alpha_c \approx 422$ dB/cm) modify the effective η_i via an exponential attenuation with intensity given by the ratio $r = \frac{\alpha_w}{\alpha_c}$, which enters a generalized fidelity formula reported in [3].

State-of-the-art SNSPD dark count rates ($\gamma \sim 30$ kHz over $\Delta t \approx 10$ ns) further modify F by the no-count Poisson multiplicative factor $e^{-\gamma L_{tot} \Delta t}$. Even in the worst case, F degrades by only a few percent compared to the lossless, zero-dark count scenario.

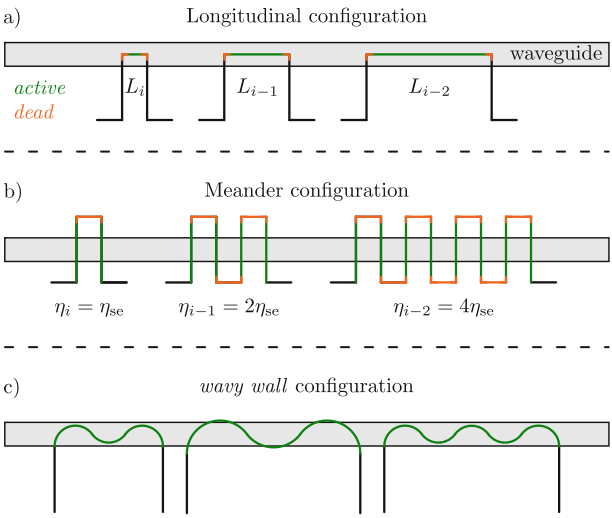

Fig. 1. Different configurations of SNSPDs on top of the waveguide. a) represents the longitudinal configuration, characterized by a variable-length and longitudinally centered nanowire. b) represents the meander configuration, characterized by being a multiple of the single-element unit SPD. c) represents the *wavy wall* configuration, characterized by nanowires with constant curvature for its length. Picture from [3].

3 Nanowire Arrangement and FEM Simulations

We compared three different nanowire layouts, as shown in Fig. (1), each with their pros and cons.

1. **Longitudinal**: the nanowire is parallel and centered on the waveguide; it allows continuous tuning of η_i by accordingly choosing the nanowire length, but prone to current crowding in 90 degrees bends.
2. **Meander**: transverse straight segments with wide U-turns away from the mode; discrete η_i as combination of single-element efficiency η_{se} but fabrication friendly.
3. **Wavy-wall**: uniform-curvature sinusoidal arcs centered on the waveguide; in principle allowing continuous η_i and no current-crowding issue but requires high resolution and fast lithography.

FEM simulations confirm that the meander layout achieves the target efficiency with negligible extra loss, while U-turn bends contribute with negligible factors if put sufficiently away from the mode (above 6 μm).

Other results obtained from FEM simulations are.

1. **Propagation stability**: Strip-loaded TE modes exhibit no lateral leakage ($\Delta n > 0$) and bend-loss critical radius $R_{crit} \approx 434$ μm, that is the radius from which radiative losses are no longer negligible.
2. **Unit absorption**: after 5 μm of transversal nanowire length the absorption saturates. Depending on the SIN thickness, comprised between 180 nm and 200 nm, η_{se} saturates to a value between 2.5% and 3.5%.

4 Conclusions and Future Perspectives

We have demonstrated a fully integrated, linearly multiplexed SNSPD array on SIN/LNOI platform, with analytic fidelity matching binary-tree spatial PNRDs and with robustness against waveguide losses and dark count rates. FEM-driven design suggests the meander geometry for balancing fabrication ease and performance.

Crucially, our linear architecture allows incremental addition of new SNSPD elements post-fabrication: adding a few SPDs at the beginning of the waveguide extends the dynamic range with little increment to the PNRD total length. The modularity and small footprint make this device readily integrable into larger LNOI-based quantum photonic circuits.

This work contributes to paving the way to compact, scalable, PNRDs for on-chip quantum state characterization, quantum communications and beyond.

References

1. Jönsson M, Björk G (2019) Evaluating the performance of photon-number-resolving detectors. Phys Rev A 99:043822
2. Gaggero A et al (2019) Amplitude-multiplexed readout of single photon detectors based on superconducting nanowires. Optica 6:823–828
3. Limongi L et al (2025) Linearly multiplexed photon number resolving single-photon detectors array. Opt Commun 575:131244

CO_2-Laser for Electrochemical and Colorimetric Sensors Development

Dounia El Fadil, Paolo Di Battista, Annalisa Scroccarello(✉), Flavio Della Pelle, and Dario Compagnone

Department of Bioscience and Agro-Food and Environmental Technology, University of Teramo, Teramo, Italy
{delfadil,pdibattista,ascroccarello}@unite.it

Keywords: laser-induced nanostructures · CO_2 laser · paper-based analytical devices · lab-made electrochemical sensors

In recent years, CO_2 lasers have emerged as powerful tools for the fabrication of functional nanomaterials, offering a unique combination of high energy, tunable parameters, and compatible with scalable manufacturing techniques [1]. The versatility of CO_2 laser approaches has positioned them at the forefront of advanced material engineering for sensor development. In particular, the CO_2 lasers application in generating laser-induced nanoparticles (LINPs) has opened new frontiers in electrochemical and colorimetric sensing technologies, where the interface plays a critical role in sensor performance [2].

Commonly, the substrates employed in laser-assisted nanostructuring include flexible polymers (e.g., polyimide), cellulose, hydrogel, glass, and carbon-based films such as graphene oxide (GO) [3, 4]. Further, the CO_2 lasers for in situ nanostructuring allow the direct synthesis of metallic nanostructures on target substrates without the need for multiple processing steps [5]. This in situ strategy simplifies fabrication workflows and enhances reproducibility, which is critical for practical sensor deployment; indeed, by finely tuning the laser parameters such as power, scanning speed, and pulse duration, researchers can control the nucleation and growth of nanoparticles within the substrate matrix, leading to well-dispersed, uniformly sized nanoparticles.

Beyond material fabrication, CO_2 laser-induced nanostructuring offers substantial advantages for sensor performance. In electrochemical sensing, laser-generated nanoparticles provide abundant electroactive sites, promote electron transfer, and improve detection sensitivity and selectivity for analytes such as biomolecules, contaminants, and, in general, redox-active species. In colorimetric sensing, metallic nanoparticles, especially those with plasmonic properties, exhibit strong optical absorbance in the visible range, enabling direct visual detection of analyte-induced color changes. These dual functional properties enable the creation of hybrid sensors capable of simultaneous electrochemical and optical readouts, thereby increasing reliability and application [5–7]. This proceeding presents recent developments of our research group in CO_2 laser-assisted nanostructuring for sensor applications, emphasizing fabrication strategies, material interfaces, and performance outcomes relevant to practical deployment.

C. Di Natale et al. (Eds.): AISEM 2025, LNEE 1497, pp. 295–298, 2025.
https://doi.org/10.1007/978-3-032-08271-8_46

1 Electrochemical Sensors

The study of Scroccarello et al. [8] presents a novel, facile, and scalable strategy to fabricate nanostructured rGO films embedded with noble metal nanoparticles (MNPs), including gold (Au), silver (Ag), and platinum (Pt). The aim is to develop high-performance, versatile electrochemical sensors for detecting biological and environmentally relevant analytes. Unlike existing methods, which tend to be complex, poorly reproducible, and limited in scalability, this work proposes a single-step, surfactant-free, laser-assisted co-reduction technique of GO and metal cations, forming conductive rGO films decorated with "naked" MNPs. The study explores the fabrication, characterization, and sensing capabilities of these nanocomposite films transferred onto lab-made screen-printed electrodes, demonstrating their analytical robustness in real sample matrices. The fabricated MNPs@rGO electrodes were tested for sensing of caffeic acid (CA), nitrite (NO_2^-) and hydrogen peroxide (H_2O_2). In detail, the CA was evaluated using Au@rGO electrodes, returning high sensitivity and low detection limit (<0.6 μM) and demonstrating the applicability in CA determination in coffee samples. The NO_2^- determination was carried out with Ag@rGO electrodes, demonstrating excellent electrocatalytic activity toward nitrite oxidation in model solutions and lake water samples, achieving a sub-micromolar detection limit and good reproducibility. Finally, the Pt@rGO electrodes were used for amperometric detection of H_2O_2 residues from indoor disinfection fogging treatments on surfaces. The sensors enabled real-time monitoring of H_2O_2 decay post-fogging, highlighting practical environmental sensing capabilities.

The single-step laser approach allows the synthesis of MNPs@rGO hybrid films via co-reduction in a single step, circumventing traditional multi-step chemical or physical methods. This laser-assisted approach offers several advantages, such as surfactant-free synthesis, simultaneous reduction and nanoparticle formation, patterned film fabrication, and reproducibility. Further, this approach improves the electrode surface area and electrical conductivity while providing catalytic sites from the noble MNPs, enhancing sensitivity and selectivity toward potential target analytes.

2 Colorimetric Sensors

The CO_2 laser plotter technique can also be employed for the in-situ scribing of different metal nanoparticles (MNPs) or nanostructures onto cellulosic substrates. Scroccarello et al. [4] Reported the synthesis of Au, Ag, Pt, Cu and Ni laser-induced MNPs (LIMs) in a few steps, with high resolution and accurate patterns, overcoming issues like uncontrolled formation of MNPs on paper. The different LIMs were characterized by peculiar optical and localized surface plasmon resonance (LSPR) features tunable according to metal precursor concentration and laser parameters.

Lab-made PADs, containing catalytic/sensing LIMs array, were manufactured via CO_2 laser approach, proving LIMs' organic dye remediation and vapor sensing ability. The catalytic activity of the produced LIMs was proved through a paper comb laser-shaped device. Methyl orange, rhodamine b, and methylene blue were selected as model dyes and deposited on the paper comb containing the different LIMs. The three dyes turned rapidly (1 min) from colored to colorless, proving the catalytic ability of LIMs

towards organic dye remediation. In detail, Cu-, Ag-, and Au-LIMs had the best catalytic ability with effective dye conversions, whereas Pt- and Ni-LIMs demonstrated lower activity. Further, the LIMs' potential as sensing elements was tested with the design of a colorimetric sensor array for peracetic acid (PAA) determination, which is widely used as a disinfectant in industrial, public, and healthcare environments. The sensor array was exposed to PAA in a vapor-saturated chamber, resulting in a LIMs visible color change induced by PAA oxidant capacity that varies LIMs' size, shape, and arrangement; the LIMs color variation resulted in proportional to PAA concentration, then proving the array quantification capacity in the vapor phase.

In another work, only Pt-LIM was assembled in a paper-based analytical device and was employed as a nanozyme for the ascorbic acid (AA) determination [5]. The proposed device exploits the oxidase-mimicking activity of Pt-LIM towards 3,3′, 5,5′-tetramethylbenzide (TMB) oxidation: this results in a blue color formation, which is inhibited by the AA antioxidant capacity than resulting in a color fading, which was monitored by a simple smartphone camera. The catalytic device returned analytical figures of merit useful for sample analysis and was applied in AA determination in different foods and food supplements, obtaining accurate (recoveries 92–114%; relative error $-11/+4\%$) and reproducible results (RSD $\leq 10\%$; $n = 3$).

This approach opens new prospects toward the rational patterning of catalytic/plasmonic-active metal nanostructures onto cellulosic substrates, without the need for additional reagents or cumbersome, long procedures.

3 Conclusions

This proceeding highlights the versatility of the CO_2 laser for integrating functional nanostructured films in electrochemical and colorimetric sensors. The single-step, surfactant-free laser-assisted synthesis enables the direct formation of rGO-metal nanoparticle hybrids (Au, Ag, Pt), leading to flexible, scalable, and highly sensitive electrochemical devices capable of detecting different analytes with excellent stability and reproducibility. Simultaneously, laser processing has proven effective in creating colorimetric paper-based sensors, using metal nanoparticles to generate visually detectable signals. This dual applicability demonstrates the broad potential of LINPs for multimode sensing platforms that combine visual and electrical outputs, supporting a wide range of real-world analytical needs.

References

1. Scroccarello A, Della Pelle F, Di Giulio T, Mazzotta E, Malitesta C, Compagnone D (2024) Single-stroke metal nanoparticle laser scribing on cellulosic substrates for colorimetric paper-based device development. ACS Sustain Chem Eng. 12:3196–3208
2. Della Pelle F, Bukhari QUA, Alvarez Diduk R, Scroccarello A, Compagnone D, Merkoçi A (2023) Freestanding laser-induced two-dimensional heterostructures for self-contained paper-based sensors. Nanoscale 15:7164–7175
3. Silveri F, Della Pelle F, Compagnone D (2025) Recent advances in sustainable strategies for the integration of nanostructured sensing surfaces in electroanalytical devices

4. Silveri F et al (2024) Exploiting CO2 laser to boost graphite inks electron transfer for fructose biosensing in biological fluids. Biosens Bioelectron 263:116620
5. Zhao, L., et al (2023) Laser reduced graphene oxide electrode for pathogenic escherichia coli detection. ACS Appl Mater Interfaces
6. Pidal, J.M.G., et al (2024) Laser-induced 2D/0D graphene-nanoceria freestanding paper-based films for on-site hydrogen peroxide monitoring in no-touch disinfection treatments. Microchimica Acta
7. Silveri F, Scroccarello A, Della Pelle F, Del Carlo M, Compagnone D (2023) Rapid pretreatment-free evaluation of antioxidant capacity in extra virgin olive oil using a laser-nanodecorated electrochemical lab-on-strip. Food Chem
8. Scroccarello A (2023) One-step laser nanostructuration of reduced graphene oxide films embedding metal nanoparticles for sensing applications. ACS Sens 8:598–609

Rapid Profiling of Flour with Near-Infrared Spectral Sensing and Chemometrics

Leonardo Ciaccheri[1](✉), Anna G. Mignani[1], Andrea A. Mencaglia[1], and Lien Smeesters[2]

[1] CNR-Istituto di Fisica Applicata "Nello Carrara" (IFAC), 50019 Sesto Fiorentino, FI, Italy
l.ciaccheri@ifac.cnr.it

[2] Department of Applied Physics and Photonics, Brussels Photonics (B-PHOT), Vrije Universiteit Brussel, 1050 Brussels, Belgium
lien.smeesters@vub.be

Abstract. This pilot study aims to rapidly and non-destructively screen flours based on key nutraceutical indicators such as fats, carbohydrates, and proteins. It has industrial relevance for both high-throughput online screening and occasional at-line sampling and testing. The study analyzed 47 commercially available flours from cereals, legumes, tubers, and others, each with varying nutraceutical values. Using the SpectraPod™ pocket-sized near-infrared spectral sensor, we measured the flour reflectance spectra. Chemometric processing of the spectroscopic data allowed us to classify flours into two fat classes with 98% accuracy and three classes for carbohydrates and proteins, each with 89% accuracy.

Keywords: Flour · Near-infrared · Spectroscopy · Fats · Proteins · Carbohydrates · Chemometrics

1 Introduction

A rapid non-destructive screening of flours based on quality indicators such as fats, carbohydrates, and proteins is important to check the nutritional consistency, to make blends for specific dietary needs, to facilitate detection of non-compliant samples, and overall for a comprehensive quality assurance.

Optical spectroscopy is a powerful analytical tool for assessing flour quality due to its non-destructive nature, speed, and ability to analyze multiple components simultaneously. Among various spectroscopic techniques, near-infrared spectroscopy (NIR) is particularly effective for evaluating flour quality. In fact, NIR's ability in measuring key nutritional indicators like fats, proteins, and carbohydrates makes it an invaluable method for ensuring the integrity and consistency of flour products [1–5].

This pilot study investigates a variety of commercially available flour samples, to demonstrate the effectiveness of NIR-enabled digital analytics for assessing an agricultural commodity fundamental to many everyday foods. Using a pocket-sized spectral sensor and chemometric analysis of the data, we classified flours into two fat classes with 98% accuracy and three classes for carbohydrates and proteins, each with 89% accuracy.

C. Di Natale et al. (Eds.): AISEM 2025, LNEE 1497, pp. 299–303, 2025.
https://doi.org/10.1007/978-3-032-08271-8_47

2 Flours and Spectral Sensor

2.1 Flours

We analyzed a collection of 47 commercially available flour samples, categorized into cereals (wheat, buckwheat, rice, corn, emmer, millet, rye, oat, kamut, quinoa, and breadcrumbs), legumes (chickpeas, peas, lupins, and red lentils), tubers (comprising potato, cassava, and arrowroot), and others (almonds, amarant coconut, and dark flax). Flour samples were contained in glass vials for spectroscopic measurements using a pocket-sized spectral sensor.

2.2 Spectral Sensor

The SpectraPod™ pocket-sized spectral sensor we used covers the 850–1700 nm wavelength range with 16 spectral bands [6, 7]. It includes a tungsten source and a chip integrating an array of filters with detectors. The sensor produces 16 distinct signals, each giving the spectroscopic response of a specific pixel. The pod connects to a laptop via USB port, and a custom software interface provides communication, data acquisition and storage. Figure 1-left illustrate the SpectraPod™ in use, and Fig. 1-right shows the measured reflectance spectra of all flours colored by type.

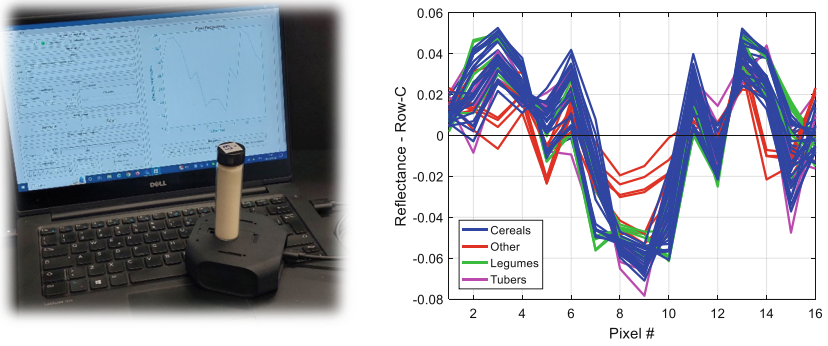

Fig.1. Left: SpectraPod™ device in use measuring flour in a glass vial. Right: Reflectance spectra of all flours considered.

3 Flour Profiling

Fats, carbohydrates and proteins were identified as the key nutraceutical indicators for four profiling, due to their abundance and significance for dietary needs. Figure 2 displays histograms of the fat, carbohydrate and protein content of the examined flours, as detailed on their packaging. Given these nutritional profiles, two or three classes of concentration of fats, carbohydrates and proteins were considered. Fats were categorized into two classes (low and high concentration), with a cutoff at 20 g/hg. Carbohydrates and proteins were categorized into three classes (low, medium and high concentration) with cut-offs of 30 and 50 g/hg for carbohydrates, and 20 and 30 g/hg for proteins. These thresholds are marked as red lines in Fig. 2.

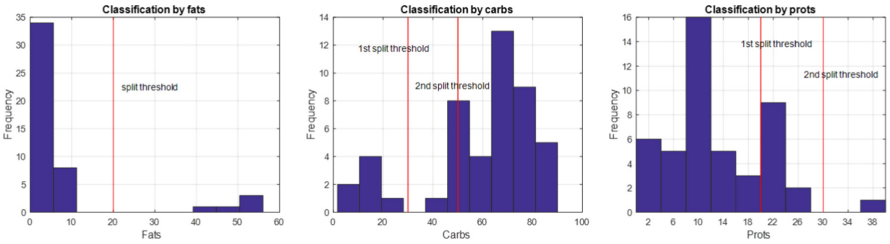

Fig.2. Pre-defined classes of concentration of fats (left), carbohydrates (center), and proteins (right) for flour profiling.

The reflectance spectra of flours were firstly interpreted using Principal Component Analysis (PCA), which is one of the most popular and effective multivariate data processing unsupervised methods [8]. PCA reduces the dimensionality of the data, linearly transforming the original set of variables into a new and smaller set of orthogonal variables known as principal components (PCs) that maximize the explained variance. PCA of the entire spectroscopic pattern revealed that only certain pixels significantly correlated with fats, carbohydrates, or proteins. Therefore, to enhance the model's accuracy, a new PCA model was developed by selecting pixels with a good correlation coefficient (absolute value $\geq$0.5) with at least one nutritional variable. This refined approach identified pixels 3, 5, 8, 9, and 14 only as having good classification ability.

To evaluate the accuracy of classifying the flour samples into low/medium/high-concentration categories, we utilized the K-Nearest Neighbors (KNN) algorithm, renowned for its simplicity, popularity, and efficacy in solving classification problems [9]. This algorithm examines a point in a vector space and assigns it to a predefined group. In essence, KNN gauges the likelihood of a data point being a member of a particular group based on the membership of the nearest neighboring training points. The KNN classifier with K = 3 and Standardized Euclidean Distance was used for evaluating the separation of the two classes for fats and three classes for carbohydrate or protein subdivision. In all cases, the PC2-PC3 plane served as the predictor space.

Figures 3, 4, and 5 illustrate the classification results for fats, carbohydrates, and proteins, respectively. The left panels display the flour spectra with selected pixels utilized in the chemometric processing. The central panels show the score plots in the PC1-PC2 spaces, highlighting the separation achieved in each classification. The right panels summarize the confusion matrices and the accuracy of classification, demonstrating the effectiveness of our method in profiling flours based on these key nutritional components.

Fats were classified with 98% accuracy, with only one sample, dark flax seeds misclassified. Carbohydrates and proteins were both classified with 89% accuracy, with five samples misclassified in each category. The misclassified samples for carbohydrates were: chickpeas, multi-cereals, peas, red lentils, and amarant. The misclassified samples for protein were: chickpeas, dark flax seeds, peas, lupins, and red lentils.

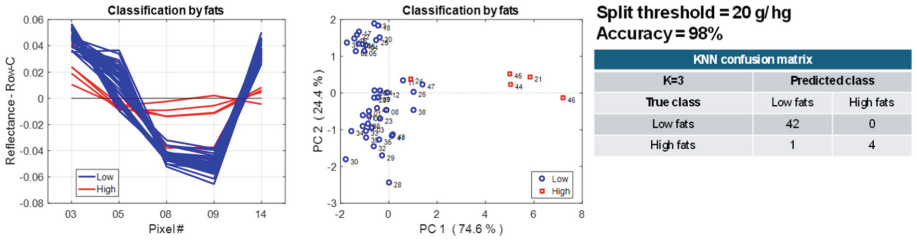

Fig. 3. Classification of fats into two classes of concentration. Left: reflectance spectra with selected pixels. Center: PC score plot grouping the flours according to low (blue) or high (red) concentration. Right: confusion matrix of classification.

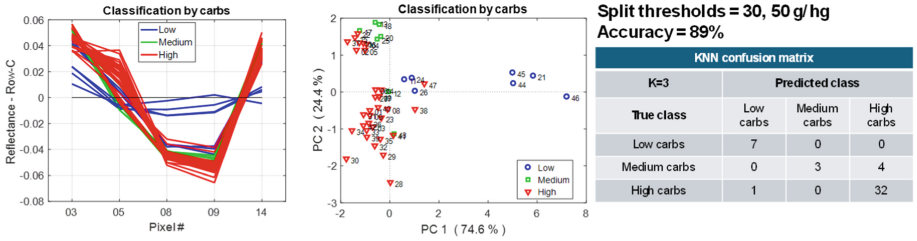

Fig. 4. Classification of carbohydrates into three classes of concentration. Left: reflectance spectra with selected pixels. Center: PC score plot grouping the flours according to low (blue), medium (green) or high (red) concentration. Right: confusion matrix of classification.

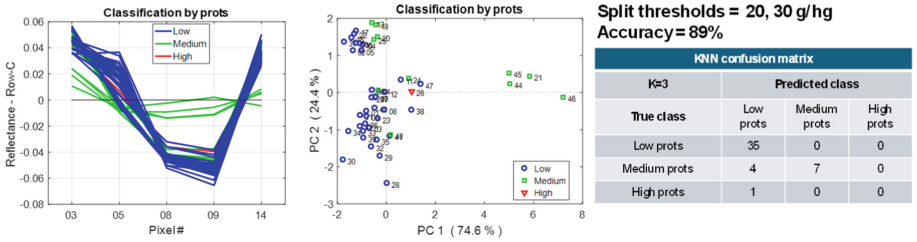

Fig. 5. Classification of proteins into three classes of concentration. Left: reflectance spectra with selected pixels. Center: PC score plot grouping the flours according to low (blue), medium (green) or high (red) concentration. Right: confusion matrix of classification.

4 Perspectives

Using the SpectraPod™ pocket-sized spectral sensor and chemometric analysis, we effectively profiled flours based on pre-defined values of fats, carbohydrates, and proteins. This approach allowed us to accurately classify the flours' nutritional content, demonstrating the potential for rapid and non-destructive assessment of key nutraceutical indicators. This pilot study lays the groundwork for developing real-time, and cost-effective quality control methods for flour production, meeting industry demands for both high-throughput on-line screening, and occasional at-line sampling and testing.

Acknowledgements. The CNR-Short Term Mobility Program 2023, and PhotonHub Europe® (European Union's Horizon 2020 research and innovation program, Grant Agreement n. 101016665) are acknowledged for partial funding.

References

1. Badaró AT, Hebling e Tavares JP, Blasco J, Aleixos-Borrás N, Barbin DF: (2022) Near infrared techniques applied to analysis of wheat-based products: Recent advances and future trends. Food Control **140**:109115
2. Barbon Junior S et al (2020) Multi-target prediction of wheat flour quality parameters with near infrared spectroscopy. Inf Process Agric 7(2):342–354
3. Chen X, Siesler HW, Yan H (2021) Rapid analysis of wheat flour by different handheld near-infrared spectrometers: a discussion of calibration model maintenance and performance comparison. Spectrochim Acta Part A Mol Biomol Spectrosc 252:119504
4. Masithoh RE, Yuliyanda I (2019) NIR reflectance spectroscopy and SIMCA for classification of crops flour. IOP Conf Ser: Earth Environ Sci 355(1):012004
5. Zhang S, Liu S, Shen L, Chen S, He L, Liu A (2022) Application of near-infrared spectroscopy for the nondestructive analysis of wheat flour: a review. Curr Res Food Sci 5:1305–1312
6. Van Klinken A et al (2023) High-performance photodetector arrays for near-infrared spectral sensing. APL Photonics 8(4):041302
7. Mantispectra: https://mantispectra.com/. Last accessed 23 May 2025
8. Souza AS et al (2024) An introductory review on the application of principal component analysis in the data exploration of the chemical analysis of food samples. Food Sci Biotechnol 33:1323–1336
9. Parul GMS (2022) A Review on analysis of K-Nearest neighbor classification machine learning algorithms based on supervised learning. Int J Eng Trends Technol 70(7):43–48

Synthesis of Silver Dendrites as a Powerful SERS Platform for Hydrated Proteins Detection

Dario Morganti[1(✉)], Antonio Alessio Leonardi[2], Maria Josè Lo Faro[3], Sabrina Conoci[2], Alessia Irrera[1], and Barbara Fazio[1]

[1] Institute for Microelectronics and Microsystems, CNR IMM-ME, Viale F. S. d'Alcontres 31, 98166 Messina, ME, Italy
dario.morganti@cnt.it
[2] Department of Chemical, Biological, Pharmaceutical, and Environmental Sciences (ChiBioFarAm), University of Messina, Viale F. S. d'Alcontres 31, 98166 Messina, ME, Italy
[3] Department of Physics and Astronomy, University of Catania, Via Santa Sofia 64, 95123 Catania, CT, Italy

Abstract. In this work, we present a highly sensitive method for the detection of biomolecules by Surface-Enhanced Raman Spectroscopy (SERS), exploiting the unique plasmonic properties of a silver (Ag) dendritic layer. This three-dimensional (3D) material is produced as a waste by-product during the metal-assisted chemical etching (MACE) process used to synthesize silicon nanowires. The fractal structure of the dendritic Ag layer is able to efficiently trap the light inside the micro- and nanocavities, forming numerous and very intense hot-spot regions that amplify Raman signals over a wide range of excitation wavelengths (from UV to IR spectral region). Furthermore, the sponge-like behavior of the Ag platform allows for the encapsulation and confinement of extremely small liquid volumes of the sample. This allows proteins to maintain their natural hydration shell, enabling the analysis of biomolecules in an environment that mimics the physiological conditions. This represents a significant advantage both in basic research and for biomedical and biochemical studies.

Keywords: Silver dendrites · Metal-assisted chemical etching · Surface-Enhanced Raman Spectroscopy · protein analysis · SARS-Cov-2

1 Introduction

Analytical detection of biomolecules is a widely investigated topic in different application fields, including chemistry, biology and biomedicine. Vibrational techniques, such as Raman spectroscopy, provide valuable information on the chemical structure and properties of various biomolecules such as proteins and nucleic acids [1–4]. However, despite its grate potential in molecular analysis, it often manifests the problem of low signal intensity, making the detection of small amounts of molecular samples a hard challenge. To overcome this drawback, surface-enhanced Raman spectroscopy (SERS) emerges as a powerful alternative to traditional Raman techniques [5]. SERS exploits

C. Di Natale et al. (Eds.): AISEM 2025, LNEE 1497, pp. 304–310, 2025.
https://doi.org/10.1007/978-3-032-08271-8_48

the amplification of the electromagnetic field in some transition metal-based nanostructures to amplify the Raman modes intensities of the analyte. This amplification of the electromagnetic field can reach very high values when the analyte lies in proximity to the metal nanostructure surface. In these regions, called *hot spots*, the electromagnetic field can reach very intense value of up to 10^8. This improvement enables the identification of molecular vibrations with high sensitivity, even when only extremely low amounts of sample are available, up to the single molecule [6].

Among the various metallic nanostructures, in this work, we use plasmonic material composed of silver (Ag) dendrites, which are a by-product generated during the synthesis of silicon nanowires via the metal-assisted chemical etching (MACE) process [7]. In this study, silver dendrites enable SERS detection of lysozyme with an enhancement factor (EF) up to ~10^6 under hydrating conditions. Additionally, this plasmonic platform enabled the first acquisition of the Raman fingerprint of the SARS-CoV-2 genome in hydrated conditions, providing a rapid and straightforward method for virus detection.

2 Results and Discussions

The highly sensitive spectroscopic detection of biomolecules via Surface-Enhanced Raman spectroscopy (SERS), was carried out exploiting the peculiar plasmonic properties of a silver (Ag) dendrite layer. This 3D material is synthesised as a by-product in the metal assisted chemical etching (MACE) process by using a commercial silicon wafer and the silver nitrate salts as precursors of metallic Ag, as shown in Fig. 1.

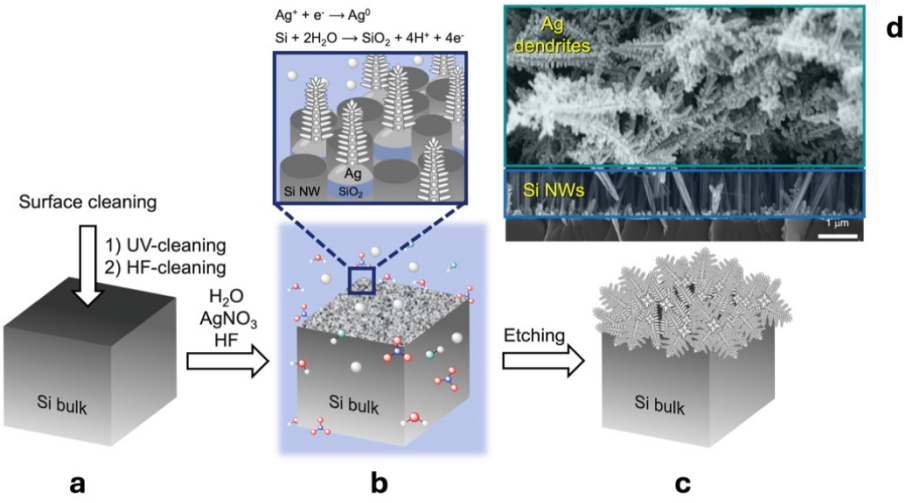

Fig. 1. Schematic representation of the synthesis of Ag dendrite. (a) cleaning procedure of the commercial Si surface; (b) sample during MACE process; (c) obtained Ag dendrites; (d) Scanning Electron Microscopy image of the as-grown Ag dendrites in plan view.

The surface of the commercial silicon substrate is initially cleaned by UV-ozone treatment and then by immersion in a HF-based solution (Fig. 1a). Silver ions (Ag^+) in

solution are reduced by the Si at the metal interface forming a discontinuous layer of Ag^0 dendrites. This method was originally developed for the realization of silicon nanowires (Si NWs) [8–10] and the silver dendrites are produced as an undesired byproduct and removed by HNO_3 etching. However, for our purposes, the silver dendrites represent the main product of interest, so they are left onto the silicon surface that acts as a support material (Fig. 1c). Figure 1d shows a Scanning Electron Microscopy image acquired in cross-section, revealing the dendritic structure of the silver platform grown above a dense array of silicon nanowires, both formed as a result of the MACE process.

A critical aspect is the presence of surface contaminants or a silver oxide layer that can limit the SERS performance of the platform. So, an UV-ozone cleaning process is performed to remove any organic or environmental contaminants. To assess the metal surface purity, Energy Dispersive X-ray profilometry measurements have been performed [1], revealing that the silver matrix grows on the Si substrate with good quality and without the presence of oxygen.

The fractal behaviour of the Ag dendrites has been demonstrated by scanning electron microscopy images [1], showing the scale invariance of the material. The unique hierarchical structure can efficiency traps the light in micro and nanocavities of different dimensions promoting an inhomogeneous electromagnetic field localization. This led to the formation of numerous and very intense hot spots 3D distributed in the whole volume of the material enhancing SERS performance in a wide range of excitation wavelengths (from UV to the infrared region) [2]. Moreover, the sponge-like behaviour of this platform promotes the encapsulation and confinement of very small liquid sample volumes, enabling proteins in solutions to maintain their natural hydration shell. This offers a great advantage as it allows to analyse biomolecules in their biologically active conformation [1].

Figure 2 shows an example of a protein study under hydration conditions using the SERS technique. For this purpose, we used lysozyme as a known target protein. In Fig. 2a the SERS spectrum of a lysozyme 10^{-5} M solution (black line) is reported, after drop casting and drying onto the silver platform. This spectrum is compared to the Raman spectrum of lysozyme 10^{-2} M in PBS water solution (blue line) and in powder state (magenta line). The enhancement factor (EF) of the Ag fractals has been estimated by comparing the phenylalanine ring breathing mode in three different samples. The EF evaluation accounted for the scaling of the molecular concentration in the solutions, for the laser power, and for the integration time, obtaining a value higher than 10^6. To demonstrate that the protein is confined in a hydration shell the SERS spectrum of lysozyme has been compared to the Raman spectrum of the protein in powder state in the high frequency region (Fig. 2b). The difference between the two spectra mainly lies in the shape of the hydroxy group stretching band between 3200 and 3600 cm^{-1}. This signal in the Raman spectrum is ascribed to the only hydroxy group present in the peptide chains, while in the SERS spectrum is present also the contribution of the distorted H-bonded network of water. To demonstrate the presence of the hydration water, the Raman spectrum of the pure water (cyan line in Fig. 2b) has been compared with the SERS spectrum of pure water drop casted onto the Ag platform (dark green in Fig. 2b). The spectra show different ratios in the OH stretching contributions.

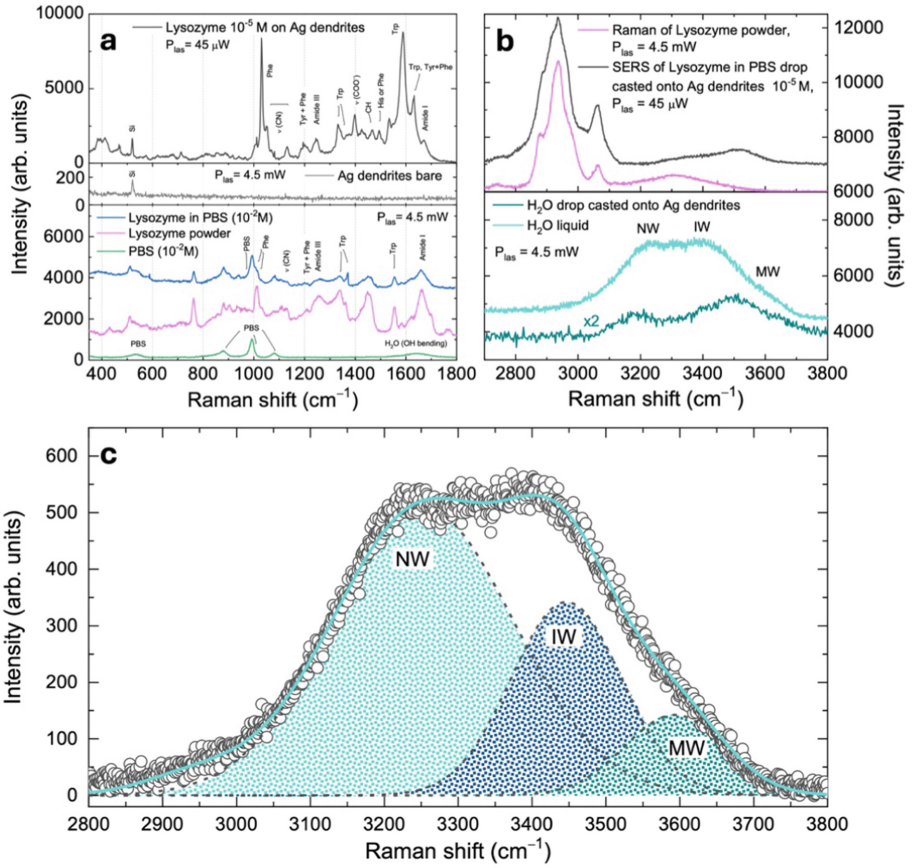

Fig. 2. (a) Comparison between the SERS spectrum of a 10^{-5} M lysozyme solution (black line) onto the Ag dendrite platform in the low frequency region and the Raman spectra of the lysozyme dry powder (blue line), the pure phosphate buffer saline (PBS) solution (green line), the lysozyme 10 mM in the PBS solution (magenta line), and the Raman spectrum of the bare Ag dendrites. (b) SERS spectrum the 10^{-5} M lysozyme solution compared to the lysozyme powder Raman spectrum in the high frequency region. Spectra are compared with water drop casted onto the Ag dendrites (dark green line), and liquid water (cyan line). (c) Raman spectrum of liquid water fitted by Gaussian distributions.

Figure 2c shows the Raman spectrum of water and the fitting of the OH stretching vibrational modes. The lowest frequency band, centered at about 3200 cm^{-1}, is called network water (NW) and is related to the stretching vibrational modes of water with the highest degrees of connectivity with tetrahedral H-bond [11]; the band at about 3450 cm^{-1} is called intermediate water (IW) due to water molecules with a low degree of connectivity and a coordination number close to three; finally the less intense multimeric water (MW) band at about 3600 cm^{-1} is typical of weakly bound water (dimers and trimers) [12]. Inside the Ag platform, the intensities of the IW and MW contributions of water increase with respect to the NW band. This behavior is also reproduced in the

spectra with lysozyme demonstrating that the protein is surrounded by a distorted water molecule, thus representing its hydration shell.

This SERS platform has proven to be an efficient tool not only for protein but also genome (DNA and RNA) analysis. Since 2019, numerous efforts have been focused on studies on SARS-Cov-2. In particular, we have dealt with the first characterization of the first Raman fingerprint of a deactivated RNA of the Omicron variant of the SARS-Cov. The RNA was quantified by RT-PCR, by which the RNA was converted into complementary DNA copies (cDNA) and amplified in real time obtaining a concentration of 10^4 cps/μL. The sample was drop casted on the Ag dendrite platform and let it to dry.

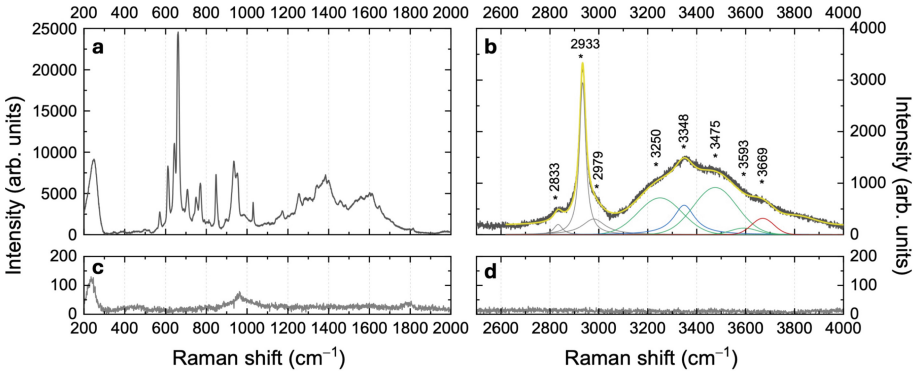

Fig. 3. SERS spectrum of the Omicron variant of SARS-CoV-2 in the low (a) and high (b) frequency region. The colored lines in (b) are the fitting curves separating the different spectral contributions. In particular, the grey lines represent the C-H stretching contributions; the green lines represent the network, intermediate, and multimers water bands, the blue and red lines indicate the N-H stretching band of nucleobases and the ribose O-H stretching band, respectively. The spectrum is compared with the SERS (grey line) of the bare Ag dendrites (c-d).

Figure 3a shows the SERS spectrum between 200 and 2000 cm^{-1}, dominated in the low-frequency region by intense peaks mainly related to symmetric stretching modes and deformations of the nucleobases and ribose rings in nucleosides [2].

Figure 2b shows the spectrum in the high-frequency region, between 2500 and 4000 cm^{-1}. The spectrum is compared with the reference Raman spectrum of bare Ag dendrites, which appears devoid of any spectroscopic signal. The C-H stretching modes vibrating between 2700 and 3100 cm^{-1} are typical of the RNA spectrum and mainly originate from the C-H [13–15] groups of ribose. Between 3000 and 3800 cm^{-1}, we find the complex spectrum formed by the N-H [16] and O-H [17] vibration bands of both RNA (nitrogenous bases and sugars) and interfacial water molecules [18]. In particular, we note the rearrangement in the hydrogen bond network, typical of liquid water, which gives rise to the three bands typical of interfacial water molecules, as previously observed in the case of lysozyme [1].

3 Conclusions

In conclusion we demonstrated that by a low cost and industrially compatible method it is possible to realize a dense array of silver dendrite platform with interesting optical properties, allowing the identification and characterization of different biomolecules via SERS effect. The intense plasmonic absorption extending throughout all the visible range guarantees resonance conditions with any excitation wavelength from UV to NIR region. Moreover, the high surface-to-volume ratio and its scale-invariant fractal properties provide the presence of numerous hot-spots in 3D that increase the Raman signal by several orders of magnitude. Furthermore, the possibility of confining water within the fractal structure allows to analyze biomolecules in hydration conditions, preserving their biologically active conformation.

Acknowledgements. CNR-IMM Messina acknowledges the Project MUR-PNRR "I-PHOQS–Integrated Infra-structure Initiative in Photonic and Quantum Sciences", grant number CUP B53C22001750006, funded by the European Union (Next Generation EU).

References

1. Faro MJL, et al (2019) Fractal Silver Dendrites as 3D SERS Platform for Highly Sensitive Detection of Biomolecules in Hydration Conditions. Nanomaterials 9. https://doi.org/10.3390/nano9111630
2. Leonardi AA et al (2022) Molecular fingerprinting of the omicron variant genome of SARS-CoV-2 by SERS spectroscopy. Nanomaterials 12:2134. https://doi.org/10.3390/nano12132134
3. Morganti D, Longo V, Leonardi AA, Irrera A, Colombo P, Fazio B (2025) First Vibrational Fingerprint of Parietaria Judaica Protein via Surface-Enhanced Raman Spectroscopy. Biosensors 15:182. https://doi.org/10.3390/bios15030182
4. Lo Faro MJ, Leonardi AA, Morganti D, Sciuto EL, Irrera A, Fazio B (2022) Surface-enhanced raman scattering for biosensing platforms: a review. Radiat Eff Defects Solids 177:1209–1221. https://doi.org/10.1080/10420150.2022.2136084
5. Moskovits M (1985) Surface-enhanced spectroscopy. Rev Mod Phys 57:783–826. https://doi.org/10.1103/RevModPhys.57.783
6. Nie S, Emory SR (1997) Probing single molecules and single nanoparticles by surface-enhanced raman scattering. Science 275:1102–1106. https://doi.org/10.1126/science.275.5303.1102
7. Huang Z, Geyer N, Werner P, de Boor J, Gösele U (2011) Metal-assisted chemical etching of silicon: a review. Adv Mater 23:285–308. https://doi.org/10.1002/adma.201001784
8. Morganti D, Faro MJL, Leonardi AA, Fazio B, Conoci S, Irrera A (2022) Luminescent silicon nanowires as novel sensor for environmental air quality control. Sensors 22:8755. https://doi.org/10.3390/s22228755
9. Morganti D, et al (2021) Ultrathin Silicon Nanowires for Optical and Electrical Nitrogen Dioxide Detection. Nanomaterials 11. https://doi.org/10.3390/nano11071767
10. Leonardi AA et al (2021) A novel silicon platform for selective isolation, quantification, and molecular analysis of small extracellular vesicles. Int J Nanomed 16:5153–5165. https://doi.org/10.2147/IJN.S310896

11. Brubach J-B, Mermet A, Filabozzi A, Gerschel A, Roy P (2005) Signatures of the hydrogen bonding in the infrared bands of water. J Chem Phys 122:184509. https://doi.org/10.1063/1.1894929
12. Brubach J-B et al (2001) Dependence of water dynamics upon confinement size. J Phys Chem B 105:430–435. https://doi.org/10.1021/jp002983s
13. Lu F-K et al (2015) Label-free DNA imaging in vivo with stimulated raman scattering microscopy. Proc Natl Acad Sci 112:11624–11629. https://doi.org/10.1073/pnas.1515121112
14. Varvarà P, et al (2024) Biotinylated polyaminoacid-based nanoparticles for the targeted delivery of lenvatinib towards hepatocarcinoma. Int J Pharmaceut 662: 124537. https://doi.org/10.1016/j.ijpharm.2024.124537
15. Morganti D et al (2024) Temporal convolutional network on raman shift for human osteoblast cells fingerprint analysis. Intelligence-Based Medicine 10:100183. https://doi.org/10.1016/j.ibmed.2024.100183
16. Chatterjee K, Dopfer O (2020) Spectroscopic identification of fragment ions of DNA/RNA building blocks: the case of pyrimidine. Phys Chem Chem Phys 22:17275–17290. https://doi.org/10.1039/D0CP02919J
17. Nikolaenko TYu, Bulavin LA, Govoruna DN (2011) Quantum mechanical interpretation of the IR spectrum of 2-Deoxy-D-Ribose in the oh group stretching vibration region. J Appl Spectrosc 78:751–754. https://doi.org/10.1007/s10812-011-9528-4
18. Halina A, Beata B-P, Jakub S, Joanna J-G, Radzislaw K (2011) hydrogen bonds of interfacial water in human breast cancer tissue compared to lipid and DNA interfaces. Journal of Biophysical Chemistry 2011. https://doi.org/10.4236/jbpc.2011.22020

Validation of On-Chip Bioluminescence Detection for Radiation-Stressed Genetically Engineered *E. Coli*

Lorenzo Nardi[1(✉)], Costanza Maria Martella[3], Parsa Abbasrezae[1], T. B. De Albuquerque[1], Domenico Caputo[2], Nicola Lovecchio[2], Giulia Petrucci[2], Francesca Costantini[2], Giampiero de Cesare[2], Daniela Billi[3], and Augusto Nascetti[1]

[1] Scuola di Ingegneria Aerospaziale, Sapienza Università di Roma, Roma, Italy
lorenzo.nardi@uniroma1.it

[2] Dip. Ingegneria dell'Informazione, Elettronica e delle Telecomunicazioni, Sapienza Università di Roma, Roma, Italy

[3] Dipartimento di Biologia, Università di Roma Tor Vergata, Roma, Italy

Abstract. The ALCYONE project, funded under the EU Horizon Europe program, aims to develop a lab-on-chip (LoC) platform for biological studies in space environments. This study focuses on validating the system's bioluminescence detection capability using genetically engineered *Escherichia coli* MG1655 cells. The cells, transformed with a luciferase-expressing plasmid, were irradiated with UV-C light for two minutes to induce stress responses, while unirradiated cells served as controls. Bioluminescence emission (520–530 nm) was measured using hydrogenated amorphous silicon (a-Si:H) photosensors integrated into the LoC platform. The experimental results confirm the system's ability to differentiate between irradiated and control samples, demonstrating its potential for real-time, low-power monitoring of biological responses in space environments. Future work will integrate thermal control and fluidic automation to enhance biological experiment autonomy.

Keywords: Lab-on-chip · Bioluminescence · Space biology · a-Si:H photosensors · Microfluidics · Radiation effects

1 Introduction

Long-duration space missions expose biological systems to extreme conditions, including ionizing radiation and microgravity, which can have significant physiological effects [1]. The ability to monitor cellular responses in real time is crucial for assessing space radiation risks and developing countermeasures [2]. Traditional laboratory equipment is not suitable for spaceflight due to size, weight, and power constraints. Therefore, miniaturized, autonomous lab-on-chip (LoC) platforms offer a promising solution for space biology studies [3].

The ALCYONE project focuses on developing a compact and low-power LoC system capable of performing real-time biological experiments in space. This system integrates thin-film sensors, microfluidic actuators, and photodetectors to monitor

C. Di Natale et al. (Eds.): AISEM 2025, LNEE 1497, pp. 311–315, 2025.
https://doi.org/10.1007/978-3-032-08271-8_49

bioluminescence-based stress responses in living cells [4]. The present study validates the system's ability to detect bioluminescent signals emitted by a bacterial biosensor obtained by genetically engineered Escherichia coli in response to radiation exposure.

2 System Overview

2.1 Lab-On-Chip Design

The ALCYONE LoC system (Fig. 1) consists of three main layers: (1) a thermal actuation layer with thin-film resistive heaters, (2) a biological incubation layer with a microfluidic network, and (3) a sensing layer with integrated a-Si:H photosensors and temperature sensors. This modular design enables precise environmental control while ensuring compatibility with spaceflight requirements [5].

The fluidic system includes tapered culture chambers designed to stabilize liquid positioning under microgravity-like conditions. Active pressure modulation enables controlled meniscus positioning, preventing bubble formation and ensuring consistent cell exposure to reagents [6].

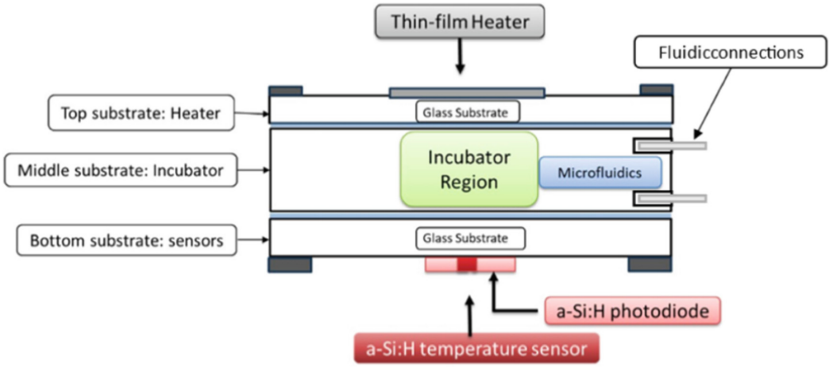

Fig. 1. ALCYONE LoC scheme.

2.2 Photosensor Design and Detection Method

Bioluminescence detection is achieved using a-Si:H photosensors, which provide high sensitivity in the visible spectrum. These sensors are optimized for low-light conditions and exhibit a spectral response that aligns with the peak emission wavelength of the luciferase reaction (520–530 nm). The sensors design is based on a half-donut shape optimized for efficient photon capture from the bioluminescent cell cultures hosted in the incubation chamber.

The a-Si:H sensor array was fabricated through a multi-step microfabrication process. After aligning photomasks on soda-lime glass substrates, ITO and Ti-W layers were deposited via magnetron sputtering to form the bottom contacts. These were patterned using two separate lithography steps and wet etching. The a-Si:H p-i-n photodiode stack was deposited by PECVD, followed by Cr/Al/Cr back contacts added via thermal

evaporation. Sensor areas were defined through photolithography, with wet etching for metals and RIE for a-Si:H. A 5 μm SU-8 insulating layer was patterned, and Ti-W was deposited and etched to define top contacts. Finally, SU-8 passivation was applied using a shadow mask, with optional annealing to enhance performance. This process yields low-noise, radiation-hardened photodiodes suitable for space applications.

The integration of these sensors within the LoC system eliminates the need for bulky optical components, reducing power consumption and system complexity in accordance with typical space systems requirements [7].

3 Materials and Methods

3.1 Biological Experimentation

Escherichis coli MG1665 was transformed with a luciferase-expressing plasmid based on a pET19b backbone and carrying the luciferase gene from *Photinus pyralis*, called BgLuc, under the control of the *recA* promoter of *E. coli*. Transformants were selected in Luria-Bertani growth medium containing ampicillin (100 $\mu g\ ml^{-1}$).

Aliquots of transformants (10^8 cells/mL) were exposed to UV-C radiation (VILBER lamp, 254 nm, 16xW, 230V) for 2 min (900 J/m2) to induce the activation of the "SOS response box," which is regulated by *recA* promoter region that drives the luciferase expression in response to DNA damage. After UV-C irradiation, D-Luciferin (5 mM, D-Luciferin sodium salt, Sigma Aldrich®) was added as a substrate for the luciferase reaction resulting in a bioluminescence with light emitted in the 520–530 nm range. Control samples were not exposed to UV-C irradiation and the luciferin substrate was added to evaluate the background luciferase-luciferin reaction.

In particular, *E. coli* cells and substrate (2.5 μL of cells and 2.5 μL of D-Luciferin) was loaded into the microfluidic chamber, ensuring precise positioning and a controlled dark environment to minimize interference.

3.2 Measurement Procedure

Initial trials involved direct droplet placement on the sensor surface, but signal inconsistencies due to substrate evaporation led to the adoption of a microfluidic channel-based measurement method. The final protocol involved preloading cells into a dark microfluidic channel and introducing them onto the sensor under control conditions to ensure reproducible readings.

4 Results

4.1 Bioluminescence Detection Performance

The a-Si:H photosensors successfully detected bioluminescence from irradiated *E. coli* cells, with a clear distinction between control and treated samples (Fig. 2). The measured photocurrent in irradiated cells exhibited a peak response significantly above background noise, confirming the system's sensitivity.

The dark reference samples showed minimal signal, ensuring that the observed bioluminescence originated from the engineered luciferase system and was not due to sensor noise or experimental artefacts.

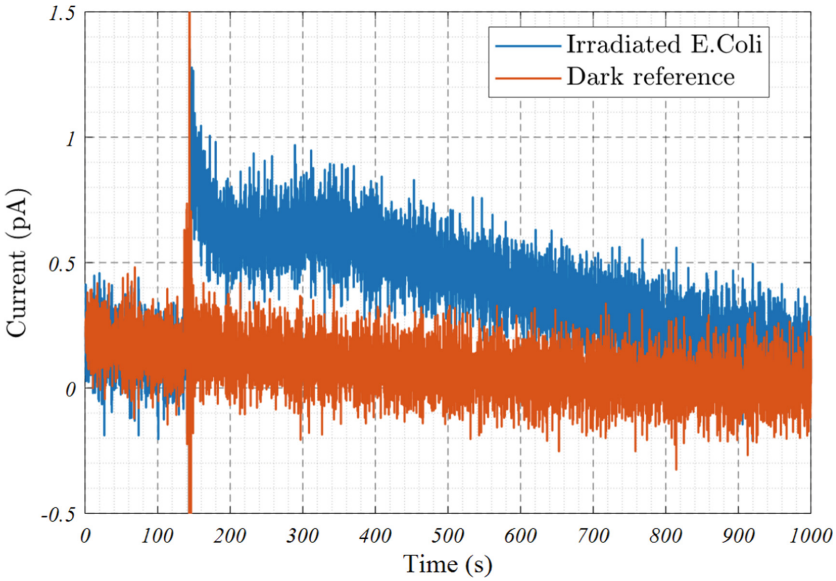

Fig. 2. Results

4.2 Signal Stability and Biological Response

Bioluminescence intensity decreased over time due to substrate depletion, aligning with expected luciferase reaction kinetics. The signal decay was consistent with previous studies on bioluminescent reporter systems, further validating the reliability of the measurement approach [8].

These results confirm that the LoC platform can effectively monitor biological stress responses, laying the groundwork for its deployment in future space missions. In addition, these results are also a confirmation of the effectiveness of the a-Si:H photosensors for detecting weak bioluminescent signals, even in low-power configurations, making the system ideal for resource-constrained environments such as space missions.

5 Conclusions

This study validates the bioluminescence detection capability of the ALCYONE LoC system, demonstrating its ability to monitor radiation-induced stress responses in a bacterial biosensor. The successful integration of a-Si:H photosensors, microfluidics, and biological elements represents a significant step toward autonomous space-based biological research.

Future work will focus on expanding the system's capabilities by integrating thermal regulation and multi-spectral sensing to enhance experimental precision. The broader

ALCYONE initiative aims to deploy this technology on CubeSats for long-term studies of biological adaptation to space environments.

References

1. Bunge F, Van Den Driesche S, Vellekoop MJ (2017) Easy-to-use microfluidic chip for long-term 3D-cell cultures. In: Van Den Driesche S, Giouroudi I, Delgado-Restituto M (eds.) Barcelona, Spain, pp. 1024706
2. Zhao Y et al (2023) Microfluidic actuated and controlled systems and application for lab-on-chip in space life science. Space Sci Technol 3:0008. https://doi.org/10.34133/space.0008
3. Dervisevic E, Tuck KL, Voelcker NH, Cadarso VJ (2019) Recent progress in lab-on-a-chip systems for the monitoring of metabolites for mammalian and microbial cell research. Sensors 19:5027. https://doi.org/10.3390/s19225027
4. Fang G, Chen Y, Lu H, Jin D (2023) Advances in spheroids and organoids on a chip. Adv Funct Materials 33:2215043. https://doi.org/10.1002/adfm.202215043
5. Ricco AJ, Parra M, Bhardwaj SR, Santa Maria SR (2022) Microfluidic biosensing and bioanalytical devices for space applications. Lab Chip 22:3576–3592. https://doi.org/10.1039/D2LC00571D
6. Strods A, Gomez D, Beysens D (2021) Microfluidic techniques for fluid control in microgravity: a review. Microfluid Nanofluid 25:56. https://doi.org/10.1007/s10404-021-02498-8
7. Smith PA, Young MA, Brown RC (2020) Advances in thin-film photosensor technology for biological sensing. J Microelectron Eng 230:111255. https://doi.org/10.1016/j.mee.2020.111255
8. Williams CL, Lee HJ, Tseng H, Sun P (2023) Bioluminescence imaging in microfluidic systems: applications in cell-based assays. Biosens Bioelectron 202:114085. https://doi.org/10.1016/j.bios.2022.114085

Amplification Strategies for the Labelling and Detection of Infectious Agents by Means Optical Sensing

G. Bella[1(✉)], M. S. Nicolò[1], E. L. Sciuto[1], and S. Conoci[1,2,3]

[1] Department of Chemical, Biological, Pharmaceutical and Environmental Sciences, University of Messina, Viale F. Stagno d'Alcontres 31, 98166 Messina, Italy
gbella@unime.it

[2] Department of Chemistry "Giacomo Ciamician", University of Bologna, Via Selmi 2, 40126 Bologna, Italy

[3] URT Lab Sens DSFTM-CNR, Viale F. Stagno D'Alcontres 37, 98166 Messina, Italy

Abstract. The present contribution describes a high challenging project aiming to develop strategies to shift the paradigm from target- to signal amplification, enabling rapid, simple and low-cost tests for viruses and bacteria using assays on paper or simple electronic read out. The vision, applicable to any pathogen and in different detection modalities, is based on signal generation from thousands of reporter molecules generated for each analyte captured and will make a breakthrough in the diagnostic field, enabling home- and point of care diagnostics. The detection strategy for the pathogens is emission, colorimetric assay or electrochemiluminescence, ECL. To achieve such a goal we have designed electrochemiluminescent polynuclear complexes able to disaggregate (to avoid self-quenching) upon a redox reaction, breakable nanoparticles able to release hundreds of reporter molecules. Phage display technology provides probes endowed with high affinity and selectivity towards the desired analyte overcoming the limitations of monoclonal antibodies, including cost, chemical stability and heterogeneity of reactions. In this research, we will demonstrate that we can detect the virus or bacterium without the need to extract any biomolecular marker.

Keywords: Later flow · biosensors · Sars-Cov2 · *pseudomonas aeruginosa* · pathogen detection

1 Introduction

The investigation of sensors with intriguing chemical [1], magnetic [2] and photophysical [3] features has been finding many applications in a multi-variegated scenario. In the biomedical field, access to effective screening and diagnostic tools is essential for public health, as recently highlighted by the *COVID-19* pandemic [4]. The need for broader access to affordable and reliable diagnostic methods is evident, particularly for infectious diseases [5]. Current diagnostics are sophisticated but often insufficient, as seen with tuberculosis, where a significant number of cases go undiagnosed, and in HIV awareness,

C. Di Natale et al. (Eds.): AISEM 2025, LNEE 1497, pp. 316–320, 2025.
https://doi.org/10.1007/978-3-032-08271-8_50

with only half of those infected knowing their status [6]. The challenges include the need for rapid, cost-effective testing solutions that can improve early detection and treatment. Enhancing these diagnostic capabilities would not only benefit patient outcomes but also strengthen health systems globally by reducing the burden of undiagnosed diseases. The present project aims to shift the paradigm in pathogen detection from target-based to signal amplification approaches. The goal is to enable rapid, simple, and low-cost tests for viruses (*SARS-Cov-2*) and bacteria (*Pseudomonas aeruginosa*) using assays on nitrocellulose (paper) or accessible electronic readouts. The vision for this project is to develop detection strategies that can be applied to any pathogen and utilize different detection modalities, such as emission, colorimetric assays, or electrochemiluminescence (ECL). The key innovation is the use of signal generation from thousands of reporter molecules generated for each captured target, which will enable a breakthrough in the diagnostic field and facilitate home and point-of-care testing. To achieve the presented goal, the project has designed the following technologies:

(1) Electrochemiluminescent polynuclear complexes that can disaggregate upon a redox reaction to avoid self-quenching.
(2) Breakable nanoparticles capable of releasing hundreds of reporter molecules.
(3) Engineered phages as sensing probes of the detection strategy.

On the following this background, colorimetric detection methods using cellulose-based materials like chromatography and filter paper will be used in our detecting platform. The main advantage of these colorimetric methods is that can potentially be observed by the naked eye. These features are of particular interest in developing countries, where clinical laboratory infrastructures are very limited and cost constraints are relevant.

2 Results and Discussion

The central part of this study is focused on creating the molecular detection assay based on a lateral flow prototype. The performance of such a new platform for detecting *SARS CoV-2* and *P. aeruginosa* will be assessed under various experimental conditions, related to:

1- The affinity and densities of phages on the nanomaterials surface for signal amplification.
2- The methods of phages immobilization on solid substrates and the varying densities of the nanomaterials on the paper medium.
3- The use of different porosity grade in the nitro-cellulose wafer for signal amplification.
4- The implementation of various detection and transduction modules.
5- The impact of varying volumes of biological fluid used in the assay.

These factors will provide a comprehensive evaluation of how effectively our sensoring system can efficiently perform in different scenarios, selecting the perfect conditions for the best specific and sensitive test to detect the presence of SARS CoV-2 or *P. aeruginosa* in the biological fluid. Figure 1 shows a schematic visualization of our assembled lateral flow device.

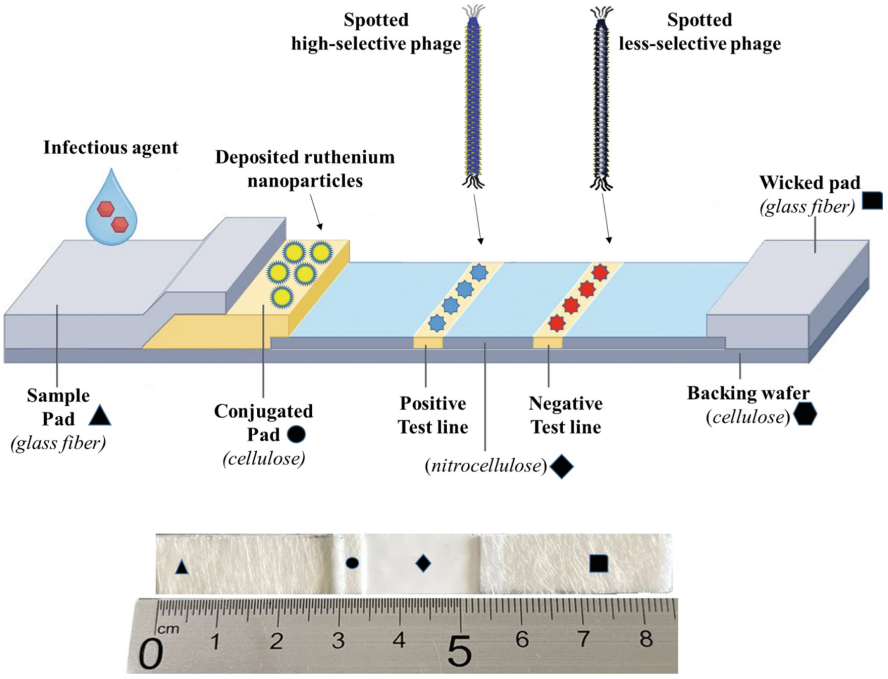

Fig. 1. Top) Lateral flow scheme. Bottom) Later flow assembled prototype.

In order to verify the interaction and the stability between phage and nitrocellulose wafer ELISA test was performed, using a Horse Radish Peroxidase-labeled antiphage antibody and subsequent colorimetric reaction adopting the chromogenic substrate TMB (Figs. 2 and 3).

Specifically, data indicates that the binding between phage and nitrocellulose is highly stable and is not compromised by the washing process. Figure 3 clearly illustrates how 10^{12} PFU/mL was the most suitable phage quantity for Elisa detection on nitrocellulose. Furthermore, several surface functionalization strategies will be assessed involving the use of membranes with different porosity.

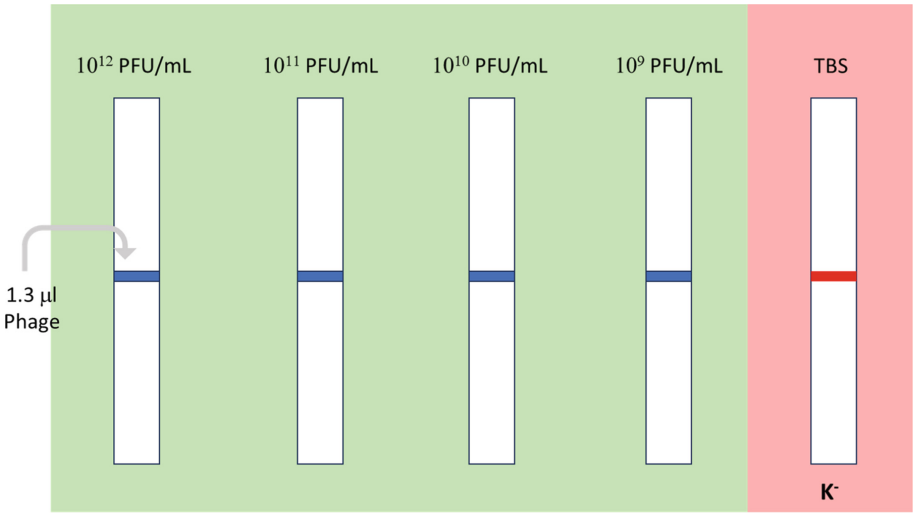

Fig. 2. Adhesion test of phage on nitrocellulose by means ELISA.

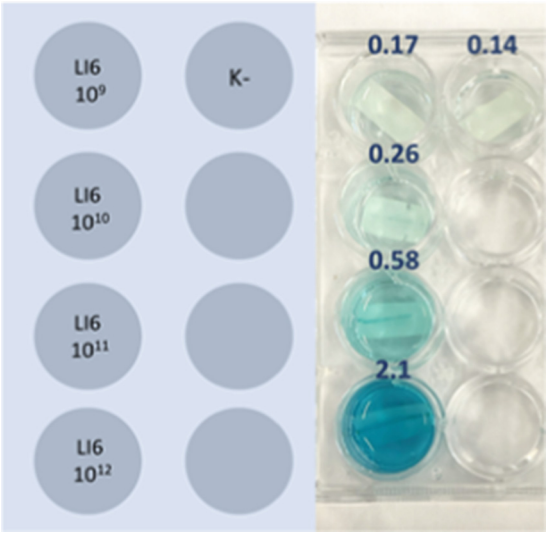

Fig. 3. Absorbance values ($\lambda = 450$ nm) of experimental ELISA test with multiple phage quantities.

3 Conclusions

The COVID pandemics has revealed the need of rapid, reliable diagnostic tests to be used by not specialized users. In the present project, a prototype of an innovative lateral flow assay for microbial pathogens has been set up. This system is based on a new capture element, in detail the selected pathogens are recognized and bound by an engineered

bacteriophage, which is a more stable and cheap alternative to common capture agents (e.g. antibodies). Data indicates that the binding of phages to nitrocellulose support is very strong, demonstrating the stability of the system. Several detection techniques can be applied to this system to reveal the pathogen capture.

References

1. Giannetto A, Nastasi F, Puntoriero F, Bella G, Campagna S, Lanza S (2021) Fast transport of HCl across a hydrophobic layer over macroscopic distances by using a Pt(II) compound as the transporter: micro- and nanometric aggregates as effective transporters. Dalton Trans 50:1422–1433
2. Bella G, Milone M, Bruno G, Santoro A (2022) Which DFT factors influence the accuracy of ^{1}H, ^{13}C and ^{195}Pt NMR chemical shift predictions in organopolymetallic square-planar complexes? New scaling parameters for homo- and hetero-multimetallic compounds and their direct applications. Phys Chem Chem Phys 24:26642–26658
3. Bella G, Bruno G, Santoro A (2023) Circular dichroism simulations of chiral buckybowls by means curvature analyses. FlatChem 40:100509
4. Cheng L et al (2023) A review of current effective COVID-19 testing methods and quality control. Arch Microbiol 205:239
5. Mardian Y, Kosasih H, Karyana M, Neal A, Lau C-Y (2021) Review of current COVID-19 diagnostics and opportunities for further development. Front Med 8:615099
6. Mukherjee S, Perveen S, Negi A, Sharma R (2023) Evolution of tuberculosis diagnostics: From molecular strategies to nanodiagnostics. Tuberculosis 140: 102340; Qashqari FS, et al (2022) Knowledge of HIV/AIDS transmission modes and attitudes toward HIV/AIDS infected people and the level of HIV/AIDS awareness among the general population in the kingdom of Saudi Arabia: A cross-sectional study. Front Public Health 10: 955458

Hybrid Optical-Fiber/Alkali-Activated Material Sensor for Structural Health Monitoring Structures: Preliminary Results

R. De Michele[1(✉)], B. Liguori[1], I. Ingrosso[2], A. Largo[2], and C. Menna[3]

[1] Department of Chemical, Materials and Industrial Engineering, University of Naples Federico II, P.le V. Tecchio 80, 80125 Naples, Italy
rosa.demichele@unina.it
[2] RINA Consulting S.p.A., Via B. Ravenna 4, 73100 Lecce, Italy
[3] Department of Structures for Engineering and Architecture, University of Naples Federico II, Via Claudio 21, 80125 Naples, Italy

Abstract. In this work, a system for detecting temperature within structures useful for monitoring structural health during fire was realized. The aim is to monitor the temperature inside building materials when their external surface is subjected to a heat wave. This is extrinsic sensing material whose self-sensing capability is realized through the incorporation of an optical fiber as an intelligent sensing element. Specifically, Fiber Bragg Grating (FBG) technology was implemented within an innovative fire resilient alkali-activated material (AAM) and within a traditional cement-based material (OPC) for comparison. The performance of the two monitoring systems was compared in a test where heat waves in the proximity of a fire were simulated. During the heat test, traditional K-thermocouples (TC) were exploited to validate FBG sensors response. The preliminary results have demonstrated the applicability of this new AAM-based detection system to structures in high fire probability areas.

Keywords: Alkali-activated materials · Fiber Bragg Grating · Smart Building Materials

1 Introduction

The safety and usefulness of concrete structures are threatened by uncontrolled fire. Concrete, though incombustible, suffers from explosive spalling and mechanical degradation at temperatures above 300 °C [1]. Consequently, it is crucial to monitor concrete infrastructure in real-time to assess their structural health and facilitate prompt maintenance. For applications in structural health monitoring (SHM), Fiber Bragg Gratings (FBGs) are considered to be very promising sensors due to their compact size, their light weight, their resistance to electromagnetic interference, their ability to be multiplexed and their high resistance to harsh chemicals [2] respect to traditional sensors (i.e. thermocouples). To address fire protection challenges, the use of Alkali-Activated Materials (AAMs),

C. Di Natale et al. (Eds.): AISEM 2025, LNEE 1497, pp. 321–326, 2025.
https://doi.org/10.1007/978-3-032-08271-8_51

particularly based on selected waste, has gained prominence in retrofitting and strengthening of fire resistance structures due to low carbon footprint, excellent performance in terms of mechanical strength and durability, good fire resistance and thermal insulation properties [3]. The integration of FBGs with advanced materials such as AAMs can be a forward-looking approach to improve the performance and longevity of structures. Therefore, in this work an experimental campaign was conducted to develop an alkali-activated material (AAM) with higher fire resistance than a conventional cement-based material (OPC). The temperature monitoring system achieved by integrating FBG into these materials was then evaluated.

2 Material and Methods

Wood ash (WA), waste from combustion processes of virgin wood, was used as a precursor in alkali-activated systems to achieve higher fire resistance. In particular, WA were used in different percentage (15, 25 and 35%) in two alkali-activated systems based on class-F fly ash (FA) and/or ground granulated blast furnace slag (GGBS), provided by Enel (Italy) and Ecocem (France) respectively. A mixture of sodium silicate (R = 3.3, Prochin) and 10 M sodium hydroxide (NaOH 98%, J.T. Baker) were used as activating solution with a silica modulus (M_s) ratios of 0.9 and varying Na_2O concentration (M) of 4% and 10%. Figure 1 shows the sample preparation procedure. Precursor and activating solution were mixed to obtain a homogenous slurry that was poured into moulds (height 5 cm) and cured at room temperature and 100% of relative humidity. After one day of curing the samples were stored into a climatic chamber at room temperature and relative humidity $70 \pm 5\%$ for 28 days. Compressive strength [4] was determined by ZwickRoell universal testing machine with a 10 kN load cell and a crossbar lowering speed of 2 mm min^{-1}. The samples with the 28 days-highest compressive strength were subjected to unstressed residual strength test [5]. Therefore, they were heated in an electric oven at a heating rate of 6 °C/min until the target temperatures (200, 400, 600, 800 °C) were reached. Each temperature was maintained for 2 h. The samples were then allowed to cool naturally to room temperature for the compressive strength test to assess residual strength. The system with the highest residual compressive strength was optimised to produce a mortar, indicated by AAM, with sand to binder ratio equal to 1. For comparison, a cement-based mortar, indicated by OPC, was also prepared according to [4]. The alkali-activated mortar (AAM) and cement-based mortar (OPC) were subjected to the same unstressed residual test strength.

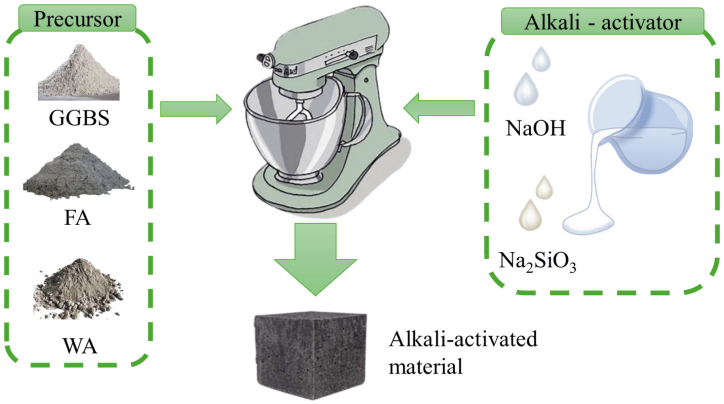

Fig. 1. Sample preparation diagram

3 Experimental Setup

The experimental set-up (Fig. 2) was realized as follow. The selected materials, AAM and OPC, were produced in a specific geometry (150 × 150 × 5 cm^3) with a 5 mm diameter capillary tube inside which the thermal sensors were incorporated as shown in Fig. 3. The incorporation of FBG into a capillary tube can mitigate the effects of transverse deformation on measurements and increase the temperature sensitivity of FBGs for sensing applications [4]. For validation a traditional K-thermocouples (TC) was also inserted into the same capillary on the opposite side to allow easy insertion of cables. The sensitive part of each sensor is located in the centre of the through hole (see Fig. 3). For FBG, it was necessary to join the fiber optic cables to the patch cables using the 90S core alignment splice-in g apparatus supplied by Fujikura. To interrogate the FBG sensors was used 4-channel high-speed interrogator Hyperion si155 provided by Micron Optics. To read the output from the thermocouples, the USB data recorder TC-08 provided by Pico Technology was needed. The specimens were placed inside a metal chamber (300 × 150 × 150 mm^3) from the open side (see Fig. 2) and a TC was installed on each sample surface to monitor the temperature inside the chamber during the test. The chamber was closed on the open side and insulated with a thermal shield material consisting of insulating glass fiber, aluminum foil and adhesive. On the closed opposite side of chamber, a circular hole of 37 mm in diameter has been made to house the nozzle of the heat gun used to deliver the heat waves. From room temperature, the system inside the chamber was subjected to cyclic heat waves to avoid overheating of the chamber. Specifically, 5 min of heating given by the thermal activity of the heat gun followed by 5 min of natural cooling given by the shutdown. The test was carried out for 11 cycles.

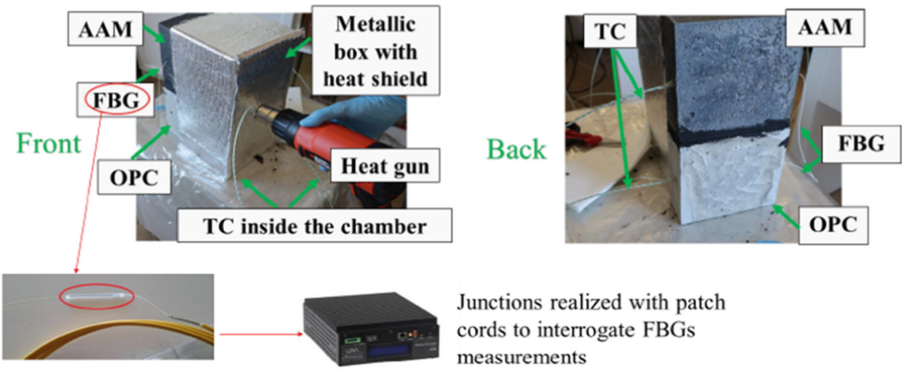

Fig. 2. Experimental set-up.

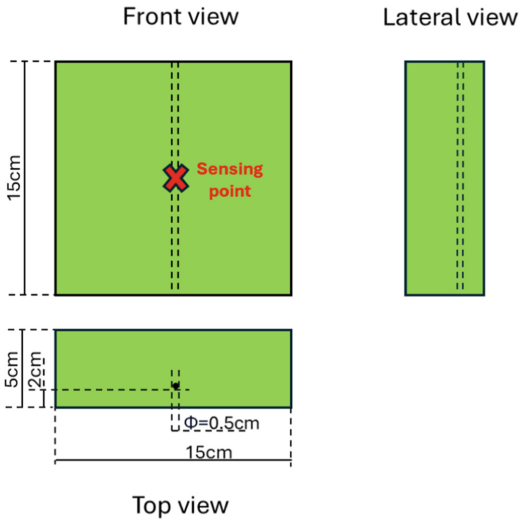

Fig. 3. Geometry with integration of FBG.

4 Results

The FA-based system with 15%WA as the lowest loss compressive strength, -39%, at the highest target temperature, 800 °C, was selected to produce an alkali-activated mortar (AAM). Figure 4 showed the percentage change in compressive strength at the target temperature compared to the room temperature value of selected mortars. The cement-based mortars (OPC) showed a linear trend in the loss of compressive strength due to the degradation reactions of the cement paste as the temperature increases [6]. For the AAM, a gradual loss of compressive strength was observed up to 600 °C due to the loss of water from the hydrated phases [7], but a recovery occurred at 800 °C, reducing the loss to 11%, due to the ceramisation of the alkali-activated paste. To correlate FBG measurements with TC, it was not necessary to reach high temperatures to validate the

system, as FBG technology can linearly measure temperatures up to 900 °C. No significant differences were found between the measurements recorded by thermocouples and FBG incorporated in materials. Therefore, the use of FBGs as a sensing element in a temperature monitoring system in building materials was found to be feasible, as they respond similarly to thermocouples. Figure 5 showed the measurements registered by thermocouples on the surface samples in the chamber and by FBG in through-holes within the samples. The monitoring systems responded differently to the thermal stress recorded by the surface TCs depending on the material used. In particular, OPC showed a slightly lower insulating capacity than AAM. This result is confirmed by the evaluation of the post-fire resistance (see Fig. 4). Instead, the integration of FBG into AAM, fire resistant materials, can provide a system for monitoring the temperature inside structures when they are subjected to the heat waves that occur during fires, as shown in Fig. 5.

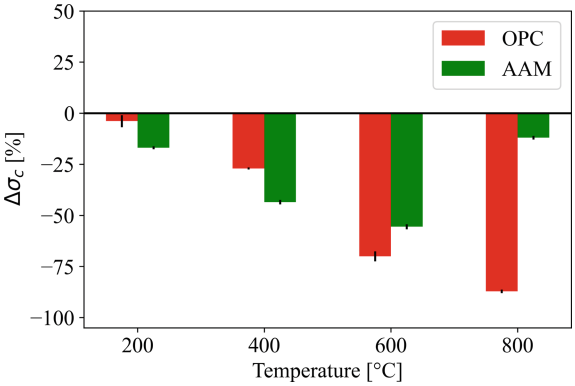

Fig. 4. Percentage change in compressive strength of AAM and OPC compared to unheated control sample.

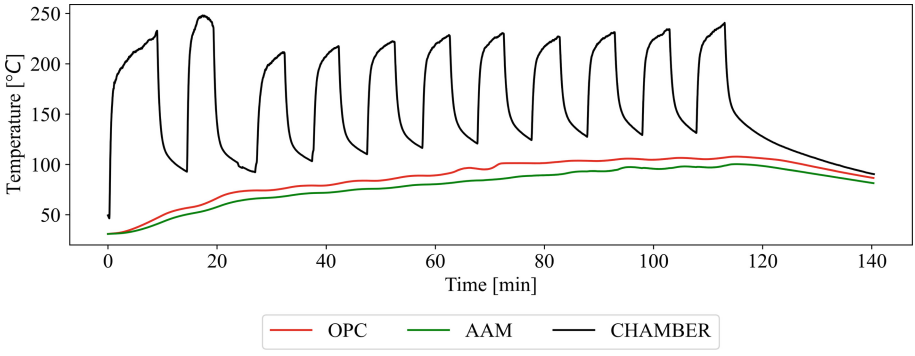

Fig. 5. Comparison between OPC and AAM under temperature stress.

5 Conclusion

Alkali-activated materials are known in the construction industry as alternative binders to cement due to their superior durability and sustainability properties. This preliminary study provided further information on these materials. Specifically, an alkali-activated mortar based on wood ash (AAM) has been developed with superior fire resistance compared to a traditional cement-based mortar (OPC). The reduction in compressive strength loss of AAM compared to traditional OPC at high temperatures paves the way for these materials in applications in extreme conditions. Although non-intrinsic self-sensing cement integrated with optical fibers has emerged for decades, in a harsh outdoor environment, such as a fire, detection properties are unstable and measurement accuracy is greatly reduced. In this study, in addition to improved fire-resistance properties, the potential advantages of alkali-activated materials in sensor technologies over cement-based sensors were highlighted. AAMs have been integrated with Fiber Bragg Grating temperature sensing to develop advanced building materials. The monitoring systems obtained through the integration of FBG showed very good correlation between outdoor and indoor temperatures as well as very good correlation with traditional sensing elements (thermocouples).

Acknowledgements. This research study has been funded by TREEADS – "A Holistic Fire Management Ecosystem for Prevention, Detection and Restoration of Environmental Disasters" CUP: E52C21000660006.

References

1. Panias D, Balomenos E, Sakkas K (2015) The fire resistance of alkali-activated cement-basedconcrete binders. Handbook of alkali-activated cements, mortars and concretes. Woodhead Publishing, pp. 423–461
2. Brindisi A, et al (2023) Fiber Bragg Grating Bonding Characterization under Long-Period Cyclic Loading. Photonics 10(8): MDPI
3. Peng X, et al (2020) Fire resistance of alkali activated geopolymer foams produced from metakaolin and Na_2O. Materials 13(3): 535
4. UNI EN 196-1:2016. Test methods of cements—Part 1: Determination of mechanical strengths
5. Guerrieri M, Sanjayan JG (2010) Behavior of combined fly ash/slag-based geopolymers when exposed to high temperatures. Fire and Mat Int J 34(4):163–175
6. Neto JADF, et al (2022) Effects of post-fire curing on the residual mechanical behavior of cement-lime masonry mortars. Constr Build Mat 327: 126613
7. Behfarnia K, Shahbaz M (2018) The effect of elevated temperature on the residual tensile strength and physical properties of the alkali-activated slag concrete. J Build Eng 20:442–454

A HDR System for the Recognition of Printed Color Markers

Michela Lecca[1] and Massimo Gottardi[2(✉)]

[1] Fondazione Bruno Kessler, Digital Industry Center, TeV, 38123 Trento, Italy
[2] Fondazione Bruno Kessler, Sensors and Devices, IRIS, 38123 Trento, Italy
gottardi@fbk.eu

Abstract. Introducing colors in barcodes and QR codes would significantly extend the data capacity of such markers, but still today represents a major challenge because of the large variety of color distortions often occurring in real world scenes. To address this problem, several constraints on the light and on the marker structure and colors have been introduced in the past, limiting the applicability range of the color markers. To overcome this issue, here we propose (i) a novel model for color markers with the only constraints of being composed of matte material and not differing from each other in color intensity solely and (ii) a HDR imaging system for the illuminant invariant recognition of such markers. In our system, an optical sensor acquires marker colors over a linear dynamic range of about 105 dB, while a microcontroller implements a nearest-neighbor classification in an illuminant invariant color space. We tested a prototype of this system on a set of 15 color markers printed on matte, white paper and acquired under 18 lights, reaching on average 99.14% of correct classification.

Keywords: Color Markers · Illuminant invariance color representation · HDR optical sensors

1 Introduction

Barcodes and QR codes are black & white visual labels of objects and services worldwide used to compactly encode data information. The development of a color technology for such markers represents a significant, intriguing advancement as it would enable bursting the marker data capacity. Several studies in this direction have begun more than 10 years ago, but such a technology is still an open issue. The main difficulty in this field is the variety of color distortions that must be modelled and handled, like e.g. the color shifts caused by light changes, by physical properties of the reading devices and by features of the support on which markers are printed or displayed [1, 2]. In the past, these problems have been addressed by imposing constraints on the markers' color number and structure [3] and/or on the environmental light conditions [4] or by including in the marker a reference palette [5] for controlling and correcting possible color variations.

This work contributes to the state of the art with (i) a new, little constrained model of color markers and (ii) a HDR imaging system for the illuminant invariant recognition of

C. Di Natale et al. (Eds.): AISEM 2025, LNEE 1497, pp. 327–332, 2025.
https://doi.org/10.1007/978-3-032-08271-8_52

these color markers. Our markers are composed by color blocks (white, black and grey tones are forbidden) with the following two constraints: (a) the blocks are printed or displayed on matte material and (b) the set of markers to be recognized cannot contain markers which only differ only in color intensity. The constraint in (a) enables representing the marker colors regardless of light changes through the Gray World algorithm. This algorithm divides the R, G, B components of each marker color by their mean values over the marker: while this operation removes possible color effects due to the light, it also discards any information about the global color intensity, so that two markers whose color blocks differ only in intensity becomes indistinguishable: the constraint in (b) is introduced just to avoid the misclassification of such markers. Our marker model is less constrained than others proposed in the past: in fact, there is no need to include in the marker structure any calibration-control patterns, there are no limitations on the number of marker blocks and chromaticities and there are no constraints on the light. The HDR imaging system we propose is composed by the HDR low power optical sensor described in [6, 7] and a microcontroller connected to it. The optical sensor captures the marker colors over a linear dynamic range of about 105 dB DB, enabling accurate color sampling even in low and high lights, while the microcontroller implements the Gray-World color normalization and a nearest-neighbour classification for recognizing the color markers (here we do not cope with the problem of detecting the marker in a scene).

We tested a prototype of the proposed imaging system on a set of 15 color markers printed on matte, white paper and acquired under 18 lights differing for color and/or intensity, reaching in the worst case the 99.14% and on average the 98.40% of right classification of the observed markers.

2 The Proposed Color Marker Technology

The proposed color marker model, the optical sensor and the operations performed by the microcontroller are described in the following Subsections.

2.1 Color Marker Model

We considered a set of N markers, each composed by m adjacent rectangular, color blocks, adjacent to each other and printed on white, matte paper with density 80 gr/m^2. We sampled the marker colors from the 18 colors of a MacBeth color checker (black, white and grey tones were excluded). As illustrated in Fig. 1 (A), each marker appears like a sequence of colored rectangles: although in principle the proposed system can manage markers with arbitrary geometric structures, here we chose a linear displacement of the color blocks to enable a simple and fast acquisition of the color markers by our prototype. Specifically, to this purpose, we located the marker on a rigid support, and we acquired its m colors under different illuminations by moving the prototype from the first block on left to the last block on right of the marker (see Fig. 1 (B)). The prototype was perpendicular to the marker support and the light sources were placed to guarantee a uniform illumination across the marker. In this work, we set $N = 15$ and $m = 6$, but other choices are possible.

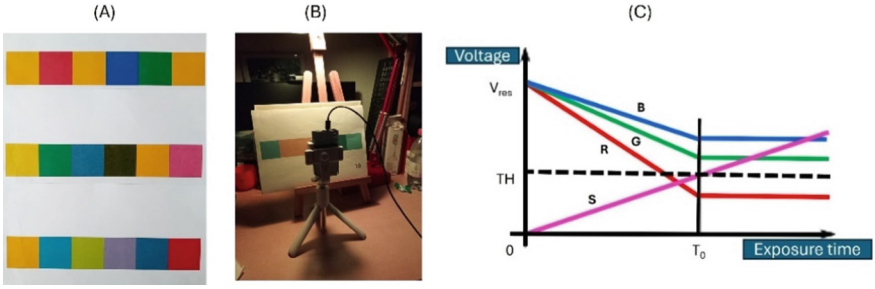

Fig. 1. (A) Some color markers printed on paper; (B) the color marker acquisition set up; (C) the HDR sensor color capturing diagram: R, G, B are sampled where their sum S reaches a pre-defined threshold TH.

2.2 The Optical Sensor

We adapted the optical sensor in [6, 7] to collect (R, G, B) data over a high, linear dynamic range instead of chromaticity information as in its original version. This sensor consists of three photodiodes, a voltage comparator that controls the exposure time, and a sample-and-hold circuit that samples the analog signals of the photodiodes when the sum of their voltages reaches a pre-defined threshold TH selected to grant a dynamic range for the pixel intensity up to 105 dB (see Fig. 1 (C)). In this way, for any point p, the sensor autonomously adjusts the exposure time of p upon the light level, enabling an accurate sample of the color of p under illumination with arbitrary intensity.

2.3 The Microcontroller

The marker colors are represented as a sequence $\left[(r_1, g_1, b_1, T_1), \ldots, (r_m, g_m, b_m, T_m)\right]$ where (r_i, g_i, b_i) is the color of the i-th block and T_i is the exposure time at which this color has been acquired. The exposure time varies from block to block, depending on the block color intensity as well as on the light intensity. To recover the relative intensity information among the marker colors, the microcontroller maps any triplet (r_i, g_i, b_i) onto the *exposure-corrected* triplet

$$(R_i, G_i, B_i) = \frac{\max\limits_{j=1,\ldots,m} T_j}{T_i}(r_i, g_i, b_i), i = 1, \ldots, m. \tag{1}$$

and achieves invariance against light changes by the following normalization:

$$\left(R_i^*, G_i^*, B_i^*\right) = \left(\frac{R_i}{\sum_{j=1}^m R_j}, \frac{G_i}{\sum_{j=1}^m G_j}, \frac{B_i}{\sum_{j=1}^m B_j}\right) \tag{2}$$

Equation (2) implements a slight variant of the Gray-World algorithm, where the the denominators are the sums of the R_j s, G_j s and B_j s instead of their mean values as in the original Gray-World implementation. According to the von Kries model [8], when applied to matte material uniformly illuminated, this normalization makes the colors robust to light changes. In fact, under these hypotheses, a color change at any point

x due to a light change can be approximated by a linear transformation rescaling the triplet $(R(x), G(x), B(x))$ to $(\alpha R(x), \beta G(x), \gamma B(x))$, where α, β, γ are strictly positive real values depending on the light energy and camera sensitivities. Dividing the color components at x by the sum (or mean value) of the colors in a neighbourhood of x allows removing their dependence on the light parameters α, β, γ and thus achieving invariance against light changes.

We observe that the normalization described by Eq. (2) also eliminates any information about the global intensity of the marker. Therefore, two markers i and j with exposure-corrected sequences $\left[\left(R_1^i, G_1^i, B_1^i\right), \ldots, \left(R_m^i, G_m^i, B_m^i\right)\right]$ and $\lambda[\left(R_1^j, G_1^j, B_1^j, ..., \left(R_m^j, G_m^j, B_m^j\right)\right]$ becomes indistinguishable after normalization (of course, here $\lambda > 0$). Consequently, to enable a fair recognition, the set of markers to be recognized cannot contain markers differing to each other in intensity only: this is the constraint (b) mentioned in Sect. 1.

2.4 Color Marker Recognition

Marker recognition is performed by a nearest-neighbour classifier. In this framework, the colors of each printed, linear marker to be recognized are acquired by the HDR sensor under a reference illumination RI, then exposure-corrected and converted by the microcontroller to the normalized RGB space according to the Gray-World principle, and finally stored as a sequence $\left[\left(R_1^*, G_1^*, B_1^*\right), \ldots \left(R_m^*, G_m^*, B_m^*\right)\right]$ in a database. Each time the color sequence $S(M)$ of a marker M under a new illumination NI is acquired by the sensor, the microcontroller corrects its colors accounting for the corresponding exposure times, normalizes the exposure-corrected colors according to the Gray-World model, computes the L^1 distance between the normalized color sequence $NS(M)$ and each reference normalized color sequence, and returns the reference marker one whose color sequence has the smallest distance from $NS(M)$.

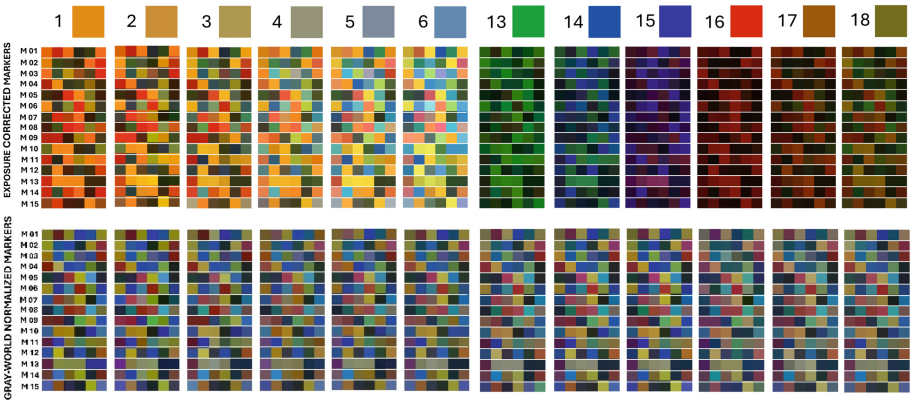

Fig. 2. On top: the colors of the lights from 1 to 6 and from 13 to 18 and the exposure-corrected color markers (labeled as M01,… M15); on bottom: the color markers after the Gray-World normalization. For constraints on paper length, here we did not report the lights and color markers under the lights from 7 to 12 that have the same chromaticities of the lights from 1 to 6 but a lower brightness.

3 Experiments

We tested our HDR imaging system under 18 lights, labeled by integer numbers from 1 to 18 and produced by a YELANGU led lamp with dimmable color (see Table 1). For the lights from 1 to 6 we set the brightness at the maximum level allowed by the lamp (L = 100%) and we tuned the light correlated color temperature (CCT) from 2500K to 7500K with steps of 1000K. For the lights from 7 to 12 we set the same CCTs of the lights from 1 to 6 but a lower brightness level (L = 40%). These 12 lights are commonly used in many real-world scenarios, like e.g. industrial and domestic environments. For the lights from 13 to 18, which have more unusual colors (like red, green, violet, blue), we tuned the values of hue (H), saturation (S) and intensity (L) of the color lamp as indicated in Table 1. Figure 2 shows the exposure-corrected color markers acquired by the sensor before and after the Gray-World color normalization for the lights with different chromaticities. From a visual inspection of the markers captured under all the lights, we observed that after the Gray-World normalization, the marker colors remain stable across light changes.

Table 1. Information about the colors of the lights used in the experiments.

Light	Color Information	Light	Color Information
1	CCT = 2500K, L = 100%	10	CCT = 5500K, L = 40%
2	CCT = 3500K, L = 100%	11	CCT = 6500K, L = 40%
3	CCT = 4500K, L = 100%	12	CCT = 7500K, L = 40%
4	CCT = 5500K, L = 100%	13	H = 90, S = 85, L = 40%
5	CCT = 6500K, L = 100%	14	H = 180, S = 85, L = 40
6	CCT = 7500K, L = 100%	15	H = 270, S = 85, L = 40%
7	CCT = 2500K, L = 40%	16	H = 360, S = 85, L = 40%
8	CCT = 3500K, L = 40%	17	H = 355, S = 50, L = 40%
9	CCT = 4500K, L = 40%	18	H = 340, S = 10, L = 40%

For evaluating the performance of the proposed system on illuminant invariant marker recognition, we took as references the markers captured under the six most common lights (i.e. lights 1, …, 6), and the other as tests. The results are reported in Fig. 3. When the reference and test markers are compared without color normalization, the percentage of the marker correctly recognized is 85.05% on average and the 33.34% in the worst case, while, when the color normalization is applied, this percentage reaches the 99,14% on average and the 93,34% in the worst case. The worst results were obtained for light 13, which has a strong green component and distorts the colors more much than the other lights. We observe that the average percentage of correct classification is very high also when no color normalization is applied. This is due to the presence of lights with similar chromaticity, like lights 1, 2, 3, 7, 9, 16, 17 and 18. Nevertheless, the use of the Gray-World normalization enables better recognition performance on every light. To conclude, the obtained results are encouraging and indicate that the proposed system can be a starting point for color marker technology.

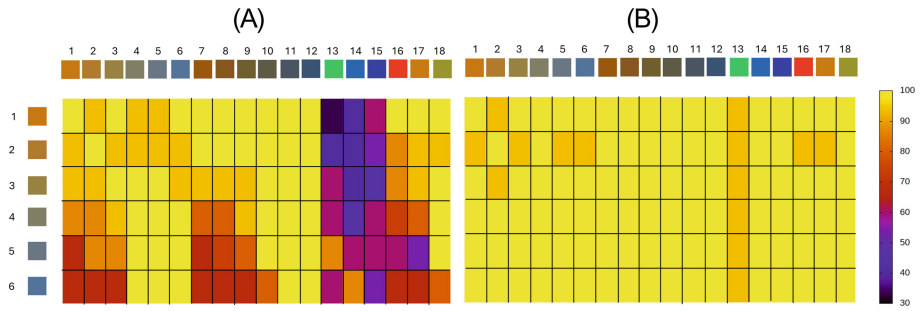

Fig. 3. Percentage of correct recognition for the markers without Gray-World normalization (A) and with Gray-World normalization (B). The colors of the reference and test lights are shown on left and on top, respectively.

References

1. Sirmen RT, Üstündağ BB (2023) Color barcodes from debut to present: a broad survey on the state of the art. Alphanumeric J 11(1):31–62
2. Lecca M, Lecca P (2024) A dataset for illuminant- and device- invariant colour barcode decoding with cameras. Data Brief 52:1–21
3. Parikh DJ, Janck G (2008) Localization and segmentation of a 2D high capacity color barcode. In: IEEE workshop on applications of computer vision. Copper Mountain, CO, USA
4. Bagherinia H, Manduchi R (2012) High information rate and efficient color barcode decoding. In: Computer Vision–ECCV 2012. Workshops and Demonstrations, Florence, Italy
5. Kato H (2010) Performance of a color 2D barcode as a pervasive computing tool. In: Int. Symposium on Intelligent Signal Processing and Communication Systems. Chendu
6. Lecca M, Gottardi M, Farella E, Miloseviic B (2016) Always-on low-power optical system for skin-based touchless machine control. J Opt Soc Am A 33: 1015–1024
7. Paissan F, Lecca M, Passerone R, Farella E, Gottardi M (2024) HDR vision sensor with neuro-memristive skin detection for edge computing. J Opt Soc Am A 41: 1009–1018
8. Lecca M (2014) On the von Kries model: estimation, dependence on light and device, and applications. In: Lecture Notes in Computational Vision and Biomechanics, pp. 95–135

Design of FMCW LiDAR for Precision Relative Navigation in Close Formation Distributed SAR

Mattia Tagliente, Giuseppe Brunetti, and Caterina Ciminelli(✉)

Optoelectronics Laboratory, Department of Electrical and Information Engineering, Politecnico di Bari, Bari, Italy
caterina.ciminelli@poliba.it

Abstract. Distributed Synthetic Aperture Radar (DSAR) missions impose stringent relative navigation requirements, including sub-millimeter position and millimeter-per-second velocity knowledge, for applications such as single-pass interferometry. This paper presents the design and performance analysis of a Frequency-Modulated Continuous-Wave (FMCW) LiDAR system for DSAR metrology. The system operates at 1550 nm and employs integrated photonics for reduced Size, Weight, and Power (SWaP). Key LiDAR parameters are derived from DSAR mission specifications, such as a 2 km maximum inter-satellite range and a 100 Hz update rate, resulting in a 150 GHz chirp bandwidth and a 10 ms coherent integration time. The proposed architecture incorporates a heterogeneous System-in-Package design. Performance analysis, with a calculated electrical Signal-to-Noise Ratio (SNR) exceeding 30 dB, indicates theoretical range precision of 28.7 μm and velocity precision of 0.71 μm/s. These findings suggest the photonic integrated LiDAR can meet the 1 mm range and 1 mm/s velocity targets for DSAR formation control.

Keywords: FMCW LiDAR · DSAR · Integrated Photonics · Formation Flying

1 Introduction

Distributed Synthetic Aperture Radar (DSAR) systems, comprising multiple cooperating spacecraft, represent a significant advancement over traditional single-satellite SAR, offering enhanced capabilities for Earth observation [1]. The successful execution of DSAR missions, especially for applications demanding high geometric accuracy like single-pass interferometry, relies fundamentally on precise formation flying, imposing stringent requirements on relative spacecraft navigation [1]. Achieving the necessary accuracy, potentially requiring sub-millimeter position knowledge for future high-frequency systems, is challenging for conventional techniques, especially under the demanding Size, Weight, and Power (SWaP) constraints typical of modern satellite constellations [1, 2]. Concurrently, the development of advanced spaceborne Light Detection and Ranging (LiDAR) systems, such as those proposed for space debris tracking [3], underscores the potential of optical metrology in space.

C. Di Natale et al. (Eds.): AISEM 2025, LNEE 1497, pp. 333–338, 2025.
https://doi.org/10.1007/978-3-032-08271-8_53

Frequency-Modulated Continuous-Wave (FMCW) LiDAR technology is particularly well-suited for formation flying as it enables simultaneous, high-precision measurement of inter-satellite range and relative velocity. Implementing FMCW LiDAR using integrated photonics allows for significant SWaP reduction compared to bulk-optic systems, making it compatible with smaller satellite platforms. This aligns with the broader trend of incorporating photonic technologies into SAR payloads to handle computationally intensive tasks like on-board data processing, aiming for higher performance and reduced SWaP. The adoption of photonic LiDAR for inter-satellite metrology is thus consistent with the technological evolution towards more integrated and capable photonic-enabled SAR systems. This paper presents the design and performance analysis of an integrated FMCW LiDAR system tailored to the metrological requirements of DSAR formation control. The derivation of key LiDAR parameters from DSAR mission requirements is outlined, and the overall system architecture along with hardware component specifications is selected to suit the intended application. Finally, mathematical models and simulations are employed to evaluate the system's anticipated range and velocity measurement performance.

2 Close-Formation DSAR

Close-formation DSAR systems, where multiple satellites operate with inter-satellite distances typically ranging from tens of meters up to a few kilometres, are important for advanced Earth observation. This configuration enables applications such as single-pass interferometric SAR (InSAR) for terrain mapping and TomoSAR for 3D imaging, that benefit from the coherent processing of signals acquired by spatially separated platforms. The "close" aspect, with an upper boundary considered here as 2 km, is determined by the need to maintain a proper interferometric baseline and ensure coherence between the received signals from different satellites. Exceeding this range can lead to decorrelation and loss of interferometric quality, diminishing the utility for high-precision measurements. For instance, the TanDEM-X mission utilized such close formations for generating high-resolution global Digital Elevation Models (DEMs) [6].

The requirements for relative navigation in close formation DSAR primarily stem from the need for SAR data processing. For InSAR and TomoSAR applications, the interferometric phase, which contains the geophysical information, is directly dependent on the baseline vector—the three-dimensional separation between SAR antenna phase centres [6]. Errors in baseline knowledge translate directly into inaccuracies in the final products. To achieve high-quality DEMs, such as those from the TanDEM-X mission, a baseline knowledge accuracy of 1 mm (1D Root Mean Square, RMS) is required during data acquisition [1]. This level of precision has been demonstrated in post-processing using carrier-phase Differential Global Navigation Satellite System (DGPS) techniques [1]; missions like TanDEM-X achieved up to 1 mm baseline measurement accuracy via onboard differential Global Navigation Satellite System (GNSS) receivers. Furthermore, precise relative velocity knowledge is essential to maintain phase stability throughout the synthetic aperture integration time. An uncompensated change in the baseline due to relative velocity error can corrupt the interferometric phase. Consequently, relative velocity knowledge at 1 mm/s level is considered necessary to complement the millimeter-level position knowledge [1].

In addition to SAR processing, active Formation Keeping (FK) systems are necessary to maintain the desired satellite constellation geometry and ensure collision avoidance [2]. These systems counteract orbital perturbations, maintaining satellites within operational baseline ranges (e.g., 200–500 m cross-track [2]) and at safe separations (e.g., minimum 150 m [2]). The sensing accuracy for FK is less demanding than for SAR processing, typically in the order of centimetres to meters for position [2]. Under nominal conditions, relative radial velocities are kept very low; e.g., TanDEM-X maintained velocity knowledge within 0.3 mm/s per axis [1]. However, a navigation system must accommodate potential off-nominal scenarios, such as during orbital manoeuvres. For Low Earth Orbit (LEO) satellites, typically orbiting at altitudes below 1000 km (e.g., TanDEM-X at 514 km), the orbital mean motion (n) at an altitude of approximately 550 km is roughly 0.0011 rad/s. In a worst-case scenario of differential orbital phasing between two spacecraft with a 2 km separation (S), the maximum relative line-of-sight speed ($v_{rel,max}$) can be approximated by $v_{rel,max} \approx n \times S$. This calculation yields 0.0011 rad/s $\times$ 2000 m $\approx$ 2.2 m/s. This is therefore set as a requirement for the LiDAR system's Doppler tolerance. The update rate for the relative navigation solution, enabling effective closed-loop control, is specified as 100 Hz [6].

Currently, DGPS is the state-of-the-art for high-accuracy baseline determination, capable of achieving millimeter-level accuracy in post-processing [1]. However, real-time onboard accuracy is often lower, and GNSS-based systems are vulnerable to signal jamming, spoofing, and ionospheric disturbances, posing risks to mission autonomy [1]. Radio Frequency (RF) Inter-Satellite Links (ISLs) offer direct ranging but with generally lower accuracy than DGPS [1]. Other optical sensors might struggle with simultaneous high-precision range and velocity over the required distances and conditions [1].

FMCW LiDAR sensors represent a compelling alternative. As an active optical sensor, a LiDAR provides an independent, onboard measurement capability, enhancing resilience. It directly measures both range and relative radial velocity with high precision by analyzing the beat frequency and Doppler shift of the laser signal [3]. This approach is well-suited for the operational distances of close formations (tens of meters to a few kilometers) and it offers the potential for real-time millimeter-level range and millimeter-per-second velocity measurements. Furthermore, the use of integrated photonics can lead to compact, low SWaP FMCW LiDAR systems, aligning with the trend toward photonic-enabled SAR payloads [5].

3 LiDAR System Design for DSAR Metrology

The design of the integrated FMCW LiDAR system is driven by the metrological requirements for DSAR formation control, as detailed in Sect. 2.

The system employs FMCW ranging for simultaneous range and velocity measurements [3], operating in the 1550 nm C-band for its mature ecosystem, eye-safety, reduced solar interference, and fiber compatibility. A coaxial bistatic architecture using integrated photonics targets a 1U CubeSat volume. The front-end is a heterogeneous System-in-Package (SiP) with InP-on-Si Photonic Integrated Circuits (PICs), SiGe BiCMOS analog Integrated Circuits (ICs), and CMOS digital/driver Application-Specific Integrated Circuits (ASICs) on a silicon interposer, minimizing path lengths and enabling thermal co-management of key components within footprint constraints.

The key LiDAR parameters are derived from DSAR mission requirements (see Sect. 2). A 150 GHz chirp bandwidth (B) yields a 1 mm intrinsic range resolution ($\Delta R = c/(2B)$), meeting the 1 mm DSAR accuracy target. A 10 ms coherent integration time (T_{meas}) provides a 100 Hz update rate. A single long up-chirp for the full 10 ms maximizes the time-bandwidth product. This single-long chirp eases hardware linearity/bandwidth demands compared to shorter, faster sub-chirps. A full triangular chirp ($T_{chirp} = T_{meas} = 10$ ms) means an up/down-chirp duration $T_{ramp} = 5$ ms. The chirp rate is $\kappa = B/T_{ramp} = 30$ THz/s. At $R_{max} = 2$ km, round-trip delay $\tau_{D,max} \approx 13.33\,\mu s$, yielding maximum beat frequency $f_{beat,\max} = \kappa\tau_{D,\max} \approx 400$ MHz. For $v_{max} = 2.2$ m/s (see Sect. 2), maximum Doppler shift $f_{Doppler,max} = 2v_{max}/\lambda_{laser} \approx 2.84$ MHz (at $\lambda_{laser} = 1.55\,\mu m$). Laser coherence length ($L_c = c/(\pi\Delta\nu)$) must exceed 4 km, requiring laser linewidth $\Delta\nu \leq 23.9$ kHz.

A hybrid InP photonic integrated laser provides the < 10 kHz linewidth (meeting the < 23.9 kHz requirement) and wide tunability for the 150 GHz chirp. An on-chip Semiconductor Optical Amplifier (SOA) amplifies output to 200 mW [4]. This is split 90:10, yielding 180 mW (P_{tx}) for the transmit Optical Phased Array (OPA) and 20 mW (P_{LO}) for the local oscillator. This split optimizes returned signal strength while ensuring P_{LO} is sufficient for shot-noise limited coherent reception.

An 8 cm diameter ($D_{aperture}$) metasurface lens collimates, transmits, and focuses received signals. These 1550 nm all-glass meta-optics offer $> 80\%$ efficiency and LEO thermal resilience [7]. The 8 cm aperture maximizes collection area (A_{rx}) for better SNR and narrows beam divergence, suitable for a 10x10 cm CubeSat face. Theoretical FWHM beam divergence is $\theta_{FWHM} \approx 1.98 \times 10^{-5}$ rad. The $1/e^2$ divergence results in a ~ 5.02 cm spot diameter at 2 km.

Two interleaved 2048-element sparse OPAs (Tx/Rx) behind the lens provide a coaxial bistatic path with a 50% fill factor, eliminating bulk beamsplitter losses and maintaining Tx/Rx isolation [8]. Apodization for sidelobe suppression (>10–19 dB) yields a practical continuous low-sidelobe steering range of ~ $\pm$ 19°, sufficient for acquisition and tracking. Hierarchical thermo-optic phase shifters at sub-array boundaries reduce heater count [9]; onboard optimization further cuts heater power.

A two-mode scan strategy is used. Initial acquisition employs a raster scan over a 10°x10° uncertainty cone. With 0.25° steps and 10 ms dwell per point (1600 points), acquisition takes ~ 16 s, acceptable for initial link-up. Upon target lock, the OPA enters tracking mode, continuously staring for 100 Hz updates.

Millimeter-level range accuracy at 2 km requires a highly linear optical frequency sweep, as nonlinearity or jitter degrades measurements. A strategy of open-loop distortion, closed-loop locking, and external calibration addresses this. CMOS Digital-to-Analog Converter (DAC) banks, potentially flip-chipped over OPA heater rows, generate control signals.

Received light is coherently mixed with P_{LO} in a high-speed balanced InGaAs photoreceiver, suppressing common-mode noise. The differential output feeds a SiGe BiCMOS Transimpedance Amplifier (TIA) providing low noise ($i_{n,TIA} \approx 1.1 \times 10^{-12}\,\mathrm{A}/\sqrt{\mathrm{Hz}}$) and meeting the 450 MHz Analog Front-End (AFE) bandwidth. This bandwidth accommodates $f_{beat,max}$ and $f_{Doppler,max}$ with margin. The amplified beat signal is digitized by a high-speed Analog-to-Digital Converter (ADC).

Received optical power (P_{rec}) for a diffuse Lambertian target (reflectivity ρ) is $P_{rec} = P_{tx} \cdot \left(\rho A_{rx}/\left(\pi R^2\right)\right) \cdot \eta_{sys}$. Parameters: $P_{tx} = 180\,\text{mW}$; $\rho = 0.1$ (conservative for unprepared surfaces); $A_{rx} \approx 0.005027\,\text{m}^2$ (8 cm lens); $R_{max} = 2000\,\text{m}$; and round-trip system optical efficiency $\eta_{sys} = 0.003$. This η_{sys} is a conservative estimate for all path losses (metasurface, OPAs, coupling, polarization, pointing) [10]. This yields $P_{rec} \approx 2.16 \times 10^{-14}\,\text{W}(0.0216\,\text{pW})$.

Electrical Signal-to-Noise Ratio (SNR) in the signal's frequency bin ($\Delta f = 1/T_{meas}$) for the coherent receiver is $SNR = \left(2\mathcal{R}^2 P_{rec} P_{LO} T_{meas}\right)/\left(2q\mathcal{R}P_{LO} + i_{n,TIA}\right)$, with photodiode responsivity $\mathcal{R} \approx 0.9\,\text{A/W}$, $P_{LO} = 20\,\text{mW}$, elementary charge $q = 1.6 \times 10^{-19}\,\text{C}$, TIA noise $i_{n,TIA} \approx 1.1 \times 10^{-12}\,\text{A}/\sqrt{\text{Hz}}$, and $T_{meas} = 10\,\text{ms}$. LO-induced shot noise ($2q\mathcal{R}P_{LO} \approx 5.76 \times 10^{-21}\,\text{A}^2/\text{Hz}$) dominates TIA noise ($i_{n,TIA}^2 \approx 1.21 \times 10^{-24}\,\text{A}^2/\text{Hz}$), confirming shot-noise limited operation for maximum sensitivity. The SNR is ≈ 1214.7 (30.8 dB), based on conservative parameters, forming the basis for measurement precision.

Fundamental range resolution (ΔR) from chirp bandwidth B is $\Delta R = c/(2B) = 1\,\text{mm}$ (for $B = 150\,\text{GHz}$). Coherent measurement time $T_{meas} = 10\,\text{ms}$ defines velocity resolution (Δv): $\Delta v = \lambda_{laser}/(2T_{meas}) = 0.08\,\text{mm/s}$ (for $\lambda_{laser} = 1.55\,\mu m$).

Measurement precision (standard deviation), limited by SNR via the Cramér-Rao Lower Bound (CRLB), is calculated for range (σ_R) and velocity (σ_v). Range precision $\sigma_R \geq \Delta R/\sqrt{SNR} \approx \left(1 \times 10^{-3}\,\text{m}\right)/\sqrt{1214.7} \approx 28.7\,\mu m$. Velocity precision $\sigma_v \geq \lambda_{laser}/\left(2\pi T_{meas}\sqrt{SNR}\right) \approx 0.71\,\mu\text{m/s}$. These values (28.7 μm range, 0.71 μm/s velocity) indicate potential to meet the 1 mm range and 1 mm/s velocity knowledge targets with significant margin.

System accuracy, distinct from precision, is governed by systematic errors minimized through calibration and advanced digital signal processing (DSP). Practical performance is affected by non-ideal factors (laser phase noise, chirp nonlinearities, etc.), but fundamental limits are positive. Super-resolution algorithms (e.g., MUltiple SIgnal Classification (MUSIC)) aim for frequency estimates finer than Fourier resolution (0.5 mm range equivalent), targeting sub-0.1 mm system accuracy. Coherent detection enables phase-based processing: range from up/down-chirp phase differences ($R = c \cdot \left(\phi_{up} - \phi_{down}\right)/(4\pi\kappa)$) with phase unwrapping. Synthetic wavelength techniques can resolve ambiguities. These DSP routines are feasible on space-grade Field-Programmable Gate Arrays (FPGAs) (e.g., Xilinx Zynq UltraScale +) within CubeSat power budgets (< 5 W) at 100 Hz. System simulations, utilizing validated models that reflect the paper's integrated design principles, confirmed the system's theoretical SNR predictions. These results demonstrated excellent agreement with theory, including the expected inverse square dependence of SNR on beat frequency, derived from the paper's equations for received power and range. For target reflectivities from 0.05 to 0.45, simulations yielded SNRs like approximately 34–43 dB at 1 km (200 MHz beat frequency), aligning with the paper's calculated ~ 30.8 dB at 2 km for a 0.1 reflectivity (Fig. 1). Even at the maximum 2 km range with a low 0.05 reflectivity, the projected ~ 28 dB SNR robustly supports the system's operational range and its targeted sub-millimeter measurement precision. Space qualification will necessitate attention to thermal management, radiation hardening, and reliability.

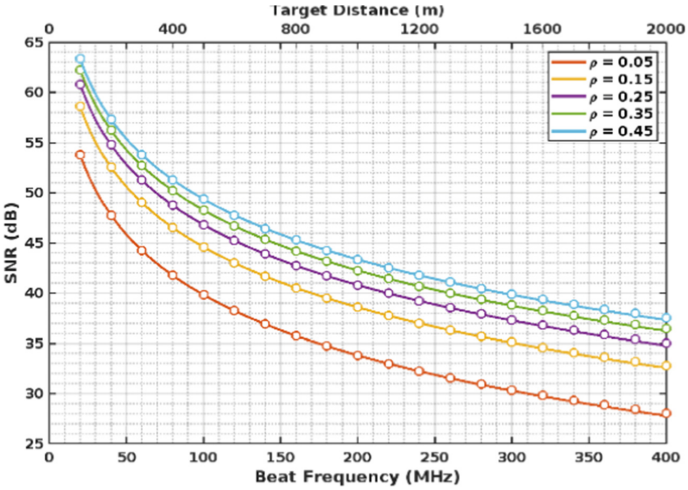

Fig. 1. SNR for the FMCW LiDAR system.

References

1. Hu C, et al (2025) Distributed Spaceborne SAR: A review of systems, applications, and the road ahead. IEEE Geosci Remote Sens Mag
2. D'Amico S, et al (2020) Satellite formation flying and rendezvous. In: Position, Navigation, and Timing Technol. In the 21st Century, pp. 1921–1946. Wiley
3. Tagliente M, et al (2023) Spaceborne LiDAR for debris detection and tracking. In: Proc. SIE 2022, Lect. Notes Electr. Eng., vol. 1005, pp. 172–177. Springer
4. Poulton CV et al (2022) Coherent LiDAR With an 8,192-element optical phased array and driving laser. IEEE J Sel Top Quantum Electron 28(5):1–8
5. di Toma A et al (2025) $LiNbO_3$-based Photonic FFT processor: an enabling technology for SAR on-board processing. J Lightw Technol 43(2):912–921
6. Xu B et al (2020) SAR interferometric baseline refinement based on flat-earth phase without a ground control point. Remote Sens 12(2):233
7. Park J-S et al (2024) All-glass 100 mm diameter visible metalens for imaging the cosmos. ACS Nano 18(4):3187–3198
8. Lei Y et al (2023) Si Photonics FMCW LiDAR chip with solid-state beam steering by interleaved coaxial optical phased array. Micromachines 14(5):1001
9. Li W et al (2022) Silicon optical phased array with calibration-free phase shifters. Opt Express 30(24):44029–44038
10. Walsh SM et al (2022) Demonstration of 100 Gbps coherent free-space optical communications at LEO tracking rates. Sci Rep 12(1):18345

Advanced NDIR Technology for CO_2 Detection: Comprehensive Laboratory Characterization

L. Barretta[1(✉)], E. Massera[2], M. Dellutri[3], and F. Formisano[2]

[1] Analog, Power and Discrete, MEMS and Sensors Group (APMS), STMicroelectronics, Via Remo de Feo 1, 80022 Arzano, NA, Italy
luigi.barretta@st.com
[2] ENEA CR Portici, Piazzale Enrico Fermi 1, 80055 Portici, Napoli, Italy
[3] Analog, Power and Discrete, MEMS and Sensors Group (APMS), STMicroelectronics, Stradale Primosole 50, 95121 Catania, Italy

Abstract. The detection and monitoring of carbon dioxide (CO_2) are critical for ensuring air quality, industrial safety, and environmental health. CO_2 is a key greenhouse gas, and its accurate measurement is essential for regulatory compliance, health hazard prevention, and climate change mitigation. Non-Dispersive Infrared (NDIR) technology has emerged as a leading solution for CO_2 sensing due to its high sensitivity, selectivity, and robustness. However, the performance of NDIR sensors can be influenced by environmental factors such as temperature, humidity, and gas composition, necessitating precise calibration in controlled laboratory environments.

This study presents the comprehensive laboratory characterization of an advanced NDIR CO_2 sensor, designed for compactness and integration into IoT applications. The sensor features a novel optical design with a gold-plated reflective surface and an optimized optical path, enabling high infrared absorption while maintaining a small form factor. A dedicated setup was developed at the ENEA gas sensor characterization laboratory, including a 15 L large volume test chamber (LVTC) with controlled air composition and environmental conditions.

The calibration procedure involved baseline recording, sensor response testing with target gas, and desorption phase evaluation. Results demonstrate excellent sensitivity (30 ppm per lsb), rapid response time (within seconds), and linearity (correlation coefficient near 1). Temperature drift was minimal and correctable via firmware, while no significant humidity-induced drift was observed. These findings validate the sensor's suitability for real-world applications, highlighting the importance of laboratory characterization in optimizing sensor performance and ensuring reliable CO_2 monitoring in diverse environments.

Keywords: CO_2 Monitoring · NDIR Technology · Sensor Calibration · Gas Sensor Characterization

1 Introduction

Carbon dioxide (CO_2) monitoring plays a vital role in addressing some of the most pressing challenges of our time, including air quality management, industrial safety, and climate change mitigation. As a major greenhouse gas, CO_2 contributes significantly

C. Di Natale et al. (Eds.): AISEM 2025, LNEE 1497, pp. 339–344, 2025.
https://doi.org/10.1007/978-3-032-08271-8_54

to global warming, making its accurate detection and monitoring essential for environmental policies and sustainable development. Beyond environmental concerns, CO_2 monitoring is critical in various industrial applications, such as HVAC systems, food storage, medical devices, and workplace safety, where elevated CO_2 levels can pose serious health risks [1, 2]. The ability to measure CO_2 concentrations with precision is therefore indispensable across a wide range of fields.

Non-Dispersive Infrared (NDIR) sensors have emerged as a leading technology for CO_2 detection [3, 4] due to their high sensitivity, selectivity, and long-term stability. Unlike other sensing technologies, NDIR sensors rely on the absorption of infrared light at a specific wavelength corresponding to CO_2 molecules, ensuring accurate and interference-free measurements. Their robustness and low maintenance requirements make them ideal for both industrial and environmental applications. Furthermore, advancements in NDIR sensor design, such as compact architectures and enhanced optical paths, have enabled their integration into portable and IoT-enabled devices, expanding their usability in modern applications.

However, the performance of NDIR sensors can be affected by environmental factors such as temperature, humidity, and gas composition. These interferences can lead to measurement inaccuracies if not properly accounted for. To address these challenges, comprehensive laboratory characterization in controlled environments is essential. By simulating real-world conditions in a controlled setting, it is possible to evaluate sensor performance, identify potential sources of error, and optimize calibration procedures. Laboratory characterization ensures that sensors deliver reliable and repeatable measurements, even in dynamic and challenging environments.

This study focuses on the importance of laboratory characterization for NDIR CO_2 sensors, highlighting the role of controlled environments in assessing sensor sensitivity, accuracy, and stability. By leveraging advanced setups and precise calibration techniques, this work aims to enhance the reliability of CO_2 monitoring technologies, paving the way for improved environmental and industrial safety applications.

2 Material and Method

To evaluate the performance of the proposed NDIR CO_2 sensor, a comprehensive laboratory characterization was conducted using a state-of-the-art gas sensor characterization system (GSCS) at the ENEA gas sensor characterization laboratory. The experimental setup includes a 15 L large volume test chamber (LVTC) (Fig. 1), which consists of a stainless-steel airtight chamber housed within an adjustable thermal box. This setup allows precise control of environmental parameters, including temperature, humidity, and gas composition, essential for assessing sensor performance under realistic yet controlled conditions.

The LVTC is equipped with certified mass flow controllers (MKS 1179 series) and certified gas bottles (Rivoira SpA) to regulate the concentration of CO_2 and other gases. Temperature and humidity are monitored using industrial-grade sensors (LSI Pt100) to ensure accurate environmental control. The calibration procedure is divided into three main steps: (1) baseline recording with synthetic air, (2) sensor response recording with the target gas, and (3) desorption phase recording while flushing the chamber with

synthetic air. This procedure enables the identification of sensing hysteresis or poisoning effects and ensures reliable sensor calibration. The chamber's characteristic time (τ) was estimated to be 1100 ± 50 s with a gas flow of 1 L/min, allowing for precise calibration of sensors with response times faster than 2 min.

Fig. 1. Photos of the gas sensor characterization setup, including the 15 L large volume test chamber (LVTC) and associated equipment.

The NDIR CO_2 sensor under study (Fig. 2) is designed for compactness and IoT integration. It features a flat lower internal wall made of PCB, where the detector and emitter are mounted, and a biconical upper internal wall with gold-plated reflective surfaces to enhance infrared (IR) radiation reflection. This innovative design extends the optical path without increasing the sensor's size, maintaining high IR absorption efficiency. The sensor also incorporates an optical filter for frequency selection, targeting the CO_2 absorption band at 4.3 µm, and includes a reference IR sensor to improve measurement accuracy.

The laboratory characterization focuses on evaluating the sensor's sensitivity, linearity, response time, and stability under varying temperature and humidity conditions. These tests aim to validate the sensor's performance and suitability for real-world applications.

3 Results

The laboratory characterization of the NDIR CO_2 sensor yielded promising results, demonstrating its suitability for accurate and reliable CO_2 monitoring in diverse applications. The calibration curves (Fig. 3a) show that the sensor closely follows the controlled chamber dynamics, with a response time significantly shorter than the chamber's characteristic time of 1100 ± 50 s. The sensor's rapid response, measured in seconds, highlights its capability to detect changes in CO_2 concentration efficiently, making it ideal for real-time monitoring applications.

The scatter plot (Fig. 3b) further validates the sensor's performance, illustrating a strong linear relationship between the chamber's CO_2 concentration and the sensor's response. The calculated correlation coefficient is near 1, confirming the sensor's excellent linearity across the tested concentration range. Sensitivity measurements indicate a resolution of 30 ppm per least significant bit (lsb), while baseline noise remains low,

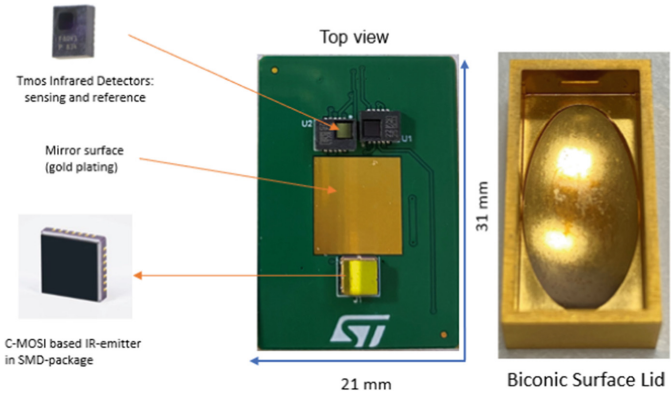

Fig. 2. DIL24 PCB with reflecting surface, right: internal shape of the lid 3D rendering of final wearable sensor node.

around 30 lsb. These characteristics ensure the sensor's ability to detect even small variations in CO_2 levels with high precision.

Environmental factors were also evaluated to assess the sensor's robustness. Temperature drift, although present, was minimal and could be effectively corrected through firmware recalibration. Humidity variations (20–70%) had negligible impact on the sensor's performance, further demonstrating its stability under varying environmental conditions. These findings confirm that the sensor meets the operational specifications required for real-world applications.

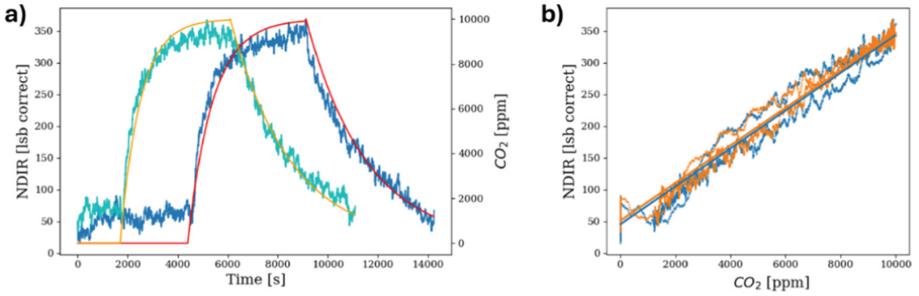

Fig. 3. Calibration curves over time, a) in yellow and red the concentration trend in the controlled chamber and in green and blue the sensor responses. b) scatter plot between chamber concentration and sensor response.

Overall, the results highlight the effectiveness of the innovative design features, including the compact optical path and gold-plated reflective surfaces, in achieving high sensitivity and accuracy. While the sensor performed well under controlled conditions, further hardware improvements, such as enhanced noise rejection, could further optimize its performance. These results validate the importance of laboratory characterization in ensuring the reliability and robustness of advanced NDIR CO_2 sensors for environmental and industrial applications.

4 Conclusion

The comprehensive laboratory characterization of the innovative NDIR CO_2 sensor highlights its strong potential for accurate and reliable CO_2 monitoring across a wide range of applications, including environmental monitoring, industrial safety, and smart building systems. The sensor demonstrated excellent performance in terms of sensitivity, linearity, and response time, meeting the operational requirements for real-world use. Its rapid response, measured in seconds, ensures timely detection of CO_2 concentration changes, making it suitable for applications where real-time monitoring is critical.

The sensor's compact design, featuring a gold-plated reflective surface and optimized optical path, proved effective in maintaining high infrared absorption while reducing size. This design innovation not only enhances sensitivity but also facilitates integration into IoT-enabled and portable devices, expanding its usability in modern applications. The inclusion of an optical filter targeting the 4.3 μm CO_2 absorption band, along with a reference IR sensor for baseline correction, further improved accuracy and selectivity, ensuring reliable measurements even in the presence of other gases.

Environmental robustness was another key strength observed during the characterization. The sensor exhibited minimal temperature drift, which could be effectively corrected through firmware recalibration, and no significant impact from humidity variations (20–70%), confirming its stability under varying environmental conditions. These features make the sensor suitable for deployment in dynamic environments where temperature and humidity fluctuations are common.

The laboratory characterization process, conducted in a controlled environment using a state-of-the-art setup, was instrumental in validating the sensor's performance. The three-step calibration procedure allowed for the identification of potential sources of error, such as sensing hysteresis or poisoning, ensuring consistent and repeatable measurements. This approach underscores the importance of controlled laboratory testing in optimizing sensor performance and reliability before deployment in real-world conditions.

While the sensor met or exceeded performance expectations, opportunities for further improvement were identified. Hardware enhancements, such as improved noise rejection and further optimization of the optical design, could enhance the sensor's accuracy and stability even further. These refinements would solidify its position as a leading solution for CO_2 monitoring in diverse applications.

In conclusion, the innovative NDIR CO_2 sensor represents a significant advancement in gas sensing technology. Its combination of high sensitivity, rapid response, compact design, and environmental stability makes it a reliable and versatile tool for CO_2 monitoring. The results of this study emphasize the critical role of laboratory characterization in ensuring the performance and reliability of advanced sensing technologies, paving the way for their successful implementation in industrial, environmental, and IoT applications.

Acknowledgment. Research reported in this publication was supported by SALVO project that has received funding from the National Programs (PON) of the Italian Ministry of Economical Development (MISE): code B48I20000050005 (Prog n. F/190012/01/X44).

References

1. Caesary D, Song SY, Yu H, Kim B, Nam MJ (2020) A review on CO2 leakage detection in shallow subsurface using geophysical surveys. Int J Greenhouse Gas Control 102:103165
2. Zhang C, Xu K, Liu K, Xu J, Zheng Z (2022) Metal oxide resistive sensors for carbon dioxide detection. Coord Chem Rev 472:214758
3. Park J, Cho H, Yi S (2010) NDIR CO2 gas sensor with improved temperature compensation. Procedia Eng 5:303–306
4. Xu M et al (2024) Development of a compact NDIR CO2 gas sensor for harsh environments. Infrared Phys Technol 136:105035

Neural Networks and Machine Learning For Sensing

A Federated Learning Universal Calibration for Low-Cost Air Quality Monitoring Networks

A. Mohamed Elamin[1], S. De Vito[2(✉)], G. Piantadosi[2], C. Sansone[1], and G. Di Francia[2]

[1] Department of Electrical Engineering and Information Technologies, University of Naples "Federico II", Naples, Italy
[2] ENEA CR-Portici, Energy and Data Science Laboratory, Portici, Italy
saverio.devito@enea.it

Abstract. Low cost air quality monitoring systems (LCAQMS) are a promising tool to increase the spatial and temporal resolution of Air quality information. Unfortunately, they suffer from limited accuracy due to a variety of factors including lack of specificity, sensitivity and sensor drifts. Fabrication variance and inherent monitored phenomena characteristics requires costly ad-hoc calibration procedures which have to be repeated on a seasonal basis. Here We propose to use an in-network Federated Learning approach to this problem analysing the results obtained in a publicly available dataset. Preliminary results show that the proposed approach could allow to obtain a single, universal and continuously updated city wide calibration law, ultimately reducing the cost burden of LCAQMS field operation.

Keywords: Low Cost Air Quality Monitoring Sensors · Calibration · Federated Learning · Universal Calibration · Machine Learning

1 Introduction

Low cost air quality monitoring nodes, based on solid state sensing devices, could be integrated with regulatory grade monitoring networks enhancing the air quality information density. To this purpose, starting from EU/2008/50 AQ and continuing with the recent EU/2024/2881, the European Commission is setting and updating data quality objectives allowing the use of LCAQM devices for specific purposes [1]. The complexity of the pollutant mixtures together with reduced specificity of sensing units requires the low cost air monitoring devices to be adequately calibrated i.e. deriving a sensing model capable to estimate actual pollutant concentrations reducing (ideally canceling) the interferents impacts. LCAQMs are furthermore affected by significant fabrication variance, leading the scientific community to develop node-specific calibration procedures. It is widely recognized that the complexity of the real world atmospheric composition cannot be fully reproduced in controlled laboratory environment which make common to resort to in field calibration procedures which, in turn, needs the access to reference grade monitoring station for ground truth data. However, field derived calibration have been

C. Di Natale et al. (Eds.): AISEM 2025, LNEE 1497, pp. 347–353, 2025.
https://doi.org/10.1007/978-3-032-08271-8_55

demonstrated to lack robusteness to relocation and multi-seasonal deployment because of temporal and spatial variance of both environmental variables and atmospheric composition (concept drift). This induced the exploration of continuous or adaptive approaches [2]. The latter may become extremely costly when considering the need to (seasonally re-)calibrate hundreds of devices at city scale.

Universal calibration, sometimes referred as global calibration, aims at obtaining a single calibration law which can be used, with or without node specific adaptations, for all sensors nodes in a sensor network avoiding node ad-hoc calibration derivation [3]. However, seasonal concept drifts and city specific pollutant mixture composition prevented the generalization of the derived calibration law to different cities and, respectively, seasons.

Federated learning is a relatively novel concept in maching learning community. It allows a distributed learning community of nodes to derive local AI models at the edge which are then fused in a centralized way [4]. The obtained AI model could be further improved at the local level in a iterative fashion. The entire mechanism promotes:

- Data privacy: no data is actually exchanged but only trained models are actually transferred.
- Network efficiency: The data stream is not transferred to the cloud
- Computing resource efficiency: The data stream is processed following an edge computing model.

More interestingly, federated learning inherently promotes data diversity, improving the variance of the dataset which is a significant and recurrent issue for the calibration of LCAQMS devices.

Exploiting Federated learning, We propose to develop a universal calibration by using a small subset of in situ co-located devices (*Calibration learners*) which continuously provide edge derived, seasonally updatable, calibration models. The latter could be fused in-cloud to be sent back to potentially hundreds of deployed nodes to allow for accurate pollutant concentration readings. As such, We introduce and present the results of federated learning based, universal calibration derivation procedure for pervasive low cost monitoring applications.

2 Methodology

2.1 Computational Architecture

The computational architecture relies on **FLOWER**™ framework which allow for implementing a federated learning scheme which completely avoid actual data transmission, relying instead on model fusion techniques at cloud level [4]. From the model point of view, We tested the implementation of XGBoost algorithm and Shallow Neural Networks architecture comparing them with Multilinear regression. In facts, the possibility to continuously update the model could allow to counteract the generalization limitations of nonlinear algorithms exploiting their improved accuracy with respect to Multilinear regression algorithms.

2.2 Dataset Description

The adopted dataset is based on MONICA™ devices (https://doi.org/10.5281/zenodo.13151960). The single node include NO2, O3, CO targeted Alphasense electrochemical sensors and 1 Plantower 7003 Optical particle counte. A STM32 Nucleo board provide for data capture, preprocessing and transmission using BLE transponder. A lightweight LiPO battery provide for 3 h continuous and autonomous operation. The devices have been co-located with regulatory grade anlaysers for three periods during a total of 1.5 year (Winter 2021, Summer 2021, and Winter 2022) in order to derive calibration functions in view of three different, citizen-driven, participatory monitoring campaigns. During the winter 2021 colocation experiment (from January 13th 15:00 to March 24th 10:00), 30 devices were partitioned in three equal-sized sets of ten devices each. Each set has been continuously co-located for three weeks on the roof of the reference station located at less than 20 m from a main street in the city of Portici, 7 km south of Naples city center in the south of Italy (Lat°:40.821721, Long°:14.324336) at Portici Waterfront entrance. Sampled data have been averaged at 1 h rate and synchronized with reference analyzer data stream to form a dataset used for calibration and validation purposes. A similar colocation experiment was then repeated during the summer/autumn time of the same year (from July 4th 00:00 to October 4th 9:20 at Portici Isola Ecologica site) (Lat:40.825580, Long°:14.33298) and final colocation experiment in winter 2022 (from Jan 11 to 13 Apr 2022 at Portici Scuola Da Vinci Comes - Viale Bernini (Lat°:40.8170813, Long°:14.3426628). Locations are shown in Fig. 1.

During the colocations, both concentrations of target particulate fractions and humidity levels changed significantly. Generally, lower concentrations and humidity levels were observed during the summer deployment, During winter time, actually, the second period/batch was characterized by the highest recorded pollution levels, while the lowest was recorded during the first period of the summer deployment see Fig. 2.

2.3 Federated Learning and Performance Comparison

The present comparison focuses on Particulate matter concentration estimation. Thus all measurements have been captured using Plantower PMS7003 sensors for particle count and weight estimation. The performance assessment foresee the use of a set of single, device and deployment location dependent, calibration models obtained by a subset of devices. These models are then fused together using model *parameters averaging technique*. The resulting model is then tested on a separate subset of devices (*Test nodes*) during a different deployment period (and, subsequently, location) wrt those encompassed in the federated learning training period. To ensure fair comparison, performance assessment is implemented with respect to the performances obtained by the *Test nodes* specific *in field calibration* laws as derived during the same period. The procedure is henceforth time-wise (sequential time stratified) and node-wise cross-validated through random selection of the 10 *Calibration learners* devices. More specifically, the question we are trying to answer in this preliminary report is: “Can we set a small number of devices in co-location with a reference analyzer in different locations and times with the aim of providing a federated calibration for the other devices ?” and “How the obtained accuracy compare with short term *in field calibration*?”.

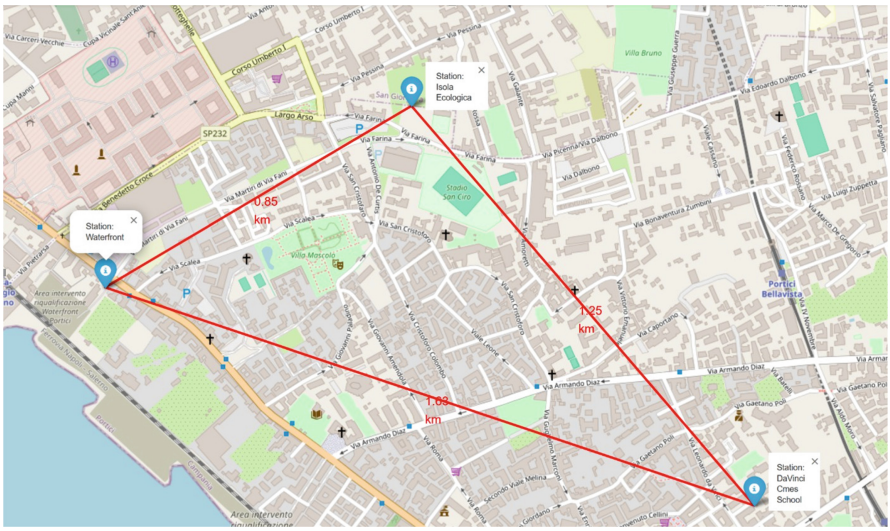

Fig. 1. Co-location deployment sites

This questions are particularly interesting because they formulate a first real world scenario in which a massive network of IoT LCAQMS devices is deployed and their global calibration is automatically and continuously updated based on a small number of devices collocated in close proximity of reference devices. Hence we adhered to the following procedure:

1 Select a single node and a season (which also carries the location), obtaining an ad hoc calibration using two consecutive weeks and test the performance on the third week. This performance will be our performance goal threshold.
2 A combination of five sensors from different locations and different seasons were randomly chosen (the other two seasons in the data sets). Obtain a federated learning calibration.
3 Repeat step 1 and 2 for k = 100 time, cross validating the choice of devices in each iteration.

Actual raw sensor concentration estimations and relative humidity have been used as input to MLR, Random Forests and Shallow Neural Network models.

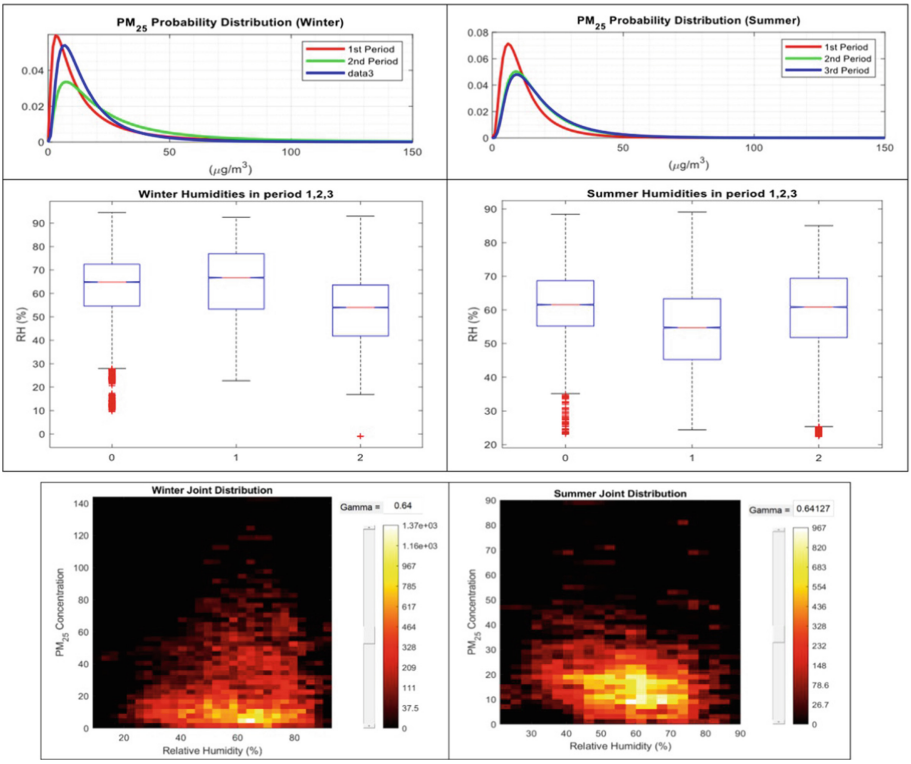

Fig. 2. Probability distribution of PM fractions concentrations during the three colocation periods in winter and summer. Box plot of relative humid- ity recordings during winter and summer colocation periods, Joint histogram (concentrations in g/m3) distribution of both forcers during (e) whole winter and (f) summer colocation periods.

3 Results

The obtained preliminary results have been condensed in Figs. 3 and 4. For space paucity, they presents the results obtained by two ad-hoc short term calibration models using MLR and respectively RFs with results obtained by Federated Learning approach using MLR. Figure 3 shows how FL obtains comparable results in terms both of R2 and Mean Absolute Error, notwithstanding the fact that the FL model has been obtained in different seasons and using data from different sensors units.

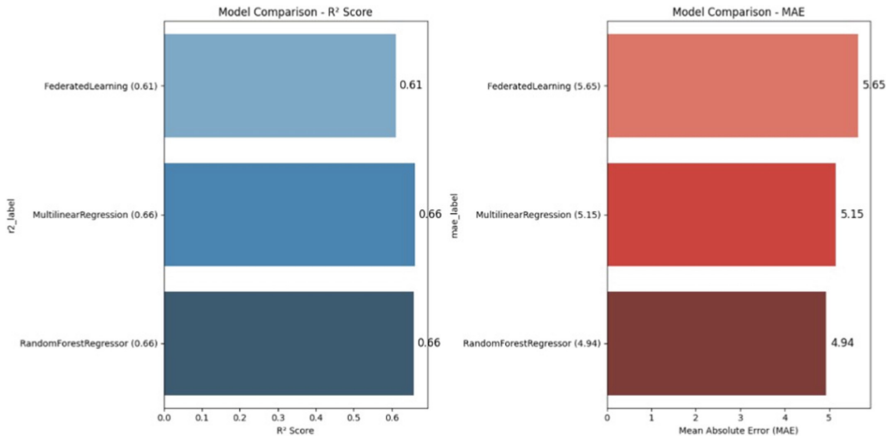

Fig. 3. Results comparison in terms of MAE obtained by the proposed approaches across the different combinations of learning and test nodes.

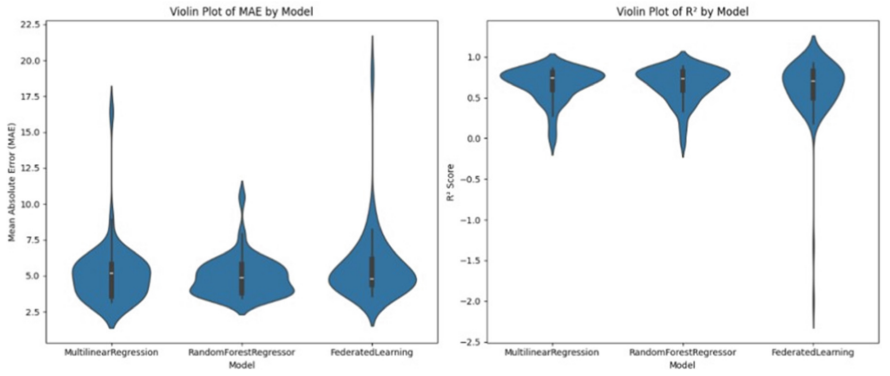

Fig. 4. Violin plot of distribution, across the different combinations of learning and test nodes, of R2 and MAE for the proposed approaches.

However, the violin plots, reported in Fig. 4, shows mixed behaviour in terms of results distribution with a larger variance shown by FL approach. Specific analysis revealed two specific nodes cases out of the total thirty in which FL performed significantly worse than RF ad hoc derived short term calibration. Further investigations will include the use of dataset in which it could be possible to compare FL models obtained in the same season but different locations in the same urban area to verify the possibility to completely equalize performance levels.

4 Conclusions

Preliminary results indicate that the universal calibration derived by federated learning methodology could achieve similar results with respect to node specific calibration. This could allow significant cost reduction without sacrificing accuracy. Though still needing colocation of a fraction of devices, this approach also allows to promote diversity in the training set providing additional robustness to extreme localized concentrations while the possibility of continuous update allows for strongly reducing if not eliminating the impacts of concept drifts.

Acknowledgments. This work has received funding from Italian Ministry of University and Research under Investment no. 1.5 of the "Piano Nazionale di Ripresa e Resilienza (PNRR)", Project "RAISE" – Robotics and AI for Socioeconomic Empowerment, Spoke 3.

References

1. European Commission (2024) Directive (EU) 2024/2881 of the European Parliament and of the Council of 23 October 2024 on ambient air quality and cleaner air for Europe
2. De Vito S et al (2024) Future low-cost urban air quality monitoring networks: insights from the EU's AirHeritage project. Atmosphere 15:1351. https://doi.org/10.3390/atmos15111351S
3. De Vito et al (2024) A global multiunit calibration as a method for large-scale IoT particulate matter monitoring systems deployments. In: IEEE Transactions on Instrumentation and Measurement, vol. 73, pp. 1–16, Art no. 2501916, https://doi.org/10.1109/TIM.2023.3331428
4. Beutel, DJ, et al (2022) Flower: A Friendly Federated Learning Research Framework, arXiv:2007.14390; Khond S, Kale V, Ballal MS (2022) Data mining methods for bad data detection and event data acquisition in microgrids. In 2022 IEEE International Conference on Power Electronics, Smart Grid, and Renewable Energy (PESGRE), pp. 1–6. IEEE

Aging Detection in Cast Resin Transformers by Vibration Data Analysis with Neural Networks

L. De Maria[1(✉)], V. Rucconi[2], D. Bartalesi[1], M. Sozzi[1], S. Garatti[2], and S. Bittanti[2]

[1] Technologies for Transmission and Distribution Department, RSE S.p.A., 20134 Milano, Italy
letizia.demaria@rse-web.it

[2] Dipartimento di Elettronica, Informazione e Bioingegneria, Politecnico di Milano, Milano, Italy

Abstract. Vibration Detection is as an effective method to detect loose or deformed windings in transformers. Authors' previous research work investigated the virtue of deep neural networks in detecting these faults in oil filled transformers. It was proven that neural networks can detect loosening fault with a high accuracy, robustly to possible misplacements in the positioning of vibration sensors, under load and no-load transformer's operation. In this paper, the analysis of vibrational spectra through neural networks is applied to a cast resin transformer, with the aim of evaluating whether progressive changes in the sampled vibrational pattern can be correlated with the aging of the transformer insulation. The proposed approach yields a classifier capable of predicting the transformer aging with satisfactory accuracy and suggests a linear and progressive deterioration of the transformer over time.

Keywords: Vibration Data · Neural Networks · Cast resin transformers · Aging detection

Cast resin transformers are applied in a wide range of power systems of Medium Voltage network, since they are more compact and require less maintenance than oil insulated transformers [1]. Windings are encapsulated in cast resin, generally an epoxy one, and are cooled by natural air or forced ventilation. The analysis of the deterioration of cast-resins, however, is more complex than that for oil-insulated transformers, and is still an open research topic in the field of fault detection. It is believed that a relevant portion of fault in cast-resins transformers is due to thermal accumulation: an overheat in the windings, which would accelerate the aging effect of insulation [2]. Several diagnostic methods are applied to check the insulation and mechanical conditions of a transformer, like partial discharge (PD) measurements, temperature values recording and analysis for overheat detection, Sweep Frequency Response Analysis (SFRA) method [3]. Vibration analysis is a method generally applied for monitoring the mechanical conditions of core or windings of transformers [4–6], while its application to monitor insulation condition of cast resin transformers is still little investigated. Another challenge is that the aging

C. Di Natale et al. (Eds.): AISEM 2025, LNEE 1497, pp. 354–359, 2025.
https://doi.org/10.1007/978-3-032-08271-8_56

profile of the transformer is unknown, being aging not directly observable, so that different behaviors ranging from a monotone decreasing of the performance to a sudden breakdown without any warning are all possible.

The aim of this work is the exploitation of vibrational data to train predictor capable of correctly estimating the aging/deterioration profile of the considered cast resin insulated transformer.

1 Experimental Setup and Data Collection

A cast resin transformer (10 kVA) was used as test transformer for vibration measurements. It was subjected to daily current cycles, for a period of about 7 months to induce accelerated thermal aging leading to failure. Daily cycles were characterized by a first heating cycle, obtained by operating the transformer with a constant current equal to the machine nominal value, and a subsequent cooling phase during which the transformer was operated in a no-load condition with nominal voltage.

The experimentation started on March 2021, and, after a first voltage failure of the transformer, which occurred at the end of July, it was temporarily interrupted and then resumed in September 2021. It continued until the complete failure of the transformer, which occurred at the beginning of October 2021. During the experimentation, some variables of interest were acquired, specifically: the temperatures of the upper part of the transformer, of the environment and an average value of temperatures collected inside the windings, the current and the voltage.

The transformer under investigation was also equipped with accelerometers positioned on the yoke of the transformer. Vibration data were acquired every 30 min in a day (although this interval may vary to 15 min in certain specific days) and each acquisition consisted of a time signal with a duration of 10 s. For each day, only the measurements collected during the transformer cooling (no-load) phase, within the time interval during which the internal temperature decreases from 130 °C to 40 °C, were maintained. The time signals were FFT transformed in spectra of which only magnitudes were considered. Only frequencies deemed significant were maintained: 50 Hz, 150 Hz, 400 Hz, 600 Hz, 800 Hz, 900 Hz, 1900 Hz, 2000 Hz, 2100 Hz, 2200 Hz. Thus, each data point consists of a 10-dimensional vector containing the magnitude of the harmonics at the previously indicated frequencies. The overall dataset is the collection of the available measurements obtained in a period of about 200 days distributed among six months (March, April, May, June, July, and September), with multiple measurements per day. To regularize the spectra, datasets obtained by averaging two [three] consecutive measurements in the original dataset were considered (without overlapping in the averaging window to avoid introducing any correlation). Given that averaging two [three] data points halves [reduces by a third] the numerosity of the dataset, all these three datasets, namely batch 1, batch 2 and batch 3 respectively, were considered and the subsequent analyses was conducted for all the three cases.

2 Classification Problem

The purpose of this study is to understand if it is possible to predict the deterioration level / aging of the transformer from a given vibrational data point. In this respect, it is to remark that the aging (deterioration) profile of the transformer is unknown (no reference has been found in the literature on how deterioration can be inferred from the signals measured in the experimentation). As is clear, the aging is somehow related to the time progression in the experimentation, but its profile could be linear and monotone, or with a sudden decreasing of performance leading to a breakdown without warnings. To highlight the deterioration profile too, the data were clustered into groups of contiguous days and each cluster was interpreted as an aging level, so that data in the same cluster were labelled the same way. Then, a multi-label classifier based on deep neural networks was created [7], capable of evaluating the aging/deterioration level of the resin transformer from a new vibrational observation (this amounts to correctly predicting the group to which the observation belongs). However, a variety of partitions was considered:

3 classes = Mar - (Apr, May, Jun, Jul) – Sept.
4 classes = Mar - (Apr, May) - (Jun, Jul) – Sept.
5 classes = Mar - Apr - May - (Jun, Jul) – Sept.
6 classes = Mar - Apr - May - Jun - Jul – Sept.

The analysis was carried out for each partition. In this way, based on the results obtained, it should be also possible to infer significant conclusions on the aging/deterioration profile. If, for example, all the clusters in each clustering were classifiable, this would mean that each cluster shows a different deterioration level from the others, signifying a progressive aging for which the degree of deterioration can be assigned depending on the position of the cluster in the experimentation timeline. The training of the classifiers followed various suggestions in the literature to improve accuracy and reduce variance [8, 9]. Specifically, we opted for a classifier obtained as an ensemble of multi-output feed-forward neural networks, with an output layer equipped with a *softmax activation* function. Each network in the ensemble is trained using cross-entropy as a cost function but using a different optimization algorithm to diversify the obtained predictions [10]. The output of the ensemble was obtained as the mode of the individual networks' outputs.

To train the final classifier, a training dataset, consisting of an 85% randomly chosen of the available data in each class, was first isolated, while the remaining 15% of the data was kept as a test dataset for later usage. The training data set was then partitioned into 10 subgroups taken randomly to have in each group a balanced number of elements for each class ("shuffled" and "stratified" partition). The stratified shuffled k-fold cross-validation method with $k = 10$ was then used to decide the hyper-parameters of each network of the ensemble. The hyper-parameters considered are the following:: the number of layers (from 4 to 7), the number of neurons per layer (which could be: 100, 150, 250, 400); the type of activation function (tanh or relu); some training parameters, such as the regularization coefficient (0.4, 0.5, 0.6) and the dropout coefficient (0.1, 0.2, 0.3). Once these hyper-parameters were calibrated for each of the 5 networks of the ensemble (each trained using a different optimization algorithm), the final classifier was trained from all the training data using the early-stopping technique to further prevent the phenomenon

of over-fitting. Early-stopping requires the use of validation data taken from the training data to decide when to stop the numerical optimization algorithm. We considered again the "shuffled" and "stratified" partition as before and the training of the neural networks and the construction of the ensemble was repeated ten times, choosing in turn which partition to use as a validation dataset. All the ten constructed ensembles were tested using the remaining part of the data not used in the training and validation phase (test dataset) to detect the actual performance (measured in terms of classification accuracy) of the obtained classifiers on new data.

Given that the data portioned were balanced, the test dataset contains measurements of each month and is representative of all the encountered operating conditions in any day (that is, the various temperatures in the cooling phases). As previously mentioned, the analysis was repeated several times, for different partitions of the initial data in aging/deterioration classes (3 classes, 4 classes, 5 classes or 6 classes), as well as for the three datasets obtained depending on whether single or average measurements of two or three contiguous measurements were considered (batch 1, batch 2, or batch 3).

3 Results

The results obtained in the test phase, with data not used in the training phase, are summarized in Table 1 which reports, for all the various cases (classes vs batches), the average with respect to the ten classifiers corresponding to the ten different early stopping of the so-called confusion matrices.

More specifically, each matrix in the table represents a case study (a choice of partitioning the data into aging classes and a choice of the dataset – batch1, 2, or 3). The confusion matrix (called this way because it allows to understand if there is a "confusion" in the classification of different classes) summarizes the classification accuracies obtained class by class. To be precise, each column represents the class predicted by the classifier, while each row represents the actual class of the test data; each matrix entry (row "i" and column "j") gives the percentage of test data in the aging class i that have been classified as belonging to class j. The higher the values on the diagonal (which corresponds to a correct classification) the better. Moreover, the confusion matrices allow one to also understand where the misclassification error is distributed among the various classes. This is quite significant in the current case of study since the aging classes come in a temporal sequence so that a concept of proximity of classes applies: misclassification errors for which a data point is incorrectly classified as belonging to a temporally contiguous class are less important than errors for which the predicted class is very distant from the true class.

Some interesting observations can be drawn from the results reported in Table 1. First, the classification performance is quite good, as the highest values of the confusion matrix are concentrated on the diagonal. This shows how the vibrational data contain indeed useful information for predicting the aging level of the transformer. It can also be noted that the use of averages of 2 or 3 data at a time (batch 2 and batch 3) significantly improves the classification.

The best performances were obtained considering 4 and 5 classes (the partition into 6 classes probably suffers from the limited number of available measurements in June,

which all correspond to the final part of the month and are therefore close to July). Since the best performance is obtained for many classes, the obtained results suggest a linear and progressive degradation profile over time. This observation is also reinforced by the fact that the misclassification errors are almost always between temporally contiguous classes, which correspond to similar aging/deterioration conditions.

Table 1. Confusion matrices.

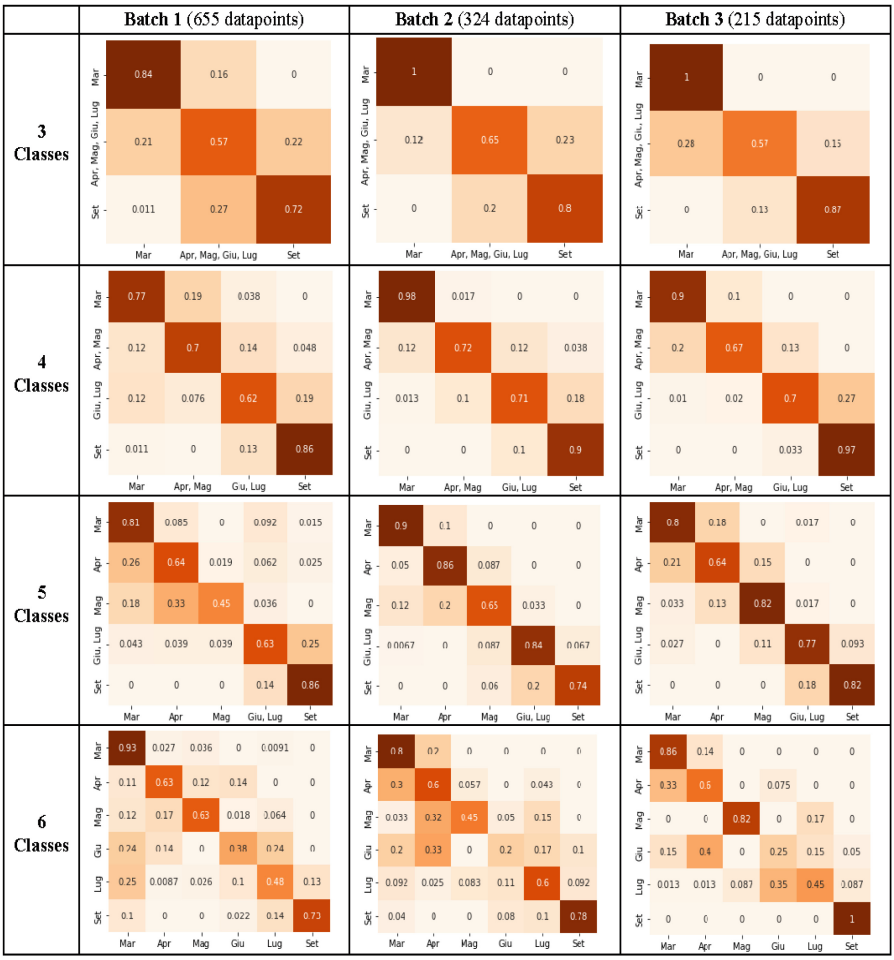

4 Conclusion

The results illustrated in the previous sections are encouraging and show that vibrational data can potentially bring very useful information about the aging/deterioration level of a cast resin transformer. A point that should be further investigated is if the prediction

obtained in the various classes is effectively due to different aging/deterioration levels of the transformer and not to operating conditions that have changed during the experiment. Our analysis seems to reveal that the latter is not the case (current and voltage are the same for all available data and temperature and its derivative change uniformly enough class by class). Finally, it would be significant to study the repeatability of this analysis on other transformers of the same type of the one used in the current experimentation and verify whether a predictor trained from the data related to a given transformer is able to predict the aging/deterioration level of another cast resin transformer of the same type.

Acknowledgement. This work has been financed by the Research Fund for the Italian Electrical System under the Three-Year Research Plan 2025–2027 (MASE, Decree n.388 of November 6*th*, 2024), in compliance with the Decree of April 12*th*, 2024".

References

1. Dolce S, Fiorucci E, Bucci G, D'Innocenzo F, Ciancetta G, Di Pasquale A (2017) Test instrument for the automatic compliance check of cast resin insulated windings for power transformers. Measurement 100:50–61
2. Xiao M, Du B (2016) Effects of high thermal conductivity on temperature rise of epoxy cast winding for power transformer. IEEE Trans on Dielectr Electr Insulat 23: 2413–2420
3. Di Pasquale A, Fiorucci E, Ometto A, Rotondale N (2012) Frequency characterization of cast resin transformers. 21st International Symposium on Power Electronics, Electrical Drives, Automation and Motion (SPEEDAM), pp. 1045–1050. IEEE, Sorrento
4. Tavakoli A, et al (2020) A Machine Learning approach to fault detection in transformers by using vibration data. 21st IFAC World Congress, pp. 13656–13661. Germany
5. Rucconi V, De Maria L, Garatti S, Bartalesi D, Valecillos B, Bittanti S (2021) Deep learning for fault detection in transformers using vibration data, 19th IFAC Symposium on System Identification, SYSID 2021. Padova, Italy, pp 262–267
6. Rucconi V, et al (2023) No-load transformers: vibration spectra analysis by deep learning methods for loose windings detection. Sensors and Microsystems. AISEM 2021. Lecture Notes in Electrical Engineering, Springer, vol 918 (2023)
7. Nielsen MA (2015) Neural Networks and Deep Learning. Determination press. San Francisco, CA
8. Brownlee J (2018) Better Deep Learning: Train Faster, Reduce Overfitting, and Make Better Predictions. Machine Learning Mastery. Melbourne, EN
9. Moss H, Leslie DS (2018) Using J-K-fold Cross Validation to Reduce Variance When Tuning NLP Models. 27th International Conference on Computational Linguistics (COLING 2018), pp. 2978–2989. Santa Fe, New Mexico, USA
10. Battiti R (1992) First- and second-order methods for learning: between steepest descent and newton's method. Neural Comput 4(2):141–166

Conditional Data Augmentation for Enhanced Forecasting Operation from Sensor Data in Photovoltaic Systems

A. Galli[1], G. Piantadosi[2(✉)], S. Dutto[1], G. Di Francia[2], and C. Sansone[1]

[1] Università Federico II di Napoli, Via Claudio 21, 80125 Napoli, Italy
[2] ENEA, CR Portici, Piazzale Enrico Fermi 1, 80055 Napoli, Italy
gabriele.piantadosi@enea.it

Abstract. The accurate forecasting of photovoltaic (PV) energy production is a critical challenge in the transition to renewable energy. Machine learning models designed for energy forecasting require vast and heterogeneous datasets to achieve robust performance. However, real-world limitations often result in incomplete or insufficient data, particularly when dealing with the inherent variability of solar irradiance and environmental conditions.

This study proposes a Conditional Time Series Generative Adversarial Network (cTimeGAN) framework tailored to augment PV-related sensor data, enabling improved training and performance of forecasting models. The methodology leverages the ability of cTimeGAN to generate synthetic, contextually rich datasets that mirror the temporal, structural, and environmental variations present in real-world PV systems.

Unlike traditional data augmentation techniques, cTimeGAN conditions the generation process on multiple factors such as weather patterns, system configuration, and seasonal profiles. This allows the network to synthesize time series that are both statistically coherent and physically plausible. The resulting synthetic data not only enhances the diversity of training sets but also supports scenario-based simulations, helping models generalize across rare or extreme operating conditions.

Preliminary evaluation on benchmark datasets shows promising generative performance in terms of realism and predictive utility. Future work will explore the integration of the synthetic data into operational PV forecasting pipelines to assess its actual impact on predictive accuracy and robustness. The proposed framework has the potential to reduce dependency on extensive data collection campaigns, accelerate model deployment in new environments, and improve anomaly detection and resilience in PV energy systems.

1 Introduction

Photovoltaic (PV) systems play a pivotal role in the clean energy transition [1, 2], yet their large-scale integration into the energy grid remains a technical challenge due to the inherent variability and intermittency of solar irradiance and rapidly changing meteorological conditions [3]. The ability to accurately forecast PV energy production is therefore essential to enable reliable energy dispatch, reduce balancing costs, support energy trading strategies, and ensure grid stability.

C. Di Natale et al. (Eds.): AISEM 2025, LNEE 1497, pp. 360–365, 2025.
https://doi.org/10.1007/978-3-032-08271-8_57

Modern forecasting approaches increasingly rely on data-driven machine learning models, which demand extensive and high-quality time series data for effective training. However, in real-world deployments, PV monitoring data is often incomplete, noisy, or geographically biased. These limitations stem from multiple factors, including sensor malfunctions, inconsistent data acquisition frequencies, and the scarcity of labeled data in underrepresented climatic or environmental conditions.

Moreover, environmental phenomena such as sudden cloud movements, seasonal variability, or system-specific features (e.g., panel orientation, degradation, inverter performance) introduce complex dependencies that are difficult to capture using conventional statistical models or naive augmentation techniques.

This study addresses these challenges by introducing a generative framework based on Conditional Time Series Generative Adversarial Networks (cTimeGAN), specifically tailored to the photovoltaic domain. Unlike general-purpose GAN-based approaches, cTimeGAN conditions the generation of synthetic data on external contextual features—such as weather parameters and PV system metadata—enabling the synthesis of temporally realistic and physically consistent sensor data. This conditional structure allows the model to simulate a wide range of plausible scenarios, including rare or extreme events, thereby enriching the training datasets used for forecasting and diagnostic tasks.

By leveraging this approach, we aim to provide a scalable and domain-aware data augmentation strategy that can improve the performance and resilience of PV forecasting models, particularly in data-scarce environments and in the early deployment phases of new installations.

2 Methods

The proposed methodology employs *cTimeGAN*, a conditional generative model that integrates the strengths of Conditional Generative Adversarial Networks (cGANs) [5] and TimeGAN [6] to synthesize realistic time series data conditioned on multiple contextual variables. This hybrid architecture is specifically tailored to address the multifaceted challenges in photovoltaic (PV) energy forecasting, particularly the representation of temporal patterns and exogenous dependencies such as weather fluctuations and system-specific features.

The overall framework is illustrated in Fig. 1, which depicts the dual-structured architecture composed of two principal modules:

The Conditional GAN Block (cGAN) module is responsible for generating latent representations of the sensor data by conditioning the generator on a vector of external variables. These include:

- **Weather Conditions**: Ambient temperature, humidity, solar irradiance, wind speed, and cloud cover.
- **System Characteristics**: Panel orientation, tilt angle, nominal power, panel technology, inverter type, and geographic location.

The generator G learns to produce time series sequences that match the distribution of real PV sensor data, while the discriminator D distinguishes between real and synthetic samples. The adversarial training process is guided by the conditional input y_n, ensuring

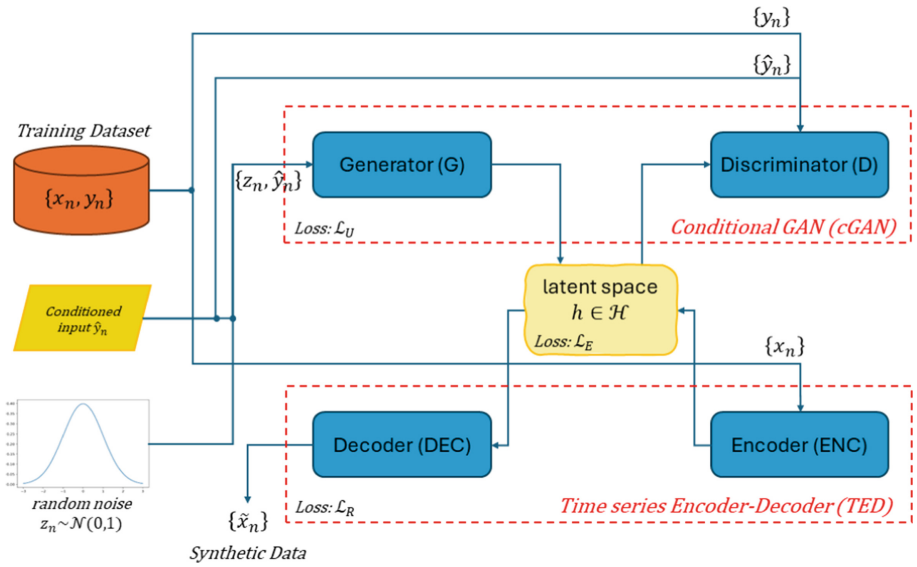

Fig. 1. Overview of the cTimeGAN architecture, composed of a Conditional GAN block (top) and a Time-aware Encoder-Decoder (TED) block (bottom).

that the generated sequences are not only statistically plausible but also contextually coherent.

To preserve temporal consistency and structural dependencies, the architecture incorporates a Time-aware Encoder-Decoder (TED) Block autoencoding module. This block comprises:

- **Encoder (ENC)**: Projects the multivariate time series into a latent representation h ∈ H, capturing temporal dependencies and contextual semantics.
- **Decoder (DEC)**: Reconstructs the time series from the latent space, ensuring fidelity through reconstruction loss.
- **Autoregressive Dependencies**: Implemented through sequential modeling layers (e.g., RNN, LSTM), these ensure that future values depend on historical context, a crucial aspect in PV forecasting.

The TED block jointly optimizes multiple loss functions:

- **Adversarial Loss L_{adv}**: Encourages realism in generated sequences.
- **Recovery Loss L_{rec}**: Ensures high-quality reconstruction of input data.
- **Embedding Loss L_{emb}**: Aligns latent dynamics with the true data manifold.

The synergistic interaction between the cGAN and TED components allows the model to generate high-fidelity synthetic sequences that retain both short-term fluctuations and long-range temporal structure. These sequences enhance the diversity and generalizability of training datasets for downstream machine learning models, especially in scenarios with sparse or imbalanced real-world data.

3 Results and Outcomes

The cTimeGAN framework is anticipated to address key challenges in PV forecasting by:

- Generating synthetic data that replicates diverse weather and system conditions, enhancing dataset representativeness.
- Improving the accuracy and robustness of machine learning models for PV energy forecasting.
- Facilitating anomaly detection by providing synthetic examples of rare or extreme events.
- Reducing dependency on extensive, costly, and time-consuming real-world data collection efforts.

To assess the generative capabilities of cTimeGAN, we conducted experiments on three benchmark datasets (Sines, Stocks, and Energy) and evaluated both discriminative quality and forecasting utility of the generated time series. The three datasets, Sines (synthetic), Stocks (financial), and Energy (real household consumption); are the same used in the original TimeGAN benchmark [6], and are commonly adopted in generative modeling of time series. To evaluate the quality of the generated time series, we adopt two widely used metrics: classification Accuracy (ACC) of a supervised model trained to distinguish real from synthetic data (lower is better) to assess the discriminative score; Mean Absolute Error (MAE) of generated values using models trained on synthetic data (lower is better) to assess the predictive score. We compare Conditional TimeGAN with several established baselines from the time-series generative modeling literature, including TimeGAN [6], RCGAN [7], C-RNN-GAN [8], WaveNet [9], and WaveGAN [10].

Table 1. Results on benchmark datasets.

	Discriminative (ACC)			Predictive (MAE)		
Method	Sines	Stocks	Energy	Sines	Stocks	Energy
Conditional TimeGAN	0.018	0.13	0.271	0.096	0.042	0.0297
TimeGAN [6]	0.011	0.102	0.236	0.093	0.038	0.273
RCGAN [7]	0.022	0.196	0.336	0.097	0.04	0.292
C-RNN-GAN [8]	0.229	0.399	0.499	0.127	0.038	0.483
WaveNet [9]	0.158	0.232	0.397	0.117	0.042	0.311
WaveGAN [10]	0.277	0.217	0.363	0.134	0.041	0.307

As shown in the Table 1, Conditional TimeGAN achieves near-best results in both metrics, with performance comparable to the top-performing approach, TimeGAN, across all datasets.

These results highlight the effectiveness of conditional generative modeling in synthesizing high-quality, context-aware time series for PV forecasting applications. Such

preliminary experiments demonstrate that synthetic data generated by cTimeGAN may improve model generalization and performance, particularly in scenarios with limited real-world data and in applications where conditioning on external variables is important.

Future evaluations will focus on integrating the synthetic data into real-world forecasting pipelines to quantify improvements in operational settings.

4 Conclusion

This study introduces Conditional TimeGAN, a context-aware generative framework designed to augment photovoltaic (PV) sensor data by conditioning the generation process on concrete external variables such as weather conditions, system characteristics, and operating states. While our approach does not outperform the current state-of-the-art (TimeGAN) in quantitative metrics, it achieves near-best performance in both discriminative and predictive evaluations across benchmark datasets, confirming its viability as a competitive alternative.

The key innovation lies in the explicit conditioning mechanism, which enables the generation of synthetic data that reflects specific real-world scenarios. This capability is particularly relevant in the PV domain, where data scarcity is often most critical under rare, extreme, or system-specific conditions.

This conditional structure offers practical advantages:

- In forecasting, the ability to generate data under controlled input conditions (e.g., seasonal variation, shading, degraded systems) allows for the targeted augmentation of underrepresented operational scenarios. This can improve generalization and robustness of predictive models, especially in early deployment phases or in regions with limited historical data.
- In fault detection, the conditioning input can encode fault-related features, enabling the synthesis of synthetic failure cases. This is especially valuable given the typical lack of diverse, labeled fault data, and it supports the training of more balanced and effective anomaly detection models.

In summary, although the current implementation of Conditional TimeGAN does not surpass unconditioned generative baselines in performance metrics, it unlocks a new axis of control in synthetic data generation that aligns closely with real-world needs in PV monitoring. Future work will focus on embedding this approach into operational pipelines and evaluating its impact in production-grade forecasting and diagnostic systems.

References

1. Hassan Q et al (2024) A comprehensive review of international renewable energy growth. Energy and Built Environment
2. IEA (2023) World energy outlook 2023 https://www.iea.org/reports/worldenergy-outlook-2023
3. Notton G et al (2018) Intermittent and stochastic character of renewable energy sources: consequences, cost of intermittence and benefit of forecasting. Renew Sustain Energy Rev 87:96–105

4. Goodfellow IJ et al (2014) Generative adversarial networks
5. Mirza M, Osindero S (2014) Conditional generative adversarial nets
6. Yoon J, Jarrett D, van der Schaar M (2019) Time-series generative adversarial networks. In: Wallach H, Larochelle H, Beygelzimer A, d'Alché-Buc F, Fox E, Garnett R (eds.) Advances in Neural Information Processing Systems, vol. 32. Curran Associates Inc. (2019)
7. Esteban C, Hyland SL, Rätsch G (2017) Real-valued (medical) time series generation with recurrent conditional gans. arXiv preprint arXiv:1706.02633
8. Mogren O (2016) C-RNN-GAN: Continuous recurrent neural networks with adversarial training. arXiv preprint arXiv:1611.09904
9. Van Den Oord A, et al (2016) Wavenet: A generative model for raw audio. arXiv preprint arXiv:1609.03499, 12
10. Donahue C, McAuley J, Puckette M (2018) Adversarial audio synthesis. arXiv preprint arXiv:1802.04208

Convolution Recurrent Neural Network for Tactile Textural Classification

Mohmad Yaacoub[1(✉)], Razan Khalifeh[1], and Ali Ibrahim[2]

[1] Department of Naval, Electrical, Electronics, and Telecommunications Engineering, University of Genoa, Genoa, Italy
mohamad.yaacoub@edu.unige.it

[2] Department of Electrical and Electronics Engineering, Lebanese International University, Beirut, Lebanon

Abstract. This paper presents a tactile-sensing fingertip based on piezoelectric materials for texture classification. The system integrates a tactile sensing glove equipped with eight P(VDF-TrFE) sensors mounted on the index finger. A dataset comprising six naturalistic textures was collected to train a Convolution Recurrent Neural Network (C-RNN) classifier. The results demonstrate the effectiveness of the proposed approach, achieving a classification accuracy of 90.91%. This study highlights the potential of combining tactile sensing technologies with machine learning techniques for advanced texture recognition applications.

Keywords: Piezoelectric sensor · texture recognition · machine learning

1 Introduction

The sense of touch, through the so-called somatosensory system, enables humans to explore, interpret, and interact with their surroundings. This system involves the activation of primary sensory units in the skin, which convert mechanical stimuli into electrical signals. These signals are interpreted, processed, and decoded by the central nervous system [1]. Over the past decade, artificial tactile sensing systems have increasingly attracted the interest of researchers for their ability to partially replicate human touch in various applications including robotics.

Moreover, the integration of these artificial sensing systems with the advancements in artificial intelligence leverages the outcome of handling complex functions such as texture classification [2], object recognition [3], hardness classification [4], and slippage detection [5]. Moreover, several machine learning (ML) and deep learning (DL) algorithms for processing tactile information have been explored. These include Support Vector Machine (SVM) [6], Convolutional Neural Network (CNN) [7], and Long-Short-Term-Memory (LSTM) [8].

Deep neural networks (DNNs) are computationally distributed models able to learn representations from raw data through a structure of hierarchical layers, similar to how the brain handles new information. Their generalization and learning capabilities, overcoming the limitations of traditional statistical approaches, offer a promising solution for these tactile sensing applications.

C. Di Natale et al. (Eds.): AISEM 2025, LNEE 1497, pp. 366–370, 2025.
https://doi.org/10.1007/978-3-032-08271-8_58

Among several tasks, texture recognition is one of the most important tasks. The characteristics of a surface, including its roughness, smoothness, can significantly influence how objects are grasped or manipulated. For instance, authors in [9] presents an object texture recognition methods based on tactile perception information from a bionic tactile sensor (BioTac). Vibration data from ten different materials were collected and several ML algorithms were implemented to differentiate between them. In [10], a PVDF-based fingerprint-inspired tactile sensor was developed to differentiate between various textures. Results demonstrated that, by combining the collected signals with machine learning algorithms, diverse textures can be effectively identified. Moreover, authors in [11] proposed a a hybrid sensor with two distinct patterns of its ridged structure, which mimic different parts of a human fingerprint. The developed tactile sensor uses the vibration signal that is generated when the sensor slides against the surface of an object. Results demonstrated that the proposed sensor was able to distinguish nine surface textures. A multimodal tactile sensor that can provide accelerometer, gyroscope, piezoresistive, and pressure data was proposed in [12] for the recognition of five different textures.

These studies emphasize the importance of dynamic actions such as sliding action in texture discrimination. To this end, this paper proposes a Convolution Recurrent Neural Network (C-RNN) for tactile texture classification. This approach leverages convolutional layers driven by its potential to extract spatiotemporal features from time series and LSTM layers to capture sequential dependencies enabling learning and classifying of tactile information, paving the way for more responsive and intelligent tactile sensing systems.

2 Materials and Methods

2.1 Tactile Sensing Glove

The tactile sensing glove used in this study is composed of 8 piezoelectric sensing array attached to the volar side of a fabric glove and embedded electronics attached to a passive PCB on the backside of the hand. In particular, the manufacturing process involves screen-printing repeated units of P(VDF-TrFE) poly (vinylidene fluoride trifluor-oethylene). The single sensor is composed of a bottom electrode, a ferroelectric polymer P(VDF-TrFE) layer (5.1 μm thick), and a top electrode (PEDOT: PSS). To collect and process tactile signals, embedded electronics configured with a sampling frequency of 2 kHz was used. The 2 kHz sampling rate is used to capture the full bandwidth of the sensor. The structure of the e-skin, the intrinsic flexibility of the sensing system, and its wide frequency bandwidth (0.5 Hz–1 kHz) make it a good candidate as a functional constituent of a flexible electronic skin measuring dynamic contacts.

2.2 Dataset

The dataset used in this study was collected in [2], comprising five natural texture materials: “Carpet,” “Soft PVC,” “Plastic Mesh,” “Paperboard,” “Wood,” and “Foam.”

During the experiment, participants were asked to wear the tactile glove and slide their index finger across the texture specified by the experimenter. The sliding motion

was performed randomly, without controlling for force or velocity. However, participants were asked to complete each motion within 5 in two directions—forward (25 times) and backward (25 times). In total, 2100 trials were collected, comprising 50 trials × 6 textures × 7 subjects.

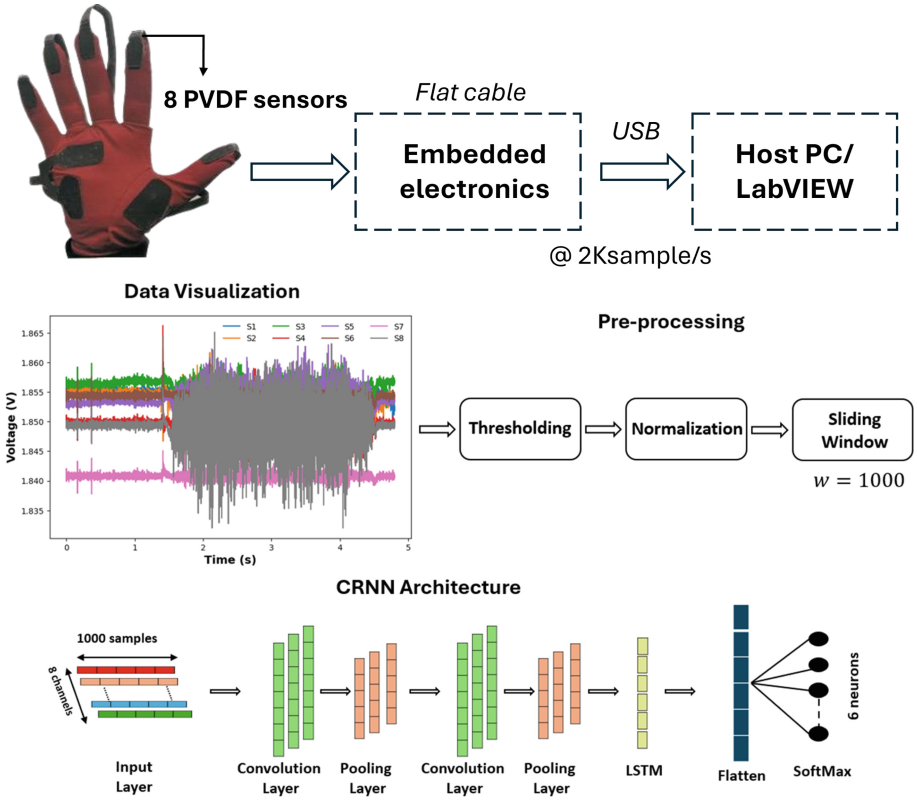

Fig. 1. Top: Experimental setup including the tactile sensing glove. Middle: Response of the eight sensors integrated on the index finger and the thresholding mechanism. Bottom: Architecture of the proposed algorithm.

2.3 Data Preprocessing

Initially, a thresholding mechanism was applied to reduce noise by removing the data exceeding the minimum and maximum noise values for the first 500 samples, when no action was taken by the participants. The dataset was then normalized along each channel using the standard scaler technique [13].

This normalization prevents any feature from affecting the algorithm performance due to the differences in scale. Additionally, a sliding window of 1000 samples was applied to segment the data from each channel to minimize the network's input, thereby reducing complexity.

2.4 Algorithms

This dataset was used to train the CRNN architecture (see Fig. 1 bottom).

The network embeds two convolution neural layers each employing the ReLU activation function, followed by batch normalization applied to the feature maps, and a max pooling layer reduces the dimensionality by a factor of two. Then an LSTM layer processes the output from the last max-pooling. Finally, the flattened layer is followed by a dense layer with six neurons corresponding to the number of textures, utilizing the softmax activation function for classification.

The network was implemented in Python using the Keras API, with the following settings: Adam optimizer (learning rate 0.01), a batch size of 32, and 300 epochs. Early stopping based on validation loss, with the patience of $p = 5$, was employed to prevent overfitting.

For the training procedure, the datasets were split into 80% for training, 10% for validation to select the best network configuration, and 10% for testing, maintaining class balance.

3 Results and Discussion

The convolutional recursive neural network (C-RNN) model has been implemented in different scenarios such as classification and recognition [14, 15].

The CRNN architecture was tested to evaluate its effectiveness in tactile texture classification. A considerable effort was made to optimize the network through a grid search method, which examined various hyperparameters. The optimal setup identified through this search consisted of two convolutional layers, each containing 64 filters with a kernel size of 4, which efficiently captured local spatial features from the tactile input. These convolutional layers were followed by a Long Short-Term Memory (LSTM) layer with 128 units, enabling the model to learn and retain sequential dependencies critical for accurate texture recognition.

The experimental results indicated that the proposed algorithm attained a classification accuracy of 90.9%, which implies that the proposed system surpassed human tactile perception in discriminating the majority of the textures**.** This performance surpasses the state-of-the-art accuracy of 87% reported in previous studies, such as in [2].

4 Conclusion

This paper presents a tactile sensing glove combined with ML algorithms for naturalistic texture discrimination. A C-RNN algorithm was employed to classify six naturalistic textures. The proposed model achieves an accuracy of 90.01%, outperforming existing methods reported in the literature. All experimental data were collected by randomly sliding either the sensorized fingertip over the textures without controlling sliding speed or force, demonstrating the system's suitability for real-time surface texture discrimination in uncontrolled environments.

References

1. Abraira VE, Ginty DD (2013) The sensory neurons of touch. Neuron 79(4):618–39
2. Abbass Y, Gianoglio C, Ali HA, Saleh M, Valle M (2024) Texture Perception Using Tactile Sensing Glove Based on PVDF Sensors and Machine Learning. IEEE Sensors Letters
3. Yaacoub M, Ibrahim A, Khansa F, Hammadi L, Gianoglio C (2025) Wearable Multisensory Glove for Shape, Size, and Stiffness Recognition Based on Off-the-Shelf Components. IEEE Sensors Letters
4. Amin Y, Gianoglio C, Valle M (2023) Embedded real-time objects' hardness classification for robotic grippers. Futur Gener Comput Syst 1(148):211–224
5. Khalifeh R, Gianoglio C, Abbass Y, Valle M (2024) Pilot study: experimental analysis of PVDF sensors response to slippage. In: Annual Meeting of the Italian Electronics Society, pp. 238–243. Springer Nature Switzerland, Cham
6. Pal M, Khasnobish A, Konar A, Tibarewala DN, Janarthanan R (2014) Classification of deformable and non-deformable surfaces by tactile image analysis. In: Proceedings of The 2014 International Conference on Control, Instrumentation, Energy and Communication (CIEC), pp. 626–630. IEEE
7. Huang S, Wu H (2021) Texture recognition based on perception data from a bionic tactile sensor. Sensors 21(15):5224
8. Yan Y, Hu Z, Shen Y, Pan J (2022) Surface texture recognition by deep learning-enhanced tactile sensing. Adv Intel Sys 4(1):2100076
9. Qin L et al (2024) Fingerprint-inspired biomimetic tactile sensors for the surface texture recognition. Sens Actuators, A 1(371):115275
10. Kim SJ, Choi JY, Moon H, Choi HR, Koo JC (2020) Biomimetic hybrid tactile sensor with ridged structure that mimics human fingerprints to acquire surface texture information. Sensors \& Materials 32
11. Kim SJ, Choi JY, Moon H, Choi HR, Koo JC (2020) Biomimetic hybrid tactile sensor with ridged structure that mimics human fingerprints to acquire surface texture information. Sensors & Materials 22:32
12. Martinez-Hernandez U, Assaf T (2023) Soft tactile sensor with multimodal data processing for texture recognition. IEEE Sens Lett 7(8):1–4
13. Huang L, Qin J, Zhou Y, Zhu F, Liu L, Shao L (2023) Normalization techniques in training dnns: Methodology, analysis and application. IEEE Trans Pattern Anal Mach Intell 45(8):10173–10196
14. Gill HS, Khalaf OI, Alotaibi Y, Alghamdi S, Alassery F (2022) Multi-Model CNN-RNN-LSTM Based Fruit Recognition and Classification. Intel Auto Soft Comp 33(1)
15. Kousik N, Natarajan Y, Raja RA, Kallam S, Patan R, Gandomi AH (2021) Improved salient object detection using hybrid convolution recurrent neural network. Expert Syst Appl 15(166):114064

Development and Optimization of an Electrochemical Sensor for Hydroxyl Radical Detection via DS110 Electrodes and Neural Network Modeling

Chafia Bouasla[1,4(✉)], Mohammed Mahdi[1], Imadeddine Belhani[2], Saidi Mohamed Racim[3], and Kharoua Amira[3]

[1] Microelectronic and Nanotechnology Division, MEMS and Sensor/Centre for the Development of Advanced Technologies CDTA, City20 Aout 1956, Algiers, Algeria
cbouasla@cdta.dz

[2] Laboratory of Theoretical Physics and Material Physics (LPTPM), University of Chlef Hassiba Benbouali, B. P 78C, 02180 Ouled Fares Chlef, Algeria

[3] Department of Electronics, Abderrahmane Mira University of Bejaia, Bejaia, Algeria

[4] MEMS Platform/Centre for the Development of Advanced Technologies CDTA, Algiers, Algeria

Abstract. The hydroxyl radical (•OH), with a redox potential of 2.8 V, is the most reactive oxygen species involved in various chemical and biological processes. Therefore, the development of simple and reliable methods for its quantitative determination is highly desirable.

In this study, an electrochemical sensor based on screen-printed electrodes, DS110 modified with naphthol blue black (NBB) dye, was developed for the detection of generated hydroxyl radicals (•OH). The degradation of the NBB film was induced by •OH radicals generated by the Fenton reaction.

The effects of different parameters, such as the H_2O_2 (0.3–2.5 mM) concentration, $FeSO_4$ (0.03–0.25 mM) concentration, and pH (1–8), on the charge transfer resistance (Rct) and double layer capacitance (Cm) were extracted and analyzed. The experimental results were also modeled via an artificial neural network (ANN) with a mean squared error of 10–5. This model was developed in MATLAB via a feed-forward back-propagation network, a multilayered perceptron. The input variables to the feed-forward neural network were various experimental variables, such as temperature, NNB concentration, $FeSO_4$ concentration, pH, and H_2O_2 concentration. The ANN successfully modeled the nonlinear relationships between the experimental inputs and the double-layer capacitance (Cm), achieving high predictive accuracy with a coefficient of determination (R2) exceeding 0.99.

Keywords: hydroxyl radicals · electrochemical sensor · neural network

C. Di Natale et al. (Eds.): AISEM 2025, LNEE 1497, pp. 371–380, 2025.
https://doi.org/10.1007/978-3-032-08271-8_59

1 Introduction

Electrochemical sensing techniques are gaining considerable attention for the detection of reactive oxygen species (ROS), including hydroxyl radicals (•OH), because of their inherent advantages, such as high sensitivity, rapid response, portability, and suitability for in situ and real-time monitoring [1–5]. These characteristics are particularly valuable in complex or biologically relevant media, where traditional spectroscopic or chromatographic methods may be limited by matrix interference, cost, or operational complexity. Despite their advantages, the electrochemical detection of •OH radicals present notable challenges, primarily because of their extremely short lifetime and high reactivity. These factors often result in low detection efficiency and signal instability, necessitating innovative approaches to enhance sensor performance.

In this context, the present study focuses on the development and optimization of an electrochemical sensor specifically tailored for •OH radical detection via the Fenton reaction (Eq. (1)) [6], which uses screen-printed carbon electrodes (DS110) modified with Naphthol blue black (NBB), a redox-active dye known to facilitate electron transfer and improve surface reactivity.

$$Fe^{2+} + H_2O_2 \rightarrow Fe^{3+} + {}^{\cdot}OH + OH^{-} \tag{1}$$

The functionalization of the electrode surface aims to increase the interaction between the target radicals and the sensing interface, thereby enhancing both selectivity and sensitivity. The use of DS110 electrodes offers advantages in terms of miniaturization, cost-effectiveness, and ease of surface modification, making the system suitable for potential field applications.

To further improve the analytical performance and reduce the reliance on extensive experimental trials, artificial neural network (ANN) modeling was integrated into the study. A multilayer perceptron (MLP) architecture was employed to model the complex, nonlinear relationships between the input parameters (e.g., pH, $Fe3^{+}$ concentration, H_2O_2 concentration, NBB concentration, and temperature) and key electrochemical outputs, such as the double-layer capacitance (C_m). The ANN was trained via experimental data derived from electrochemical impedance spectroscopy (EIS) to ensure robustness and generalizability across varying operational conditions.

This combined experimental and computational approach not only provides deep insights into the behavior of the electrochemical system under Fenton reaction conditions but also demonstrates the feasibility of intelligent sensor design using machine learning tools. The findings of this study lay the groundwork for developing next-generation electrochemical sensors with enhanced performance for the detection of short-lived ROS, with promising applications in environmental monitoring, industrial process control, and biomedical diagnostics where oxidative species serve as critical indicators.

2 Experimental Section

2.1 Materials and Methods

All the electrochemical experiments were conducted at room temperature via a DS110 screen-printed electrochemical sensor comprising a carbon working electrode (WE), a carbon counter electrode (CE), and an Ag/AgCl pseudoreference electrode (RE) connected to a potentiostat system (N302). The working electrode was functionalized by drop-casting a defined volume of naphthol blue black (NBB) solution and left to dry under ambient conditions to increase the sensitivity toward hydroxyl radicals (Fig. 1). The Fenton reaction, which is used to generate •OH radicals, was carried out in a beaker containing freshly prepared Fe^{2+} and H_2O_2 in 5 mM Na_2SO_4 (pH 7). After 5 min of reaction initiation, a 20 μL droplet of the reaction mixture was deposited onto the modified working electrode. Electrochemical impedance spectroscopy (EIS) measurements were then performed in the frequency range of 100 MHz–100 kHz using a 10 mV AC perturbation and a DC bias of –100 mV. The resulting Nyquist plots were analyzed via ZView® software to extract key parameters such as the solution resistance (Rs), charge transfer resistance (R_{ct}), and double-layer capacitance (C_m), enabling detailed characterization of the electrode's response to hydroxyl radicals.

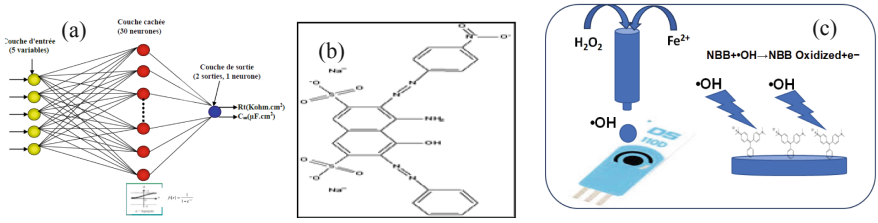

Fig. 1. (a) Architecture of the MLP network, (b) structure of naphthol blue black (NBB), (c) DS110 electrode with the Fenton reaction

2.2 Neural Network Technique

In chemical processes, MLP neural networks serve as powerful tools for predictive modeling and system optimization [7–9]. They allow researchers to understand complex, nonlinear relationships between multiple interacting variables, reduce the number of required experiments, and unveil patterns that are often undetectable via traditional statistical approaches.

Additionally, in this work, experimental data were modeled by an MLP with 3 layers: an input layer, hidden layers, and an output layer. This three-layered feed-forward back propagation network consists of 5, 30, and 1 neurons in the first, second, and third layers, respectively. MLP was performed in MATLAB. The input variables to the network were as follows: initial Fe^{3+} concentration (0.03–0.12 mM), initial pH (2–3), H_2O_2 concentration (0.9–2.5 mM), temperature (303 K), and NBB concentration (0.06 mM). The double-layer capacitance (Cm) was chosen as the experimental response or output variable. The hyperbolic sigmoid transfer functions have been tested in a hidden layer network (6) [10]. The optimal architecture of the MLP (Fig. 1), and its parameter variation

was determined on the basis of the minimum value of the mean square error (MSE) of the training and validation sets [11].

The MSE was used as the error function. It measures the performance of the network according to the following equation:

$$MES = \frac{1}{Q} = \sum_{i=1}^{i=Q} \left(y_{i,pred} - y_{i,exp}\right)^2 \tag{2}$$

where Q is the number of data points, $y_{i,pred}$ network prediction, $y_{i,exp}$ experimental response.

3 Results and Discussion

3.1 Cyclic Voltammetry Characterization

3.1.1 Effect of NBB

To evaluate the effect of naphthol blue black (NBB) modification on the electrochemical behavior of the working electrode, cyclic voltammetry (CV) measurements were performed using the well-known reversible redox couple $[Fe(CN)_6]^{3-}/[Fe(CN)_6]^{4-}$ as a redox probe (Fig. 2a). Prior to the adsorption of NBB, the voltammogram exhibited well-defined anodic and cathodic peaks with a peak-to-peak separation (ΔE_p) of approximately 100 mV, indicative of a quasireversible electron transfer process at the bare DS110 electrode surface.

Following surface modification with NBB (Fig. 2a), significant suppression of both redox peaks was observed, and the faradaic current decreased drastically, almost disappearing. This marked attenuation in the electrochemical response suggests that the adsorbed NBB layer acts as a barrier to electron transfer, effectively blocking the access of the redox probe to the underlying conductive surface. The disappearance of the redox peaks is also indicative of the formation of an electroactive film, likely due to the oxidation of the NBB molecules, leading to a passivating layer that impedes interfacial electron exchange.

These findings confirm that the NBB film was successfully immobilized onto the electrode surface and substantively altered the electron transfer kinetics, a factor that is critical in tuning the sensitivity and selectivity of the electrode for hydroxyl radical detection in subsequent experiments.

3.1.2 Effect of the $K_4[Fe(CN)_6]$ Concentration

To investigate the influence of the $K_4[Fe(CN)_6]$ concentration on the electrochemical response of the DS110 working electrode, cyclic voltammetry (CV) was performed over a potential window ranging from –0.6 V to +0.7 V at a fixed scan rate of 100 mV/s. Solutions with increasing concentrations of $K_4[Fe(CN)_6]$ (from 1 M to 5 M) were analyzed to assess the electrode's charge transfer behavior under varying redox probe availability.

As depicted in Fig. 2b, all recorded voltammograms exhibit a pair of well-defined redox peaks: a cathodic peak located at approximately +0.05 V and an anodic peak

above +0.1 V. These peaks correspond to the classic one-electron redox reaction of the ferri-/ferrocyanide couple, described by the following equations:

Oxidation:

$$Fe(CN)_6^{4-} \rightarrow Fe(CN)_6^{3-} + e^- \tag{3}$$

Reduction:

$$Fe(CN)_6^{3-} + e^- \rightarrow Fe(CN)_6^{4-} \tag{4}$$

As the concentration of $K_4[Fe(CN)_6]$ increases, the intensity of both the anodic and cathodic peaks increases proportionally. Conversely, a decrease in concentration leads to a noticeable decline in peak current intensity. This behavior reflects a diffusion-controlled process, where the availability of redox species directly affects the charge transfer at the electrode–electrolyte interface. The results confirm that the electron transfer kinetics are significantly influenced by the concentration of the redox couple in the solution, validating the DS110 electrode's responsiveness and sensitivity to changes in the electrochemical environment.

3.1.3 Effect of the Fenton Reaction

To evaluate the impact of hydroxyl radicals (•OH) generated via the Fenton reaction on the electrochemical behavior of the modified DS110 electrode, cyclic voltammetry was performed in two different electrolytic environments: (a) 0.1 M Na_2SO_4 containing Fenton's reagent (a mixture of H_2O_2 and Fe^{2+}) and (b) 0.1 M Na_2SO_4 alone, over a potential range from 0–1.6 V vs. SCE, at a scan rate of 100 mV/s (Fig. 2c).

In the presence of Fenton's reagent, the voltammogram recorded during the first scan shows two distinct oxidation peaks centered at approximately 0.55 V and 1.0 V. These peaks are absent in subsequent cycles, indicating that they correspond to nonreversible processes likely associated with the oxidative degradation of the naphthol blue black (NBB) layer immobilized on the electrode surface. The transient nature of these peaks suggests that they result from the attack of •OH radicals on the adsorbed dye molecules, leading to their decomposition and the loss of redox activity on the electrode surface.

In contrast, the voltammogram recorded for Na_2SO_4 without Fenton's reagent shows no such oxidation peaks, confirming that the observed electrochemical behavior is directly linked to the presence of hydroxyl radicals generated in situ by the Fenton reaction.

These findings provide strong electrochemical evidence for the interaction between the hydroxyl radicals and the NBB-modified electrode surface, thereby supporting the ability of the sensor to detect •OH through changes in its voltametric signature**.**

3.2 Influence of Operational Parameters on Double-Layer Capacitance (C_m) and Charge Transfer Resistance (R_{ct})

Electrochemical impedance spectroscopy (EIS) was employed to investigate how varying operational conditions—namely, H_2O_2 concentration, $FeSO_4$ concentration, and pH—affect the electrochemical properties of the DS110 sensor modified with naphthol

blue black (NBB). The Nyquist plots presented in Fig. 3 reveal valuable information about two key parameters, the charge transfer resistance (R_{ct}) and the double-layer capacitance (C_m), which are both indicative of the sensor's interfacial behavior and overall reactivity toward hydroxyl radical (•OH) detection.

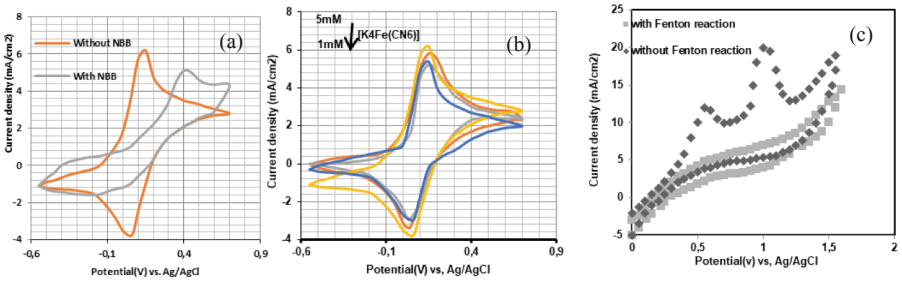

Fig. 2. Cyclic voltammetry characterization of the DS110 electrode.

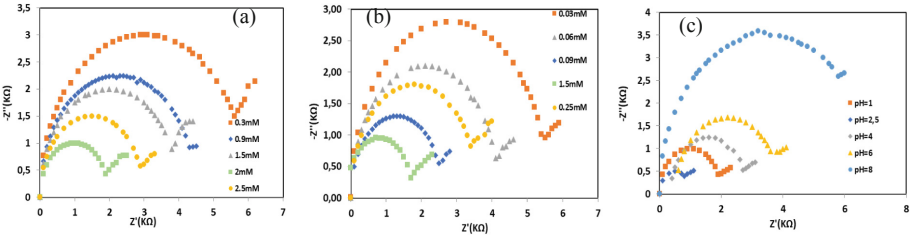

Fig. 3. Nyquist plots: (a) effect of H_2O_2 concentration, (b) effect of $FeSO_4$, (c) effect of pH.

3.2.1 Effect of the H_2O_2 Concentration

Increasing the H_2O_2 concentration from 0.3 to 2.5 mM resulted in a progressive reduction in the diameter of the semicircles in the Nyquist plots (Fig. 3a). This reduction corresponds to a significant decrease in R_{ct}, implying an acceleration of electron transfer processes at the electrode–electrolyte interface. This increase is directly associated with the greater generation of •OH radicals via the Fenton reaction, which increases the redox activity on the modified electrode surface.

Simultaneously, C_m increases with increasing H_2O_2 concentration, reflecting the expansion of the electrochemically active area and the development of a more structured electric double layer. This behavior suggests enhanced adsorption of redox-active species and improved interfacial charge accumulation, both of which are crucial for sensitive and selective hydroxyl radical detection.

3.2.2 Effect of the $FeSO_4$ Concentration

A similar effect was observed when the $FeSO_4$ concentration was varied from 0.03 to 0.25 mM (Fig. 3.b). As the concentration of Fe^{2+} increases, the Nyquist plots again exhibit shrinking semicircle diameters, corresponding to a decrease in R_{ct}. The availability of Fe^{2+} ions is critical in catalyzing the Fenton reaction, thereby accelerating •OH production and facilitating charge transfer at the sensor surface.

Concurrently, higher Fe^{2+} levels contribute to an increase in C_m, suggesting improved charge storage capability and more active interaction sites on the electrode surface. These results confirm that $FeSO_4$ plays a pivotal role in driving the electrochemical generation of •OH and enhancing the sensor's response characteristics.

3.2.3 Effect of pH

The impact of pH on R_{ct} and C_m is more nuanced but equally significant (Fig. 3c). The optimal performance is observed in the mildly acidic range of pH 2.5–3, where R_{ct} is minimized and C_m reaches its peak. This condition ensures the maximum stability and solubility of Fe^{2+} ions, as well as sufficient proton availability to maintain an efficient Fenton reaction.

At extremely low pH values (e.g., pH 1), although Fe^{2+} remains fully soluble, the excess protons may interfere with •OH generation or promote side reactions that limit radical availability. On the other hand, at relatively high pH values ($\geq$4), Fe^{2+} undergoes hydrolysis, leading to the precipitation of $Fe(OH)_3$, which sequesters active iron species and impedes the Fenton mechanism. This results in elevated R_{ct} values and a marked decrease in C_m, highlighting the critical role of pH balance in sustaining efficient radical production.

3.2.4 Determination of Optimal Operating Conditions

As illustrated in Fig. 3, the double-layer capacitance (C_m) is significantly influenced by three key parameters: the $FeSO_4$ concentration, the solution pH, and the H_2O_2 concentration. These variables are closely linked to the efficiency of hydroxyl radical (•OH) production through the Fenton reaction and therefore play a pivotal role in shaping the electrochemical behavior of the DS110/NBB-modified sensor. The maximum C_m value, reflecting optimal interfacial charge accumulation and enhanced redox activity, was achieved under the following operating conditions: 0.06 mM $FeSO_4$, pH 2.5, and 2 mM H_2O_2.

These conditions reflect the optimal balance for Fenton chemistry, where the generation of •OH radicals is maximized. At pH 2.5, iron remains in its soluble Fe^{2+} form while avoiding the excessive proton interference that occurs at lower pH values and the precipitation of $Fe(OH)_3$ at higher pH values [12]. Moreover, 0.06 mM $FeSO_4$ provides sufficient catalytic activity without leading to passivation or excessive side reactions, and 2 mM H_2O_2 ensures that a high oxidant concentration can sustain radical production without causing sensor degradation or radical quenching.

The elevated C_m observed under these conditions signifies a well-structured electric double layer and enhanced interfacial activity, which are essential for rapid and sensitive electron transfer processes. Since C_m is closely related to the density of electroactive

sites and the degree of electrode polarization, its maximization directly corresponds to improved sensor performance.

3.3 Artificial Neural Network (ANN) Modeling with a Multilayer Perceptron (MLP)

To predict and optimize the performance of an electrochemical sensor, an artificial neural network (ANN) model based on the multilayer perceptron (MLP) architecture was developed. The model architecture was optimized to include one hidden layer composed of 30 neurons and a single output neuron, which yielded the best performance in terms of minimizing prediction error and improving generalizability.

The ANN was trained via a supervised learning approach, where experimental data on the double-layer capacitance (C_m) and rate constant of dye degradation were used as outputs, and the input parameters included the $FeSO_4$ concentration, pH, H_2O_2 concentration, NBB concentration, and temperature. The training algorithm focused on minimizing the mean squared error (MSE) between the predicted and experimental outputs. The resulting model demonstrated excellent predictive power, with a coefficient of determination (R^2) of 0.99, indicating a very strong correlation between the experimental and predicted values (see Table 1 and Fig. 2) (Fig. 4).

Table 1. Values of C_m for different parameters.

	PH	Temperature (K)	[$FeSO_4$] (Mm)	[H_2O_2] (Mm)	[NBB] (Mm)	$C_m(\mu f.Cm^2)$
1	2.00	303	0.06	0.9	0.06	4.085
2	2.50	303	0.06	0.9	0.06	4.8
3	3.00	303	0.06	0.9	0.06	4.42
4	3.50	303	0.06	0.9	0.06	4.268
5	4.00	303	0.06	0.9	0.06	3.822
6	3.00	303	0.03	0.9	0.06	3.874
7	3.00	303	0.05	0.9	0.06	4.44
8	3.00	303	0.06	0.9	0.06	5.159
9	3.00	303	0.07	0.9	0.06	4.659
10	3.00	303	0.09	0.9	0.06	4.42
11	3.00	303	0.12	0.9	0.06	4.036
12	3.00	303	0.06	0.9	0.06	4.517
13	3.00	303	0.06	1.2	0.06	4.92
14	3.00	303	0.06	1.5	0.06	4.993
15	3.00	303	0.06	1.8	0.06	4.769
16	3.00	303	0.06	2.1	0.06	5.384
17	3.00	303	0.06	2.5	0.06	4.981

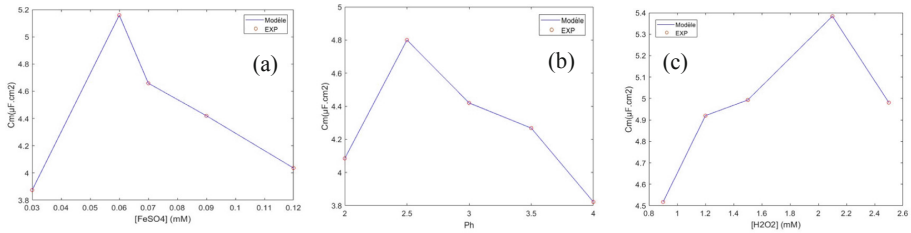

Fig. 4. (a) Model outputs as a function of (a) the $FeSO_4$ concentration variation, (b) pH, and (c) the H_2O_2 concentration.

4 Conclusion

In this study, an innovative electrochemical sensor platform was developed using DS110 electrodes functionalized with naphthol blue black (NBB) dye for the detection of hydroxyl radicals (•OH) generated via the Fenton reaction. The electrochemical characterization was carried out via cyclic voltammetry (CV) and electrochemical impedance spectroscopy (EIS), enabling the evaluation of key interfacial parameters such as the charge transfer resistance (R_{ct}) and double-layer capacitance (C_m). The NBB layer was shown to significantly alter electron transfer at the electrode surface, which in turn facilitated specific interactions with reactive oxygen species. The electrochemical response of the modified sensor was highly dependent on three crucial experimental variables: the $FeSO_4$ concentration, pH, and H_2O_2 concentration. Through a systematic investigation, the optimal sensing conditions were determined to be 0.06 mM $FeSO_4$, pH 2.5, and 2 mM H_2O_2. To predict sensor performance under a broader range of experimental parameters, a multilayer perceptron (MLP) artificial neural network was constructed. The model incorporated six key inputs: the Fe^{3+} concentration, pH, Na_2SO_4 concentration, applied current, temperature, and H_2O_2 concentration. An optimal MLP architecture with one hidden layer containing 30 neurons and one output neuron was established. The model demonstrated excellent agreement with the experimental data, with a coefficient of determination (R^2) of 0.99 for both the kinetic rate constant and dye degradation efficiency. These results underscore the ability of the MLP to capture complex, nonlinear relationships inherent in electrochemical processes and provide reliable predictions for sensor behavior. Overall, this work demonstrates the successful integration of functionalized electrochemical platforms with artificial intelligence-based modeling. This hybrid approach enhances the detection capabilities for highly reactive species such as •OH in complex environments.

References

1. Zhao S et al (2021) Recent advances of electrochemical sensors for detecting and monitoring ROS/RNS. Biosens Bioelectron 179:113052
2. Ju J, Liu X, Yu JJ, Sun K, Fathi F, Zeng X (2020) Electrochemistry at bimetallic Pd/Au thin film surfaces for selective detection of reactive oxygen species and reactive nitrogen species. Anal Chem 92:6538–6547

3. Zou H, Tai C, Gu XX, Zhu RH, Guo QH (2002) A new simple and rapid electrochemical method for the determination of hydroxyl radical generated by Fenton reaction and its application. Anal Bioanal Chem 373(1–2):111–115
4. Cao Si J, Lu L, Gao ZF, Zhang Y, Luo HQ, Li NB (2014) A sensitive electrochemical method based on Fenton-induced DNA oxidation for detection of hydroxyl radical. Anal Methods 6(17):6793–6798
5. Duanghathaipornsuk S, Kanel S, Haushalter EF, Ruetz JE, Kim D-S (2020) Detection of hydroxyl radicals using cerium oxide/graphene oxide composite on prussian blue. Nanomaterials 10(6):1136
6. Bouasla C, Samar MH, Ismail F (2010) Degradation of methyl violet 6B dye by the Fenton process. Desalination 254:35–41
7. Bury D, Jakubczak M, Bogacki J, Jastrzębska AM (2023) Phenazopyridine degradation by electro-fenton process with magnetite nanoparticles-activated carbon cathode: artificial neural networks modeling. Nanomaterials 13(4):674
8. Gholizadeh AM, Zarei M, Ebratkhahan M, Hasanzadeh A (2021) Phenazopyridine degradation by electro-fenton process with magnetite nanoparticles-activated carbon cathode: artificial neural networks modeling. J Environ Chem Eng 9(1):104999
9. Ganzenko O, et al (2014) Techniques d'intelligence artificielle dans la modélisation du procédé électro-Fenton pour le traitement des eaux usées. INRS Espace
10. Morgan DP, Scofield CL (1991) Neural Networks and Speech Processing. Kluwer Academic Publishers, London
11. Salari D, Niaei A, Khataee A, Zarei M (2009) Electrochemical treatment of dye solution containing C.I. Basic Yellow 2 by the peroxi-coagulation method and modeling of experimental results by artificial neural networks. J Electroanal Chem 629:117–125
12. Bouasla C (2024) Optimization of electrochemical oxidation for the degradation of acid yellow 99 via sulfate and hydroxyl radical activation: a study using Plackett–Burman and Box–Behnken designs. J Water Process Eng, 106362

Effectiveness of Performance Ratio Measure for Photovoltaic Anomaly Detection

S. Dutto[1], G. Piantadosi[2(✉)], A. Galli[1], C. Sansone[1], and G. Di Francia[2]

[1] Università Federico II di Napoli, Via Claudio 21, 80125 Napoli, Italy
[2] ENEA, CR Portici, Piazzale Enrico Fermi 1, 80055 Napoli, Italy
gabriele.piantadosi@enea.it

Abstract. Photovoltaic (PV) systems play a growing role in the global shift toward renewable energy, but they remain vulnerable to a wide range of failures that can compromise performance and reliability. This study evaluates the effectiveness of the Performance Ratio (PR), a standardized metric from IEC 61724-1, as a tool for anomaly detection in PV systems. Using real-world data from five PV plants and manually labeled fault events, we assess the PR's ability to identify system anomalies and benchmark its performance against four machine learning (ML) models, including LSTM and Transformer architectures. Results show that the PR achieves an AUC score of 78.98, serving as a reliable baseline for fault detection, while ML-based virtual sensing models trained on meteorological and modeled irradiance data offer competitive accuracy. However, issues such as class imbalance and binary fault labeling highlight the need for more refined, granular classification methods. Ultimately, the findings support combining traditional PR metrics with advanced data-driven approaches to improve the robustness, interpretability and scalability of PV monitoring systems.

1 Introduction

PV systems are susceptible to a diverse range of failures that can affect all system components, including modules, cabling, protective devices, power converters and inverters. These components can degrade or malfunction due to various internal or external factors. Environmental and operating conditions - such as extreme temperatures, humidity, dust, and mechanical stress - are among the most influential causes, making PV systems particularly vulnerable. As PV systems continue to play a pivotal role in the global transition to renewable energy [1], undetected failures can significantly reduce energy yield, increase operational and maintenance costs and even pose safety risks due to electrical or thermal anomalies. Common faults - such as panel soiling, inverter malfunctions or progressive degradation - may cause minor efficiency losses initially, but can evolve into critical failures that shorten the system's operational lifespan and compromise its return on investment. Effective and timely fault detection mechanisms are therefore critical to ensuring optimal functioning, long-term reliability and financial sustainability. The literature emphasizes the strategic importance of accurate, data-driven fault detection techniques, which reinforce the dependability of PV production and advance the renewable energy transition [2]. The ability to detect and diagnose system anomalies at an early

C. Di Natale et al. (Eds.): AISEM 2025, LNEE 1497, pp. 381–386, 2025.
https://doi.org/10.1007/978-3-032-08271-8_60

stage plays a crucial role in plant performance monitoring, allowing for rapid intervention and targeted maintenance. This proactive approach not only minimizes downtime but also supports asset preservation and efficiency optimization over time. Fault detection systems that can operate autonomously, interpret data in real time and provide actionable insights are becoming indispensable tools for operators, investors and energy planners, as they help guarantee stable energy production and predictable returns in the energy market.

Fault detection approaches vary by input data, techniques and level of analysis. Broadly, they fall into two categories: module-level and signal-level detection. Module-level detection targets individual PV units to identify localized issues such as cracks, corrosion, soiling, or hotspots, often using visual assessments - either manual or assisted by automatic computer vision (CV) algorithms [3] - and specialized imaging - e.g., thermal infrared or electroluminescence - via UAVs, drones or fixed cameras. This enables high-resolution inspection of physical anomalies and performance losses. Signal-level detection, on the other hand, analyzes inverter-generated time series data - such as voltage, current, and power output - to identify deviations from expected patterns. This approach enables scalable, cost-effective monitoring without physical inspection. Among the methodologies applied at the signal level, compliance with international standards is essential for ensuring consistency, comparability, and performance benchmarking. In this regard, the IEC 61724-1 standard [4], serves as a globally recognized reference for the accurate measurement, monitoring and evaluation of PV system performance. While the primary objective of the standard is to guide performance assessment rather than fault detection per se, its metrics and recommended practices provide a valuable framework for validating the effectiveness of a detection model, which should strive to achieve accuracy levels that surpass the performance monitoring criteria implied by the standard. In particular, the PR - a central indicator defined by the IEC - offers a normalized measure of system efficiency that accounts for both the installed system's nominal capacity and the environmental irradiation conditions. This makes PR a practical and widely adopted benchmark for gauging overall system health. However, despite its utility, PR is not without limitations. For instance, it does not adequately reflect performance losses due to certain real-world conditions such as temperature-induced efficiency drops, gradual material degradation or operational curtailment, which can lead to under- or overestimation of true performance.

Building on these considerations, the present study investigates the PR as a baseline for evaluating more advanced diagnostic approaches. By examining its behavior across multiple plants and comparing it to the performance of ML-based detection, the study aims to assess the effectiveness of more advanced, accurate and data-informed diagnostic systems. Ultimately, the goal is to contribute to the optimization of PV system operation and maintenance strategies, paving the way for more intelligent and resilient PV infrastructures.

2 Methods

To conduct a rigorous and quantitative assessment of anomaly detection in PV systems, real-world data collected from five distinct, fully operational PV plants were utilized. To create a reliable ground truth for our anomaly detection system, malfunction events

were labeled by hand. The collected data, including power output and irradiation levels, were used to derive typical performance and classification KPI metrics. A central component of this analysis was the use of the PR, a standardized and widely accepted indicator for assessing the operational efficiency of PV systems. The PR is defined in the IEC 61724-1 standard, developed by the International Electrotechnical Commission (IEC), which provides a globally recognized framework for monitoring and analyzing PV performance. This parameter enables the normalization of a system's energy output by accounting for the local climatic and technical operating conditions. Expressed as a percentage, the PR is calculated as the ratio between the actual energy yield of the PV system and the theoretical energy that could be produced based on the solar radiation incident on the plane of the modules. The formula used is as follows:

$$Performance\ Ratio(PR) = \frac{E_{DC}}{P_0} / \frac{H_{PoA}}{H_0}$$

where:

- E_{DC} is the actual energy yield by the system, measured at the inverter output [kWh];
- H_{PoA} is the irradiance measured on the plane of the module array (Plane of Array, PoA), using field sensors [kWh/m^2];
- P_0 is the nominal power of the system, determined from the factory specifications of the inverters and the connected modules, measured under Standard Test Conditions (STC), as defined in international standards IEC 61215, IEC 61646, and UL 1703 (i.e., with irradiance of 1000 W/m^2, an air mass (AM) of 1.5, and a module temperature of 25 °C) [kW];
- H_0 is the irradiance used to calculate P_0 under standard test conditions [conventionally fixed at 1000 W/m^2].

By leveraging this formulation, a standardized benchmark could be established to assess system performance across different plants and operating conditions, enabling the identification of underperformance and potential anomalies in a consistent manner. In addition to such performance-based metric, a suite of pre-trained ML techniques [5, 6] was employed to construct a virtual sensing framework for anomaly detection, aimed at minimizing reliance on physical instrumentation such as pyranometers. Although pyranometers provide accurate irradiance measurements, their susceptibility to hardware failures underscores the value of data-driven alternatives capable of estimating irradiance from external sources, thereby enhancing the resilience and reliability of monitoring systems. The predictive capabilities of four different ML architectures were evaluated: linear regression [7] (LR), multi-layer perceptron [8] (MLP), long short-term memory network [9] (LSTM) with attention [10] blocks and Transformer network [11] (TRN). Each of these models was trained using a heterogeneous dataset that integrated three main categories of input features:

1. **Meteorological data,** collected from four sources: two commercial providers, Open-Meteo (OM) and OpenWeatherMap (OWM); two numerical weather prediction models, European Centre for Medium-Range Weather Forecasts (ECMWF) and Global Forecast System (GFS).
1. **Modelled irradiance**, simulated at the five PV plant locations using the Clear-sky model implemented in the *pvlib* [12] Python library.

2. **Plant-specific configuration data**, including technical specifications of each PV installation.

This multi-source approach enabled us to train models capable of approximating irradiance levels and power outputs without the need for locally measured solar data, thereby enhancing fault detection capabilities in situations where sensor data are missing, noisy or unreliable.

3 Results and Discussion

The adoption of the PR as a foundational benchmark for the development of advanced PV system performance monitoring frameworks has demonstrated notable effectiveness. This is particularly evident when considering the significant improvement margin in the baseline results achieved in this work.

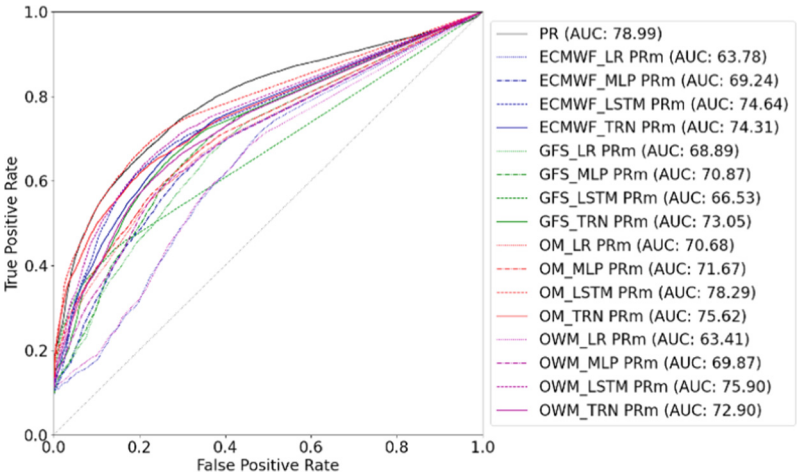

Fig. 1. Comparative analysis of the ROC curve between the PR-based anomaly detection model and a range of ML models trained using different meteorological data sources, as listed in the previous paragraph.

As shown in Fig. 1, the ROC curve for the PR-based fault detection model yields an Area Under the Curve (AUC) score of 78.98, which indicates a moderately good ability to discriminate between faulty and non-faulty instances.

At the same time, the four ML models – particularly the LSTM architecture trained with data from OM, with an AUC score of 78.29 - demonstrate highly competitive performance. These results highlight the potential of data-driven virtual sensing frameworks as viable alternatives to traditional sensor-dependent monitoring, especially when physical sensors are unavailable or faulty. The promising outcomes obtained by the specific data-model pairings suggest that further optimization, including model fine-tuning and feature engineering, could enhance predictive accuracy and ultimately surpass the baseline performance.

Furthermore, it should be noted that, unlike the ML models considered, the PR formula explicitly incorporates irradiance measured by on-site sensors to evaluate inverter performance, thereby gaining an advantage in the comparison.

Finally, the effectiveness of any fault detection system is critically influenced by the characteristics of the dataset used for training and evaluation. In this context, the dataset employed in the current study exhibits a pronounced class imbalance, with only approximately 21% of the recorded days labeled as anomalous. This imbalance calls for the implementation of targeted class balancing strategies, both in the design of learning algorithms and in the assessment of their performance. Without such adjustments, models risk producing misleading outcomes - for instance, achieving high specificity while suffering from low precision or recall - thus compromising their practical utility. Addressing class imbalance is therefore essential to ensure the development of reliable and generalizable models capable of accurately detecting anomalies in real-world conditions. Moreover, the current binary fault labeling scheme, although useful as a first step, may overlook important differences between types of anomalies. A systematic re-evaluation of the initial labeling process is recommended, with the aim of introducing a more granular classification of anomalous events. Sub-categorizing faults into distinct types - such as energy yield losses, data acquisition failures, unexpected signal spikes, or prolonged periods of missing data - would enable a more nuanced understanding of fault dynamics. This, in turn, would support a more accurate interpretation of deviations and foster the development of more sophisticated and interpretable anomaly detection methodologies. Ultimately, refining both the labeling and the evaluation processes is expected to contribute significantly to improving the sensitivity, specificity, and overall reliability of PV system fault detection tools.

4 Conclusion and Future Work

The PR, due to its computational simplicity and minimal input data requirements, demonstrates potential as an anomaly detection system, achieving an AUC score of around 80% and 78% accuracy. However, the relatively low F1-score of 54% indicates wide optimisation margin. While these results confirm the value of PR as a robust baseline, its inherent simplicity also highlights its limitations, emphasizing the need for complementary data-driven methodologies that can leverage its strengths while compensating for its shortcomings. The improvements achieved in this work using PR as a baseline further support the potential for integrating traditional performance metrics with ML-based anomaly detection techniques to enhance the accuracy and robustness of PV system monitoring. To this end, a series of ML models were explored to develop a virtual sensing framework aimed at reducing dependence on physical sensors such as pyranometers, which are prone to failure and require regular maintenance. Among the tested models, those based on recurrent neural networks – especially the LSTM trained with weather data from Open Meteo - demonstrated promising results, achieving an AUC close to that of the PR-based approach. These findings suggest that data-driven models, when properly tuned and trained on reliable and diverse input sources, can complement or even surpass traditional metrics in identifying system anomalies. Future research should focus on fine-tuning model hyperparameters, expanding the diversity and granularity of

training datasets and incorporating fault sub-classification to enable more granular and interpretable anomaly detection. Additionally, integrating uncertainty quantification and explainability into the ML framework could significantly increase the trustworthiness and practical applicability of these approaches in real-world PV monitoring systems. Ultimately, the synergistic combination of interpretable performance metrics like PR with the adaptability of advanced ML models offers a promising path toward more resilient and intelligent PV system diagnostics.

References

1. IEA (2023) World energy outlook 2023. International Energy Agency, IEA, Paris, France
2. Mellit A, Tina GM, Kalogirou SA (2018) Fault detection and diagnosis methods for photovoltaic systems: a review. Renew Sustain Energy Rev 91:1–17
3. Akram MW et al (2020) Automatic detection of photovoltaic module defects in infrared images with isolated and develop-model transfer deep learning. Sol Energy 198:175–186
4. IEC (2021) Photovoltaic system performance - part 1: monitoring. International Electrotechnical Commission. IEC, Geneva, Switzerland
5. Piantadosi G, Ferlito S, Dutto S, Di Francia G (2025) Long-term photovoltaic power forecasting with transformer NN. In: Conoci S, Di Natale C, Prodi L, Valenti G (eds.) Sensors and Microsystems, AISEM 2024. Lecture Notes in Electrical Engineering 1334: 250–256. Springer
6. Piantadosi G, et al (2024) Photovoltaic power forecasting: a transformer based framework. Energy and AI 18
7. Montgomery DC, Peck EA, Vining GG (2021) Introduction to linear regression analysis. John Wiley & Sons
8. Minsky M, Papert S (1969) An introduction to computational geometry. Cambridge Tiass, HIT 479(480): 104
9. Graves A, Graves A (2012) Long short-term memory. Supervised sequence labelling with recurrent neural networks, 37–45
10. Luong MT, Pham H, Manning CD (2015) Effective approaches to attention-based neural machine translation. arXiv preprint arXiv:1508.04025
11. Vaswani A, et al (2017) Attention is all you need. Advances in neural information processing systems, 30
12. Holmgren WF, Hansen CW, Mikofski MA (2018) Pvlib python: a python package for modeling solar energy systems. J Open Sour Softw 3(29):884

False Data Injection Identification in Energy Microgrids Through an Anomaly Detection Approach

A. Sgueglia[1], G. Spinelli[2(✉)], C. A. Visaggio[3], S. De Vito[2], and G. Di Francia[2]

[1] Department of Engineering, University of Sannio, Benevento, Italy
[2] ENEA CR-Portici, Energy and Data Science Laboratory, Portici, Italy
giovanni.spinelli@enea.it
[3] Department of Agricultural Sciences, Food, Natural Resources and Engineering, University of Foggia, Foggia, Italy

Abstract. This paper presents an application of unsupervised approaches to anomaly detection in smart meter log data within Smart Grids, with a specific focus on detecting False Data Injection (FDI) cyber-attacks. The proposed solution leverages the DBSCAN algorithm, selected for its ability to detect clusters of arbitrary shape and isolate noise without prior knowledge of the number of clusters. To validate the model, a realistic and reproducible test dataset was generated by injecting controlled Gaussian noise into a portion of the data. DBSCAN was then trained and evaluated on this dataset, demonstrating robust performance in distinguishing between normal behavior and simulated anomalies. Results achieved include 87% accuracy, 95% precision, and an F1-score of 89%, highlighting the algorithm's effectiveness in detecting subtle anomalies while minimizing false positives. Parameter tuning, based on k-distance curve analysis, led to the identification of an optimal configuration (eps = 0.25, min samples = 10), which significantly contributed to the quality of clustering and anomaly separation. Overall, the study confirms the viability of unsupervised techniques like DBSCAN in detecting cyber threats and operational issues in Smart Grid environments..

Keywords: False Data Injection · Cybersecurity · Microgrids · DBSCAN · Attacks Detection · Anomaly Detection

1 Introduction

Clustering, as an unsupervised learning technique, enables the grouping of data into homogeneous sets without the need for predefined labels. This makes it particularly suitable for the detection of anomalies and attacks, such as False Data Injection (FDI), which aims to manipulate sensor measurements and compromise system state estimation. The use of clustering algorithms for anomaly detection has therefore become a key tool in ensuring the security of Smart Grids and, more generally, modern energy systems.

Several studies in literature have proposed and evaluated clustering algorithms to detect anomalies in both microgrids and distribution networks. Among these, the

C. Di Natale et al. (Eds.): AISEM 2025, LNEE 1497, pp. 387–392, 2025.
https://doi.org/10.1007/978-3-032-08271-8_61

Density-Based Spatial Clustering of Applications with Noise (DBSCAN) stands out for its ability to identify arbitrarily shaped clusters and isolate outliers, without requiring a predefined number of clusters [1, 2]. These characteristics make it especially effective in handling complex and non-linear data, such as those generated by smart meters and IoT devices commonly found in microgrids [3, 4].

In summary, clustering algorithms provide a robust and flexible solution for anomaly detection in Smart Grids, offering a solid balance between effectiveness, adaptability, and the ability to operate in dynamic and unpredictable environments like the ones generated by cyber attacks.

2 Methodology

Given the growing threat posed by False Data Injection (FDI) attacks in modern smart microgrids, this work adopts a data-driven, unsupervised approach for anomaly detection. To simulate such attacks and evaluate the detection capabilities of clustering algorithms, a labeled dataset was generated by injecting artificial anomalies into real or simulated smart meter data. The dataset includes measurements such as active and reactive power, recorded at 15-min time intervals, reflecting users load profiles and time-of-day variations. In particular, loads include both office alike loads and HVAC machines for ENEA C.R. Portici supercomputing facility.

False data were injected by altering a configurable percentage of rows through controlled noise injection, including Gaussian noise to simulate realistic fluctuations. Parameters such as FDI (faults) ratio and noise scale control the frequency and intensity of the alterations, respectively. The resulting dataset includes a binary anomaly label column to distinguish normal from tampered data and is split into a training set (80% normal data) and a test set (10% normal + 10% anomalous data). Preprocessing steps included normalization, removal of missing values, and filtering of irrelevant columns.

DBSCAN is especially effective in the context of electrical microgrids due to its ability to:

- operate without prior knowledge of the number of clusters;
- detect arbitrarily shaped clusters, ideal for nonlinear data;
- isolate noisy data as outliers, thus facilitating anomaly detection;
- adapt to the dynamic behavior of microgrids, where operating conditions may vary.

The algorithm identifies dense regions of data points as clusters, and its behavior is mainly governed by two parameters:

eps: the maximum distance between two points to be considered part of the same cluster;

min samples: the minimum number of points required to form a dense region.

These parameters directly affect clustering performance and the algorithm's sensitivity to structural patterns in the data.

To fine-tune DBSCAN's performance, particular focus was placed on selecting appropriate values for its two core parameters. The optimal ***eps*** value was estimated using the k-distance curve, identifying the "elbow" point where density sharply changes. Actually, the plot clearly showed an inflection point which suggested an optimal eps of

0.25. Meanwhile, ***min samples*** was chosen based on data density and DBSCAN best practices, aiming to balance sensitivity and false alarm rates. A min samples value of 10 was selected, aiming to balance detection sensitivity and the number of false positives (Figs. 1, 2 and 3).

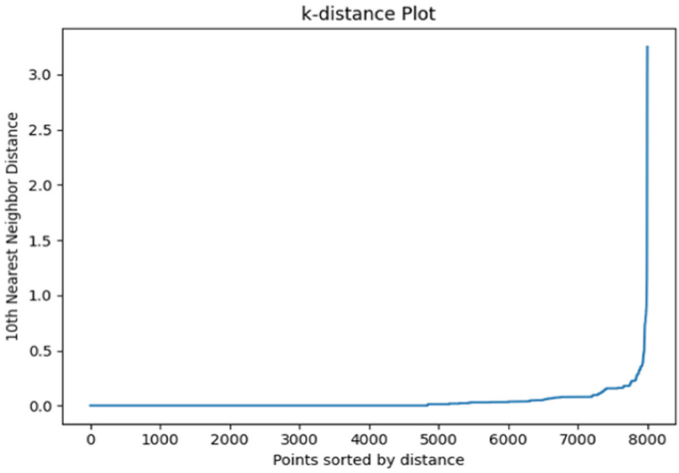

Fig. 1. Visualization of the k-distance curve for estimating the optimal value of eps

3 Results

To evaluate the system's effectiveness, a labeled and structured dataset was created through the controlled injection of anomalies. These anomalies were introduced by adding Gaussian noise to a randomly selected portion of the dataset rows. The random selection was seeded to ensure reproducibility, while the noise intensity was calibrated based on the standard deviation of the original variables. This method allowed for the simulation of realistic attack scenarios where data tampering is subtle and difficult to detect visually.

Varying the proportion of altered timeseries rows, defined by a fault ratio parameter, enabled the creation of diverse testing conditions. Specifically, when fault ratio ranged between 1% and 3%, anomalies were harder to detect, especially with low-intensity noise. As the ratio increased to 10%, the tampered data became more distinguishable while still maintaining plausibility.

By adjusting both the proportion of altered rows and the intensity of the noise, a versatile and robust dataset was generated. It was well-suited for testing the algorithm's ability to detect subtle and sophisticated forms of anomalous behavior, ultimately contributing to a reliable evaluation of the model's detection capabilities.

The effectiveness of DBSCAN strongly depends on the appropriate tuning of its main parameters: eps (neighborhood radius) and min samples (minimum number of points per cluster). Optimal values have been selected with the previously mentioned methodology. Once applied, these parameters enabled the model to clearly distinguish between dense clusters of normal data and isolated outliers, which corresponded to injected anomalies. The best separation was observed in datasets where anomalies accounted for at least 5% of the total entries. Visual validation using scatter plots further confirmed the model's ability to detect even low-intensity anomalies, which would otherwise go unnoticed in manual inspection. Using the optimized configuration, the DBSCAN algorithm was applied to the generated dataset containing simulated anomalies. The results were encouraging, with the model successfully separating anomalous observations from normal data. Table 1 summarizes the key performance metrics.

Table 1. Detection Key performance metrics

Metric	Value
Accuracy	87%
Precision	95%
Recall	87%
F1-Score	89%
Silhouette Score	0.57
Davies-Bouldin Index	1.32

These results confirm the model's robustness and accuracy. A high precision (95%) indicates that most detected anomalies were true positives, while the strong recall (87%) confirms its ability to capture a majority of actual anomalies. The F1-score of 89% reflects a balanced trade-off between these two metrics. Clustering validity scores reinforce this interpretation: a Silhouette Score of 0.57 points to well-formed clusters, while a Davies-Bouldin Index of 1.32 suggests good inter-cluster separation. Notably, DBSCAN was also able to identify irregularities unrelated to the injected anomalies, such as acquisition errors or natural fluctuations in the data. This suggests good generalization performance and highlights the algorithm's potential not only for attack detection but also for overall data quality monitoring.

Fig. 2. Training Set Anomalies

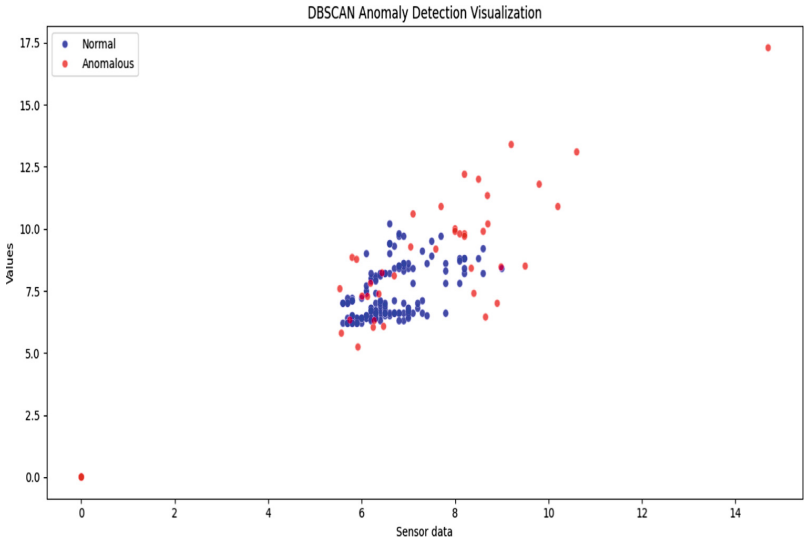

Fig. 3. Test Set Anomalies

4 Conclusions

This study aimed to select, implement, and evaluate algorithms for detecting attacks in electrical microgrids, with a focus on False Data Injection (FDI) attacks, which compromise measurement reliability and operational security. DBSCAN was selected for its ability to detect anomalies without labeled data and to identify arbitrarily shaped clusters.

The implemented pipeline includes:

- Simulation of FDI attacks via controlled noise injection on voltage, current, and power, affecting 1–10% of the data.
- Parameter tuning (eps, min samples) using k-distance plots and empirical validation.
- Automated anomaly detection and visualization of results.

The model performed well on simulated data, clearly separating normal and anomalous clusters reaching accuracies in excess of 85% at high (>90%) precision rate.

Finally, a semi-real-time analysis architecture was proposed for deployment on the ENEA infrastructure. It involves acquiring smart grid data via an MQTT queue, storing them, and processing with the developed algorithm.

Acknowledgments. This work has received funding from Italian Minisitry of Environment and Energy Security and European Union under the Piano Operativo di Ricerca (POR) and NextGeneration EU frameworks respectively, POR H2 AdP MMES/ENEA, PNRR–Mission 2, Component 2, Investment 3.5 “Ricerca e sviluppo sull’ idrogeno”.

References

1. Sharma R, Joshi AM, Sahu C, Nanda SJ (2023) Detection of false data injection in smart grid using PCA based unsupervised learning. Electr Eng 105(4):2383–2396
2. Mohammadpourfard M, Ashkan S, Seifi AR (2017) A statistical unsupervised method against false data injection attacks: a visualization-based approach. Expert Syst Appl 84:242–261
3. Bhattacharjee A, Mondal AK, Verma A, Mishra S, Saha TK (2022) Deep latent space clustering for detection of stealthy false data injection attacks against AC state estimation in power systems. IEEE Trans Smart Grid 14(3):2338–2351
4. Khond S, Kale V, Ballal MS (2022) Data mining methods for bad data detection and event data acquisition in microgrids. In: 2022 IEEE International Conference on Power Electronics, Smart Grid, and Renewable Energy (PESGRE), pp 1–6. IEEE

Flight Altitude Estimation for Unmanned Aerial Vehicles Using GNSS-Barometer Data Fusion

Gennaro Ariante(✉), Pierluigi Falco, and Giuseppe Del Core

Department of Science and Technology, University of Naples "Parthenope", Naples, Italy
{gennaro.ariante,pierluigi.falco001}@studenti.uniparthenope.it,
giuseppe.delcore@uniparthenope.it

Abstract. The emerging frontier in urban transportation, encompassing both goods delivery and passenger transport, is represented by Urban Air Mobility (UAM). UAM seeks to exploit the "third dimension" of airspace to mitigate traffic congestion in daily urban commutes while advancing the decarbonization of transportation systems. UAM is conceived as an innovative transportation mode that utilizes Unmanned Aerial Vehicles (UAVs), commonly referred to as drones, and Vertical Take-Off and Landing (VTOL) vehicles for the aerial transport of people and goods in urban and suburban areas. This class of UAVs will operate in a designated airspace known as Very Low Level (VLL), defined as altitudes below 500 feet. Consequently, accurate altitude measurement will be critical during missions, especially in urban environments where a high level of safety is required. This is due to the presence of people, vehicles, and various obstacles, both stationary and moving, that necessitate precise navigation and obstacle avoidance to ensure safe operations. In this work, a data fusion algorithm that integrates GNSS and barometric measurements is proposed to enhance altitude estimation accuracy, during UAS missions, especially those operations conducted in Beyond Visual Line of Sight (BVLOS) or fully autonomous mode.

Keywords: UAS · UAV · UAM · Altitude Estimation · Sensor Fusion · GNSS · Barometer · Data Fusion

1 Introduction

Urban Air Mobility (UAM) is emerging as a crucial solution for addressing growing traffic congestion in major cities, caused by the imbalance between limited transportation infrastructure and increasing mobility demands. One of the key areas of development within UAM is the advancement of electric vertical take-off and landing (eVTOL) aircraft, which are fundamental for enabling safe, efficient, and sustainable air transportation in urban environments [1].

Another rapidly expanding sector within UAM is drone-based goods delivery, which is revolutionizing the logistics industry. Traditional ground-based transport methods are gradually being complemented, or even replaced, by autonomous cargo drones, which offer faster, more flexible, and cost-efficient delivery solutions. These drones are at the

C. Di Natale et al. (Eds.): AISEM 2025, LNEE 1497, pp. 393–398, 2025.
https://doi.org/10.1007/978-3-032-08271-8_62

forefront of UAM operations, pioneering real-world applications that demonstrate the feasibility of on-demand aerial logistics [2, 3].

As UAM continues to evolve, overcoming technological, regulatory, and infrastructural challenges will be essential to fully integrating aerial transportation systems into urban settings. Ensuring safety, air traffic management, and public acceptance will be key to making urban aviation a mainstream transportation mode in the near future [4].

Real-time knowledge of an aircraft's position during a mission is crucial, particularly in Beyond Visual Line of Sight (BVLOS) operations or fully autonomous flights. As is well established, in outdoor operations, UAV positioning relies on onboard Global Navigation Satellite System (GNSS) receivers, which provide location coordinates in a geographical reference system. However, in many scenarios, the accuracy of GNSS positioning (typically ranging from 5 to 10 m or more) may be insufficient for precision navigation tasks [5]. This limitation becomes particularly critical in scenarios such as maneuvering through crowded areas, landing in challenging environments, or executing precision landings. The inaccuracies may arise from factors such as signal attenuation, multipath errors, or reflections of signals in urban canyons [6].

This work presents a data fusion algorithm designed to integrate GNSS and barometric sensor measurements to improve altitude estimation accuracy during UAV operations. By combining data from these two sources, the algorithm compensates for individual sensor limitations, such as GNSS altitude drift and barometric pressure variations due to weather changes.

The proposed approach leverages sensor fusion techniques, ensuring a more robust and reliable altitude estimation, which is crucial for UAV applications, including precision navigation, obstacle avoidance, and autonomous flight stability. The results demonstrate the potential of this method to enhance situational awareness and flight safety, particularly in challenging environments where accurate altitude data is essential.

1.1 Sensors Description

In this work, the primary objective of the data fusion module is to enhance altitude estimation accuracy, minimizing measurement errors that could pose risks during UAV navigation. By integrating data from GNSS and barometric sensors (Fig. 1), the system compensates for individual sensor inaccuracies, ensuring a more reliable altitude estimate.

This integration plays a crucial role in automatic navigation safety, particularly in scenarios where precise altitude data is essential, such as urban air mobility, obstacle avoidance, and autonomous landing operations. The proposed approach improves the UAV's ability to adapt to environmental conditions, reducing the likelihood of navigation errors and enhancing overall mission reliability.

The barometer operates by using pressure-sensitive elements, such as temperature, humidity, and air flow sensors, to measure atmospheric pressure. This measurement is then used to indirectly calculate the altitude of the carrier based on the relationship between atmospheric pressure and elevation.

The tests were conducted using a GNSS sensor (U-blox 8) and a barometric sensor (ST LPS22HB). These sensors were employed to gather data for evaluating the

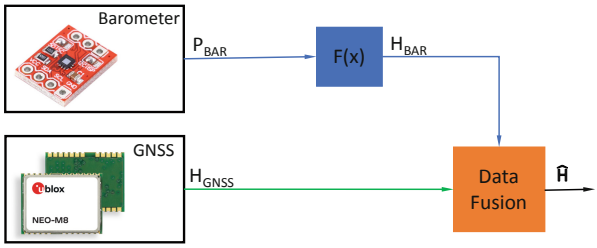

Fig. 1. Sensor fusion block diagram.

performance of the proposed altitude measurement approach, with the GNSS providing geolocation coordinates (WGS-84 system) and the barometer offering atmospheric pressure-based altitude readings.

1.2 Data Fusion Method

The sensor fusion technique plays a crucial role in system identification. By combining data from multiple sensors, such as the GNSS and barometer, the fusion approach enhances the accuracy and reliability of altitude measurements, particularly in scenarios where individual sensor readings may be affected by errors, such as noise, multipath, or external disturbances. The algorithms used for estimation and removal of systematic errors and noise is Gelb's method. Gelb's method is a computational algorithm that processes measurements to deduce a minimum-square estimation error of the state of a system, utilizing knowledge of system and measurement dynamics, assuming normal (Gaussian) statistics of system noise and measurement errors [7]:

$$z_{GNSS} = x + \upsilon_{GNSS} and z_{BAR} = x + \upsilon_{BAR} \tag{1}$$

It is possible to define an optimal x estimate, which is a linear function of the data collection:

$$\hat{x} = k_{BAR} z_{BAR} + k_{GNSS} z_{GNSS} \tag{2}$$

Defining the estimation error $\bar{x}$:

$$\bar{x} = \hat{x} - x \tag{3}$$

As criterion of optimality, the mean square value of $\bar{x}$ must be computed.

$$E[\bar{x}] = E[k_{BAR}(x + \upsilon_{BAR}) + k_{GNSS}(x + \upsilon_{GNSS}) - x] = 0 \tag{4}$$

where E is denoted the average. Letting $E[\upsilon_{BAR}] = E[\upsilon_{GNSS}] = 0$ and $E[x] = x$, since x is "nonrandom". Combining Eqs. (1) and (4), the mean square error will be:

$$E\left[\bar{x}^2\right] = k_{BAR}^2 \sigma_{BAR}^2 + (1 - k_{BAR})^2 \sigma_{GNSS}^2 \tag{5}$$

where σ^2_{BAR} and σ^2_{GNSS} denote the variance of υ_{BAR} and υ_{GNSS}, respectively. Differentiating this quantity with respect to k_{BAR} and setting the result to zero yields:

$$2k_{BAR}\sigma^2_{BAR} - 2(1 - k_{BAR})\sigma^2_{GNSS} = 0 \tag{6}$$

or

$$k_{BAR} = \frac{\sigma^2_{BAR}}{\sigma^2_{BAR} + \sigma^2_{GNSS}} \tag{7}$$

The corresponding minimum mean square estimation error is the following:

$$E\left[\bar{x}^2\right] = \left(\frac{1}{\sigma^2_{BAR}} + \frac{1}{\sigma^2_{GNSS}}\right) \tag{8}$$

Considering Eq. (2), the algorithm will be:

$$\hat{x} = \left(\frac{\sigma^2_{GNSS}}{\sigma^2_{GNSS} + \sigma^2_{BAR}}\right) z_{BAR} + \left(\frac{\sigma^2_{BAR}}{\sigma^2_{GNSS} + \sigma^2_{BAR}}\right) z_{GNSS} \tag{9}$$

where z_{GNSS} and z_{BAR} represent the measurements obtained from the GNSS and barometer sensors, respectively, and σ^2_{GNSS} and σ^2_{BAR} denote the variances associated with each measurement.

2 Simulations and Results

To validate the proposed data fusion technique, preliminary tests were conducted using a quadrotor UAV. During these trials, the device was mounted onboard the UAV, and data collection was performed throughout key mission phases, including take-off, hovering, and landing.

Data acquisition began when the UAV was positioned at the take-off site and continued until landing completion. Figure 2 illustrates the recorded GNSS and barometric data during the flight test, highlighting instances where the GNSS signal was lost (marked as a circle slip error). These interruptions demonstrate the critical need for data fusion methods to maintain continuous altitude estimation.

By integrating GNSS and barometric measurements, the data fusion approach ensures availability and continuity of altitude information, reducing measurement uncertainty and enhancing mission safety, especially in environments where GNSS signals may be unreliable or temporarily unavailable.

Figure 3 illustrates the altitude estimation obtained by integrating GNSS and barometric measurements, processed in a MATLAB environment during post-processing. The results demonstrate how the proposed data fusion approach effectively mitigates the effects of GNSS signal loss, ensuring a continuous and reliable altitude estimation throughout the entire UAV mission.

As observed in Fig. 3, the fusion of GNSS and barometric data significantly reduces the impact of GNSS unavailability, thereby improving the accuracy and robustness of altitude estimation. This enhancement is particularly valuable for autonomous UAV operations, where maintaining precise altitude information is crucial for safe navigation and obstacle avoidance.

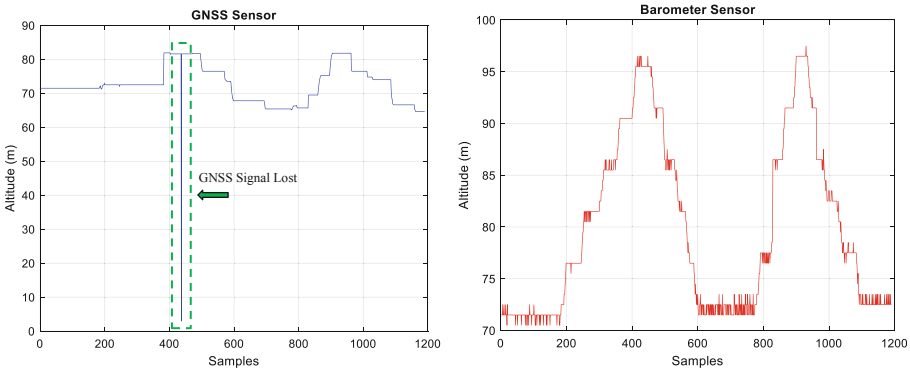

Fig. 2. GNSS and barometer measurements during flight test.

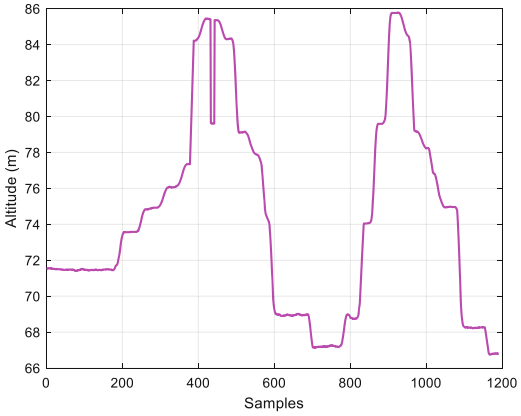

Fig. 3. Altitude estimation by data fusion method.

3 Conclusions

This study presents an altitude estimation method for UAVs, by using GNSS–barometer data fusion. Accurate flight altitude information is crucial for ensuring safe navigation, particularly during drone operations in urban environments. UAVs frequently operate in complex and confined areas where GNSS signals may be compromised due to signal loss and multipath effects. Consequently, integrating on-board sensors become essential to maintain reliable navigation. In this work, a low-computation data fusion technique was implemented to estimate flight altitude by combining data from GNSS and barometer sensors. The results demonstrate that the proposed integration method significantly improves performance compared to using the GNSS sensor alone, particularly in terms of stability and accuracy of the vertical component. Future work will focus on integrating an IMU (Inertial Measurement Unit) to enhance measurement redundancy and availability. Additionally, an Extended Kalman Filter (EKF) will be implemented as a data fusion technique to further improve altitude estimation accuracy. The EKF will enable more

robust filtering of sensor noise, reduce uncertainty, and provide a more consistent and reliable altitude measurement, even in challenging operational conditions.

References

1. Cohen AP, Shaheen SA, Farrar EM (2021) Urban air mobility: history, ecosystem, market potential, and challenges. IEEE Trans Intell Transp Syst 22(9):6074–6087. https://doi.org/10.1109/TITS.2021.3082767
2. Ariante G, Del Core G (2025) Unmanned aircraft systems (UASs): current state, emerging technologies, and future trends. Drones 9(1):59. https://doi.org/10.3390/drones9010059
3. Li X, Tupayachi J, Sharmin A, Martinez Ferguson M (2023) Drone-aided delivery methods, challenge, and the future: a methodological review. Drones https://doi.org/10.3390/drones7030191
4. Bauranov A, Rakas J (2021) Designing airspace for urban air mobility: a review of concepts and approaches. Progress Aerospace Sci https://doi.org/10.1016/j.paerosci.2021.100726
5. Ariante G, Papa U (2024) Embedded platforms for UAS landing path and obstacle detection II: navigation support systems for urban air mobility operations: Second Edition vol 530 https://doi.org/10.1007/978-3-031-59754-1
6. Yang Y, Khalife J, Morales JJ, Kassas ZM (2022) UAV waypoint opportunistic navigation in GNSS-denied environments. IEEE Trans Aerosp Electron Syst 58(1):663–678. https://doi.org/10.1109/TAES.2021.3103140
7. Papa U, Ariante G, Del Core G (2018) UAS aided landing and obstacle detection through LIDAR-Sonar data. In: 5th IEEE International Workshop on Metrology for AeroSpace, MetroAeroSpace 2018. Proceedings, Institute of Electrical and Electronics Engineers Inc., pp 478–483 https://doi.org/10.1109/MetroAeroSpace.2018.8453594

Integration of Machine Learning for Next Generation Gas Sensor Technology

Donatella Puglisi[1](✉), Ivan Shtepliuk[1], and Jens Eriksson[1,2]

[1] Department of Physics, Chemistry and Biology, Linköping University, 58183 Linköping, Sweden
donatella.puglisi@liu.se
[2] VOC Diagnostics, 58330 Linköping, Sweden

Abstract. Today's challenges and demands for advanced and economically viable gas sensor systems necessitate the development of innovative solutions that can achieve not merely incremental improvements of existing technology, but rather a true paradigm shift in the current state-of-the-art. Here, we demonstrate that the integration of chemical gas sensors with machine learning (ML) techniques has reached a level of maturity that can significantly accelerate innovation and broaden their application across a variety of real-world scenarios. We present three different case studies that illustrate the application of ML-enhanced electronic nose (e-nose) technology in the key areas of food quality control, forensic analytics, and early cancer diagnostics. We trained all available machine learning models in MATLAB's Classification Learner to select the best-performing model, and used custom MATLAB code for a more thorough analysis of the chosen model. Performance metrics such as validation and test accuracy, precision, sensitivity, and specificity were used to evaluate the effectiveness of the models for binary classification tasks. Our results demonstrate that the Optimizable Ensemble model, implemented using Gentle Adaptive Boosting, outperformed all other models across all performance metrics. In all cases, our classification model achieved remarkable performance between 95% and 98% accuracy, sensitivity, and specificity, demonstrating the potential of ML-enhanced e-nose technology as a versatile and reliable analytical tool.

Keywords: Electronic Nose · Machine Learning · Forensic Analytics · Food Quality Control · Cancer Diagnostics

1 Introduction

Since the development of the first metal oxide semiconductor (MOS) gas sensors by Taguchi in the early 1960s [1], extensive research efforts have focused on the development of novel sensing materials, innovative devices, and intelligent operation modes to enhance the performance of chemical gas sensors [2–4]. However, such technology, although largely investigated, continues to face persistent issues such as inadequate selectivity, signal drift, and cross-sensitivity to even small variations in humidity, temperature, and other environmental factors. These disadvantages ultimately lead to poor

C. Di Natale et al. (Eds.): AISEM 2025, LNEE 1497, pp. 399–403, 2025.
https://doi.org/10.1007/978-3-032-08271-8_63

accuracy and reliability of measurement readings, which hinder their applicability in many real-world scenarios. It is therefore necessary to explore new interdisciplinary approaches and research paths to achieve high technology readiness levels suitable for scalability and commercialization [5].

The integration of gas sensor technology with machine learning (ML) has been explored since the 1990s [6]. However, early studies often relied on classical ML models such as k-nearest neighbors (k-NN), support vector machine (SVM), and linear discriminant analysis (LDA), which, while useful, are limited in handling high-dimensional, nonlinear, or noisy sensor data, thus lacking the robustness needed to fully address the challenges of analyzing complex gas mixtures. Furthermore, limitations in available sensor technologies, materials, computing power and memory, and data quality have hindered the development of accurate, transferable models and their use in real-world and real-time applications. Since then, critical advancements in both hardware and software have made such integration much more viable [7]. Deep learning techniques, ensemble methods, and continual learning models today offer robust pattern recognition in complex and highly variable environments. Affordable, and high-performance processors combined with Internet of Things (IoT) ecosystems enable scalable and real-time collection and processing of big data, even on portable devices. Improved sensor fusion, including integration with temperature, humidity, proximity, and global positioning system (GPS) sensors, advances contextual understanding and compensates for variability. These developments enable faster, smarter, more reliable, and scalable ML-enhanced gas sensor systems, finally making them viable for practical applications and real-world use cases [8–10]. An example of such integrated systems is the electronic nose (e-nose), a device that mimics the human olfactory receptors to detect odors [11, 12]. Although the e-nose concept was introduced by Persaud and Dodd in the 1980s [13], only in recent years has the widespread availability of sophisticated ML techniques, supported by access to considerable computational power and the ability to perform complex analyses of large datasets, opened up unprecedented opportunities for the practical implementation of e-nose technology [14–16].

Here, we present three case studies in the relevant fields of food quality assessment, forensic investigations, and early cancer diagnostics, aiming to demonstrate the broad application potential of ML-enhanced e-nose technology in key sectors such as defense and security, healthcare, environment, and agriculture.

2 Material and Methods

Our instrument consists of 32 MOS chemiresistive gas sensors (TGS2X series, Figaro USA Inc.) distributed across four temperature-controlled banks [14–17]. The sample is placed in a custom designed aluminum holder that is inserted into the e-nose system at the start of each measurement. Following an initial equilibration phase where volatile organic compounds (VOCs) emitted from the sample diffuse into the instrument's headspace, a downstream ventilation system propels these gases across the sensor array. Data acquisition occurs at 10 Hz throughout 10 min measurement period (including 5 min of sensor exposure to VOCs and 5 min of recovery to the baseline), meaning that, for each measurement, we obtain 32 voltage-time signals, resulting in a dataset

with dimensions of 32 × 6000. Signal processing, feature extraction, and dataset formation were conducted within the MATLAB R2024a environment. We trained all available ML models in MATLAB's Classification Learner for best-performing model selection, while custom MATLAB code has been developed for more sophisticated analysis of the selected model. Performance metrics such as validation and test accuracy, precision, sensitivity, and specificity were used to assess the model's effectiveness in performing binary classification tasks. The results for all models were obtained using a consistent methodological approach, which involved the use of 60 or 85 features, based on the specific case study, and implementation of a 10-fold or 5-fold cross-validation (CV) scheme with a 90%−10% train-test split.

Samples used for our experiments consisted of fresh, urine-contaminated, and rotten pig meat (CASE I: food quality assessment), blood, putrefaction fluids, and muscle tissue from autopsies (CASE II: forensic analytics), and plasma blood samples from healthy and oncological patients (CASE III: early cancer diagnostics). Samples were prepared in aliquots of 1 ml or approximately 1.5 g, transported under standard conditions at Linköping University, Sweden, stored at −20 °C ± 1 °C, and thawed immediately prior to VOC measurements at ambient temperature (+21 °C ± 1 °C). All ethical aspects of handling biological materials from deceased humans and oncological patients have been carefully considered and appropriate Ethical Committee approval has been obtained from the Swedish Ethical Review Authority in accordance with ethical review legislation, Act (SFS 2003:460), Reg. Nos. 2025-01121-02, 2023-05783-01, 2023-01881-01, 2022-03015, 2019-02140. Written informed consent was obtained from all study participants in accordance with the Swedish legislation. No Ethical Committee approval was required for handling meat samples.

3 Results and Discussion

Our results demonstrate that the Optimizable Ensemble model, based on Gentle Adaptive Boosting, outperformed all other models across all performance metrics.

Specifically, in food quality assessment (CASE I, Fig. 1a), the model achieved remarkable performance with 96% sensitivity and 95% specificity in discriminating fresh from urine-contaminated meat samples. The model's robustness was further demonstrated in forensic applications (CASE II, Fig. 1b), where it achieved 98% accuracy in distinguishing *post-mortem* from *ante-mortem* samples, with near-perfect signal-level classification in test cases (313/313 *post-mortem* and 309/314 *ante-mortem* samples were correctly identified). In early cancer diagnostics, our approach of estimating sensor utility and removing data from less informative sensors, combined with majority voting, achieved 97% test accuracy and excellent specificity (CASE III, Fig. 1c).

These results underscore the exceptional capability of the proposed ML-enhanced e-nose technology across diverse applications, demonstrating its potential as a versatile and reliable analytical tool.

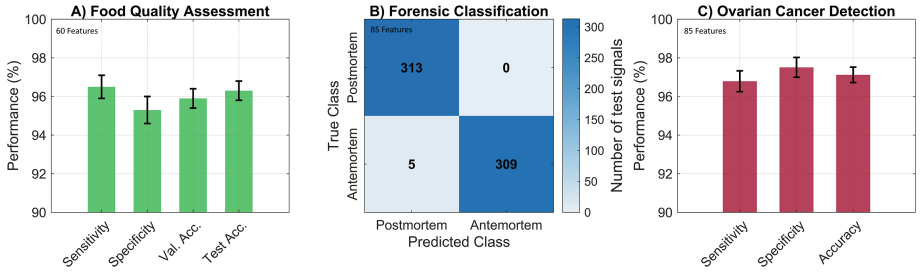

Fig. 1. Performance evaluation of the ML-enhanced e-nose technology across three critical applications: (a) Food quality assessment results showing high discrimination capability between fresh (50 samples) and urine-contaminated meat (50 samples), with validation and test accuracy exceeding 95%. Error bars represent 95% confidence intervals; (b) Forensic application test confusion matrix demonstrating exceptional classification performance between *post-mortem* and *ante-mortem* biological samples, achieving 98% test accuracy; (c) Cancer detection performance metrics showing 97% test accuracy and excellent specificity in discriminating between healthy individuals (103 samples) and ovarian cancer patients (102 samples).

4 Conclusions

We used a 32-element MOS-based electronic nose combined with machine learning to measure and analyze VOC emissions from human and animal samples in three relevant case studies. Our models demonstrate remarkable sensitivity, specificity, and accuracy in successfully solving different binary classification tasks, highlighting the enormous potential and versatility of this technology in real-world applications that do not require the identification of single target gases. Further research will include the analysis of larger and more diverse datasets as well as the development of more robust algorithms to assess model stability and reliability.

Acknowledgements. This work was supported by the Strategic Innovation Programs Swelife, grant No. 2023-03874, and Swelife and MedTech4Health, grant No. 2022-03464, a joint venture of Vinnova, Formas and the Energy Agency, the US National Science Foundation (NSF) Convergence Accelerator Program 2023, with funding from the Swedish Research Council, Vetenskapsrådet, grant No. 2023-07219, and Sweden's Innovation Agency, Vinnova, grant No. 2023-04186, the Swedish Food Agency, Dnr 2021/00918, the Swedish Police Authority, Dnr A170.261/2024, the Strategic Research Area in Forensic Sciences (SOFO), Dnr. IFM-2023-00208, the Faculty of Science and Engineering at Linköping University, Dnr LiU-2025-00019, and the EU's Horizon Europe research and innovation programme under GA No. 101214318 (DISARM). The computations and data handling were enabled by resources provided by the National Academic Infrastructure for Supercomputing in Sweden (NAISS), partially funded by the Swedish Research Council through grant agreement no. 2022-06725. The authors would like to thank all partners and collaborators of these research and innovation projects, as well as students and colleagues who contributed to sampling and measurements.

References

1. Figaro USA Inc. https://www.figarosensor.com/. Last accessed 23 May 2025

2. Jung H-T (2022) The present and future of gas sensors. ACS Sens 7:912–913
3. Saruhan B, Fomekong RL, Nahirniak S (2021) Review: influences of semiconductor metal oxide properties on gas sensing characteristics. Front Sens 2:657931
4. Domènech-Gil G, Puglisi D (2021) Benefits of virtual sensors for air quality monitoring in humid conditions. Sens Actuators B Chem 344:130294
5. Eriksson, J., et al.: Toward self-learning sensor devices for precision molecular identification, Chem, **11**, 102612 (2025)
6. Nakamoto T, Fukunishi K, Moriizumi T (1990) Identification capability of odor sensor using quartz-resonator array and neural-network pattern recognition. Sens Actuators, B Chem 1(1–6):473–476
7. Friedman J, Hastie T, Tibshirani R (2000) Additive logistic regression: a statistical view of boosting (With discussion on a rejoinder by the authors). Ann Stat 28(2):337–407
8. Smith K (2024) The most mysterious sense: cracking the odour code. Nature 633:26–29
9. Sung S-H, Suh JM, Hwang YJ, Jang HW, Park JG, Jun SC (2024) Data-centric artificial olfactory system based on the eigengraph. Nat Commun 15(1211):1–16
10. Chen M, Cui D, Haick H, Tang N (2024) Artificial Intelligence-based medical sensors for healthcare system. Adv Sens Res 3:2300009
11. Liu T et al (2023) Review on algorithm design in electronic noses: challenges, status, and trends. Intell Comput 2:0012
12. Karakaya D, Ulucan O, Turkan M (2020) Electronic nose and its applications: a Survey. Int J Autom Comput 17:179–209
13. Persuad D, Dodd G (1982) Analysis of discrimination mechanisms in the mammalian olfactory system using a model nose. Nature 299:352
14. Shtepliuk I et al (2025) Electronic nose and machine learning for modern meat inspection. J Big Data 12:96
15. Shtepliuk, I., et al.: Adaptive machine learning for electronic nose-based forensic VOC classification, Adv. Sci. 12, e04657 (2025)
16. Eriksson J, Puglisi D, Borgfeldt C (2024) Electronic nose for early diagnosis of ovarian cancer. Proceedings **97**:145
17. VOC Diagnostics AB. https://vocdiagnostics.com/. Last accessed 23 May 2025

Digital Twin Development for Hydrogen Transport Network with Machine Learning-Based Anomaly Detection

M. Villari[1], S. De Vito[2], E. Esposito[2(✉)], A. Senese[3], A. Longobardi[1], and G. Di Francia[2]

[1] Department of Engineering, University of Salerno, Via Giovanni Paolo II, 132, 84084 Fisciano, Italy

[2] Energy and Data Science Laboratory (TERIN-SSI-EDS), ENEA Research Centre of Portici, Piazzale Enrico Fermi, 1, 80055 Portici, Italy
elena.esposito@enea.it

[3] Department of Physics "Ettore Pancini", University of Naples Federico II, Via Cinthia 21, Building 6, 80126 Naples, Italy

Abstract. The transition toward a hydrogen-based energy system introduces significant challenges for infrastructure monitoring, particularly in transport networks. The hydrogen's properties, such as high flammability, diffusivity and its propensity to cause embrittlement of materials, need robust and continuous safety monitoring. Pipelines, compressors and storage systems are subject to operational risks such as pressure fluctuations, leaks and malfunctions, which can affect both safety and system efficiency.

Anomaly Detection (AD) is crucial for addressing these challenges, as it enables the early identification of irregularities and supports predictive maintenance strategies. Traditional rule-based systems often struggle with complex, multivariate patterns, making Machine Learning (ML) approaches increasingly attractive. When integrated into a Digital Twin (DT) framework, ML techniques can enhance the capability to detect subtle or emerging faults in real time.

This work presents the development of a MATLAB/Simulink-based Digital Twin of a hydrogen transport network operating with methane-hydrogen mixtures. The model includes pipelines, tanks, and compressors, with embedded pressure sensors generating time-series data. The anomalies, such as compressors malfunctions or local restrictions, are artificially injected to simulate fault scenarios. Two ML-based AD algorithms, One-Class SVM and Isolation Forest, are then evaluated for their ability to detect these anomalies. The aim is to validate a flexible, simulation-driven approach to improve the safety and resilience of hydrogen infrastructures.

Keywords: Anomaly Detection · Hydrogen Transport Networks · Digital Twin · Machine Learning

C. Di Natale et al. (Eds.): AISEM 2025, LNEE 1497, pp. 404–409, 2025.
https://doi.org/10.1007/978-3-032-08271-8_64

1 Introduction

The increasing global push toward decarbonization and sustainable energy systems has accelerated the development of hydrogen as a key energy vector. As a lightweight, energy-dense, and clean fuel, hydrogen plays a central role in sectors ranging from mobility to industrial processing and power storage. However, the infrastructure required for hydrogen production, storage, and especially transport, such as pipelines and compressor stations, poses significant challenges due to hydrogen's physical and chemical properties, including its high diffusivity, low ignition energy, and tendency to embrittle metals.

Digital Twin (DT) technology, defined as a virtual representation of a physical asset or system updated in real time with sensor data, is increasingly being adopted in industrial settings for operational optimization, diagnostics, and predictive maintenance. In the hydrogen sector, recent studies have explored the use of DTs to simulate electrolyzers, optimize hydrogen production and storage, and improve overall supply chain management. For example, Gerard et al. [1] developed a digital twin framework to support the smart design of green hydrogen production facilities, focusing on performance monitoring and optimization. Similarly, Ahmed et al. [2] proposed a DT-enabled predictive maintenance framework for hydrogen fuel cell systems, emphasizing early fault detection and degradation modeling.

Despite these advances, DT applications for hydrogen transport networks are still unexplored, particularly in the real-time anomaly detection (AD) framework. Transport systems, being characterised by dynamic conditions and complex dependencies between components, need continuous monitoring to detect potential malfunctions such as pressure fluctuations, leaks, valve failures and compressor inefficiencies. Traditional threshold or rule-based diagnostics systems are often unable to detect subtle or compound faults.

Machine Learning (ML)-based anomaly detection provides a promising approach, especially when dealing with high-dimensionality time series data from multiple sensors. Unsupervised and semi-supervised approaches, such as One-Class Support Vector Machines (OC-SVMs) [3], Isolation Forest [4] and Deep Learning-based models, such as LSTM autoencoders [5], have performed well in fault detection in several domains, including water networks, industrial plants and energy systems.

This research addresses this gap by integrating ML-based fault detection techniques into a MATLAB/Simulink-based digital twin of a hydrogen transport network. The proposed approach simulates dynamic gas transport using physical laws and system components (e.g., pipes, tanks, compressors) and generates multivariate time series data for training and testing of ML algorithms. The anomalies are injected into the simulation (e.g. local restrictions, compressor malfunctions) and then, they are evaluated using the selected ML models.

This work contributes to the literature by proposing a novel DT-ML integrated architecture tailored to hydrogen transport systems and showing the effectiveness of data-driven anomaly detection on simulated sensor data.

2 Methodology

This study presents the development of a digital twin for a gas transport network involving methane-hydrogen mixtures, modeled in MATLAB/Simulink. The aim is to simulate real-world network behavior and reproduce malfunctioning scenarios to generate data for ML-based anomaly detection and predictive maintenance.

The model is built based on a realistic pipeline segment of Italy's SNAM Rete Gas network, leveraging cartographic and public documentation data. Collaboration with SNAM [6] provided insight into operational constraints and regulatory frameworks governing pipeline design and sensor deployment.

The digital twin allows simulation of both normal and faulty conditions, focusing on time-series pressure data collected via virtual sensors. These data are critical to developing robust anomaly detection models capable of identifying pressure fluctuations, equipment faults, or structural anomalies.

2.1 Reference Pipeline and Geographical Context

A real pipeline segment has been isolated from national and regional infrastructure for simulation. The selected segment spans:

- 68.7 km on the national network (diameter: 1200 mm)
- 19 km on the regional network (variable diameter)

The route runs from Moliterno (a mixing node) to Contursi, passing through a recompression station in Montesano. Geographical data were extracted from official SNAM documents, which include operational pressure values such as:

- Operating pressure: 74 bar
- Minimum guaranteed pressure: 24 bar
- Inlet pressure: ~75 bar

The infrastructure is modeled as bidirectional, with pipelines used variably to match seasonal gas demands (5:1 ratio between winter and summer).

2.2 Digital Twin Construction

The digital twin of the methane-hydrogen transport network has been developed within the MATLAB/Simulink environment, using the Simscape libraries to accurately simulate the physical behavior of the system. The simulation has been configured to operate in the time domain, with a steady-state solver managing the underlying mathematical equations. This setup allowed for the realistic reproduction of pressure dynamics throughout the pipeline infrastructure.

The network itself was represented as a simplified but coherent system composed of 9 pipeline segments and 7 compression stations, reflecting the main elements of the real-world gas transport layout. Additional components such as valves were placed at key strategic points along the route to regulate flow and simulate control operations. To monitor the behavior of the gas under varying conditions, 5 virtual pressure sensors were

placed at significant points: upstream and downstream of the main compressors, as well as near the terminal section of the pipeline.

Each element within the model was defined by its physical and geometric characteristics, length, diameter, surface roughness, and other relevant parameters. The simulation of gas dynamics was based on the ideal gas law, which governs the relationships between pressure, temperature, and volume in a compressible fluid.

To capture transient behaviors such as gradual or abrupt changes in pressure, the model incorporated dynamic input signals using *PS Ramp* and *PS Step* blocks. These allow for fine control over pressure variations during the simulation, simulating realistic operational events or anomalies. Pressure outputs from the five sensors were collected in two formats: visualized in real time via the Scope block and recorded as structured time series data using the *To Workspace block*. This data, structured for efficient processing and interpretation, provides a robust foundation for training and validating machine learning models aimed at anomaly detection and predictive maintenance.

A mixture of 90% methane and 10% hydrogen was selected based on literature, which suggests this concentration minimizes material degradation (hydrogen embrittlement) and mechanical stress on pipelines. The main impact of this mixture is improved calorific value, with limited influence on pipeline dynamics, especially at low percentages.

The simulation encompasses this mixture by weight-averaging the physical properties of the two gases.

The output of the simulated system is shown in Fig. 1.

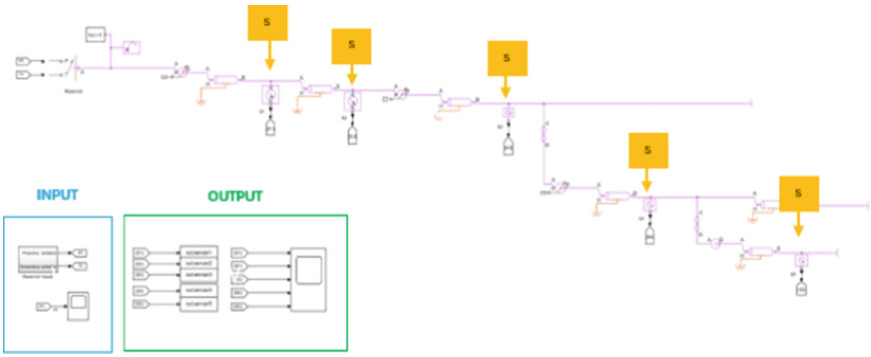

Fig. 1. Digital Simulink/Simscape model and pressure sensor positioning.

2.3 Normal Operation vs Anomalous Scenarios

The system has been simulated under steady-state conditions. The pressure remained within safe operational limits (24–75 bar), with a consistent profile across the sensors. This baseline is used to characterize "normal" system behavior. Based on the network properties, with the perfect gas equations formulations already implemented, the input of constant pressure regime at the reservoir and balancing the compressor stations, we obtain a possible trend of the pressure values over time measured by the 5 sensors under normal operating conditions (Fig. 2).

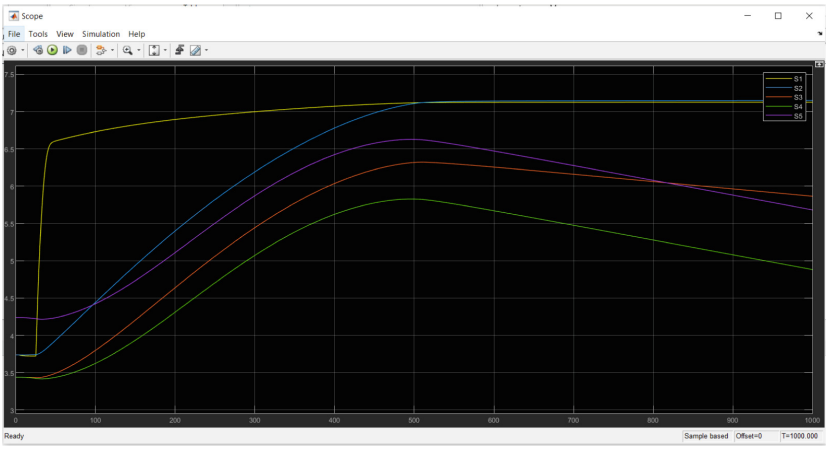

Fig. 2. Pressure values over time measured by the 5 sensors under normal operating conditions.

3 Anomaly Detection Framework

A first simulation scenario considers a malfunction in Compressor 1, which experiences a startup delay of 375 s and is only able to provide a pressure differential (Δp) of 3.5 Pa. This anomaly affects all sensors installed throughout the network.

A second scenario involves the introduction of a local restriction (a valve or an orifice), which models the pressure drop due to a localised reduction in flow area. This malfunction causes a significant disturbance specifically at Sensors 4 and 5.

Figure 3 shows overlaid time-series plots of pressure values recorded by the sensors, highlighting the temporal patterns and impacts of the two fault scenarios.

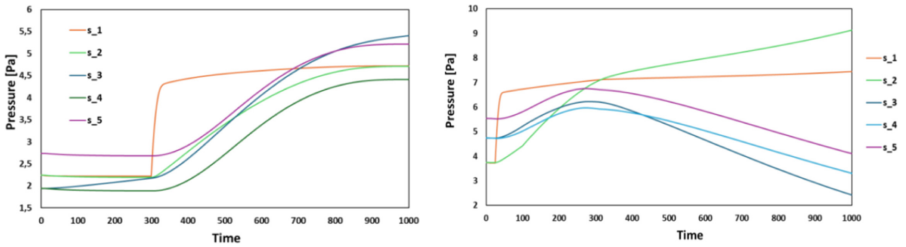

Fig. 3. Example of injected anomalies: compressor malfunction (left) and local restriction (right).

The obtained dataset simulates system behaviour through multivariate time series collected from the five pressure sensors. Two AD algorithms have been applied on the dataset: OC-SVM [3] and Isolation Forest [4], using a dataset split of 70% training, 10% validation and 20% testing. The hyper-parameters of both models have been optimised by a grid search procedure.

The preliminary results show that both models have been able to effectively distinguish between normal and anomalous states. The One-Class SVM demonstrated a

slightly higher sensitivity in detecting gradual pressure drops across all sensors, particularly in the compressor failure scenario. Nevertheless, Isolation Forest showed better performance in isolating localized anomalies, such as the abrupt pressure change at sensors 4 and 5 caused by the simulated restriction.

Overall, both algorithms proved effective, with Isolation Forest achieving an average ROC-AUC score of 0.88 and the OC-SVM scoring of 1.00. These results suggest that ML-based anomaly detection integrated within a simulation-driven Digital Twin framework offers a promising tool for early fault detection in hydrogen transport networks. However, model performance could further benefit from hyperparameter fine-tuning and from the inclusion of additional sensor types or features, such as temperature or flow rate data.

4 Conclusions

This work presented the development of a Digital Twin for a hydrogen transport network operating with a methane-hydrogen gas mixture. The system was used to simulate both normal and faulty operating conditions, generating realistic sensor data for machine learning-based anomaly detection.

The integration of One-Class SVM and Isolation Forest algorithms within this Digital Twin environment enabled the detection of both global and localized anomalies with high accuracy. The simulation-driven approach facilitates the testing and validation of anomaly detection methods under controlled conditions, offering a scalable solution for enhancing the operational safety and reliability of hydrogen infrastructures.

Future work will focus on expanding the model to incorporate more complex network topologies, real-world sensor data, and advanced deep learning techniques for anomaly detection. Additionally, deployment of the framework in edge computing environments will be explored to support real-time monitoring in operational settings.

References

1. Gerard B, Carrera E, Bernard O, Lun D (2022) Smart design of green hydrogen facilities: a digital twin-driven approach. E3S Web Conf **334**:02001 https://doi.org/10.1051/e3sconf/202233402001
2. Ahmed A, Choi S, Lee M (2021) Digital twin-driven predictive maintenance for hydrogen fuel cell systems. Int J Hydrogen Energy 46(13):9352–9361
3. Yang S, Kun K, Feamster N (2021) An efficient one-class SVM for anomaly detection in the internet of things. arXiv preprint arXiv:2101.00451
4. Liu FT, Ting KM, Zhou ZH (2008) Isolation forest. In: 2008 Eighth IEEE International Conference on Data Mining (pp 413–422). IEEE
5. Malhotra P, Vig L, Shroff G, Agarwal P (2016) Long Short-term memory networks for anomaly detection in time series. ESANN 2015 SNAM. https://www.snam.it/it/home.html. (Last accessed on 16 May 2025)

Hybrid-Quantum Machine Learning Approach for Anomaly Detection in Complex Industrial Systems

A. Senese[1], E. Esposito[2(✉)], S. De Vito[2], G. Acampora[1], and G. Di Francia[2]

[1] Department of Physics "Ettore Pancini", University of Naples Federico II, Via Cinthia 21, Building 6, 80126 Naples, Italy
[2] Energy and Data Science Laboratory (TERIN-SSI-EDS), ENEA Research Centre of Portici, Piazzale Enrico Fermi, 1, 80055 Portici, Italy
elena.esposito@enea.it

Abstract. Quantum computing is increasingly explored in artificial intelligence and anomaly detection due to its potential to model complex data structures using high-dimensional feature embeddings. One of the most promising directions in this field involves quantum kernel methods, which allow for the computation of similarities between data samples in the Hilbert space of a quantum system. These kernels can capture nonlinear relationships and hidden patterns that are often inaccessible to traditional classical techniques, making them particularly useful in scenarios where subtle correlations are critical. In this work, we propose a hybrid quantum-classical approach for anomaly detection in industrial control systems. The method combines classical autoencoder for dimensionality reduction with parameterized quantum circuits (PQCs), which are used to compute quantum kernel-based similarity measures. To optimize the structure of the quantum kernel, the Evolutionary Variational Quantum Algorithm (EVOVAQ) is employed, allowing task-specific tuning to maximize performance in terms of classification or detection metrics. The proposed approach is applied to two different datasets: a simulated Hydrogen Transport Network (HTN), which reflects physical sensor data in the gas transport framework and leakage monitoring, and the Secure Water Treatment (SWaT) scenario, which simulates the behavior of a cyber-physical water treatment system. Both datasets present real-world challenges such as noisy measurements, correlated sensor data, and complex temporal dynamics. By embedding data into quantum Hilbert spaces, our method aims to improve the sensitivity to anomalous patterns that may resemble normal operational fluctuations, offering a novel strategy for enhancing the robustness of anomaly detection in critical infrastructure systems.

Keywords: Anomaly Detection · Evolutionary Optimization · Quantum Kernels · Cyber-Physical Systems · Hydrogen Transport Networks

C. Di Natale et al. (Eds.): AISEM 2025, LNEE 1497, pp. 410–416, 2025.
https://doi.org/10.1007/978-3-032-08271-8_65

1 Introduction

The growing focus on energy transition has driven the exploration of alternative solutions for hydrogen distribution, which is increasingly recognized as a key energy vector to decarbonize sectors such as industry, transportation, and power generation. Among these solutions, repurposing existing natural gas infrastructure for hydrogen transport offers a practical opportunity, but also presents significant technical and safety challenges. Hydrogen's unique physical and chemical properties, including high diffusivity and its tendency to cause material embrittlement, make it more difficult to handle safely, especially in critical components such as joints, valves, and welds. To study these dynamics and the impact of potential faults, a simulated model of a Hydrogen Transport Network (HTN) has been developed using MATLAB/Simulink/Simscape (Fig. 1). The model emulates a physical system and generates multivariate sensor data, primarily pressure measurements, from strategically placed virtual sensors. Anomalies have been injected at selected locations to simulate leaks and other operational issues, enabling the evaluation of anomaly detection algorithms in a controlled yet realistic setting. In parallel, the Secure Water Treatment (SWaT) testbed presents a more complex cyber-physical scenario (Fig. 2) where cyberattacks can subtly alter sensor readings, mimicking natural fluctuations [1]. SWaT is a fully operational small-scale water treatment plant that provided a labeled dataset combining normal operations and various cyber and physical attacks, offering a rich environment for studying anomaly detection in industrial control systems. Both use cases share several challenges: high-dimensional and noisy data, strong inter-sensor correlations, and complex temporal dynamics. Traditional threshold-based or statistically rigid methods often struggle under such conditions. To address this, our work introduces a hybrid quantum-classical framework that leverages parameterized quantum circuits to compute optimized quantum kernels [2] via EVOVAQ [3]. These kernels map data into high-dimensional Hilbert spaces, making it easier to capture hidden correlations and improve the effectiveness of classical anomaly detection algorithms like One-Class SVM and Isolation Forest. This approach aims to enhance early detection capabilities for subtle or masked anomalies, improving robustness in critical infrastructure domains such as hydrogen networks and water treatment systems.

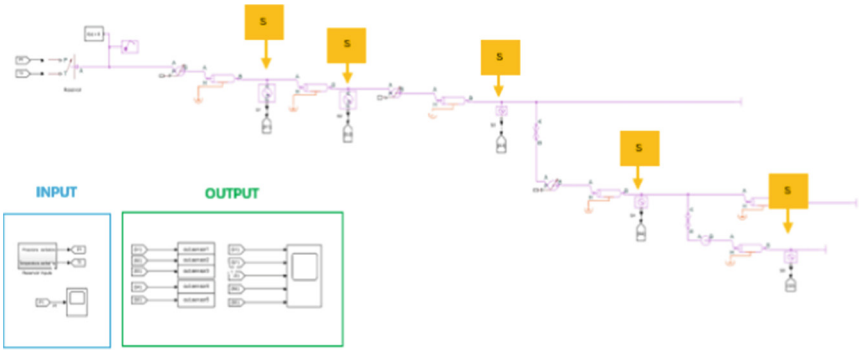

Fig. 1. Simulated hydrogen transport network in MATLAB/Simulink/Simscape equipped with 5 pressure sensors.

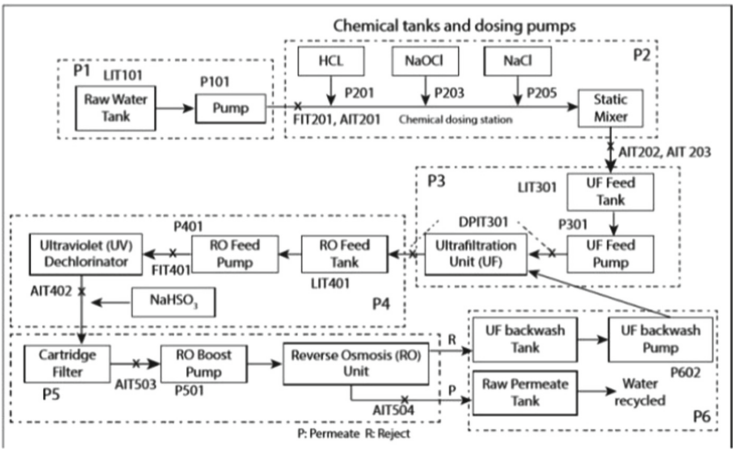

Fig. 2. The schematic layout of the SWaT testbed representing the physical structure of the water treatment plant.

2 Architecture

The proposed architecture is based on a hybrid quantum-classical approach designed for anomaly detection in complex industrial systems. The processing pipeline (Fig. 3) begins with data normalization using z-score transformation, which ensures comparability across features and reduces the impact of scale variability. The normalized data is then passed into a parameterized quantum circuit (PQC), which computes similarity measures between data samples through quantum kernel evaluations. Different quantum circuit architectures are explored, employing gates such as CX, Hadamard, and SWAP, to assess how circuit design affects kernel performance [4]. To optimize the kernel for the anomaly detection task, the Evolutionary Variational Quantum Algorithm (EVOVAQ) is employed. EVOVAQ uses evolutionary strategies to search for the most effective quantum kernel configuration, with performance measured in terms of the Area Under the Receiver Operating Characteristic Curve (AUC-ROC). Once the optimized quantum kernel is obtained, it is integrated into classical anomaly detection models, specifically One-Class Support Vector Machine [5] and Isolation Forest [6]. This integration allows the system to leverage the quantum kernel's ability to map data into high-dimensional Hilbert spaces, enhancing sensitivity to subtle or non-linear patterns that are often missed by traditional models. The architecture is modular and adaptable to different application domains, offering a balance between interpretability and performance.

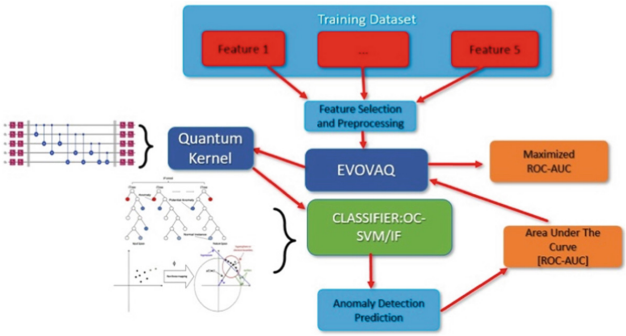

Fig. 3. Overview of the hybrid quantum-classical anomaly detection pipeline applied to industrial datasets.

2.1 Datasets Description

Two datasets were used to evaluate the proposed hybrid quantum-classical anomaly detection approach. The first dataset was generated through the simulated HTN model developed in MATLAB/Simulink/Simscape. This model replicates a simplified pipeline system equipped with five virtual pressure sensors placed at critical junctions. The simulation includes normal operating conditions as well as injected anomalies, such as artificial leaks, introduced at specific locations to evaluate the sensitivity of anomaly detection methods. The resulting dataset contains 10.700 time-series samples across five features, offering a controlled environment to study complex multivariate dynamics under varying physical states. The second dataset is derived from the SWaT testbed, a realistic industrial-scale cyber-physical system representing a fully operational water treatment plant. SWaT comprises six process stages and includes 51 sensors and actuators that continuously monitor and control the system. The dataset contains over 496.000 labeled data samples, collected over 11 days: the first 7 days under normal operation and the remaining 4 days under a series of simulated cyber and physical attacks. Each record includes timestamped sensor and actuator readings, along with corresponding labels indicating whether the system was in a normal or attack state.

For the classical methods, the HTN dataset was split into 70% training, 10% validation, and 20% test. In contrast, the hybrid quantum approach was trained on a subset of 500 samples. This limitation was imposed by the computational overhead associated with simulating quantum circuits on classical hardware, which is particularly demanding in terms of memory and processing time. Unfortunately, the available local computational resources were insufficient to handle larger datasets without encountering significant slowdowns or memory issues.

For the SWaT dataset, anomaly detection algorithms were trained directly on the transformed data using 70% training, 10% validation, and 20% test split. As with the HTN dataset, the hybrid quantum variant was trained on only 500 samples, again due to the computational constraints of quantum simulation on classical hardware.

For the classical methods, the HTN dataset was split into 70% training, 10% validation, and 20% test. In contrast, the hybrid quantum approach was trained on a subset of

500 samples. This limitation was imposed by the computational overhead associated with simulating quantum circuits on classical hardware, which is particularly demanding in terms of memory and processing time. Unfortunately, the available local computational resources were insufficient to handle larger datasets without encountering significant slowdowns or memory issues.

For the SWaT dataset, anomaly detection algorithms were trained directly on the transformed data using 70% training, 10% validation, and 20% test split. As with the HTN dataset, the hybrid quantum variant was trained on only 500 samples, again due to the computational constraints of quantum simulation on classical hardware.

The hyperparameters for the models were selected using GridSearchCV, a technique that performs an exhaustive search over a specified parameter grid. For each model, a set of candidate values for the key parameters was defined, and GridSearchCV was used to identify the optimal combination based on performance metrics. This approach ensures the selection of the best-performing model configuration while minimizing overfitting and enhancing generalization. The parameters tuned during this process include the kernel function, regularization parameters, and others specific to the anomaly detection algorithms.

3 Experimental Results

In this section, we present the experimental evaluation of classical and hybrid quantum-classical models for anomaly detection on two industrial datasets: SWaT and HTN. The hybrid quantum-classical approach integrates a parametrized Two-Local quantum circuit within an autoencoder framework for dimensionality reduction, followed by a classical anomaly detector (Isolation Forest or One-Class SVM). The quantum circuits were executed on 4 qubits for SWaT and 5 qubits for HTN, with parameters optimized via EVOVAQ, an evolutionary algorithm specifically designed for quantum circuit parameter tuning.

In the SWaT dataset experiments, several quantum circuit configurations were tested by varying the entanglement topology (circular or full), gate types (CX, Hadamard, SWAP), and circuit depth (number of repetitions). Among these, the configuration employing full entanglement with CX gates and two repetitions yielded the highest performance, achieving an AUC of 0.73. Increasing the circuit depth or introducing Hadamard gates led to a noticeable decline in performance, likely due to increased quantum noise. Configurations using only SWAP gates produced results comparable to simpler setups, underscoring the importance of careful gate selection and circuit architecture design in hybrid quantum anomaly detection models.

Experiments performed on the HTN dataset revealed a significant performance improvement when using hybrid quantum-classical models, particularly the Quantum One-Class SVM (QOC-SVM), which consistently achieved a perfect AUC of 1.0 across all tested configurations. The Quantum Isolation Forest (QIF), on the other hand, demonstrated more variable results and in some configurations, such as full CX entanglement performed worse than its classical counterpart. Notably, the combination of RX, RY, RZ rotation gates with full SWAP entanglement enabled both QOC-SVM and QIF to reach perfect AUC scores, highlighting the ability of quantum feature spaces to effectively

model complex inter-sensor correlations. A summary comparison of the AUC-ROC scores across classical and quantum-inspired models on both datasets is shown in Fig. 4.

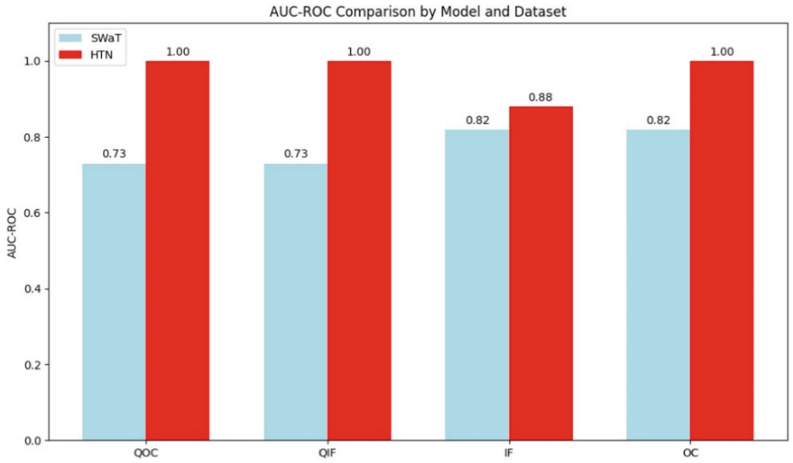

Fig. 4. Comparison of AUC-ROC scores across classical and quantum-inspired models on SWAT and HTN datasets.

4 Conclusion

This work presents a hybrid quantum-classical framework for anomaly detection in industrial control systems, combining classical algorithms, and quantum kernel-based methods. Through experiments on both a simulated hydrogen transport network and the real-world SWaT testbed, the proposed approach was evaluated in terms of its ability to capture latent dependencies and identify anomalous behavior. While quantum-enhanced models do not universally outperform their classical counterparts, the results highlight their potential in scenarios characterized by strong inter-feature correlations and non-linear patterns. The findings suggest that, with careful circuit design and parameter optimization, quantum kernels can be effectively integrated into anomaly detection pipelines, paving the way for future applications in complex industrial settings.

References

1. Goh J, Adepu S, Junejo KN, Mathur A (2016) A dataset to support research in the design of secure water treatment systems. *iTrust, Center for Research in Cyber Security, Singapore University of Technology and Design*, Singapore
2. M.Incudini M, Martini F, Pierro AD (2024) Toward useful quantum kernels. Adv Quantum Technol 2300298
3. Acampora Gutiérrez G, et al (2024) EVOVAQ: evolutionary algorithms-based toolbox for variational quantum. SoftwareX **26**(101756):0–8
4. Ivan D (2012) Chapter 2-Quantum mechanics fundamentals. Ivan D (ed.) Quantum Information Processing and Quantum Error Correction, Academic Press, pp 29–89

5. Yang S, Kun K, Feamster N (2021) An efficient one-class svm for anomaly detection in the internet of things. ArXiv e-prints
6. Al Fariz WS (2021) Isolation forest based anomaly detection: a systematic literature review. In: *2021 8th International Conference on Information Technology, Computer and Electrical Engineering (ICITACEE)* pp 118–122
7. Berahmand K, Daneshfar F, Salehi ES, Li Y, Xu Y (2024) Autoencoders and their applications in machine learning: a survey. Artif Intell Rev 57(2):28

Author Index

C. Di Natale et al. (Eds.): AISEM 2025, LNEE 1497, pp. 417–420, 2025.
https://doi.org/10.1007/978-3-032-08271-8